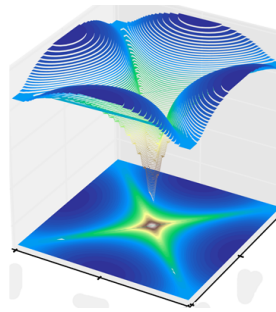




Thèse présentée pour obtenir le grade de
DOCTEUR DE L'ÉCOLE POLYTECHNIQUE

Nonlocal Coulomb Interactions and Electronic Correlations: Novel Many-Body Approaches

THOMAS AYRAL



Soutenue publiquement le 28 septembre 2015 à l'École Polytechnique
devant le jury composé de

| | | |
|-------------------|--|-----------------------|
| Massimo Capone | SISSA, Trieste (Italie) | (Rapporteur) |
| Andrew J. Millis | Columbia University, New York (Etats-Unis) | (Rapporteur) |
| Silke Biermann | Ecole Polytechnique, Palaiseau (France) | (Directrice de thèse) |
| Olivier Parcollet | Institut de Physique Théorique, Saclay (France) | (Directeur de thèse) |
| Benoît Douçot | Université Pierre et Marie Curie, Paris (France) | (Président) |
| Antonio Tejeda | Université Paris-Sud, Paris (France) | (Examinateur) |
| Simone Fratini | Institut Néel, Grenoble (France) | (Examinateur) |

Abstract

In strongly correlated materials, quantum fluctuations taking place at the level of atomic sites play a central role. These *local* processes are captured nonperturbatively in dynamical mean field theory (DMFT). *Nonlocal* mechanisms, however, are also suspected to be essential for the proper description of some of these materials, including the well-known high-temperature cuprate superconductors and the more exotic systems of atoms adsorbed on semiconducting surfaces.

In this thesis, the effect of nonlocal, potentially long-range fluctuations beyond the DMFT framework is investigated from two angles.

First, long-ranged interactions in adatom systems, computed from first principles within the constrained random-phase approximation (cRPA), are treated within the extended DMFT (EDMFT) framework and its combination with the diagrammatic *GW* method (*GW*+EDMFT). They are shown to explain some material trends observed in these compounds. In addition, thanks to the spatial and temporal information delivered by *GW*+EDMFT, they solve existing puzzles raised by different experimental conclusions drawn from different probes.

Second, a new approach to the Hubbard model including nonlocal correlation effects is proposed. Formally based on the local expansion of the triply-irreducible functional, this approach, dubbed TRILEX, approximates the renormalized three-leg electron-boson vertex by a local but frequency-dependent vertex computed from an impurity model with retarded density-density and spin-spin interactions. This local vertex is used to construct frequency- and momentum-dependent self-energies capturing nonlocal correlation effects. By construction, this method reconciles two theoretical pictures of cuprate superconductors, namely the spin fluctuation theory at weak interaction strengths and the doped-Mott-insulator picture at strong coupling.

This novel approach is applied to the single-band Hubbard model. It is shown to reduce to DMFT at strong coupling and high temperatures, and to fluctuation-exchange theories at weak coupling, while substantial deviations from both limits are observed at intermediate coupling. There, upon doping, antiferromagnetic spin fluctuations are observed to lead to a momentum-differentiated spectral intensity on the Fermi surface, which is reminiscent of the formation of Fermi arcs in photoemission measurements on cuprate superconductors.

These two methodological developments are intrinsically linked to algorithmic aspects which are reviewed in the last part of this work. In particular, an open-source library dedicated to massively parallel computations in the field of quantum many-body physics, TRIQS, is presented, with a focus on error estimation through the binning and jackknife methods. The hybridization-expansion continuous-time quantum Monte-Carlo algorithm in the segment picture – central to the TRILEX method – and its state-of-the-art implementation are explained. Finally, as a further illustration, a new lightweight method relying on this algorithm and designed for realistic systems, the combined screened-exchange and dynamical DMFT method (SEx+DDMFT), is presented together with an application to the BaCo_2As_2 compound.

Résumé

Dans les matériaux à fortes corrélations électroniques, un rôle central est joué par les fluctuations quantiques à l'échelle de l'atome. Ces processus *locaux* sont pris en compte de façon non perturbative dans la théorie du champ moyen dynamique (DMFT). Cependant, les mécanismes *non locaux* sont supposés être essentiels pour décrire de façon adéquate certains de ces matériaux, dont font partie les fameux supraconducteurs à haute température critique mais aussi les moins connus systèmes d'atomes adsorbés sur surfaces semiconductrices. Dans cette thèse, j'étudie l'effet des fluctuations non locales – éventuellement à longue portée – au-delà de DMFT sous deux angles.

Pour commencer, je montre que dans les systèmes d'ad-atomes, les interactions à longue portée, calculées à partir des premiers principes dans le cadre de la “constrained random phase approximation” (cRPA), et traitées par la méthode de DMFT étendue (EDMFT) et sa combinaison avec la méthode *GW* (*GW*+EDMFT), permettent d'établir une classification de certains systèmes d'ad-atomes, et aussi de résoudre, grâce aux informations tant spatiales que temporelles fournies par *GW*+EDMFT, des questions soulevées par des conclusions expérimentales divergentes selon les techniques expérimentales utilisées pour caractériser ces matériaux.

Ensuite, je propose une nouvelle approche pour traiter le modèle de Hubbard incluant des effets de corrélations non locales. Se fondant formellement sur l'expansion locale de la fonctionnelle triplement irréductible, cette approche, baptisée TRILEX, approxime le vertex d'interaction électron-boson renormalisé par un vertex local, mais fonction de la fréquence, calculé à partir d'un modèle d'impureté avec des interactions retardées entre charges et entre spins. Ce vertex local est utilisé pour calculer des self-énergies et polarisations fonctions de la fréquence et de l'impulsion, et pouvant donc rendre compte d'effets de corrélations non locales. Par construction, cette méthode réconcilie deux visions théoriques des supraconducteurs à haute température critique, à savoir la théorie de la fluctuation de spin en régime d'interactions faibles, et l'image de l'isolant de Mott dopé en régime d'interactions fortes.

Cette nouvelle approche est appliquée au modèle de Hubbard à une bande. Je montre qu'elle se ramène à DMFT à fort couplage et à haute température, et aux théories dites d'échange de fluctuations à bas couplage, tandis que des déviations substantielles vis-à-vis de ces deux limites sont observées à couplage intermédiaire. Dans ce régime de paramètres, sous dopage, les fluctuations antiferromagnétiques ont pour conséquence une différenciation de l'intensité spectrale sur la surface de Fermi dans l'espace des impulsions. Ceci n'est pas sans rappeler la formation d'arcs de Fermi dans les mesures de photoémission sur les matériaux cuprates supraconducteurs.

Ces deux développements méthodologiques sont intrinsèquement liés à des aspects algorithmiques qui font l'objet de la dernière partie de ce travail. En particulier, j'y présente une librairie “open-source” dédiée au calcul massivement parallèle dans le domaine du problème à *N* corps quantique, avec une illustration sur l'estimation d'erreurs par la méthode du “jackknife”. J'y décris également l'algorithme de Monte-Carlo quantique en temps continu avec expansion de l'hybridation dans le cas spécial d'une représentation par “segments”, indispensable à la méthode TRILEX, ainsi que son implémentation dans l'état de l'art. Enfin, à titre d'illustration, une nouvelle méthode pour décrire les systèmes réalistes et également basée sur cet algorithme, la méthode “SEx+DDMFT” (combined screened-exchanged and dynamical DMFT), est exposée ainsi que son application au composé BaCo_2As_2 .

Contents

| | |
|--|-----------|
| Abstract | 2 |
| Contents | 4 |
| I Context | 9 |
| 1 Introduction | 10 |
| 1.1 Challenges | 10 |
| 1.2 Approach | 11 |
| 1.3 Contributions | 12 |
| 1.4 Structure of this work | 12 |
| 2 Dynamical Mean-Field Theory: a local approach to Mott physics | 14 |
| 2.1 Mott insulators: a Coulombic thorn in Fermi liquid theory's side | 15 |
| 2.2 Dynamical Mean Field Theory: local physics to capture "Mottness" | 19 |
| 2.3 Summary: successes and limitations of DMFT | 24 |
| II Long-range interactions in surface systems: insights from combined <i>GW</i> and Extended Dynamical Mean Field Theory | 26 |
| 3 Adatoms on semiconducting surfaces: experiments and theoretical puzzles | 27 |
| 3.1 Surface systems: the basics of α -phases | 27 |
| 3.2 Experiments on surfaces: a variety of puzzling phases | 29 |
| 3.3 Early theoretical attempts and open puzzles | 31 |
| 4 <i>Ab initio</i> effective kinetic and interaction parameters for α-phases | 34 |
| 4.1 How to describe materials in a realistic way? | 34 |
| 4.2 <i>Ab initio</i> kinetic parameters from density-functional theory | 35 |
| 4.3 Constrained RPA (cRPA): Application to surfaces | 36 |
| 4.4 Conclusion: an extended Hubbard model with long-range interactions | 38 |
| 5 Nonlocal interactions: Extended Dynamical Mean Field Theory and combined <i>GW</i> and Extended Dynamical Mean Field Theory | 40 |
| 5.1 Extended Dynamical Mean Field Theory (EDMFT) | 40 |
| 5.2 Combined <i>GW</i> and Extended DMFT: <i>GW</i> +EDMFT | 42 |
| 5.3 Application to the extended Hubbard model on square lattice | 44 |
| 5.4 Conclusions | 53 |

| | | |
|------------|---|------------|
| 6 | Local and long-range interactions in surface systems: insights from combined GW and Extended Dynamical Mean Field Theory | 54 |
| 6.1 | Incorporating long-ranged interactions in $GW+EDMFT$ | 54 |
| 6.2 | A materials trend: from Mott physics to charge-ordering... | 56 |
| 6.3 | Experimental timescales: a solution to the Sn/Si puzzle | 59 |
| III | Nonlocal correlations in cuprates: unifying spin fluctuation and Mott physics with TRILEX | 65 |
| 7 | Introduction to high-temperature superconductors | 66 |
| 7.1 | Experiments: strong correlations and nonlocal effects | 66 |
| 7.2 | Theory: two viewpoints on high-temperature superconductivity | 74 |
| 8 | A local approximation to the three-leg vertex, TRILEX | 85 |
| 8.1 | Motivations | 85 |
| 8.2 | An intuitive picture | 87 |
| 8.3 | Functional derivation | 88 |
| 8.4 | Algorithmic scheme | 99 |
| 8.5 | Around the three-leg vertex | 102 |
| 8.6 | Discussion: relation to other methods | 103 |
| 9 | Application to the single-band Hubbard model | 105 |
| 9.1 | An interpolation between fluctuation-exchange theories and DMFT | 105 |
| 9.2 | A first-order Mott transition | 108 |
| 9.3 | Fermi arcs upon doping | 110 |
| 9.4 | The question of antiferromagnetic ordering | 110 |
| 9.5 | Influence of the decoupling choice | 111 |
| 9.6 | Conclusions and perspectives | 114 |
| IV | Modern computational methods for the quantum many-body problem | 115 |
| 10 | TRIQS: flexible yet fast codes for the quantum many-body problem | 116 |
| 10.1 | Structure of the TRIQS library | 116 |
| 10.2 | Three illustratory examples of usage of the TRIQS library | 117 |
| 10.3 | Error analysis: Binning and Jackknife | 120 |
| 11 | Continuous-time quantum Monte Carlo solver in the hybridization expansion with dynamical spin spin interactions | 128 |
| 11.1 | Hybridization and \mathcal{J}_\perp expansion: derivation | 129 |
| 11.2 | Implementation notes | 140 |
| 12 | Dynamical screening in solids: Combined Screened Exchange and dynamical DMFT | 149 |
| 12.1 | Density functional theory combined to DMFT: LDA+DMFT in a nutshell | 149 |
| 12.2 | Beyond LDA+DMFT combined with cRPA: $GW+DMFT$ and $SEx+DDMFT$ | 150 |

| | | |
|-------------|---|------------|
| V | Conclusions and perspectives | 155 |
| | Acknowledgments | 156 |
| VI | Appendix: conventions | 157 |
| A | Notations | 158 |
| A.1 | Time and frequencies | 158 |
| A.2 | Space and momentum | 158 |
| A.3 | Operators | 158 |
| A.4 | Indices | 159 |
| A.5 | Pauli matrices | 159 |
| B | Fourier conventions | 160 |
| B.1 | Fourier transforms in the imaginary time-frequency domain | 160 |
| B.2 | Fourier transform in the space-momentum domain | 161 |
| VII | Appendix: technical developments for TRILEX | 162 |
| C | Bosonic and fermionic correlation functions: relations | 163 |
| D | Three-point correlation function: various properties | 165 |
| D.1 | Time-translation symmetries and Fourier properties | 165 |
| D.2 | Symmetries in the $(i\omega, i\Omega)$ plane | 168 |
| D.3 | Partial sum on Matsubara frequencies | 169 |
| D.4 | High-frequency expansion of the three-point correlation function | 170 |
| D.5 | Equations of motion for the three-point function, and Ward identity | 171 |
| E | Atomic limit | 175 |
| E.1 | Simple observables: Z , $\langle n_\sigma \rangle$, $\chi(i\Omega)$, $G(i\omega)$, $\Sigma(i\omega)$ | 175 |
| E.2 | Three-point correlation function $\tilde{\chi}(i\omega, i\Omega)$ | 176 |
| E.3 | Three-leg vertex $\Lambda(i\omega, i\Omega)$ | 180 |
| F | Equations of motion | 181 |
| F.1 | Prerequisite: Schwinger-Dyson equations | 181 |
| F.2 | Equations of motion for G and W | 182 |
| F.3 | General formulae for the self-energy and polarization | 182 |
| G | A selection of many-body methods seen from a “parquet” perspective | 185 |
| G.1 | Prerequisite: four-leg observables and parquet equations | 185 |
| G.2 | The fluctuation-exchange (FLEX) approximation | 187 |
| G.3 | The two-particle self-consistent theory (TPSC) | 188 |
| G.4 | The dynamical vertex approximation: an example of strong-coupling approach with long-range correlations | 190 |
| VIII | Appendix: general background | 194 |
| H | Experimental probes for condensed matter physics: a brief theoretical overview | 195 |

| | | |
|---------------------|--|------------|
| H.1 | Surface probes: electron diffraction, electron energy loss spectroscopy, photoemission | 195 |
| H.2 | Bulk probes: neutron scattering, nuclear magnetic resonance, optics | 203 |
| I | Reminder on many-body theory | 211 |
| I.1 | Correlation functions: general properties | 211 |
| I.2 | Time-dependent perturbation theory: the Golden Rule | 217 |
| I.3 | Analytical continuation techniques | 220 |
| I.4 | Around the Lindhard function and the random-phase approximation | 222 |
| I.5 | GW self-energy on the real axis | 224 |
| I.6 | Weak-coupling charge and spin density wave scenarios | 226 |
| J | Reminder: realistic calculations for correlated materials | 234 |
| J.1 | Density functional theory | 234 |
| J.2 | Density functional theory combined to many-body techniques: LDA+DMFT | 238 |
| J.3 | The constrained random-phase approximation (cRPA) | 240 |
| IX | Appendix: details of some derivations | 244 |
| K | Appendix to chapter 6 | 245 |
| L | Appendix to chapter 8 | 247 |
| L.1 | Non-interacting free energy | 247 |
| L.2 | Simplifications in the homogeneous phase | 248 |
| L.3 | Spin rotation invariance: properties | 248 |
| M | Appendix to chapter 11 | 249 |
| M.1 | Dynamical trace factor in CTQMC | 249 |
| M.2 | Hamiltonian formulation the impurity model | 250 |
| M.3 | Computation of $K(\tau)$ from $U(iv)$ | 251 |
| M.4 | A code example: the insert move | 252 |
| N | Appendix to chapter 10 | 254 |
| N.1 | Simple-minded estimates for $f(\langle X \rangle)$ | 254 |
| N.2 | Relationship between the error estimate and the intrinsic variance | 255 |
| N.3 | Relationship between empirical and intrinsic variance | 256 |
| N.4 | Details for paragraph 10.3.4.1.2 | 257 |
| N.5 | Autocorrelation time estimation from the autocorrelation function | 258 |
| Index | | 260 |
| Bibliography | | 262 |
| X | Publications | 277 |
| O | EDMDT and GW+EDMFT applied to the extended Hubbard model on the square and cubic lattices | 278 |
| O.1 | Paper 1: Ayrál <i>et al.</i> (2012) | 278 |
| O.2 | Paper 2: Ayrál <i>et al.</i> (2013) | 284 |
| O.3 | Paper 3: Huang <i>et al.</i> (2014) | 306 |

| | | |
|----------|---|------------|
| P | Adatoms on semiconducting surfaces | 326 |
| P.1 | Paper 4: Hansmann <i>et al.</i> (2013a) | 326 |
| P.2 | Preprint 1:Hansmann <i>et al.</i> (2015) | 332 |
| Q | TRILEX: formalism and first implementation | 342 |
| Q.1 | Paper 5: Ayrat and Parcollet (2015) | 342 |
| R | Computational developments | 349 |
| R.1 | Paper 6: Parcollet <i>et al.</i> (2015) | 349 |
| R.2 | Paper 7: van Roekeghem <i>et al.</i> (2014) | 368 |

Part I

Context

Introduction

1.1 Challenges

In a world where larger and larger swaths of the economy are said to have become “dematerialized”, materials have never mattered so much.

The very computers and “smart” phones that convey the flow of this digital economy need to be constantly improved; their electronic components need to be further miniaturized and more energy-efficient; their screens more highly-resolved and soon flexible or even pliable; their batteries lighter while able to store more energy. More and more “smart” objects need “smart” materials whose properties can be controlled by an electronic device.

Materials design – the creation of materials with given specifications – is a challenging task. From the large palette of chemical elements, finding the combination leading to a specific electronic property is an incremental procedure: it first requires the precise understanding of existing materials, that is, the ability to relate a given set of macroscopic electronic properties to the internal microscopic structure of the material and to external parameters such as temperature, pressure or exposition to light. This implies the description of the material by a “model” supposed to capture the properties at stake. Only with this understanding can one then predict what properties a prospective new material, with a new chemical composition or microscopic structure, will have.

The task of relating the microscopic structure to the macroscopic electronic properties is perhaps nowhere so arduous as in strongly correlated materials. Conversely, perhaps no other materials display so many transitions between exotic phases upon sometimes minute changes in the external parameters, an appealing feature for potential applications. In these materials, the interactions between the electrons of partially filled shells induce peculiar behaviors and collective phenomena giving rise to macroscopic effects such as high-temperature superconductivity or metal-insulator transitions. These interactions, however, hamper simple approaches describing electrons as independent particles or on the contrary as tightly bound to their atom. What makes strongly-correlated materials interesting – the fact that they are always “on the verge” – is also what calls for sophisticated theoretical approaches.

The main complexity of strongly-correlated materials originates from the intricate interplay of several degrees of freedom: high-energy and low-energy, local and nonlocal, short and long-ranged, charge and spin. This makes both the task of constructing a minimal model adequate for a given phenomenon, and the task of understanding the mechanisms described by this model, a tall order.

Headway in the latter direction has been made in the last two decades thanks to the advent of dynamical mean field theory (DMFT, *Georges et al. (1996)*). This approach to the strong correlations problem gives prominence to the local degrees of freedom as the main ingredients to account for the transition between

a “normal” (quasi-non-interacting) metal and a “Mott” insulator, where electronic motion is jammed by electronic interactions. This locality assumption is embodied by a local “impurity” problem describing one or a few atoms embedded in a non-interacting environment, which DMFT uses as an effective description of the solid.

DMFT has since been extended in several respects. One direction is its application to systems with long-range interactions, as opposed to the local interactions which it has originally been developed for. Another is the inclusion of nonlocal degrees of freedom beyond the size of the impurity problem, motivated by the experimental observation of extended spin correlations in high-temperature cuprate superconductors.

Systems of adatoms adsorbed on semiconducting surfaces are an original example of competing phenomena triggered by strong correlations in low dimensions. Depending on the nature of the adatom and of the substrate, as well as on the temperature, the surface system can be metallic or insulating, ordered or disordered. Even more intriguing, different experimental probes “see” different phases. While previous theoretical studies have focused on weak-coupling scenarios or mostly restricted attention to local physics, a first-principles determination of the relevant low-energy model, including the range of its interactions, and dedicated theoretical treatment thereof, are still lacking.

High-temperature cuprate superconductors pose a different challenge: while most researchers in the field agree that interactions in cuprates are mostly of local character, and that spin fluctuations play an important role in the superconducting mechanism, a unified method taking into account both strong short-range correlations and long-range fluctuations in an unbiased way has so far been out of reach. The recently discovered iron-based superconductors, pose different but no less difficult challenges: there, the combination of spin density wave fluctuations with moderate correlations has to be handled in a *multi-band context*. Methods are thus needed that are lightweight enough to be extended to such multiorbital situations.

1.2 Approach

In this work, the problem of strong correlations in solids will be approached from a dynamical mean field perspective, that is, with a focus on the nonperturbative treatment of local correlations. This ensures that Mott physics, in the relevant interaction regime, will be properly taken into account. The general purpose of this work is to further take into account contributions from nonlocal degrees of freedom.

These contributions may come directly from *nonlocal interactions* between electrons – which will be shown to be relevant to surface adatoms – or from *nonlocal fluctuations induced by local correlations*, as will be seen in the case of cuprate superconductors. In either case, instead of resorting to the complex machinery of parquet equations or approximations thereof such as ladder resummations, the nonlocal degrees of freedom will be represented as bosonic fields corresponding to physical two-particle fluctuations directly accessible to experiments.

The coupled system of the bosonic modes and the fermionic degrees of freedom will then be studied either through an extension of the DMFT lens, extended DMFT (EDMFT, Sengupta and Georges (1995); Kajueter (1996); Si and Smith (1996)), or through an extension of EDMFT to nonlocal self-energies and polarizations, *GW+EDMFT* (Biermann *et al.* (2003); Sun and Kotliar (2004)). In the former method, nonlocal interactions merely translate into retarded interactions in the DMFT impurity model. In the latter, they additionally lead to momentum-dependent self-energy and polarization effects which can be studied in connection with *e.g.* charge-ordering phenomena in systems of adatoms on surfaces.

The electron-boson system will also be studied from a brand new perspective. Instead of making a locality assumption on the self-energy, as DMFT does, an approach will be developed that consists in approximating the three-leg vertex by a local vertex. From the local diagrams generated by this approximation, less irreducible diagrams with nonlocal contributions, including self-energies and polarizations, can be computed at a far lower cost than solving an impurity model with multiple sites. Moreover, long-range fluctuations are captured in this approach.

1.3 Contributions

The contributions of this work are the following:

First, I present the first fully self-consistent implementation of the EDMFT and $GW+EDMFT$ methods with continuous-time quantum Monte-Carlo impurity solvers with retarded interactions, applied to the extended Hubbard model on a square and cubic lattice with short-range interactions. The effect of vertex corrections in the construction of self-energies (Aryal *et al.* (2012)), the detailed local-nonlocal interactions phase diagram, with a characterization of the energy scales of the screened interaction (Aryal *et al.* (2013)), and the influence of longer-range hoppings and doping (Huang *et al.* (2014)) are studied.

Second, this work gives new insights into systems of adatoms on silicon surfaces: it maps out the general phase diagram as a function of local interaction and nonlocal interactions; using the constrained random-phase approximation (cRPA), it places different compounds on this phase diagram, thus providing orientation in the intriguing phenomena observed in these systems (Hansmann *et al.* (2013a)). It also resolves long-standing questions elicited by apparently contradictory experimental conclusions coming from different probes (Hansmann *et al.* (2014)).

Third, I present a novel method for unifying Mott physics and spin fluctuation physics (Aryal and Parcollet (2015)). At the price of solving an impurity model with dynamical charge-charge and spin-spin interactions, this method, called TRILEX, constructs nonlocal self-energies and polarizations from a local three-leg electron-boson coupling vertex. Applied to the Hubbard model in two dimensions, this method captures, like DMFT, the Fermi-liquid-to-Mott-insulator transition, but also long-ranged spin fluctuations physics. Away from half-filling, it yields Fermi arcs similar to those observed in photoemission experiments on cuprates.

Fourth, this work puts an emphasis on algorithmic developments: through the contribution to an open-source library for many-body computations, TRIQS (Parcollet *et al.* (2015)), and the implementation of state-of-the-art continuous-time Monte-Carlo solvers with dynamical charge-charge and spin-spin interactions; besides being needed in the TRILEX method, this solver is used in another new method for realistic materials, the combined screened-exchange and dynamical DMFT method (van Roekeghem *et al.* (2014)).

1.4 Structure of this work

This work is structured as follows:

In part I, besides this Introduction, I introduce the dynamical mean field approach to Mott physics (chapter 2).

In part II, systems of adatoms on semiconducting surfaces are studied from first principles: after a general introduction to these systems and a review of the open puzzles (chapter 3), I present the derivation of the low-energy effective model through the constrained random-phase approximation (chapter 4). Chapter 5 is devoted to the theoretical framework for solving such a model – the EDMFT method and the $GW+EDMFT$ method. Finally, I apply this methodology to surface systems in chapter 6.

In part III, I give an experimental and theoretical overview of high-temperature cuprate superconductors in chapter 7. Then, I present the formal derivation of TRILEX, a new method to approach this problem, in chapter 8. Finally, chapter 9 summarizes the first results of this method applied to the single-band Hubbard model.

In part IV, I touch on some computational aspects. Chapter 10 gives a glimpse of the TRIQS library and my contributions to it. Chapter 11 is a detailed description of an extension of continuous-time quantum Monte-Carlo algorithms to retarded spin-spin interactions, as well as the corresponding implementation notes. Finally, chapter 12 presents an example of usage of this algorithm for a recently developed method for realistic calculations in strongly-correlated materials, the combined screened exchange and dynamical DMFT method.

Part V presents the conclusions of this work.

This work has four main appendices. Part VI gathers the conventions used in the main text. Part VII presents technical developments necessary for TRILEX. Part VIII is an appendix presenting general background material for the field of strongly-correlated materials, with mainly a pedagogical purpose. Finally, part IX contains details of some calculations.

The publications corresponding to this work are enclosed in part X.

Dynamical Mean-Field Theory: a local approach to Mott physics

In a solid, about 10^{23} electrons interact with one another. To describe their motion and hence the electronic properties of a solid, one should in principle solve 10^{23} coupled equations, an impossible task even for state-of-the-art computers – and for any computer in the foreseeable future. Yet, in the same way as biologists can study the human body without keeping track of every single protein, solid-state physicists can predict the electronic properties of matter without monitoring every single electron. Instead of focusing on the behavior of individual entities, the task of the physicist is to identify the *relevant degrees of freedom* of the problem. Indeed, in the words of Anderson (1972), “more is different”: more particles give rise to new states of matter – superconductivity, giant magnetoresistance, superfluidity, charge density waves... These *emergent* macroscopic phenomena result from, but are not the simple addition of, the complex behaviors of the microscopic entities. Physics (and science at large) consists in writing down the minimal equations that account for the macroscopic behavior *at a given scale*.

A formal procedure for doing so is “renormalization group theory”, a theory developed in the 1970s. It allows to write down an “effective” model describing the physics of a system at a given scale. As one goes down in energy scale, the high-energy degrees of freedom “renormalize” the low-energy degrees of freedom. The constrained random-phase approximation, which can be seen as a concrete way of performing this renormalization procedure, will be described in a later part (section J.3). The renormalized model, albeit much simpler than the original “high-energy” model, still requires some work.

Here, I will focus on such a low-energy model, the Hubbard model. As the minimal model describing the competition of the localizing effect of Coulomb interactions and the itinerancy favored by the tunnel effect, it has been widely studied since the 1960s. Here, I will restrict my attention to one class of methods – dynamical mean field theory (DMFT) – that has been developed to handle it.

In this chapter, I describe dynamical mean field theory (DMFT) in its single-site version (section 2.1). The “cluster” versions of DMFT will be introduced in section 7.2.2.2, while the application of DMFT to realistic materials (as opposed to the “model” approach of this section) is briefly introduced in section J.2. Examples of “weak-coupling” approaches to the Hubbard model such as spin fluctuation theory will be dealt with in part III in the context of cuprate materials.

In this chapter, $\hbar = k_B = 1$. In case of doubt, the general notation conventions are summarized in appendix VI.

2.1 Mott insulators: a Coulombic thorn in Fermi liquid theory's side

This section is a brief introduction to the Mott mechanism and to the Hubbard model, a minimal model to describe the transition from a “normal metal” to a Mott insulator.

2.1.1 Fermi liquid theory and Mott physics: of the (surprising) robustness and (eventual) failure of band theory

In the early twentieth century, the electronic structure of matter – namely the description of electron propagation in solids – was described within the so-called “band theory”. One of the consequences of this theory, which is based on the image of “quasi-free” electrons (non-interacting electrons in the periodic potential of the crystal), is that solids with an odd number of electrons per unit cell cannot be insulating. Indeed, in this case, the Fermi level falls inside of a continuum of allowed states – a “band” – and thus the excitation cost to create an electrical current is small.

While band theory provided a good classification for many solids at the time, Verwey and de Boer (1936) discovered that some materials with “unpaired electrons and incomplete outer shells” (understand: with an odd number of electrons per unit cell and thus partially filled valence bands) such a nickel oxide (NiO), an oxide with 3d valence electrons, were very poor conductors. This prompted Mott and Peierls (1937) to hypothesize that in these materials, “the electrostatic interaction between the electrons prevents them from moving at all”, explaining their insulating behavior. Mott’s paper was the opening remark of the field of strongly correlated materials.

“Mott insulators”, as these special insulators have later been called, are characterized by a blocking of electronic conduction due to the Coulomb repulsion: electrons are deterred from tunneling or “hopping” from site to site by a too large energetical cost. A simple-minded estimate of this cost – about 14 eV for electrons distant of 1 in free space¹ – would indicate that this effect is huge in most solids – even in solids well described by band theory: indeed, typical kinetic energies – the other important energy scale – are in the range of a few electron volts.

2.1.1.1 Why band theory (suprisingly) works in many solids: Fermi liquid theory

Two additional factors must be taken into account to mitigate the previous argument and explain the surprising robustness of band theory against the effect of Coulomb repulsion.

The first is the screening of the Coulomb interaction. In the same way as in electrolytic solutions, the range of the electrostatic potential of charge carriers is reduced to a characteristic length (called the Debye length) due to the shielding or “screening” of this potential by other ions, in a solid, the interelectronic potential is screened by the presence of the other electrons. As will be explained more quantitatively in section J.3.1, the screened potential has both a shorter range (with a typical length scale called the Thomas-Fermi length) and a reduced magnitude. This screening effect can be seen as one of the “renormalization” effects of high-energy electrons that have been mentioned in the introduction of this part.

The second factor is the Pauli exclusion principle. It effectively reduces the phase space for the scattering of an electron, or more precisely of a “quasi-electron” – an electron dressed with elementary excitations. The existence of these “quasiparticles”, namely of well-defined excitations in momentum space which reduce to the original electrons when the interactions are turned off, is the essence of Landau’s Fermi liquid (FL) theory. Within this theory, interactions merely endow (quasi-)electronic excitations with a finite lifetime and an enhanced mass (among others). The scattering rate at temperature T of a quasiparticle of energy ε with respect to the Fermi energy is given by the expression:

$$\Gamma_{\text{FL}} \propto \varepsilon^2 + \pi^2 T^2 \quad (2.1)$$

¹ $V(r) = \frac{e^2}{4\pi\epsilon_0 r}$ with $r = 10^{-10} \text{ m}$, $\epsilon_0 = 8.85 \cdot 10^{-12} \text{ F/m}$

Thus, a quasiparticle on the Fermi surface ($\varepsilon = 0$) has an infinite lifetime at $T = 0$. The ε^2 term is a direct consequence of the Pauli principle, which restricts the possible scattering states for a given particle. A finite temperature opens up the phase space of allowed transitions to a range $k_B T$ of the Fermi surface, whence the second term. The details of this calculation can be found *e.g.* in Abrikosov *et al.* (1965) or in a more modern form in section 7.7 of Coleman (2011). The renormalized mass of quasiparticles is denoted as $m^* > m$: in Fermi liquid theory, interelectronic interactions merely make electrons “heavier”.

2.1.1.2 Green’s functions and the self-energy: quantifying correlations

Both the finite lifetime effect and the mass enhancement effect can be described mathematically by a complex function of momentum (\mathbf{k}) and energy (ω), the self-energy $\Sigma(\mathbf{k}, \omega)$ of the electron. It is defined by the following relation:

$$\Sigma(\mathbf{k}, \omega) \equiv G_0^{-1}(\mathbf{k}, \omega) - G^{-1}(\mathbf{k}, \omega) \quad (2.2)$$

where $G(\mathbf{k}, \omega)$ is the “propagator” or “Green’s function” of the electron, defined in imaginary time as $G_{ij}(\tau) \equiv -\langle T c_i(\tau) c_j^\dagger(0) \rangle$: it characterizes the propagation of an electron from a site j (where it is created by c_j^\dagger) to a site i (where it is annihilated by c_i) between times 0 and τ . G_0 is the propagator in the absence of interactions. Thus, the self-energy Σ – which vanishes in the absence of interactions – measures the *effect of correlations on the propagation of an electron*.

The physical content of the propagator itself is easily understood by looking at its expression in the non-interacting case, $G_0(\mathbf{k}, \omega) = (\omega - \xi_{\mathbf{k}})^{-1}$. In this formula, $\xi_{\mathbf{k}} \equiv \varepsilon_{\mathbf{k}} - \mu$, where $\varepsilon_{\mathbf{k}}$ denotes the energy of a single electron of momentum \mathbf{k} (for instance, $\varepsilon_{\mathbf{k}} = \frac{\hbar^2 |\mathbf{k}|^2}{2m}$ for a free electron), and μ is the chemical potential. Thus the poles of G_0 , $\omega_{\mathbf{k}} = \xi_{\mathbf{k}}$, correspond to the single-particle energies. As shown in appendix H.1.4, the imaginary part of $G(\mathbf{k}, \omega)$ (or the “spectral function” $A(\mathbf{k}, \omega) \equiv -\frac{1}{\pi} \text{Im} G(\mathbf{k}, \omega + i\eta)$, with η an infinitesimal positive factor) is directly related to the signal that can be measured in angle-resolved photoemission (ARPES). In the non-interacting case:

$$A_0(\mathbf{k}, \omega) = \delta(\omega - \xi_{\mathbf{k}}) = \lim_{\eta \rightarrow 0} \frac{\eta/\pi}{(\omega - \xi_{\mathbf{k}})^2 + \eta^2}$$

The non-interacting Fermi surface corresponds the locus of the momenta \mathbf{k}_F such that $\omega_{\mathbf{k}_F} = 0$. The levels observed in photoemission in this case are infinitely sharp ($\eta \rightarrow 0$).

In the presence of interactions, the propagator becomes $G^{-1}(\mathbf{k}, \omega) = [\omega - \xi_{\mathbf{k}} - \text{Re}\Sigma(\mathbf{k}, \omega)] - i\text{Im}\Sigma(\mathbf{k}, \omega)$. Thus, the new dispersion is given by the solutions $\tilde{\omega}_{\mathbf{k}}$ of $\tilde{\omega}_{\mathbf{k}} - \xi_{\mathbf{k}} - \text{Re}\Sigma(\mathbf{k}, \tilde{\omega}_{\mathbf{k}}) = 0$, while the interacting Fermi surface corresponds to $\tilde{\omega}_{\tilde{\mathbf{k}}_F} = 0$, *i.e.* $-\tilde{\xi}_{\tilde{\mathbf{k}}_F} - \text{Re}\Sigma(\tilde{\mathbf{k}}, \tilde{\omega}_{\tilde{\mathbf{k}}_F}) = 0$. The corresponding spectral function is given by:

$$A(\mathbf{k}, \omega) = \frac{-\text{Im}\Sigma(\mathbf{k}, \omega)/\pi}{[\omega - \xi_{\mathbf{k}} - \text{Re}\Sigma(\mathbf{k}, \omega)]^2 + [\text{Im}\Sigma(\mathbf{k}, \omega)]^2} \quad (2.3)$$

Roughly speaking (*i.e.* forgetting about the momentum- and energy-dependence of the self-energy), the real part of the self-energy shifts the energy levels, while its imaginary part broadens them.

2.1.1.3 The self-energy in Fermi-liquid theory

The connection of Σ to the mass enhancement predicted by Fermi liquid theory is seen by making a Taylor expansion the self-energy in the vicinity of the interacting Fermi surface, namely around $\omega \approx \tilde{\omega}_{\tilde{\mathbf{k}}_F} = 0$ and $\mathbf{k} \approx \tilde{\mathbf{k}}_F$, which yields $\omega - \xi_{\mathbf{k}} - \text{Re}\Sigma(\mathbf{k}, \omega) = Z_{\tilde{\mathbf{k}}_F}^{-1} (\omega - \tilde{\xi}_{\tilde{\mathbf{k}}_F})$, where I have defined the so-called quasiparticle residue:

$$Z_{\tilde{\mathbf{k}}_F} \equiv \frac{1}{1 - \partial_{\omega} \text{Re}\Sigma(\mathbf{k}, \omega)|_{\text{FS}}} \quad (2.4)$$

and the renormalized energy $\tilde{\xi}_{\tilde{\mathbf{k}}} \equiv Z_{\tilde{\mathbf{k}}_F} (\mathbf{k} - \tilde{\mathbf{k}}_F) \cdot \nabla_{\mathbf{k}} [\xi_{\mathbf{k}} + \text{Re}\Sigma(\mathbf{k}, \omega)]|_{\text{FS}}$. The effective mass (tensor) is defined as the curvature of the renormalized energy $\frac{1}{m_{\alpha\beta}^*} = \frac{1}{\hbar^2} \partial_{k_{\alpha}} \partial_{k_{\beta}} \tilde{\xi}_{\tilde{\mathbf{k}}}|_{\text{FS}}$. If one neglects the momentum dependence

of Σ and considers an isotropic $\xi_{\mathbf{k}}$, then $m^*/m = 1/Z$: the effective mass of quasiparticles is directly given by the inverse of Z . The smaller Z , the heavier the quasiparticles.

Following the previous reasoning, the spectral function of a Fermi liquid should in principle read:

$$A_{\text{FL}}(\mathbf{k}, \omega) = Z_{\mathbf{k}} \frac{\Gamma_{\text{FL}}(\omega)/\pi}{\left[\omega - \xi_{\mathbf{k}}\right]^2 + \Gamma_{\text{FL}}^2(\omega)}$$

with the identification $\Gamma_{\text{FL}} = -Z_{\mathbf{k}} \text{Im}\Sigma_{\text{FL}}(\mathbf{k}, \omega)$. The connection to the scattering rate computed within Fermi liquid theory, Eq. (2.1), is made (at zero temperature) by setting: $\text{Im}\Sigma_{\text{FL}}(\mathbf{k}, \omega) \propto \omega^2$.

At this point, one might think that the only effect of interactions as described by FL theory is to renormalize the width of the bands (through Z) and give the electrons a finite lifetime $\tau \propto 1/\Gamma_{\text{FL}}$. However, the energy integral of $A_{\text{FL}}(\mathbf{k}, \omega)$ is $Z_{\mathbf{k}}$ instead of the expected 1: only a fraction $Z_{\mathbf{k}}$ of the spectrum is described by quasiparticles (which explains the name given to $Z_{\mathbf{k}}$). The total spectrum is in fact $A(\mathbf{k}, \omega) = A_{\text{FL}}(\mathbf{k}, \omega) + A_{\text{inc}}(\mathbf{k}, \omega)$ where the “incoherent” part $A_{\text{inc}}(\mathbf{k}, \omega)$ describes the excitations which cannot be described in terms of quasiparticles and are thence outside the realm of FL theory.

2.1.1.4 Mott insulators: solids are made up of atoms, after all

The kind of insulator envisioned by Mott corresponds to the extreme case² $Z \rightarrow 0$. In such a case, all the spectral weight goes into $A_{\text{inc}}(\omega)$. In the previous section, all the “incoherent” excitations had conveniently been lumped into this term, while the focus was on the coherent excitations, of weight Z . In Mott insulators, since the Fermi-liquid quasiparticles do not exist anymore, the excitations hidden in $A_{\text{inc}}(\omega)$ can no longer be glossed over: a change of paradigm is necessary.

Such a change can be easily operated when taking another viewpoint on solids. While band theory regards electrons in solids essentially as free waves in the periodic potential of the ions, one may as well consider a solid as a collection of atoms, with electrons sitting on their respective ionic site. Pushed to the extreme, this vision leads to the neglect of tunnelling between neighboring ionic sites – the so-called atomic limit approximation. In this limit and within a much simplified model of an atom (a single orbital), the self-energy of an electron sitting on an atomic site is (see appendix E for a derivation):

$$\Sigma_{\text{at}}(\omega) = \frac{U}{2} + \frac{U^2}{4\omega} \quad (2.5)$$

where U parametrizes the cost of a double occupation of this atomic site (this U will be more precisely defined in the framework of the Hubbard model introduced in the next section). The form of this self-energy is very different from the Fermi-liquid form studied in the previous section; in particular, the self-energy *diverges* at low energy. The corresponding Green’s function is:

$$G_{\text{at}}(\omega) = \frac{1/2}{\omega - U/2} + \frac{1/2}{\omega + U/2}$$

i.e. the spectral function is composed of two peaks separated with an energy interval U . Each peak has a weight $1/2$, in contrast to the bands of band theory, which can accommodate two electrons each.

Note that while in the non-interacting limit, there is no *correlation* (in the statistical sense) between the occupation of the up level and the occupation of the down level ($\langle n_{\uparrow} n_{\downarrow} \rangle_0 = \langle n_{\uparrow} \rangle \langle n_{\downarrow} \rangle = 1/4$ at half-filling), in the atomic limit, the probability for double occupancy is given by

$$\langle n_{\uparrow} n_{\downarrow} \rangle_{\text{at}} = \frac{1}{2(1 + e^{U\beta/2})} \approx \frac{1}{2} e^{-\beta U/2} \ll 1$$

²If the momentum-dependence of the self-energy is neglected, $Z \rightarrow 0$ also corresponds to a diverging effective mass m^* of Landau’s quasiparticles, as first shown by Brinkman and Rice (1970) – which explains why conduction is impossible in a Mott insulator.

2.1.1.5 Conclusion: how to interpolate between these pictures?

In the two previous sections, solids have been considered from two main vantage points: the non-interacting limit, where interactions merely give a lifetime and an enhanced mass to electrons, and the atomic limit, in which electrons simply occupy atomic levels. These two images, however, are but caricatures of strongly-correlated solids, where interactions are strong enough that the transfer of spectral weight from A_{FL} to A_{inc} must be described more precisely than just with Fermi-liquid parameters, and the kinetic energy is not so weak as to warrant a description of the solid solely in terms of isolated atoms.

Before I turn to dynamical mean field theory, a method designed to bridge this gap, I first introduce the minimal model encapsulating the interplay of interaction energy and kinetic energy, the Hubbard model.

2.1.2 The Hubbard model: the spherical, yet challenging cow of strongly correlated materials

Electrons in a solid-state environment are both (charged) particles and waves: as waves, they “like” to be delocalized to minimize (by tunnelling) their kinetic energy; as charged particles, they repel one another and thus try to be as localized as possible in order to avoid paying this potential energy price.

This essential “schizophrenia” of electrons is minimally captured by the Hubbard model, a model due to Hubbard (1963), Kanamori (1963) and Gutzwiller (1963). It contains two terms: a kinetic energy term favoring a wave-like behavior and a potential energy term favoring localization. In its single-band form, it reads:

$$H_{\text{Hubbard}} = -t \sum_{\langle ij \rangle \sigma} (c_{i\sigma}^\dagger c_{j\sigma} + \text{h.c.}) + U \sum_i n_{i\uparrow} n_{i\downarrow} \quad (2.6)$$

i and j denote lattice sites, $\langle ij \rangle$ denote nearest-neighbor sites, $c_{i\sigma}^\dagger$ ($c_{i\sigma}$) creates (annihilates) an electron of spin $\sigma = \uparrow, \downarrow$ at site \mathbf{R}_i . t is the hopping (tunnelling) amplitude between two neighboring sites: it parametrizes the kinetic energy of the electron. U parametrizes the inter-electronic Coulomb repulsion. In the Hubbard model, this interaction is assumed to be purely local as a consequence of screening (see above, subsection 2.1.1.1, for a qualitative discussion).

The Hubbard model can be taken as the starting point of a calculation (with “knobs” t , U and the chemical potential μ in a grand canonic ensemble), or derived from first principles as described in the appendix (chapter J.3). As will be seen later (chapter 7), this model is conjectured, following Anderson (1987), to be a reasonable description of high-temperature superconductors. It may easily be extended to the case of nonlocal interactions (see chapter 5), or to the multi-orbital case.

The ratio t/U controls the importance of the kinetic energy over the interaction energy:

- if $t/U \rightarrow \infty$, the Hamiltonian can be diagonalized in momentum space, $H_{\text{Hubbard}}(U = 0) = \sum_{\mathbf{k}\sigma} \epsilon(\mathbf{k}) c_{\mathbf{k}\sigma}^\dagger c_{\mathbf{k}\sigma}$, where $c_{\mathbf{k}\sigma}^\dagger = \sum_i e^{i\mathbf{k}\cdot\mathbf{R}_i} c_{i\sigma}^\dagger$ creates a wave-like state with (quasi) momentum \mathbf{k} . The many-body ground state is a Slater determinant made up of these modes of energy $< \epsilon_{\text{F}}$ propagating with the dispersion relation $\epsilon(\mathbf{k})$ (for instance, $\epsilon(\mathbf{k}) = -2t [\cos(k_x) + \cos(k_y)]$ on a two-dimensional square lattice).
- if $t/U = 0$, H_{Hubbard} can be diagonalized in real space, its eigenstates being the many-body states $|n_\uparrow^{i=0}, n_\downarrow^{i=0}, n_\uparrow^{i=1}, n_\downarrow^{i=1}, \dots, n_\uparrow^{i=N}, n_\downarrow^{i=N}\rangle$ with $n_\sigma = 0, 1$. At half-filling, the ground state is a degenerate state with one localized electron per site, with an energy gap U to the first excited state: it is a “Mott” insulator.

Thus, the Hubbard model encompasses both the non-interacting and atomic limits that have been introduced in the previous section. As such, it contains the essential ingredients to study the transition between a Fermi liquid and a Mott insulator.

Despite its apparent simplicity, the Hubbard model has been a challenge to theoreticians since its introduction. A direct diagonalization of this model is limited to small system sizes: without using symmetries, it requires diagonalizing matrices of size 4^N (with N : number of atoms), and even with symmetries, the sizes that can be reached are so small that finite-size effects prevent the extrapolation to the thermodynamic limit in interesting regimes of parameters. Likewise, quantum Monte-Carlo methods are hampered by the negative sign problem (see chapter 11) except for special cases like the half-filled case.

On the other hand, mean-field theories, which are valid in the thermodynamic limit, must be considered with care. For instance, Hartree mean field theory, which consists in approximating the interaction term as

$$U \sum_i n_{i\uparrow} n_{i\downarrow} \approx U \sum_i n_{i\uparrow} \langle n_{i\downarrow} \rangle + n_{i\downarrow} \langle n_{i\uparrow} \rangle + \text{const.}$$

or equivalently the self-energy as

$$\Sigma_{\sigma}^H(\mathbf{k}, \omega) = U \langle n_{i\bar{\sigma}} \rangle \quad (2.7)$$

is not valid in the atomic limit (compare to equation (2.5)), despite the fact that it can open an antiferromagnetic gap of order U on a bipartite sublattice: this happens under a certain critical temperature $T_c \sim e^{-1/UN(\varepsilon_F)}$ ($N(\varepsilon)$ is the noninteracting density of states), in which case $\langle n_{A\uparrow} \rangle = \langle n_{B\downarrow} \rangle = 0$ and $\langle n_{A\downarrow} \rangle = \langle n_{B\uparrow} \rangle = 1$ (where A and B denote sites on different sublattices; this calculation is carried out in appendix I.6.2).

This failure highlights the special nature of the Mott gap: as first hinted at by Mott's remark, it is intrinsically a *charge gap*, associated to a freezing of the charge degrees of freedom. By contrast, the mechanism described by static mean-field theory is based on the opening of a *spin gap*. One may also trace back this failure to a wrong choice of mean field, as will be argued in the next section.

2.2 Dynamical Mean Field Theory: local physics to capture ‘‘Mottness’’

2.2.1 Intuitive picture: a mean field theory, only dynamical

In the previous section, the static (Hartree) mean-field treatment of the Hubbard model has been discarded on the basis that it could not capture the opening of a charge gap. Still, mean field theory (as introduced by Weiss (1907)) has appealing features: after selecting the relevant variable (the mean field), it reduces a complicated lattice problem to a simpler local problem which is then solved, if not exactly, at least taking many-body effects into account.

The prototypical example for this is the mean-field solution of the Ising model, defined by the Hamiltonian:

$$H_{\text{Ising}} = -J \sum_{\langle ij \rangle} s_i s_j - h \sum_i s_i \quad (2.8)$$

which describes the ferromagnetic ($J > 0$) coupling of neighboring ($\langle ij \rangle$) classical spins $s_i = \pm 1$ in a magnetic field h . If one is interested in the possibility for magnetic ordering of the spin system, the relevant degree of freedom or ‘‘order parameter’’ is the local magnetization

$$m = \langle s_i \rangle \quad (2.9)$$

After decoupling the interaction term by neglecting fluctuations of the order parameter, one can write down a local effective Hamiltonian, $H_{\text{eff}}[h_{\text{eff}}] = -h_{\text{eff}} s$, with the ‘‘Weiss field’’ h_{eff} defined as $h_{\text{eff}}[m] = Jzm + h$. In this simple model, the local model, H_{eff} , can be solved exactly for $\langle s \rangle_{\text{eff}}$: $\langle s \rangle_{\text{eff}}[h_{\text{eff}}] = \tanh(\beta [h_{\text{eff}}])$. This set of two equations (with three unknowns $\langle s \rangle_{\text{eff}}$, m and h_{eff}) is closed by imposing the self-consistency condition:

$$\langle s \rangle_{\text{eff}} = m \quad (2.10)$$

Solving for m for a given inverse temperature β and field h , one obtains the final equation $m = \tanh(\beta [Jzm + h])$ which, at zero field, has one “disordered” solution $m = 0$ for $T > Jz/k_B \equiv T_c^{\text{MF}}$, and two ordered solutions $|m| \neq 0$ for $T < T_c^{\text{MF}}$.

Dynamical mean field theory is based on a similar reasoning. The key difficulty, however, consists in identifying the order parameter. The discussion of the previous sections has taught us that one possible observable to describe both a non-interacting or weakly-interacting system and a Mott insulator is the one-particle local spectral function $A(\omega)$ or, equivalently, the local Green’s function $G_{ii}(\omega)$ defined as (in imaginary time):

$$G_{ii}(\tau) = -\langle T c_i(\tau) c_i^\dagger(0) \rangle \quad (2.11)$$

This object is *dynamical* (it depends on imaginary time), as opposed to m which is static in the Ising case. These dynamics describe electronic motion, and encompasses, in particular, Fermi liquid behavior (as in $A_{\text{FL}}(\omega)$) as well as incoherent structures at high energies ω . From there, DMFT constructs the analog of h_{eff} , the dynamical Weiss field “ $\mathcal{G}(\omega)$ ”. Based on this Weiss field, one then solves for the propagator $G_{\text{imp}}(\omega)$ of a local effective problem (the analog of H_{eff} , called an impurity problem). The three unknowns G_{ii} , G_{imp} and \mathcal{G} can be determined by imposing a self-consistency condition:

$$G_{\text{imp}}(\omega) = G_{ii}(\omega) \quad (2.12)$$

One can then solve for G_{imp} for a given inverse temperature β and interaction-to-kinetic energy ratio U/t . In the next section, I specify the various building blocks of this calculation.

2.2.2 The cavity construction: impurity physics in the spotlight

Thus far, I have described the structure of a DMFT calculation based on an analogy with the mean-field treatment of the Ising model. Here, I specify the effective model of DMFT (the analog of H_{eff}) following Georges *et al.* (1996).

2.2.2.1 Definition of the effective model of DMFT

The Hubbard model can be expressed in a path integral formalism (see *e.g.* Negele and Orland (1988)), namely the partition function can be written as $Z = \int \mathcal{D}[\bar{c}c] e^{-S_{\text{Hubbard}}}$, where

$$S_{\text{Hubbard}} = \int_0^\beta d\tau \left\{ \sum_{ij,\sigma} \bar{c}_{i\sigma\tau} \left((\partial_\tau - \mu) \delta_{ij} + t_{ij} \right) c_{j\sigma\tau} + U \sum_i n_{i\uparrow\tau} n_{i\downarrow\tau} \right\} \quad (2.13)$$

$\bar{c}_{i\sigma\tau}$ and $c_{i\sigma\tau}$ are conjugate Grassmann antiperiodic fields; $t_{ij} = -t\delta_{\langle ij \rangle}$ in the case of nearest-neighbor hopping.

The local effective model of DMFT is found by singling out one site of the lattice in the above action, and integrate out all the other sites. The local model obtained after integration of the other sites and a truncation in the limit of infinite dimensions is a “renormalized” local model describing one site embedded in a host which is described by a dynamical “mean field” \mathcal{G} .

More precisely, let us focus on a given site (denoted by the index 0) and define the effective action S_{imp} of this single site – which is akin to an “impurity” atom hosted in a lattice – as:

$$\frac{1}{Z_{\text{imp}}} e^{-S_{\text{imp}}[\bar{c}_0, c_0]} \equiv \frac{e^{-S_0}}{Z} \int \mathcal{D}_{i \neq 0}[\bar{c}_i, c_i] e^{-(S^{(0)} + \Delta S)}$$

I have split the action as $S_{\text{Hubbard}} = S_0 + S^{(0)} + \Delta S$, where S_0 denotes the action of the site 0, $S^{(0)}$ the action of the lattice with site 0 removed (the lattice with a “cavity” at site 0) and ΔS the remaining part. In the limit of infinite dimensions, S_{imp} simplifies to (Georges *et al.* (1996)):

$$S_{\text{imp}} = \iint_0^\beta d\tau d\tau' \bar{c}(\tau) \{-\mathcal{G}^{-1}(\tau - \tau')\} c(\tau') + \int_0^\beta d\tau U n_{\uparrow\tau} n_{\downarrow\tau} \quad (2.14)$$

where the Weiss field is given by:

$$\mathcal{G}^{-1}(i\omega) = G_{ii}^{-1}(i\omega) + \Sigma_{\text{imp}}(i\omega) \quad (2.15)$$

with

$$G_{ii}(i\omega) = \int_{-\infty}^{\infty} \frac{d\varepsilon N(\varepsilon)}{i\omega + \mu - \varepsilon - \Sigma_{\text{imp}}(i\omega)} \quad (2.16)$$

$N(\varepsilon)$ is the non-interacting density of states, and $\Sigma_{\text{imp}}(i\omega)$ the self-energy associated with S_{imp} , defined as $\Sigma_{\text{imp}}(i\omega) \equiv \mathcal{G}^{-1}(i\omega) - G_{ii}^{-1}(i\omega)$. In the limit of infinite dimensions, since the lattice self-energy becomes local (Metzner and Vollhardt (1989); Müller-Hartmann (1989)), the lattice and the impurity self-energies are equal.

This closes the set of DMFT equations: for a given self-energy $\Sigma_{\text{imp}}(i\omega)$, obtained by solving the effective local model S_{imp} parametrized by $\mathcal{G}(i\omega)$, one can compute G_{ii} using (2.16), and then find a new Weiss field $\mathcal{G}(i\omega)$ (using (2.15)), until convergence.

2.2.2.2 Physical content of the local effective model

The physical content of the effective local problem, Eq. (2.14), is made clearer by defining a “hybridization” function $\Delta(i\omega)$ as:

$$\Delta(i\omega) \equiv i\omega + \mu - \mathcal{G}^{-1}(i\omega)$$

Then, Eq. (2.14) reads:

$$S_{\text{imp}} = \iint_0^\beta d\tau d\tau' \bar{c}(\tau) \{(\partial_\tau - \mu) \delta_{\tau-\tau'} + \Delta(\tau - \tau')\} c(\tau') + \int_0^\beta d\tau U n_{\uparrow\tau} n_{\downarrow\tau} \quad (2.17)$$

This local action can be contrasted with the action describing the Hubbard model, Eq. (2.13): roughly speaking, the nonlocal but static hopping term t_{ij} has been traded for a local, yet dynamical hybridization term $\Delta(\tau - \tau')$. Therefore, one can view S_{imp} as an auxiliary model whose hybridization term $\Delta(\tau - \tau')$ is adjusted in such a way that the impurity Green’s function G_{imp} reproduces the local lattice Green’s function G_{ii} . $\Delta(\tau)$ is thus supposed to mimic the incursions of electrons to and from the impurity site. This dynamical process intrinsically depends on the strength of the interactions (U) in the system.

The problem described by S_{imp} can be cast in a Hamiltonian form as the coupling of an interacting fermionic level (at energy $-\mu$ and with interactions U) with a non-interacting fermionic bath described by the hybridization function $\Delta(\omega)$ (see appendix M.2 for more details). This is the so-called Anderson impurity model (Anderson (1961)) which, among others, captures Kondo physics.

Contrary to static mean field theory, the effective local model of DMFT, S_{imp} , albeit local, is a nontrivial many-body problem. Its solution is the main technical hurdle of DMFT. As will be described in chapter 11, however, the advent of continuous-time quantum Monte-Carlo solvers has made it easier to obtain an exact – up to statistical noise – solution of S_{imp} .

Let us emphasize that since DMFT is in general applied to finite-dimensional problems, the locality of the self-energy, an exact property in infinite dimensions, becomes an approximation to the true self-energy in finite dimensions.

In the next section, I give a more formal justification of the exactness of DMFT in infinite dimensions.

2.2.3 Functional aspect: DMFT as a local approximation to the Luttinger-Ward functional

In this section, I give another interpretation of DMFT based on energy functionals. This derivation will be performed in more details as part of a more general framework in chapter 8. Here, I merely recall the main results.

Let us take the action for the Hubbard model, Eq. (2.13), as a starting point. Defining its free energy in the presence of a bilinear source term $F_{i\tau, j\tau'} \bar{c}_{i\tau} c_{j\tau'}$, $\Omega[F] = -\ln Z[F]$, one can perform a Legendre transform of Ω (which, as the generating functional of correlation functions, satisfies $\delta\Omega/\delta F = G$) with respect to F , which can be shown³ to be expressed as:

$$\Gamma[G] = -\text{Tr} \log [G^{-1}] + \text{Tr} \left[(G^{-1} - G_0^{-1}) G \right] + \Phi[G] \quad (2.18)$$

Here, G_0 is the non-interacting Green's function, and $\Phi[G]$ is the so-called Luttinger-Ward functional (Luttinger and Ward (1960)), which is the sum of all graphs constructed with $G_{ij}(\tau - \tau')$ lines and $Un_{i\uparrow}n_{i\downarrow}$ vertices which do not fall apart if two G lines are cut. Such graphs are called two-particle irreducible (2PI) graphs. Examples of graphs contributing (or not) to $\Phi[G]$ will be shown later (Fig. 8.3 in chapter 8).

DMFT can be regarded as a nonperturbative approximation to $\Phi[G]$. One way to see this is to compare the structure of the impurity action, Eq. (2.17), with that of the Hubbard action, Eq. (2.13): apart from the fact that one is local and the other not, the diagrammatic content of both actions is the same, they will generate diagrams with fermionic lines G and a local vertex $Un_{\uparrow}n_{\downarrow}$. Thus, the 2PI functional of the Hubbard model $\Phi_{\text{Hubbard}}^{\text{exact}}[G_{ij}, U]$ and the 2PI functional of the impurity model $\Phi_{\text{imp}}^{\text{exact}}[G, U]$ correspond to the same series, except that the Hubbard functional contains diagrams with non local propagators G_{ij} (with $i \neq j$).

Thus, DMFT consists in constructing a 2PI functional where the internal lines of the exact 2PI functional are replaced by local propagators:

$$\Phi^{\text{DMFT}}[G] = \sum_{\mathbf{R}_i \in \text{BL}} \Phi^{\text{exact}}[G_{ii}] \quad (2.19)$$

This approximation becomes exact in the limit of infinite dimensions since, due to the irreducibility property of Φ , all contributions to Φ with nonlocal propagators vanish in this limit (Georges *et al.* (1996)).

The locality of the self-energy directly follows from the approximation of Φ (Eq. (2.19)). Indeed, setting the sources $F = \frac{\delta\Gamma}{\delta G}$ to zero leads to $0 = G^{-1} - G_0^{-1} + \frac{\delta\Phi}{\delta G}$. Comparing this relation to the definition of Σ , Eq. (2.2), one sees that $\Sigma_{ij} = \frac{\delta\Phi}{\delta G_{ji}}$. Thus, plugging the DMFT approximation of Φ , Eq. (2.19), one gets

$$\Sigma_{ij}^{\text{DMFT}} = \frac{\delta\Phi}{\delta G_{ii}} \delta_{ij}$$

i.e. Σ^{DMFT} is local.

2.2.4 Summary: set of DMFT equations

Based on the previous discussions, the self-consistent DMFT loop, illustrated in Fig. 2.1, consists in the following steps:

³see section 8.3

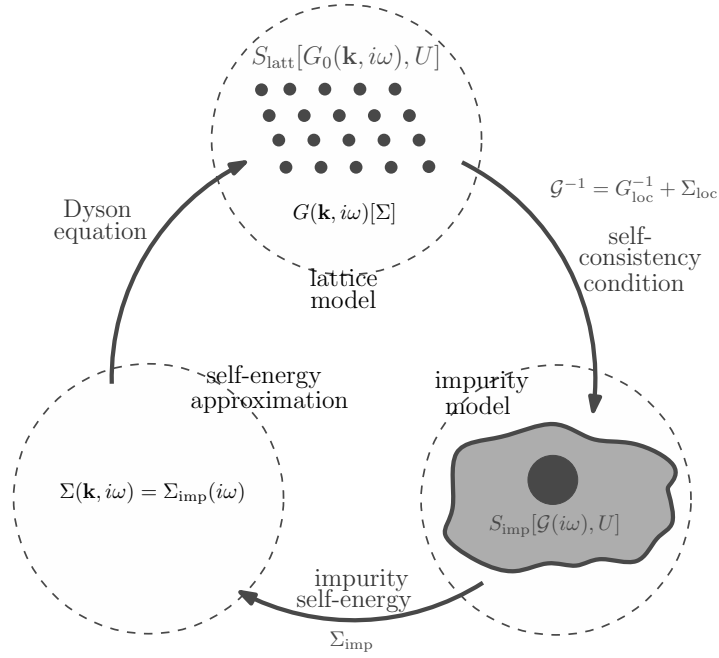


Figure 2.1: the DMFT loop

1. Start with an initial self-energy $\Sigma_{\text{imp}}(i\omega)$ (for instance $\Sigma_{\text{imp}} = 0$)
2. Compute the local fermionic Green's functions G using Dyson's equations:

$$G_{\text{loc}}(i\omega) = \sum_{\mathbf{k} \in \text{BZ}} \frac{1}{i\omega + \mu - \varepsilon(\mathbf{k}) - \Sigma_{\text{imp}}(i\omega)} \quad (2.20)$$

3. Compute the fermionic "Weiss field" $\mathcal{G}(i\omega)$:

$$\mathcal{G}(i\omega) = \left[G_{\text{loc}}(i\omega)^{-1} + \Sigma_{\text{imp}}(i\omega) \right]^{-1} \quad (2.21)$$

4. Solve the impurity model, Eq. (2.14), for $\Sigma_{\text{imp}}(i\omega)$
5. Go back to step 2 until convergence

2.2.5 Selected results, and limitations of single-site DMFT

This section is not intended to be an exhaustive review of DMFT results. I refer the reader to *Georges et al.* (1996) for a detailed overview of the early results.

By construction, DMFT interpolates between the Mott insulator and the non-interacting limit. It can thus capture the Mott transition, as illustrated in the left panel of Fig. 2.2, which shows a (T, U) phase diagram. This phase diagram has been obtained on the Bethe lattice (where the density of states $N(\varepsilon)$ is semicircular, namely $N(\varepsilon) = \frac{2}{\pi D} \sqrt{\left(\frac{\varepsilon}{D}\right)^2 - 1}$). The impurity action is solved approximately using an iterated-perturbation-theory (IPT) solver, which corresponds to a second-order approximation of the self-energy (with bare lines, *i.e.* $\Sigma_{\text{IPT}}(\tau) = -U^2 \mathcal{G}(\tau) \mathcal{G}(\tau) \mathcal{G}(-\tau)$).

For small values of the interaction ($U/D < 2.5$), a metallic solution is found, while for large values a Mott

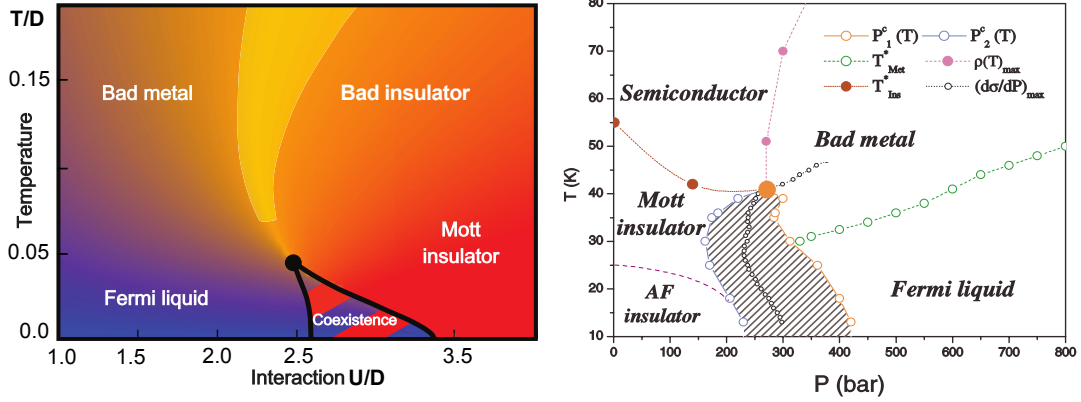


Figure 2.2: *Left*: (U, T) phase diagram of single-site DMFT on the Bethe lattice with an IPT impurity solver. Blue: small resistivity. Red: large resistivity (adapted from Vučićević *et al.* (2013)). *Right*: Temperature vs. Pressure phase diagram of the organic salt κ -(BEDT - TTF) $_2$ Cu [N(CN) $_2$] Cl (from Limelette *et al.* (2003)). Hatched region: coexistence region. AF stands for “antiferromagnetic”. D denotes the half-bandwidth.

insulating solution is found, characterized by a Mott gap of order U , by a vanishing quasiparticle residue Z , by a very small local double occupancy $\langle n_{\uparrow}n_{\downarrow} \rangle$ and large local susceptibility. The hatched region – the “coexistence” region – is a region where a metallic and an insulating solution coexist: DMFT predicts the Mott transition to be a first-order metal-to-insulator transition. The first-order line is terminated by a critical point located, in this approximation, at $U_c/D = 2.45$ and $T_c/D = 0.046$. At higher temperatures, there is a crossover between a bad metal and a bad insulator. The bad metal is characterized by an anomalous behavior of the resistivity (which is no longer quadratic in T as is the case in a Fermi liquid).

In this calculation, spin ordering has not been allowed for: as any mean field approximation, DMFT can restrict the search space; here, paramagnetism is enforced by symmetrizing the up and down components of the impurity Green’s function or self-energy. If DMFT, however, is extended to the case of two distinct sublattices (and hence spin differentiation is allowed), antiferromagnetism can be studied. This yields a Néel temperature line (T_N^{DMFT}) which is higher than the exact Néel temperature computed in three dimensions⁴, T_N^{3D} : DMFT overestimates the ordering temperature; indeed, it neglects spatial fluctuations of the order parameter which can destabilize the ordered phase (in two dimensions, they even destroy the order down to $T = 0$: this is the Mermin-Wagner theorem). The same caveat can be extended to the vicinity of the Mott transition, where spatial fluctuations are expected to play an important role: is the value of the critical interaction robust to the inclusion of spatial fluctuations? This and other issues related with short-range spatial fluctuations is addressed by a first possible extension of DMFT, cluster DMFT, which will be reported on in more detail in section 7.2.2.2 in the context of cuprate materials.

The somewhat “artificial” suppression of antiferromagnetism in “paramagnetic” DMFT calculations is however relevant to materials where frustration does suppress antiferromagnetism. This is the case in organic salts, as shown in the right panel of Fig. 2.2. Pressure controls the ratio D/U : the larger P , the larger D/U . There is a qualitative agreement with the single-site DMFT phase diagram.

The extension of single-site DMFT to multiorbital Hubbard models and more generally to realistic materials (the “LDA+DMFT” method) is briefly described in section J.2.

2.3 Summary: successes and limitations of DMFT

As we have seen in the previous section, DMFT succeeds in unifying the Mott and the Fermi liquid viewpoints, insofar as it smoothly connects those two exact limits. As any mean field theory, however, its validity is

⁴These lines are shown in Fig. 7.14 in chapter 7, where DMFT and its cluster extension are compared.

questionable in regions of the phase space where fluctuations are expected to play an important role: close to phase transitions and in low-dimensional systems, for instance.

One natural route to include spatial fluctuations is provided by “cluster extensions” of DMFT, which can be seen as an extension of DMFT to “extended” impurity models, namely impurity models with a finite spatial extent, contrary to the single-impurity model used in single-site DMFT. These extensions will be described in section 7.2.2.2.

Single-site DMFT provides a unified description of spectral properties on either side of the Mott transition, namely of the low-energy Fermi-liquid-like features and incoherent high-energy features like Hubbard bands in the correlated metal – and of the Hubbard bands in the Mott insulator.

The local approximation of the self-energy, which becomes exact in the limit of infinite dimensions, is improved by cluster extensions of DMFT which will be discussed in chapter 7.

In the next part, I show that DMFT can be extended to systems with nonlocal interactions such as systems of adatoms on semiconducting surfaces.

Part II

Long-range interactions in surface systems: insights from combined *GW* and Extended Dynamical Mean Field Theory

Systems of adatoms on semiconducting surfaces are original systems where the interplay of strong local and nonlocal interactions and low dimensionality leads to a mozaic of phases, insulating or metallic, ordered or disordered, magnetic or paramagnetic. These complex behaviors pose many challenges to theory.

I will cover this topic in four chapters. In chapter 3, I give a basic description of these systems, an overview of the main experimental findings and a summary of the theoretical questions that will be dealt with in the following chapters. In chapter 4, I explain how to construct from first principles low-energy models for the adatoms systems. In chapter 5, two methods of solution of these low-energy models – extended DMFT (EDMFT) and its self-consistent combination with the *GW* method, *GW*+EDMFT – are presented as well as their application to the extended Hubbard model. Finally, in chapter 6, I describe the application of these methods to surface systems.

| | | |
|----------|--|----|
| 3 | Adatoms on semiconducting surfaces: experiments and theoretical puzzles | |
| 3.1 | Surface systems: the basics of α -phases | 27 |
| 3.2 | Experiments on surfaces: a variety of puzzling phases | 29 |
| 3.3 | Early theoretical attempts and open puzzles | 31 |
| 4 | <i>Ab initio</i> effective kinetic and interaction parameters for α-phases | |
| 4.1 | How to describe materials in a realistic way? | 34 |
| 4.2 | <i>Ab initio</i> kinetic parameters from density-functional theory | 35 |
| 4.3 | Constrained RPA (cRPA): Application to surfaces | 36 |
| 4.4 | Conclusion: an extended Hubbard model with long-range interactions | 38 |
| 5 | Nonlocal interactions: Extended Dynamical Mean Field Theory and combined <i>GW</i> and Extended Dynamical Mean Field Theory | |
| 5.1 | Extended Dynamical Mean Field Theory (EDMFT) | 40 |
| 5.2 | Combined <i>GW</i> and Extended DMFT: <i>GW</i> +EDMFT | 42 |
| 5.3 | Application to the extended Hubbard model on square lattice | 44 |
| 5.4 | Conclusions | 53 |
| 6 | Local and long-range interactions in surface systems: insights from combined <i>GW</i> and Extended Dynamical Mean Field Theory | |
| 6.1 | Incorporating long-ranged interactions in <i>GW</i> +EDMFT | 54 |
| 6.2 | A materials trend: from Mott physics to charge-ordering... | 56 |
| 6.3 | Experimental timescales: a solution to the Sn/Si puzzle | 59 |

Adatoms on semiconducting surfaces: experiments and theoretical puzzles

Systems of adsorbed atoms (adatoms) on semiconducting surfaces (introduced in section 3.1) display a rich phase diagram upon varying the adatom or substrate species, the temperature or the surface coverage. Different experimental probes have pointed to metallic or insulating phases with various symmetries of the electronic system under consideration (section 3.2). Theoretical accounts for these contrasted behaviors have been put forth early on, but have left a number of open questions (section 3.3).

3.1 Surface systems: the basics of α -phases

Historically, systems of adsorbed metallic atoms on semiconducting surfaces have been studied because of the critical role played by metal-semiconductor junctions in the semiconductor industry, for instance at the junction between the (metallic) source or drain and the semiconductor in a transistor. This has spurred a number of experiments consisting in first depositing various atomic species (which I shall generically call X in the following) on top of a semiconducting sample (mainly Si or Ge) cleaved along a crystallographic axis (e.g. (111) or (110) in Miller indices), and then characterizing the state of the surface in terms of conductivity, symmetry, etc.

The cleaving of the sample leaves dangling bonds on the surface which form a two-dimensional Bravais lattice (or net) with unit vectors \mathbf{a} and \mathbf{b} (see Fig.3.1). The adatoms in turn form a Bravais lattice on top of these dangling bonds. This adatom Bravais lattice is conventionally denoted as $L_x \times L_y - R\theta^\circ$ with unit vectors \mathbf{A} and \mathbf{B} of respective length $L_x a$ and $L_y b$ and rotated with respect to (\mathbf{a}, \mathbf{b}) by an angle θ (this is Wood's notation (Wood (1964))). In practice, the angle is often dropped, which is what I shall do in the following. The full notation is thus

$$X/X'(hkl)L_x \times L_y$$

where X is the adatom species, X' the semiconductor species, (hkl) the cleaving plane in Miller indices, and L_x and L_y the relative length with respect to the smaller unit cell. Examples for $X/\text{Si}(111)\sqrt{3} \times \sqrt{3}$ and $Y/\text{Si}(111)3 \times 3$ are illustrated in Fig. 3.2. By definition, the dangling bonds form a 1×1 lattice. A letter c in front of $L_x \times L_y$ means that there is an additional atom at the *center* of the adatom unit cell. More terminological details can be found in Wood (1964).

In the following, I will focus on silicon (Si) and germanium (Ge) substrates cleft along the (111) direction. Both Si and Ge crystallize in the diamond structure, a face-centered cubic phase with two atoms per

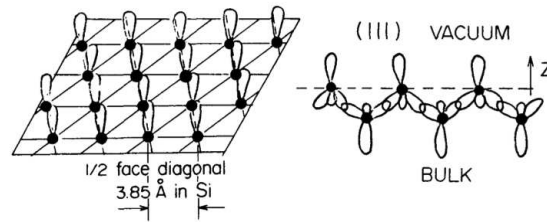


Figure 3.1: Sketch of the silicon orbitals and dangling bonds. *Left*: (111) surface of silicon. *Right*: Side view (from Tosatti and Anderson (1974))

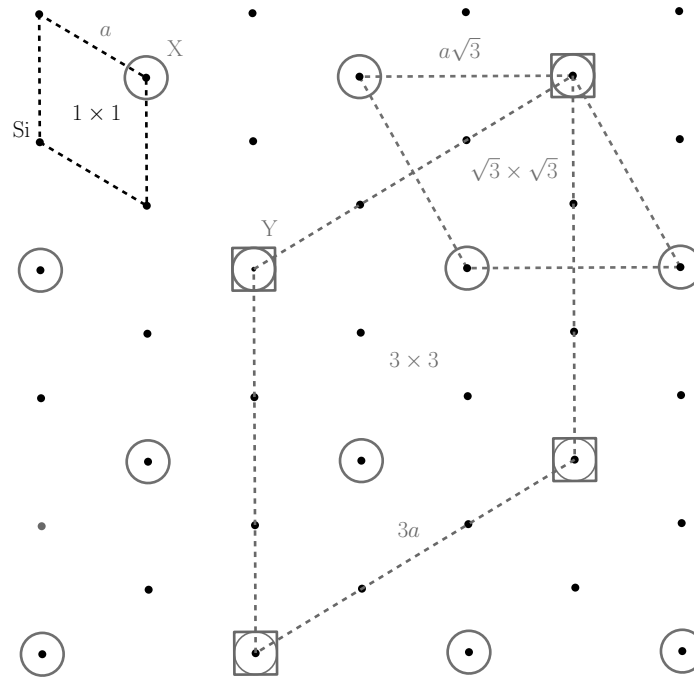


Figure 3.2: Various reconstructions of the silicon surface. Small dots: Si atoms in a triangular lattice. Large circles: $\sqrt{3} \times \sqrt{3}$ adatoms of type X. Large squares: 3×3 adatoms of type Y.

face-centered unit cell; cleaving along the (111) plane leaves one dangling bond per surface Si/Ge atom (as illustrated in Fig.3.1). A clean Si(111) 1×1 surface is not stable, it reconstructs in a 7×7 pattern, a reconstruction which has been observed in real space for the first time by Binnig et al (Binnig *et al.* (1983b)) as one proof of concept of scanning tunneling microscopy (STM, described in appendix H.1.3).

When depositing metallic atoms on top of the surface, a metallic surface state should appear in the absence of reconstruction (X/Si(111) 1×1 phase). However, in most cases, a reconstruction to larger unit cells is more favorable energetically, leading to a more stable, passivated surface which does not lend itself to more instabilities. Tetravalent atoms (of the group IV: C, Sn, Pb, ...) are a notable exception¹. These so-called “ α -phases” reconstruct to the $\sqrt{3} \times \sqrt{3}$ geometry (see Fig. 3.3); their band structure has a metallic band in the band gap according to density functional theory (DFT) in the local density approximation (LDA), as will be explained later in chapter 4, see Fig. 4.1. In the following, I shall restrict to these α -phases.

¹In general, the state of the surface depends on the position of the adatom, the amount of coverage of the surface, and the valence of the adatom.

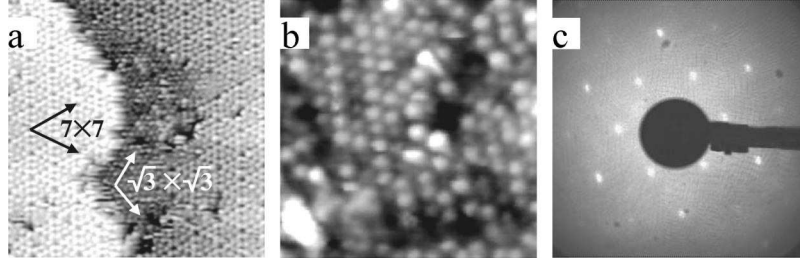


Figure 3.3: C/Si(111) system. *Left*: STM images with 7×7 and $\sqrt{3} \times \sqrt{3}$ regions. *Middle*: zoom on the $\sqrt{3} \times \sqrt{3}$ region. *Right*: LEED pattern (from Pignedoli *et al.* (2004))

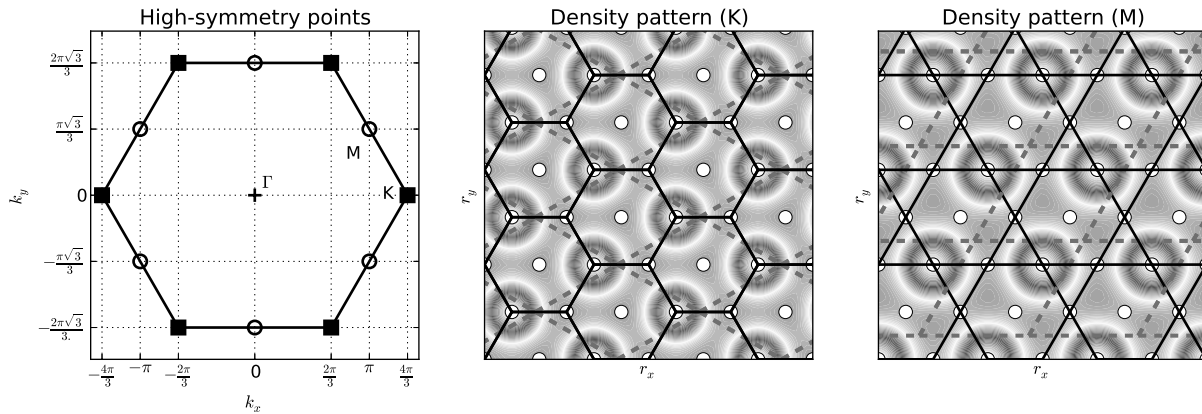


Figure 3.4: *Left*: Brillouin zone of the $\sqrt{3} \times \sqrt{3}$ phase. *Middle and right*: Color plot of the density patterns $\rho(r) \propto e^{i\mathbf{Q}\cdot\mathbf{r}}$ corresponding to $\mathbf{Q} = K$ (3×3 , “honeycomb”) and $\mathbf{Q} = M$ ($2\sqrt{3} \times 2\sqrt{3}$, “Kagome”) symmetries, respectively. The white dots denote adatoms. The dotted lines denote the unit cell.

I now turn to an overview of the relevant experimental literature.

3.2 Experiments on surfaces: a variety of puzzling phases

Surface systems have been probed using various experimental setups including scanning-tunnelling microscopy (STM), angle-resolved photoemission spectroscopy (ARPES), core-level spectroscopy, low-energy electron diffraction (LEED) and electron energy loss spectroscopy (EELS). All of them are particularly suited for α -phases as they are *surface* probes.

In appendix H.1, the reader will find a brief theoretical overview of these probes with a focus on what observables they give access to.

A selection of experimental studies of the α -phases described in subsection 3.1 is summarized in Table 3.1.

Experiments on α -phases with a germanium substrate (Pb/Ge(111) and Sn/Ge(111)) all point to a transition from a $\sqrt{3} \times \sqrt{3}$ phase at high temperatures to a 3×3 phase at low temperatures, namely a commensurate charge-density wave (CDW) order. Signatures of a 3×3 symmetry (illustrated in Fig. 3.4) include: a 3×3 density pattern (STM by Carpinelli *et al.* (1996, 1997)), Bragg peaks of the 3×3 symmetry (LEED by Carpinelli *et al.* (1996); Uhrberg *et al.* (2000b)), two or three components in cPES spectra (Göthelid *et al.* (1995); Uhrberg and Balasubramanian (1998); Avila *et al.* (1999); Uhrberg *et al.* (2000b)), surface-state bands and band back-foldings at the Γ point (ARPES, Uhrberg and Balasubramanian (1998); Avila *et al.* (1999); Uhrberg *et al.* (2000b)). There are also indications of a 3×3 symmetry at high temperatures based on PES, namely two components in cPES spectra (Uhrberg and Balasubramanian (1998); Avila *et al.* (1999)), and indications for surface-state bands in ARPES (Uhrberg and Balasubramanian (1998); Uhrberg *et al.* (2000b)). A significant

| System | Reference | Probe | Main observations |
|------------|------------------------------------|------------------------|---|
| Pb/Ge(111) | Carpinelli <i>et al.</i> (1996) | LEED, EELS, STM | Transition between a metallic $\sqrt{3} \times \sqrt{3}$ phase at high temperature and a gapped phase with 3×3 geometry at low temperature ($T < 250K$) |
| Sn/Ge(111) | Göthelid <i>et al.</i> (1995) | cPES | cPES: two components (room temperature). |
| | Carpinelli <i>et al.</i> (1997) | STM, EELS | Transition between a metallic $\sqrt{3} \times \sqrt{3}$ phase at high temperature and a <i>metallic</i> phase with 3×3 geometry and structural distortion at low temperature ($T < 210K$) |
| | Uhrberg and Balasubramanian (1998) | cPES, ARPES | cPES: two components. ARPES: two surface bands at low temperature (arguably also at high temperature); band back-folding |
| | Avila <i>et al.</i> (1999) | cPES, ARPES | cPES: two components. ARPES: Split surface band at low temperature ($T = 100K$) |
| | Uhrberg <i>et al.</i> (2000b) | LEED, cPES, ARPES | cPES: three components ($T = 70K$). ARPES: Surface-state peaks. |
| Pb/Si(111) | Horikoshi <i>et al.</i> (1999) | RHEED | Streaks of 3×3 symmetry appear in $\sqrt{3} \times \sqrt{3}$ structures upon cooling (and other symmetries) |
| | Slezak <i>et al.</i> (1999) | STM | Transition between 1×1 and $c(5 \times \sqrt{3})$ geometry upon cooling, and the appearance of 3×3 islands within $\sqrt{3} \times \sqrt{3}$ portions of the surface |
| | Custance <i>et al.</i> (2001) | STM | Coexistence of 1×1 and $\sqrt{3} \times \sqrt{3}$ at high temperatures, and of 3×3 and $c(5 \times \sqrt{3})$ at low temperatures |
| Sn/Si(111) | Göthelid <i>et al.</i> (1995) | cPES | cPES: two components (room temperature) |
| | Uhrberg <i>et al.</i> (2000a) | STM, LEED, cPES, ARPES | LEED: $\sqrt{3} \times \sqrt{3}$ symmetry down to low temperature ($T = 70K$). cPES: two major components. ARPES: two surface bands. |
| | Morikawa <i>et al.</i> (2002) | RHEED, STM | STM: $\sqrt{3} \times \sqrt{3}$ phase down to $T = 6K$. RHEED: streaks of 3×3 symmetry at $T = 120K$. |
| | Lobo <i>et al.</i> (2003) | ARPES | Band foldings at low temperature (3×3 symmetry) |
| | Modesti <i>et al.</i> (2007) | STM, cPES, ARPES | STM: $\sqrt{3} \times \sqrt{3}$ down to $T = 5K$, and <i>gapped</i> phase at low temperature. cPES: two components. ARPES: Band back-folding. |
| | Li <i>et al.</i> (2013) | ARPES | Band back-folding |
| C/Si(111) | Pignedoli <i>et al.</i> (2004) | STM | $\sqrt{3} \times \sqrt{3}$ structure (see Fig. 3.3) |

Table 3.1: Summary of experiments on α -phases

difference between Pb/Ge(111) and Sn/Ge(111) at low temperature is that Pb/Ge(111) is gapped (EELS, Carpinelli *et al.* (1996)), while Sn/Ge(111) is not (EELS, Carpinelli *et al.* (1997)).

The situation for α -phases with a silicon substrate is more diverse. While C/Si(111) remains in the $\sqrt{3} \times \sqrt{3}$ symmetry all the way down to low temperatures (Pignedoli *et al.* (2004)), Pb/Si(111) shows clear tendencies to 3×3 ordering at low temperatures (as seen by RHEED (Horikoshi *et al.* (1999)) and STM (Slezak *et al.* (1999); Custance *et al.* (2001))). Sn/Si(111) is the most controversial compound, since STM experiments all point to a $\sqrt{3} \times \sqrt{3}$ symmetry (i.e. no CDW) down to very low temperatures ($T = 5K$, Morikawa *et al.* (2002); Modesti *et al.* (2007)), LEED patterns do not reveal traces of 3×3 symmetry either (down to $T = 70K$, Uhrberg *et al.* (2000a)), whereas PES experiments show signs of 3×3 symmetry at low temperatures (in the form of band back-foldings for ARPES (Uhrberg *et al.* (2000a); Lobo *et al.* (2003); Modesti *et al.* (2007); Li *et al.* (2013)), and two components for cPES (Göthelid *et al.* (1995); Uhrberg *et al.* (2000a); Modesti *et al.* (2007), see Fig.6.5) and even high temperatures in some cases.

3.3 Early theoretical attempts and open puzzles

I start this section by listing the most salient physical facts from a theoretical point of view (3.3.1). Then, I give a short overview of the recent theoretical endeavors on surfaces, before concluding with a list of the yet unanswered questions (3.3.2).

3.3.1 α -phases: important physical facts

As we have seen in the previous section, experiments on α -phases show evidence for metal/insulator transitions as well as various orderings, most notably from the “homogeneous” $\sqrt{3} \times \sqrt{3}$ phase to the ordered 3×3 phase. To theoretically account for these observations, one must bear in mind the following basic facts about α -phases:

1. **Narrow bandwidth and sizable local interaction:** in α -phases (i.e. in a $\sqrt{3} \times \sqrt{3}$ reconstruction), adatoms are very far apart (7\AA for germanium substrates), leading to weak hopping matrix elements:

$$t_{ij} \equiv \iiint_{\mathcal{V}} d\mathbf{r} w_{\mathbf{R}_i}^*(\mathbf{r}) \left(-\frac{\hbar^2}{2m} \nabla^2 + V_{\text{eff}}(\mathbf{r}) \right) w_{\mathbf{R}_j}(\mathbf{r}) \quad (3.1)$$

and thus very narrow bandwidths, i.e. small kinetic energies. Here, $w_{\mathbf{R}_i}(\mathbf{r})$ denotes a wavefunction localized at surface site \mathbf{R}_i (a Wannier function, see appendix J.1.1 for an intuitive explanation), and $V_{\text{eff}}(\mathbf{r})$ is an effective one-body potential, comprising the ionic potential and possibly the Kohn-Sham potential (this is discussed at greater length in appendix 4). Nonetheless, if one were to take an atomic wave function to approximate the Wannier function, one would get a much smaller bandwidth than that computed from density functional theory (DFT), which is of order 0.5 eV. Indeed, the Wannier functions at adatom sites extend quite deeply into the bulk (see Fig. 4.2 for an illustration) so that part of the hopping is mediated by the bulk. Comparatively, the Hubbard U computed from constrained RPA (of the order of 1 eV, see section J.3) is quite large with respect with the bandwidth. This hints at the importance of electron-electron interactions in α -phases.

2. **Long-ranged interactions:** the insulating character of the substrate leads to a *dielectric* screening of the long-range tail of Coulomb interaction:

$$v_{\text{Coul}}(\mathbf{r}) \propto \frac{1}{\epsilon|\mathbf{r}|} \rightarrow v_{\text{screened}}(\mathbf{r}) \propto \frac{1}{\epsilon_{\text{surf}}|\mathbf{r}|}$$

where ϵ_{surf} is related to the bulk dielectric constant ϵ through $\epsilon_{\text{surf}} = \frac{\epsilon+1}{2}$ (screening by an infinite half-plane, I refer the reader to chapter 4 for more details about screening). Thus, contrary to a number of systems where *metallic* screening leads to a very local (Yukawa-type $v(\mathbf{r}) \propto \frac{1}{|\mathbf{r}|} e^{-|\mathbf{r}|/\xi_{\text{TF}}}$) interactions, here the long-range tail of the Coulomb interaction should be taken into account.

3. **Low-dimensions:** the two-dimensional character of surfaces is conducive to Fermi surface instabilities whenever the Fermi surface displays nested portions. These instabilities can conspire with electron-phonon interactions to create charge density waves (Peierls instability), or lead to spin density waves in the presence of (even very weak) local interactions. These arguments are reviewed in appendix I.6.

3.3.2 Beyond the weak-correlation picture and towards realistic calculations

After the first experiments on Pb/Ge, Carpinelli *et al.* (1996) proposed that the observed transition to a low-temperature charge-ordered phase could be accounted for by a weak-coupling charge-density wave (CDW) scenario (this scenario is described in more details in appendix I.6). There is however no compelling evidence that it can explain the variety of behaviors observed in α -phases. Carpinelli *et al.* (1996) already point to electron-electron correlations as necessary ingredients to explain the discrepancies between the experimental results and the predictions of the weak coupling CDW scenario.

A selection of recent theoretical works on α -phases is summarized in Table 3.2. While first-principles DFT calculations investigating the weak-interaction regime have confirmed the existence of a surface band (in Sn/Si, Profeta *et al.* (2000)) and possibility for 3×3 spin-ordering (in C/Si, Profeta and Tosatti (2007)), the influence of local Hubbard interactions has been investigated early on using Hartree-Fock theory (Santoro *et al.* (1998), see paragraph I.6.2.2 in the appendix) and more recently with LDA+ U (Profeta and Tosatti (2007), see subsection J.1.2.2 in the appendix) and many-body techniques beyond Hartree-Fock (Hellberg and Erwin (1999); Schuwalow *et al.* (2010); Li *et al.* (2011, 2013)). In Sn/Si, at large U values, the most stable state is claimed to be either 3×3 (Profeta and Tosatti (2007); Schuwalow *et al.* (2010); Li *et al.* (2013)) or $2\sqrt{3} \times 2\sqrt{3}$ (Li *et al.* (2011)). Distorted (charge-ordered) 3×3 phases are obtained only within LDA+ U for weaker U values.

Santoro *et al.* (1998) have been the first to stress the relevance of nonlocal interactions (parametrized by V). On the basis of Hartree-Fock calculations (see paragraph I.6.2.2), they find that while no CDW phase can be stabilized in the absence of U and V (except as a secondary instability of a spin-density wave (SDW) in the presence of electron-phonon interactions), at moderate U and V values a variety of orders can be found. In particular, for moderate U values (and small V values), SDWs can be stabilized. For moderate U and V values, a CDW is found to be the most stable phase. Finally, in the large U limit, Mott physics (with spin ordering on top) dominate.

3.3.3 Theoretical wish-list

The theoretical approaches summarized in the previous subsection call for further effort in two main directions:

- **Ab initio determination of effective parameters:** while the kinetic parameters have been quite accurately determined using DFT-type methods, a proper derivation of the effective interaction parameters (be it their strength or their range) from first principles, *i.e.* without fitting parameters, is essential in view of the variety of phenomena observed in various α -phases.
- **Appropriate treatment (strong) long-range interactions:** so far, nonlocal interactions have been treated only at the Hartree-Fock level, whereas local interactions U have been treated at the DMFT level. A many-body treatment of nonlocal interactions is also possible, and potentially important.

In the next three chapters, I will present our work in both directions.

Table 3.2: Theory summary

| Reference | System | Low-energy model | Method | U/V | Main findings |
|--------------------------------|------------------|--|--|--|---|
| Santoro <i>et al.</i> (1998) | α -phases | single-band extended Hubbard model + electron-phonon | Hartree Fock + strong-coupling limit | whole phase diagram | V -driven CDW, U -driven SDW, Mott+magnetic phase at large U |
| Hellberg and Erwin (1999) | K/Si(111)-B | Hubbard model | Mean-field + Finite-size diagonalization | $U = 1.2$ eV $U_c \approx 0.95$ eV | Mott insulator |
| Profeta <i>et al.</i> (2000) | Sn/Si | “Kohn-Sham” | DFT (LDA) | - | Surface (metallic) band. Agreement of calculated STM profile with experiment |
| Profeta and Tosatti (2005) | C/Si | “Kohn-Sham” | DFT (LSDA) with various symmetries | - | Most stable: 3×3 phase with 3 inequivalent sites (doubly, singly occupied, and empty site with AF order) |
| Profeta and Tosatti (2007) | Sn/Si and Sn/Ge | “Kohn-Sham” | DFT (LDA+ U) | $U \approx 4$ eV ($U_c \approx 2$ eV) | Magnetic (3×3 AF), undistorted insulators. Note: Sn/Ge: 3×3 distortion for smaller U values |
| Schuwalow <i>et al.</i> (2010) | Sn/Si and Sn/Ge | single and multi-band Hubbard model | DFT + [(C)DMFT / slave boson] | $U_{c(\text{Sn/Si})}^{\text{DMFT}} \approx 0.6$ eV | Weak-coupling: spin ordering. Realistic coupling: Mott AF state |
| Li <i>et al.</i> (2011) | Sn/Si | single-band Hubbard model | DFT + [DMFT / dual-fermion / VCA] | $U_c^{\text{DF}} \approx 0.65$ eV | Increasing U : from 3×3 to $2\sqrt{3} \times 2\sqrt{3}$ (stripe) AF order |
| Li <i>et al.</i> (2013) | Sn/Si | single-band Hubbard model | DFT + CDMFT | $U \approx 0.66$ eV | 3×3 AF spiral order, band backfoldings |

Ab initio effective kinetic and interaction parameters for α -phases

In the previous chapter, I have underlined the need for a parameter-free determination of the properties of various surface systems. A first step towards this goal is the computation of effective kinetic and interaction parameters for the low-energy model.

In this chapter, I will show how the effective kinetic and interaction parameters have been determined *from first principles* for a family of surface systems, namely the X/Si(111) family, with X = Pb, Sn, Si, C.

I will use these results, obtained by Philipp Hansmann, in the next two chapters which are dedicated to the solution of the low-energy models derived here.

4.1 How to describe materials in a realistic way?

The physics of electrons in a solid at equilibrium is determined, if the ionic cores are assumed to be fixed, by the following Hamiltonian:

$$H_{\text{ES}} \equiv \iiint_{\mathcal{V}} d\mathbf{r} \psi^\dagger(\mathbf{r}) \left(-\frac{\hbar^2 \nabla^2}{2m} + V_{\text{ext}}(\mathbf{r}) \right) \psi(\mathbf{r}) + \frac{1}{2} \iiint_{\mathcal{V}} d\mathbf{r} \iiint_{\mathcal{V}} d\mathbf{r}' \psi^\dagger(\mathbf{r}) \psi^\dagger(\mathbf{r}') v_{\text{Coul}}(\mathbf{r} - \mathbf{r}') \psi(\mathbf{r}') \psi(\mathbf{r}) \quad (4.1)$$

$V_{\text{ext}}(\mathbf{r})$ contains the ionic potential (specific to each material) and (optionally) external driving fields, m is the electron mass, \mathcal{V} denotes the solid's volume, $v_{\text{Coul}}(\mathbf{r} - \mathbf{r}') = \frac{e^2}{|\mathbf{r} - \mathbf{r}'|}$ is the (bare) Coulomb interaction, and $\psi^\dagger(\mathbf{r})$ and $\psi(\mathbf{r})$ are fermionic field operators. \mathbf{r} denotes the continuous real-space coordinate. As explained in appendix J.1, if it were not for the second term, one could write H_{ES} as a sum of one-body Hamiltonians describing independent electrons, and thus compute the many-body state of any solid (neglecting phonons) from the mere knowledge of V_{ext} .

When electron-electron interactions do not vanish, however, H_{ES} can no longer be directly diagonalized. The quartic term (term with four fermionic fields) makes it non-separable.

Traditionally, there have been two strategies to deal with this problem:

- **Keep all degrees of freedom and construct a “representative” one-body Hamiltonian** h_{eff} that can reproduce some properties of the many-body Hamiltonian H_{ES} . This is the essence of density functional theory (DFT), whose basic principles are reminded in appendix J.1.
- **“Integrate out” the high-energy degrees of freedom to get a low-energy many-body Hamiltonian** (such as the Hubbard model, which has been introduced in chapter 2) which, despite its many-body

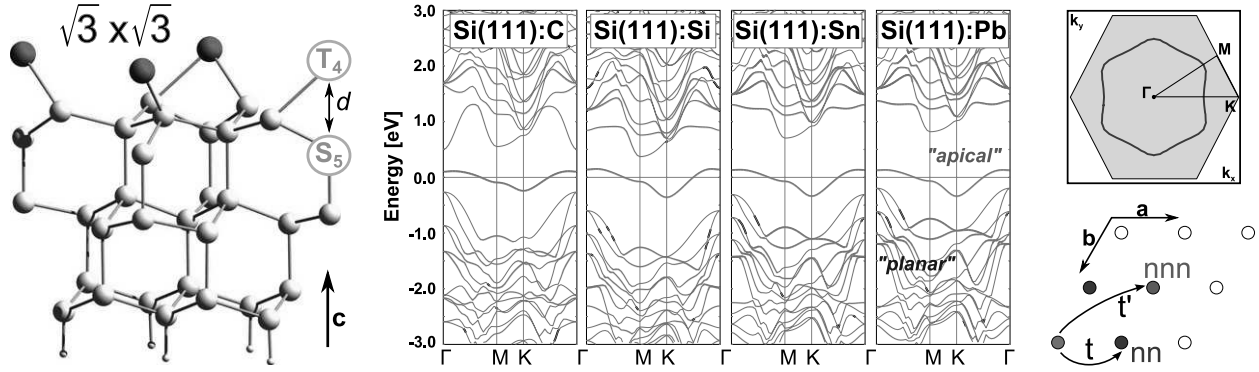


Figure 4.1: *Left:* Slab geometry. *Middle:* Low-energy band structure $\epsilon(\mathbf{k})$ for four adatom systems. *Right:* shape of the Fermi surface (top) and tight-binding hopping parameters (bottom) (from Hansmann *et al.* (2013b))

character, can still be solved in an approximate way by adequate techniques thanks to its reduced number of degrees of freedom. In practice, in this second approach, the low-lying Hamiltonian is often a clever educated guess whose parameters (*e.g.* the strength and range of interaction parameters) are usually chosen with a certain degree of arbitrariness for lack of a controlled procedure to perform the actual renormalization procedure, so that material specificities are lost in the process.

This apparent contradiction – density-functional theory vs. low-energy many-body theory – is currently being challenged by the development of methods such as the constrained random-phase approximation (cRPA) which aim at constructing low-energy models from the first principles, *i.e.* at deriving the low-energy many-body Hamiltonian starting from the mere crystal structure of the solid, as encoded in H_{ES} . The low-energy model – whose parameters are now material-specific – can then be dealt with using appropriate many-body techniques. In the next section, I describe how to determine the kinetic parameters of this low-energy model.

4.2 *Ab initio* kinetic parameters from density-functional theory

Density functional theory is a powerful first-principles technique which is routinely used to compute the ground-state energy of a wide class of materials (more details can be found in appendix J.1). Although it is strictly speaking not designed to give spectral information, it can nevertheless be used as a starting point for a low-energy many-body computation.

In this section, I present density-functional theory results for α -phases obtained by Philipp Hansmann and published in Hansmann *et al.* (2013b,a). They are summarized in Fig. 4.1. The substrate-adatom system has been represented by a silicon slab with three bilayers covered with adatoms at $1/3$ monolayer coverage in the $\sqrt{3} \times \sqrt{3}$ geometry. All adatoms occupy the T_4 sites, except carbon (C) adatoms which occupy the subsurface site S_5 , as shown in the left panel of Fig. 4.1. The band structure obtained using the Vasp (for the structural relaxation) and Wien2k (for the band structure itself) electronic structure packages is shown in the middle panel. The Kohn-Sham bands $\epsilon_n^{KS}(\mathbf{k})$ consist in high-energy bands with mostly planar character (the blue intensity is proportional to $\langle \psi_{\mathbf{k}n} | w_{\mathbf{k},\text{planar}} \rangle$, where $w_{\mathbf{k},\text{planar}}$ is a Wannier function with planar geometry), and a well-separated, single, low-energy, metallic band with predominantly apical character (red intensity; the corresponding Wannier function is shown in Fig. 4.2).

The dispersion of this band is well fitted by a tight-binding dispersion on a triangular lattice given by:

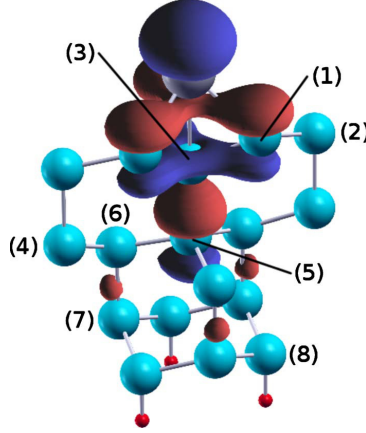


Figure 4.2: Adatom Wannier function. The turquoise and grey spheres are substrate and ad atoms, respectively. The blue and red volumes represent the negative and positive lobes of the Wannier function (from Schuwalow *et al.* (2010)).

| (meV) | Pb | Sn | Si | C |
|------------|-----|-----|-----|-----|
| t_{nn} | 42 | 42 | 50 | 38 |
| t_{nnn} | -20 | -20 | -23 | -15 |
| t_{nnnn} | 10 | 10 | 5 | 0.5 |

Table 4.1: Tight-binding parameters for the 4 adatom systems

$$\begin{aligned}
 \varepsilon(\mathbf{k}) &= 2t_{nn} \left(\cos(k_x) + 2 \cos(k_x/2) \cos(k_y \sqrt{3}/2) \right) \\
 &+ 2t_{nnn} \left(\cos(k_x \sqrt{3}) + 2 \cos(3k_x/2) \cos(k_y \sqrt{3}/2) \right) \\
 &+ 2t_{nnnn} \left(\cos(2k_x) + 2 \cos(k_x) \cos(k_y \sqrt{3}) \right)
 \end{aligned} \tag{4.2}$$

with t_{nn} and t_{nnn} defined in Fig. 4.1. This determines the kinetic parameters of the low-energy model, which are summarized in Table 4.1 for the four compounds under study.

As we will see from quantitative estimates of the interactions in the next section, the low-lying band is very narrow compared to the interaction value, so that correlation effects are expected to be strong and a dedicated many-body treatment must be applied.

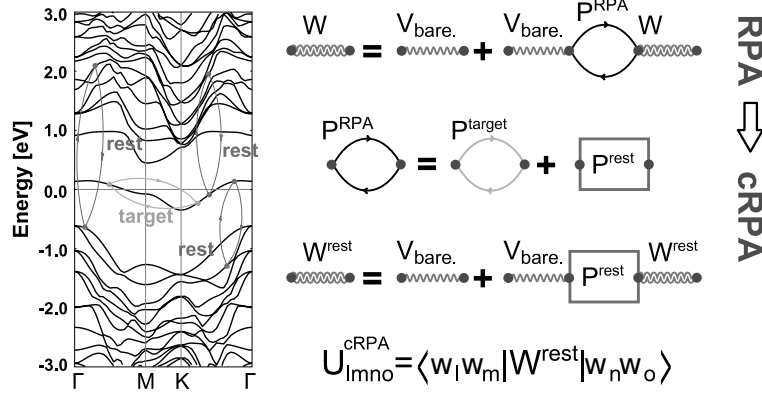
4.3 Constrained RPA (cRPA): Application to surfaces

4.3.1 cRPA in a nutshell

The constrained random-phase approximation (Aryasetiawan *et al.* (2004)), described in detail in appendix J.3, consists in computing Hubbard's U (or extended/multiorbital generalization thereof) by partially screening the long-ranged Coulomb interaction $v_{\text{Coul}}(\mathbf{r} - \mathbf{r}')$. The partially screened interaction is defined as:

$$W_{\text{rest}}(\mathbf{r}, \mathbf{r}', \omega) \equiv \iiint_{\bar{\mathbf{r}}} v_{\text{Coul}}(\mathbf{r}, \bar{\mathbf{r}}, \omega) \left\{ 1 - \int_{\mathbf{r}''} v_{\text{Coul}}(\mathbf{r}, \mathbf{r}'') P_{\text{rest}}(\mathbf{r}'', \mathbf{r}', \omega) \right\}_{\bar{\mathbf{r}}, \mathbf{r}'}^{-1} \tag{4.3}$$

where P_{rest} contains screening originating from high-energy pair-hole creation processes, illustrated in red in the left panel of Figure 4.3: P_{rest} is the random-phase approximation's "bubble" where particle-hole processes

Figure 4.3: the cRPA method. From Hansmann *et al.* (2013b)

within a low-energy “target” space have been removed. Hubbard’s U is computed by taking matrix elements of W_{rest} in a Wannier (localized) basis $\{w_{\mathbf{R}a}\}$ (a is an orbital index and \mathbf{R} a Wannier site index):

$$U_{abcd}^{\mathbf{R}_1\mathbf{R}_2\mathbf{R}_3\mathbf{R}_4}(\omega) = \langle w_{\mathbf{R}_1a} w_{\mathbf{R}_2b} | W_{\text{rest}}(\mathbf{r}, \mathbf{r}', \omega) | w_{\mathbf{R}_3c} w_{\mathbf{R}_4d} \rangle$$

The resulting interaction $U_{abcd}^{\mathbf{R}_1\mathbf{R}_2\mathbf{R}_3\mathbf{R}_4}(\omega)$ is:

1. **frequency dependent**, *i.e.* it includes retardation effects coming from high-energy modes. This indicates that generically, Hubbard’s U is *dynamical*. While it is the case in some materials (see for instance the material studied in chapter 12), in the case of surface systems, this frequency dependence is weak compared to the energy scales given by the kinetic and interaction parameters;
2. in general, **shorter-ranged** than v_{Coul} (this can be understood intuitively within a simpler screening model, see the discussion on the Thomas-Fermi approximation in subsection J.3.1 of the appendix). For some systems, this an *a posteriori* justification for restraining the range of interactions in the correlated subspace to *local* interactions (as done in the Hubbard model). In α -phases, however, while the value of the local interaction is indeed reduced with respect to the bare Coulomb value, longer-range matrix elements are not negligible.

4.3.2 cRPA in α -phases: the importance of long-range interactions

In α phases, the low-energy subspace contains only one band: the interaction matrix is of the form $U^{\mathbf{R}_1\mathbf{R}_2\mathbf{R}_3\mathbf{R}_4}$. Only the density-density terms are non-negligible, so that I adopt the simplified notation:

$$v_{\text{screened}}(\mathbf{R}, \tau) \equiv U_{\mathbf{R},0,0,\mathbf{R}}(\tau) \quad (4.4)$$

Figure 4.4 presents the interaction parameters obtained for 4 adatom systems from cRPA (Hansmann *et al.* (2013b,a)).

Going from lead to carbon, the local screened interactions (Hubbard’s U , red squares) increase from 0.9 eV to 1.4 eV, while the nearest-neighbor screened interactions (denoted by V , blue squares) are virtually constant, $V = 0.5$ eV. Before interpreting this trend, let us note that (a) Hubbard’s U is very large compared to the bandwidth (see Fig. 4.1) and (b) the nearest-neighbor interaction V is sizable compared to U : an extended Hubbard modelling is required.

Interestingly, the image-charge estimate $v \cdot \frac{\epsilon_{\text{Si}+1}}{2}$ for the screened interaction yields the same results as cRPA for nearest-neighbor interactions (pale blue squares), whereas it fails to reproduce the cRPA value for the local interactions. This can be ascribed to the large intersite distance between adatom sites: since there is

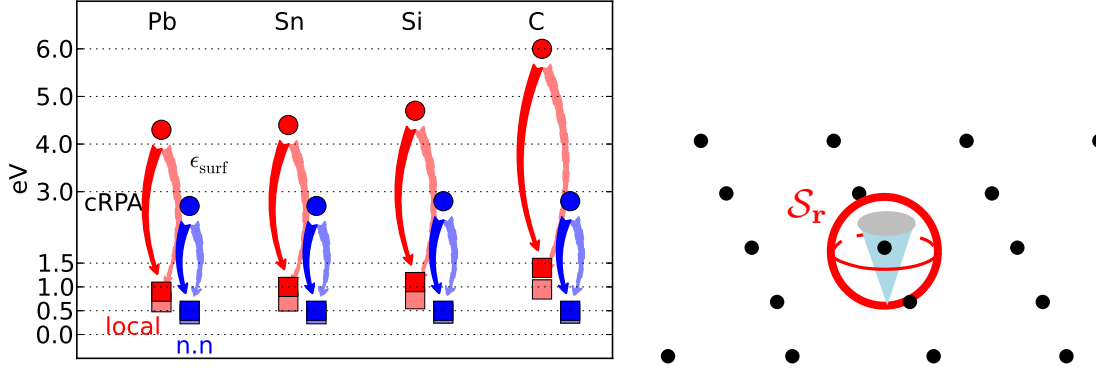


Figure 4.4: *Left*: Interaction parameters from cRPA. The red (blue) disks represent the bare onsite (nearest-neighbor) interaction (local matrix elements of v_{Coul}), while the red (blue) squares represent the screened onsite (nearest-neighbor) interaction computed from cRPA. The pale squares represent the screened interaction computed from a surface image charge estimate $v_{\text{screened}} = v_{\text{bare}}/\epsilon_{\text{surf}}$, with $\epsilon_{\text{surf}} = (\epsilon_{\text{Si}} + 1)/2$, ϵ_{Si} being the relative dielectric permittivity of silicon ($\epsilon_{\text{Si}} = 11.68$). *Right*: sketch of the Gauss surface (see Eq.4.5). The blue cone stands for the Wannier function (Fig. 4.2).

| (eV) | Pb | Sn | Si | C |
|------|-----|-----|-----|-----|
| U | 0.9 | 1.0 | 1.1 | 1.4 |
| V | 0.5 | 0.5 | 0.5 | 0.5 |

Table 4.2: Interaction parameters for the 4 adatom systems

almost no overlap between the Wannier functions of neighboring sites, one can apply Gauss's theorem to obtain the electrostatic potential at a distant site:

$$\oiint_{\mathcal{S}_r} \mathbf{E} \cdot d\mathbf{S} = \iiint_{\gamma_r} \frac{\rho(\mathbf{r})}{\epsilon_{\text{surf}}} d\mathbf{r} = -\frac{e}{\epsilon_{\text{surf}}} \quad (4.5)$$

where \mathcal{S}_r ($\mathbf{r} > \mathbf{r}_{\text{Wannier}}$) is a surface containing the whole charge of the Wannier function (see Fig.4.4, right panel), so that $E(\mathbf{r}) = -e/(4\pi\epsilon_{\text{surf}}|\mathbf{r}|^2)$ and hence

$$v_{\text{screened}}(\mathbf{r}) = \frac{e^2}{4\pi\epsilon_{\text{surf}}|\mathbf{r}|} = \frac{v(\mathbf{r})}{\epsilon_{\text{surf}}}, \quad (\mathbf{r} > \mathbf{r}_{\text{Wannier}}) \quad (4.6)$$

Since for $\mathbf{r} > \mathbf{r}_{\text{Wannier}}$, $E(\mathbf{r})$ is an integrated quantity, it does not depend on the specific shape of the Wannier functions. Conversely, the local Hubbard U depends on the details of the Wannier functions (see e.g. Eq. J.34).

An important consequence of this remark is that one can use Eq. (4.6) to see that the (partially) screened interaction is long-ranged, so that one can parametrize the full interaction as:

$$v_{\text{screened}}(\mathbf{R}) = U_X \delta_{\mathbf{R}} + V_X \frac{a}{|\mathbf{R}|} (1 - \delta_{\mathbf{R}}) \quad (4.7)$$

with $X = \text{Pb, Sn, Si, C}$. In this study, we neglect the frequency-dependence of v_{screened} after checking that it is relatively weak. The specific values for each adatom (illustrated in Fig. 4.4) are tabulated in Table 4.2.

4.4 Conclusion: an extended Hubbard model with long-range interactions

In the end, one is thus facing the following low-energy Hamiltonian, obtained from the first principles:

$$H_{\text{EHM}} = \sum_{ij} t_{ij} c_i^\dagger c_j + \frac{1}{2} \sum_{ij} v_{ij} n_i n_j \quad (4.8)$$

where latin indices denotes Bravais lattice (or Wannier) sites $i \equiv \mathbf{R}_i$, c_i^\dagger and c_i create and annihilate electrons with wavefunction $w_{\mathbf{R}_i}(\mathbf{r})$ (I drop the band index since I am dealing with the surface band of Fig. 4.1 only). t_{ij} is the tight-binding hopping matrix (whose Fourier transform is the bare dispersion $\varepsilon(\mathbf{k})$ given in Eq. 4.2), and v_{ij} is the partially screened interaction, which I have so far denoted as $v_{\text{screened}}(\mathbf{R}_i - \mathbf{R}_j)$. In the following chapters, I shall drop the “screened” subscript because I shall henceforth work only the low-energy correlated subspace, where v_{screened} plays the role of a bare interaction. The transcription of Eq. (4.7) in this new notation is

$$v_{ij} = U\delta_{ij} + V \frac{a}{|\mathbf{R}_i - \mathbf{R}_j|} (1 - \delta_{ij}) \quad (4.9)$$

This Hamiltonian is called the extended Hubbard model. In the next chapter, I shall present two methods to solve this Hamiltonian. These methods will then be applied to surface systems (chapter 6).

Nonlocal interactions: Extended Dynamical Mean Field Theory and combined GW and Extended Dynamical Mean Field Theory

In the previous chapter, we have seen that systems of adatoms on semiconducting surfaces cannot be described only by local interactions. There, the repulsion between electrons located on distant sites cannot be neglected, which is the source of interesting physical phenomena such as charge ordering. To solve the corresponding low-energy model, the extended Hubbard model, new methods beyond dynamical mean field theory must be used.

In this chapter, I briefly present two extensions of DMFT aimed at treating these nonlocal interactions, “extended DMFT” (EDMFT) (section 5.1) and the combination of *GW* with EDMFT, *GW*+EDMFT (section 5.2). These methods are applied to the extended Hubbard model on the square lattice in section 5.3.

The corresponding results are published in *Ayral et al.* (2012, 2013); *Huang et al.* (2014) (included in chapter O).

The application to α -phases will be the topic of the next chapter (chapter 6).

5.1 Extended Dynamical Mean Field Theory (EDMFT)

Extended DMFT (Sengupta and Georges (1995); Kajueter (1996); Si and Smith (1996)) applies to models with “extended” interactions such as the extended Hubbard model,

$$H_{\text{EHM}} = \sum_{ij,\sigma} t_{ij} c_{i\sigma}^\dagger c_{j\sigma} + \frac{1}{2} \sum_{ij} v_{ij} n_i n_j \quad (5.1)$$

where t_{ij} is the tight-binding hopping matrix (e.g. $t_{ij} = -t\delta_{\langle ij \rangle}$ for nearest-neighbor hopping only) and v_{ij} is the interaction matrix, containing possibly local and nonlocal interactions. In the case of local interactions only, $v_{ij} = U\delta_{ij}$, and one recovers the Hubbard model introduced in chapter 2 (Eq. (2.6)). If, furthermore, there is a repulsion between electrons on neighboring sites, $v_{ij} = U\delta_{ij} + V\delta_{\langle ij \rangle}$. On a square lattice, the Fourier transform reads $v_{\mathbf{q}} = U + 2V(\cos(q_x) + \cos(q_y))$. In particular, this interaction is minimum at $\mathbf{q} = (\pi, \pi)$. True long-ranged interactions can also be considered – this will be done in chapter 6.

To solve this problem, one encounters the same difficulties as for the Hubbard model, with the extra complexity brought by the nonlocal interactions. A first straightforward step is to treat the nonlocal interactions separately from the local ones, for instance at the Hartree level, and perform plain-vanilla DMFT calculations on top. This is what is done for instance in *Pietig et al.* (1999).

5.1.1 Introducing bosonic variables: the Hubbard-Stratonovich transformation

Another more sophisticated possibility is to consider the four-fermion interaction term $\frac{1}{2}v_{ij}n_in_j$ not as purely fermionic, but as the exchange of an auxiliary boson between two pairs of fermions. Then, appropriate approximations can be applied to this bosonic mode, with the hope that approximations made on the bosonic mode will nonetheless lead to nontrivial effects on the remaining fermionic modes.

Mathematical substance is given to this intuition by the Hubbard-Stratonovich transformation (Hubbard (1959)):

$$e^{\int_0^\beta d\tau \sum_{ij} \frac{1}{2} v_{ij} n_{i\tau} n_{j\tau}} = \int \mathcal{D}[\phi] e^{-\int_0^\beta d\tau \frac{1}{2} \sum_{ij} \phi_{i\tau} [-v^{-1}] \phi_{j\tau} \pm \int_0^\beta \sum_i \phi_{i\tau} n_{i\tau}} \quad (5.2)$$

where $\phi_{i\tau}$ is a real bosonic periodic field. Thus, one has traded a nonlocal interaction term (in the left-hand side) for a propagating boson with bare propagator v coupled to the fermionic density by a local electron-boson coupling term $\int_0^\beta \sum_i \phi_{i\tau} n_{i\tau}$ (in the right-hand side).

In essence, extended DMFT (EDMFT, Sengupta and Georges (1995); Si and Smith (1996); Kajueter (1996)) consists in transposing the DMFT equations (section 2.2.4) to the bosonic operator, with the transpositions $G \rightarrow W = -\langle \phi \phi \rangle$, $\mathcal{G} \rightarrow \mathcal{U}$, and $\Sigma \rightarrow P$. The bosonic “self-energy”, P , is called the polarization; it is related to the charge susceptibility, $\chi(\mathbf{q}, i\omega)$ (defined as the Fourier transform of $\chi_{ij}(\tau) \equiv \langle n(\tau)n(0) \rangle_{\text{conn}}$), by the exact equation (see appendix C)

$$P(\mathbf{q}, i\Omega) = \frac{-\chi(\mathbf{q}, i\Omega)}{1 - v(\mathbf{q})\chi(\mathbf{q}, i\Omega)}$$

The same cavity construction that led to the impurity action Eq. (2.14) yields the following impurity model (see *e.g.* Ayrál *et al.* (2013)):

$$S_{\text{imp}} = \iint_0^\beta d\tau d\tau' \bar{c}(\tau) \left\{ -\mathcal{G}^{-1}(\tau - \tau') \right\} c(\tau') + \frac{1}{2} \iint_0^\beta d\tau d\tau' \mathcal{U}(\tau - \tau') n_\tau n_{\tau'} \quad (5.3)$$

This describes an impurity with dynamical interactions $\mathcal{U}(\tau - \tau')$ which, like the fermionic Weiss field \mathcal{G} , are computed self-consistently. Note that the bosonic field ϕ has been integrated out. EDMFT thus consists in transposing a problem with nonlocal spatial interactions to an effective problem with nonlocal *temporal* interactions.

The impurity model with retarded interactions can be solved efficiently using continuous-time quantum Monte-Carlo (CTQMC) algorithms as described in chapter 11.

5.1.2 Summary: set of EDMFT equations

The self-consistent EDMFT algorithm, illustrated in Fig. 5.1, consists in the following steps:

1. Start with an initial self-energy $\Sigma_{\text{imp}}(i\omega)$ and polarization $P_{\text{imp}}(i\Omega)$ ($i\Omega$ denotes a bosonic Matsubara frequency)
2. Compute the local fermionic and bosonic Green’s functions G and W using Dyson’s equations:

$$G_{\text{loc}}(i\omega) = \sum_{\mathbf{k} \in \text{BZ}} \frac{1}{i\omega + \mu - \varepsilon(\mathbf{k}) - \Sigma_{\text{imp}}(i\omega)} \quad (5.4)$$

$$W_{\text{loc}}(i\Omega) = \sum_{\mathbf{q} \in \text{BZ}} \frac{v(\mathbf{q})}{1 - v(\mathbf{q})P_{\text{imp}}(i\Omega)} \quad (5.5)$$

3. Compute the fermionic and bosonic “Weiss fields” $\mathcal{G}(i\omega)$ and $\mathcal{U}(i\Omega)$:

$$\mathcal{G}(i\omega) = \left[G_{\text{loc}}^{-1}(i\omega) + \Sigma_{\text{imp}}(i\omega) \right]^{-1} \quad (5.6)$$

$$\mathcal{U}(i\Omega) = \left[W_{\text{loc}}^{-1}(i\Omega) + P_{\text{imp}}(i\Omega) \right]^{-1} \quad (5.7)$$

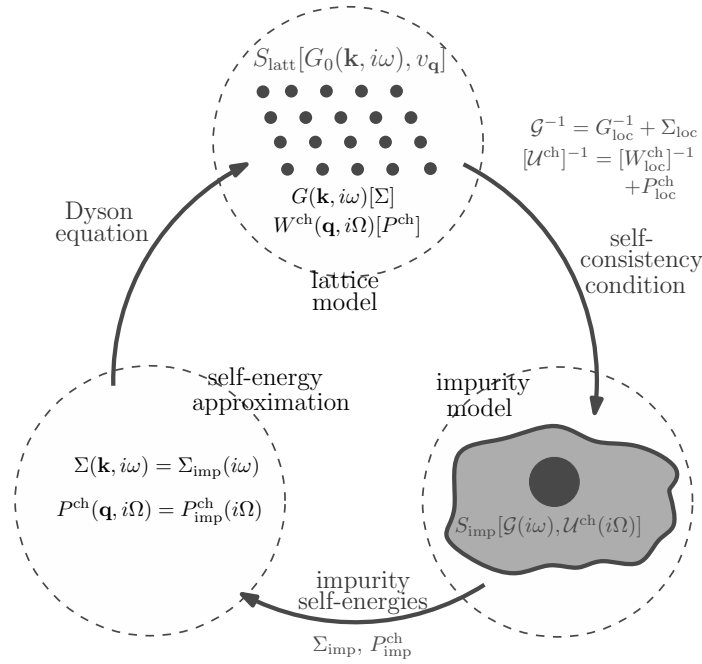


Figure 5.1: The EDMFT loop. It contains, compared to the DMFT loop, presented in Fig. 2.1, an additional self-consistency cycle on bosonic quantities W^{ch} , \mathcal{U}^{ch} , $P_{\text{imp}}^{\text{ch}}$.

4. Solve the impurity model, Eq. (5.3), for $\Sigma_{\text{imp}}(i\omega)$ and $P_{\text{imp}}(i\Omega)$
5. Go back to step 2 until convergence.

$P_{\text{imp}}(i\Omega)$, an observable written only in terms of the bosonic field ϕ , cannot be directly computed from the impurity solver, since the impurity action Eq. (5.3) is written only in terms of fermionic operators. It is computed from the connected charge-charge correlation function of the impurity $\chi_{\text{imp}}(\tau) = \langle n(\tau)n(0) \rangle_{\text{imp}}^{\text{conn}}$ through the relation:

$$P_{\text{imp}}(i\Omega) = \frac{-\chi_{\text{imp}}(i\Omega)}{1 - \mathcal{U}(i\Omega)\chi_{\text{imp}}(i\Omega)} \quad (5.8)$$

If the interactions are local ($v_{\mathbf{q}} = U$), the above equations reduce to the DMFT equations presented in section 2.2.4.

A variant to the above equations has been proposed in Sun and Kotliar (2002). Instead of defining $v(\mathbf{q})$ as the Fourier transform of the total bare interaction term, one can define $\tilde{v}(\mathbf{q})$ as the Fourier transform of nonlocal interactions only, and define a screened interaction $\tilde{W}_{\text{loc}}(i\Omega)$ as $\tilde{W}_{\text{loc}}(i\Omega) = \sum_{\mathbf{q}} \tilde{v}_{\mathbf{q}} (1 - \tilde{v}_{\mathbf{q}} \tilde{P}_{\text{imp}}(i\Omega))^{-1}$. In this case, \tilde{W} contains the screening effects coming from the nonlocal part of interactions only. The retarded interactions are then computed as $\tilde{\mathcal{U}}(i\Omega) \equiv U + [\tilde{W}_{\text{loc}}^{-1}(i\Omega) + \tilde{P}_{\text{imp}}(i\Omega)]^{-1}$. In the following, I shall call this variant “HS-V” (because it formally corresponds to a Hubbard-Stratonovich decoupling of the V -term only), whereas in case of doubt, I shall call “HS-UV” the algorithm presented above.

5.2 Combined GW and Extended DMFT: GW+EDMFT

In DMFT and EDMFT, the self-energy – whether fermionic (Σ) or bosonic (P) – is local. The GW+EDMFT method (Sun and Kotliar (2002, 2004); Biermann *et al.* (2003)) can be seen – in the context of the model calculations presented in this part – as a way of restoring the spatial dependence of the self-energy by adding to the impurity self-energy the first non-trivial nonlocal diagrammatic correction.

The combination of GW with DMFT in the context of realistic calculations, as introduced in Biermann *et al.* (2003), is more ambitious as it takes into account all electronic degrees of freedom; its explanation is deferred to section 12.2.

5.2.1 Motivation: the GW approximation

After applying the Hubbard-Stratonovich transformation to the interaction term of the extended Hubbard model (see subsection 5.1.1), one is facing an electron-boson coupling problem, with a fermionic propagator called G and a bosonic propagator called W . W encodes the charge fluctuations of the system. If the system is close to a charge instability, this should be reflected in W .

The simplest self-energy diagrams corresponding to this action are the following:

$$\Sigma_{i\tau,j\tau'}^{\text{GW}} = -G_{i\tau,j\tau'} W_{i\tau,j\tau'} \quad (5.9a)$$

$$P_{i\tau,j\tau'}^{\text{GW}} = 2G_{i\tau,j\tau'} G_{j\tau',i\tau} \quad (5.9b)$$

The form of Σ – which explains the name “GW approximation” (introduced by Hedin (1965)) – reflects the coupling of the bosonic fluctuations to the fermionic modes. If W has a sharp momentum structure, so should Σ . P is given by the particle-hole excitation processes in the system. To zeroth order in the interaction, it reduces to the charge response of free electrons, called the Lindhard function, $\chi_0 = -2G_0G_0$. The physical content of the Lindhard function is explained in more detail in appendix I.6.1.1. For instance, if large portions of the Fermi surface are parallel to each other (with a vector \mathbf{Q} between them) or “nested”, $\chi_0(\mathbf{q}, i\Omega)$ will be peaked at $\mathbf{q} = \mathbf{Q}$. Thus, through Eqs (5.9a-5.9b), fermionic instabilities feed back on bosonic modes, and vice versa.

However appealing, this approximation to the self-energies turns out to be rather poor in the context of strongly correlated materials. In this regime, “vertex corrections” become important, *i.e.* instead of the bare electron-boson coupling $\lambda = 1$ implied by Eqs (5.9a-5.9b), the *renormalized* electron-boson coupling should be inserted. As will be proven in section 5.3, this coupling largely departs from the bare coupling as the strength of correlations is increased. In part III, this basic fact is taken as the starting point for a new method. For the time being, a simple way of improving on this approximation is to combine it with EDMFT, namely by adding the impurity self-energies to the GW self-energies (subtracting the local part of the latter to avoid double counting some terms).

5.2.2 Summary: set of GW+EDMFT equations

The self-consistent GW+EDMFT algorithm (applied in the context of the extended Hubbard model, Eq. (5.1)), is illustrated in Fig. 5.2. It consists in the following steps:

1. Start with an initial self-energy $\Sigma(\mathbf{k}, i\omega)$ and polarization $P(\mathbf{q}, i\Omega)$
2. Compute the lattice fermionic and bosonic Green’s functions G and W using Dyson’s equations,

$$G(\mathbf{k}, i\omega) = \frac{1}{i\omega + \mu - \varepsilon(\mathbf{k}) - \Sigma(\mathbf{k}, i\omega)}$$

$$W(\mathbf{q}, i\Omega) = \frac{v(\mathbf{q})}{1 - v(\mathbf{q})P(\mathbf{q}, i\Omega)}$$

3. Compute the fermionic and bosonic “Weiss fields” $\mathcal{G}(i\omega)$ and $\mathcal{U}(i\Omega)$

$$\mathcal{G}(i\omega) = \left[G_{\text{loc}}(i\omega)^{-1} + \Sigma_{\text{loc}}(i\omega) \right]^{-1}$$

$$\mathcal{U}(i\Omega) = \left[W_{\text{loc}}(i\Omega)^{-1} + P_{\text{loc}}(i\Omega) \right]^{-1}$$

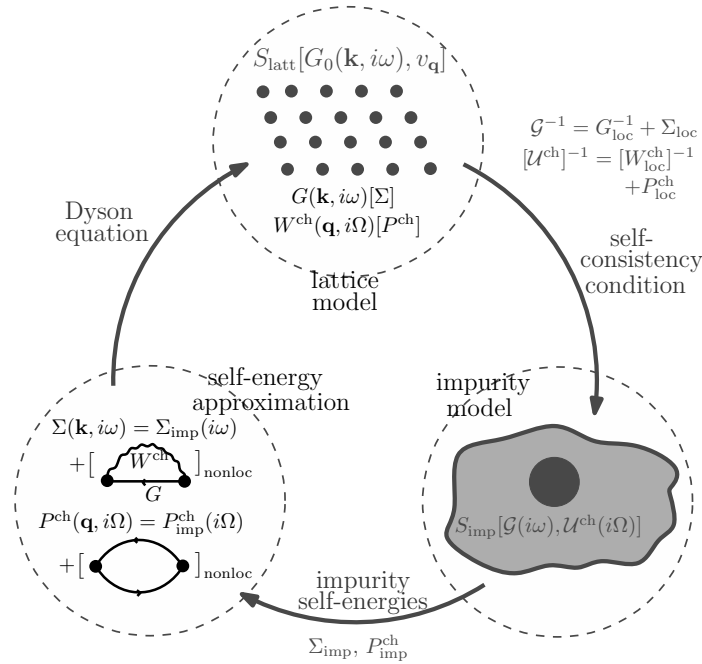


Figure 5.2: The GW+EDMFT loop.

4. Solve the impurity model, Eq. (5.3), for $\Sigma_{\text{imp}}(i\omega)$ and $P_{\text{imp}}(i\Omega)$
5. Compute the momentum dependent self-energies $\Sigma(\mathbf{k}, i\omega)$ and $P(\mathbf{q}, i\Omega)$ as the following combination:

$$\begin{aligned} \Sigma(\mathbf{k}, i\omega) &= \Sigma_{\text{imp}}(i\omega) + \left[- \sum_{\mathbf{q}, i\Omega} G(\mathbf{k} + \mathbf{q}, i\omega + i\Omega) W(\mathbf{q}, i\Omega) \right]_{\text{nonloc}} \\ P(\mathbf{q}, i\Omega) &= P_{\text{imp}}(i\Omega) + \left[2 \sum_{\mathbf{k}, i\omega} G(\mathbf{k} + \mathbf{q}, i\omega + i\Omega) G(\mathbf{k}, i\omega) \right]_{\text{nonloc}} \end{aligned} \quad (5.10)$$

The suffix “nonloc” denotes, for any quantity $X(\mathbf{k}, i\omega)$, $X_{\text{nonloc}}(\mathbf{k}, i\omega) = X(\mathbf{k}, i\omega) - X_{\text{loc}}(i\omega)$.

6. Go back to step 2 until convergence

The charge susceptibility is an interesting physical by-product of this calculation. It can be computed as (see appendix C):

$$\chi(\mathbf{q}, i\Omega) = \frac{-P(\mathbf{q}, i\Omega)}{1 - v(\mathbf{q})P(\mathbf{q}, i\Omega)} \quad (5.11)$$

Contrary to EDMFT, GW+EDMFT does not boil down to DMFT in the case of local interactions $v(\mathbf{q}) = U$.

In the “HS-V” scheme proposed by Sun and Kotliar (2002), since $\tilde{W}(\mathbf{q}, i\Omega)$ does not contain the local part of the interaction, expression (5.10) is supplemented by the second order self-energy contribution with local interactions only ($- [U^2 GGG]_{\text{nonloc}}$).

5.3 Application to the extended Hubbard model on square lattice

In this section, EDMFT and GW+EDMFT are applied to the extended Hubbard model with short-range interactions on the square and cubic lattice. The corresponding papers (Aryal *et al.* (2012), Aryal *et al.* (2013) and Huang *et al.* (2014)) are included in chapter O at the end of this thesis.

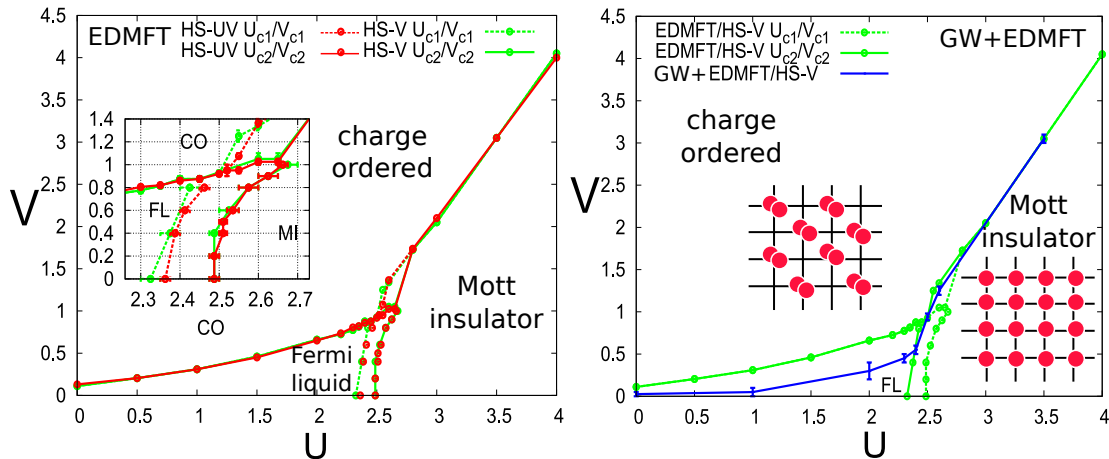


Figure 5.3: (U, V) phase diagram on the square lattice with nearest-neighbor hopping only (in units of the half-bandwidth), $\beta D = 100$. *Left*: EDMFT phase diagram (HS-UV (red) and HS-V (green)). *Inset*: zoom on the Mott transition region. *Right*: $GW+EDMFT/HS-V$ phase diagram (solid blue line). $GW+EDMFT/HS-UV$ is on top of EDMFT/HS-UV within error bars.

Unless otherwise stated, all results are given for the square lattice at half-filling, without frustration, in units of the half-bandwidth, $D = |4t|$. The temperature is kept fixed to $\beta D = 100$. U parametrizes the local Hubbard repulsion, while V parametrizes the nearest-neighbor repulsion.

5.3.1 Phase diagram: charge ordering and effective local interactions

I start this section by giving the final phase diagram in the EDMFT as well as in the $GW+EDMFT$ approximations. I will then explain how this diagram has been mapped out and what is the physical content of each phase.

The (U, V) phase diagram is given in Fig. 5.3. Whether in EDMFT or in $GW+EDMFT$, one can observe three phases:

- At weak values of the local and nearest-neighbor repulsion, one observes a Fermi-liquid (FL) phase characterized by a Fermi-liquid behavior for the self-energy (see top part, panel (b) of Fig. 5.5; the corresponding spectra will be described in the next subsection);
- At weak values of the nearest-neighbor repulsion V but large local interaction U , one observes a Mott insulating (MI) phase driven by the localizing effect of Hubbard's U ; this phase is characterized by a very large low-energy self-energy (see bottom part, panel (b) of Fig. 5.5)
- At large values of the nearest-neighbor repulsion V , the system turns charge-ordered (CO), namely there is a symmetry-breaking where one sublattice is doubly occupied and one sublattice is empty, as depicted in Fig. 5.3. This checkerboard pattern minimizes the Coulomb repulsion stemming from V . Since these calculations are performed in the disordered phases (without breaking the symmetry explicitly), one cannot enter this phase. I will come back to the charge-ordering criterion.

The transition lines in EDMFT and $GW+EDMFT$ are very similar, except for the variant HS-V where the FL-CO transition line is much lower in $GW+EDMFT$ than in EDMFT. This can be ascribed to the fact that in HS-V, the contributions from the local and the nonlocal interactions to the nonlocal self-energy are not summed at the same level: while nearest-neighbor interactions (V) are summed up to infinite order, local interactions (U) are summed to second order only in the nonlocal contribution. In addition, the condition for charge-

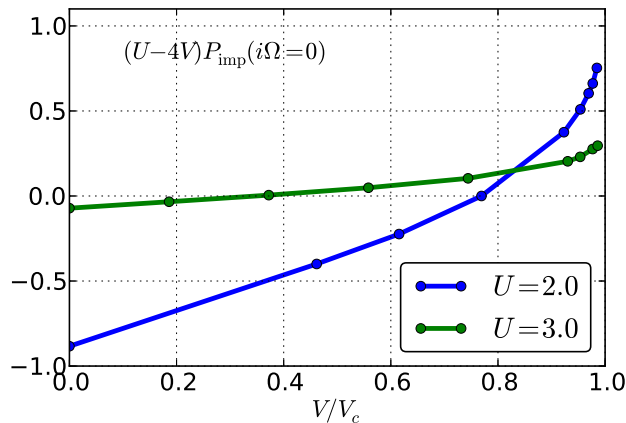


Figure 5.4: Evolution of $(U - 4V)P_{\text{imp}}(i\Omega = 0)$ as a function of V ($V_c(U = 2.0) = 0.65$; $V_c(U = 3.0) = 2.15$).

ordering is different. The FL-MI phase transition is of first-order character. The order of the FL-CO and MI-CO transitions cannot be decided from these calculations since they are limited to the disordered phases.

Charge ordering can in principle be detected by putting a staggered chemical potential or field h coupling to the density on two sublattices, and by looking at the corresponding response $dn_i/dh_j = \langle n_i n_j \rangle = \chi_{ij}$. In EDMFT and GW+EDMFT, the static charge response $\chi(\mathbf{q}, i\Omega = 0)$ is given by Eq. (5.11). In a second-order transition, ordering is signalled by a divergence of $\chi(\mathbf{q}, i\Omega = 0)$ at a given wavevector. In the square lattice, checkerboard charge-ordering is signalled by a divergence at $\mathbf{Q} = (\pi, \pi)$. Thus, one can locate the phase transition by looking at the point where the denominator of χ , $1 - v_{\mathbf{q}}P(\mathbf{q}, i\Omega = 0)$, vanishes, or equivalently when $v_{\mathbf{q}}P(\mathbf{q}, i\Omega = 0) = 1$. In EDMFT and on the square lattice with nearest-neighbor repulsion only, this condition reduces to

$$(U - 4V)P_{\text{imp}}(i\Omega = 0) = 1 \quad (5.12)$$

This quantity is plotted in Fig. 5.4 for two selected values of U . The charge-ordering criterion is met for a given value of V . Indeed, as one increases V , the impurity polarization P_{imp} becomes stronger (see panels (d) in Fig. 5.5). Beyond V_c (and in the near vicinity of V_c), the divergence in the charge susceptibility precludes convergence. The FL-CO and MI-CO transition lines shown in Fig. 5.3 are determined by extrapolating the $(U - 4V)P_{\text{imp}}(i\Omega = 0)$ curve to 1. While the convergence of $(U - 4V)P_{\text{imp}}(i\Omega = 0)$ towards 1 as V is increased is quite gradual in the metallic phase ($U = 2$), this quantity remains quite far from 1 until the close vicinity of V_c in the insulating phase ($U = 3$).

The transition between the Fermi-liquid phase and the Mott insulating phase is of first-order nature as in DMFT, namely there is a region where a metallic and an insulating solution coexist (between the dashed and the solid line), at $U \approx 2.4$ for $V = 0$ (see inset of the left panel in Fig. 5.3). As one increases V , the critical value of the local interaction $U_c(V)$ increases, namely larger V s favor the Fermi-liquid phase over the Mott insulating phase.

Both the transition to the charge-ordered phase and the $U_c(V)$ curve can be intuitively understood by looking at the self-consistently determined dynamical interactions $\mathcal{U}(\omega)$ shown in Fig. 5.6. While $\mathcal{U}(i\Omega)$ (like $P_{\text{imp}}(i\Omega)$ and $W_{\text{loc}}(i\Omega)$) is a real function, $\mathcal{U}(\omega)$ is a complex function whose real and imaginary part are related by the Kramers-Kronig relations (see appendix I.1.2.4). Here, I have obtained $\mathcal{U}(\omega)$ from $\mathcal{U}(i\Omega)$ by Padé analytical continuation (a technique which is described in appendix I.3.1). The real part, shown in panel (a) for different values of V , displays a characteristic screening frequency (of the order of $\omega = 1.5$ for the curves shown) separating a high-energy part close to the bare value $U = 2$ and a low-energy, screened value which strongly depends on V : as V increases, $\text{Re}\mathcal{U}(\omega = 0)$ is more and more reduced. Thus, the effect of nonlocal interactions at the local level is to reduce the effective cost of a double occupancy for processes of energies lower than the screening frequency. The dependence of $\text{Re}\mathcal{U}(\omega = 0)$ on V strongly differs in the

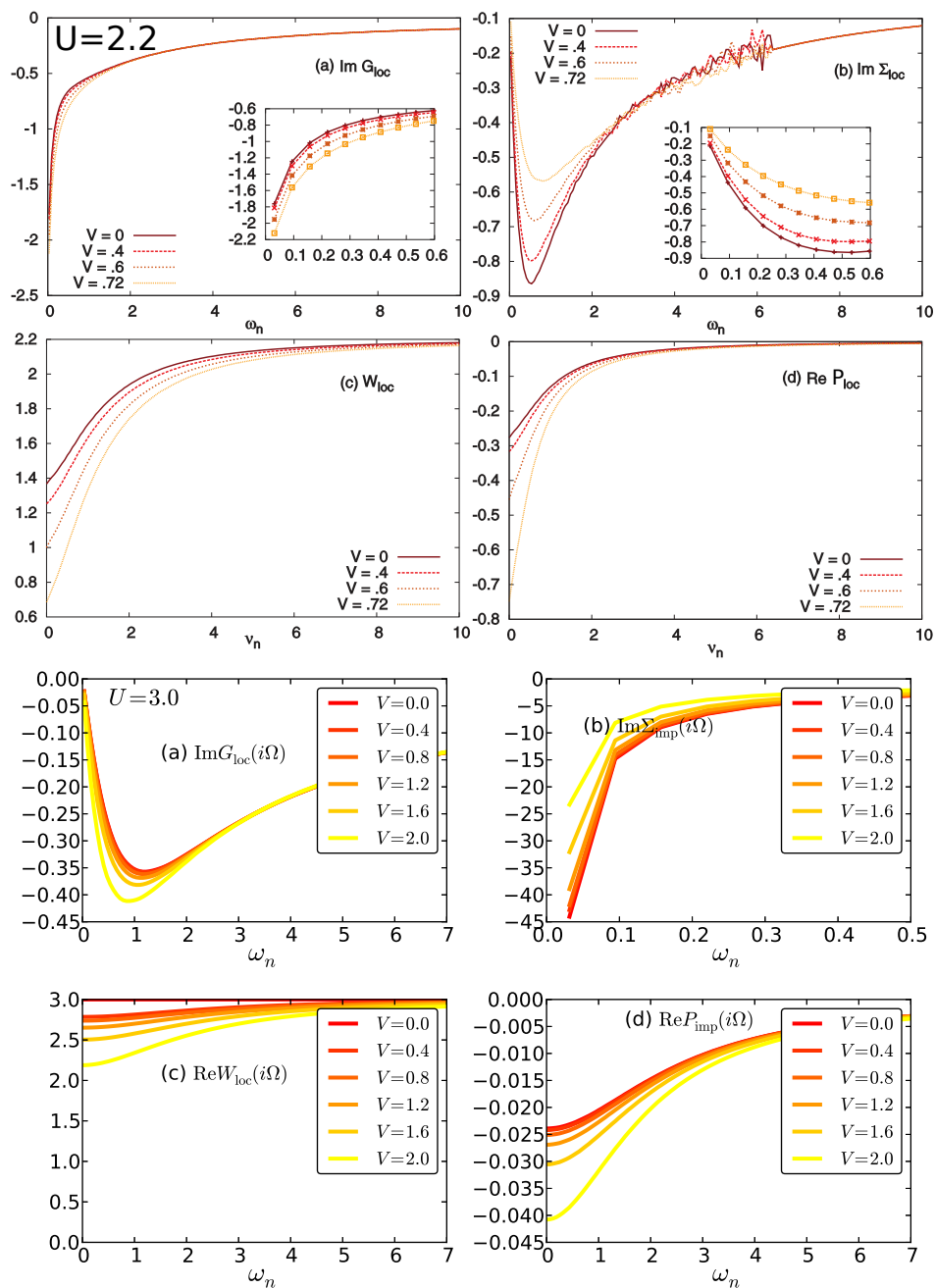


Figure 5.5: Imaginary-frequency data in EDMFT at $U = 2.2$ (top) and $U = 3.0$ (bottom). (a) $\text{Im}G_{\text{loc}}(i\omega)$ (b) $\text{Im}\Sigma_{\text{imp}}(i\omega)$ (c) $\text{Re}W_{\text{loc}}(iv)$ (d) $\text{Re}P_{\text{imp}}(iv)$.

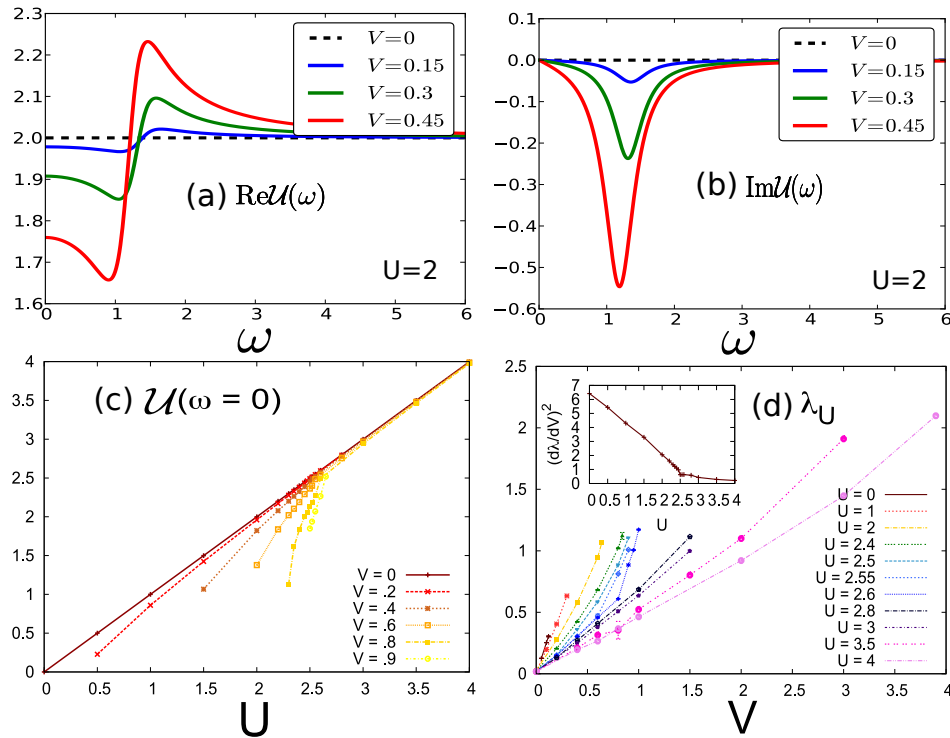


Figure 5.6: Dynamical interactions $\mathcal{U}(\omega)$ in EDMFT on the square lattice. (a) and (b): real and imaginary part (obtained by Padé analytical continuation). (c) Evolution of $\mathcal{U}(\omega = 0)$ as a function of U . (d) Evolution of the “screening strength” λ_U as a function of V . *Inset*: $(d\lambda_U/dV)^2$ as a function of U .

FL and in the MI phase, as shown in panel (c) of Fig. 5.6: the dependence is much stronger in the FL phase. Indeed, the compressibility of a Mott insulator is vanishing, hence screening (which is related to the charge response) is much less efficient.

The strength of the screening can be quantified. Looking at panel (b) in Fig. 5.6, one sees that a measure of the screening strength is given by the following energy scale:

$$\lambda_U \equiv \sqrt{\left| \int_0^\infty \text{Im}\mathcal{U}(\omega) d\omega \right|} \quad (5.13)$$

This is inspired by the simple case of the Holstein model (discussed in more details in subsection 11.1.4.2.2), where Einstein phonons of energy ω_0 coupled to fermions with strength λ give rise to retarded interactions characterized by $\text{Im}\mathcal{U}(\omega) = \lambda^2 (\delta(\omega - \omega_0) - \delta(\omega + \omega_0))$ for which $\lambda_U = \lambda$. In our case, λ_U is seen to be proportional to V far enough from the CO phase transition (panel (d) of Fig. 5.6). The slope, shown in the inset, strongly depends on the phase where it is considered. I shall come back to the dependence of the screening frequency on U and V in subsection 5.3.3.

5.3.2 Spectra: self-consistent and one-shot schemes, the importance of local vertex corrections

In this section, I give an overview of the spectra obtained in EDMFT and $GW+EDMFT$, as well as in various implementations of the GW method. The goal of the latter comparison is to show the importance of local vertex corrections absent in GW .

Fig. 5.7 show spectra obtained at different points of the phase diagram for various self-consistent methods. These spectra have been obtained by MaxEnt analytical continuation (explained in appendix I.3.2) with a slight sophistication due to the dynamical kernel (discussed in Ayrat *et al.* (2013)).

The GW method, summarized in section 5.2.1, always yields metallic spectra, namely spectra with a quasi-particle peak at the Fermi level. The same holds for a variant of the GW method, the quasi-particle GW method (“QPGW”, Kotani *et al.* (2007)), which consists (in this simple model context) in expressing $G(\mathbf{k}, i\omega)$ as

$$G(\mathbf{k}, i\omega) = \left[i\omega + \mu - Z_{\mathbf{k}}(\epsilon_{\mathbf{k}} - \text{Re}\Sigma^{\text{GW}}(\mathbf{k}, i\omega)) \right]^{-1}$$

with the quasiparticle weight $Z_{\mathbf{k}} \approx \left[1 - \text{Im}\Sigma^{\text{GW}}(\mathbf{k}, i\omega_0)/\omega_0 \right]^{-1}$.

The spectra from the EDMFT and GW+EDMFT methods, in contrast, have spectral weight transfers from the quasiparticle peak to incoherent bands as U is increased, and eventually a Mott gap opens (see spectra for $U = 3.5$). The GW+EDMFT spectra are in general slightly less coherent than EDMFT spectra (more weight goes to the high-energy features, see *e.g.* $U = 2$). This trend is more pronounced when inspecting the momentum-dependent spectral function, shown in panel (d) of Fig. 5.7. Another feature can be observed in the spectra in the Mott phase for large values of V , namely when the coupling to the screening modes is important: symmetric high-energy “bumps”, distinct from the Hubbard bands, can be observed at $|\omega| \approx 3$ for $U = 3.5$, $V = 3$ (panel (c)). This is a direct consequence of the frequency-dependence of the interactions $\mathcal{U}(\omega)$. These features are most easily understood in the limit of zero bandwidth, where the impurity Green’s function factorizes as (Florens (2003)):

$$G_{\text{imp}}(\tau) = G_{\text{imp}}(\tilde{U}, \tau)e^{-K(\tau)} \quad (5.14)$$

where $G_{\text{imp}}(U, \tau)$ is the Green’s function computed for static interactions U , and $\tilde{U} = U - 2K'(0)$, the “dynamical kernel” $K(\tau)$ is defined as $K''(\tau) = \mathcal{U}(\tau)$ for $\tau \in [0^+, \beta^-]$ and $K(0) = K(\beta) = 0$. In real frequencies, $G_{\text{imp}}(\omega)$ (and hence $A(\omega)$) is thus given by the convolution of the atomic-limit spectrum with a bosonic kernel with a characteristic screening frequency. It should therefore display, in addition to the Hubbard bands, a series of bosonic shakeoff peaks (Casula *et al.* (2012)). Here, only one of these replicaes is visible.

Finally, Fig. 5.8 gives further insights in the failure of GW to capture incoherent spectral weight transfers to Hubbard bands. Panels (a) and (b) show results obtained from various one-shot calculations, which usually give better spectra in GW applied to realistic materials (see *e.g.* Aryasetiawan and Gunnarsson (1998) for a discussion). In all cases, however, while the GW+EDMFT spectra have emergent Hubbard bands in the correlated metal and full-fledged Hubbard bands in the Mott insulator, the GW spectra are metallic with a very weak renormalization of the quasiparticle peak. The reason for this discrepancy can be traced back to the lack of vertex corrections in GW.

In EDMFT, in contrast, the impurity self-energy, being computed exactly within statistical error in the CTQMC algorithm, can be expressed as¹:

$$\Sigma_{\text{imp}}(i\omega) = - \sum_{i\Omega} G_{\text{imp}}(i\omega + i\Omega) W_{\text{imp}}(i\Omega) \Lambda_{\text{imp}}(i\omega, i\Omega)$$

where $\Lambda_{\text{imp}}(i\omega, i\Omega)$ is the renormalized electron-boson vertex which will be rigorously dealt with in chapter 8. For the time being, one can compute a rough estimate of the order of magnitude of this vertex by defining $\tilde{W}(\tau) = \Sigma_{\text{imp}}(\tau)/G(\tau)$ and then $\tilde{\Lambda}(i\Omega) = \tilde{W}(i\Omega)/W_{\text{imp}}(i\Omega)$. The GW approximation consists in setting $\tilde{\Lambda} = 1$. The static component $\tilde{\Lambda}(i\Omega = 0)$ of this crude estimate is shown in Fig. 5.8, panel (c), for GW+EDMFT. As one approaches the Mott transition, this estimate of the vertex is seen to grow substantially. GW misses this trend.

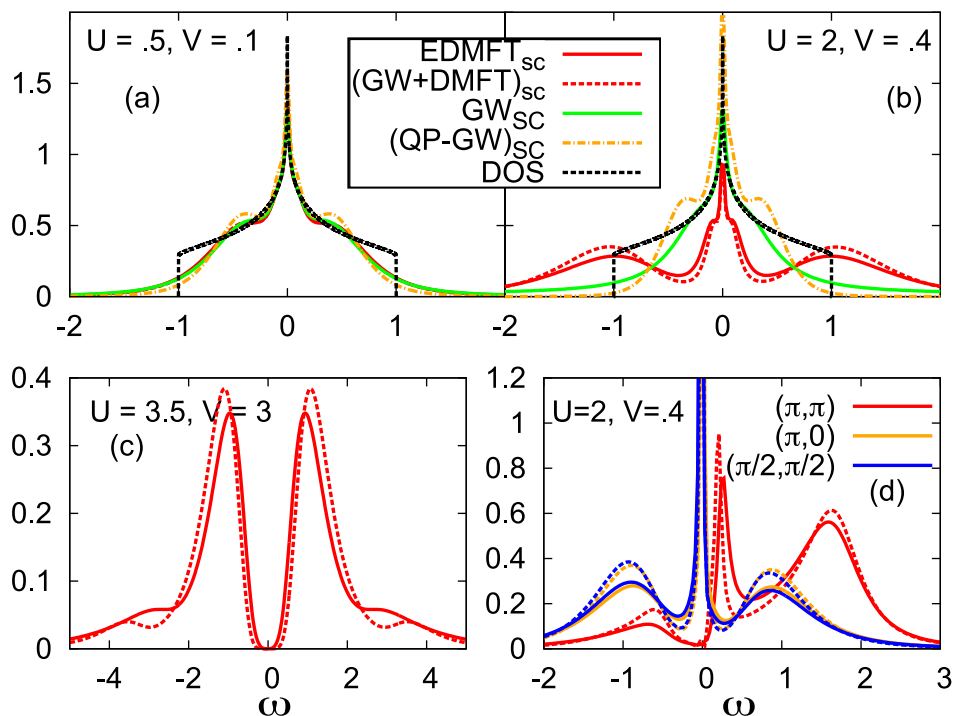


Figure 5.7: Panels (a), (b) and (c): local spectra $A_{loc}(\omega)$ for different points of the phase diagram obtained within different self-consistent schemes. Panel (d): $A(\mathbf{k}, \omega)$ for $\mathbf{k} = (\pi, \pi)$, $\mathbf{k} = (\pi, 0)$ and $\mathbf{k} = (\pi/2, \pi/2)$ at $U = 2$, $V = 0.4$ in EDMFT (solid lines) and GW+EDMFT/HS-UV (dashed lines)

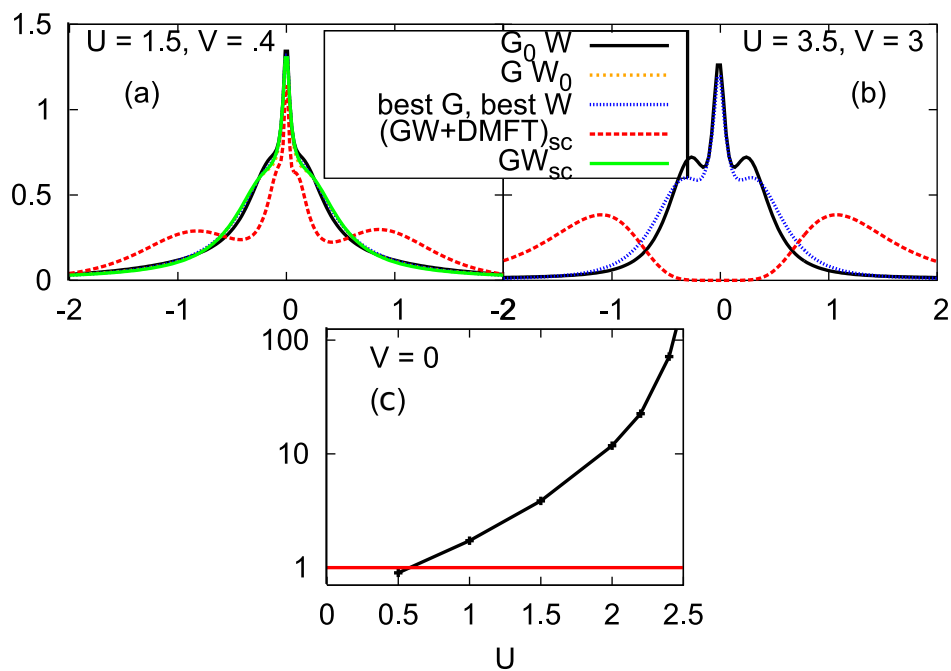


Figure 5.8: Panels (a) and (b): comparison of local spectra $A_{loc}(\omega)$ for one-shot schemes and self-consistent schemes. Panel (c): estimate of the vertex $\tilde{\lambda}(i\Omega = 0)$.

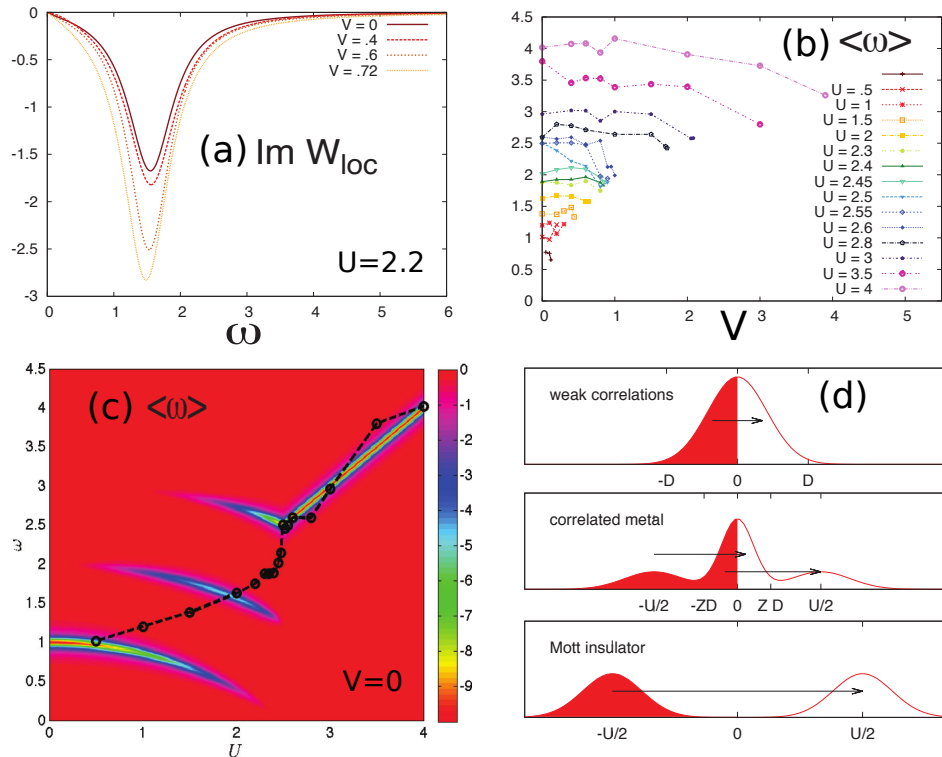


Figure 5.9: Study of the screening frequency in EDMFT ($\beta D = 100$). (a) $\text{Im}W_{\text{loc}}(\omega)$ (obtained by Padé analytical continuation). (b) $\langle\omega\rangle$ as a function of V . (c) Black dotted curve: $\langle\omega\rangle$ in EDMFT at $V = 0$. Colorplot: $\text{Im}\chi_{\text{loc}}^{I\text{-DMFT}}$ in the (ω, U) plane.

5.3.3 Screening properties

In this section, I further investigate the dependence of the screening frequency introduced in the previous sections. This frequency is visible both in $\mathcal{U}(\omega)$ and $W_{\text{loc}}(\omega)$. In this section, I focus on $W_{\text{loc}}(\omega)$. $\text{Im}W_{\text{loc}}(\omega)$ is very similar to $\text{Im}\mathcal{U}(\omega)$. It is shown in panel (a) of 5.9. This panel already gives an indication that the screening frequency is weakly dependent on V . One can quantify the screening frequency by defining:

$$\langle\omega\rangle \equiv \frac{\int_0^\infty \text{Im}W_{\text{loc}}(\omega)\omega d\omega}{\int_0^\infty \text{Im}W_{\text{loc}}(\omega)d\omega} \quad (5.15)$$

Our intuition is confirmed by panel (b) which displays the dependence of $\langle\omega\rangle$ on V for a wide range of values of U : in all cases, $\langle\omega\rangle$ is virtually independent of V . To understand the remaining dependence on U , one gets an estimate of $\chi_{\text{imp}}(i\Omega)$ (which is linked to W_{loc} by $W_{\text{loc}}(i\Omega) = U - U\chi_{\text{imp}}(i\Omega)U$) within the simple “linearized-DMFT” scheme (Potthoff (2001)). The imaginary part of the function so obtained is plotted as a color plot in panel (c). The first line of poles, starting from $\omega = 1$ at $U = 0$, corresponds to transitions within the quasiparticle peak (within linearized DMFT, this peak is mimicked by two levels; a more realistic sketch is shown in panel (d), under the label “weak correlations”). As the correlation strength is cranked up, incoherent bands appear at $\pm U/2$, opening up the possibility for particle-hole processes between the quasiparticle band and either Hubbard band (“correlated metal”), with a characteristic energy scale $U/2$. Finally, in the Mott state, the only remaining particle-hole transitions are inter-Hubbard-band transitions with energy scale U . This explains the trend observed in $\langle\omega\rangle$ in EDMFT.

¹This result will be derived rigorously in chapter 8.

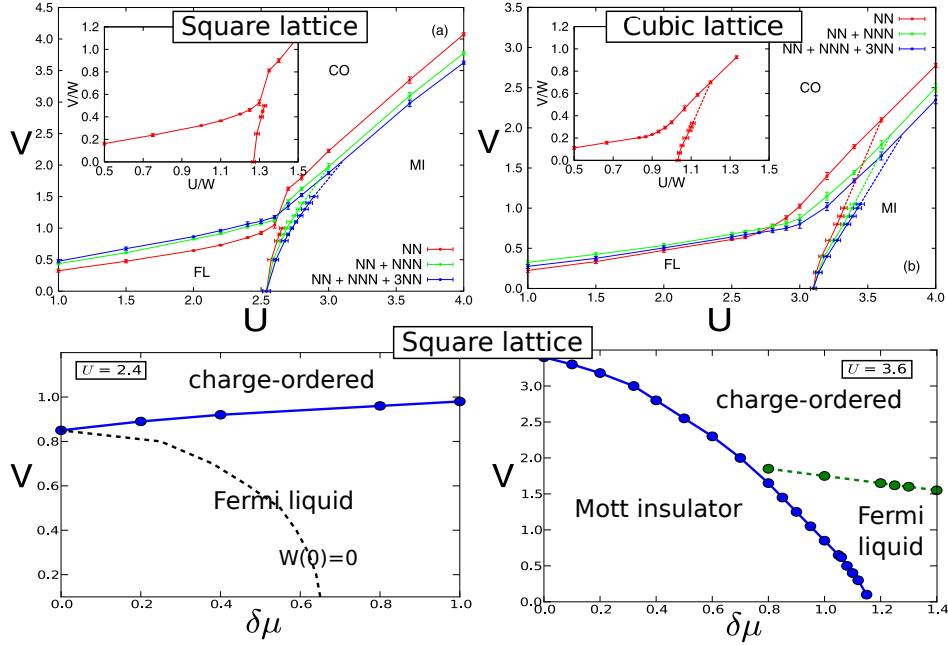


Figure 5.10: *Top panels:* (U, V) phase diagram with various interaction ranges in two (left) and three (right) dimensions obtained within EDMFT ($\beta D = 100$) NN: nearest neighbor, NN+NNN: nearest and next-nearest-neighbor; NN+NNN+3NN: nearest, next-nearest and third-nearest neighbors. *Lower panels* $(V, \delta\mu = \mu - U/2)$ diagrams in two dimensions for $U = 2.4$ (left) and $U = 3.6$ (right).

5.3.4 Dimension, interaction range and doping

I end up the discussion on EDMFT and GW+EDMFT by investigating the robustness of the above results with respect to dimension, range of the hopping parameters and doping.

The top left and top right panels of Fig. 5.10 show the phase diagrams in two and three dimensions for different interaction ranges. In all cases, the qualitative picture, with three phases, is identical. The main effect of more extended interactions in two dimensions is a small destabilization of the charge-ordered phase for small U s (larger V_c), and a small enhancement of the MI phase with respect to the CO phase for large U s (lower V_c). In three dimensions, the trend is similar for the MI-CO phase boundary, but the boundaries for NN+NNN and NN+NNN+3N interactions (see the caption for a definition of these abbreviations) are reversed with respect to the two-dimensional case. In the next chapter, the effect of truly long-ranged interactions (with a $1/r$ behavior) will be investigated in the case of surface systems.

In the lower panels of Fig. 5.10, the influence of doping is investigated in two dimensions starting from the Fermi-liquid phase (left panel) and from the Mott insulating phase (right panel). In the former case, doping slightly enhances the Fermi-liquid phase with respect to the charge-ordered phase. Interestingly, for large dopings the low-energy part of the fully screened interaction $W_{loc}(i\Omega)$ becomes negative (see the black dashed line): creating doublons in this region becomes energetically favorable. In the latter case (right panel), the charge-ordering domain is enhanced by doping. While at low values of V , a transition to a Fermi liquid phase occurs (when the chemical potential reaches the upper Hubbard band), for larger values of V one runs into a charge-ordered phase.

5.4 Conclusions

The EDMFT and $GW+EDMFT$ approximations place bosonic fluctuations in the charge sector at the center of the stage.

In particular, these methods capture **charge-ordering phenomena at weak and strong coupling** through the introduction of a bosonic Weiss field, $\mathcal{U}(\omega)$, which measures the impact of nonlocal screening effects (caused by nonlocal interactions v_q) on the local physics. In the next chapter, these methods will be applied to systems of adatoms on semiconducting surfaces, systems where electrons interact through effective long-ranged interactions.

A second appealing aspect of $GW+EDMFT$ is the lightweight construction of a **momentum-dependent self-energy**. Here, contrary to cluster DMFT, the range of accessible fluctuations is unlimited: the bosonic fluctuations included in W can be long-ranged. This comes at the cost of a relative loss of control, as the choice of GW diagrams to supplement the impurity self-energies is somewhat arbitrary and there is no well-defined way of measuring the corresponding error.

Finally, let us note that EDMFT and $GW+EDMFT$ can be straightforwardly extended to the spin channel, where cluster DMFT sees most of the interesting deviations from single-site DMFT.

Local and long-range interactions in surface systems: insights from combined GW and Extended Dynamical Mean Field Theory

In chapter 4, I have explained how, starting from the Hamiltonian describing all the electrons in the solid, one can derive a low-energy model whose kinetic parameters have been obtained by fitting the DFT (LDA) low-energy band by a tight-binding dispersion (section 4.2), and whose interaction parameters have been computed in the constrained RPA approximation (section J.3).

The Hamiltonian describing the low-energy physics of α -phases, the extended Hubbard model, combines the physical ingredients which we had surmised in the introductory chapter (see section 3.3.1), to wit: narrow bandwidths, strong local interactions U , sizable *and* long-ranged nonlocal interactions parametrized by V , in two dimensions.

To handle these elements, and in particular the combination of strong local interactions and nonlocal interactions, one method of choice is the EDMFT or GW +EDMFT methods, which have been explained and applied to the square and cubic lattices the previous chapter (chapter 5).

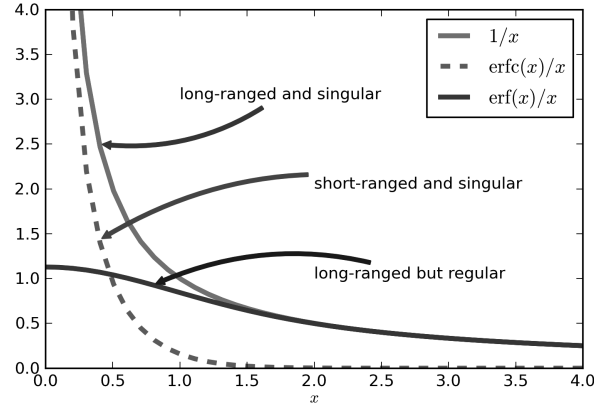
In this chapter, EDMFT/ GW +EDMFT are applied to the triangular lattice with long-ranged interactions. This extension is discussed in section 6.1. Then, the family of compounds whose interactions have been computed in chapter 4 are characterized with the help of a common phase diagram in terms of local and nonlocal interactions, where each compound is placed according to its first-principles interaction parameters (section 6.2). Finally, in section 6.3, the emphasis is put on Sn/Si(111) and the long-standing puzzles concerning this compound, which are solved by investigating the question of experimental timescales.

The results of section 6.2 have been published in Hansmann *et al.* (2013a), included in appendix P.1. The results of section 6.3 are in preprint Hansmann *et al.* (2015), included in appendix P.2.

6.1 Incorporating long-ranged interactions in GW +EDMFT

The solution of the GW +EDMFT equations (summarized in section 5.2.2) in the context of surface systems is very similar to the solution on the square and cubic lattice presented in the previous chapter. The only notable difference is the lattice geometry and the range of interactions.

The bare dispersion $\varepsilon(\mathbf{k})$ has been given in Eq. (4.2) and the tight-binding parameters for the four compounds in Table 4.1 (chapter 4). These tightbinding parameters are quite similar for all four compounds.


 Figure 6.1: Decomposition of $1/x$ using the error function.

Because of the long-range character of the bare interaction v (Eq. (4.9)), the numerical Fourier transform has to be performed with special care:

$$v(\mathbf{q}) = \sum_i e^{i\mathbf{q}\cdot\mathbf{R}_i} v_{i,0} = U + V \underbrace{\sum_{i \neq 0} \frac{1}{|\mathbf{R}_i|/a} e^{i\mathbf{q}\cdot\mathbf{R}_i}}_{\equiv \tilde{v}(\mathbf{q})} \quad (6.1)$$

The contribution from the long-ranged tail, $\tilde{v}(\mathbf{q})$, cannot be directly summed numerically because of its slow spatial decay. One possibility to handle this difficulty is to decompose the summand using the error function and its complementary ($\text{erfc}(x) = 1 - \text{erf}(x)$), with a parameter η controlling their range:

$$\tilde{v}(\mathbf{q}) = \underbrace{\sum_{i \neq 0} \frac{\text{erf}(|\mathbf{R}_i|/\eta)}{|\mathbf{R}_i|/a} e^{i\mathbf{q}\cdot\mathbf{R}_i}}_{\equiv v_{\text{LR}}(\mathbf{q})} + \underbrace{\sum_{i \neq 0} \frac{\text{erfc}(|\mathbf{R}_i|/\eta)}{|\mathbf{R}_i|/a} e^{i\mathbf{q}\cdot\mathbf{R}_i}}_{\equiv v_{\text{SR}}(\mathbf{q})}$$

As illustrated in Fig. 6.1, $\text{erfc}(x/\eta)/x$, though singular at $x = 0$, is short-ranged (with a range η), so that the numerical lattice sum to be performed to compute $v_{\text{SR}}(\mathbf{q})$ will be accurate provided the lattice sums extends to neighbors within a range η , namely $Na \gtrsim \eta$, where N is the linear size of the lattice. On the other hand, $\text{erf}(x/\eta)/x$, though long-ranged, is regular at $x \rightarrow 0$ and very smooth, so that it can be approximated by its continuum limit to high accuracy, *viz.*

$$\sum_i \frac{\text{erf}(R_i/\eta)}{R_i/a} e^{i\mathbf{q}\cdot\mathbf{R}_i} \approx \iint_{\mathcal{L}} d\rho \frac{\text{erf}(a\rho/\eta)}{\rho} e^{ia\mathbf{q}\cdot\rho} \equiv \tilde{v}_{\text{LR}}^{\text{cont}}(\mathbf{q}) \quad (6.2)$$

As shown in appendix K, this continuum approximation is valid if

$$\eta \gg a\sqrt{N} \quad (6.3)$$

Then, using the identities $\int_0^{2\pi} dx e^{ia \cos x} = 2\pi J_0(a)$ (J_0 is the Bessel function of the first kind) and $\int_0^\infty \text{erf}(ax) J_0(x) dx = \text{erfc}(\frac{1}{2a})$, one finds:

$$\tilde{v}_{\text{LR}}^{\text{cont}}(\mathbf{q}) = \int_0^\infty \rho d\rho \int_0^{2\pi} d\theta \frac{\text{erf}(a\rho/\eta)}{\rho} e^{ia|\mathbf{q}|\rho \cos \theta} = \int_0^\infty d\rho \text{erf}(a\rho/\eta) 2\pi J_0(a|\mathbf{q}|\rho) = \frac{2\pi}{a|\mathbf{q}|} \text{erfc}\left(\frac{|\mathbf{q}|\eta}{2}\right) \quad (6.4)$$

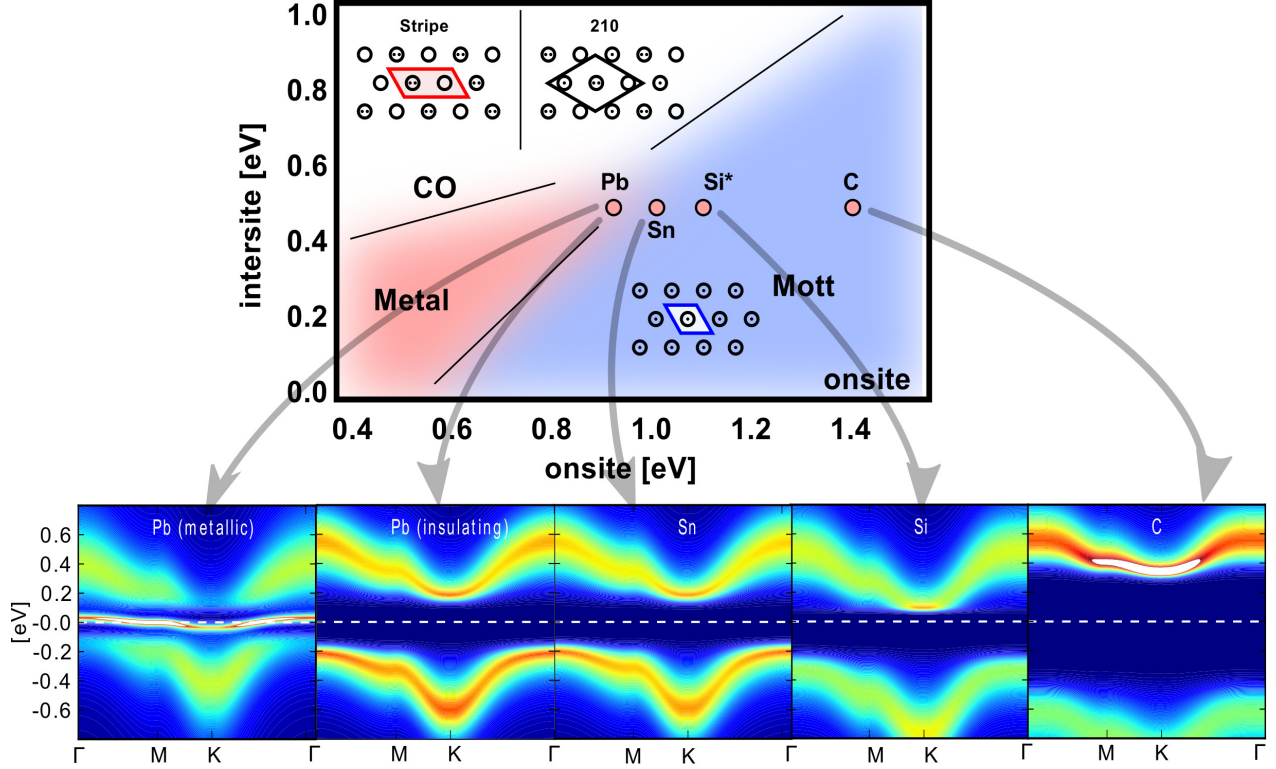


Figure 6.2: Phase diagram in the plane of onsite (U) and intersite (V) interactions ($T = 116$ K). The inset sketches show the unit cell and occupation patterns in the Mott, stripe ($2\sqrt{3} \times 2\sqrt{3}$ symmetry) and 210 (3×3 geometry) phases. Lower row: momentum-resolved spectral function $A(\mathbf{k}, \omega)$ along a high-symmetry path obtained from MaxEnt analytical continuation.

Thus, $\tilde{v}_{LR}(\mathbf{q}) = \sum_i \frac{\text{erf}(R_i/\eta)}{R_i/a} e^{i\mathbf{q}\cdot\mathbf{R}_i} - \lim_{R \rightarrow 0} \frac{\text{erf}(R/\eta)}{R/a} e^{i\mathbf{q}\cdot\mathbf{R}} = \frac{2\pi}{a|\mathbf{q}|} \text{erfc}\left(\frac{|\mathbf{q}|\eta}{2}\right) - \frac{a}{\eta} \frac{2}{\sqrt{\pi}}$, and the final formula reads:

$$v(\mathbf{q}) = U + V \left(\sum_{\substack{\mathbf{R} \in \text{BL} \setminus \{0\} \\ |\mathbf{R}| < Na}} \frac{\text{erfc}(|\mathbf{R}|/\eta)}{|\mathbf{R}|/a} e^{i\mathbf{q}\cdot\mathbf{R}} + \frac{2\pi}{a|\mathbf{q}|} \text{erfc}\left(\frac{|\mathbf{q}|\eta}{2}\right) - \frac{a}{\eta} \frac{2}{\sqrt{\pi}} \right) \quad (6.5)$$

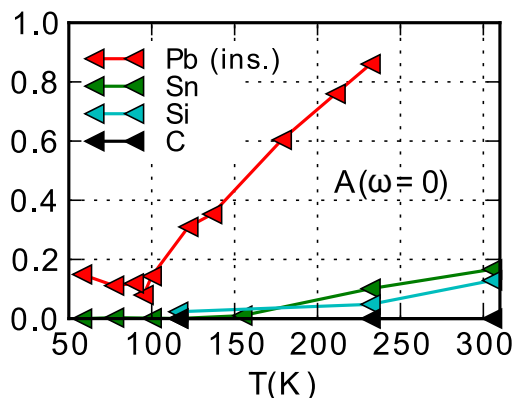
with η chosen such that:

$$\sqrt{N} \ll \frac{\eta}{a} \lesssim N \quad (6.6)$$

The last two terms do not depend on the Bravais lattice as they come from the continuum approximation (6.2), but they govern the long wavelength ($|\mathbf{q}| \rightarrow 0$) behavior of $v(\mathbf{q})$, $v(\mathbf{q}) \sim 1/|\mathbf{q}|$, which in term stems from the long-range character of the interaction $v(\mathbf{R})$. A plot of the corresponding $v(\mathbf{q})$ will be given in the following (Fig. 6.10).

6.2 A materials trend: from Mott physics to charge-ordering...

In this section, the GW+EDMFT formalism is applied to the extended Hubbard mode with long-range interactions. The kinetic parameters for each adatom species are summarized in Table 4.1.


 Figure 6.3: Temperature dependence of $A_{\text{loc}}(\omega)$.

6.2.1 A phase diagram to classify α -phases

For each adatom species, namely for each set of kinetic parameters, the (U, V) phase diagram is sketched out in the same way as in the previous chapter for the extended Hubbard model on the square lattice with short-range interactions. Due to the similarity of the kinetic parameters of each adatom, the boundary lines are analogous for the four adatoms. Thus, one can gather all adatoms on the same (U, V) phase diagram, as shown in Fig. 6.2. The blurring in the final phase boundaries means that they in fact correspond to several slightly different curves, each one corresponding to a different set of kinetic parameters.

As in the square lattice, the metal-to-Mott transition is of first-order character with a coexistence region between a metallic and an insulating phase. The three phases one observes are the following:

- A **metallic, Fermi-liquid phase** at low onsite and intersite interactions, reflecting the low-energy band structure: a half-filled metallic band at the Fermi level.
- A **Mott phase** at large onsite interactions, with a critical U_c of the order of the bandwidth (roughly 0.5 eV) in the absence of intersite interactions.
- A **charge-ordered phase** at large intersite interactions. In a triangular lattice at half-filling, there are two possible charge orders illustrated in the upper-left cartoons, the “stripe” order, corresponding to a $2\sqrt{3} \times 2\sqrt{3}$ symmetry (or the M point, see Fig. 3.4), and the “210” order, corresponding to a 3×3 symmetry (or the K point). The nature of the ordered phase as predicted from our GW+EDMFT calculations in the unordered phase is discussed in the next subsection (6.2.2).

Once this phase diagram is established, one can place the compounds according to the interaction parameters computed in constrained RPA (see Fig. 4.4 in chapter 4). One thus observes a clear material trend: while C/Si(111) is predicted to be a *bona fide* Mott insulator owing to its large onsite-to-intersite interaction ratio, the lead and tin compounds sit quite close to the metallic phase (within GW+EDMFT, Pb/Si is even found to be in the metal-insulator first-order coexistence region), and most importantly to charge order – in close agreement with experimental findings, with 3×3 patches observed in Pb/Si, band back-foldings and core-level structures for Sn/Si (see Table 3.1).

In the bottom row of Fig. 6.2, I show the momentum-resolved spectral function $A(\mathbf{k}, \omega)$ obtained by MaxEnt analytical continuation of the imaginary-frequency data (a method briefly explained in appendix I.3.2). As the onsite-to-intersite interaction ratio decreases, so does the Mott gap decrease (from C to Pb). For the metallic solution of Pb/Si, one sees a very narrow quasi-particle peak.

Fig. 6.3 shows the temperature evolution of the momentum-integrated spectrum. The temperature evolution for the insulating solutions is typical of the gradual filling of a gap by thermal excitations, and, as we will

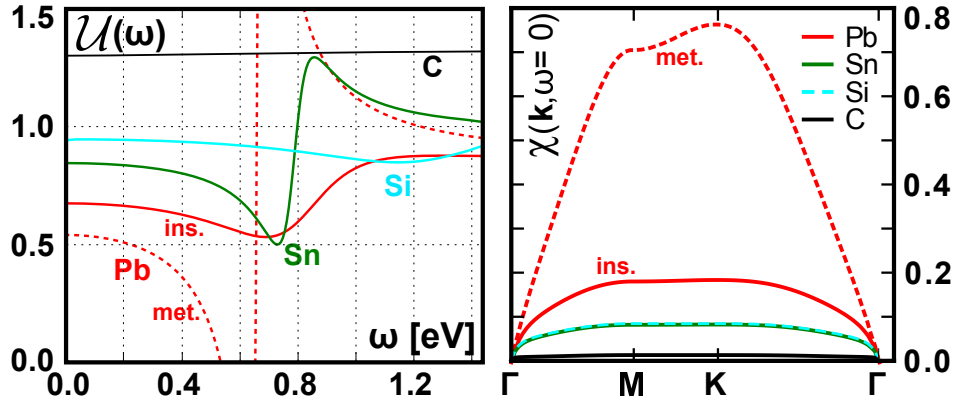


Figure 6.4: Left panel: effective local interactions, $\mathcal{U}(\omega)$. Right panel: charge susceptibility, $\chi(\mathbf{k}, \omega = 0)$.

discuss in greater detail in the next section, agrees with experimental data available for Sn/Si (see also the first arXiv version of Li *et al.* (2013)).

6.2.2 Screened interactions and nature of the charge-ordered phase

In this subsection, I give an interpretation of the phase diagram by relating the onsite-to-intersite interaction ratio to the shape of the self-consistently computed effective dynamical local interaction $\mathcal{U}(\omega)$, displayed in the left panel of Fig. 6.4.

$\mathcal{U}(\omega)$ reflects the effect of nonlocal interactions at the local level. It can be viewed as the partially screened interaction, with screening processes coming only from the nonlocal interactions. When nonlocal interactions are comparatively weak (as in the carbon compound, black curve), $\mathcal{U}(\omega)$ is almost static and equal to the bare onsite interaction, U . As the relative strength of nonlocal interactions increases, $\mathcal{U}(\omega)$ is screened at energies below a characteristic screening frequency which can be related to the gap width in an insulating phase, or to the bandwidth in a metallic phase, as we have seen in the previous chapter (Fig 5.9). As an interesting consequence, the screened value $\mathcal{U}(\omega = 0)$ depends on the phase of the system, *i.e.* if the bare U and V are such that the compound is in a coexistence region (like lead), there are two different $\mathcal{U}(\omega = 0)$ depending on which solution is considered (red curves). As expected, $\mathcal{U}(\omega = 0)$ is lower for the metallic solution, where screening is more efficient due to the absence of a finite energy gap in the spectrum.

Physically, one can interpret this screening mechanism by saying that larger intersite interactions make the creation of doubly-occupied sites comparatively more energetically favorable than in the absence of intersite repulsion, thus lowering the effective Hubbard repulsion. When intersite interactions grow, $\mathcal{U}(\omega = 0)$ can even reach a threshold where it becomes more favorable to go into a phase with static double occupations, namely a charge-ordered phase.

In the case of the square lattice with nearest-neighbor repulsion studied in the previous chapter, there was no ambiguity as to which charge-ordering pattern was favored by the nonlocal interactions (in that case, it was a checkerboard pattern). On the triangular lattice, the situation is not so clear-cut. First, several ordering patterns, presented in the introductory chapter (see Fig. 3.4), are possible. Second, the long-ranged character of the interactions causes many possible ordering possibilities to become entangled; in a way, it “frustrates” patterns corresponding to high-symmetry points.

Despite being limited to the phase without order, our *GW*+EDMFT computations give further information about the nature of the ordered-phase thanks to the charge susceptibility $\chi(\mathbf{q}, i\Omega)$, computed from $P(\mathbf{q}, i\Omega)$ and $v(\mathbf{q})$ by Eq. (5.11). Its momentum-resolved static value (shown in the right panel of Fig. 6.4) gives the relative contribution to the various charge-ordering symmetries to the instability. Hence, one can infer from these calculations that in all compounds, the M and K geometries are *both* relevant, with a slight preference for K (3×3 or “210” phase) in the case of lead, as seen in experiment.

6.2.3 Conclusions and open questions

In conclusion, this study shows that

- the C/Si(111) compound is a Mott insulator ($\sqrt{3} \times \sqrt{3}$ symmetry),
- the Pb/Si(111) compound is the closest to charge-ordering (3×3 symmetry, in agreement with experiments)
- the Sn/Si(111) case is less clear-cut, being less close to charge-ordering than Pb/Si(111), but much more so than C/Si(111). This situation is also in agreement with experiments, which show apparently conflicting evidence of $\sqrt{3} \times \sqrt{3}$ and 3×3 symmetries. In the next section, we propose a simple explanation to this remaining puzzle.

6.3 Experimental timescales: a solution to the Sn/Si puzzle

As seen in section 3.2, the Sn/Si(111) compound is subject to experimental controversies: while scanning tunneling microscopy sees no trace of charge ordering in this compound (Uhrberg *et al.* (2000a); Morikawa *et al.* (2002); Modesti *et al.* (2007); Li *et al.* (2013)), photoemission spectroscopies such as ARPES and core-level spectroscopy (cPES) see clear signs of the symmetries associated with the ordered phase (Göthelid *et al.* (1995); Uhrberg *et al.* (2000a); Lobo *et al.* (2003); Modesti *et al.* (2007)). In this section, I explain that this puzzle can be solved by examining the temporally and spatially resolved susceptibility computed within the GW+EDMFT approximation.

These results can be found in preprint Hansmann *et al.* (2015), included in section P.2.

6.3.1 Two snapshot-like probes: core-level spectroscopy and ARPES

Photoemission spectroscopies are fast experimental probes. In this section, I show that these probes can only be understood if incorporating symmetry-breaking contributions ($2\sqrt{3} \times 2\sqrt{3}$ and 3×3) to the total spectrum.

6.3.1.1 Inequivalent adatoms from core-level spectroscopy

Core-level photoemission experiments have led to the identification of several components in the cPES spectra (see the discussion in section 3.2 and the experimental data, grey and black dots in Fig. 6.5), a sign that 4d core electrons with different valence environments are present in the compound. This observation can be quantified by performing configuration-interaction (CI) simulations of the excitation of a 4d core electron in three valence configurations, namely an empty surface orbital, a half-filled surface orbital or a doubly occupied surface orbital (see left panel in Fig. 6.5). The spectra corresponding to the three environments are shown in the central panel in the form of red, blue and green narrow peaks.

To compute the total spectrum, one must estimate the relative weight of each environment in our system. In the Mott phase, all tin sites are in a singly-occupied environment. In the CO phase, we perform a 6-site exact diagonalization (ED) calculation where we project the ground-state wavefunction on the 3 states of interest, namely $\sqrt{3} \times \sqrt{3}$, 3×3 and $2\sqrt{3} \times 2\sqrt{3}$. The projection is shown in the lower right panel. One can see that the relative contributions of the three states are of $\eta_{\sqrt{3} \times \sqrt{3}} = 13\%$, $\eta_{3 \times 3} = 56\%$ and $\eta_{2\sqrt{3} \times 2\sqrt{3}} = 31\%$ (note that there are other states which we neglect here), which corresponds to 32% half-filled sites and 68% of empty/doubly-occupied sites.

Using these proportions, one can compute the cPES spectrum separately for the Mott phase ($A_{\text{Mott}}^{\text{cPES}}(\omega)$) and for the CO phase ($A_{\text{CO}}^{\text{cPES}}(\omega)$). The total spectrum is then $A_{\text{tot}}^{\text{cPES}}(\omega) = \alpha A_{\text{Mott}}^{\text{cPES}}(\omega) + (1 - \alpha) A_{\text{CO}}^{\text{cPES}}(\omega)$, where α is the proportion of Mott domains and $1 - \alpha$ the proportion of charge-ordered domains in the sample, if one

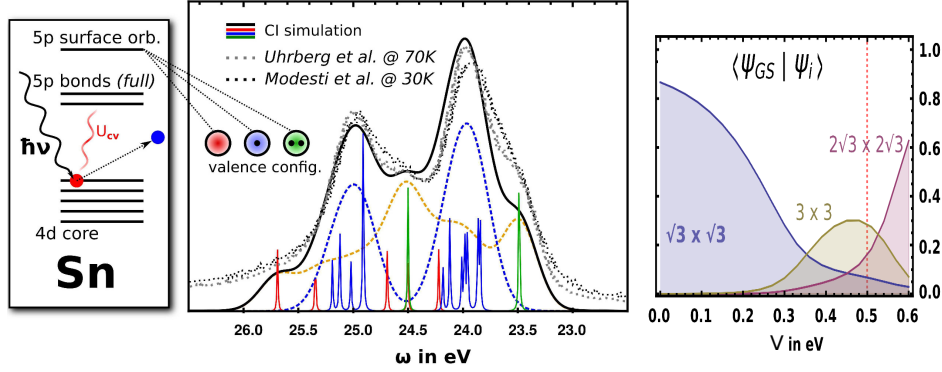


Figure 6.5: cPES of the Sn adatom 2p-shell. *Left*: Cartoon of the Sn 4d core electron emission process. *Middle*: comparison between experimentally obtained spectra (black solid line) and theoretical simulations with full multiplet cluster calculations (upper panel $T=140$ K; lower panel $T=9$ K): The red dashed curve is the sum of the three specifically weighted contributions (corresponding to the three axial surface orbital configurations) with an overall Gaussian broadening of 0.37 eV ($T=9$ K) and 0.41 eV ($T=140$ K). *Right*: projection of the exact ground-state of a finite 6×6 cluster on the $\sqrt{3} \times \sqrt{3}$, 3×3 and $2\sqrt{3} \times 2\sqrt{3}$ states (*The CI and ED computations have been performed by Philipp Hansmann.*).

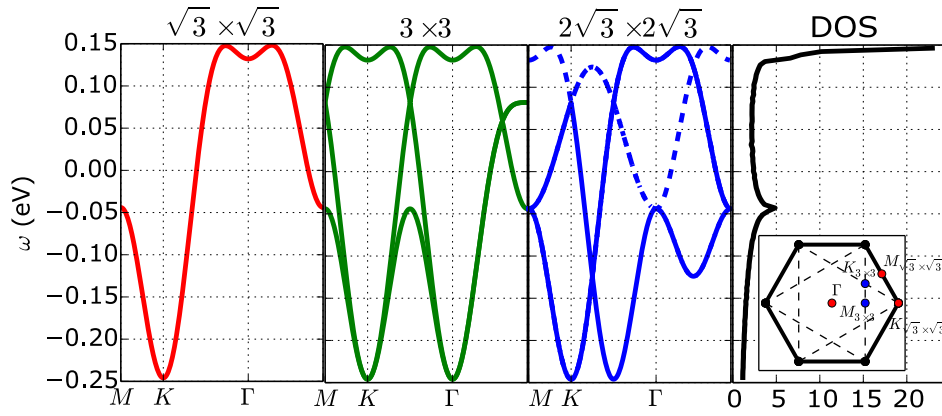


Figure 6.6: *Left panels*: tight-binding bands in the three symmetries for Sn/Si(111) (with the parameters of Table 4.1). *Right panel*: non-interacting density of states. *Inset*: reminder of the high-symmetry points.

assumes that Sn/Si is in the vicinity of a first-order phase transition (which we suspect due to our previous work on the phase diagram, Fig. 6.2, and ongoing calculations in the ordered phase). We estimate these proportions by using the available experimental spectra (middle panel). The outcome is $\alpha = 30\%$. The blue and yellow dashed curves correspond to $\alpha A_{\text{Mott}}^{\text{cPES}}(\omega)$ and $(1 - \alpha)A_{\text{CO}}^{\text{cPES}}(\omega)$, respectively (with a broadening factor); the solid black curve is the total theoretical spectrum $A_{\text{tot}}^{\text{cPES}}(\omega)$. The agreement with the experimental spectra is very good.

6.3.1.2 Traces of ordered phase: band backfoldings in ARPES

Based on the cPES study, we have quantified the relative importance of the three phases. We can use this information to compute the ARPES spectrum.

The effect of symmetry-breaking from the $\sqrt{3} \times \sqrt{3}$ unit cell to the $2\sqrt{3} \times 2\sqrt{3}$ and 3×3 unit cells can be understood in a simple way by looking at the tight-binding bands for the three phases. These are shown in Fig. 6.6. While in the $\sqrt{3} \times \sqrt{3}$ symmetry (red curve), the band goes down when going to point K and up when going to point Γ , the trend is more complex due to the backfoldings in the $2\sqrt{3} \times 2\sqrt{3}$ and 3×3 symmetries.

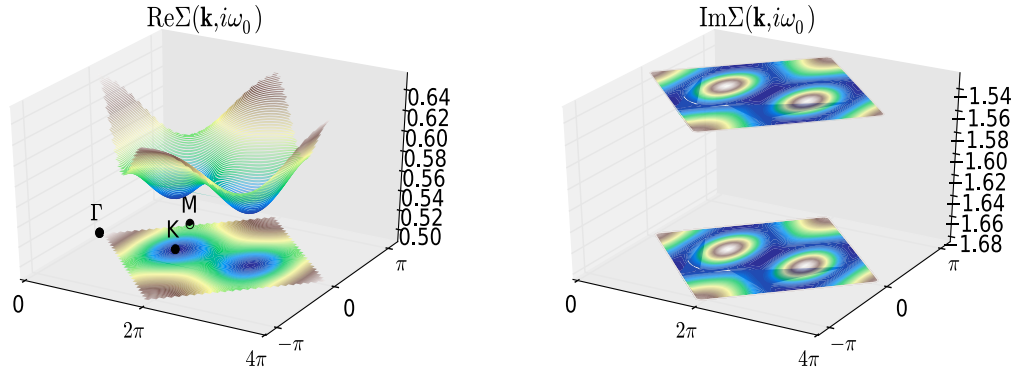


Figure 6.7: GW+EDMFT self-energy for Sn/Si(111) at $T = 116\text{K}$. Left: $\text{Re}\Sigma(\mathbf{k}, i\omega_0)$. Right: $\text{Im}\Sigma(\mathbf{k}, i\omega_0)$.

In particular, in the 3×3 symmetry (green curves) a band goes down to Γ . This observation is reminiscent of the measured ARPES data, shown in the bottom right panel of Fig. 6.9: there, while the band goes down to K , one also sees a shoulder when going from K to Γ , an indication that the band is going down to Γ . In any case, this shoulder would not be present in the experimental spectrum if the system were containing only the $\sqrt{3} \times \sqrt{3}$ symmetry.

Since ARPES is an extended probe (the ARPES signal integrates over several unit cells), it contains contributions both from MI domains (in proportion α) and from CO domains (in proportion $1 - \alpha$). The composition of the latter has been determined thanks to the analysis of the cPES spectrum. Thus, one can compute the total ARPES spectrum as the following sum:

$$A_{\text{tot}}^{\text{ARPES}}(\mathbf{k}, \omega) = \alpha A_{\sqrt{3} \times \sqrt{3}}^{\text{ARPES}}(\mathbf{k}, \omega) + (1 - \alpha) \left[\eta_{\sqrt{3} \times \sqrt{3}} A_{\sqrt{3} \times \sqrt{3}}^{\text{ARPES}}(\mathbf{k}, \omega) + \eta_{3 \times 3} A_{3 \times 3}^{\text{ARPES}}(\mathbf{k}, \omega) + \eta_{2 \sqrt{3} \times 2 \sqrt{3}} A_{2 \sqrt{3} \times 2 \sqrt{3}}^{\text{ARPES}}(\mathbf{k}, \omega) \right] \quad (6.7)$$

where $A_{\varphi}^{\text{ARPES}}(\mathbf{k}, \omega)$ is the spectrum corresponding to the phase φ , i.e. $A_{\varphi}^{\text{ARPES}}(\mathbf{k}, \omega) \equiv -\frac{1}{\pi N_{\varphi}} \text{ImTr} G_{\varphi}(\mathbf{k}, \omega + i\eta)$, with N_{φ} the number of electrons per unit cell in phase φ , and as usual,

$$G_{\varphi}(\mathbf{k}, \omega) = \left[(\omega - \mu) \mathbf{1} - \varepsilon_{\varphi}(\mathbf{k}) - \Sigma_{\varphi}(\mathbf{k}, \omega) \right]^{-1}$$

The tight-binding dispersions $\varepsilon_{\varphi}(\mathbf{k})$ are those depicted in Fig. 6.6.

In principle, this expression requires the computation of $\Sigma_{\varphi}(\omega)$ for each of the three phases. For the $\sqrt{3} \times \sqrt{3}$ phase, the GW+EDMFT and the EDMFT self-energy are very close to each other, namely the nonlocal contributions to $\Sigma(\mathbf{k}, i\omega)$ are rather small, especially for the imaginary part. This is shown in Fig. 6.7. There are some nonlocal deviations in the real part of the GW+EDMFT self-energies, but they do not induce large changes in the local observables. Thus, we decide to work with the EDMFT result $\Sigma_{\text{imp}}(i\omega)$. We note that this self-energy is close to the atomic limit self-energy, but not identical, as shown in the inset of Fig. 6.8. The main panel of this figure shows the same self-energy on the real-frequency axis after Padé analytical continuation.

For the $2 \sqrt{3} \times 2 \sqrt{3}$ and 3×3 phases, computing $\Sigma(\mathbf{k}, \omega)$ would require performing GW+EDMFT calculations in the ordered phase. While this is feasible, we resort instead to a simpler estimate of the self-energy in those phases. For the empty or full bands (corresponding to empty and doubly-occupied sites), where correlations are expected to be negligible, we approximate the self-energy by the Hartree estimate computed for a model with nearest-neighbor interactions only. For the half-filled site of the 3×3 site, we use the EDMFT self-energy $\Sigma_{\text{imp}}(i\omega)$ computed in the $\sqrt{3} \times \sqrt{3}$ phase.

The Hartree estimates read:

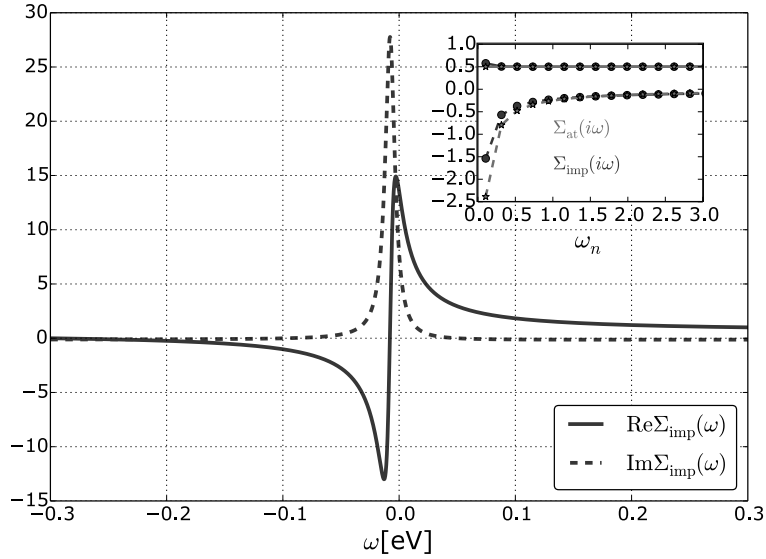


Figure 6.8: Self-energy $\Sigma_{\text{imp}}(\omega)$ after Padé analytical continuation. Solid lines: real part; dashed lines: imaginary part. *Inset*: imaginary-frequency self-energy. Gray curves: atomic-limit self-energy $\Sigma_{\text{at}}(i\omega) = \frac{U^2}{4i\omega} + \frac{U}{2}$.

$$\tilde{\Sigma}_{\sigma,3\times 3}^{\text{Hartree}} = \begin{pmatrix} \frac{U}{2} - 3V & & \\ & 0 & \\ & & -\frac{U}{2} + 3V \end{pmatrix} \quad (6.8)$$

$$\tilde{\Sigma}_{\sigma,\text{stripe}}^{\text{Hartree}} = \begin{pmatrix} \frac{U}{2} - 2V & & \\ & & \\ & & -\frac{U}{2} + 2V \end{pmatrix} \quad (6.9)$$

Here, the chemical potential is absorbed in $\tilde{\Sigma}$ ($\tilde{\Sigma} \equiv \Sigma - \mu$). The final approximate form of the self-energies is taken to be:

$$\tilde{\Sigma}_{\sigma, \sqrt{3}\times\sqrt{3}}(i\omega) = \tilde{\Sigma}_{\text{imp}}(i\omega) \quad (6.10)$$

$$\tilde{\Sigma}_{\sigma,3\times 3}(i\omega) = \begin{pmatrix} \frac{U}{2} - 3V & & \\ & \tilde{\Sigma}_{\text{imp}}(i\omega) & \\ & & -\frac{U}{2} + 3V \end{pmatrix} \quad (6.11)$$

$$\tilde{\Sigma}_{\sigma,\text{stripe}}(i\omega) = \begin{pmatrix} \frac{U}{2} - 2V & & \\ & & \\ & & -\frac{U}{2} + 2V \end{pmatrix} \quad (6.12)$$

These expressions for $\tilde{\Sigma}$ are analytically continued and plugged in Dyson's equation to compute the spectrum. The corresponding plots are shown in Fig. 6.9.

As expected from the above discussion of the tight-binding band back-foldings, the contribution from the $2\sqrt{3} \times 2\sqrt{3}$ and 3×3 phases lead to a shoulder in the path from K to Γ in the combined spectrum (middle right panel). The agreement with the experimental spectra (bottom right panel) is good.

6.3.2 Time and space-dependent susceptibilities, or why STM sees the $\sqrt{3} \times \sqrt{3}$ symmetry only

I now turn to the missing piece: why does STM not sense the ordered phases observed in cPES and ARPES? The answer lies in the discrepancies between the experimental timescales. While ARPES and cPES are fast

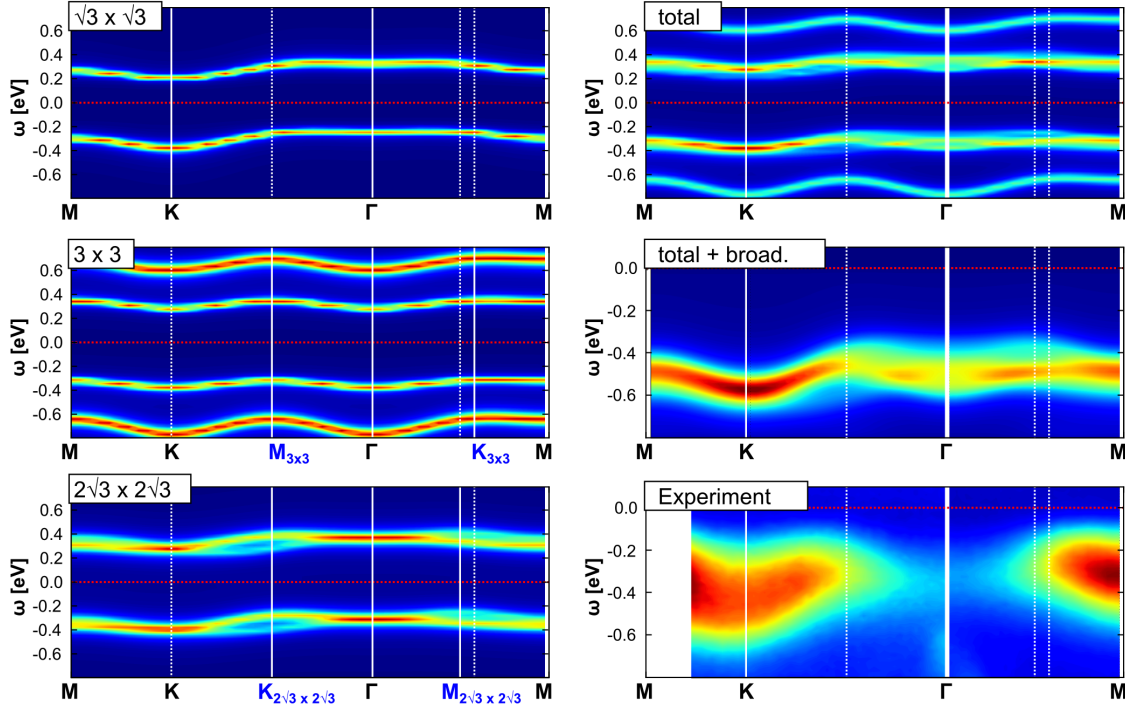


Figure 6.9: ARPES spectra from experiment and theory ($\varepsilon_F = 0.0$). *Upper panels*: Experiment (left); Broadened electron removal part of the full GW+DMFT spectral function $A(\mathbf{k}, \omega)$ in the experimentally measured k-space window (right). *Middle panels*: high resolution full spectral function $A(\mathbf{k}, \omega)$ of GW+DMFT along the complete $\Gamma \rightarrow M \rightarrow K \rightarrow \Gamma$ path (left); Contribution of the Mott ($\sqrt{3} \times \sqrt{3}$)-phase to the full spectral function (right). *Lower panels*: Contribution of the (3×3)-phase to the full spectral function (right); Contribution of the stripe-type ($2\sqrt{3} \times 2\sqrt{3}$)-phase to the full spectral function (right). For sketches of the respective unit cells see Fig.6.5.

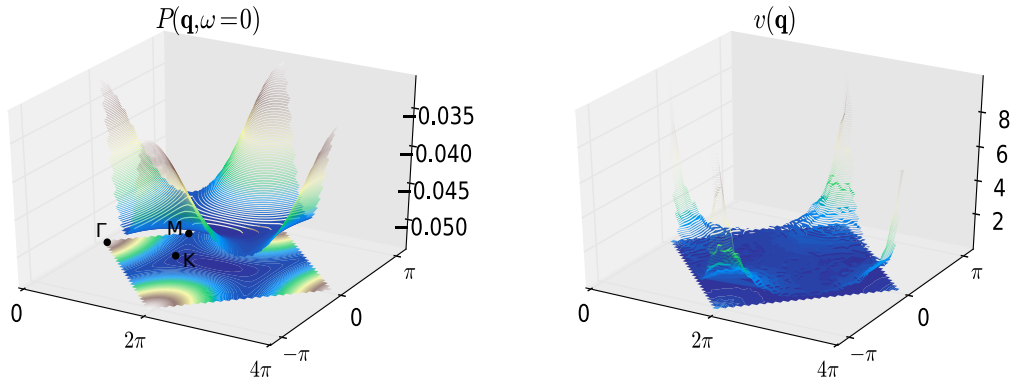


Figure 6.10: Momentum-dependence of $P(\mathbf{q}, \omega = 0)$ (left) and $v(\mathbf{q})$ (right) in SnSi.

probes, STM is a time-integrated, *i.e.* slow, probe. This discrepancy is visible in the imaginary-time charge-charge correlation function computed in GW+DMFT by Eq. (5.11).

In GW+EDMFT, the \mathbf{q} -dependence of $\chi(\mathbf{q}, i\Omega)$ comes both from $P(\mathbf{q}, i\Omega)$ and $v(\mathbf{q})$ (through Eq. (5.11)). Both are plotted in Fig. 6.10. $P(\mathbf{q}, \omega = 0)$ is largest (in absolute value) in the region of M and K , without a relevant difference in magnitude between both points. $v(\mathbf{q})$ is peaked at $\mathbf{q} = 0$ owing to its long-ranged character.

Next, let us discuss the behavior of $\chi(\mathbf{R}, \tau)$, computed from $\chi(\mathbf{q}, i\Omega)$ by first computing the charge-charge correlation function $\chi(\mathbf{q}, i\Omega)$ and then Fourier transforming to \mathbf{R}, τ coordinates. Indeed, the imaginary-time

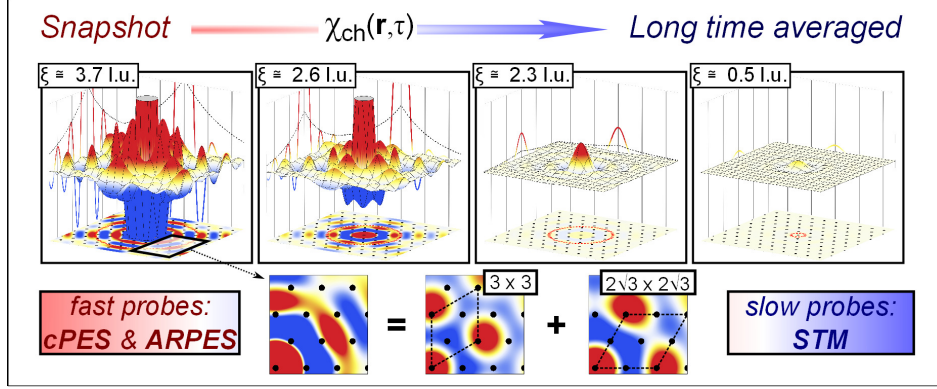


Figure 6.11: Charge correlation function $\chi(\mathbf{R}, \tau)$ plotted on the surface lattice x - y -plane for four different values of τ . At $\tau = 0.0$, we find large charge fluctuations of correlation lengths ξ exceeding 3.5 lattice units (l.u.) which are picked up by core-level and photoemission spectroscopies. Due to decay on a fs time-scale (see evolution with τ) they are invisible to slow probes like STM. On the bottom of the figure we show how such fluctuations can be decomposed into two contributions related to 3×3 (“210”) and $2\sqrt{3} \times 2\sqrt{3}$ (stripes) symmetry.

dependence of $\chi(\mathbf{R}, \tau)$ contains different pieces of information: while $\chi(\mathbf{q}, \tau = 0)$ corresponds to instantaneous probes (cPES and ARPES), $\chi(\mathbf{q}, \tau = \beta/2)$ roughly corresponds to the time-integrated response. To see this, let us use the Kramers-Kronig relations (see appendix I.1.2.4). This yields:

$$\chi_{\mathbf{q}}(\tau) = \text{FT} [\chi_{\mathbf{q}}(i\omega)] = \text{FT} \left[- \int_{-\infty}^{\infty} \frac{d\omega}{\pi} \frac{\chi_{\mathbf{q}}''(\omega)}{i\omega - \omega} \right] = - \int_{-\infty}^{\infty} \frac{d\omega}{\pi} \frac{e^{-\tau\omega}}{e^{-\beta\omega} - 1} \chi_{\mathbf{q}}''(\omega) = \int_{-\infty}^{\infty} \frac{d\omega}{\pi} \frac{e^{-(\tau-\beta/2)\omega}}{\sinh\left(\frac{\beta\omega}{2}\right)} \chi_{\mathbf{q}}''(\omega)$$

Hence:

$$\begin{aligned} \chi_{\mathbf{q}}(\tau = \beta/2) &= \int_{-\infty}^{\infty} \frac{d\omega}{\pi} \frac{\chi_{\mathbf{q}}''(\omega)}{\sinh\left(\frac{\beta\omega}{2}\right)} \\ &\approx 2T \int_{-\infty}^{\infty} \frac{d\omega}{\pi} \frac{\chi_{\mathbf{q}}''(\omega)}{\omega} = 2T \chi_{\mathbf{q}}(\omega = 0) = 2T \int_0^{\infty} dt \chi_{\mathbf{q}}^{\text{R}}(t) \end{aligned}$$

The approximation of the second line is valid only if $\beta\omega \ll 1$, which is the case if most of the spectral weight of $\chi_{\mathbf{q}}''(\omega)$ is concentrated at small frequencies compared to the temperature. This is not really verified in our system (the poles of $\chi_{\mathbf{q}}''$ are roughly at $\pm U$), but we nevertheless keep in mind this simple estimate to understand the meaning of $\chi_{\mathbf{q}}(\tau = \beta/2)$.

The evolution of $\chi(\mathbf{R}, \tau)$ is shown in Fig. 6.11: while instantaneous probes “see” strong charge modulations corresponding to a mixture of the 3×3 and $2\sqrt{3} \times 2\sqrt{3}$ phases (left panels), slow probes see a uniform charge density corresponding to the homogenous $\sqrt{3} \times \sqrt{3}$ phase (right panels). From $\chi(\mathbf{R}, \tau)$ one extracts a typical correlation length “seen” by each experimental probe. This is done by fitting $\chi(\mathbf{R}, \tau)$ to the expression $e^{-|\mathbf{R}|/\xi(\tau)} \sqrt{\xi(\tau)/|\mathbf{R}|}$ (the large $|\mathbf{R}|$ limit of the 2D Fourier transform of the Ornstein-Zernike form $\chi(\mathbf{q}, \tau) \propto 1/(\mathbf{q}^2 + \xi(\tau)^{-2})$). While “snapshot probes”, such as ARPES and core-level PES, see correlation lengths of several lattice units (3.7 l.u. for $\tau = 0$), STM (corresponding to long imaginary times) sees virtually no charge-charge correlations.

Part III

Nonlocal correlations in cuprates: unifying spin fluctuation and Mott physics with TRILEX

The field of strong correlations owes much to the discovery – in the mid 1980s – of copper-oxide (or “cuprate”) superconductors with a critical temperature above the boiling point of liquid nitrogen. In contrast with the “conventional” superconductors discovered by Onnes (1911), which need to be cooled down to a few Kelvin to superconduct, and are in general *bona fide* metals at room temperature, the new high-temperature superconductors are characterized by *strong interelectronic correlations*.

How can superconductivity – a state of matter where the electric current can flow seamlessly through the material – coexist with strong Coulomb repulsion between electrons? How can correlations – in general regarded as a hindrance to the flow of electrons – turn into a blessing? These fundamental puzzles have spawned an exciting field of research.

In chapter 7, I give a glimpse of the main experimental body of knowledge on cuprates, followed by an overview of the theoretical landscape after almost three decades of research. Based on these introductory elements, I then introduce, in chapter 8, a new method – dubbed TRILEX – which, drawing inspiration from the emphasis on *locality* of dynamical mean field theory, unifies the two main theoretical views on cuprates. Finally, chapter 9 presents a first application of TRILEX to the two-dimensional Hubbard model, the simplest model to describe cuprates.

7 Introduction to high-temperature superconductors

| | |
|--|----|
| 7.1 Experiments: strong correlations and nonlocal effects | 66 |
| 7.2 Theory: two viewpoints on high-temperature superconductivity | 74 |

8 A local approximation to the three-leg vertex, TRILEX

| | |
|---|-----|
| 8.1 Motivations | 85 |
| 8.2 An intuitive picture | 87 |
| 8.3 Functional derivation | 88 |
| 8.4 Algorithmic scheme | 99 |
| 8.5 Around the three-leg vertex | 102 |
| 8.6 Discussion: relation to other methods | 103 |

9 Application to the single-band Hubbard model

| | |
|---|-----|
| 9.1 An interpolation between fluctuation-exchange theories and DMFT | 105 |
| 9.2 A first-order Mott transition | 108 |
| 9.3 Fermi arcs upon doping | 110 |
| 9.4 The question of antiferromagnetic ordering | 110 |
| 9.5 Influence of the decoupling choice | 111 |
| 9.6 Conclusions and perspectives | 114 |

Introduction to high-temperature superconductors

In this chapter, I give a general overview of copper-oxide materials from an experimental (section 7.1) and theoretical (sections 7.2.1 and 7.2.2) point of view. Far from being exhaustive, this introduction intends to give the necessary background to understand the open challenges in the field.

There is a vast literature on the subject. For instance, a recent textbook by Plakida (2010) gives a pedagogical, yet detailed general introduction to the subject. On the theory side, Manske (2004) is one reference among others.

7.1 Experiments: strong correlations and nonlocal effects

In this section, some important experimental findings on cuprate materials are summarized. I first give a short description of the cuprate compounds from a structural and electronic point of view for orientation (section 7.1.1). Then, I review the main experimental findings (section 7.1.2), with a focus on nuclear magnetic resonance (NMR), neutron scattering, optics and angle-resolved photoemission (ARPES) experiments. This selection underlines the importance of strong correlations and of nonlocal effects in cuprate materials.

A theoretical description of the experimental probes mentioned in the text can be found in the appendix, chapter H.

7.1.1 A brief description of cuprate materials

In 1986, Bednorz and Muller (1986), who were seeking after materials with a strong electron-phonon coupling¹ “ λ ”, discovered that the $\text{Ba}_x\text{La}_{5-x}\text{Cu}_5\text{O}_{5(3-y)}$ compound becomes superconducting at 30 Kelvin. A few months later, Wu *et al.* (1987) found a critical temperature of 90 K in the ceramic $\text{YBa}_2\text{Cu}_3\text{O}_{7-\delta}$, above the boiling point of liquid nitrogen, 77 K. These critical temperatures were far above other “conventional” superconductors, well described by BCS theory (in fact magnesium diboride, well described by BCS theory, surpasses BaLaCuO with a T_c of 39 K – but it was discovered only in 2001). Fig. 7.1 gives a graphical illustration this breakthrough. As one can see, the commonality of these materials is the presence of copper and oxygen atoms. On this figure, a representative of the more recently discovered iron-based superconductors, FeAs, is also shown.

¹Their goal was to reach higher critical temperatures based on the theory of conventional superconductors, the Bardeen-Cooper-Schrieffer (BCS) theory, which stipulates that the critical temperature is given by $T_c \propto e^{-1/\lambda N(\epsilon_F)}$, see Eq. (1.51b) in appendix I.6.

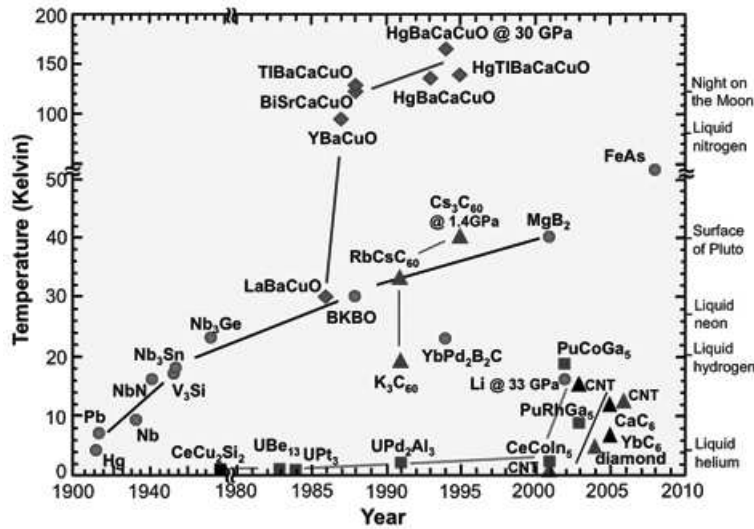


Figure 7.1: Critical temperature in conventional and unconventional superconductors: timeline (from Wikipedia). Cuprate superconductors are represented as diamonds. FeAs (on the right) belongs to the family of iron-based superconductors.

All cuprate materials contain two-dimensional copper-oxygen planes, the remaining atoms forming other planes or “blocks” acting as charge reservoirs whose chemical composition can be changed to adjust the doping level (usually denoted as x or δ) of the copper-oxygen planes. The crystal structure of one typical cuprate, “LSCO” (for $\text{La}_{2-x}\text{Sr}_x\text{CuO}_4$), is shown in Fig. 7.2. The copper atoms are located inside oxygen octahedra (which may be distorted); the material itself is made up of alternating layers of copper-oxide planes and La/Sr-O planes/blocks. In the case of LSCO, there is one copper-oxide plane between the blocks, LSCO is called a *monolayer* compound (like BiSCO). The first compound with a critical temperature above 77 K, “YBCO” (for $\text{YBa}_2\text{Cu}_3\text{O}_{7-\delta}$), is a *bilayer* compound, for instance. In general, the critical temperature increases with the number of CuO layers (with a maximum for three layers).

The experimental phase diagram of LSCO, a hole-doped material², is shown in Fig. 7.2. For very low dopings x (*i.e.* for close to one electron per copper site on average), the system is **antiferromagnetically** (AF) ordered (green region). At low temperatures, one finds a **superconducting dome** centered at a so-called *optimal doping* of $x \approx 15\%$. The region left of the dome, on the *underdoped* side, is the **pseudo-gap** phase. Above and right of this phase, the system is said to be in a “**strange metal**” state in the sense that the resistivity in this region (among others) has an anomalous behavior. On the far right, it becomes a “normal” metal again. Furthermore, there are small regions of **spin density wave** (SDW) order at the junction of the antiferromagnetic region with the superconducting dome. Finally, a **charge-density wave** (CDW) phase is seen at $x \approx 1/8 = 12\%$ doping.

The charge-density-wave phase has recently been under intense scrutiny both experimentally (Tranquada *et al.* (1995); Hoffman *et al.* (2002); Doiron-Leyraud *et al.* (2007); LeBoeuf *et al.* (2012); Ghiringhelli *et al.* (2012); Wu *et al.* (2013); Fujita *et al.* (2014); Cyr-Choinière *et al.* (2015)...) and theoretically (Nie *et al.* (2014); Efetov *et al.* (2013); De Carvalho and Freire (2014); Atkinson *et al.* (2014); Allais *et al.* (2014); Chowdhury and Sachdev (2014); Corboz *et al.* (2014); Wang *et al.* (2015)...). The experimental meaning of the pseudogap phase will be explained later.

The diversity of phases observed in cuprates – ranging from spin-ordered phases (AF) and superconducting phases (SC) to CDW and SDW phases over the intriguing “pseudo-gap” phase – already raises several issues:

²I will not deal with electron-doped materials for the sake of simplicity.

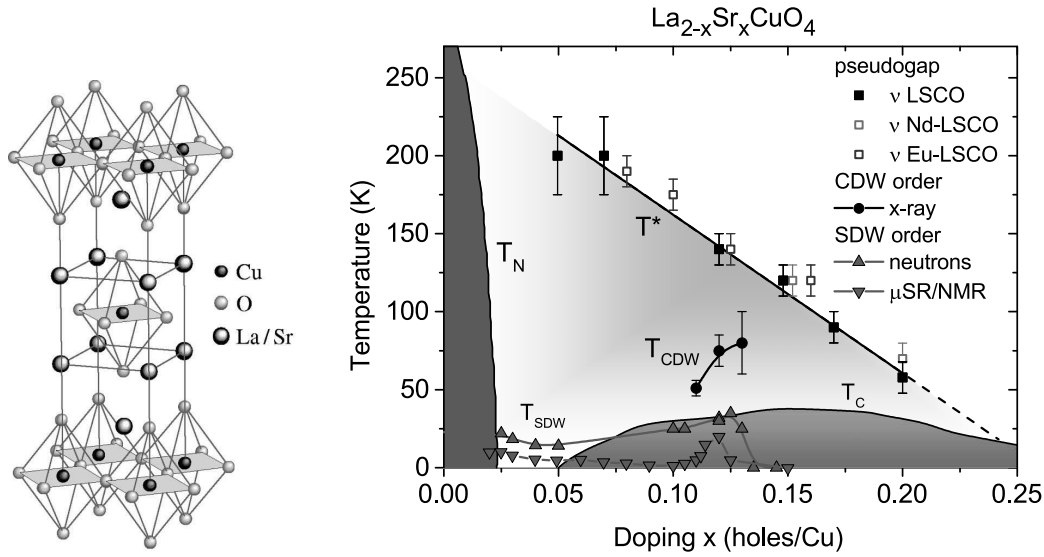


Figure 7.2: LSCO compound. *Left*: crystal structure (from Damascelli *et al.* (2003)). *Right*: experimental phase diagram (from Croft *et al.* (2014)). The T^* line is the crossover temperature to the pseudogap phase, determined as the upturn of the Nernst coefficient; T_{CDW} is the onset temperature of a CDW phase, determined by X-ray diffraction; T_{SDW} is determined by neutron scattering, nuclear magnetic resonance (NMR) and muon spin resonance (μ SR).

- What is the mechanism responsible for each individual phase and in particular for superconductivity: phonons like in BCS theory? Fermi-surface instabilities (like nesting)? Electronic correlations? Spin or charge dynamics?
- Are the various phases competing or collaborating with each other, is one the precursor of the other?

I now briefly outline the electronic structure of cuprates. The top left panel of Fig. 7.3 is a sketch of the level structure of LSCO (which I take as a prototypical example): the valence configuration is Cu $3d^9$ and O $2p^6$. In the cubic environment of the oxygen atoms, the degeneracy of the d level is lifted into e_g ($x^2 - y^2$ and $3z^2 - r^2$) and t_{2g} (xy , yz , zx) levels, which are further split by a tetragonal distortion (the octahedron is elongated along the c axis, this is the Jahn-Teller effect) into 4 distinct levels (yz and zx are still degenerate). The tetragonal distortion also splits the oxygen $2p$ orbitals into σ and π levels. By symmetry, only the in-plane $x^2 - y^2$ and σ orbitals strongly hybridize, yielding a low-lying bonding band and an antibonding band at the Fermi-level. Counting the electrons, this latter band turns out to be half-filled. The rest of the states do not really hybridize and form non-bonding bands in-between the bonding and antibonding bands.

This justifies the use of a model with three bands – the in-plane $x^2 - y^2$ orbital and the two σ orbitals – to describe the physics of cuprates. The spatial arrangement of these orbitals is illustrated in the top-right panel of Fig. 7.3, and the wavefunction overlaps are parametrized by the tight-binding hopping terms t_{pd} and t_{pp} (with a different sign depending on which lobes overlap). Here, I take values that reproduce well density functional theory (within the local density approximation) calculations (see caption), and obtain the tight-binding bands shown in the bottom left panel. There is a dispersionless nonbonding (N) band at $\epsilon = \epsilon_p$ and a pair of bonding (B) and antibonding (AB) bands, the antibonding band being half-filled. The corresponding density of states is shown under label (a): there are two deep-lying bands (N and B) and one isolated band at the Fermi level³. This band is used as the starting point for a description in terms of a single-band model.

As will be seen later, the role of Coulomb interactions in cuprates has been surmised early on. However, even supposing there is a sizable Hubbard U interaction, one should be careful in writing down a single-band

³There are many other bands between -5 and 2 eVs; only they are not relevant for the problem at stake.

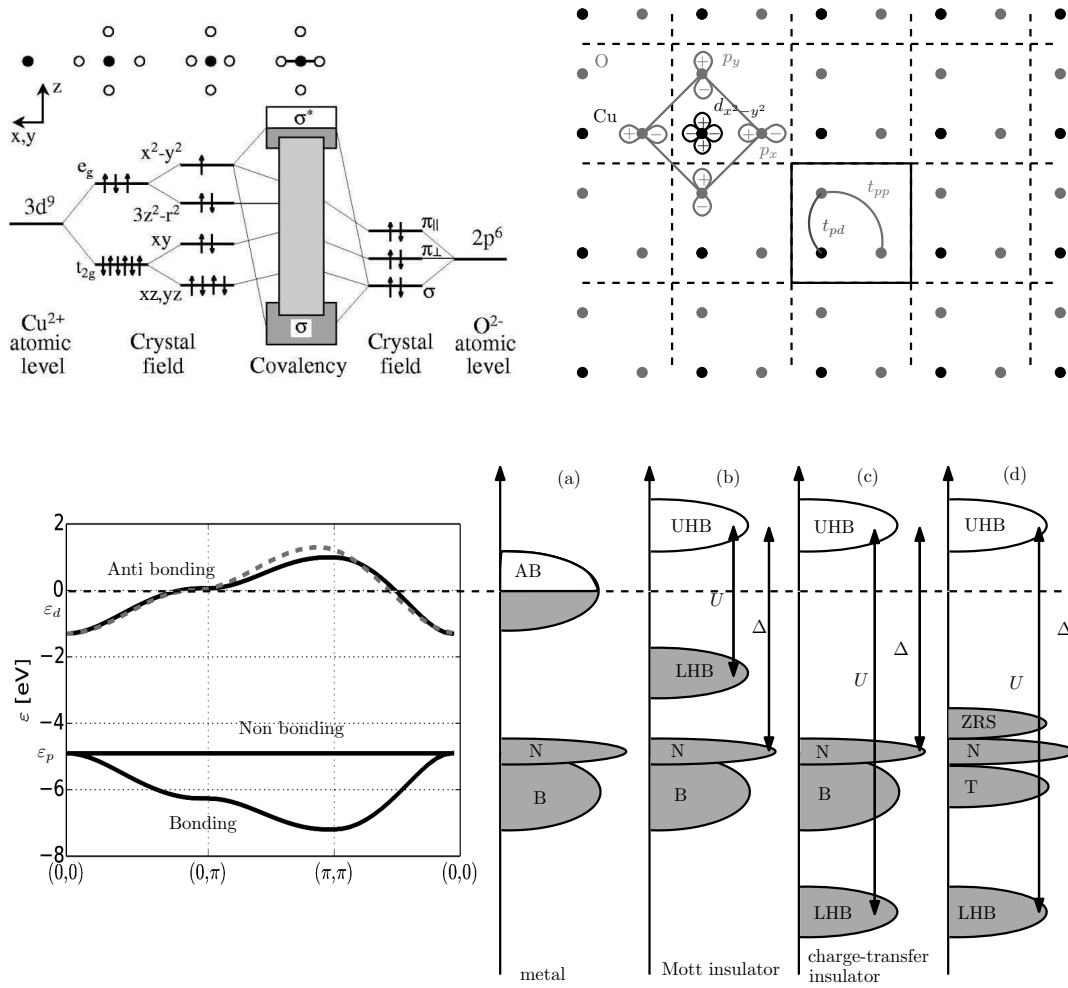


Figure 7.3: Electronic structure of cuprates: basics. *Top left*: Level structure of LSCO (from Fink *et al.* (1994); Damascelli *et al.* (2003)). *Top right*: CuO_2 plane: tight-binding parametrization in the (xy) plane. *Bottom left*: tight-binding dispersion for a three-band model (solid black curves; $t_{pd} = 1.3$ eV, $t_{pp} = 0$, $\epsilon_p = -4.9$ eV, $\epsilon_d = -1.3$ eV). Dashed curve: one-band tight-binding dispersion ($t_{dd,\text{eff}} = -0.325$ eV). *Bottom right*: various scenarios (UHB: Upper Hubbard Band; LHB: Lower Hubbard Band; ZRS: Zhang-Rice Singlet band; T: Triplet band; U is Hubbard's U , Δ is the charge-transfer energy) (adapted from Fink *et al.* (1994); Damascelli *et al.* (2003)).

model (Zhang and Rice (1988)). Let us call U the $d-d$ local interaction and Δ the charge-transfer energy ($\Delta \sim \varepsilon_d - \varepsilon_p$). Then:

- If $U \ll \Delta$ (case (b) in Fig. 7.3), then the nonbonding and bonding bands can be considered as inert and one can readily write down a single-band model with the antibonding band and an interaction U (I have plotted a corresponding band with an effective tightbinding hopping, see the red dashed line). This situation is not realized in cuprate materials which are in fact charge-transfer insulators (Zaanen *et al.* (1985)) (the situation $U \ll \Delta$ rather corresponds to early transition metal oxides, *e.g.* vanadates and titanates; see Imada *et al.* (1998) for an in-depth review).
- If, however, U and Δ are comparable in strength or if $U \gg \Delta$ (cases (c) and (d)) – which is the case in cuprate (and also nickelate) materials, then the N and B bands have to be taken into account, at least in an effective way by taking the correct “ U ” parameter in a single-band model, or with a proper three-band model if one suspects the oxygen degrees of freedom to be important. For completeness, let us note that as shown under label (c), the spin of the hole in the upper Hubbard band and the one of the electron on the bonding band interact and lead to the formation of an additional triplet band (T) and so-called Zhang-Rice singlet band (ZRS, Zhang and Rice (1988)).

As a bottom line of this discussion, one can remember that the single-band Hubbard model comes out as a natural low-energy model for cuprates, with the following caveats: (a) its effective parameters are not straightforward and (b) effects beyond the single band are not ruled out.

7.1.2 Experiments on cuprates: the importance of momentum dependence

In this section, I give a short overview of some experimental facts with a focus on the momentum dependence of the spin susceptibility and of the spectral function. I also show conductivity data which have been used to support important theoretical scenarios.

The relevant probes, with a focus on the observables they give access to, are briefly discussed in appendix H.2.

7.1.2.1 Antiferromagnetic spin fluctuations and pseudo gap from neutron scattering and nuclear magnetic resonance

Figure (7.4) gives an overview of experimental insights on the magnetic properties of cuprates as seen by neutron scattering. Neutron scattering has provided the early indication that the undoped compounds are antiferromagnetic at low temperatures: a peak at the AF wavevector (an angle $\theta \approx 26^\circ/2$ corresponds to $q \approx \pi/a$ for $\lambda_{\text{neutron}} = 2.37$ and $a_{\text{LSCO}} = 3.79$) appears at low temperatures in the static scattering intensity (panels (a) and (b) from Vaknin *et al.* (1987); in fact, the ordering wavevector is slightly canted, see panel (c) (Yamada *et al.* (1989))). In the Néel phase, the spin-wave dispersion $\tilde{\omega}(\mathbf{q})$ can be obtained by using “hot” neutrons; at long wavelengths, the slope c of $\tilde{\omega}(\mathbf{q}) \approx c\mathbf{q}$ gives access to the antiferromagnetic exchange scale J , related to c by the relation⁴: $c \equiv \sqrt{2zS}Ja \cdot 1.158$. In Aeppli *et al.* (1989), $c = 0.85$ eV, leading to $J = 160$ meV ($S = 1/2$, $z = 4$).

Furthermore, neutrons reveal dynamical spin fluctuations, as illustrated in panel (d) (from Bourges *et al.* (1996)), which shows that $\chi''_{\text{spin}}(\mathbf{q}, \omega = 39$ meV) features AF fluctuations that are enhanced at low temperatures. Such curves can be fitted by a Lorentzian or Ornstein-Zernicke form

$$\Gamma(\mathbf{q}, \omega) = \frac{\Gamma(\mathbf{q} = 0, \omega)}{\xi^2 (\mathbf{q} - \mathbf{Q}_{\text{AF}})^2 + 1} \quad (7.1)$$

⁴This relation can be obtained by starting from the Heisenberg model and performing a $1/S$ expansion or using Schwinger bosons. See *e.g.* Chap. 8 of Auerbach (1994).

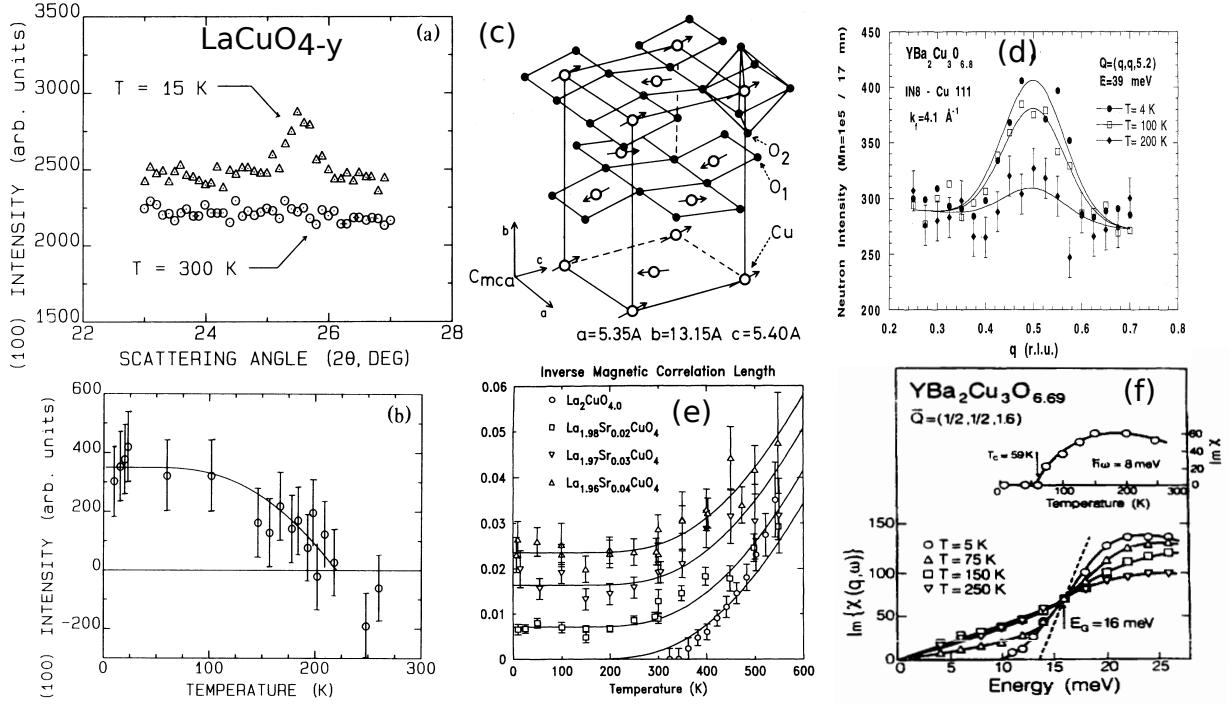


Figure 7.4: Neutron scattering: early experiments. (a) (from Vaknin *et al.* (1987)): Dependence of the (static) scattering intensity ($\sim \Gamma_1(\mathbf{q}, \omega = 0)$) as a function of the scattering angle 2θ [$q = \frac{4\pi}{\lambda_{\text{neutron}}} \sin(\theta/2)$] in the 100 direction. (b) Temperature dependence of the same intensity. (c) (from Yamada *et al.* (1989)) AF spin order in LSCO [note: the definition of \mathbf{a}, \mathbf{b} , and \mathbf{c} is different from my conventions] (d) (from Bourges *et al.* (1996)): scattering intensity as a function of wavevector \mathbf{q} at $\omega = 39$ meV ($\sim \Gamma_2(\mathbf{q}, \omega)$). (e) (from Keimer *et al.* (1992)): inverse correlation length extracted from spin correlation function vs. T . (f) (from Rossat-Mignod *et al.* (1991)): $\text{Im} \chi_{\text{spin}}(\mathbf{q}, \omega) \propto \Gamma_2(\mathbf{q}, \omega)$ for different temperatures.

Here $\Gamma(\mathbf{q}, \omega)$ denotes the neutron scattering rate ($\propto \text{Im} \chi_{\text{sp}, \perp}(\mathbf{q}, \omega)$, see appendix H.2.1), ξ is the AF correlation length and $\mathbf{Q}_{\text{AF}} = (\pi, \pi)$. The result of such a fit for YBCO is shown in panel (e) for a range of dopings: while diverging at half-filling upon cooling the system, signalling the onset of long-range AF order, the correlation length remains finite for the doped system until zero temperature, with correlation lengths of the order of 50 : albeit far-reaching, the spin correlations away from half-filling are too short-ranged to induce an ordered phase (see the phase diagram, Fig. 7.2). Panel (f) shows the energy dependence of $\Gamma(\mathbf{q}, \omega)$ at fixed momentum in the same region of the phase diagram: upon cooling, a “soft” gap in the spin spectrum appears well above the superconducting critical temperature ($T_c = 59$ K). This spin gap is called a “pseudogap”.

This depletion of the spin susceptibility at low energy upon cooling was first observed in early NMR measurements reproduced in Fig. 7.5. While the Knight shift of a normal metal is supposed to be constant and proportional to the density of states at the Fermi level (see Eqs. (H.38-H.39) in appendix H.2.2) – which is roughly what is observed at half-filling ($x = 1$), the Knight shift, and hence $\chi_{\text{spin}}(\mathbf{q} = 0, \omega = 0)$, of doped compounds decreases for decreasing temperature; the same phenomenon is seen for the spin-lattice relaxation rate $1/T_1$ (right panel). This suppression of spectral weight at low energies is in agreement with the above neutron experiments.

7.1.2.2 Conductivity: the puzzle of the mid-infrared peak

While the importance of spin fluctuations and the opening of a pseudogap has been stressed by neutron and NMR measurements, conductivity measurements, such as those shown in Fig. 7.6 for LSCO at various

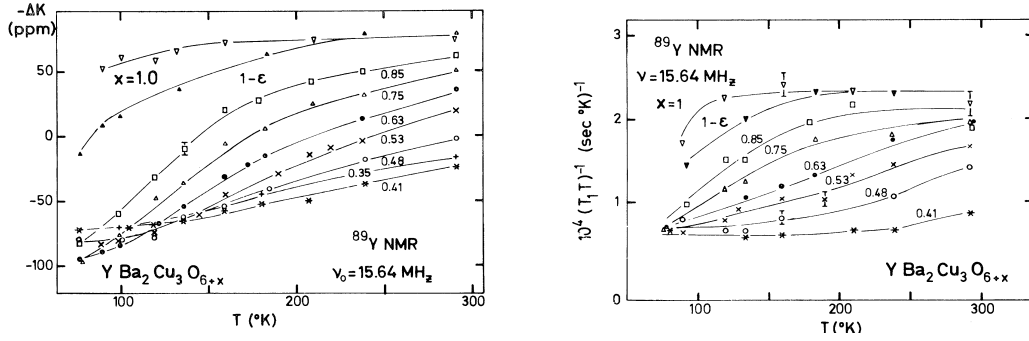


Figure 7.5: NMR: early experiments on $\text{YBa}_2\text{Cu}_3\text{O}_{6+x}$ (from Alloul *et al.* (1989)). *Left*: Knight shift as a function of temperature for several dopings. *Right*: Spin-lattice relaxation rate $1/T_1 T$ as a function of temperature for several dopings.

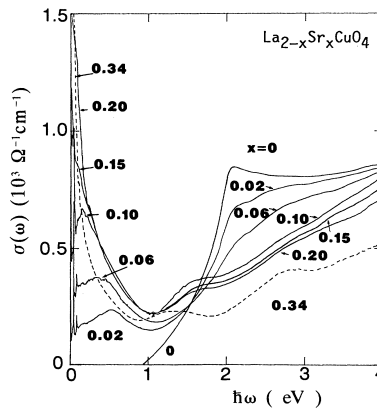


Figure 7.6: Optical conductivity $\sigma(\omega)$ of LSCO for various dopings at room temperature (from Uchida *et al.* (1991))

dopings, have brought up new questions. The optical spectrum at half-filling ($x = 0$) displays a gap with an “edge” at about 2 eV, which roughly corresponds to the charge-transfer energy Δ and can be explained by the opening of a Mott gap in the antibonding $x^2 - y^2$ band (with $U \gg \Delta$) (see the band structure arguments presented above, section 7.1.1). This corroborates the importance of correlations as touched on in section 7.1.1.

Upon doping, however, the situation is less clear-cut. At intermediate dopings (see *e.g.* $x = 0.02 - 0.06$), a peak at $\lesssim 0.5$ eV appears (the “mid-infrared peak”, whose origin is still subject to discussion), and for large doping a Drude peak at $\omega = 0$ appears, albeit with an unconventional $1/\omega$ dependence (instead of $1/\omega^2$, see Eq. (H.50)).

7.1.2.3 Angle-resolved photoemission: momentum differentiation on the Fermi surface

Contrary to NMR, neutron scattering and optics, which measure two-particle correlation functions, ARPES probes the one-particle spectral function $A(\mathbf{k}, \omega)$, as is shown in appendix H.1.4. Hence, one can look into ARPES spectra for signs or signatures of the two-particle correlations. Indeed, collective modes seen in two-particle probes can have consequences on the propagation of electrons in the solid; these effects are encoded in the self-energy $\Sigma(\mathbf{k}, \omega)$. Let us remember that $\Sigma(\mathbf{k}, \omega)$ enters $A(\mathbf{k}, \omega)$ in the following way (for a one-band

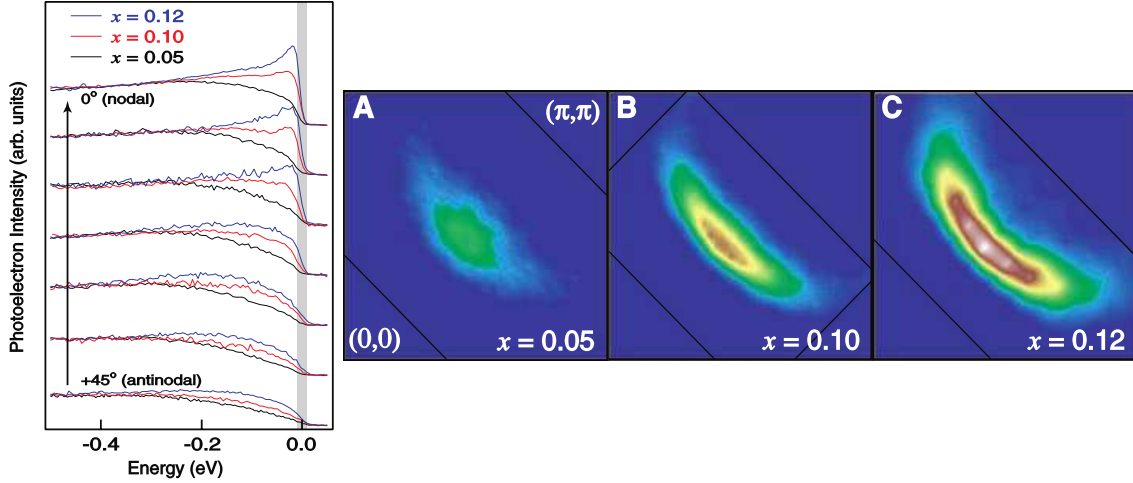


Figure 7.7: ARPES on $\text{Ca}_{2-x}\text{Na}_x\text{CuO}_2\text{Cl}_2$ at $T = 15\text{K}$, from Shen *et al.* (2005): *Left*: EDCs from $\mathbf{k} = (\pi, 0)$ (antinode, bottom) to $\mathbf{k} = (\pi/2, \pi/2)$ (node, top). *Right*: MDCs at ϵ_F for three dopings 5, 10 and 12% (with $T_c = 13\text{K}$ and 22K for the latter two)

model with bare dispersion $\epsilon(\mathbf{k})$:

$$A(\mathbf{k}, \omega) = -\frac{1}{\pi} \frac{\text{Im}\Sigma(\mathbf{k}, \omega)}{(\omega - \epsilon_{\mathbf{k}} - \text{Re}\Sigma(\mathbf{k}, \omega))^2 + \text{Im}\Sigma(\mathbf{k}, \omega)^2} \quad (7.2)$$

In particular, the spectral weight on the Fermi surface is given by:

$$A(\mathbf{k}_F, \omega = 0) = -\frac{1}{\pi} \frac{1}{\text{Im}\Sigma(\mathbf{k}_F, \omega = 0)}$$

Thus, momentum distribution curves (MDCs) at $\omega = 0$ can be directly related to the imaginary part of the self-energy. Such curves for “CCOC” ($\text{Ca}_{2-x}\text{Na}_x\text{CuO}_2\text{Cl}_2$) for different dopings are shown in Fig. 7.7. As the doping is decreased from close to optimal doping ($x = 0.12$) to close to half-filling ($x = 0.05$), the spectral intensity on the Fermi surface becomes weaker and weaker in the “antinode” region (around the $(\pi, 0)$ and $(0, \pi)$ points) (right panels, MDCs). The energy dispersion curves (EDCs, on the left) show that while there is a sharp Fermi surface at the node ($\mathbf{k} = (\pi/2, \pi/2)$ region), a soft gap opens at the antinode for the lower dopings. This phenomenon was first observed in bismuth samples (BiSCO) in the mid 1990s (Marshall *et al.* (1995, 1996); Ding *et al.* (1996); Loeser *et al.* (1996)).

7.1.2.4 The generic cuprate phase diagram

Let us conclude this short experimental overview by a description of the generic phase diagram of the CuO_2 planes on the hole-doped side, shown in Fig. 7.8. The AF and pseudogap phases have been explained in the previous sections. They cover the undoped and underdoped portions of the phase diagram. The temperature T^* is the crossover temperature to the pseudogap phase. Above the superconducting dome, the “strange metal” phase is characterized by anomalous behaviors in several observables such as the resistivity and the conductivity. In the overdoped phase, Fermi-liquid behavior is recovered. The superconducting phase is characterized with a gap of d -wave symmetry, to be contrasted with the s -wave (spherical) symmetry of the BCS gap. At 12% or one eighth doping, a charge-density wave is seen in many experiments and has been the subject of much interest in recent years, although incommensurate stripe order in LBCO and LSCO has been observed as early as 1995 by Tranquada *et al.* (1995).

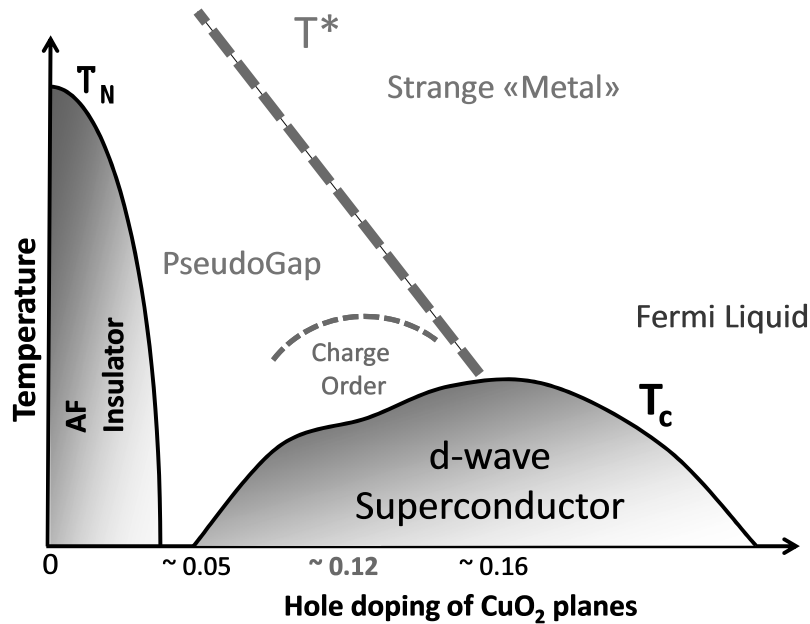


Figure 7.8: Generic cuprates phase diagram. Adapted from Le Tacon (2015).

7.1.3 Summary

The experiments reviewed in the previous section point to a number of facts:

- **strong correlations** have to be reckoned with: the parent compounds are Mott/charge-transfer insulators;
- **spin fluctuations** are strong in the underdoped regime;
- there are **sizable nonlocal correlations** at the two-particle level (spin correlations) and the one-particle level (as seen in the momentum-resolved spectral function);
- the **BCS theory** with electron-phonon coupling as the “pairing glue” **does not account for the experimental findings** (see e.g. *Perfetti et al. (2007)*)

7.2 Theory: two viewpoints on high-temperature superconductivity

To account for the experimental evidence, two main classes of theories have been put forward from the early days. The starting point of both families is the antiferromagnetic Mott insulator, albeit with a different emphasis:

- According to a first class of theories, the essential point is that the parent compound is an **antiferromagnet**. The key observation is that there is a $T = 0$ transition between an ordered phase and a disordered (Fermi-liquid) phase at a critical doping x_c . This is a quantum critical point. Strong (spin) fluctuations – paramagnons – emanate from the quantum critical point at finite temperatures. These critical, long-ranged spin fluctuations act as the pairing glue between electrons. At low temperature, around this critical point, the fluctuations are so strong that the electrons form pairs, leading to a superconducting dome. This – essentially weak-coupling – approach was first proposed by *Monthoux et al. (1991)*; it is illustrated by the left panel of Fig. 7.9 and will be elaborated on in section 7.2.1.

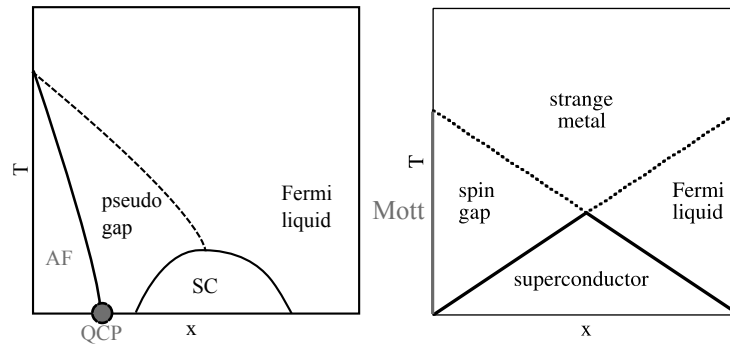


Figure 7.9: Two scenarios for cuprates (right panel adapted from Norman and Pépin (2003))

- According to a second class of theories, the **Mott** character of the parent compound is essential for superconductivity. Strong correlations open a charge gap and cause the particles to localize. These localized moments (only) then order antiferromagnetically at low temperatures. Upon doping, the main quasiparticles are claimed to be spin singlets of these localized moments (“spinons”) and propagating holes (“holons”). This “spin liquid” undergoes ordering at low enough temperatures because spinons induce attractive interactions between holons. This theory – called “Resonating Valence Bonds” (RVB) was put forward by Anderson (1987). It is illustrated in the right panel of Fig. 7.9 and will be developed in section 7.2.2.

Other theories have been proposed, such as the concept of “marginal Fermi liquid” by Varma *et al.* (1989) or “loop current phases” (Varma (1999), consistent with neutron experiments by *e.g.* Fauqué *et al.* (2006)), but I will restrict to the two above classes.

7.2.1 Spin fluctuation theory: The importance of long-range fluctuations (weak coupling)

The observation of strong and rather long-ranged spin fluctuations in neutron scattering experiments has prompted many authors to devise methods incorporating a coupling of spin fluctuations to the fermionic degrees of freedom, either phenomenologically – by choosing a form for the spin susceptibility fitting the available experimental data – or starting from low-energy models such as the Hubbard model.

The more phenomenological works, initiated by Monthoux *et al.* (1991), were spurred by pre-cuprates works showing that in low dimensions, spin fluctuations stemming from Fermi surface instabilities – a weak-coupling mechanism – can act as a pairing glue (Scalapino *et al.* (1986, 1987)), leading to *d*-wave superconductivity. An alternative weak-coupling approach also based on spin fluctuations has been proposed by Schrieffer *et al.* (1989): in this work, the authors show that in a spin-density wave (SDW) background, quasiparticles called “spin bags”, consisting of a hole surrounded by spins excitations depressing the local SDW order (a sort of polaron), experience an attractive force to one another, leading to an *s*-wave superconducting instability. This scenario is quite different from the “spin fluctuation” scenario which will be presented in the next section, where there are strong spin fluctuations, however not in a SDW background.

Other approaches such as the fluctuation exchange approximation (FLEX) and the two-particle self-consistent theory (TPSC) also emphasize two-particle fluctuations in the spin and charge channels (and also superconducting singlet channel for FLEX). As weak-coupling diagrammatic approaches, they are limited to the weak-interaction regime. They are described in more details in appendices G.2 and G.3.

7.2.1.1 The spin-fermion model

After the early NMR experiments, Millis *et al.* (1990) have shown that the NMR experiments are well described by the following phenomenological form of the spin susceptibility:

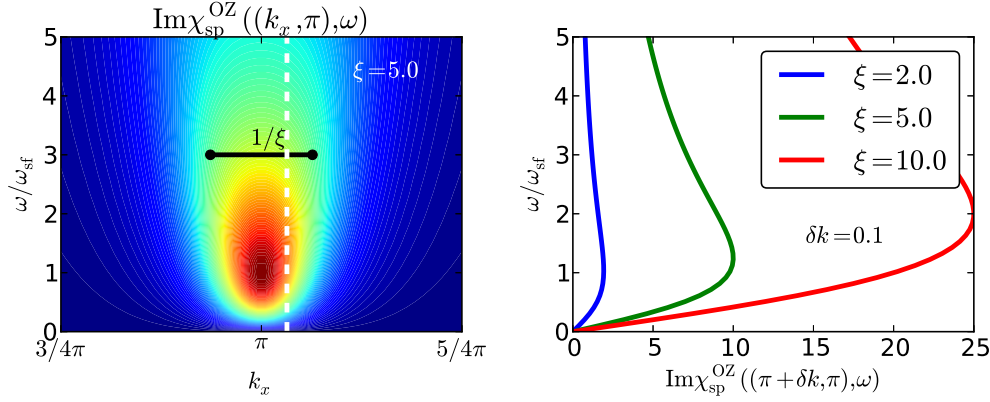


Figure 7.10: Ornstein-Zernicke susceptibility (here, $\chi_0 = \xi^2$; see text). *Left*: color plot $\text{Im}\chi_{\text{sp}}^{\text{OZ}}((k_x, \pi), \omega)$. *Right*: vertical cut (along the white dashed line), i.e. at $k_x = \pi + \delta k$, for various values of ξ .

$$\chi_{\text{sp}}^{\text{OZ}}(\mathbf{q}, \omega) = \frac{\chi_0}{1 + \xi^2 (\mathbf{q} - \mathbf{Q})^2 - i \frac{\omega}{\omega_{\text{sf}}}} \quad (7.3)$$

In this work, the parameters χ_0 , ξ and ω_{sf} are fitted to the available experimental data, with $\mathbf{Q} = (\pi, \pi)$ denoting the antiferromagnetic wavevector. ξ is the magnetic correlation length, ω_{sf} the typical spin fluctuation energy, as illustrated in Fig.7.10. This form, traditionally called the ‘‘Ornstein-Zernicke’’ form, can be obtained from the susceptibility in the RPA approximation in the limit $\mathbf{q} \rightarrow \mathbf{Q}$ and $\omega \rightarrow 0$ (see appendix I.4.2.2, with $\chi_0 = \frac{1}{U_{\text{sp}}} \xi^2 / \xi_0^2$ and $\omega_{\text{sf}} = \frac{D}{\xi^2}$).

What the NMR and inelastic neutron scattering experiments were indicating is that the spin degrees of freedom, governed by the correlator $\chi_{\text{sp}}^{\text{OZ}}(\mathbf{q}, \omega)$, are ‘‘relevant’’ (in the renormalization group sense) low-energy degrees of freedom in the underdoped region of the phase diagram. This prompted Monthoux *et al.* (1991) to propose a superconducting pairing scenario based on the spin degrees of freedom. Spin fluctuation theory (see Schmalian *et al.* (1998) for a review) revolves around this idea.

It consists in an effective phenomenological low-energy model where the fermionic degrees of freedom are coupled to their own spin fluctuations (the so-called ‘‘spin-fermion model’’):

$$S_{\text{sf}} = \sum_{k\sigma} \bar{c}_{k\sigma} [-G_0^{-1}] c_{k\sigma} + \frac{1}{2} \sum_q [\chi_{\text{sp}}^{\text{OZ}}(q)]^{-1} \vec{\phi}_q \cdot \vec{\phi}_{-q} + \sum_{k'} \lambda_{\mathbf{k}'-\mathbf{k}} \vec{\phi}_{\mathbf{k}'-\mathbf{k}} \cdot \left\{ \sum_{\sigma\sigma'} \bar{c}_{k'\sigma} \vec{\sigma}_{\sigma\sigma'} c_{k\sigma'} \right\} \quad (7.4)$$

Here, $k \equiv (\mathbf{k}, i\omega)$, \bar{c}_k and c_k are conjugate Grassmann antiperiodic fields describing the fermionic degrees of freedom (with spin $\sigma = \uparrow, \downarrow$ and non-interacting propagator $G_0^{-1}(k) \equiv i\omega - \xi_{\mathbf{k}}$); $\vec{\phi}_q$ is a vector bosonic field (with three components $I = x, y, z$) describing the spin fluctuations degrees of freedom⁵, $\lambda_{\mathbf{q}}$ is the coupling constant between the fermions and the bosonic fields, and $\vec{\sigma} = (\sigma^x, \sigma^y, \sigma^z)$ is the vector of Pauli matrices. One can check that in the absence of coupling ($\lambda = 0$), $\langle \phi^I(q) \phi^I(-q) \rangle = \chi_{\text{sp}}^{\text{OZ}}(q)$.

In the 1990s, this model was introduced as a phenomenological model based on NMR and INS evidence. It can also be thought of as having been formally derived from a weak-coupling renormalization procedure starting from the Hubbard model (see *e.g.* Rech *et al.* (2006); Chubukov *et al.* (2002) for a discussion). Indeed, functional renormalization group (fRG) studies (see Metzner *et al.* (2012) for a review) have shown that, at least at weak coupling, the low-energy effective action is close to (7.4), giving an *a posteriori* justification at weak coupling.

⁵ ϕ^I has bosonic commutation rules, not spin commutation rules, despite what is conveyed by the usual notation in terms of spin variables ‘‘s’’.

Figure 7.11: The self-energy in the spin fluctuation approximation.

7.2.1.2 *d*-wave superconductivity in the spin-fermion model

In this section, I briefly show that *d*-wave superconductivity can emerge from the spin-fermion model, using a few crude approximations. A more detailed discussion can be found *e.g.* in Chubukov *et al.* (2002).

The emergence of *d*-wave superconductivity in the spin-fermion model defined by Eq. (7.4) was predicted before the discovery of cuprate superconductors (Kohn and Luttinger (1965) had argued that the Friedel oscillations in the susceptibility due to the singularity of $\chi_0(\mathbf{q}, \omega = 0)$ at $2k_F$ could lead to a *d*-wave attraction; Béal-Monod *et al.* (1986); Scalapino *et al.* (1986, 1987) had examined the possibility of superconductivity mediated by antiferromagnetic fluctuations or paramagnons).

This attraction can be proven in a similar way as I have derived the CDW instability in two dimensions in appendix I.6.1.3, namely by directly assuming that the boson mode ϕ condenses and then writing the corresponding self-consistent equations. Here, I give a slightly different derivation based on Nambu-Gor'kov Green's functions (Nambu (1960)), inspired from one derivation of generalized Eliashberg equations (an extension of BCS theory taking into account the full energy dependence of the gap function and self-energy effects, however without vertex corrections (Migdal (1958); Eliashberg (1960))). Instead of the spinor $\Psi_{k\sigma}^\dagger \equiv [\bar{c}_{k+Q,\sigma}, \bar{c}_{k,\sigma}]$ which I have used for the CDW instability, I define the spinor $\Psi_k^\dagger \equiv [\bar{c}_{k\uparrow}, c_{-k\downarrow}]$ to rewrite Eq. (7.4) as:

$$S_{sf}^{\text{Nambu}} = \sum_{\mathbf{k} \in \text{BZ}, i\omega} \Psi_k^\dagger [-G_0^{-1}] \Psi_k + \frac{1}{2} \sum_q [\chi_{sp}^{\text{OZ}}(q)]^{-1} \phi_q^z \cdot \phi_{-q}^z + \sum_{k'} \phi_{k'-k}^z \Psi_{k'}^\dagger [\lambda_{\mathbf{k}'-\mathbf{k}} \mathbf{1}] \Psi_k \quad (7.5)$$

Here, bold symbols act in the 2×2 spin space. In particular, $G_0^{-1}(k) = \begin{bmatrix} G_0^{-1}(k) & 0 \\ 0 & -G_0^{-1}(-k) \end{bmatrix}$. In going from Eq. (7.4) to (7.5), I have assumed that the Brillouin zone is invariant under the inversion $\mathbf{k} \rightarrow -\mathbf{k}$ and considered the simplified case of longitudinal fluctuations ϕ^z only. Defining the Nambu-Gor'kov Greens function $G(k) \equiv -\langle \Psi(k) \Psi^\dagger(-k) \rangle$ and the self-energy $\Sigma(k) = G_0^{-1}(k) - G^{-1}(k) \equiv \begin{bmatrix} \Sigma(k) & S(k) \\ S^*(k) & -\Sigma(-k) \end{bmatrix}$ (Σ/S is the normal/anomalous self-energy), one gets:

$$G(k) = \frac{1}{(G_0^{-1}(k) - \Sigma(k)) (-G_0^{-1}(-k) + \Sigma(-k)) - |S(k)|^2} \begin{bmatrix} -G_0^{-1}(-k) + \Sigma(-k) & S(k) \\ S^*(k) & G_0^{-1}(k) - \Sigma(k) \end{bmatrix} \quad (7.6)$$

To lowest order in the electron-boson coupling λ (*i.e.* neglecting vertex corrections), the self-energy reads:

$$\Sigma(k) = - \sum_q \lambda_q G(k+q) [-\chi_{sp}^{\text{OZ}}(q)] \lambda_{-q} \quad (7.7)$$

or equivalently $\Sigma(k) = - \sum_{k'} \lambda_{k'-k} G(k') [-\chi_{sp}^{\text{OZ}}(k'-k)] \lambda_{k-k'}$. This diagram is illustrated in Fig. 7.11. Combining Eq. (7.6) and (7.7), one finds that the anomalous self-energy $S(k)$, which is proportional to the superconducting gap, obeys the equation:

$$S(k) = \sum_{k'} \frac{|\lambda_{k'-k}|^2 \chi_{sp}^{\text{OZ}}(k'-k) S(k')}{(G_0^{-1}(k') - \Sigma(k')) (-G_0^{-1}(-k') + \Sigma(-k')) - |S(k')|^2} = \sum_{k'} \frac{|\lambda_{k'-k}|^2 \chi_{sp}^{\text{OZ}}(k'-k) S(k')}{(i\omega' - \xi_{\mathbf{k}'} - \Sigma(k')) (i\omega' + \xi_{-\mathbf{k}'} + \Sigma(-k')) - |S(k')|^2}$$

For now, I suppose that the normal self-energy $\Sigma(\mathbf{k}, i\omega)$ is vanishing or constant (absorbed in the chemical potential); furthermore, supposing that $\xi_{\mathbf{k}'} = \xi_{-\mathbf{k}'}$, looking for a static solution $S(\mathbf{k}, i\omega) = S(\mathbf{k})$, and linearizing for small $S(\mathbf{k}')$ (i.e. $T \approx T_c$), I obtain:

$$S(\mathbf{k}) = - \sum_{\mathbf{k}', i\omega'} \frac{|\lambda_{\mathbf{k}'-\mathbf{k}}|^2 \chi_{\text{sp}}^{\text{OZ}}(\mathbf{k}' - \mathbf{k}, i\omega')}{\omega'^2 + \xi_{\mathbf{k}'}^2} S(\mathbf{k}') \quad (7.8)$$

Let us now examine the possible solutions for this equation. If, as in BCS theory, one chooses a constant $S(\mathbf{k}) = S$, one sees that since $\chi_{\text{sp}}^{\text{OZ}} > 0$, the left-hand side and the right-hand side have opposite signs, so that such a s -wave solution is forbidden. Since $\chi_{\text{sp}}^{\text{OZ}}$ is sharply peaked at $\mathbf{k}' - \mathbf{k} = \mathbf{Q} = (\pi, \pi)$ (see Eq. (7.3)), if one considers $\mathbf{k} = (\pi, 0)$ on the left-hand side, then the most important contribution to the integral will be for $\mathbf{k}' = (0, \pi)$. Hence, a gap function $S(\mathbf{k})$ such that $S(\mathbf{k} = (\pi, 0))$ and $S(\mathbf{k} = (0, \pi))$ have opposite signs – i.e. a solution with d -wave symmetry – can be a solution to this equation.⁶

7.2.1.3 Spin-fluctuation theory, hot and cold spots: main results

The phenomenological susceptibility introduced in Eq. (7.3) can be tuned via ξ to approach the quantum critical point (corresponding to $\xi \rightarrow \infty$ at $T = 0$; see right panel of Fig. 7.9). The computations in the resulting critical region account for a number of experimental results such as the temperature dependence of the NMR data (Onufrieva *et al.* (1998)) (and hence the dependence of T^* on doping), the opening of a pseudogap (Onufrieva and Pfeuty (1999)), STM data (Onufrieva and Pfeuty (2012)), kinks in the ARPES dispersions (Dahm *et al.* (2008)). Indeed, the normal self-energy in this approximation (computed from Eq. (7.7) and continued analytically, see Eq. (I.36) in appendix I.5) is given by:

$$\Sigma(\mathbf{k}, \omega) = - \sum_{q, \pm} |\lambda_q|^2 \int_0^\infty \frac{d\bar{\omega}}{\pi} \text{Im} \chi_{\text{sp}}^{\text{OZ}}(\mathbf{q}, \bar{\omega}) \frac{n_B(\bar{\omega}) + n_F(\pm \epsilon_{\mathbf{k}+\mathbf{q}})}{\omega - i\eta \pm \bar{\omega} - \epsilon_{\mathbf{k}+\mathbf{q}}}$$

Since $\text{Im} \chi_{\text{sp}}^{\text{OZ}}(\mathbf{q}, \bar{\omega})$ is peaked at $\bar{\omega} = \omega_{\text{sf}}$ and $\mathbf{q} = \mathbf{Q}$, this can be approximated as:

$$\Sigma(\mathbf{k}, \omega) \approx - \sum_{\pm} \frac{n_B(\omega_{\text{sf}}) + n_F(\pm \epsilon_{\mathbf{k}+\mathbf{Q}})}{\omega - i\eta \pm \omega_{\text{sf}} - \epsilon_{\mathbf{k}+\mathbf{Q}}} \quad (7.10)$$

The scattering on the Fermi surface is defined as $\gamma_{\mathbf{k}_F} = \Sigma''(\mathbf{k}_F, \omega = 0) = \sum_{\pm} \frac{\{n_B(\omega_{\text{sf}}) + n_F(\pm \epsilon_{\mathbf{k}_F+\mathbf{Q}})\} \eta}{(\pm \omega_{\text{sf}} - \epsilon_{\mathbf{k}_F+\mathbf{Q}})^2 + \eta^2}$. It is large for momenta \mathbf{k}_F such that $\epsilon_{\mathbf{k}_F+\mathbf{Q}} = \omega_{\text{sf}}$. In the limit $\xi \rightarrow \infty$, $\omega_{\text{sf}} \rightarrow 0$, i.e. $\gamma_{\mathbf{k}_F}$ is large if and only if $\epsilon_{\mathbf{k}_F+\mathbf{Q}} \approx 0$, i.e. if $\mathbf{k}_F + \mathbf{Q}$ lies on the Fermi surface. For the Fermi surface of cuprates, there are two such points in the upper quadrant of the Brillouin zone, at the intersection of the non-interacting Fermi surface and of the antiferromagnetic Brillouin zone boundary. At these points, the quasi-particles have a short lifetime because

⁶The sign of the bosonic propagator is crucial here. In the case of the electron-phonon interaction, the phononic propagator D_0 is negative and hence the gap of d -wave symmetry: had one started from the Fröhlich action, Eq. (I.38) in appendix I.6, one would have gotten:

$$S_{\text{eb}}^{\text{Nambu}} = \sum_{\mathbf{k} \in \text{BZ}, i\omega} \Psi_{\mathbf{k}}^\dagger [-G_0^{-1}] \Psi_{\mathbf{k}} + \frac{1}{2} \sum_q [-D_0(q)^{-1}]^{-1} \phi_q \phi_{-q} + \sum_{\mathbf{k}'} \phi_{\mathbf{k}'-\mathbf{k}} \Psi_{\mathbf{k}'}^\dagger [\lambda_{\mathbf{k}'-\mathbf{k}} \sigma^z] \Psi_{\mathbf{k}}$$

where $D_0(q)$ is now the phonon propagator (note the σ^z matrix). When performing a similar computation as above for this action, the minus sign in front of D_0 and the σ^z matrix instead of 1 lead to a cancellation of minus signs and one gets the Matsubara-frequency version of the BCS gap equation:

$$S(\mathbf{k}) = - \sum_{\mathbf{k}', i\omega'} \frac{|\lambda_{\mathbf{k}'-\mathbf{k}}|^2 D_0(\mathbf{k}' - \mathbf{k}, i\omega')}{\omega'^2 + \xi_{\mathbf{k}'}^2} S(\mathbf{k}') \quad (7.9)$$

with the important difference that D_0 is *negative* at low frequencies. Hence, this equation accepts a uniform – s -wave – solution $S(\mathbf{k}) = S$, the BCS gap.

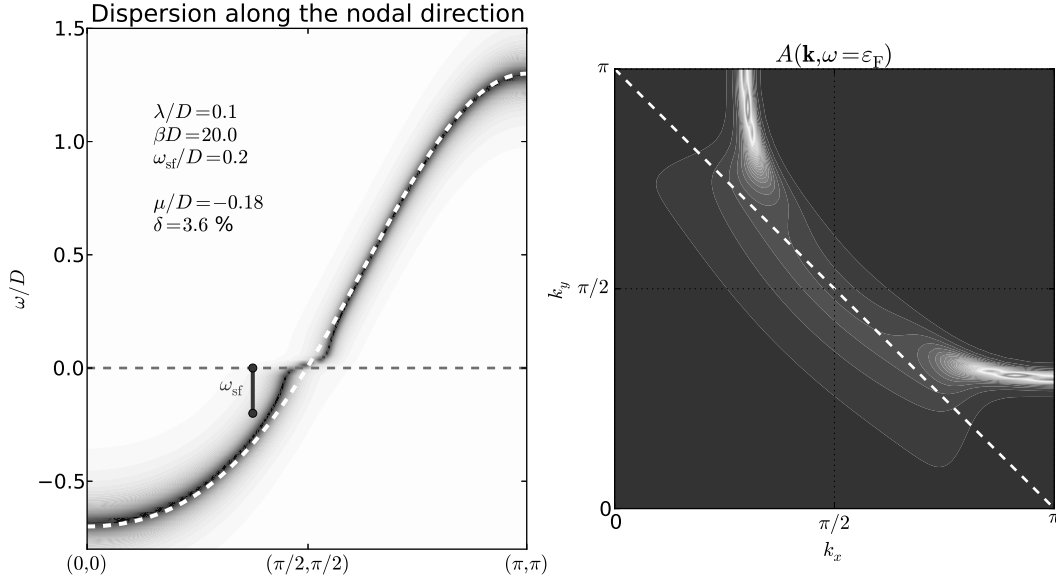


Figure 7.12: Kinks and hot regions in spin fluctuation theory computed from Eq. (7.10). *Left*: renormalized dispersion (computed keeping only the real part of Σ). The white dashed line is the bare dispersion ($t = -0.25$, $t' = -0.3 \cdot t$). *Right*: MDC at $\omega = \epsilon_F$ in the upper quadrant of the Brillouin zone. The white dashed line is the antiferromagnetic Brillouin zone boundary

they are scattered by spin fluctuations. These points are called “hot spots”. The real part of the above self-energy deforms the bands with a characteristic energy scale ω_{sf} ; this results in a kink in the nodal direction. Fig. 7.12 illustrates these features. A more detailed discussion of the doping dependence of ω_{sf} and of the resulting kink can be found in Manske *et al.* (2002).

The main advantage of spin fluctuation theory lies in the fact that it captures the momentum dependence of the spin susceptibility and of the self-energy; a phenomenological approach, it agrees well with experiments. However, this interesting feature is offset by the lack of control inherent to the *choice* of the phenomenological form of the spin susceptibility and more generally of the low-energy model (7.4). Secondly, even within this model, the neglect of vertex corrections implied by the form of the self-energy (Eq. (7.7)) is not justified: contrary to the phononic case, where the vertex correction scales as $\sqrt{m_e/M}$ (ratio of the electronic to the ionic mass), for the spin-fermion coupling, there is no such Migdal theorem. While this could be seen as a blessing to attain high critical temperatures, this has to be taken into account when computing the self-energy.

7.2.2 Another viewpoint: The importance of Mottness

The approaches presented above are valid when Mott physics do not play an important role compared to long-ranged spin fluctuations. Another class of approaches takes a fundamentally different point of view by asserting that the Mott phenomenon is key to understanding cuprate physics.

7.2.2.1 Resonating valence bonds (RVB): the strong-coupling scenario of high-temperature superconductivity

The standard-bearer of this class of approaches is Anderson (1987), who has proposed that cuprate materials should be regarded primarily as doped Mott insulators. Doping the Mott insulator frustrates the antiferromagnetic order, causing the electron spins to form disordered singlet pairs, or “resonating valence bonds” (RVB, as they were called in the original paper (Anderson (1973))); see Fig. 7.13 for an illustration). In this

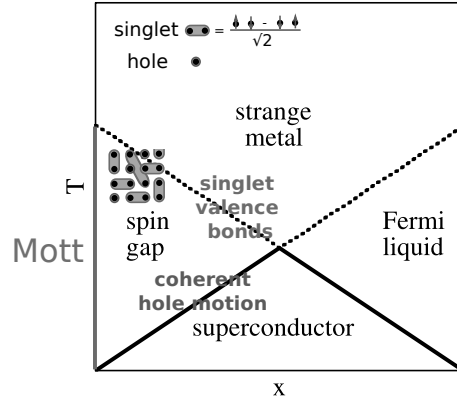


Figure 7.13: RVB scenario

“spin liquid”, the holes have a certain mobility. This pairing of localized spins in singlets explains the pseudogap temperature T^* . Above T^* (in the “strange” metal phase), the singlet pairs disappear. At large enough doping and low enough temperatures, the motion of the holes becomes coherent, leading to a d -wave superconducting state. A central point in this approach is the realization that the antiferromagnetism of cuprates is of Heisenberg type, namely it involves localized spins as opposed to weak-coupling itinerant antiferromagnetism, whose main mechanism is a minimization of the kinetic energy by a halving of the Brillouin zone (this “Slater” mechanism is discussed in appendix I.6.2.3).

The road to superconductivity can be studied by taking the $U \rightarrow \infty$ limit of the Hubbard model, which leads to the $t - J$ model (see *e.g.* Auerbach (1994) for more details):

$$H_{t-J} = -t \sum_{\langle ij \rangle} [\tilde{c}_{i\sigma}^\dagger \tilde{c}_{j\sigma} + \text{h.c.}] + J \sum_{ij} \left[\vec{s}_i \cdot \vec{s}_j - \frac{1}{4} n_i n_j \right] \quad (7.11)$$

where $\sum_{\langle ij \rangle}$ denotes a sum over all nearest-neighbor bonds, $\tilde{c}_{i\sigma}^\dagger$ is a modified creation operator which projects out double occupancies: $\tilde{c}_{i\sigma}^\dagger \equiv c_{i\sigma}^\dagger (1 - n_{i\bar{\sigma}})$, and $\vec{s}_i \equiv \tilde{c}_{i\sigma}^\dagger \vec{\sigma}_{\sigma\sigma'} \tilde{c}_{i\sigma'}$ ($\vec{\sigma}$ is the vector of Pauli matrices), and $J = \frac{4t^2}{U}$ is an antiferromagnetic superexchange coupling. Noting the formal similarity between this Hamiltonian and the spin fermion action Eq. (7.5) upon integration of the ϕ fields (with the replacement $J(\cos(q_x) + \cos(q_y)) \leftrightarrow \frac{1}{2} \lambda^2 \chi_{\text{sp}}^{\text{OZ}}(\mathbf{q}, i\Omega)$), one can directly write the gap equation:

$$\mathcal{S}(\mathbf{k}) = -3 \sum_{\mathbf{k}', i\omega'} \frac{J(\mathbf{k}' - \mathbf{k})}{\omega'^2 + \xi_{\mathbf{k}'}} \mathcal{S}(\mathbf{k}') \quad (7.12)$$

which has a d -wave solution for the same reason as the one discussed for the spin-fermion model (the factor of 3 comes from the three spin components). The notable difference is that at this simple mean-field level, the effective interaction is instantaneous (which has lead Anderson (2007) to question the use of the word “pairing glue” for cuprate superconductors; the issue is however more subtle, since a more detailed analysis of the full pairing vertex by Maier *et al.* (2008) stresses the importance of retarded contributions). Other approaches such as the Gutzwiller method (Zhang *et al.* (1988)) have been implemented to study superconductivity in this model.

The RVB idea can also be implemented directly in the Hubbard model by decomposing the original fermionic operators, which carry a spin 1/2 and a charge $-e$, in the following way:

$$c_{i\sigma}^\dagger = f_{i\sigma}^\dagger b_i \quad (7.13)$$

where $f_{i\sigma}^\dagger$ creates a *neutral* spin 1/2 particle (akin to a “singlet” state, a *spinon*) and b_i annihilates a boson carrying charge e , a *holon*. At the cost of introducing a Lagrange multiplier to constrain the overall filling,

one can then treat the resulting “slave-boson” Hamiltonian (Coleman (1984)) in a mean-field way. Among others, one gets a d -wave instability (Kotliar and Liu (1988a); Kotliar (1988); Kotliar and Liu (1988b)). Among the shortcomings of this approach, one may mention that it is intrinsically uncontrolled, and leads to an overestimation of T_c and an underestimation of antiferromagnetic correlations, probably due to its mean-field character.

A related approach is the “dimer model” approach which also consists in zeroing in on cleverly chosen states of the Hilbert state and diagonalizing the corresponding Hamiltonian (see e.g. Punk *et al.* (2015) for a recent work).

These approaches give valuable insights into the relevant physical degrees of freedom in the system. Yet, they lack a control parameter to assess their reliability with respect to the exact solution of the Hubbard model.

7.2.2.2 Cluster DMFT, or the importance of local physics and short-range spin correlations

As discussed in part 2, dynamical mean field theory places local physics at the center of the stage. In single-site DMFT (section 2.1), the Hubbard problem is dealt with by replacing the space-dependent lattice problem by a time-dependent or dynamical *local* problem. This problem describes an impurity embedded in a noninteracting bath mimicking the lattice degrees of freedom; the coupling of this bath to the impurity is described by a dynamical mean-field $\Delta(\omega)$. This much simpler problem is solved exactly by powerful continuous-time Quantum Monte-Carlo techniques (see chapter 11 for details). The mean-field $\Delta(\omega)$ is adjusted in such a way that at the end of the calculation, the impurity Green’s function coincides with the local component of the lattice’s Green’s function. The sole – if drastic – approximation involved in the process is the assumption that the self-energy is *local*, $\Sigma(\mathbf{k}, i\omega) \approx \Sigma(i\omega)$. Nevertheless, keeping frequency-dependence of the self-energy and of the mean-field $\Delta(\omega)$ (at variance with “static” mean field theories) allows DMFT to interpolate between a Fermi liquid at weak interactions and a Mott insulator in the atomic limit (including the transition between the two phases).

However, as we have just seen, experiments on cuprates show direct evidence of the *nonlocality* of the self-energy.

7.2.2.2.1 Basic description: DCA and CDMFT To improve on the aforementioned limitation, a cluster version of DMFT has been introduced which replaces the lattice problem by a finite-size *cluster* of impurities. There are many ways of reinstating spatial dependence in the impurity model. One, called cellular DMFT (CDMFT, Lichtenstein and Katsnelson (2000); Kotliar *et al.* (2001)) is based on a real-space picture: it replaces the single-site impurity problem with an impurity model with several (N_c) impurities. The self-energy computed from this model has thus e.g. intersite components, instead of only local components. This first method breaks translation invariance within the cluster. A second variant, called the dynamical cluster approximation (DCA, Hettler *et al.* (1998, 1999)), is based on a momentum-space picture, namely on a coarse graining of the Brillouin zone into N_c patches. Examples of such patches are shown in Fig. 7.14(d). The self-energy computed in the impurity model is thence a piecewise constant function on these patches. DCA can also be understood in real space by considering a real-space cluster of impurities with periodic boundary conditions.

Thus, in cluster DMFT, short-range correlations within the cluster are taken into account and the self-energy is now approximated by the coarse-grained self-energy of the finite-size cluster.

An extended review of cluster DMFT and of DCA results can be found in Maier *et al.* (2005a).

7.2.2.2.2 Insights in cuprate physics Cluster DMFT methods have been applied to the 2D Hubbard model with tight-binding parameters relevant for cuprate materials.

Numerous studies have demonstrated that cluster DMFT captures a large part of the physics of cuprate superconductors. This includes momentum-differentiation and in particular the pseudo gap phase or Fermi

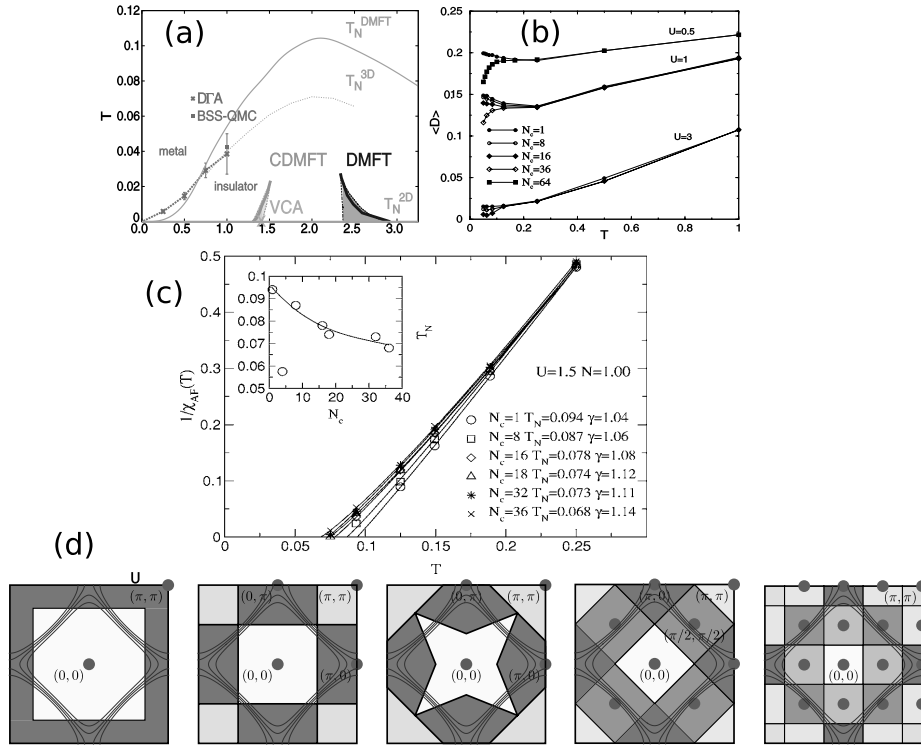


Figure 7.14: Cluster DMFT (DCA) results in two dimensions (energies expressed in units of the half-bandwidth D). (a) (T, U) phase diagram. Left of the CDMFT region: metallic solution; right: Mott insulating solution (from Schäfer *et al.* (2015a)) (b) Double occupancy vs. temperature for various cluster sizes N_c and U 's (from Moukouri and Jarrell (2001)) (c) Inverse static AF susceptibility vs. temperature for various cluster sizes. Inset: $T_{N\acute{e}el}$ as a function of N_c (from Jarrell *et al.* (2001)) (d) Various DCA Brillouin zone tilings (from Gull *et al.* (2010))

arcs (Maier *et al.* (2000); Huscroft *et al.* (2001); Parcollet *et al.* (2004); Civelli *et al.* (2005); Kyung *et al.* (2006); Ferrero *et al.* (2008); Kancharla *et al.* (2008); Werner *et al.* (2009); Ferrero *et al.* (2009); Gull *et al.* (2009, 2010, 2013)), and d -wave superconductivity (Maier *et al.* (2004, 2005b); Capone and Kotliar (2006); Maier *et al.* (2006); Civelli *et al.* (2008); Kancharla *et al.* (2008); Civelli (2009); Kyung *et al.* (2009); Gull *et al.* (2013)). These results have been studied with cluster sizes up to $N_c = 16$ in the superconducting region (Gull *et al.* (2013)); a minimal cluster of two sites only ($N_c = 2$), however, already captures the formation of Fermi arcs (Ferrero *et al.* (2008)), underlining the importance of singlet physics. The values of U reached by cluster DMFT are out of the reach of the weak-coupling methods discussed above.

Thus, cluster DMFT arguably captures the “big picture” of cuprate physics. Two elements are however missing: long-range antiferromagnetic fluctuations, and convergence with respect to the number of cluster sites or momentum patches N_c .

7.2.2.2.3 Dependence on N_c

In this section, I focus on the influence of the number of patches N_c . The cluster size N_c (be it the number of impurity sites or the number of patches) provides a control parameter to dynamical mean field theory. In the same way as finite-site methods such as exact diagonalization or quantum Monte-Carlo methods can be analyzed by studying the dependence of their observables on the system size, the reliability of cluster DMFT can be quantified by looking at the N_c dependence of its observables. Contrary to finite-size methods, however, cluster DMFT, as a mean field theory, is formulated in the thermodynamic limit.

Fig. 7.14 illustrates the dependence on N_c of selected observables.

In panel (b), the double occupancy $\langle n_{\uparrow}n_{\downarrow} \rangle$ can be seen to be independent of cluster size at high temperatures (and even equal to the single-site result): this illustrates the fact that single-site DMFT provides a good description at high and intermediate temperatures. In general, cluster DMFT converges fast with respect to N_c for local thermodynamic quantities (Capone *et al.* (2004)). At lower temperatures, however, $\langle n_{\uparrow}n_{\downarrow} \rangle$ becomes strongly dependent on N_c : for the largest cluster sizes, one even sees a downturn of the double occupancy, indicating an onset of insulating behavior at very low temperatures. This observation is corroborated by another method, the dynamical vertex approximation (explained in section G.4 of the appendix).

In panel (c), one sees that the AF spin susceptibility also depends on N_c at low temperatures and that, as shown in the inset, the extrapolated Néel temperature – which should vanish as a result of the Mermin-Wagner theorem, converges very slowly as a function of N_c . This indicates that the fluctuations responsible for the destruction of long-range AF order in two dimensions are essentially long-range spin fluctuations, not captured by cluster DMFT unless the cluster is very large.

The short-range fluctuations included by cluster DMFT, however, strongly modify the single-site picture. They quantitatively change the value of the critical interaction for the metal-to-Mott insulator transition (panel (a)): U_c is decreased from $U_c^{\text{single-site}}/D \approx 2.5$ to $U_c^{\text{cluster}}/D \approx 1.5$.

In Gull *et al.* (2010), the influence of the momentum-space coarse graining on the momentum-selective Mott transition is studied systematically. While the maximal resolution obtained in this method ($N_c = 16$, see rightmost sketch of panel (d) in Fig. 7.14) allows to differentiate important regions such as the antinodal and the nodal region, the resolution is still quite coarse, and one is still far from convergence with respect to N_c .

7.2.2.2.4 Conclusions Cluster DMFT yields interesting and precise insights into cuprate physics: it has a control parameter, namely the cluster size N_c which can in principle be used to *quantify* the error made at one cluster size with respect to the next.

The exponential complexity of the Hubbard model, however, comes back in the form of the Monte-Carlo sign problem which becomes more and more acute as N_c grows. This effectively precludes the convergence of cluster DMFT with respect to N_c at low temperatures. The situation is even worse for more realistic systems such as multiorbital models, which are currently simply out of reach for cluster DMFT.

Thus, new methods must be devised to overcome this limitation.

7.2.3 Open questions: short-range vs. long-range fluctuations

The class of approaches reviewed in the previous two sections share commonalities: among others, they can describe d -wave superconductivity, the opening of a pseudogap, the ordering to an antiferromagnetic phase at low doping. In either case, however, the mechanisms behind the phenomena are poles apart: the AF gap described by spin fluctuation theory is essentially a Slater gap of itinerant antiferromagnetism, while the AF strong-coupling is a Heisenberg gap; the pseudogap is driven in one case by long-range spin fluctuations, in the other by short-range fluctuations of localized moments.

The experimental evidence, however, yields clear-cut conclusions: to describe cuprates, one should incorporate at least two ingredients: (very) **strong correlations** (absent in spin-fluctuation theories and the likes, but captured by CDMFT) and (quite) **large antiferromagnetic correlation lengths**, out of cluster DMFT's reach but described by spin fluctuation theory.

Recently, extensions of DMFT such as dual fermion and dual boson methods (Rubtsov *et al.* (2008, 2012)) or the dynamical vertex approximation (DVA, presented in appendix G.4) have been developed to bridge the gap between both worlds. They are however saddled with issues of their own – related to the complexity of grappling with (or circumventing) parquet equations.

In the next chapter, I describe a method that overcomes these difficulties by placing the focus on bosonic fluctuations – as in spin fluctuation theory – while still capturing local physics, without having to deal with the parquet equations. Its starting point is the local approximation of a three-leg vertex which is easier to manipulate than the four-leg vertices of D Γ A.

A local approximation to the three-leg vertex, TRILEX

In the previous chapter, I have shown that the properties of cuprate materials can be approached from two main vantage points: one – the family of “fluctuation theories” – places the emphasis on long-range two-particle fluctuations with a more or less phenomenological underpinning; the other – the family of “doped Mott insulator theories” – stresses instead “Mottness” as the indispensable beachhead to enter cuprate territory.

Both schools of thought contain appealing ingredients towards the understanding of cuprate materials. While endeavors to capture both long-range fluctuations and strong-interaction physics such as the dual fermion and dual boson methods or the dynamical vertex approximation (DFA) have been proposed, they are stalemated by the formidable complexity of parquet equations.

In this chapter, I describe a method aimed at solving this conundrum. The focus is on the Hubbard model, but the arguments also hold for more general strongly-correlated models.

8.1 Motivations

In this section, I summarize the teachings of the previous chapter by establishing a theoretical wish-list of the indispensable ingredients of a method designed to describe strongly-correlated materials.

8.1.1 Strong-coupling physics

We want to capture Mott physics.

For this, the mechanism of local Coulomb repulsion between electrons must be captured in a dedicated way, beyond mean-field theory. Dynamical mean-field theory (chapter 2.1) is a tool of choice to achieve this goal, since its guiding principle is the many-body description of local physics through the solution of a local impurity model.

This impurity model is used to approximate the lattice self-energy by the impurity self-energy, a local or (in the cluster case) short-range quantity. This way, local correlations are treated in a nonperturbative way, and the Mott transition with the accompanying short-range fluctuations (in cluster DMFT) is captured. Long-range correlations are out of reach because of the large complexity of solving an extended impurity problem.

In the dynamical vertex approximation (DFA, *Toschi et al. (2007)*), explained in appendix G.4) and dual methods (*Rubtsov et al. (2008, 2012)*), the focus is shifted from the one-particle impurity self-energy to the two-particle impurity vertex function. In DFA, the irreducible vertex is approximated by a local vertex. This

approximation is based on the insight that the more “irreducible” objects are, the more local they become. This vertex is then used to approximate the *lattice* vertex function (F) and from it construct a momentum-dependent lattice self-energy $\Sigma(\mathbf{k}, \omega)$. Since parquet or Bethe-Salpether equations are solved to compute F and then Σ , the latter contains information about some long-range fluctuations.

8.1.2 Nonlocal fluctuations and correlations

We want long-range fluctuations in the right channel (mainly spin) to be properly taken into account.

For this, bosonic fluctuations must be treated in a dedicated way. In particular, their momentum dependence is crucial. Moreover, they should have a feedback effect of the self-energy. This is what is done in spin fluctuation theory (section 7.2.1), the fluctuation-exchange approximation (FLEX, appendix G.2) or two-particle self-consistent theory (TPSC, appendix G.3), where the self-energy is constructed as the product of the fermionic propagator with the relevant bosonic fluctuations (see Eqs.7.10-G.13-G.17). Thus, the self-energy acquires a nontrivial momentum dependence due to the fluctuations of the system.

8.1.3 Simplicity

We want a method than can be extended to models beyond the single-band Hubbard model.

The dynamical vertex approximation and dual methods correct for the main shortcoming of DMFT – namely the locality of the self-energy – but are computationally very demanding. For instance, the dynamical vertex approximation in its full implementation has been applied only to an eight-site Hubbard molecule (Valli *et al.* (2015)), and one would be hard pressed to extend even its ladder version to cluster impurity models, let alone multiorbitals models. On the other hand, dual methods resort to dual fields which are difficult to trace back to physical fluctuations, and also require the choice of certain classes of nonlocal diagrams.

8.1.4 Control

We want a method where the approximation to the exact solution can be systemically controlled.

The only well-defined control parameter is the “size” N_c of the cluster impurity model of cluster DMFT, which corresponds to the number of sites in cellular DMFT (CDMFT) or to the number of momentum patches in the dynamical cluster approximation (DCA). For given observable $\hat{O}(N_c)$, one can perform a finite-size analysis, namely one can in principle check that $\hat{O}(N_c)$ converges to a certain value for $1/N_c \rightarrow 0$.

The big catch in cluster DMFT methods is that in interesting parameter regimes, one cannot reach large enough N_c to perform this extrapolation.

8.1.5 Conclusion: A combination of all this?

The method we propose to meet the above requirements is based on the following ideas:

1. Since bosonic modes are important, they should appear explicitly in the action. This is achieved by decoupling the Hubbard interaction with a Hubbard-Stratonovich field.
2. Since local physics must be treated nonperturbatively, an effective many-body impurity model is used to represent the lattice problem and solved nonperturbatively.
3. Since nonlocal correlation effects should be retained, what is extracted from the impurity model is not the one-particle self-energy, but a more sophisticated correlator.
4. Since the method must be simple enough, not a four-leg impurity vertex, but the three-leg electron-boson impurity vertex, is used to approximate the corresponding lattice vertex. From this vertex, momentum-dependent self-energies are constructed.

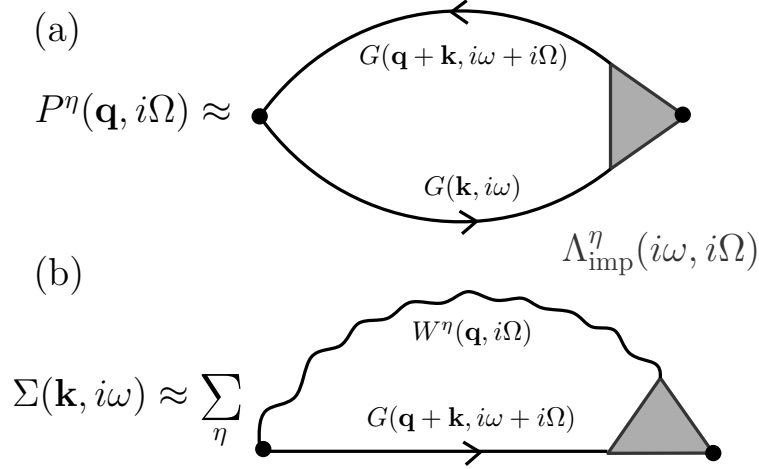


Figure 8.1: Lattice self-energy Σ and polarization P^η in the TRILEX approximation. η denotes the channel. G (W^η) is the fermionic (bosonic) propagator. $\Lambda_{\text{imp}}^\eta(i\omega, i\Omega)$ is the impurity vertex in channel η .

- Finally, our method lends itself to a cluster extension: we thus have a control parameter N_c . The conjecture is that for a given observable \hat{O} , the series $\hat{O}(N_c)$ converges faster than in cluster DMFT schemes thanks to the inclusion of long-range physics.

8.2 An intuitive picture

In the “fluctuation-exchange” approaches to the cuprates, correlations are described by a self-energy computed as the product of the electronic propagator G with the relevant fluctuation propagators which I shall call W^η (η denoting “spin” or “charge”, for instance):

$$\Sigma_{\text{fluctuation}}(\mathbf{k}, i\omega) \sim - \sum_{\mathbf{q}, i\Omega, \eta} \lambda_{\mathbf{q}}^\eta G_{\mathbf{k}+\mathbf{q}}(i\omega + i\Omega) W_{\mathbf{q}}^\eta(i\Omega) \lambda_{\mathbf{q}}^\eta \quad (8.1)$$

The fluctuations are bosonic fields ϕ^η obtained by decoupling the interaction term *via* a Hubbard-Stratonovich transformation. W^η is their propagator $W^\eta = -\langle \phi^\eta \phi^\eta \rangle$. λ^η is the bare coupling between the fermionic fields and the bosonic Hubbard-Stratonovich fields ϕ^η .

On the other hand, DMFT approximates the self-energy by a local impurity self-energy:

$$\Sigma_{\text{DMFT}}(\mathbf{k}, i\omega) = \Sigma_{\text{imp}}(i\omega) \quad (8.2)$$

The connection between these two approximations is given by the exact expression of the self-energy in a problem describing the coupling of electrons with fluctuating fields ϕ^η :

$$\Sigma_{\text{exact}}(\mathbf{k}, i\omega) = - \sum_{\mathbf{q}, i\Omega, \eta} \lambda_{\mathbf{q}}^\eta G_{\mathbf{k}+\mathbf{q}}(i\omega + i\Omega) W_{\mathbf{q}}^\eta(i\Omega) \Lambda^\eta(\mathbf{k}, \mathbf{q}; i\omega, i\Omega) \quad (8.3)$$

Here, the central quantity is the renormalized electron-boson coupling vertex¹ $\Lambda^\eta(\mathbf{k}, \mathbf{q}, i\omega, i\Omega)$, which encodes the effect of correlations on the bare vertex $\lambda_{\mathbf{q}}^\eta$. Diagrammatically, it amounts to the connected three-point correlation function $\langle cc^\dagger \phi^\eta \rangle$ stripped of its “legs” (hence represented as a triangle).

The fluctuation exchange form of Eq. (8.1) comes from neglecting the vertex corrections to λ^η , namely by approximating $\Lambda^\eta \approx \lambda^\eta$. While this approximation is justified by Migdal’s theorem in the case of the coupling

¹It must not be confounded with the fully irreducible, four-leg vertex of DΓA.

of electrons to phonons (in this case $\Lambda - \lambda \sim \sqrt{m_e/M}$, where M is the ionic mass), for the spin-fermion problem or more general actions, there is no *a priori* reason to neglect vertex corrections.

The DMFT approximation to the self-energy is a good example where *local* vertex corrections are crucial. Indeed, Eq. (8.2) can be cast in the form of Eq. (8.3):

$$\Sigma_{\text{imp}}(i\omega) = - \sum_{i\Omega, \eta} \lambda^\eta G_{\text{imp}}(i\omega + i\Omega) W_{\text{imp}}^\eta(i\Omega) \Lambda_{\text{imp}}^\eta(i\omega, i\Omega) \quad (8.4)$$

Here, the momentum dependence of G , W and Λ is neglected but their full frequency dependence is retained. By construction, this formula gives the exact impurity self-energy. At half-filling, in the strong-correlation limit, where Σ_{imp} is insulating (it is diverging at low frequencies), replacing $\Lambda_{\text{imp}}^\eta(i\omega, i\Omega)$ by the bare value λ^η yields a *metallic* self-energy, even if an insulating propagator $G_{\text{imp}}(i\omega)$ is used (for more details, see the discussion in section 5.3.2, or Ayrál *et al.* (2012), included in chapter O.1). This indicates that the Mott mechanism is intrinsically linked to the frequency structure of the vertex. Still, the DMFT self-energy given by Eq.(8.4) is local.

The idea of our method is to use the exact form Eq. (8.3) to construct a momentum-dependent self-energy (as in fluctuation theories) which can still describe Mott physics (as in DMFT).

This is achieved by replacing the momentum-dependent electron-boson coupling vertex $\Lambda^\eta(\mathbf{k}, \mathbf{q}, i\omega, i\Omega)$ by a *local* vertex computed from an impurity model:

$$\Lambda^\eta(\mathbf{k}, \mathbf{q}, i\omega, i\Omega) \approx \Lambda_{\text{imp}}^\eta(i\omega, i\Omega)$$

The resulting self-energy is illustrated in panel (b) of Fig. 8.1. While the local vertex captures strong-correlation physics (as in DMFT), the momentum-dependence of the self-energy comes from the momentum-dependence of G and more importantly W (as in fluctuation theories). In the $U \rightarrow 0$ limit, Λ_{imp} naturally becomes the bare vertex λ , so that one recovers fluctuation theories, while in the $t \rightarrow 0$ limit, all propagators become local and the vertex reduces to the atomic-limit vertex, by construction: thus, one recovers DMFT at strong-coupling.

In the following section, I give a formal derivation of this method. In particular, I address the following issues:

- how can one go from a fermion-only model to a fermion-boson coupling problem?
- how can one cast this approximation as the approximation of a functional?
- what impurity model has to be solved? what are the dynamical mean fields?

8.3 Functional derivation

In this section, I derive the main equations of the method with a focus on energy functionals.

8.3.1 From the Hubbard model to an electron-boson coupling problem

The starting point is the single-band Hubbard model. To establish notation, I recall its Hamiltonian form:

$$H_{\text{Hubbard}} = \sum_{\mathbf{R}\mathbf{R}'\sigma} t_{\mathbf{R}\mathbf{R}'} c_{\mathbf{R}\sigma}^\dagger c_{\mathbf{R}'\sigma} + U \sum_{\mathbf{R}} n_{\mathbf{R}\uparrow} n_{\mathbf{R}\downarrow} \quad (8.5)$$

\mathbf{R} denotes a point of the Bravais lattice, $\sigma = \uparrow, \downarrow$, $t_{\mathbf{R}\mathbf{R}'}$ is the tight-binding hopping matrix (its Fourier transform is $\varepsilon(\mathbf{k})$), U is the local Hubbard repulsion, $c_{\mathbf{R}\sigma}^\dagger$ and $c_{\mathbf{R}\sigma}$ create and annihilate electrons in a state localized around site \mathbf{R} , $n \equiv n_\uparrow + n_\downarrow$, with $n_\sigma \equiv c_\sigma^\dagger c_\sigma$. The action corresponding to this model reads:

$$S_{ee} = \bar{c}_u \left[-G_0^{-1} \right]_{uv} c_v + \frac{1}{2} U n_{\mathbf{R}\uparrow\tau} n_{\mathbf{R}\downarrow\tau} \quad (8.6)$$

Latin indices $u, v, w \dots$ gather space ($\mathbf{R} \in \text{BL}$), imaginary time ($\tau \in [0, \beta]$) and spin: $u \equiv (\mathbf{R}, \tau, \sigma)$. Repeated indices are summed over (Einstein convention); summation may mean continuous integration or discrete summation, namely $\sum_u = \sum_{\mathbf{R} \in \text{BL}} \int_0^\beta d\tau \sum_{\sigma=\uparrow, \downarrow}$. $\bar{c}_{\mathbf{R}\tau\sigma}$ and $c_{\mathbf{R}\tau\sigma}$ are conjugate β -antiperiodic Grassmann fields, while $G_{0,uv}$ is the non-interacting fermionic propagator: $G_{0,\sigma}^{-1}(\mathbf{k}, i\omega) = i\omega + \mu - \varepsilon(\mathbf{k})$, $i\omega$ denoting fermionic Matsubara frequencies and μ the chemical potential.

8.3.1.1 Rewriting in terms of density and spin operators

Let us for the time being focus on the interaction term:

$$S_{\text{int}} = \frac{1}{2} U n_{\mathbf{R}\uparrow\tau} n_{\mathbf{R}\downarrow\tau} \quad (8.7)$$

From the original fermionic operators, let us define the following operators, for $I = 0, x, y, z$:

$$n_{\mathbf{R}\tau, I} \equiv \sum_{\sigma\sigma'} \bar{c}_{\mathbf{R}\sigma\tau} \sigma_{\sigma\sigma'}^I c_{\mathbf{R}\sigma'\tau} \quad (8.8)$$

where σ^0 is the identity matrix and $\sigma^{x/y/z}$ are the Pauli matrices. Hence, $n_0 = n_\uparrow + n_\downarrow$, $n_z = s_z$, $n_x = s_x$ etc. I now proceed to show that the Hubbard interaction term, Eq. (8.7), can be written in terms of these operators up to a constant shift of the chemical potential.

There are several ways of performing this rewriting. If one sums over all possible I indices and define the numbers $U^0 \equiv U^{\text{ch}}$, $U^x = U^y = U^z \equiv U^{\text{sp}}$, one gets, using the properties of the Pauli matrices ($I = 0, x, y, z$) :

$$\begin{aligned} \frac{1}{2} \sum_I U^I n_I n_I &= \frac{1}{2} \bar{c}^u c^v \bar{c}^w c^l \sigma_{uv}^I \sigma_{wl}^I U^I \\ &= \frac{1}{2} \bar{c}^u c^v \bar{c}^w c^l \delta_{uv} \delta_{wl} U^{\text{ch}} + \frac{1}{2} \bar{c}^u c^v \bar{c}^w c^l (2\delta_{ul} \delta_{vw} - \delta_{uv} \delta_{wl}) U^{\text{sp}} \\ &= \frac{1}{2} \bar{c}^u c^u \bar{c}^v c^v U^{\text{ch}} + \frac{1}{2} (2\bar{c}^u c^v \bar{c}^v c^u - \bar{c}^u c^u \bar{c}^v c^v) U^{\text{sp}} \\ &= \frac{1}{2} (2n_\uparrow n_\downarrow + n_\uparrow n_\uparrow + n_\downarrow n_\downarrow) (U^{\text{ch}} - 3U^{\text{sp}}) \end{aligned}$$

Using $n_\sigma n_\sigma = n_\sigma$ (which is nothing but the Pauli principle), one obtains, up to a density term which can be absorbed in the chemical potential, $\frac{1}{2} \sum_I U^I n_I n_I = U n_\uparrow n_\downarrow$, provided

$$U = U^{\text{ch}} - 3U^{\text{sp}} \quad (8.9)$$

Since the Hubbard interaction is now written in terms of a density-density term and a term of the form $\vec{s} \cdot \vec{s}$, we call this rewriting a ‘‘Heisenberg’’ rewriting. Similarly, if one decides to sum only on the $I = 0$ and $I = z$ indices, one gets:

$$\frac{1}{2} (U^{\text{ch}} n n + U^{\text{sp}} s^z s^z) = \frac{1}{2} U^{\text{ch}} (n_\uparrow + n_\downarrow)^2 + \frac{1}{2} U^{\text{sp}} (n_\uparrow - n_\downarrow)^2 = \left(n_\uparrow n_\downarrow + \frac{n}{2} \right) (U^{\text{ch}} - U^{\text{sp}})$$

so that the Hubbard term is recovered up to a chemical potential term provided

$$U = U^{\text{ch}} - U^{\text{sp}} \quad (8.10)$$

This rewriting is called ‘‘Ising’’ rewriting in analogy with the form of the interaction term of the Ising model.

8.3.1.2 Channel decomposition and Hubbard-Stratonovich transformation

Both above rewritings can be gathered in a unified notation, namely the interaction term can be rewritten, up to a density term which can be absorbed in the chemical potential:

$$S_{\text{int}} = \frac{1}{2} U_{\alpha\beta} n_{\alpha} n_{\beta} \quad (8.11)$$

where Greek indices denote $\alpha \equiv (\mathbf{R}, \tau, I)$ (where I runs over a subset of $\{0, x, y, z\}$ which depends on the rewriting, Heisenberg or Ising), and $n_{\alpha} \equiv \bar{c}_u \lambda_{uv\alpha} c_v$. One recovers the Hubbard model by specifying (I recall: $u = (\mathbf{R}, \tau, \sigma)$, $v = (\mathbf{R}', \tau', \sigma')$, $\alpha = (\mathbf{R}'', \tau'', I) \dots$):

$$\lambda_{uv\alpha} \equiv \sigma_{\sigma\sigma'}^I \delta_{\mathbf{R}-\mathbf{R}'} \delta_{\mathbf{R}'-\mathbf{R}''} \delta_{\tau-\tau'} \delta_{\tau'-\tau''} \quad (8.12)$$

$$U_{\alpha\beta} \equiv U^I \delta_{IJ} \delta_{\mathbf{R}-\mathbf{R}'} \delta_{\tau-\tau'} \quad (8.13)$$

but I will keep the generic form (8.11) for the rest of the derivation, as it encompasses a large spectrum of interaction terms, including nonlocal and multiorbital interactions. I now decouple the interaction (8.11) with a real bosonic Hubbard-Stratonovich field ϕ_{α} :

$$e^{-\frac{1}{2} U_{\alpha\beta} (\bar{c}_u \lambda_{uv\alpha} c_v) (\bar{c}_w \lambda_{wx\beta} c_x)} = \int \mathcal{D}[\phi] e^{-\frac{1}{2} \phi_{\alpha} [-U^{-1}]_{\alpha\beta} \phi_{\beta} \pm \lambda_{uv\alpha} \phi_{\alpha} \bar{c}_u c_v} \quad (8.14)$$

In principle, the interaction kernel $[-U^{-1}]_{\alpha\beta}$ should be positive definite for this integral to be convergent. Should it be negative definite, positive definiteness can be restored by redefining $\phi \rightarrow i\phi$ and $\lambda \rightarrow i\lambda$, which leaves the final equations unchanged. After this transformation, the electron-electron action (8.6) becomes a mixed electron-boson action with a Yukawa-type coupling between the bosonic and the fermionic field:

$$S_{\text{eb}} = \bar{c}_u [-G_0^{-1}]_{uv} c_v + \frac{1}{2} \phi_{\alpha} [-U^{-1}]_{\alpha\beta} \phi_{\beta} + \lambda_{uv\alpha} \bar{c}_u c_v \phi_{\alpha} \quad (8.15)$$

Here, I have chosen the minus sign for the Yukawa coupling in Eq. (8.14). This action will be the starting point of the derivation.

At this point, one can notice the analogy between our starting point Eq. (8.15) and the spin-fermion and Fröhlich actions, Eqs (7.4) and (I.38) (in appendix I.6), respectively. Indeed, this action captures the very general coupling of a fermionic field \bar{c}, c with bosonic degrees of freedom ϕ_{α} . These degrees of freedom may be physical (as is the case for the Fröhlich action) or auxiliary, as in the spin-fluctuation case or when the ϕ field stems from the Hubbard-Stratonovich decoupling of a quartic fermionic interaction term. In the latter case, there is an infinity of Hubbard-Stratonovich fields for a set interaction term. This well-known ambiguity – which is present, among others, in any static mean field theory – is discussed in the next subsection.

8.3.1.3 The Fierz ambiguity

Before carrying on with the derivation, let us discuss the subtleties associated with the decoupling and the subsequent introduction of ϕ^I . Due to the freedom in rewriting the interaction term, there are several possible Hubbard-Stratonovich decoupling fields. Since the reshuffling is exact, an exact treatment of the mixed fermion-boson action S_{eb} would lead to *exact* results. However, approximations to the electron-boson action will lead to *a priori* different results depending on the choice of the decoupling.

This ambiguity – called the Fierz ambiguity – has been thoroughly investigated in “functional integral” literature in the past (Castellani and Castro (1979); Cornwall *et al.* (1974); Gomes and Lederer (1977); Hamann (1969); Hassing and Esterling (1973); Macêdo *et al.* (1982); Macêdo and Coutinho-Filho (1991); Schulz (1990); Schumann and Heiner (1988)) and in more recent years (Baier *et al.* (2004); Bartosch *et al.* (2009); Borejsza and Dupuis (2003, 2004); Dupuis (2002)) in the context of “partial bosonization” within the functional renormalization group (fRG) framework. There is no *a priori* heuristics to find an optimal decoupling

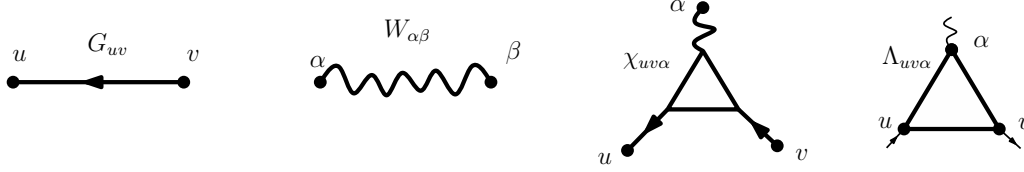


Figure 8.2: Graphical representation of the diagrammatic objects of the electron-boson model (Eq. 8.15): the fermionic propagator G_{uv} (Eq. (8.17c)), the bosonic propagator $W_{\alpha\beta}$ (Eq. (8.23)), the three-point correlation function $\chi_{uv\alpha}$ (Eq. (8.28)) and the three-leg vertex $\Lambda_{uv\alpha}$ (Eq. (8.29)). Note that the first index, u , of $\chi_{uv\alpha}$ corresponds to an outgoing leg, while it is an ingoing leg in $\Lambda_{uv\alpha}$.

without previous knowledge of the physically relevant instabilities of the system, except when it comes to symmetries. At least, one may require the decoupling to preserve the symmetry of the original Hamiltonian, for instance spin-rotational symmetry. Apart from these symmetry reasons, in most cases of physical interest, where several degrees of freedom – charge, spin, superconducting fluctuations... – are competing with one another, the conventional wisdom is that many decoupling channels should be taken into account. This ambiguity can only be dispelled by an *a posteriori* control of the error with respect to the exact solution. As we will see in a later section, our method comes with such a control parameter, the cluster size N_c .

8.3.2 Three-particle irreducible formalism

In this subsection, I construct $\mathcal{K}[G, W, \Lambda]$, the three-particle irreducible (3PI) functional. This construction has first been described in the pioneering works of de Dominicis and Martin (1964a,b). It consists in successive Legendre transformations of the free energy of the interacting system.

Let us first define the free energy of the system in the presence of linear (h_α), bilinear ($B_{\alpha\beta}$, F_{uv}) and trilinear sources ($\lambda_{uv\alpha}$, which are already present by construction) coupled to the bosonic and fermionic operators,

$$\Omega[h, B, F, \lambda] \equiv -\log \int \mathcal{D}[\bar{c}, c, \phi] e^{-S_{\text{eb}} + h_\alpha \phi_\alpha - \frac{1}{2} \phi_\alpha B_{\alpha\beta} \phi_\beta - \bar{c}_u F_{uv} c_v} \quad (8.16)$$

$\Omega[h, B, F, \lambda]$ is the generating functional of correlation functions, *viz.*:

$$\varphi_\alpha \equiv \langle \phi_\alpha \rangle = -\frac{\partial \Omega}{\partial h_\alpha} \quad (8.17a)$$

$$W_{\alpha\beta}^{\text{nc}} \equiv -\langle \phi_\alpha \phi_\beta \rangle = -2 \frac{\partial \Omega}{\partial B_{\beta\alpha}} \quad (8.17b)$$

$$G_{uv} \equiv -\langle c_u \bar{c}_v \rangle = \frac{\partial \Omega}{\partial F_{vu}} \quad (8.17c)$$

The above correlators contain disconnected terms, as indicated by the superscript “nc” (for “non-connected”). The graphical representations of the main diagrammatic objects are shown in Fig. 8.2. $W_{\alpha\beta}/W_{\alpha\beta}^{\text{nc}}$ is depicted by an unoriented line since it is the correlator of real fields ($W_{\alpha\beta} = W_{\beta\alpha}$). If the legs of an object f_{ij} have a certain direction, then the legs of $\partial/\partial f_{ij}$ have the opposite direction.

8.3.2.1 First Legendre transform: renormalization of propagators

I now define a first Legendre transform with respect to the sources h , B and F :

$$\Gamma_2[\varphi, G, W^{\text{nc}}, \lambda] \equiv \Omega[h, F, B, \lambda] - \text{Tr}(FG) + \frac{1}{2} \text{Tr}(BW^{\text{nc}}) + \text{Tr}(h\varphi) \quad (8.18)$$

The trace operator is defined as $\text{Tr}AB = A_{uv}B_{vu}$ for two-leg quantities, and $\text{Tr}AB = A_uB_u$ for one-leg quantities. By construction, the sources are related to the derivatives of Γ_2 through the reciprocal relations:

$$\frac{\partial \Gamma_2}{\partial G_{vu}} = -F_{uv} \quad (8.19a)$$

$$\frac{\partial \Gamma_2}{\partial W_{\beta\alpha}^{\text{nc}}} = \frac{1}{2}B_{\alpha\beta} \quad (8.19b)$$

$$\frac{\partial \Gamma_2}{\partial h_\alpha} = \varphi_\alpha \quad (8.19c)$$

In a fermion-only context, Γ_2 is often called the Baym-Kadanoff functional (Baym and Kadanoff (1961); Baym (1962)) or effective action. One can decompose it in the following way:

$$\Gamma_2[\varphi, G, W^{\text{nc}}, \lambda] = \Gamma_{2,0} + \Psi[\varphi, G, W^{\text{nc}}, \lambda] \quad (8.20)$$

$\Gamma_{2,0} \equiv \Gamma_2[\varphi, G, W^{\text{nc}}, \lambda = 0]$ is the non-interacting contribution, while Ψ is defined as:

$$\Psi[\varphi, G, W^{\text{nc}}, \lambda] \equiv \int_0^1 dx \frac{\partial \Gamma_2[\varphi, G, W^{\text{nc}}, x\lambda]}{\partial x} \quad (8.21)$$

The computation of $\Gamma_2[\varphi, G, W, \lambda = 0]$ is straightforward since in this case relations (8.17c-8.17b-8.27) are easily invertible (as shown in appendix L.1), yielding:

$$\begin{aligned} \Gamma_2[\varphi, G, W, \lambda] &= -\text{Tr} \log [G^{-1}] + \text{Tr} [(G^{-1} - G_0^{-1}) G] \\ &+ \frac{1}{2} \text{Tr} \log [W^{-1}] + \frac{1}{2} \text{Tr} [(W - \varphi^2) U^{-1}] \\ &+ \Psi[\varphi, G, W, \lambda] \end{aligned} \quad (8.22)$$

where the connected correlation function has been defined as:

$$W_{\alpha\beta} \equiv -\langle (\phi_\alpha - \varphi) (\phi_\beta - \varphi) \rangle = W_{\alpha\beta}^{\text{nc}} + \varphi^2 \quad (8.23)$$

The physical Green's functions (obtained by setting $F = B = 0$ in Eqs. (8.19a-8.19b)) obey Dyson equations:

$$\Sigma_{uv} = [G_0^{-1}]_{uv} - [G^{-1}]_{uv} \quad (8.24a)$$

$$P_{\alpha\beta} = [U^{-1}]_{\alpha\beta} - [W^{-1}]_{\alpha\beta} \quad (8.24b)$$

where the fermionic and bosonic self-energies have been defined as functional derivatives of Ψ with respect to the propagators:

$$\Sigma_{uv} \equiv \frac{\partial \Psi}{\partial G_{vu}} \quad (8.25a)$$

$$P_{\alpha\beta} \equiv -2 \frac{\partial \Psi}{\partial W_{\beta\alpha}} \quad (8.25b)$$

The two Dyson equations (8.24a-8.24b) and the functional derivative equations (8.25a-8.25b) form a closed set of equations that can be solved self-consistently once the dependence of Ψ on G and W is specified.

The functional $\Psi[\varphi, G, W_c, \lambda]$ is called the Almladh functional (Almladh *et al.* (1999)). It is the extension of the Luttinger-Ward functional $\Phi[G]$ (Luttinger and Ward (1960); Baym (1962)), which is defined for fermionic actions, to mixed electron-boson actions. While $\Phi[G]$ contains two-particle irreducible graphs with

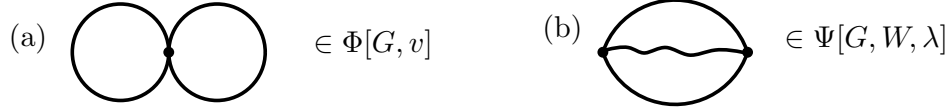


Figure 8.3: Simplest contribution to 2PI functionals. (a) Luttinger-Ward functional Φ (b) Almlbladh functional Ψ . Solid (wiggly) lines stand for G (W), while small dots stand for λ .

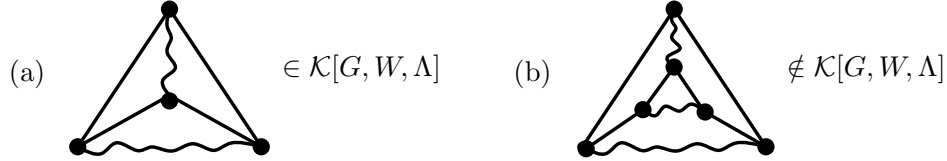


Figure 8.4: Examples of diagrams contributing (a) or not (b) to the 3PI functional \mathcal{K} . Solid (wiggly) lines stand for G (W), while large dots stand for Λ .

fermionic lines G and bare interactions U (see *e.g.* diagram (a) of Fig. 8.3), $\Psi[\varphi, G, W, \lambda]$ contains two-particle irreducible graphs with fermionic (G) and bosonic (W) lines, and bare electron-boson interactions vertices λ (see *e.g.* diagram (b) of Fig. 8.3).

Both Φ and Ψ can be approximated in various ways, which in turn leads to an approximate form for the self-energies, through Eqs (8.25a-8.25b). Any such approximation, if performed self-consistently, will obey *global* conservation rules (Baym and Kadanoff (1961)). A simple example is the GW approximation, which consists in approximating Ψ by its most simple diagram (diagram (b) of Fig. 8.3)²:

$$\Psi^{\text{EDMFT}}[G_{\mathbf{R},\mathbf{R}'}, W_{\mathbf{R},\mathbf{R}'}, \lambda_{\mathbf{R}\mathbf{R}\mathbf{R}}] = \frac{1}{2} \sum_{\mathbf{R}\mathbf{R}'} \lambda_{\mathbf{R}\mathbf{R}\mathbf{R}} G_{\mathbf{R}\mathbf{R}'} W_{\mathbf{R}\mathbf{R}'} G_{\mathbf{R}'\mathbf{R}} \lambda_{\mathbf{R}'\mathbf{R}'\mathbf{R}'}$$

DMFT (chapter 2), EDMFT (explained in section 5.1) and GW +EDMFT (explained in section 5.2) are more sophisticated examples, as discussed in Ayril *et al.* (2013): DMFT and EDMFT consist in approximating Φ and Ψ by the sum over all lattice sites of the exact Φ and Ψ with *local* propagators, namely:

$$\begin{aligned} \Phi^{\text{DMFT}}[G_{\mathbf{R},\mathbf{R}'}] &= \sum_{\mathbf{R} \in \text{BL}} \Phi^{\text{exact}}[G_{\mathbf{R}\mathbf{R}}] \\ \Psi^{\text{EDMFT}}[G_{\mathbf{R},\mathbf{R}'}, W_{\mathbf{R},\mathbf{R}'}, \lambda_{\mathbf{R}\mathbf{R}\mathbf{R}}] &= \sum_{\mathbf{R} \in \text{BL}} \Psi^{\text{exact}}[G_{\mathbf{R}\mathbf{R}}, W_{\mathbf{R}\mathbf{R}}, \lambda_{\mathbf{R}\mathbf{R}\mathbf{R}}] \end{aligned}$$

The GW +EDMFT method, on the other hand, consists in adding nonlocal corrections to the EDMFT functional in the form of GW diagrams:

$$\Psi^{GW+\text{EDMFT}}[G_{\mathbf{R},\mathbf{R}'}, W_{\mathbf{R},\mathbf{R}'}, \lambda_{\mathbf{R}\mathbf{R}\mathbf{R}}] = \sum_{\mathbf{R} \in \text{BL}} \Psi^{\text{exact}}[G_{\mathbf{R}\mathbf{R}}, W_{\mathbf{R}\mathbf{R}}, \lambda_{\mathbf{R}\mathbf{R}\mathbf{R}}] + \frac{1}{2} \sum_{\mathbf{R}\mathbf{R}', \mathbf{R} \neq \mathbf{R}'} \lambda_{\mathbf{R}\mathbf{R}\mathbf{R}} G_{\mathbf{R}\mathbf{R}'} W_{\mathbf{R}\mathbf{R}'} G_{\mathbf{R}'\mathbf{R}} \lambda_{\mathbf{R}'\mathbf{R}'\mathbf{R}'}$$

I now perform an additional Legendre transform to go one step further in terms of irreducibility.

8.3.2.2 Second Legendre transform: renormalization of the three-leg vertex

I introduce the Legendre transform of Γ_2 with respect to λ :

$$\Gamma_3[\varphi, G, W, \chi^{\text{nc}}] \equiv \Gamma_2[\varphi, G, W, \lambda] + \text{Tr}(\lambda \chi^{\text{nc}}) \quad (8.26)$$

²The bare coupling stemming from a Hubbard-Stratonovich transformation is local, hence the notation $\lambda_{\mathbf{R}\mathbf{R}\mathbf{R}}$ instead of the more general $\lambda_{\mathbf{R}\mathbf{R}'\mathbf{R}'}$

where the trace denotes: $\text{Tr}AB = A_{ab\alpha}B_{ab\alpha}$ and $\chi_{uv\alpha}^{\text{nc}}$ is the three-point correlator:

$$\chi_{uv\alpha}^{\text{nc}} \equiv \langle c_u \bar{c}_v \phi_\alpha \rangle = -\frac{\partial \Omega}{\partial \lambda_{vua}} \quad (8.27)$$

The connected three-point function χ and the three-leg vertex Λ are defined as:

$$\chi_{uv\alpha} \equiv \langle c_u \bar{c}_v (\phi_\alpha - \varphi_\alpha) \rangle = \chi_{uv\alpha}^{\text{nc}} + G_{uv} \varphi_\alpha \quad (8.28)$$

$$\Lambda_{uv\alpha} \equiv [G^{-1}]_{xu} [G^{-1}]_{vw} [W^{-1}]_{\alpha\beta} \chi_{wx\beta} \quad (8.29)$$

Λ is the amputated, connected correlation function (depicted in Fig. 8.2). I now define the three-particle irreducible functional \mathcal{K} as:

$$\mathcal{K}[\varphi, G, W, \Lambda] \equiv \Psi[\varphi, G, W, \lambda] + \text{Tr}(\lambda \chi^{\text{nc}}) - \frac{1}{2} \Lambda_{ux\alpha} G_{wx} G_{uv} W_{\alpha\beta} \Lambda_{wv\beta} \quad (8.30)$$

\mathcal{K} is the three-particle irreducible (3PI) functional (it was first introduced in de Dominicis and Martin (1964b) as $\mathcal{K}^{3/2}$). A 3PI diagram is defined as follows: for any set of three lines whose cutting leads to a separation of the diagram in two parts (“an articulation triplet”), one and only one of those parts is a simple three-leg vertex (such articulation triplets are called “trivial”). For instance, diagram (b) of Fig 8.3 contains one articulation triplet, but both disconnected parts are simple three-leg vertices. Conversely, one can check that diagram (a) of Fig. 8.4 contains only trivial articulation triplets, it is 3-particle irreducible. Diagram (b) has nontrivial articulation triplets, it is not 3PI.

Let us now show that Λ obeys the equivalent of Dyson’s equations at the 3PI level. Combining (8.30) and (8.22) trivially leads to:

$$\Gamma_3[\varphi, G, W, \Lambda] = \Gamma_{2,0} + \mathcal{K}[\varphi, G, W, \Lambda] + \frac{1}{2} \Lambda_{uw\beta} G_{uv} G_{xw} W_{\beta\alpha} \Lambda_{xv\alpha} \quad (8.31)$$

Furthermore, since $\lambda_{uv\alpha} = \frac{\partial \Gamma_3}{\partial \chi_{uv\alpha}} = \frac{\partial \Gamma_3}{\partial \Lambda_{wx\beta}} \frac{\partial \Lambda_{wx\beta}}{\partial \chi_{uv\alpha}}$, decomposing both factors using (8.31) and (8.29) yields:

$$\begin{aligned} \lambda_{uv\alpha} &= \left(\frac{\partial \mathcal{K}}{\partial \Lambda_{wx\beta}} + G_{ws} G_{rx} W_{\beta\gamma} \Lambda_{rs\gamma} \right) (G_{vw}^{-1} G_{xu}^{-1} W_{\beta\alpha}^{-1}) \\ &= G_{vw}^{-1} G_{xu}^{-1} W_{\beta\alpha}^{-1} \frac{\partial \mathcal{K}}{\partial \Lambda_{wx\beta}} + \Lambda_{uv\alpha} \end{aligned}$$

Hence, the three-leg vertex Λ is related to \mathcal{K} by the relation:

$$\Lambda_{uv\alpha} = \lambda_{uv\alpha} + K_{uv\alpha} \quad (8.32)$$

where $K_{uv\alpha}$, the generalization of the self-energy at the three-particle irreducible level, has been defined as:

$$K_{uv\alpha} \equiv - [G^{-1}]_{xu} [G^{-1}]_{vw} [W^{-1}]_{\alpha\beta} \frac{\partial \mathcal{K}}{\partial \Lambda_{wx\beta}} \quad (8.33)$$

In the context of Hedin’s equations and the GW approximation (see *e.g.* Aryasetiawan and Gunnarsson (1998)), K is often decomposed as $K \sim \frac{\delta \Sigma}{\delta G} G G \Lambda$, where $\delta K / \delta G$ is the irreducible (four-leg) vertex in one channel (see Eq. (G.19) in appendix G.3). Here, however, all quantities – most importantly \mathcal{K} – are functionals of G , W and Λ only. The four-leg vertex does not play any role in this set of equations.

Similarly, one obtains relations between the one-particle self-energies and derivatives of \mathcal{K} (using Eq. (8.32)):

$$\Sigma_{uv} = \frac{\partial \Psi}{\partial G_{vu}} = \frac{\partial \mathcal{K}}{\partial G_{vu}} + \lambda_{uv\alpha} \varphi_\alpha + \Lambda_{wu\alpha} G_{wx} W_{\alpha\beta} \Lambda_{vx\beta} - 2 \lambda_{wu\alpha} G_{wx} W_{\alpha\beta} \Lambda_{vx\beta} \quad (8.34a)$$

$$P_{\alpha\beta} = -2 \frac{\partial \Psi}{\partial W_{\beta\alpha}} = -2 \frac{\partial \mathcal{K}}{\partial W_{\beta\alpha}} - \Lambda_{wu\alpha} G_{vu} G_{wx} \Lambda_{vx\beta} + 2 \lambda_{wu\alpha} G_{vu} G_{wx} \Lambda_{vx\beta} \quad (8.34b)$$

At this point, one can notice the analogy between equations (8.25a) and (8.25b) and the two equations above. Instead of being functional derivatives of the 2PI functional Ψ , the self-energies are now expressed as the sum a functional derivative of the 3PI functional \mathcal{K} and of some diagrams which should be reminiscent of GW -type diagrams. Equations (8.33), (8.34a) and (8.34b) combined with the Dyson-like equations (8.24a), (8.24b) and (8.32) and a given \mathcal{K} form a closed set of equations which can be solved self-consistently for G , W and Λ .

This system can be further simplified. Let us first rewrite Eqs (8.34a-8.34b) as (using 8.33):

$$\begin{aligned}\Sigma_{uv} &= -\lambda_{wu\alpha}G_{wx}W_{\alpha\beta}\Lambda_{vx\beta} + \lambda_{uv\alpha}\varphi_{\alpha} + \left[\frac{\partial\mathcal{K}}{\partial G_{vu}} + K_{wu\alpha}G_{wx}W_{\alpha\beta}\Lambda_{vx\beta} \right] \\ P_{\alpha\beta} &= \lambda_{wu\alpha}G_{vu}G_{wx}\Lambda_{vx\beta} - \left[2\frac{\partial\mathcal{K}}{\partial W_{\beta\alpha}} + K_{wu\alpha}G_{vu}G_{wx}\Lambda_{vx\beta} \right]\end{aligned}$$

Owing to its 3PI character, \mathcal{K} is a functional of $f_{uv\alpha} \equiv G_{wu}d_{\alpha\beta}\Lambda_{wv\beta}$, where $d_{\alpha\beta}$ is pictorially a ‘‘half bosonic line’’, i.e. $W_{\alpha\beta} = d_{\alpha\gamma}d_{\gamma\beta}$. This causes the bracketed terms in the above equations to vanish. Indeed, using the property: $\frac{\partial d_{\alpha\delta}}{\partial W_{\kappa\eta}} = \frac{1}{2}d_{\eta\delta}^{-1}\delta_{\alpha\kappa}$, one gets:

$$\begin{aligned}\frac{\partial\mathcal{K}}{\partial G_{vu}} &= \frac{\partial\mathcal{K}}{\partial f_{pq\gamma}} \frac{\partial f_{pq\gamma}}{\partial G_{vu}} = \frac{\partial\mathcal{K}}{\partial f_{uq\gamma}} (d_{\gamma\beta}\Lambda_{vq\beta}) \\ \frac{\partial\mathcal{K}}{\partial W_{\beta\alpha}} &= \frac{\partial\mathcal{K}}{\partial f_{pq\gamma}} \frac{\partial f_{pq\gamma}}{\partial d_{\delta\kappa}} \frac{\partial d_{\delta\kappa}}{\partial W_{\beta\alpha}} = \frac{\partial\mathcal{K}}{\partial f_{pq\beta}} (G_{rp}\Lambda_{rq\kappa}) \left(\frac{1}{2}d_{\alpha\kappa}^{-1} \right)\end{aligned}$$

On the other hand:

$$\begin{aligned}K_{wu\alpha} &= -G_{rw}^{-1}G_{uy}^{-1}W_{\alpha\beta}^{-1} \frac{\partial\mathcal{K}}{\partial f_{pr\gamma}} (G_{yp}d_{\gamma\beta}) \\ &= -G_{rw}^{-1}d_{\gamma\alpha}^{-1} \frac{\partial\mathcal{K}}{\partial f_{ur\gamma}}\end{aligned}$$

Putting these relations together, one sees that the bracketed terms vanish. One thus gets the final equations:

$$\Sigma_{uv} = -\lambda_{wu\alpha}G_{wx}W_{\alpha\beta}\Lambda_{vx\beta} + \lambda_{uv\alpha}\varphi_{\alpha} \quad (8.36a)$$

$$P_{\alpha\beta} = \lambda_{wu\alpha}G_{wx}G_{vu}\Lambda_{vx\beta} \quad (8.36b)$$

These equations are the ones introduced in a simplified form in section 8.2. The second term in Σ is the Hartree contribution. I remind that lattice indices denote $u \equiv (\mathbf{R}, \tau, \sigma)$ and Greek indices $\alpha = (\mathbf{R}, \tau, I)$ ($\sigma = \uparrow, \downarrow$ and $I = 0, x, y, z$ in the single-band case, but one could extend this to a, σ and a, I , where a in an orbital index). These two equations encompass both paramagnetic and broken-symmetry phases. An alternative derivation using equations of motion is given in appendix F.

8.3.2.3 Three-particle irreducible cycle

The equations discussed in the previous sections form a set of equations that can be solved self-consistently.

The central quantity in this cycle is the three-particle irreducible functional $\mathcal{K}[G, W, \Lambda]$ or equivalently $\mathcal{K}[G, W, \chi]$ (where $\chi_{uv\alpha}$ is the connected three-point function, $\chi \sim \Lambda G G W$). Once its – most often approximate – dependence on G , W and Λ/χ is specified, the self-consistent cycle is closed, as illustrated in Figure 8.5.

This cycle has first been proposed by Hedin (1965) for the charge channel in a somewhat different, but equivalent form; the spin-dependent version of this cycle (which is contained in the present derivation) has been derived in Aryasetiawan and Biermann (2008) using Schwinger functional derivatives.

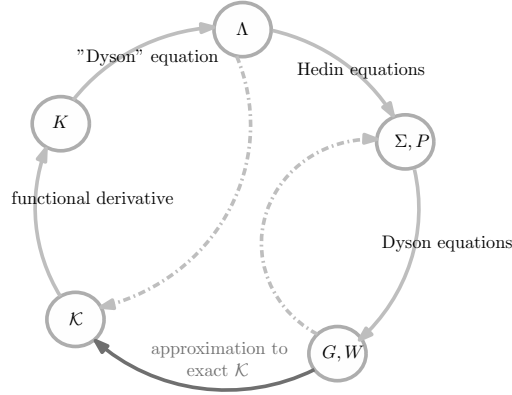


Figure 8.5: Self-consistent three-particle irreducible cycle

8.3.2.4 Phases without broken symmetry and spin rotational invariance

In the absence of symmetry breaking, $G_{uv} = G_{ij}\delta^{\sigma\sigma'}$, $W_{\alpha\beta} = W_{ij}^I\delta^{IJ}$, where $i, j, k \dots$ indices now denote space-time indices (without spin): $i \equiv (\mathbf{R}, \tau)$ (as opposed to $u = (\mathbf{R}, \tau, \sigma)$). One defines $W^0 \equiv W^{\text{ch}}$; spin rotational invariance further implies $W^x = W^y = W^z \equiv W^{\text{sp}}$. Moreover, in the rotation-invariant case, the property $\langle n^I \phi^J \rangle \propto \delta_{IJ}$ is equivalent to $\Lambda_{uv\alpha} \propto \sigma_{\sigma\sigma'}^I$ (see appendix L.3), i.e. one has $\Lambda_{uv\alpha} = \Lambda_{ijk}^{\eta(I)} \sigma_{\sigma\sigma'}^I$, with $\eta(0) = \text{ch}$, and $\eta(x/y/z) = \text{sp}$. To fix Λ_{ijk}^{η} , one can specify: $\Lambda_{i\uparrow, j\uparrow, k0} = \Lambda_{ijk}^{\text{ch}} \sigma_{\uparrow\uparrow}^0$ and $\Lambda_{i\uparrow, j\uparrow, kz} = \Lambda_{ijk}^{\text{sp}} \sigma_{\uparrow\uparrow}^z$, i.e. $\Lambda_{ijk}^{\text{ch}}$ and $\Lambda_{ijk}^{\text{sp}}$ can be computed from

$$\Lambda_{ijk}^{\text{ch}} = \Lambda_{i\uparrow, j\uparrow, k0} \quad (8.37a)$$

$$\Lambda_{ijk}^{\text{sp}} = \Lambda_{i\uparrow, j\uparrow, kz} \quad (8.37b)$$

Hence, in the Heisenberg decoupling, Eqs (8.36a-8.36b) simplify to (as shown in appendix L.2.1):

$$\Sigma_{ij} = -G_{il} W_{in}^{\text{ch}} \Lambda_{jln}^{\text{ch}} - 3G_{il} W_{in}^{\text{sp}} \Lambda_{jln}^{\text{sp}} + \varphi_{j, \text{ch}} \delta_{ij} \quad (8.38a)$$

$$P_{mn}^{\eta} = 2G_{ml} G_{jm} \Lambda_{jln}^{\eta} \quad (8.38b)$$

I recall that the latin indices $i, j \dots$ stand for space-time indices here: $i = (\mathbf{R}, \tau)$. The factor of 3 in the self-energy comes from the rotation invariance, while the factor of 2 in the polarization comes from the spin degree of freedom. φ_{ch} can be related to $\langle n \rangle$ via (see Eq. (C.1a)):

$$\varphi_{\text{ch}} = U^{\text{ch}} \langle n \rangle \quad (8.39)$$

As mentioned before, this is the Hartree term. In the following, I omit this term in the expressions for Σ as it can be absorbed in the chemical potential.

8.3.2.5 Fluctuation-exchange approximations: $\mathcal{K} = 0$

The approximation $\mathcal{K} = 0$, which leads to $K = 0$ and hence to $\Lambda_{ljn}^{\text{ch}} = \Lambda_{ljn}^{\text{sp}} = \delta_{lj} \delta_{jn}$, leads to the ‘‘fluctuation-exchange’’ forms of the self-energies and polarizations:

$$\Sigma_{ij} = -G_{ij} W_{ji}^{\text{ch}} - 3G_{ij} W_{ji}^{\text{sp}} \quad (8.40a)$$

$$P_{ij}^{\text{ch/sp}} = 2G_{ji} G_{ij} \quad (8.40b)$$

This corresponds to the FLEX approximation restricted to the particle-hole sector. The GW approximation is a restriction of the above to the charge channel, while spin fluctuation theory in its most simple form is a restriction to the spin channel. I refer the reader to the previous chapter, section 7.2.1, for a more detailed discussion of these approximations.

8.3.3 A local approximation to the three-leg vertex

The functional derivation discussed in the previous section suggests a natural extension of the local approximations on the 2PI functionals Φ (DMFT) or Ψ (EDMFT) to the 3PI functional \mathcal{K} .

Such an approximation reads, in the case when \mathcal{K} is considered as functional of $\chi_{\nu\alpha}$ (instead of $\Lambda_{\nu\alpha}$):

$$\mathcal{K}^{\text{TRILEX}}[G, W, \chi] = \sum_{\mathbf{R}} \mathcal{K}^{\text{exact}}[G_{\mathbf{RR}}, W_{\mathbf{RR}}, \chi_{\mathbf{RRR}}] \quad (8.41)$$

Like DMFT, this approximation becomes exact in the limit of infinite dimensions. The extension of the proof to 3PI diagrams is trivial, since by definition, $\mathcal{K} \subset \Psi$. An example of this is given by diagram (d) in Fig.8.4. This shows that in the limit of infinite dimensions, the three-particle irreducible functional \mathcal{K} becomes local.

In the same way as in the 2PI case, the local approximation of the 2PI functional leads to a local approximation to the self-energies, in the 3PI case considered here, the local approximation of the 3PI functional leads to a local approximation of the 3PI analog of the self-energy, K . Indeed, noticing that $\partial\mathcal{K}/\partial\chi_{\nu\alpha} = K_{\nu\alpha}$, Eq. (8.41) leads to:

$$K(\mathbf{k}, \mathbf{q}, i\omega, i\Omega) \approx K_{\text{imp}}(i\omega, i\Omega) \quad (8.42)$$

with the prescriptions:

$$\chi_{\text{loc}}^{\eta}(i\omega, i\Omega) = \chi_{\text{imp}}^{\eta}(i\omega, i\Omega) \quad (8.43a)$$

$$G_{\text{loc}}(i\omega) = G_{\text{imp}}(i\omega) \quad (8.43b)$$

$$W_{\text{loc}}^{\eta}(i\Omega) = W_{\text{imp}}^{\eta}(i\Omega) \quad (8.43c)$$

A direct consequence of Eq. (8.42) is the locality of the lattice vertex:

$$\Lambda(\mathbf{k}, \mathbf{q}, i\omega, i\Omega) = \lambda + K_{\text{imp}}(i\omega, i\Omega) \quad (8.44)$$

8.3.3.1 Construction of impurity vertex

In practice, in order to construct this functional, or in other words, to resum the infinity of diagrams contained in $\mathcal{K}^{\text{exact}}[G_{\mathbf{RR}}, W_{\mathbf{RR}}, \chi_{\mathbf{RRR}}]$, one follows a procedure akin to that of DMFT by introducing a local effective model.

Instead of being solved only for the local self-energy $\Sigma_{\text{imp}}(i\omega)$ – a one-particle irreducible object – this model is solved for the three-particle irreducible vertex $K_{\text{imp}}^{\eta}(i\omega, i\Omega)$. It is related to $\Lambda_{\text{imp}}^{\eta}(i\omega, i\Omega)$ through (see Eq. (8.32)),

$$\Lambda_{\text{imp}}^{\eta}(i\omega, i\Omega) = \lambda_{\text{imp}}^{\eta}(i\omega, i\Omega) + K_{\text{imp}}^{\eta}(i\omega, i\Omega) \quad (8.45)$$

At this stage, the frequency-dependence of the impurity bare electron-boson vertex $\lambda_{\text{imp}}(i\omega, i\Omega)$ is unspecified. Like $\mathcal{G}(i\omega)$ and $\mathcal{U}(i\Omega)$, it must be determined self-consistently.

Using Eq. (8.43a), the left-hand side of Eq. (8.45), Λ_{imp} , is given by

$$\Lambda_{\text{imp}}^{\eta}(i\omega, i\Omega) = \frac{\sum_{\mathbf{kq}} \chi^{\eta}(\mathbf{k}, \mathbf{q}, i\omega, i\Omega)}{G_{\text{imp}}(i\omega + i\Omega)G_{\text{imp}}(i\omega)W_{\text{imp}}^{\eta}(i\Omega)}$$

$\chi^{\eta}(\mathbf{k}, \mathbf{q}, i\omega, i\Omega)$ is given as function of $K_{\text{imp}}^{\eta}(i\omega, i\Omega)$ (after using Eqs. (8.32) and (8.42)), by

$$\chi^{\eta}(\mathbf{k}, \mathbf{q}, i\omega, i\Omega) = G_{\mathbf{k+q}, i\omega+i\Omega} G_{\mathbf{k}, i\omega} W_{\mathbf{q}, i\Omega}^{\eta} \left(\lambda^{\eta} + K_{\text{imp}}^{\eta}(i\omega, i\Omega) \right)$$

where I recall that λ is the bare vertex *on the lattice*. Thus, $\lambda_{\text{imp}}^{\eta}(i\omega, i\Omega)$ is found to be given, as a function of K_{imp}^{η} , as:

$$\boxed{\lambda_{\text{imp}}^\eta(i\omega, i\Omega) = \lambda^\eta + \zeta^\eta(i\omega, i\Omega) \left\{ \lambda^\eta + K_{\text{imp}}^\eta(i\omega, i\Omega) \right\}} \quad (8.46)$$

with

$$\zeta^\eta(i\omega, i\Omega) \equiv \frac{\sum_{\mathbf{k}\mathbf{q}} \tilde{G}_{\mathbf{k}+\mathbf{q}, i\omega+i\Omega} \tilde{G}_{\mathbf{k}, i\omega} \tilde{W}_{\mathbf{q}, i\Omega}^\eta}{G_{\text{imp}}(i\omega + i\Omega) G_{\text{imp}}(i\omega) W_{\text{imp}}^\eta(i\Omega)} \quad (8.47)$$

where for any X , $\tilde{X}(\mathbf{k}, i\omega) \equiv X(\mathbf{k}, i\omega) - X_{\text{loc}}(i\omega)$. Thus, making a local approximation to the 3PI functional leads to a renormalization of the impurity bare vertex. The corresponding impurity model has a bare electron-boson vertex which depends on two times:

$$S_{\text{imp}} = \iint_{\tau\tau'} \sum_{\sigma} \bar{c}_{\sigma}(\tau) \left[-\mathcal{G}^{-1}(\tau - \tau') \right] c_{\sigma}(\tau') + \frac{1}{2} \iint_{\tau\tau'} \phi_I(\tau) \left[-[\mathcal{U}^I]^{-1}(\tau - \tau') \right] \phi_I(\tau') + \iint_{\tau\tau'} \lambda_{\text{imp}, \sigma\sigma'}^I(\tau, \tau') \phi_I(\tau) \bar{c}_{\sigma}(\tau) c_{\sigma'}(\tau) \quad (8.48)$$

The fermionic action obtained when integrating out the bosonic modes has an interaction term of the form: $\frac{1}{2} \iiint_{\tau_1\tau_2\tau_3\tau_4} \sum_{\sigma_1\sigma_2\sigma_3\sigma_4} \tilde{\mathcal{U}}_{\sigma_1\sigma_2\sigma_3\sigma_4}(\tau_1, \tau_2, \tau_3, \tau_4) \bar{c}_{\tau_1}^{\sigma_1} c_{\tau_2}^{\sigma_2} \bar{c}_{\tau_3}^{\sigma_3} c_{\tau_4}^{\sigma_4}$ with the interaction function³:

$$\tilde{\mathcal{U}}_{\sigma_1\sigma_2\sigma_3\sigma_4}(\tau_1, \tau_2, \tau_3, \tau_4) = \sum_I \iint_{\tau\tau'} \lambda_{\text{imp}, \sigma_1\sigma_2}^I(\tau_1 - \tau_2, \tau - \tau_2) \mathcal{U}^I(\tau - \tau') \lambda_{\text{imp}, \sigma_3\sigma_4}^I(\tau_3 - \tau_4, \tau' - \tau_4) \quad (8.49)$$

Solving an impurity model with such a complex interaction term is feasible with for instance a continuous-time quantum Monte-Carlo solver in the interaction expansion (“CT-int”). However, the behavior of the sign problem, among others, cannot be predicted *a priori*.

8.3.3.2 A further simplification: reduction to density-density and spin-spin terms

The form (8.46) of the bare impurity vertex suggests a further approximation as a preliminary step before the full-fledged interaction term is taken into account, namely we take:

$$\lambda_{\text{imp}}^\eta(i\omega, i\Omega) \approx \lambda^\eta \quad (8.50)$$

This approximation is justified when $\zeta^\eta(i\omega, i\Omega)$, defined in Eq. (8.47), is small. Let us already notice that ζ^η vanishes in the atomic limit (when $t \rightarrow 0$, $\tilde{G} = \tilde{W} = 0$) and in the weak-coupling limit (then $W^\eta \rightarrow U^\eta$ so that $\tilde{W}^\eta \rightarrow 0$).

A corollary of this simplification is that (using (8.44)):

$$\boxed{\Lambda^\eta(\mathbf{k}, \mathbf{q}, i\omega, i\Omega) = \Lambda_{\text{imp}}^\eta(i\omega, i\Omega)} \quad (8.51)$$

This approximation can be seen as the starting point of the TRILEX method. This simplified scheme is not a local approximation of the 3PI functional yet. However, it possesses the properties that have been listed in the introduction. In particular, it trivially interpolates between the spin fluctuation method at weak-coupling (there, $\Lambda_{\text{imp}}^\eta$ reduces to the bare vertex), and the atomic limit at strong-coupling (there, $\Lambda_{\text{imp}}^\eta$ reduces to the atomic limit vertex).

Within this scheme, integrating the bosonic modes leads to a fermionic impurity model with retarded density-density and spin-spin interactions:

$$S_{\text{imp}} = \iint_{\tau\tau'} \sum_{\sigma} \bar{c}_{\sigma}(\tau) \left[-\mathcal{G}^{-1}(\tau - \tau') \right] c_{\sigma}(\tau') + \frac{1}{2} \iint_{\tau\tau'} \sum_I n_I(\tau) \mathcal{U}(\tau - \tau') n_I(\tau') \quad (8.52)$$

³In $\tilde{\mathcal{U}}_{\sigma_1\sigma_2\sigma_3\sigma_4}(\tau_1, \tau_2, \tau_3, \tau_4)$, only three times are independent.

The sum \sum_I runs on $I = 0, z$ in the z -decoupling, and on $I = 0, x, y, z$ in the xyz -decoupling. I recall that $n_x \equiv s_x$, $n_y \equiv s_y$ and $n_z \equiv s_z$ have spin commutation rules, that is, in the Heisenberg decoupling, the spin part of the interactions explicitly reads $S_{\text{int}}^{\text{SP}} = \frac{1}{2} \iint_{\tau\tau'} \mathcal{U}^{\text{SP}}(\tau - \tau') \vec{s}(\tau) \cdot \vec{s}(\tau')$.

The solution of this impurity action – an Anderson impurity model with retarded density-density and spin-spin interactions – is much easier than that of the impurity action with general interactions of the form given in Eq. (8.49). It can be solved by a continuous-time quantum Monte-Carlo algorithm with a double expansion, in powers of hybridization and of the perpendicular component of the spin interactions (Otsuki (2013)). The description of this solver and its implementation will be elaborated on in chapter 11.

Some bosonic correlators and mixed fermionic-bosonic correlators can be expressed as a function of fermionic correlators. In particular, defining $\tilde{\chi}_{\text{imp}}^\eta(i\omega, i\Omega)$ as $\tilde{\chi}_{\text{imp}}^{\text{ch/sp}}(i\omega, i\Omega) = \tilde{\chi}_{\text{imp}}^{\uparrow\uparrow}(i\omega, i\Omega) \pm \tilde{\chi}_{\text{imp}}^{\uparrow\downarrow}(i\omega, i\Omega)$, with:

$$\tilde{\chi}_{\text{imp}}^{\sigma\sigma'}(\tau, \tau') \equiv \langle c_\sigma(\tau) \bar{c}_\sigma(0) (n_{\sigma'}(\tau') - \langle n_{\sigma'} \rangle) \rangle \quad (8.53)$$

one can show (see appendix C) that the three-point electron-boson correlation function $\chi_{\text{imp}}^\eta(i\omega, i\Omega)$ (defined in its general form in Eq. (8.28)) is related to $\tilde{\chi}_{\text{imp}}^\eta(i\omega, i\Omega)$ by the relation:

$$\chi_{\text{imp}}^\eta(i\omega, i\Omega) = \mathcal{U}^\eta(i\Omega) \tilde{\chi}_{\text{imp}}^\eta(i\omega, i\Omega) \quad (8.54)$$

8.3.3.3 Alternative self-consistency conditions

This choice of self-consistency conditions is not unique. In particular, inspired by the sum rules on the charge and spin susceptibilities imposed in the two-particle self-consistent approximation (see section G.3 in the appendix), one may replace Eq. (8.43c) by:

$$\chi_{\text{loc}}^\eta(i\Omega) = \chi_{\text{imp}}^\eta(i\Omega) \quad (8.55)$$

where χ_{ij}^η denotes the (connected) susceptibility⁴ in channel η :

$$\chi_{ij}^\eta \equiv \langle (n_i^\eta - \langle n_i^\eta \rangle) (n_j^\eta - \langle n_j^\eta \rangle) \rangle \quad (8.56)$$

This relation enforces sum rules on the double occupancy (among others) and has been shown to yield good results in the TPSC context, namely excellent agreement with exact Monte-Carlo results as well as the fulfillment of the Mermin-Wagner theorem. In the following, however, I will concentrate on the self-consistency condition Eq. (8.43c). I will also show that in the regimes we have explored, the self-consistency with W does not violate the sum rules.

8.4 Algorithmic scheme

In this section, the TRILEX equations in their practical implementation are summarized. This scheme is based on the local approximation to the three-leg vertex (Eq. (8.51)) introduced in subsection 8.3.3.2. The full-fledged scheme, corresponding to the local approximation of the 3PI functional \mathcal{K} , is left for future investigations, as it requires the handling of a more complex interaction term.

8.4.1 The TRILEX loop

The self-consistent TRILEX loop consists in the following steps (illustrated by Fig. 8.6):

1. *Initialization.* The initialization consists in finding initial guesses for the self-energy and polarization. Usually, converged EDMFT self-energies provide suitable starting points for $\Sigma(\mathbf{k}, i\omega)$ and $P^\eta(\mathbf{q}, i\Omega)$.

⁴The symbol χ can denote a two-point ($\langle nn \rangle$) or three-point function ($\langle \langle c\bar{c}\phi \rangle \rangle$).

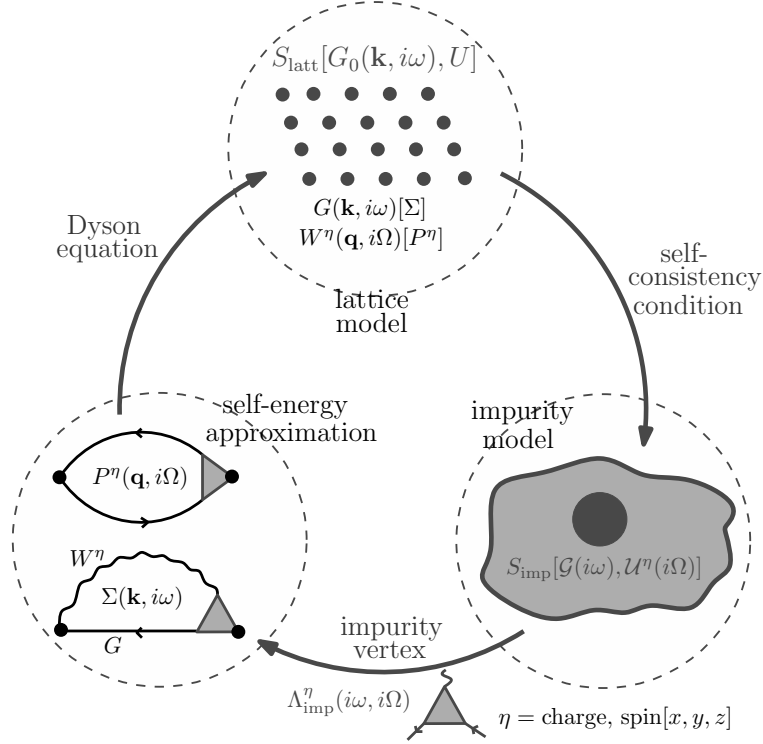


Figure 8.6: The TRILEX loop.

2. *Dyson equations.* Compute lattice observables through Dyson equations:

$$G(\mathbf{k}, i\omega) = \frac{1}{i\omega + \mu - \varepsilon(\mathbf{k}) - \Sigma(\mathbf{k}, i\omega)} \quad (8.57a)$$

$$W^\eta(\mathbf{q}, i\Omega) = \frac{U^\eta}{1 - U^\eta P^\eta(\mathbf{q}, i\Omega)} \quad (8.57b)$$

Eqs (8.57a-8.57b) are Fourier transforms of the generic equations (8.24a-8.24b). The relation between the bare interaction value U^η on the Hubbard U depends on the choice of decoupling, as mentioned in section 8.3.1.3. This relation is specified in section 8.4.2.

3. *Weiss fields.* Update the Weiss fields:

$$\mathcal{G}(i\omega) = \left[G_{\text{loc}}^{-1}(i\omega) + \Sigma_{\text{loc}}(i\omega) \right]^{-1} \quad (8.58a)$$

$$\mathcal{U}^\eta(i\Omega) = \left[\left[W_{\text{loc}}^\eta(i\Omega) \right]^{-1} + P_{\text{loc}}^\eta(i\Omega) \right]^{-1} \quad (8.58b)$$

The loc suffix denotes summation over the Brillouin zone.

4. *Impurity model.* Solve the impurity action (8.52) for $\Lambda_{\text{imp}}^\eta(i\omega, i\Omega)$, $\Sigma_{\text{imp}}(i\omega)$ and $P_{\text{imp}}(i\Omega)$. They are given in terms of the correlators $\tilde{\chi}_{\text{imp}}^\eta(i\omega, i\Omega)$ (defined above, see section 8.3.3.1), $G_{\text{imp}}(i\omega)$ and $\chi_{\text{imp}}^\eta(i\Omega)$ by the relations:

$$\Lambda_{\text{imp}}^\eta(i\omega, i\Omega) = \frac{\tilde{\chi}_{\text{imp}}^\eta(i\omega, i\Omega)}{G_{\text{imp}}(i\omega)G_{\text{imp}}(i\omega + i\Omega) \left\{ 1 - \mathcal{U}^\eta(i\Omega)\chi_{\text{imp}}^\eta(i\Omega) \right\}} \quad (8.59a)$$

$$\Sigma_{\text{imp}}(i\omega) = \mathcal{G}^{-1}(i\omega) - G_{\text{imp}}^{-1}(i\omega) \quad (8.59b)$$

$$P_{\text{imp}}(i\Omega) = \frac{-\chi_{\text{imp}}^\eta(i\Omega)}{1 - \mathcal{U}^\eta(i\Omega)\chi_{\text{imp}}^\eta(i\Omega)} \quad (8.59c)$$

5. *Momentum-dependent self-energy and polarization.* Construct momentum-dependent lattice self-energies as (see Fig. 8.1 and Eqs (8.38a-8.38b)):

$$\Sigma_{\mathbf{k},i\omega} = - \sum_{\eta, \mathbf{q}, i\Omega} m_{\eta} G_{\mathbf{k}+\mathbf{q}, i\omega+i\Omega} W^{\eta}_{\mathbf{q}, i\Omega} \Lambda_{\text{imp}}^{\eta, i\omega, i\Omega} \quad (8.60a)$$

$$P^{\eta}_{\mathbf{q}, i\Omega} = 2 \sum_{\mathbf{k}, i\omega} G_{\mathbf{k}+\mathbf{q}, i\omega+i\Omega} G_{\mathbf{k}, i\omega} \Lambda_{\text{imp}}^{\eta, i\omega, i\Omega} \quad (8.60b)$$

The factor m_{η} depends on the decoupling. In the case of the Heisenberg decoupling, $m_{\text{sp}} = 3$ and $m_{\text{ch}} = 1$, while in the Ising decoupling, $m_{\text{sp}} = m_{\text{ch}} = 1$. The practical implementation of these equations is detailed in subsection 8.4.3.

6. Go back to step 2 until convergence.

8.4.2 Bare interaction U^{η} for various decouplings

Based on Eqs. (8.9-8.10), the ratio of the bare interaction in the charge and spin channels can be parametrized by a parameter α . In the Heisenberg decoupling,

$$\tilde{U}^{\text{ch}} = (3\alpha - 1)U \quad (8.61a)$$

$$\tilde{U}^{\text{sp}} = (\alpha - 2/3)U \quad (8.61b)$$

In the Ising decoupling,

$$U^{\text{ch}} = \alpha U \quad (8.62a)$$

$$U^{\text{sp}} = (\alpha - 1)U \quad (8.62b)$$

The choice of an “optimal” α is not obvious. The influence of this parameter on the method in its single-site version will be discussed in the next chapter.

A well-defined way to choose α is to measure the relative deviation between observables computed for clusters of increasing size N_c for different α 's. The “best” α is then the one minimizing the relative deviation.

8.4.3 A convenient decomposition of the bubbles

In practice, decomposing the calculation of the self-energies (8.60a-8.60b) (see appendix L.2.2) in the following way turns out to be more stable numerically:

$$\Sigma(\mathbf{k}, i\omega) = \Sigma^{\text{nonloc}}(\mathbf{k}, i\omega) + \Sigma_{\text{imp}}(i\omega) \quad (8.63a)$$

$$P^{\eta}(\mathbf{q}, i\Omega) = P^{\eta, \text{nonloc}}(\mathbf{q}, i\Omega) + P_{\text{imp}}^{\eta}(i\Omega) \quad (8.63b)$$

with

$$\Sigma_{\mathbf{k}, i\omega}^{\text{nonloc}} \equiv - \sum_{\eta, \mathbf{q}, i\Omega} m_{\eta} \tilde{G}_{\mathbf{k}+\mathbf{q}, i\omega+i\Omega} \tilde{W}^{\eta}_{\mathbf{q}, i\Omega} \Lambda_{\text{imp}}^{\eta, i\omega, i\Omega} \quad (8.64a)$$

$$P_{\mathbf{q}, i\Omega}^{\eta, \text{nonloc}} \equiv 2 \sum_{\mathbf{k}, i\omega} \tilde{G}_{\mathbf{k}+\mathbf{q}, i\omega+i\Omega} \tilde{G}_{\mathbf{k}, i\omega} \Lambda_{\text{imp}}^{\eta, i\omega, i\Omega} \quad (8.64b)$$

and, for any X , $\tilde{X}(\mathbf{k}, i\omega) \equiv X(\mathbf{k}, i\omega) - X_{\text{loc}}(i\omega)$. One also performs a further decomposition at the level of the vertex:

$$\Lambda_{\text{imp}}^{\eta, \text{reg}}(i\omega, i\Omega) \equiv \Lambda_{\text{imp}}^{\eta}(i\omega, i\Omega) - l^{\eta}(i\Omega) \quad (8.65)$$

where $l^{\eta}(i\Omega) \equiv \frac{1 - \tilde{\mathcal{U}}^{\eta}(i\Omega) \chi_{\text{imp}}^{\eta}(i\Omega)}{1 - \mathcal{U}^{\eta}(i\Omega) \chi_{\text{imp}}^{\eta}(i\Omega)}$, and $\tilde{\mathcal{U}}^{\eta}$ is computed with U^{η} given by Eqs. (8.62a-8.62b) with $\alpha = 1/2$. This choice corresponds to a subtraction from $\tilde{\chi}_{\text{imp}}^{3, \eta}(i\omega, i\Omega)$ of its asymptotic behavior.

The final expressions are:

$$\Sigma(\mathbf{k}, i\omega) = - \sum_{\eta, \mathbf{q}, i\Omega} m_\eta \tilde{G}_{\mathbf{k}+\mathbf{q}} \left[\tilde{W}_{\mathbf{q}}^\eta l_{i\Omega}^\eta \right] - \sum_{\eta, \mathbf{q}, i\Omega} m_\eta \tilde{G}_{\mathbf{k}+\mathbf{q}} \tilde{W}_{\mathbf{q}}^\eta \left[\Lambda_{\text{imp}}^{\eta, \text{reg}} \right]_{i\Omega} + \Sigma_{\text{imp}}(i\omega) \quad (8.66)$$

$$P^\eta(\mathbf{q}, i\Omega) = 2 \left[\sum_{\mathbf{k}, i\omega} \tilde{G}_{\mathbf{k}+\mathbf{q}} \tilde{G}_{\mathbf{k}} \right] l_{i\Omega}^\eta + 2 \sum_{\mathbf{k}, i\omega} \tilde{G}_{\mathbf{k}+\mathbf{q}} \tilde{G}_{\mathbf{k}} \left[\Lambda_{\text{imp}}^{\eta, \text{reg}} \right]_{i\Omega} + P_{\text{imp}}^\eta(i\Omega) \quad (8.67)$$

The first term of each expression is computed as a simple product in time and space instead of a convolution in frequency and momentum. The second term, which contain factors which decay fast in frequencies (\tilde{G} , \tilde{W} , $\Lambda_{\text{imp}}^{\text{reg}}$), is computed as a product in space and convolution in frequencies.

The spatial Fourier transforms are performed using Fast Fourier Transforms, so that the computational expense of such calculations scales as $N_\omega^2 N_k \log N_k$, where N_ω is the number of Matsubara frequencies and N_k the number of discrete points in the Brillouin zone.

8.5 Around the three-leg vertex

In this section, I describe the most important properties of the three-leg vertex $\Lambda^\eta(\mathbf{k}, \mathbf{q}, i\omega, i\Omega)$. The derivations can be found in the corresponding appendices.

8.5.1 Asymptotics

In the large $i\omega$, large $i\Omega$ limit, the three-point correlation function is equivalent to its lowest-order contribution (see appendix D.4):

$$\chi(i\omega, i\Omega) \underset{i\omega \rightarrow \infty}{\overset{i\Omega \rightarrow \infty}{\sim}} \lambda G_0(i\omega + i\Omega) G_0(i\omega) W_0(i\Omega) \sim \lambda \frac{1}{i\omega + i\Omega} \frac{1}{i\omega}$$

where λ is the bare vertex. Thus, one can single out a “bare” contribution and a “regular” contribution to the three-leg vertex:

$$\Lambda^{\text{reg}}(i\omega, i\Omega) \equiv \Lambda(i\omega, i\Omega) - 1 \quad (8.68)$$

Thus, given the above asymptotic behavior, the regular part of the vertex, Λ^{reg} , vanishes for large $i\omega$ and $i\Omega$.

8.5.2 Symmetries

The vertex obeys the following symmetry relations (see Appendix D.2):

$$\Lambda(i\omega - i\Omega, i\Omega) = \Lambda(i\omega, -i\Omega) \quad (8.69a)$$

$$\Lambda^*(i\omega, -i\Omega) = \Lambda(-i\omega, i\Omega) \quad (8.69b)$$

A pictorial representation of these symmetries is given in Fig. 8.7.

8.5.3 Ward identity

Let us define the following correlation function:

$$\chi_{\mathbf{k}, \mathbf{q}, \mathbf{k}'}^{\sigma\sigma'I}(\tau_1, \tau_2, \tau_3) \equiv \langle T_\tau s_{\mathbf{k}', \mathbf{q}}^I(\tau_1) c_{\sigma, \mathbf{k}+\mathbf{q}}^\dagger(\tau_2) c_{\sigma', \mathbf{k}}(\tau_3) \rangle \quad (8.70)$$

which becomes the three-point correlation function when summed over \mathbf{k}' . This function obeys the following sum rule (see appendix D.5):

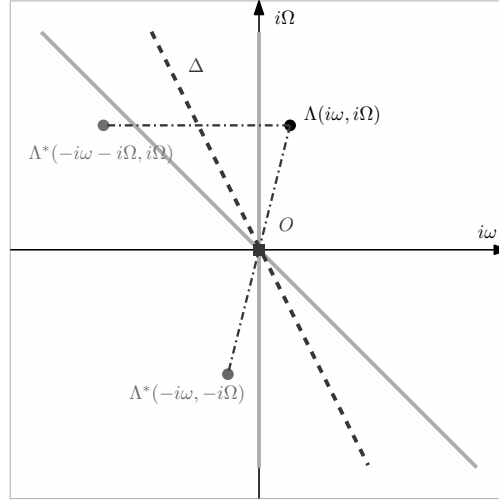


Figure 8.7: Vertex symmetries in the $(i\omega, i\Omega)$ plane ($i\omega$: fermionic Matsubara frequency; $i\Omega$: bosonic Matsubara frequency).

$$\sum_{\mathbf{k}'} \left[i\Omega - (\varepsilon_{\mathbf{k}'} - \varepsilon_{\mathbf{k}'-\mathbf{q}}) \right] \chi_{\mathbf{k}, \mathbf{q}, \mathbf{k}'}^{\sigma\sigma'I}(i\omega, i\Omega) = \sigma_{\sigma'\sigma''}^I G_{\sigma''\sigma}(\mathbf{k} + \mathbf{q}, i\omega + i\Omega) - \sigma_{\sigma''\sigma}^I G_{\sigma'\sigma''}(\mathbf{k}, i\omega) \quad (8.71)$$

This relation is useful in the atomic limit where the k dependence disappears (see next subsection). In the normal phase, $G_{\sigma\sigma'} = G_{\sigma}\delta_{\sigma\sigma'}$.

8.5.4 Atomic limit

In the atomic limit ($t \rightarrow 0$ in the Hubbard model), the three-leg vertex can be computed exactly (see Appendix E). The result is:

$$\Lambda_{\eta=\text{ch/sp}}^{\text{at}}(i\omega, i\Omega) = \frac{1}{1 - U\eta\chi^{\eta, \text{conn}}\delta_{i\Omega}} \left[1 + \frac{U^2/4}{i\omega(i\omega + i\Omega)} + \frac{U\beta}{4} \left\{ 1 - \frac{U^2}{4(i\omega)^2} \right\} \left\{ \tanh\left(\frac{\beta U}{4}\right) \mp 1 \right\} \delta_{i\Omega} \right] \quad (8.72)$$

with $\chi_c^{\text{ch/sp}} = \frac{\beta}{4} \frac{e^{\mp\beta U/4}}{\cosh(\beta U/4)}$. Note that for $i\Omega \neq 0$, one finds

$$\Lambda^{\text{ch}}(i\omega, i\Omega \neq 0) = \Lambda^{\text{sp}}(i\omega, i\Omega \neq 0) = \frac{U^2/4}{i\omega(i\omega + i\Omega)} + 1$$

as stipulated by the Ward identity (see equation (8.71) in the previous subsection). As alluded to in the intuitive introduction of TRILEX (section 8.2), this vertex is very different from the bare vertex. Most importantly, there is a very strong frequency dependence at low frequencies.

8.6 Discussion: relation to other methods

The TRILEX method has analogies with existing methods:

- *EDMFT*. TRILEX (in its full-fledged form) can be seen as the promotion of EDMFT from the two-particle level to the three-particle level. Indeed, while EDMFT approximates the fermionic and bosonic self-energies Σ and P – derivatives of the two-particle irreducible functional $\Psi[G, W, \lambda]$ – by a local approximation computed by an impurity model, TRILEX approximates the fermion-boson “self-energy”

$K(\mathbf{k}, \mathbf{q}, i\omega, i\Omega)$ – the derivative of the three-particle irreducible functional $\mathcal{K}[G, W, \chi]$ with respect to χ – by the corresponding impurity three-leg “self-energy” $K_{\text{imp}}(i\omega, i\Omega)$.

- *GW+EDMFT*. The formulae (8.63a-8.63b) are reminiscent of the form of Σ and P in the *GW+EDMFT* approximation (see chapter 5). The main difference is that in *GW+EDMFT*, (a) there is no local vertex correction in (8.64a-8.64b), and (b) so far *GW+EDMFT* has been formulated for the charge channel only.
- *Fluctuation-exchange theories*. By construction, in the weakly-correlated regime, the vertex Λ_{imp} becomes equal to the bare vertex, $\Lambda_{\text{imp}}(i\omega, i\Omega) \sim 1$. As a result, the fermionic and bosonic self-energies become equal to the *GW*, spin fluctuation or *FLEX* self-energies depending on the decoupling channel, namely: decoupling in the charge channel only leads to *GW*, decoupling in the spin channel leads to spin fluctuation-like results, which simultaneously decoupling in the charge and spin channel leads to a part of *FLEX* diagrams (*FLEX* also resums diagrams in the particle-particle channels). An important feature of spin fluctuation theory is that the form of the spin propagator is chosen on a phenomenological basis, whereas in *TRILEX* W^η is determined self-consistently.
- *Two-particle self-consistent approximation (TPSC)*. *TPSC*, described in the appendix (section G.3), approximates vertex corrections in the charge and spin susceptibilities by a constant g^η ($\eta = \text{ch, sp}$). Instead of computing the vertex from an impurity model, in *TPSC*, its value is set by requiring the fulfillment of sum rules on the susceptibility. Contrary to *TRILEX*, it takes bare propagators in the expression of the polarization.
- *Dynamical vertex approximation (DGA)*. *DGA*, described in the appendix (chapter G.4) approximates four-leg vertices (the fully irreducible vertex in the parquet version of *DGA*, the channel-wise irreducible vertex in the ladder version), objects which are much more costly in terms of computation (at the impurity model level) and storage. Second, the computation of Σ requires the solution of the parquet equations or Bethe-Salpether equations on the lattice (in the latter, easier case, corrections must be performed on the irreducible vertex to ensure numerical stability).

Application to the single-band Hubbard model

In the previous chapter, I have introduced the TRILEX formalism. In this chapter, this method is applied to the single-band Hubbard model in two dimensions.

I shall show that TRILEX interpolates between “fluctuation-exchange” theories such as spin fluctuation theory at low interaction strength U and dynamical mean-field theory at large interaction strength U , while deviating from both limits in the intermediate coupling regime.

As in DMFT, the (U, T) phase diagram features a first-order Mott transition line if antiferromagnetic fluctuations are suppressed by frustration. If the antiferromagnetic fluctuations are not suppressed, as in the square lattice with nearest-neighbor hopping only, TRILEX converges well below the Néel temperature computed within single-site DMFT. In this region, the self-energy and polarization have a sizable momentum dependence, so that upon doping, the quasiparticle lifetime on the Fermi surface is momentum dependent in a way which is reminiscent of the Fermi arcs observed in angle-resolved photoemission in cuprate materials.

These results are in the preprint [Ayral and Parcollet \(2015\)](#) included in chapter Q.1. Unless otherwise specified, the hoppings are restricted to nearest-neighbors: $t_{\mathbf{R}\mathbf{R}'} = -t\delta_{\langle\mathbf{R}\mathbf{R}'\rangle}$. All energies are given in units of the half-bandwidth $D = |4t|$. The results have been obtained by discretizing the Brillouin zone on a 64×64 momentum mesh.

9.1 An interpolation between fluctuation-exchange theories and DMFT

By construction, TRILEX interpolates between Mott physics at large interaction strengths and fluctuation-exchange theories at low interaction strengths. Here, I show that this is indeed the case in the explicit solution of TRILEX for the two-dimensional Hubbard model on a square lattice, at half-filling, with nearest-neighbor hopping only.

In the (U, T) diagram shown in Figure 9.1, the green squares stand for converged TRILEX calculations. The hatched region is a region of instable solutions. The temperature $\bar{T}^{xyz}(U)$ marking the boundary of this region corresponds to the extrapolation of the high-temperature inverse static AF susceptibility, $\chi^{\text{sp}}(\mathbf{q} = (\pi, \pi), i\Omega = 0)^{-1}$, to zero (see Fig. 9.7). For the temperatures below and slightly above this temperature, very small denominators in $W^{\text{sp}}(\mathbf{q} = (\pi, \pi), i\Omega = 0)$ preclude convergence of the method. This issue will be further discussed in section 9.4. For the time being, let us notice that TRILEX, which explicitly takes into account spin fluctuations in its self-consistent loop (through $W^{\text{sp}}(\mathbf{q}, i\Omega)$), converges far below the Néel temperature of single-site DMFT.

In the following, I will focus on three points in this phase diagram: A ($U/D = 0.5$, $\beta D = 96$) is a typical point in the weak-interaction regime; B ($U/D = 2$, $\beta D = 24$) is a point in the intermediate regime; C ($U/D = 4$, $\beta D = 48$) is a point in the strong-interaction regime. A and C are located far away from the single-site DMFT

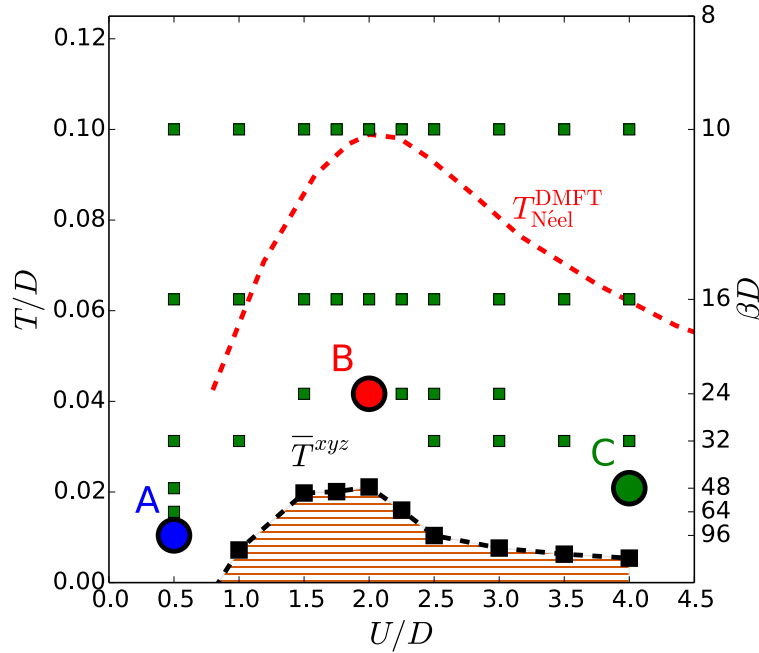


Figure 9.1: Phase diagram in the (T, U) plane at half-filling. The red dashed line is the Néel temperature computed in single-site DMFT (from Kuneš (2011)). \bar{T}^{xyz} is determined by extrapolating the inverse AF static susceptibility, see Fig. 9.7. In the hatched region, vanishing denominators in $W^{\text{sp}}(\mathbf{q}, i\Omega = 0)$ preclude convergence. The green squares denote converged TRILEX calculations. The A, B and C points are defined as: A: $U/D = 0.5$, $\beta D = 96$; B: $U/D = 2$, $\beta D = 24$; C: $U/D = 4$, $\beta D = 48$.

estimate for the critical interaction strength for the metal to insulator transition (which is located at around $U_c/D \approx 2.5$).

Let us first discuss the behavior of local observables at the A, B and C points, shown in Fig. 9.2:

- at point A ($U/D = 0.5$), the impurity vertex $\Lambda_{\text{imp}}^{\eta}(i\omega, i\Omega)$ (left and middle column) is almost constant and equal to the bare vertex, namely $\Lambda_{\text{imp}}^{\eta}(i\omega, i\Omega) \approx 1$. Deviations start to appear in the zeroth bosonic Matsubara component of $\Lambda_{\text{imp}}^{\text{sp}}$. The local component of the TRILEX $\Sigma(\mathbf{k}, i\omega)$ is identical to the DMFT impurity self-energy;
- at point C ($U/D = 4$), the impurity vertex $\Lambda_{\text{imp}}^{\eta}(i\omega, i\Omega)$ displays a strong frequency dependence. This dependence is that of the atomic-limit vertex whose expression has been given in section 8.5.4 and plotted in the bottom line with dashed lines. The numerical results are almost on top of the atomic-limit vertex except for the lowest bosonic Matsubara component of $\Lambda_{\text{imp}}^{\text{sp}}$. The local component of the TRILEX self-energy coincides with the DMFT self-energy;
- at point B ($U/D = 2$), the impurity vertex has a substantial frequency dependence which strongly departs from the bare vertex. The location of the poles is similar to that of the atomic vertex. The local component of the TRILEX self-energy deviates from the DMFT self-energy. In particular, it is more coherent than the DMFT self-energy. This point will be discussed later.

As has been hinted at in the context of the GW+EDMFT method in section 5.3.2, Mott physics are encoded in the enhancement of the impurity vertex $\Lambda_{\text{imp}}(i\omega, i\Omega)$. TRILEX allows to assess the precise frequency structure of the vertex. Already at intermediate coupling strengths ($U/D = 2$), local vertex corrections should be taken into account.

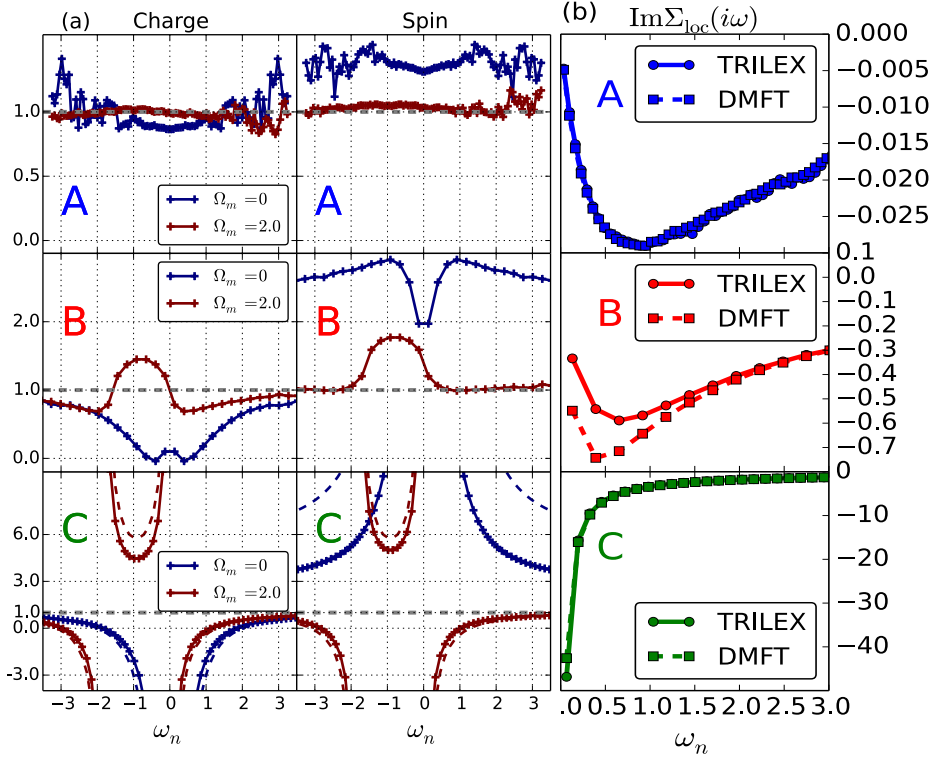


Figure 9.2: *Left and middle column*: Impurity three-leg vertex $\Lambda_{\text{imp}}^{\text{ch}}(i\omega, i\Omega)$ and $\Lambda_{\text{imp}}^{\text{sp}}(i\omega, i\Omega)$ plotted as function of the fermionic Matsubara frequency $i\omega$ for various bosonic frequencies $i\Omega$. Full lines with crosses denote the numerical data from CTQMC. Dashed line in the bottom line denote the atomic-limit vertex $\Lambda_{\text{at}}(i\omega, i\Omega)$ (see section E). *Right column*: imaginary part of the impurity self-energy, $\text{Im}\Sigma_{\text{loc}}(i\omega)$. Solid (dashed) lines denote TRILEX (DMFT) results. The points A, B and C are defined in Fig. 9.1.

The local vertex, in TRILEX, is used to compute momentum-dependent self-energies and polarizations. The lowest Matsubara components of $P^{\text{ch}}(\mathbf{q}, i\Omega)$, $P^{\text{sp}}(\mathbf{q}, i\Omega)$ and $\Sigma(\mathbf{k}, i\omega)$ are shown in Fig. 9.3:

- At point A (weak-coupling regime), the momentum dependence of the polarization and self-energy, albeit weak in absolute value, is sizable in relative values. In particular, the charge and spin polarizations, which are very similar to each other, are peaked at the nesting vector $\mathbf{q} = (\pi, \pi)$: indeed, in this limit both reduce to the bare Lindhard “bubble”, $P_0 = 2G_0G_0$. As a consequence, the self-energy is also strongly momentum-dependent (although the absolute magnitude of these variations is weak). Scattering is maximal at $\mathbf{k} = (\pi, 0)$;
- At point C (strong-coupling regime), the momentum dependence of P^n and Σ is weak, as expected in a Mott insulator. One may also note that the \mathbf{q} -averaged charge polarization is very small (due to the opening of a charge gap), while the spin polarization is quite large (corresponding to the Curie susceptibility of isolated atoms). The self-energy, while large in magnitude, is very weakly momentum-dependent;
- At point B, the momentum dependence of the polarizations and self-energy is weaker in relative terms than in the weak-interaction regime, but still sizable.

From the width of the peaks at (π, π) in P^{ch} and P^{sp} , one can estimate the correlation length. These correlation lengths, in the weak-coupling regime, are larger than those accessible to cluster schemes. Thus, TRILEX allows to incorporate long-range physics *at the cost of solving a single-site impurity problem*.

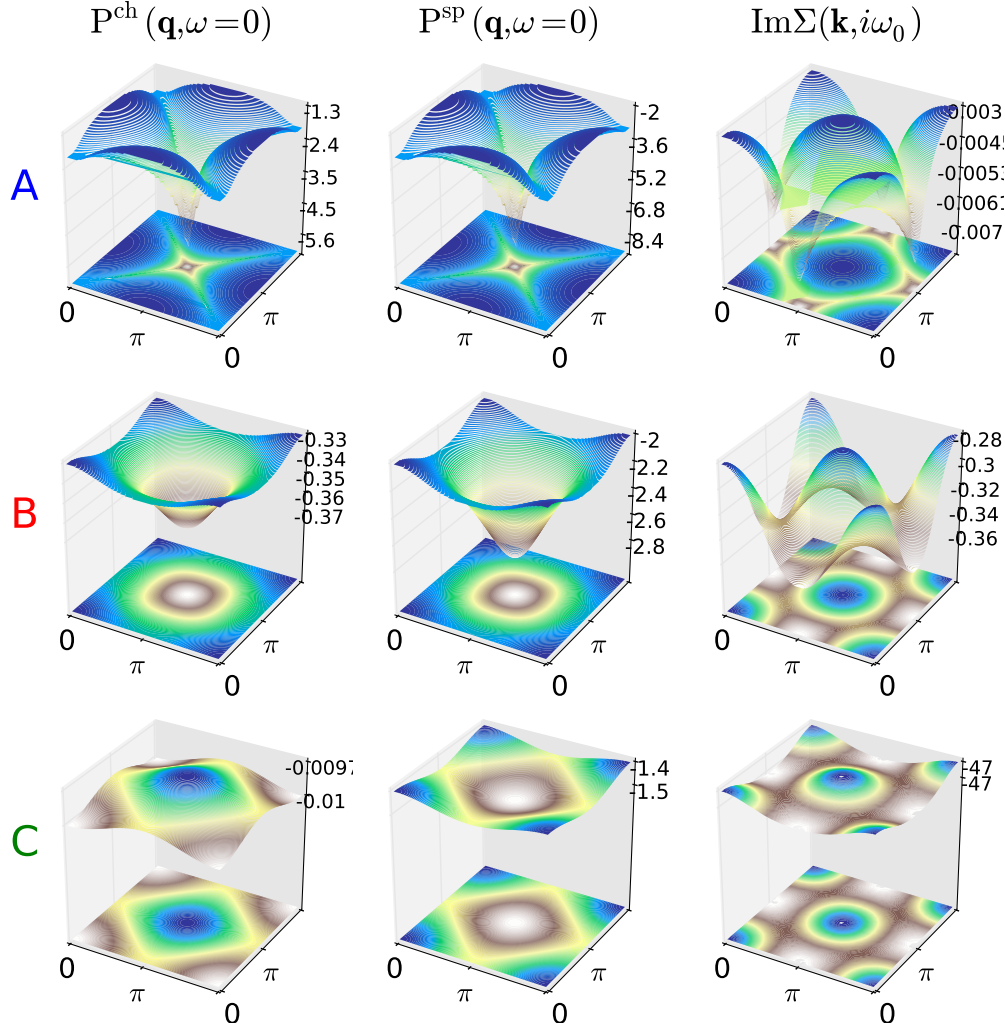


Figure 9.3: Momentum dependence of the self-energy and polarization (square lattice, half-filling, $t' = 0$). *Left:* $\text{Re}P^{\text{ch}}(\mathbf{q}, i\Omega_0)$. *Middle:* $\text{Re}P^{\text{sp}}(\mathbf{q}, i\Omega_0)$. *Right:* $\text{Im}\Sigma(\mathbf{k}, i\omega_0)$. The A, B and C points are defined in Fig. 9.1.

9.2 A first-order Mott transition

In the previous section, several points in the phase diagram have been studied. Due to extremely small denominators in $W^{\text{sp}}(\mathbf{q}, i\Omega = 0)$, no stable solution could be obtained at low enough temperatures to go below the temperature of the critical end point of the Mott transition line ($T_{\text{Mott}}/D \approx 0.045$ on the Bethe lattice, see Fig. 2.2 in the introduction to DMFT, chapter 2).

In this section, I turn to the triangular lattice in two dimensions and at half-filling. Here, geometrical frustration mitigates the low-temperature instabilities, insofar as the inverse AF susceptibility is reduced with respect to the square lattice.

In Fig. 9.4, the evolution of $-\beta/\pi \cdot G_{\text{imp}}(\tau = \beta/2)$ is monitored for two temperatures as a function of U/D . At low enough temperatures, $-\beta/\pi \cdot G_{\text{imp}}(\tau = \beta/2)$ is an accurate estimate of $A_{\text{imp}}(\omega = 0)$ (as proven in appendix I.1.2.5.1), and can thus be used to observe the transition between a Fermi liquid ($A_{\text{imp}}(\omega = 0) > 0$) and a Mott insulator ($A_{\text{imp}}(\omega = 0) \approx 0$). At low temperatures ($\beta D = 64$), both DMFT and TRILEX display a hysteretic behavior, namely there is a coexistence region between a metallic and insulating solution. At a higher temperature ($\beta D = 32$), the hysteretic region has shrunk. With these two estimates for U_c , one can draw a rough sketch of the (T, U) phase diagram in the triangular lattice (see the inset).

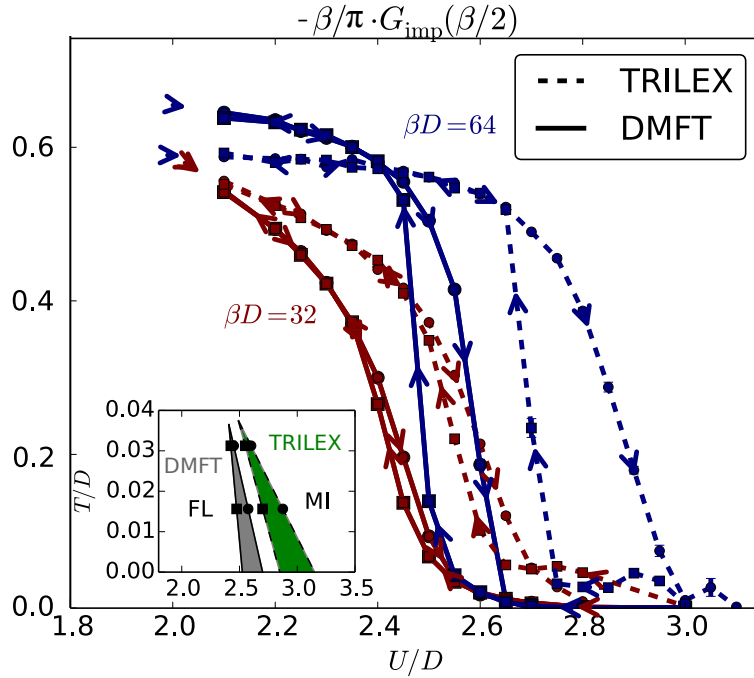


Figure 9.4: Evolution of $-\beta/\pi G_{\text{imp}}(\tau = \beta/2)$ as a function of U/D on the triangular lattice (half-filling). Solid lines: DMFT. Dashed lines: TRILEX. Red: $\beta D = 32$. Blue: $\beta D = 64$. *Inset*: sketch of the coexistence regions in DMFT (grey) and TRILEX (green) in the (U, T) plane.

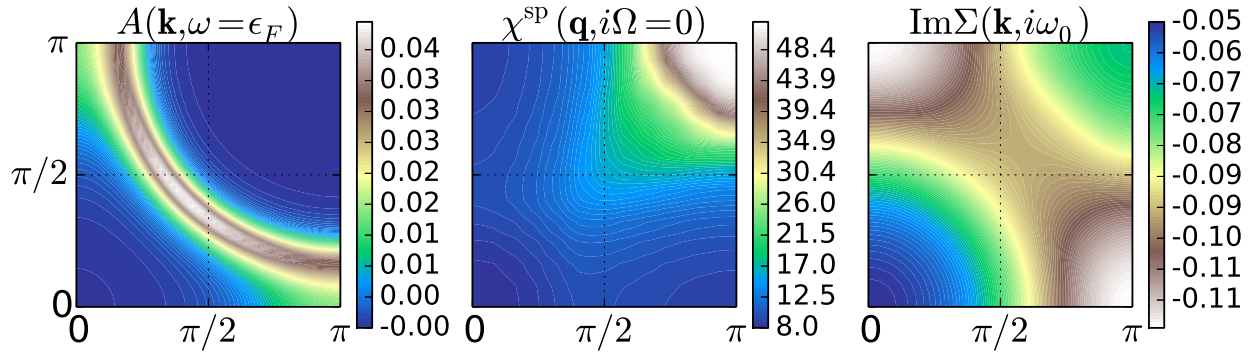


Figure 9.5: From left to right: $A(\mathbf{k}, \omega = 0)$, $\chi^{\text{sp}}(\mathbf{q}, i\Omega = 0)$ and $\text{Im}\Sigma(\mathbf{k}, i\omega_0)$ in the doped case (square lattice): $U/D = 1.8$, $t' = -0.4t$, $\beta D = 96$, $\delta = 10\%$. $A(\mathbf{k}, \omega = 0)$ is estimated from $\beta/2G(\mathbf{k}, \tau = \beta/2)$.

The first conclusion is that TRILEX also features a first-order Mott transition. The second conclusion is that in TRILEX, the critical interaction strength for the Mott transition, U_c , is slightly enhanced with respect to the single-site DMFT value, consistently with the difference that has been observed between the local component of the TRILEX self-energy and the single-site DMFT self-energy (middle right panel on Fig. 9.2).

This points to the importance of short-range fluctuations in the mechanism of the Mott transition. In cluster DMFT, these short-range fluctuations are treated non-perturbatively in the extended impurity model, leading to a substantial *reduction* of U_c with respect to the single-site value. It seems that single-site TRILEX misses local singlet physics. This motivates the need for a cluster extension of TRILEX.

9.3 Fermi arcs upon doping

The long-range fluctuations captured in TRILEX can have drastic effects on the lifetime of the quasiparticles on the Fermi surface. In this section, TRILEX is applied to the Hubbard model on a square lattice away from half-filling and with a nearest-neighbor hopping close to the one describing cuprate materials ($t' = -0.4t$), and $U/D = 1.8$, a value which is slightly smaller than that believed to describe high-temperature superconductors ($U/D \approx 2.25$, Comanac *et al.* (2007)).

Fig. 9.5 shows the results for $\beta D = 96$ and a 10% doping level. The static AF susceptibility $\chi^{\text{sp}}(\mathbf{q}, i\Omega = 0)$ has a rather broad peak at (π, π) due to relatively short-range AF fluctuations. This results, via W^{sp} (related to χ^{sp} through $W^{\text{sp}} = U^{\text{sp}} - U^{\text{sp}} \chi^{\text{sp}} U^{\text{sp}}$), in a momentum-dependent self-energy $\Sigma(\mathbf{k}, i\omega)$. $\text{Im}\Sigma(\mathbf{k}, i\omega_0)$ is larger at the antinodal points $(\pi, 0)$ and $(0, \pi)$, so that the corresponding spectral function $A(\mathbf{k}, \omega = 0)$ (left panel) displays substantial intensity variations on the Fermi surface.

These variations, although less strong than those observed experimentally and *e.g.* in cluster DMFT (Ferrero *et al.* (2008)), are reminiscent of the “Fermi arcs” seen in ARPES (Fig. 7.7 in chapter 7).

9.4 The question of antiferromagnetic ordering

In this section, I discuss the issue of the hatched region in the (U, T) phase diagram (Fig 9.1).

As previously mentioned, as the temperature is decreased, the strength of the antiferromagnetic fluctuations grows, namely the product $U^{\text{sp}} P^{\text{sp}}(\mathbf{q}, i\Omega)$ approaches the “Stoner” criterion $U^{\text{sp}} P^{\text{sp}}(\mathbf{q}, i\Omega) = 1$. This is illustrated in Fig. 9.6, where the top panels show the evolution of the inverse static AF susceptibility, $\chi^{\text{sp}}(\mathbf{Q}, i\Omega = 0)^{-1}$, as a function of temperature for the unfrustrated case ($t' = 0$) and in the presence of frustration ($t' = -0.3t$).

In the unfrustrated case, its evolution is linear for high temperatures. As temperature decreases, deviations to this linear behavior seem to appear, but the error bars (computed as the mean deviation of the last converged results divided by the square root of the number of samples) also become large. This is due to the fact that as $U^{\text{sp}} P^{\text{sp}}(\mathbf{Q}, i\Omega = 0)$ approaches the “Stoner” criterion, a small variation in $P^{\text{sp}}(\mathbf{q}, i\Omega)$ (coming for instance from the statistical noise in $\Lambda_{\text{imp}}^{\text{sp}}(i\omega, i\Omega)$) can translate into large variations in W^{sp} ; in addition, to properly integrate the corresponding peak in W^{sp} in momentum space, one must in principle refine the momentum mesh or equivalently increase the lattice size to accommodate for these longer correlation lengths. Thus, the computation becomes heavier; in this first implementation, we have preferred to defer these refinements to a later study and have instead extrapolated the linear behavior of the inverse susceptibility to compute the temperature \bar{T}^{xyz} under which we cannot safely perform the calculation.

To decide whether at low temperatures, the inverse AF susceptibility indeed intercepts the x -axis at a finite $T_{\text{Néel}}$, as the high-temperature behavior seems to indicate, or if it displays a bending (as observed in the correlation length in experiments – see the trend extracted from neutron scattering experiments in Fig. 7.4 – or in theory – see the results of the dynamical vertex approximation in appendix G.4), requires a more refined study. The issue could also be settled by allowing for a symmetry breaking with two sublattices. This idea is straightforward to implement, but requires another impurity solver, since in the AF phase the longitudinal (z) and perpendicular (x, y) spin components are no longer equivalent. In this phase, one has to measure the perpendicular components $\Lambda_{\text{imp}}^{x/y}$ of the vertex instead of Λ_{imp}^z only.

Moreover, one can expect that the low-temperature behavior of the single-site method will be affected by using the full form of the interaction term, Eq. (8.49) in the previous chapter, which derives from a local approximation of the 3PI functional \mathcal{K} . In particular, the low-energy behavior of the retarded interactions will probably be renormalized by the term $\zeta^\eta(i\omega, i\Omega)$ neglected in the present implementation. The solution of these more general equations, however, requires different impurity solvers, such as the continuous-time quantum Monte-Carlo solver in the interaction expansion (“CT-int”).

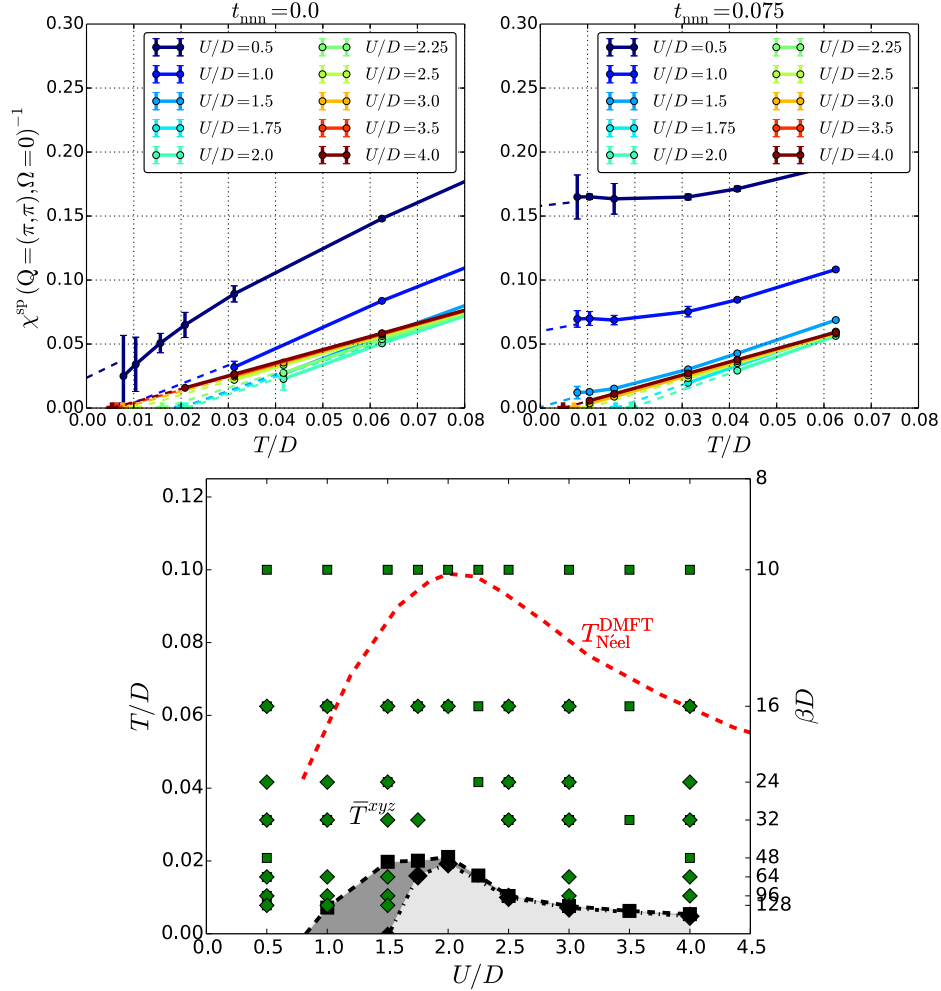


Figure 9.6: Influence of t' on \bar{T}^{xyz} (square lattice). *Top panels:* inverse static AF susceptibility as a function of temperature for various U/D values. *Left:* $t' = 0$. *Right:* $t' = -0.3t$. *Bottom panel:* (U, T) phase diagram. Squares (dark grey): $t' = 0$; diamonds (light grey): $t' = -0.3t$.

To further understand the behavior of the TRILEX equations, Fig. 9.6 also shows data for the frustrated case ($t' \neq 0$). There, one sees that frustration does lead to a “bending” of the inverse static AF susceptibility curve and that the “forbidden” region shrinks in the weak-interaction regime.

9.5 Influence of the decoupling choice

In this section, I discuss the practical implications of the way the Hubbard interaction term is decoupled in terms of Hubbard-Stratonovich terms. The ambiguity associated with this choice has already been mentioned in section 8.3.1.3.

Here, I will focus on two different levels of choice: the first is the rewriting of the Hubbard interaction in terms of a density-density and “Ising” term $s_z s_z$ or of a density-density and “Heisenberg” term $\vec{s} \cdot \vec{s}$. The second level is the subsequent choice of the ratio between the interactions in the charge and spin channels. This ratio is parametrized by the parameter α , introduced in section 8.4.2.

To compare the results of the rewriting in terms of Ising or Heisenberg spins (at fixed α), I show, in Fig. 9.7, the evolution of the inverse static AF susceptibility as a function of temperature for both decouplings. The

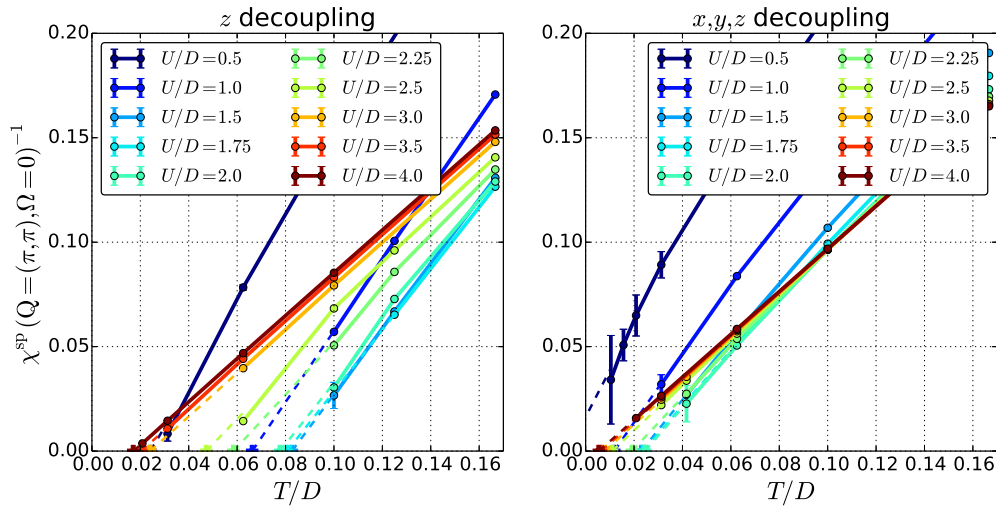


Figure 9.7: Inverse AF static susceptibility as a function of temperature (square lattice). *Left*: Ising or “z” decoupling. *Right*: Heisenberg or “xyz” decoupling.

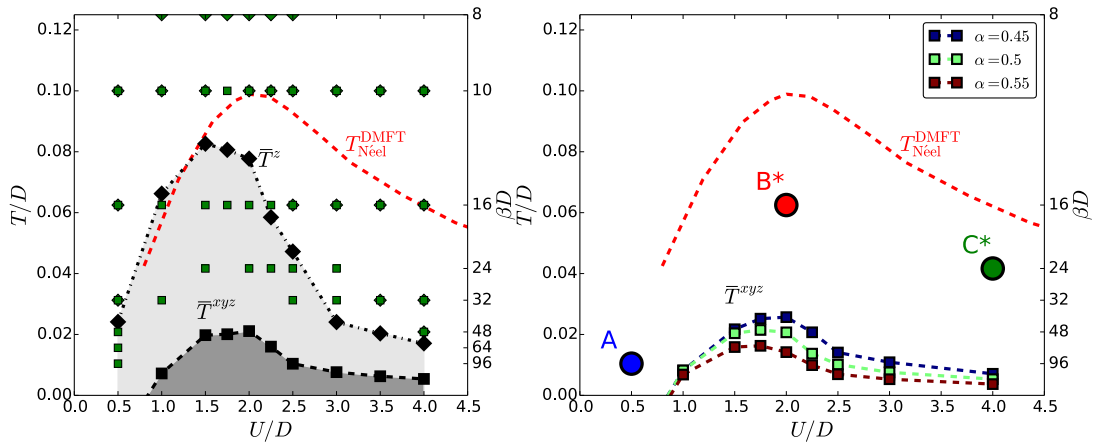


Figure 9.8: Phase diagram in the (T, U) plane at half-filling (square lattice, $t' = 0$). The dashed red line is the Néel temperature computed in single-site DMFT (from Kuneš (2011)). *Left*: Heisenberg (T_{AF}^{xyz}) vs. Ising (T_{AF}^z) decoupling (squares: Heisenberg; diamonds: Ising). T_{AF} is determined by extrapolating the inverse AF static susceptibility, see Fig. 9.7. *Right*: influence of the charge to spin channel ratio α in the Heisenberg decoupling. The points B^* and C^* are defined as B^* : $U/D = 2.0$, $\beta D = 16$; C^* : $U/2 = 4$, $\beta D = 24$.

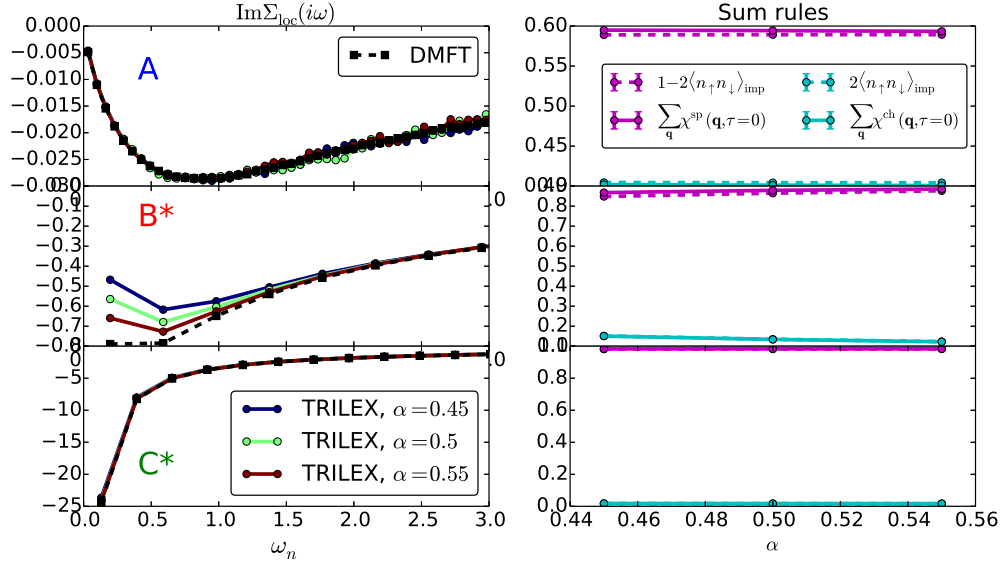


Figure 9.9: Influence of α on local observables and “sum rules”. *Left*: $\text{Im}\Sigma_{\text{loc}}(i\omega)$ for three characteristic points (defined in Fig. 9.8) and three values of α . *Right*: dependence of the susceptibility “sum rules” on α .

extrapolated \bar{T} (discussed in the previous section) strongly depends on the decoupling: the Ising decoupling yields a higher \bar{T} than the Heisenberg decoupling. This can be understood in the following intuitive way: in the Ising decoupling, the spin has fewer degrees of freedom to fluctuate than in the Heisenberg decoupling. Thus, the propensity for ordering is higher in the Ising decoupling than in the Heisenberg decoupling. In either case, \bar{T} is lower than the Néel temperature computed in single-site DMFT (except for a few points in the Ising decoupling at weak coupling, but the difference is within the error bar (not shown)): TRILEX contains spatial fluctuations beyond (dynamical) mean field theory. These results are summarized in the left panel of Fig. 9.8.

In the right panel of Fig. 9.8, the dependence of \bar{T}^{xyz} (within the Heisenberg decoupling) on α is investigated. \bar{T}^{xyz} depends on α : the larger $|U^{\text{sp}}|$, the higher \bar{T}^{xyz} , as one could have expected from the form of the Stoner criterion ($U^{\text{sp}}P^{\text{sp}}(\mathbf{Q}, i\Omega = 0) = 1$).

However, this dependence has substantial implications on physical observables only in the intermediate regime of correlations, as shown in Fig. 9.9. At points A and C* (due to the proximity to the ordered phase, we could not obtain converged results for all three values of α at points C and B), corresponding to the weak and strong-coupling limit, respectively, α has no influence on the local component of the TRILEX self-energy. Only at point B* does it lead to variations in this observable. This is another motivation for extending TRILEX to its cluster version.

However, irrespective of the value of α , sum rules on the charge and spin susceptibilities are fulfilled, namely the following identities are preserved:

$$\sum_{\mathbf{q}} \chi^{\text{ch}}(\mathbf{q}, \tau = 0) = \langle n \rangle_{\text{imp}} + 2\langle n_{\uparrow} n_{\downarrow} \rangle_{\text{imp}} - \langle n \rangle_{\text{imp}}^2 = 2\langle n_{\uparrow} n_{\downarrow} \rangle_{\text{imp}} \quad (9.1a)$$

$$\sum_{\mathbf{q}} \chi^{\text{sp}}(\mathbf{q}, \tau = 0) = \langle n \rangle_{\text{imp}} - 2\langle n_{\uparrow} n_{\downarrow} \rangle_{\text{imp}} = 1 - 2\langle n_{\uparrow} n_{\downarrow} \rangle_{\text{imp}} \quad (9.1b)$$

This is shown in the left panel of Fig. 9.9. These sum rules have been observed to be crucial for the fulfillment of the Mermin-Wagner theorem within the two-particle self-consistent theory (TPSC, Vilk and

Tremblay (1997)) or in the ladder version of the dynamical vertex approximation (Katanin *et al.* (2009)). There is thus no obvious way to fix α .

9.6 Conclusions and perspectives

The TRILEX method in its single-site version has been applied, in this chapter, to the single-band Hubbard model at and away from half-filling, on the square and on the triangular lattice.

As expected from the construction of the method, TRILEX interpolates between (a) the fluctuation-exchange limit, where the self-energy is given by the one-loop diagram computed with the propagator associated to long-range fluctuations in channel η , $W^\eta(\mathbf{q}, i\Omega)$, and (b) the dynamical mean field limit which approximates the self-energy by a local, but frequency-dependent impurity self-energy which reduces, in the strong-coupling regime, to the atomic limit self-energy.

The central quantity of TRILEX, the impurity three-leg vertex $\Lambda_{\text{imp}}(i\omega, i\Omega)$, encodes the passage from both limits, and can be used to construct momentum-dependent self-energies and polarizations *at a reduced cost* compared to cluster DMFT and diagrammatic extensions of DMFT. This cost is the cost of solving a *single-site* local impurity model with dynamical interactions. Contrary to spin fluctuation theory, the method covers the full range of interactions. At intermediate coupling, upon doping, strong AF fluctuations cause a sizable momentum differentiation of the Fermi surface, as observed in photoemission in cuprate materials.

This study opens up a number of questions and perspectives:

1. *Low-temperature phase.* The issue of the instabilities in the low-temperature regime, which is related to the fulfillment or not of the Mermin-Wagner theorem and the associated Fierz ambiguity, deserve further studies. This is all the more interesting as related methods such as TPSC and a variant of D Γ A fulfill the Mermin-Wagner theorem; understanding what are the minimal ingredients to enforce this property is needed. In particular, the role of the simplification of the impurity vertex $\lambda_{\text{imp}}(i\omega, i\Omega)$, introduced in subsection 8.3.3.2 and consisting in neglecting the quantity $\zeta^\eta(i\omega, i\Omega)$, ought to be investigated.
2. *Extension to cluster schemes.* As stated in the introduction of the TRILEX formalism, controllability is paramount. In the TRILEX formalism, the extension to cluster versions similar to those of DMFT is formally rather straightforward. In practice, the behavior of the multi-site impurity solvers (and most importantly of the sign problem) in TRILEX cannot be predicted. However, all the technological tools needed for this extension are already in the TRIQS toolbox (see chapter 10 and our paper Parcollet *et al.* (2015)). One can hope that, in the physically relevant channel, cluster-TRILEX will converge faster than cluster-DMFT with respect to the cluster size N_c due to the inclusion of long-range fluctuations.
3. *Extension to multiorbital systems.* Thanks to the simplicity of solving the single-site impurity model, single-site TRILEX can be applied to multiorbital systems to study momentum-dependent self-energy effects. Such an endeavor is currently out of the reach of cluster DMFT due to the sheer size of the corresponding Hilbert space (3 bands times a 2×2 cluster is effectively a 12-site calculation, already a large numerical effort in view of the poor momentum resolution obtained). Yet, this extension may be crucial for multiorbital systems where long-range spin physics as well as correlations are thought to play an important role. The recently discovered pnictide superconductors, where bosonic spin-density-wave fluctuations are sizable but correlations effects are not so strong, are such an example. They may prove an ideal playing ground for TRILEX.
4. *Extension to “anomalous” phases.* TRILEX can be straightforwardly extended to study charge-ordered phases (as shown by its relation to $GW + \text{EDMFT}$). Moreover, its application to superconducting phases is also possible: in this context, it interpolates between generalized Migdal-Eliashberg theory (or spin-fermion superconductivity) and the superconducting version of DMFT. As such, it can capture d -wave superconductivity at the cost of solving a single-site impurity problem (which is not possible in single-site DMFT).

Part IV

Modern computational methods for the quantum many-body problem

The methods I have presented in the previous parts of this thesis share a common feature: they are at the same time based on analytical calculations – such as the construction of energy functionals and appropriate approximations thereof, inspired by physical intuition and previous works – and they are nevertheless usually not amenable to fully analytical resolutions. They can all, however, be formulated in various algorithmic forms.

Beyond the effort that has been put into designing a method “on paper”, whether this method works or not (and proving it) mainly depends on (a) how *quickly* the algorithm can be transcribed as computer code, (b) how *efficient* the resulting program is and, most importantly, (c) how *reliably* it can be checked and tested. Meeting all three conditions is a subtle art, especially as conventional wisdom has it that (a) and (b) are mutually exclusive (a short syntax is often thought to be slow), and that the fulfillment of either (a) or (b) usually jeopardizes condition (c) (“writing checks slows down the coding”, “an optimized code is hard to read and thus to keep an overview of”).

The goal of this part is to give technical details about some of the computational methods touched on in the previous parts, with an emphasis on the algorithmic thinking behind these developments. This careful process, and the tools that support it, aim at overcoming the above contradictions.

In chapter 10, I give a brief overview of the TRIQS library, a Toolbox for Research on Interacting Quantum Systems, with a focus on one of my contributions to the library, namely error estimation through the binning and jackknife methods. In chapter 11, I describe one family of continuous-time quantum Monte-Carlo solvers on which relies, for instance, the TRILEX method presented in the previous chapters. Finally, as a further example of the use of this CTQMC solver, I describe a new method designed for realistic materials, the combined screened exchange and dynamical DMFT method (SEx+DDMFT) (chapter 12).

10 TRIQS: flexible yet fast codes for the quantum many-body problem

| | |
|--|-----|
| 10.1 Structure of the TRIQS library | 116 |
| 10.2 Three illustratory examples of usage of the TRIQS library | 117 |
| 10.3 Error analysis: Binning and Jackknife | 120 |

11 Continuous-time quantum Monte Carlo solver in the hybridization expansion with dynamical spin spin interactions

| | |
|--|-----|
| 11.1 Hybridization and \mathcal{J}_1 expansion: derivation | 129 |
| 11.2 Implementation notes | 140 |

12 Dynamical screening in solids: Combined Screened Exchange and dynamical DMFT

| | |
|---|-----|
| 12.1 Density functional theory combined to DMFT: LDA+DMFT in a nutshell | 149 |
| 12.2 Beyond LDA+DMFT combined with cRPA: GW+DMFT and SEx+DDMFT | 150 |

TRIQS: flexible yet fast codes for the quantum many-body problem

As alluded to in the introduction to this part, *flexibility* – the ease with which a new program is written and modified – and *speed* – which measures the efficiency of a given code – are often thought to be mutually exclusive. Furthermore, these two requirements are also sometimes put forward as arguments to justify the lack of *readability* of some computer codes.

The TRIQS project (Toolbox for Research on Interacting Quantum Systems, <http://ipht.cea.fr/triqs>), developed primarily by Olivier Parcollet and Michel Ferrero in Saclay (Institut de Physique Théorique) and Palaiseau (Ecole Polytechnique), aims at reconciling all three requirements by providing basic building blocks for many-body calculations. This goal is met by using modern programming techniques. This includes the combined use of modern versions of the compiled C++ language – used for writing fast yet readable code for critical parts such as Monte-Carlo algorithms – together with Python, an interactive high-level programming language. The latter language makes data post-processing and the manipulation of many-body objects much easier than the widespread “output-to-text-file-plot-with-command-line-include-in-latex-output-pdf-and-analyze-results” process. This combination is made possible and seamless by an automated generation of Python wrappers for C++ objects.

The TRIQS project also stresses the importance of *collaborative efforts* via a pedagogical documentation (see <http://ipht.cea.fr/triqs/1.2/documentation.html>), version control using the git versioning system (also essential for debugging), and the use of public or private code repositories (e.g. github.com or bitbucket.org). More details about the library can be found in our paper, Parcollet *et al.* (2015), included in chapter R.1.

My contributions to the library are the implementation, maintenance and user support of a segment-picture hybridization-expansion continuous-time quantum Monte Carlo code, presented in the next chapter. I have also implemented a library for error estimation using the binning and jackknife methods, presented in section 10.3. Before coming to this, I briefly describe the structure of the TRIQS library (section 10.1) and give three illustrative examples of uses of TRIQS in section 10.2.

10.1 Structure of the TRIQS library

The TRIQS project comprises a core library and “applications”, as illustrated in Fig. 10.1.

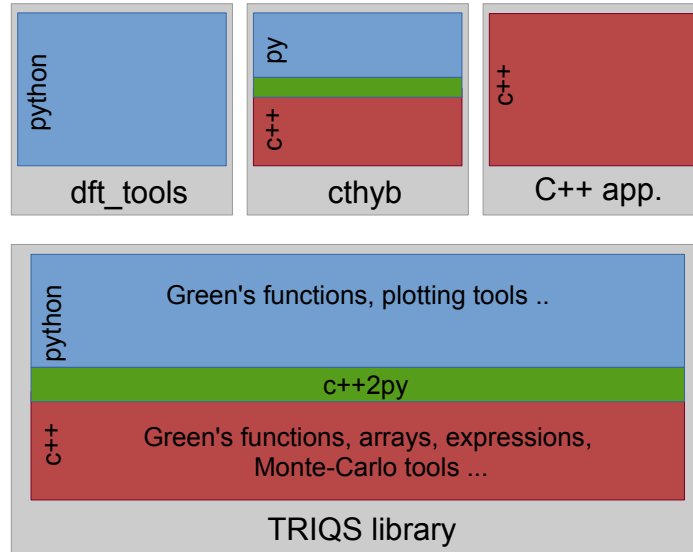


Figure 10.1: Structure of the TRIQS project, with a C++ and Python layer (from Parcollet *et al.* (2015))

10.1.1 The core library

The core TRIQS library contains basic building blocks for quantum many-body calculations such as real and imaginary time as well as real-frequency and Matsubara Green's functions with one or several variables. Also included are multidimensional arrays and an “expressions” library. A Monte-Carlo library provides a generic Metropolis-Hastings algorithm for writing any code based on this method (such as continuous-time quantum Monte-Carlo algorithms, described in the next chapter).

Most core objects are implemented at the C++ level and then automatically wrapped in Python using the “c++2py” tool of TRIQS. They can then be directly manipulated at the Python level, for instance plotted in an “ipython notebook”, a Mathematica-type browser-based interface to Python (see *e.g.* subsection 10.2.1 for an example).

10.1.2 TRIQS applications

The objects of the core library can then be used in “applications”. This may refer to existing ones such as “dft_tools” (http://ipht.cea.fr/triqs/1.2/applications/dft_tools/), an interface to density-functional theory codes, or “cthyb” (<http://ipht.cea.fr/triqs/1.2/applications/cthyb/>), an implementation of the continuous-time quantum Monte-Carlo solver in the hybridization expansion for general interactions (as opposed to the “segment picture” solver presented in the next chapter, an optimization of the hybridization-expansion solver for the case of density-density interactions). This may also simply be one's own code, written either in C++ or in Python, or in both. For instance, the segment solver code presented in the chapter (chapter 11) is one such application. The TRILEX code is another.

The common core library of all applications make them interoperable and thus facilitates collaborative efforts.

10.2 Three illustrative examples of usage of the TRIQS library

In this short section, I give three examples to illustrate the use of TRIQS. The first one illustrates the high-level usage of TRIQS. The second and third ones illustrate the implementation tools provided by TRIQS to write one's own code.

10.2.1 A DMFT calculation in one loop

Figure 10.2 illustrates the high-level use of TRIQS to write a DMFT loop in Python. This code implements the DMFT equations (subsection 2.2.4) for the case of a semicircular density of states. In this specific case, the new hybridization function $\Delta(\tau)$ is related to the impurity Green’s function by $\Delta(\tau) = (D/2)^2 G_{\text{imp}}(\tau)$ (D : half-bandwidth). Here, an interaction-expansion solver (“CT-int”) is used as impurity solver. Plotted are the imaginary parts of the impurity Green’s function $\text{Im}G_{\text{imp}}(i\omega)$ for increasing iteration index: the impurity Green’s function gradually turns from non-interacting (see $\text{Im} G_0$) to (Mott) insulating (see $\text{Im} G_{20}$).

10.2.2 Efficient and short writing of complex expressions

TRIQS simplifies the writing of complex algebraic expressions in C++. Using TRIQS, the following complicated expression:

$$\chi_{\nu\nu'\omega}^{0\sigma\sigma'} = \beta(g_{\nu}^{0\sigma} g_{\nu'}^{0\sigma'} \delta_{\omega} - g_{\nu}^{0\sigma} g_{\nu+\omega}^{0\sigma} \delta_{\nu\nu'} \delta_{\sigma\sigma'})$$

can be coded in C++, after having defined a three-frequency Green’s function $\chi_{\nu,\nu',\omega}^{0\sigma\sigma'}$, as simply as:

```
chi0(s_, sp_)(nu_, nup_, om_) <<
    beta * ( g[s_](nu_) * g[sp_](nup_) * kronecker(om_)
            - beta * ( g[s_](nu_) * g[s_](nu_ + om_)
                    * kronecker(nu_, nup_) * kronecker(s_, sp_));
```

The five variables $s_$, $sp_$, $nu_$, $nup_$, and $om_$ are “placeholders”, namely the above expression is automatically interpreted by the C++ compiler as a five-fold nested “for loop” traversing the respective domains of definition of these variables, namely $\{\uparrow, \downarrow\}$ for σ and σ' and Matsubara frequencies for ν , ν' and ω .

The syntax, while directly reflecting the mathematical formula, enhances possibilities of optimization by the library and the compiler (for instance of the memory traversal).

10.2.3 The Monte-Carlo library

As a more complex example and as a preliminary to the next chapter, I explain in this section how TRIQS simplifies the writing of Metropolis-Hastings algorithms.

The principle of the Metropolis-Hastings algorithm (Metropolis *et al.* (1953); Hastings (1970)) is illustrated in Fig. 10.3. A formal explanation is provided in section 11.1.3, but the sketch of Fig. 10.3 is self-contained: it illustrates the transition process from a “configuration” x to a configuration y . After the initialization of the simulation (with a given configuration x_0), the current configuration x can be “updated” with several updates. Each update $x \rightarrow y$ has a proposal probability $P_{x,y}^{\text{prop}}$ and $P_{y,x}^{\text{prop}}$ (probability to propose the update from x to y and conversely) as well as an associated weight ratio $p(y)/p(x)$. These are combined into a number $P_{x,y}^{\text{acc}}$. Under a certain condition on $P_{x,y}^{\text{acc}}$, the update is either accepted, in which case x becomes y , or not, in which case x remains unchanged. In either case, observables on this configuration can be “measured” at regular intervals.

This general algorithm subsumes simulations as different as the simulation of a Ising model (cf Eq. (2.8) in chapter 2) or the sampling of Feynman diagrams in *e.g.* the interaction-expansion of the continuous-time quantum Monte-Carlo algorithm (an implementation of which is given in Parcollet *et al.* (2015), included in chapter R.1). Because of this generality, it need not be rewritten from scratch for each individual code: once the generic algorithm is tested, simplified and optimized, it can be used in many codes.

The only work left to the physicist is the specification of the Metropolis updates (with the accompanying probability ratios) and measures on the configurations of the problem at hand. For instance, the parallelization of the algorithm is already implemented in the generic library.

IP[y]: Notebook

dmft_bethe (unsaved changes)

File Edit View Insert Cell Kernel Help

Code Cell Toolbar: None

```
In [1]: from pytrigs.gf.local import *
from pytrigs.archive import *
import pytrigs.utility.mpi as mpi
from pytrigs.applications.impurity_solvers.ctint_tutorial import CtintSolver
from pytrigs.plot.mpl_interface import oplot

# Parameters
U = 2.5          # Hubbard interaction
mu = U/2.0      # Chemical potential
half_bandwidth=1.0 # Half bandwidth (energy unit)
beta = 40.0     # Inverse temperature
n_iw = 128      # Number of Matsubara frequencies
n_cycles = 10000 # Number of MC cycles
delta = 0.1     # delta parameter
n_iterations = 21 # Number of DMFT iterations

S = CtintSolver(beta, n_iw) # Initialize the solver

S.G_iw << SemiCircular(half_bandwidth) # Initialize the Green's function

with HDFArchive("dmft_bethe.output.h5", 'w') as A:
    A['n_iterations'] = n_iterations # Save a parameter

for it in range(n_iterations): # DMFT loop
    for name, G0 in S.G0_iw:
        G0 <<= inverse(iOmega_n + mu - (half_bandwidth/2.0)**2 * S.G_iw[name] ) # Set G0
        # Change random number generator on final iteration
        random_name = 'mt19937' if it<n_iterations-1 else 'lagged_fibonacci19937'

    S.solve(U, delta, n_cycles, random_name=random_name) # Solve the impurity problem

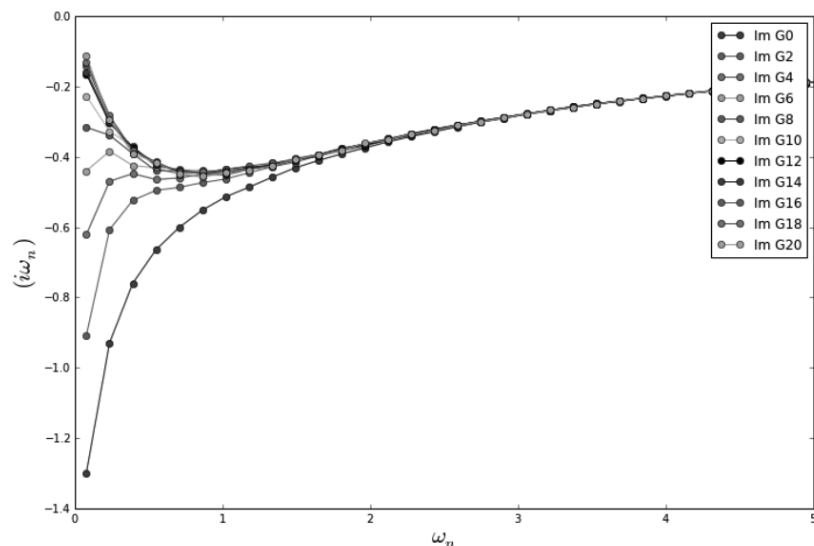
    G_sym = (S.G_iw['up']+S.G_iw['down'])/2 # Impose paramagnetic solution
    S.G_iw << G_sym

    if mpi.is_master_node():
        A['G%i'%it] = G_sym # Save G from every iteration to file
```

Starting on 1 Nodes at : 2014-10-22 18:06:12.886058

```
In [2]: A = HDFArchive("dmft_bethe.output.h5", 'r') # Open file
n_iterations = A['n_iterations'] # Load a parameter
for it in range(n_iterations): # Use parameter in the analysis
    if not it%2: oplot(A['G%i'%it].imag, '-o', name='Im G%i'%it) # Plot every second result
xlim(0,5)
```

Out[2]: (0, 5)

Figure 10.2: A DMFT calculation on the Bethe lattice, in one page (from Parcollet *et al.* (2015))

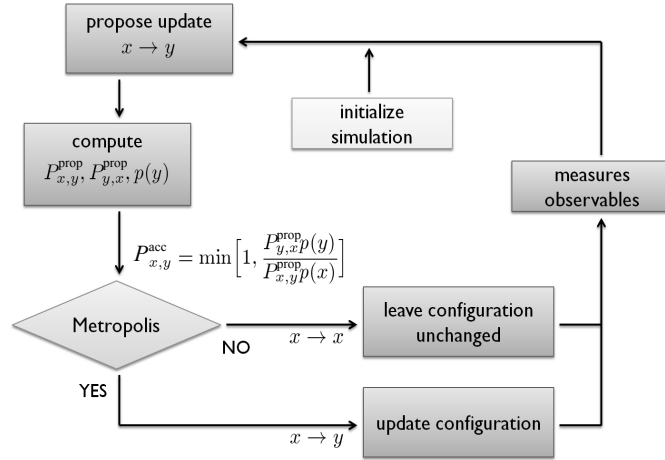


Figure 10.3: Metropolis-Hastings algorithm. x and y denote configurations (from <http://ipht.cea.fr/triqs/1.2/reference/montecarlo/loop.html>)

A concrete example can be found on the following page: http://ipht.cea.fr/triqs/1.2/reference/statistical_analysis/ising2d.html. The “segment solver” presented in the next chapter is a more complex code making use of the Metropolis-Hastings library. An example of code corresponding to a Metropolis update for this algorithm is given in Listing M.1 in appendix M.4.

10.3 Error analysis: Binning and Jackknife

This section presents one of my contributions to the TRIQS library, which can be used for instance to estimate the error bars in Monte-Carlo simulations.

10.3.1 Statement of the problem

10.3.1.1 Failure of a simple-minded estimate of the error bar

Let us consider a simple case to establish notation. Let X denote a random variable with probability densities $P(X)$. Suppose we want to obtain an estimate for its expectation value

$$f = \langle X \rangle$$

where the expectation value is defined as

$$\langle X \rangle \equiv \int dX X P(X) \quad (10.1)$$

We also define the variance of X :

$$\text{Var}(X) \equiv \langle (X - \langle X \rangle)^2 \rangle \quad (10.2)$$

As will be seen in the following, if we have N samples of X , $\{x_i\}_{i=1\dots N}$, the estimate of f is straightforwardly given by the “empirical” average of these samples:

$$f_{\text{est}} = \bar{x}$$

where the “empirical” average (or sample mean) is defined as

$$\bar{x} \equiv \frac{1}{N} \sum_{i=1}^N x_i \quad (10.3)$$

The estimation of the error bar on f_{est} is also quite straightforward if the samples are independent. The square of this error bar is defined as

$$\Delta f^2 \equiv \langle [f_{\text{est}} - f]^2 \rangle \quad (10.4)$$

In the case of independent samples, the estimate of Δf^2 is given by

$$\Delta f_{\text{est}}^2 = \frac{\sigma_x^2}{N}$$

where σ_x^2 is the “empirical” variance (or sample variance):

$$\sigma_x^2 \equiv \frac{1}{N} \sum_{i=1}^N (x_i - \bar{x})^2 \quad (10.5)$$

In this section, I shall address two issues:

- how to extend this error bar estimation to correlated samples? This question will be addressed by the binning method;
- how to extend this error bar estimation to more complex observables? This question will be addressed by the jackknife method, introduced by Quenouille (1949).

As a motivating example for the latter issue, let us consider, in addition to X , a second random variable Y , and let us estimate the error bar on the following quantity:

$$f = \frac{\langle X \rangle}{\langle Y \rangle}$$

While the estimate of f is straightforwardly given by $f_{\text{est}} = \bar{x}/\bar{y}$, the estimate of the squared error bar is *not* given by the simple-minded generalization of the one-variable case, namely it is *not* given by $\sigma_{x/y}^2/N$, where $\sigma_{x/y}^2 = \frac{1}{N} \sum_{i=1}^N (x_i/y_i - \bar{x}/\bar{y})^2$.

Let us emphasize that ratios of the form given above are ubiquitous. In particular, in fermionic Monte-Carlo algorithms, we shall see in the next chapter that the Monte-Carlo estimate of an observable O is expressed as

$$f = \frac{\langle O \cdot \text{sign} \rangle}{\langle \text{sign} \rangle}$$

where sign denotes the sign of the current Markov-chain configuration.

10.3.1.2 Algorithmic challenges and an example of the final code

As will be seen in the following, the formulae for the jackknife method are relatively simple. Here, the challenge is to write a library which applies to any function f of an arbitrary number of observables X, Y, Z, \dots

To be more specific, we want to cover the following cases:

| Random variable | Observable f | Function |
|------------------------|---|--|
| X | $\langle X \rangle$ | $f(x) = x$ |
| X | $\langle X \rangle^2$ | $f(x) = x^2$ |
| X, Y | $\langle X \rangle / \langle Y \rangle$ | $f(x, y) = x/y$ |
| X, Y | $\langle X/Y \rangle$ | $f(x) = x$ |
| $G(\tau), \text{sign}$ | $\frac{\langle \int_0^\beta G(\tau) G(-\tau) d\tau \text{sign} \rangle_{\text{MC}}}{\langle \text{sign} \rangle_{\text{MC}}}$ | $f(x, y) = x/y$ with $x = \int_0^\beta G(\tau) G(-\tau) d\tau \cdot s$ and $y = s$ |
| $G(\tau), \text{sign}$ | $\frac{\langle G(\tau) \text{sign} \rangle_{\text{MC}}}{\langle \text{sign} \rangle_{\text{MC}}}$ | $f(x, y) = x/y$ with $x = G(\tau)s$ and $y = s$ |

The last two examples are drawn from Monte-Carlo simulations. Note the difference between lines 3 ($\langle X \rangle / \langle Y \rangle$) and 4 ($\langle X/Y \rangle$).

In the final code, if X and Y denote “observables”, namely objects containing a number N of samples for the random variables X and Y , the estimation of lines 1 to 3 of the above table will be done by the following lines (see section 10.3.6 for a full example):

```
average_and_error_bar(X)
average_and_error_bar(X*X)
average_and_error_bar(X/Y)
```

This works for independent samples. The case of correlated samples will be elaborated on later.

10.3.1.3 Generic problem

Given an observable

$$O = f(\langle X \rangle, \langle Y \rangle, \langle Z \rangle, \dots)$$

with random variables $X, Y, Z \dots = \vec{X}$ and a function $f(x, y, z \dots) = f(\vec{x})$, the goal is to measure an estimate for the above observable as well as an estimate of the error on this estimate, given N samples

$$\{x_i, y_i, z_i, \dots\}_{i=1 \dots N}$$

of the random variables. Two issues need to be distinguished:

- **Autocorrelation:** the samples $\{\vec{x}_i\}_{i=1 \dots N}$ may not be independent of each other, ie $\langle x_i x_j \rangle_{i \neq j} \neq 0$. This will be dealt with by the so-called binning method (section 10.3.3)
- **Bias:** the function f may not be linear (e.g $f(x, y) = x/y$), causing simple-minded estimates of the uncertainty on the observable to be wrong. This will be dealt with by the so-called jackknife method (section 10.3.4)

In the following, I shall be looking for estimates which reduce to the exact quantity for large sample sizes N in expectation value. Such estimates are called *unbiased* estimates. More specifically, a quantity A is an unbiased estimate of another observable B if and only if

$$\langle A \rangle = B + \mathcal{O}\left(\frac{1}{N}\right)$$

I introduce the following notation to denote an unbiased estimate:

$$A \cong B$$

10.3.2 Basic results

In appendix N, I prove the following basic results which will be used in the derivations:

$$\begin{aligned} \bar{x} &\cong \langle X \rangle \\ f(\bar{x}) &\cong f(\langle X \rangle) \\ \overline{f(x)} &\not\cong f(\langle X \rangle) \end{aligned} \tag{10.6}$$

For independent samples:

$$\frac{\text{Var}(X)}{N} \cong \Delta\langle X \rangle^2 \quad (10.7)$$

$$\sigma_x^2 \cong \text{Var}(X) \quad (10.8)$$

For correlated samples:

$$\frac{\text{Var}(X)}{N} (1 + 2\tau_{\text{int}}) \cong \Delta\langle X \rangle^2 \quad (10.9)$$

$$\sigma_x^2 \cong \text{Var}(X) (1 + 2\tau_{\text{int}}) \quad (10.10)$$

where τ_{int} is the integrated autocorrelation time

$$\tau_{\text{int}} \equiv \sum_{t=1}^{\infty} A_{f,x}(t) \quad (10.11)$$

and $A_{f,x}(t)$ the autocorrelation function:

$$A_{f,x}(t) \equiv \frac{\langle f(x_{i+t})f(x_i) \rangle - \langle f(x_i) \rangle^2}{\langle f(x_i)^2 \rangle - \langle f(x_i) \rangle^2} \quad (10.12)$$

which is independent of i .

10.3.3 The binning method: autocorrelation suppression

The samples $\{x_i\}_{i=1\dots N}$ of a random variable X may not always be statistically independent of each other. The level of autocorrelation is measured by the autocorrelation time, which measures the minimal time τ for which a sample $x_{i+\tau}$ can be considered independent from a sample x_i . Autocorrelation effects are particularly relevant for Monte-Carlo sampling, especially in the vicinity of a phase transition, where the correlation time between the samples increases. See for instance [Krauth \(2006\)](#) for more details.

The binning (or bunching) method consists in removing the correlations between the samples by defining a new series $\{x_i^{\text{B}}\}$ from the original series $\{x_i\}$ through the relation

$$x_i^{\text{B}} \equiv \frac{1}{b} \sum_{j=bi}^{b(i+1)-1} x_j \quad (10.13)$$

for $i = 1 \dots N_b$. b is the bin size and $N_b \equiv N/b$ the number of bins or size of the binned series. Clearly,

$$\overline{x^{\text{B}}} \cong \langle X \rangle$$

If b is larger than the autocorrelation time (cf Eq. (N.7)), the binned series contains independent samples. One can thus use Eqs (10.7-10.8) to estimate the error on the estimate:

$$\Delta\langle X \rangle^2 \cong \frac{\text{Var}(X)}{N_b} \cong \frac{\sigma_{\text{B}}^2}{N_b} \quad (10.14)$$

One can also use this to estimate the autocorrelation time: using (10.14) and (10.9), one obtains

$$\tau_{\text{int}}^{\text{B}}(b) \cong \frac{1}{2} \left(\frac{b\sigma_{\text{B}}^2}{\text{Var}(X)} - 1 \right) \quad (10.15)$$

This estimation is only possible if one knows the intrinsic variance. The latter is given by σ^2 (Eq. (10.8)) only if the binned series becomes uncorrelated, namely for a bin size exceeding the autocorrelation time.

10.3.4 The jackknife method: bias suppression

The jackknife method has been introduced by Quenouille (1949). A detailed discussion of the uses and variants of jackknife methods can be found in *e.g.* Shao and Tu (1995). In this section, I will focus on the use of jackknife for the computation of error bars of observables which are nonlinear expressions of averages.

10.3.4.1 Jackknife on a single variable

10.3.4.1.1 Case $f = \text{Id}$ Given a series $\{x_i\}_{i=1\dots N}$, one defines the so-called jackknifed series $\{x_i^J\}_{i=1\dots N}$ by the expression:

$$x_i^J \equiv \frac{1}{N-1} \sum_{j=1, j \neq i}^N x_j \quad (10.16)$$

Clearly, $\langle \overline{x^J} \rangle = \langle X \rangle = \langle \bar{x} \rangle$, namely:

$$\overline{x^J} \cong \langle X \rangle$$

If the original series contains independent variables, then the error estimate can be computed as

$$\Delta \langle X \rangle^2 \cong (N-1) \sigma_J^2 \quad (10.17)$$

where σ_J^2 is the empirical variance of the jackknifed series. Eq. (10.17) will be proven in the general case below.

10.3.4.1.2 For a general f From the jackknifed series $\{x_i^J\}_{i=1\dots N}$, one defines the series $\{f_i^J\}_{i=1\dots N}$ with $f_i^J \equiv f(x_i^J)$ (this easily generalizes to the case $f_i^J \equiv f(x_i^J, y_i^J, z_i^J, \dots)$). An estimate for $f(\langle X \rangle)$ is then

$$f(\langle X \rangle) \cong \overline{f^J} \quad (10.18)$$

This is to be contrasted with Eq. (10.6). The error estimate is

$$\Delta f_{\text{est}}^2 \cong (N-1) \sigma_{f^J}^2 \quad (10.19)$$

Let us now prove Eqs. (10.18) and (10.19). Let us first look at:

$$\begin{aligned} f_i^J &= f\left(\frac{1}{N-1} \sum_{j=1, j \neq i}^N x_j\right) = f\left(\langle X \rangle + \frac{1}{N-1} \sum_{j=1, j \neq i}^N (x_j - \langle X \rangle)\right) \\ &= f(\langle X \rangle) + \frac{1}{N-1} \sum_{j=1, j \neq i}^N (x_j - \langle X \rangle) f'(\langle X \rangle) + \left(\frac{1}{N-1} \sum_{j=1, j \neq i}^N (x_j - \langle X \rangle)\right)^2 \frac{f''(\langle X \rangle)}{2} + \dots \end{aligned}$$

Therefore

$$\begin{aligned} \langle \overline{f^J} - f(\langle X \rangle) \rangle &= \left\langle \frac{1}{N} \sum_{i=1}^N f\left(\frac{1}{N-1} \sum_{j=1, j \neq i}^N x_j\right) - f(\langle X \rangle) \right\rangle \\ &= \frac{1}{N} \frac{1}{(N-1)^2} \sum_{i=1}^N \left\langle \left(\sum_{j=1, j \neq i}^N (x_j - \langle X \rangle) \right)^2 \right\rangle \frac{f''(\langle X \rangle)}{2} + \dots \\ &= \frac{1}{(N-1)^2} \sum_{(j,k)=1}^{N-1} \langle (x_j - \langle X \rangle) (x_k - \langle X \rangle) \rangle \frac{f''(\langle X \rangle)}{2} + \dots \\ &= \frac{1}{N-1} \text{Var}(X) \frac{f''(X)}{2} + \dots \end{aligned}$$

The last line holds only if the variables are independent. Otherwise, one has to replace $\text{Var}(X)$ by $\text{Var}(X)(1 + 2\tau_{\text{int}})$. This proves (10.18).

Let us now turn to the uncertainty estimation. After a straightforward, but lengthy calculation (detailed in appendix N.4), one finds that the right-hand side of (10.19) averages to:

$$(N - 1) \langle \sigma_{f^J}^2 \rangle = f'(\langle X \rangle)^2 \langle (\bar{x} - \langle X \rangle)^2 \rangle + \dots$$

The left-hand side is given by:

$$\Delta f(\langle X \rangle)^2 = \langle [f(\bar{x}) - f(\langle X \rangle)]^2 \rangle = f'(\langle X \rangle)^2 \langle (\bar{x} - \langle X \rangle)^2 \rangle + \dots$$

This proves (10.19).

The autocorrelation time can be obtained from a jackknife calculation by writing $\Delta \langle X \rangle^2 \cong N_b \sigma_{B,J}^2 = \frac{\text{Var}(X)}{N} (1 + 2\tau_{\text{int}})$, so that

$$\tau_{\text{int}}^J(b) \cong \frac{1}{2} \left(\frac{NN_b \sigma_{B,J}^2}{\text{Var}(X)} - 1 \right) \quad (10.20)$$

This estimation is only possible if one knows the intrinsic variance.

10.3.5 Autocorrelation time estimation through binning

The autocorrelation time of a series can be estimated by examining the autocorrelation function $A_{f,X}(t)$ defined in section 10.3.2. As shown in appendix N.5, this estimation is accurate but too slow (it is a $O(N^2)$ calculation). In this section, I show how to compute the autocorrelation via the binning method.

For testing purposes, a correlated Gaussian series with autocorrelation time τ_c is artificially generated. This is done by generating a first independent Gaussian series $\{y_i\}$ and defining a correlated series by the recursion relation:

$$\begin{cases} x_0 & = y_0 \\ x_{i+1} & = \eta x_i + \sqrt{1 - \eta^2} y_{i+1} \end{cases}$$

where $\eta \equiv e^{-1/\tau_c}$.

Using Eq. (10.15) to estimate the autocorrelation time, one finds the results shown in Fig. 10.4b. Note that the error bar depends on the correlation time (this is obvious from Eq. (N.8) and from Fig. 10.4a). Indeed, a larger autocorrelation time means a smaller effective number of independent measurements, and thence a larger error bar by virtue of Eq. (N.5). Most importantly, the estimated autocorrelation is independent of bin size for large enough bin sizes. This property is used to compute the estimate of the autocorrelation time, using (10.15), as:

$$\tau_B = \frac{1}{n_s} \sum_{n > n_c}^{n_s - n_c} \frac{1}{2} \left\{ \frac{2^n \sigma_B^2(2^n)}{\sigma^2} - 1 \right\} = \frac{1}{n_s} \sum_{n > n_c}^{n_s - n_c} \tau_{\text{int}}^B(2^n) \quad (10.21)$$

The bin size is doubled from iteration to iteration, allowing one to reuse the binned series of the previous step. The minimum bin size for computing τ_{int} , parametrized by n_c , is chosen so that the asymptotic behavior of τ_{int} is reached, i.e. $\frac{\tau_{\text{int}}(2^{n_c}) - \tau_{\text{int}}(2^{n_c-1})}{\tau_{\text{int}}(2^{n_c-1})} \ll 1$ (thus, beyond this point $\text{Var}(X) \cong \sigma^2$). In practice, a threshold of 10^{-5} is used. n_s is chosen such that there are at least $n_s = 5$ samples while ensuring that $2^{n_s} < N/10$. This is a robust and quick way of computing the autocorrelation time

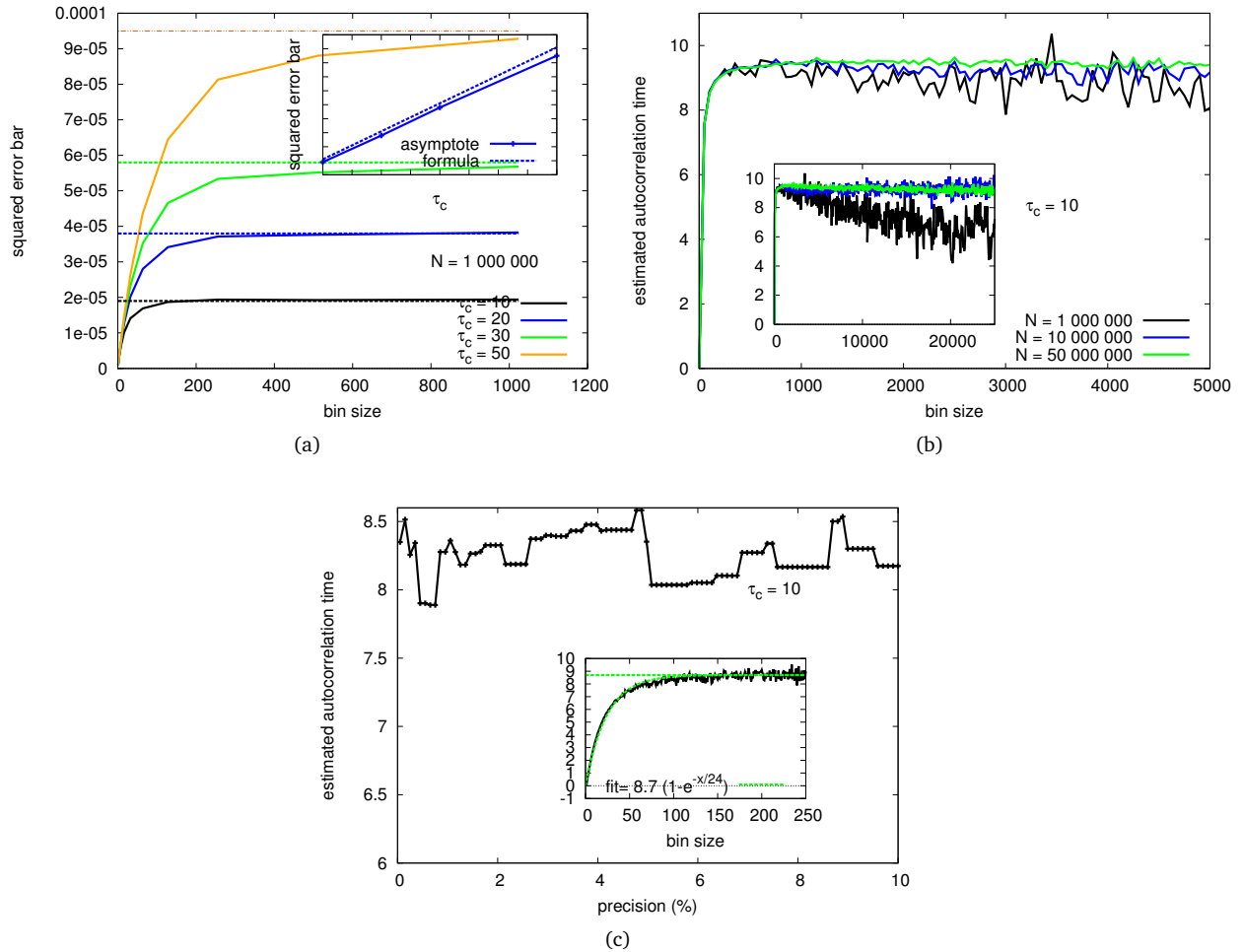


Figure 10.4: Binning analysis . (a) **Dependence of the estimated error bar on the bin size.** The error bar estimate converges to $(N.8)$ as the bin size increases. It converges faster for lower τ_c . (b) Dependence of the estimated autocorrelation time on the bin and sample size (c) **Estimated autocorrelation time:** dependence on the precision of the asymptote detection.

10.3.6 Implementation notes

The binning and jackknife methods are implemented in TRIQS and documented on the following page: http://ipht.cea.fr/triqs/1.2/reference/statistical_analysis/contents.html.

While the basic formulae (see section 10.3.2) are easy to implement, the main jackknife result, Eq. (10.18), deserves more attention. Indeed, it should work for any expression f of a variable number of arguments, such as the examples presented in the introduction to this chapter. More precisely, for each argument of $f(x, y, z, \dots)$, the jackknifed series x^J, y^J, z^J , must be computed and the estimate of $f(\langle X \rangle, \langle Y \rangle, \langle Z \rangle, \dots)$ will be $f(x^J, y^J, z^J)$ (the error bar is the square root of $\sigma_{f^J}^2$ given by Eq. (10.19)).

In our implementation, this is done by using the expression library of TRIQS (clef), while allows to “see” $f(\langle X \rangle, \langle Y \rangle, \langle Z \rangle, \dots)$ as an expression tree. For instance, $f(X, Y, Z) = \frac{X}{Y+Z}$ is nothing but the expression tree shown in Fig. 10.5 (a). The algorithm traverses the tree and replaces the leaves of this tree by the jackknife series (Fig. 10.5 (b)).

Then, the jackknife average (variance) is computed by evaluating the expression tree with the empirical average (variance) of the leaves. The series on the leaves can also optionally be binned if required by the

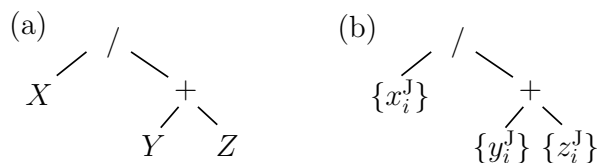


Figure 10.5: Expression trees

user.

An example of use is given below:

```

#include <triqs/clef.hpp>
#include <triqs/statistics.hpp>
using namespace triqs::statistics;
int main() {
  observable<double> X;
  X << 1.0;
  X << -1.0;
  X << .5;
  X << .0;
  std::cout << average_and_error(X) << std::endl;
  std::cout << average_and_error(X * X) << std::endl;
  return 0;
}
----- Result is -----
0.125 +/- 0.426956
0.0763889 +/- 0.174719

```

Listing 10.1: Example of error bar computation

The class **observable** can be filled with any object which has at least the following two public methods: `value_type operator[](int i)` and `int size()`, where `value_type` is any type which belongs to an algebra, namely has `+`, `-` and `*` operations. Any expression made up of observables can be input to the function `average_and_error`. If the series is known to be correlated, one can specify the bin size as a second argument to be used for a binning step before the jackknife step.

Continuous-time quantum Monte Carlo solver in the hybridization expansion with dynamical spin spin interactions

In this chapter, I describe an algorithm to compute observables associated with a local action S_{AIM} describing a correlated level hybridized with a bath. In its most simple form, this action reads:

$$S_{\text{AIM}} = \int_0^\beta d\tau \int_0^\beta d\tau' \sum_\sigma \left\{ \bar{c}_\sigma(\tau) \left[(\partial_\tau + \varepsilon_{f\sigma}) \delta(\tau - \tau') + \Delta_\sigma(\tau - \tau') \right] c_\sigma(\tau') \right\} + \int_0^\beta d\tau U n_\uparrow(\tau) n_\downarrow(\tau) \quad (11.1)$$

where ε_f is the energy of the correlated level, $\Delta_\sigma(\tau)$ is the so-called hybridization function and U the interaction between electrons of opposite spin. \bar{c}_σ and c_σ are conjugate Grassmann antiperiodic fields. Among the most prominent observables, one is mainly interested in the one-particle Green's function $G_\sigma(\tau_i - \tau_j) \equiv -\langle c_\sigma(\tau_i) \bar{c}_\sigma(\tau_j) \rangle$. This Green's function can formally be obtained by differentiating the partition function $Z = \int \mathcal{D}[\bar{c}c] e^{-S_{\text{AIM}}}$ with respect to the hybridization function:

$$G_\sigma(\tau_i, \tau_j) = \frac{1}{Z} \frac{\delta Z}{\delta \Delta_\sigma(\tau_j, \tau_i)} \quad (11.2)$$

The above expression shows that the central quantity for computing G is the partition function Z . Continuous-time quantum Monte-Carlo (CTQMC) (Rubtsov *et al.* (2005); Werner *et al.* (2006); Gull (2008)) algorithms for impurity solvers consist in first expanding the partition function in powers of one of the terms of action (11.1) and then computing the resulting infinite summation using a Metropolis-Hastings algorithm.

Hereafter, I will be interested in a specific flavor of these CTQMC algorithms, the so-called hybridization-expansion algorithm (CT-hyb, Werner *et al.* (2006); Gull *et al.* (2007)), which consists in expanding Z in powers of the hybridization Δ . The algorithm presented below applies to a generalization of Eq. (11.1) to time-dependent density-density and spin-spin interactions which are needed in the TRILEX method presented in part III. This requires, in addition to the hybridization expansion, an expansion in powers of the perpendicular component of the spin-spin interactions.

For general review on the topic of CTQMC algorithms, I refer the reader to Gull *et al.* (2011).

In section 11.1, I derive the main results and describe the underlying principles of the CT-hyb algorithm. In section 11.2, I describe how these general principles are implemented.

11.1 Hybridization and \mathcal{J}_\perp expansion: derivation

11.1.1 Definition and notations

Instead of the simple model introduced in Eq. (11.1), let us consider a more general local action describing a correlated level with hybridization function $\Delta(\tau)$, static and dynamical (first implementation: Werner and Millis (2007)) density-density interactions $\mathcal{U}(\tau)$ and dynamical spin-spin interactions $\mathcal{J}(\tau)$ (first introduced by Otsuki (2013)):

$$S_{\text{AIM}} = \iint_0^\beta d\tau d\tau' \sum_{a,b} \left\{ \bar{c}_{a\sigma}(\tau) \left((\partial_\tau + \varepsilon_{a\sigma}) \delta_{ab}^{\sigma\sigma'} \delta_{\tau-\tau'} + \Delta_{ab}^{\sigma\sigma'}(\tau - \tau') \right) c_{b\sigma'}(\tau') \right\} + \frac{1}{2} \iint_0^\beta d\tau d\tau' \mathcal{U}_{ab}(\tau - \tau') n_a(\tau) n_b(\tau') \\ + \frac{1}{2} \iint_0^\beta d\tau d\tau' \sum_{a,\xi=x,y,z} s_a^\xi(\tau) \mathcal{J}_a^\xi(\tau - \tau') s_a^\xi(\tau')$$

a denote orbital indices, σ spin indices ($\sigma = \uparrow, \downarrow$), $n_a \equiv \sum_{\sigma=\uparrow\downarrow} n_{a\sigma}$, $s_a^\xi \equiv \frac{1}{2} \sum_{\sigma\sigma'} \bar{c}_{a\sigma} \sigma_{\sigma\sigma'}^\xi c_{a\sigma'}$ and σ^ξ are the Pauli matrices². $\bar{c}_{a\sigma}(\tau)$ and $c_{a\sigma}(\tau)$ are β -antiperiodic Grassmann fields. The hybridization term $\Delta_{ab}^{\sigma\sigma'}(\tau - \tau')$ (resp. interaction terms $\mathcal{U}_{ab}(\tau - \tau')$ and $\mathcal{J}_a^\xi(\tau - \tau')$) of Eq. (11.3) may be seen as the result of the integration of a bath of uncorrelated fermionic levels hybridized to the correlated level (resp. a bath of uncorrelated bosonic levels coupled to the density and spin of the correlated level). This is shown in greater detail in appendix M.2. Note that $\mathcal{U}(\tau) = \mathcal{U}(-\tau)$ and $\mathcal{J}(\tau) = \mathcal{J}(-\tau)$ ³.

Using the spin raising and lowering operators $s_a^+ \equiv s_a^x + i s_a^y = \bar{c}_{a\uparrow} c_{a\downarrow}$ and $s_a^- \equiv s_a^x - i s_a^y = \bar{c}_{a\downarrow} c_{a\uparrow}$, the spin-spin interaction term is rewritten as:

$$\frac{1}{2} \sum_{\xi=x,y,z} s_a^\xi(\tau) \mathcal{J}_a^\xi(\tau - \tau') s_a^\xi(\tau') = \frac{1}{2} s_a^z(\tau) \mathcal{J}_a^z(\tau - \tau') s_a^z(\tau') + \frac{1}{2} \frac{\mathcal{J}_a^\perp(\tau - \tau')}{2} \{ s_a^+(\tau) s_a^-(\tau') + s_a^-(\tau) s_a^+(\tau') \}$$

with $\mathcal{J}_\perp \equiv \mathcal{J}_x = \mathcal{J}_y$. Let us decompose the action in three terms: $S = S_{\text{loc}} + S_{\text{hyb}} + S_\perp$ with

$$S_{\text{hyb}} \equiv \sum_{uv} \bar{c}_u \Delta_{uv} c_v \quad (11.4a)$$

$$S_{\text{loc}} \equiv \sum_u \{ \bar{c}_u (\partial_\tau + \varepsilon_u) c_u \} + \frac{1}{2} \sum_{uv} \mathcal{U}_{uv} n_u n_v \quad (11.4b)$$

$$S_\perp \equiv \frac{1}{2} \sum_{\alpha\beta} \mathcal{J}_{\alpha\beta}^\perp s_\alpha^+ s_\beta^- \quad (11.4c)$$

I have adopted a compact notation, $u \equiv (a, \sigma, \tau)$ and $\alpha \equiv (a, \tau)$. In particular, $\sum_u \equiv \sum_a \sum_\sigma \int_0^\beta d\tau$. The S_\perp term has been manipulated in the following way: due to the symmetry properties of \mathcal{J} and commutativity of s^+ and s^- (this is a Grassmann integral):

$$S_\perp^a = \frac{1}{2} \iint_0^\beta d\tau d\tau' \left[\frac{\mathcal{J}_a^\perp(\tau - \tau')}{2} s_a^+(\tau) s_a^-(\tau') + \frac{\mathcal{J}_a^\perp(\tau' - \tau)}{2} s_a^+(\tau) s_a^-(\tau') \right] = \frac{1}{2} \iint_0^\beta d\tau d\tau' \mathcal{J}_a^\perp(\tau - \tau') s_a^+(\tau) s_a^-(\tau')$$

In S_{hyb} , $\Delta_{uv} = \Delta_{ab}^{\sigma\sigma'}(\tau - \tau')$, while in S_\perp , $\mathcal{J}_{\alpha\beta}^\perp = \mathcal{J}_a^\perp(\tau - \tau') \delta_{ab}$. The \mathcal{J}_a^z term has been absorbed in the \mathcal{U}_{uv} term:

$$\mathcal{U}_{uv} \equiv \mathcal{U}_{ab}(\tau - \tau') + (-)^{\sigma\sigma'} \frac{1}{4} \mathcal{J}_a^z(\tau) \delta_{ab}$$

In the following, I shall successively expand the partition function Z of this model in powers of S_{hyb} and S_\perp , and show how to sample the terms of this expansion by a Monte-Carlo procedure.

¹The Fourier transform $\mathcal{U}(i\nu)$ of $\mathcal{U}(\tau)$ generally has a nonzero high-frequency limit U corresponding to static Hubbard interactions

²Hence: $s^x = \frac{1}{2} (\bar{c}_\uparrow c_\downarrow + \bar{c}_\downarrow c_\uparrow)$, $s^y = \frac{i}{2} (-\bar{c}_\uparrow c_\downarrow + \bar{c}_\downarrow c_\uparrow)$, $s^z = \frac{1}{2} (n_\uparrow - n_\downarrow)$. Note the factor of two compared to the definitions I have used in the previous parts.

³This comes from the fact that the interactions are between *real* fields

11.1.2 Hybridization and \mathcal{J}^\perp expansion

The partition function Z is defined as:

$$Z \equiv \int \mathcal{D} [\bar{c}_u c_u] e^{-S_{\text{loc}} - S_{\text{hyb}} - S_\perp} \quad (11.5)$$

Expanding it in powers of S_{hyb} and S_\perp yields:

$$Z = Z_{\text{loc}} \sum_{nk} \frac{(-)^{n+k}}{n!k!} \sum_{\substack{u_1 \dots u_n \\ v_1 \dots v_n}} \Delta_{u_1 v_1} \dots \Delta_{u_n v_n} \sum_{\substack{\alpha_1 \dots \alpha_k \\ \beta_1 \dots \beta_k}} \frac{\mathcal{J}_{\alpha_1 \beta_1}^\perp}{2} \dots \frac{\mathcal{J}_{\alpha_k \beta_k}^\perp}{2} \langle \bar{c}_{u_1} c_{v_1} \dots \bar{c}_{u_n} c_{v_n} s_{\alpha_1}^+ s_{\beta_1}^- \dots s_{\alpha_k}^+ s_{\beta_k}^- \rangle_{\text{loc}}$$

with $\langle \dots \rangle_{\text{loc}} = \frac{1}{Z_{\text{loc}}} \int \mathcal{D} [\bar{c}_u c_u] e^{-S_{\text{loc}}} [\dots]$. Noticing that the sums are invariant by reshuffling the dummy indices with permutations p and q yields:

$$Z = Z_{\text{loc}} \sum_{nk} \frac{(-)^{n+k}}{(n!)^2 (k!)^2} \sum_{\substack{u_1 \dots u_n \\ v_1 \dots v_n}} \sum_{p \in \mathfrak{S}_n} \Delta_{p(u_1) v_1} \dots \Delta_{p(u_n) v_n} \\ \sum_{\substack{\alpha_1 \dots \alpha_k \\ \beta_1 \dots \beta_k}} \sum_{q \in \mathfrak{S}_k} \frac{\mathcal{J}_{q(\alpha_1) \beta_1}^\perp}{2} \dots \frac{\mathcal{J}_{q(\alpha_k) \beta_k}^\perp}{2} \langle \bar{c}_{p(u_1)} c_{v_1} \dots \bar{c}_{p(u_n)} c_{v_n} s_{q(\alpha_1)}^+ s_{\beta_1}^- \dots s_{q(\alpha_k)}^+ s_{\beta_k}^- \rangle_{\text{loc}}$$

Using the anticommutation (commutation) properties of the \bar{c} , c (s^+ , s^-) operators, the signature of the permutation appears, and identifying the determinant of Δ via Leibniz's formula yields:

$$Z = Z_{\text{loc}} \sum_{nk} \frac{(-)^{n+k}}{(n!)^2 (k!)^2} \sum_{\substack{u_1 \dots u_n \\ v_1 \dots v_n}} \sum_{\substack{\alpha_1 \dots \alpha_k \\ \beta_1 \dots \beta_k}} \sum_{q \in \mathfrak{S}_k} \det \Delta \prod_{i=1}^k \frac{\mathcal{J}_{q(\alpha_i) \beta_i}^\perp}{2} \langle \bar{c}_{u_1} c_{v_1} \dots \bar{c}_{u_n} c_{v_n} s_{\alpha_1}^+ s_{\beta_1}^- \dots s_{\alpha_k}^+ s_{\beta_k}^- \rangle_{\text{loc}}$$

with $\det \Delta = \sum_{p \in \mathfrak{S}_n} \text{sign}(p) \Delta_{p(u_1) v_1} \dots \Delta_{p(u_n) v_n}$. One could as well identify the permanent of $\mathcal{J}_{\alpha\beta}^\perp$, but there is no fast update formula for the permanent, contrary to the determinant (see section 11.1.6.1). I now fix the (lexicographical) ordering the labels and permute the \bar{c} , c operators to cancel the $(-)^n$ factor, while absorbing the $(-)^k$ factor in the \mathcal{J} product:

$$Z = Z_{\text{loc}} \sum_{nk} \sum_{\substack{u_1 > \dots > u_n \\ v_1 > \dots > v_n}} \sum_{\substack{\alpha_1 > \dots > \alpha_k \\ \beta_1 > \dots > \beta_k}} \sum_{q \in \mathfrak{S}_k} \left\{ \det \Delta \prod_{i=1}^k \left[-\frac{\mathcal{J}_{q(\alpha_i) \beta_i}^\perp}{2} \right] \langle c_{v_1} \bar{c}_{u_1} \dots c_{v_n} \bar{c}_{u_n} s_{\alpha_1}^+ s_{\beta_1}^- \dots s_{\alpha_k}^+ s_{\beta_k}^- \rangle_{\text{loc}} \right\}$$

Finally, I expand the trace factor: $\langle \dots \rangle = Z_{\text{loc}}^{-1} \sum_{\psi} \langle \psi | e^{-S_{\text{loc}}} \dots | \psi \rangle$ (where the states $|\psi\rangle$ form a basis of S_{loc}), and get:

$$Z = \sum_n \sum_{\substack{u_1 > \dots > u_n \\ v_1 > \dots > v_n}} \sum_{\substack{\alpha_1 > \dots > \alpha_k \\ \beta_1 > \dots > \beta_k}} \sum_{q \in \mathfrak{S}_k} \sum_{\psi} \left\{ \det \Delta \prod_{i=1}^k \left[-\mathcal{J}_{q(\alpha_i) \beta_i}^\perp \right] \langle \psi | e^{-S_{\text{loc}}} c_{v_1} \bar{c}_{u_1} \dots c_{v_n} \bar{c}_{u_n} s_{\alpha_1}^+ s_{\beta_1}^- \dots s_{\alpha_k}^+ s_{\beta_k}^- | \psi \rangle_{\text{loc}} \right\}$$

This multidimensional sum can be rewritten in a compact form:

$$Z = \sum_{C \in \Omega} w_C \quad (11.6)$$

where C denotes a “configuration”

$$C \equiv \{\mathbf{u}, \mathbf{v}, \boldsymbol{\alpha}, \boldsymbol{\beta}, q, \psi\} \quad (11.7)$$

of the whole phase space Ω (with $\mathbf{u} \equiv (u_1, \dots, u_n)$ and so forth; q is a permutation of order k), and w_C its weight:

$$w_C \equiv \det \Delta \prod_{i=1}^k \left[-\frac{\mathcal{J}_{q(\alpha_i)\beta_i}^\perp}{2} \right] w_{\text{loc}} \quad (11.8)$$

I have singled out a “local” factor:

$$w_{\text{loc}} \equiv \langle \psi | e^{-S_{\text{loc}}} c_{v_1} \bar{c}_{u_1} \dots c_{v_n} \bar{c}_{u_n} s_{\alpha_1}^+ s_{\beta_1}^- \dots s_{\alpha_k}^+ s_{\beta_k}^- | \psi \rangle \quad (11.9)$$

The configurations could have been defined otherwise. An important variant is the choice $\tilde{C} \equiv \{\mathbf{u}, \mathbf{v}, \boldsymbol{\alpha}, \boldsymbol{\beta}, q\}$ with the corresponding weight:

$$w_{\tilde{C}} \equiv Z_{\text{loc}} \det \Delta \prod_{i=1}^k \left[-\frac{\mathcal{J}_{q(\alpha_i)\beta_i}^\perp}{2} \right] \langle c_{v_1} \bar{c}_{u_1} \dots c_{v_n} \bar{c}_{u_n} s_{\alpha_1}^+ s_{\beta_1}^- \dots s_{\alpha_k}^+ s_{\beta_k}^- \rangle_{\text{loc}} \quad (11.10)$$

11.1.3 Metropolis-Hastings algorithm

11.1.3.1 Basic description

The multidimensional sum of Eq. (11.6) is computed by stochastic sampling. Stochastic sampling of a random variable C of (normalized and positive) probability distribution $w(C)$ in a universe Ω consists in constructing a transition matrix $p(C \rightarrow C')$ in Ω that satisfies *detailed balance*:

$$w(C_i)p(C_i \rightarrow C_f) = w(C_f)p(C_f \rightarrow C_i) \quad (11.11)$$

and *ergodicity*, namely the probability to transition from any given element C to any other element C' in a finite time is 1. Under these two conditions, the phase (or space) average of any observable $O(C)$ is equal to the time average of the configurations generated by this transition matrix:

$$\langle O \rangle \equiv \frac{\int_{C \in \Omega} \mathcal{D}[C] O(C) w(C)}{\int_{C \in \Omega} \mathcal{D}[C] w(C)} = \lim_{N \rightarrow \infty} \frac{1}{N} \sum_{i=0}^N O(C_i) \quad (11.12)$$

N denotes the number of sampled configurations. Stochastic sampling comes at a double price: the probability distribution $w(C)$ may be hard to compute explicitly, and one may not be able to store or even write down the full transition matrix explicitly.

The Metropolis-Hastings algorithm (Metropolis *et al.* (1953); Hastings (1970)) provides a *sufficient condition* for achieving detailed balance and ergodicity provided one can compute the *ratio* of the weights. It consists in decomposing the transition probability into two parts:

$$p(C_i \rightarrow C_f) = p_{\text{prop}}(C_i \rightarrow C_f) \cdot p_{\text{acc}}(C_i \rightarrow C_f) \quad (11.13)$$

and following the procedure:

- from an initial configuration C_i , propose to transition to a final configuration C_f ; this update happens with *proposal probability* $p_{\text{prop}}(C_i \rightarrow C_f)$;
- draw a random number u between 0 and 1 and accept the proposed transition if $p_{\text{acc}}(C_i \rightarrow C_f) > u$, where the *acceptance probability* p_{acc} is defined as

$$p_{\text{acc}}(C_i \rightarrow C_f) \equiv \min \left(1, \frac{p_{\text{prop}}(C_f \rightarrow C_i) w(C_f)}{p_{\text{prop}}(C_i \rightarrow C_f) w(C_i)} \right) \quad (11.14)$$

One can check that the transition matrix defined by Eqs. (11.13) and (11.14) satisfies detailed balance (11.11). Most importantly, only the ratio $w(C_f)/w(C_i)$ is needed to compute the so-called Metropolis ratio:

$$R(C_i \rightarrow C_f) \equiv \frac{p_{\text{prop}}(C_f \rightarrow C_i)w(C_f)}{p_{\text{prop}}(C_i \rightarrow C_f)w(C_i)} \quad (11.15)$$

A pedagogical introduction to Monte-Carlo algorithms can be found in Krauth (1996). An illustration of the algorithm is shown in Fig. 11.1.3 in the previous chapter.

11.1.3.2 The Monte-Carlo fermionic sign problem

In practice, the weight of a configuration, $w(C)$, is not necessarily positive. To implement a Metropolis algorithm, one has to use $|w(C)|$ instead and compensate this modification by computing observables as follows:

$$\langle O \rangle_{\text{MC}} \equiv \frac{\int_{C \in \Omega} \mathcal{D}[C] O(C) w(C)}{\int_{C \in \Omega} \mathcal{D}[C] w(C)} = \frac{\int_{C \in \Omega} \mathcal{D}[C] O(C) |w(C)| \text{sign}(C)}{\int_{C \in \Omega} \mathcal{D}[C] |w(C)| \text{sign}(C)} \approx \frac{\langle O \text{sign} \rangle_{\text{MC}}}{\langle \text{sign} \rangle_{\text{MC}}} \quad (11.16)$$

where I have defined:

$$\langle O \rangle_{\text{MC}} \equiv \frac{1}{N} \sum_{i=0}^N O(C_i) \quad (11.17)$$

From (11.16), one can see that if $\langle \text{sign} \rangle \approx 0$, the computation of $\langle O \rangle$ can become highly inaccurate. The sign problem becomes worse for low-temperatures, since it is given by

$$\langle \text{sign} \rangle = e^{-\beta(F-F_b)}$$

where F is the free-energy ($F = -T \log Z$) associated with the model and F_b the free energy associated with the same model with bosons instead of fermions (Gull *et al.* (2011)).

In the case of density-density interactions (static and dynamical), if $[H_{\text{loc}}, n_{a\sigma}] = 0$, the sign of a configuration can be proven to be always 1 by mapping the impurity action onto a Hamiltonian problem describing the coupling of one impurity site with a *one-dimensional* chain of uncorrelated bath sites (Yoo *et al.* (2005)). In the presence of retarded spin-spin interactions, if $\mathcal{J}_{\perp}(\tau) < 0$ (“ferromagnetic” dynamical interactions), the sign is also always 1. In the reverse case ($\mathcal{J}_{\perp}(\tau) > 0$), a sign problem arises. Thus, in most cases, the hybridization expansion solver in the “segment picture” (see next section) is free of the sign problem.

In the case when $\langle \text{sign} \rangle \neq 1$, the fact that $\langle O \rangle_{\text{MC}}$ is expressed as a ratio of expectation values must not be overlooked when computing the estimate of the error bar on $\langle O \rangle$. For this, a special treatment by *e.g.* the jackknife method (presented above, see section 10.3) must be implemented.

11.1.4 Segment picture: local trace factor

Before showing how to compute correlators associated with action (11.3) using the Metropolis-Hastings algorithm, let us examine the properties of the local trace factor defined in Eq. (11.9).

11.1.4.1 Static case

In the absence of dynamical interactions the local trace factor reads (remember that $u \equiv (a, \sigma, \tau)$ and $\alpha \equiv (\tilde{a}, t)$):

$$\begin{aligned} w_{\text{loc}} &\equiv \langle \psi | T e^{-\beta H_{\text{loc}}} c_{v_1} c_{u_1}^{\dagger} \dots c_{v_n} c_{u_n}^{\dagger} s_{\alpha_1}^+ s_{\beta_1}^- \dots s_{\alpha_k}^+ s_{\beta_k}^- | \psi \rangle \\ &= \langle \psi | T e^{-\beta H_{\text{loc}}} c_{b_1 \sigma'_1}(\tau'_1) c_{a_1 \sigma_1}^{\dagger}(\tau_1) \dots c_{b_n \sigma'_n}(\tau'_n) c_{a_n \sigma_n}^{\dagger}(\tau_n) s_{\alpha_1}^+(t_1) s_{\beta_1}^-(t'_1) \dots s_{\alpha_k}^+(t_k) s_{\beta_k}^-(t'_k) | \psi \rangle \end{aligned}$$

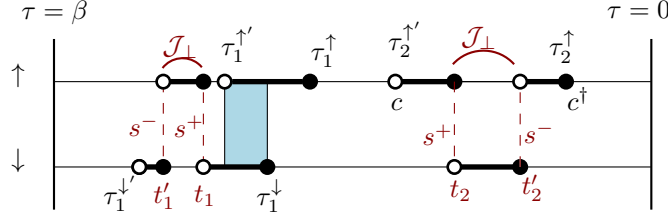


Figure 11.1: Segment picture in the case of retarded spin-spin interactions

with $H_{\text{loc}} = \sum_{a\sigma} \varepsilon_{a\sigma} c_{a\sigma}^\dagger c_{a\sigma} + \frac{1}{2} \sum_{a\sigma, b\sigma'} U_{a\sigma, b\sigma'} n_{a\sigma} n_{b\sigma'}$ and ψ is a basis state for H_{loc} (I switched back to second-quantized operators here).

In the absence of any special property, computing this expectation value involves (costly) matrix multiplications. Here, since $[H_{\text{loc}}, n_{a\sigma}] = 0$, the exponential factors coming from the Heisenberg representation of the operators ($c_{a\sigma}(\tau) = e^{\tau H_{\text{loc}}} c_{a\sigma} e^{-\tau H_{\text{loc}}}$) merely keep track of the imaginary-time history between $\tau = 0$ (right of the trace) and $\tau = \beta$ (left) with Boltzmann factors. In particular, they do not change the states. Thus, the configuration C can be represented in terms of imaginary-time “segments”: a segment in imaginary time on line $(a\sigma)$ represents time intervals when the orbital a, σ is occupied. This is illustrated in Fig. 11.1 for the case of a single orbital. Hence the name given to this specific flavor of the algorithm: the “segment picture”.

To perform the computation of the weight, one must first time-order all operators (they are so far sorted in lexicographical order). This permutation p_T generates a sign s_T . This being done, the local trace factor evaluates to:

$$w_{\text{loc}}^{\text{static}} = e^{-\sum_{ij, i \neq j} U_{ij} O_{ij} + \sum_i \mu_i l_i} s_T \langle \psi | \prod_i A_i | \psi \rangle \quad (11.18)$$

where O_{ij} is the overlap between line $i \equiv (a\sigma)$ and $j \equiv (b\sigma')$ and l_i the portion of line i which is occupied; A_i denotes any operator (c_i^\dagger, c_i, s_a^+ or s_a^-); the operators are now all time-ordered. I will now call each line i a “color”. Henceforth, $\mu_i = -\varepsilon_i$.

The last factor in Eq. (11.18), $\langle \psi | \prod_i A_i | \psi \rangle$, only contributes a sign to the weight. To determine this sign, let us regroup the operators by color starting from the time-ordered configuration. This permutation p_{regroup} generates a sign s_{regroup} :

$$w_{\text{loc}}^{\text{static}} = \underbrace{s_T s_{\text{regroup}}}_{s_{\text{config}}} e^{-\sum_{ij, i \neq j} U_{ij} O_{ij} + \sum_i \mu_i l_i} \underbrace{\langle \psi | \psi \rangle}_1 \quad (11.19)$$

The product $p_T p_{\text{regroup}}$ is itself a permutation turning a product of pairs cc^\dagger grouped by color ($\equiv a, \sigma$) to a product of pairs cc^\dagger or $c^\dagger c$ also grouped by color, as illustrated in Fig. 11.2. Hence, the sign of this permutation, s_{config} , is -1 if the number of “hybridized” antisegments is odd. By “hybridized”, I mean the operators stemming from the expansion of the hybridization term (as opposed to those in the spin term, which do not contribute to the sign). An antisegment is a segment “starting” with a creation operator (which I will loosely call a ‘dagger’), namely its left point is a dagger.

In the density-density case (and in the density-density case only⁴), due to the compulsory alternation of c and c^\dagger , the sign is -1 if the number of lines starting with a creation operator and containing an odd number of segments is odd.

The computation of $w_{\text{loc}}^{\text{static}}$ is of order $O(N^2)$, where N is the number of operators/segments. In the Metropolis-Hastings algorithm, only the ratio of two such weights is needed; this ratio is computed with complexity $O(N)$.

⁴In particular, this does not apply to when there are some composite operators

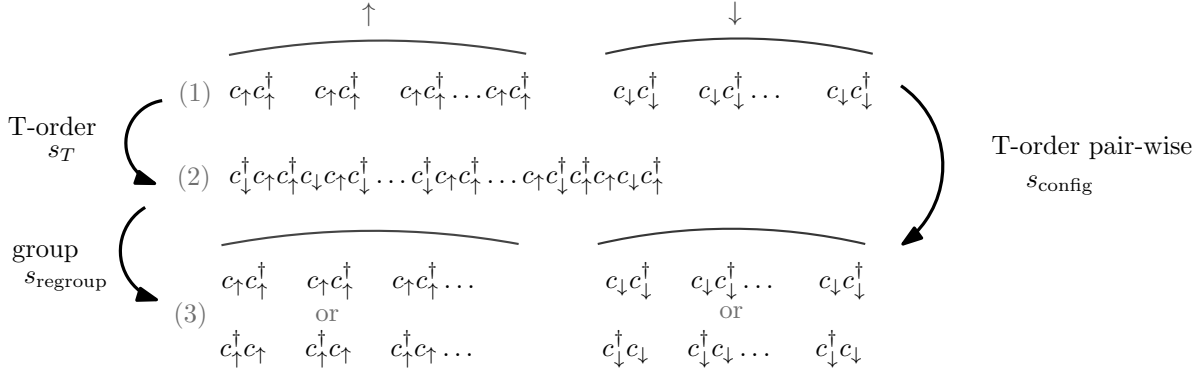


Figure 11.2: Operator permutations to compute the sign of a configuration

11.1.4.2 Dynamical interactions

11.1.4.2.1 Computation of the trace factor In the case of dynamical interactions, $S_{\text{loc}} = S_{\text{loc}}^{\text{static}} + \frac{1}{2} \iint_{\tau\tau'} \sum_{ij} \mathcal{D}_{ij}(\tau - \tau') n_i(\tau) n_j(\tau')$ where \mathcal{D}_{ij} is the retarded part of the interactions. It is a β -periodic function, and symmetric around $\beta/2$. One has to compute the following additional weight: $w_{\text{dyn}} = \exp \left[-\frac{1}{2} \sum_{ij} \iint_0^{\beta} d\tau d\tau' n_i(\tau) \mathcal{D}_{ij}(\tau - \tau') n_j(\tau') \right]$. In the segment picture, the density on a line $i(\equiv a\sigma)$ is a piecewise constant function:

$$n_i(\tau) = \sum_{k_i} \left[\theta(\tau - \tau_{k_i}) - \theta(\tau - \tau'_{k_i}) \right] \quad (11.20)$$

so that $\ln w_{\text{dyn}} = -\frac{1}{2} \sum_{ij} \sum_{k_i k_j} \int_{\tau_{k_i}}^{\tau'_{k_i}} d\tau \int_{\tau_{k_j}}^{\tau'_{k_j}} d\tau' \mathcal{D}_{ij}(\tau - \tau')$. This integral can be evaluated in terms of the “dynamical kernel” $K_{ij}(\tau)$, defined as:

$$K_{ij}''(\tau) \equiv \mathcal{D}_{ij}(\tau) \quad (11.21a)$$

$$K_{ij}(\tau = 0^+) = K_{ij}(\beta^-) = 0$$

After a few simple but tedious steps (detailed in appendix M.1), Eq. (11.19) is found to become, in the presence of dynamical interactions:

$$w_{\text{loc}}^{\text{dyn}}(\tilde{U}_{ij}, \tilde{\mu}_i) = w_{\text{loc}}^{\text{static}}(\tilde{U}_{ij}, \tilde{\mu}_i) \cdot \exp \left\{ \sum_{(\alpha, \beta)}^{\text{op. pairs}} s_{\alpha} s_{\beta} K_{i(\alpha)j(\beta)}(\tilde{\tau}_{\alpha} - \tilde{\tau}_{\beta}) \right\} \quad (11.22)$$

with $s_{\alpha} = 1$ for creation operators and -1 otherwise. The dynamical interactions renormalize the value of the static interactions as:

$$\tilde{U}_{ij} \equiv U_{ij} - 2K'_{ij}(0) \quad (11.23a)$$

$$\tilde{\mu}_i \equiv \mu_i + K'_{ii}(0) \quad (11.23b)$$

The additional exponential factor has a complexity $O(N^2)$, where N is the number of operators. Therefore, the ratio of two such factors (needed for evaluating the Metropolis ratio (Eq. (11.15))), evaluates as $O(N)$. This is of the same order as the calculation of the static trace factor, which is itself much faster than the computation of the updated (inverse) hybridization matrix, which is of order $O(N^2)$.

11.1.4.2.2 Physical interpretation: polaron effect The renormalization of the static interaction and chemical potential comes as no surprise: when fermions are coupled to bosonic modes, the position of the

fermionic level as well as the effective interaction between electrons is renormalized. One observes this when integrating out the bosonic modes *e.g.* in the Fröhlich model (section I.6 in the appendix): the effective fermion-fermion interaction becomes $U + \lambda^2 D_0(\mathbf{q}, \omega) = U + \frac{2\lambda^2 \omega_{\mathbf{q}}}{\omega^2 - \omega_{\mathbf{q}}^2}$ (D_0 is the bare bosonic propagator). In particular, the effective low-energy interaction value is reduced by the coupling to bosons: $U(\omega = 0) = U - \frac{2\lambda^2}{\omega_{\mathbf{q}}}$. Another common way of understanding this is by performing a unitary transformation on the electron-boson Hamiltonian to get rid of the electron-boson coupling at the cost of renormalizing some parameters as well as redefining the operators. I illustrate this in the context of the Hubbard-Holstein model with a single fermionic level. The Holstein model (Holstein (1959)) is the simplification of the Fröhlich model (Eq. (I.38)) to a single phonon. Thus, the Hubbard-Holstein model reads:

$$H_{\text{HH}} = \sum_{\sigma} \varepsilon c_{\sigma}^{\dagger} c_{\sigma} + U n_{\uparrow} n_{\downarrow} - \mu n + \omega_0 b^{\dagger} b + \lambda n (b + b^{\dagger}) \quad (11.24)$$

where b^{\dagger} and b respectively create and annihilate bosons (these fields are related to the ϕ field of the previous sections by $\phi = b + b^{\dagger}$). It describes the physics of polarons (see *e.g.* Ciuchi *et al.* (1997) for a discussion of this problem in relation with DMFT). The last term in H_{HH} makes the problem difficult to solve. One would like to get rid of it by “rotating” the Hamiltonian. This is done via a unitary transformation, namely one defines a new Hamiltonian \tilde{H}_{HH} as:

$$\tilde{H}_{\text{HH}} = e^S H_{\text{HH}} e^{-S} = H_{\text{HH}} + [S, H_{\text{HH}}] + \frac{1}{2!} [S, [S, H_{\text{HH}}]] + \dots$$

where S is an antihermitian operator ($S^{\dagger} = -S$) to keep \tilde{H}_{HH} hermitian. Such transformations are widely used; a prominent example is the Schrieffer-Wolff transformation (Schrieffer and Wolff (1966)) which was introduced to reduce the Anderson model (Eq. (11.1)) to the Kondo Hamiltonian. Here, one is looking for a S such that $[S, H_{\text{HH}}]$ cancels the coupling term $\lambda n (b + b^{\dagger})$. One can check⁵ that

$$S \equiv \frac{\lambda}{\omega_0} (b^{\dagger} - b) n$$

fulfills this condition. This transformation has first been introduced by Lang and Firsov (1968). Under this transformation, a few algebraic steps lead to

$$\tilde{H}_{\text{HH}} = \sum_{\sigma} \varepsilon \tilde{c}_{\sigma}^{\dagger} \tilde{c}_{\sigma} + \tilde{U} \tilde{n}_{\uparrow} \tilde{n}_{\downarrow} - \tilde{\mu} \tilde{n} + \omega_0 b^{\dagger} b + O(\lambda^2) \quad (11.25)$$

where the renormalized parameters read: $\tilde{U} = U - \frac{2\lambda^2}{\omega_0}$ and $\tilde{\mu} = \mu + \frac{\lambda^2}{\omega_0}$. The renormalized operators are $\tilde{c}_{\sigma} \equiv e^{-\frac{\lambda}{\omega_0} (b^{\dagger} - b)} c_{\sigma}$. They annihilate and create a new type of quasiparticles, (Holstein) polarons which can be interpreted as electrons surrounded by a phononic cloud. These polarons interact with a reduced interaction compared to the original electrons.

This physics is exactly included in the Monte-Carlo weight Eq. (11.22) and the corresponding renormalized values (11.23a-11.23b). Indeed, retarded interactions of the Holstein form $(\lambda^2 D_0(i\Omega) = \frac{2\lambda^2 \omega_0}{(i\Omega)^2 - \omega_0^2})$ lead to a dynamical kernel:

$$K(\tau) = - \left(\frac{\lambda}{\omega_0} \right)^2 \frac{\cosh \left(\left(\frac{\beta}{2} - \tau \right) \omega_0 \right) - \cosh \left(\frac{\beta \omega_0}{2} \right)}{\sinh \left(\frac{\beta \omega_0}{2} \right)} \quad (11.26)$$

Another effect of dynamical interactions is to renormalize the bandwidth of the original fermions, as shown in Casula *et al.* (2012). This can be seen by projecting the problem on the space of zero bosonic modes (using

⁵Indeed, $[S, H_{\text{HH}}] = \frac{\lambda}{\omega_0} [(b^{\dagger} - b) n, \omega_0 b^{\dagger} b + \lambda n (b + b^{\dagger})] = \lambda n [(b^{\dagger} - b), b^{\dagger} b] + O(\lambda^2) = -\lambda n (b^{\dagger} + b) + O(\lambda^2)$

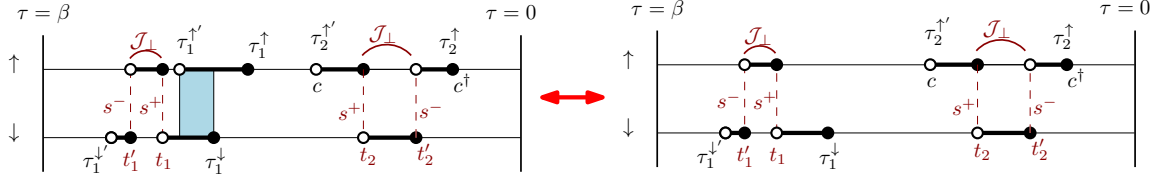


Figure 11.3: Monte-Carlo update: segment addition and removal. Empty (filled) circles denote annihilation (creation) operators. Each horizontal line represents the imaginary-time evolution for a given spin. The blue region emphasizes an overlap in occupation of the up and down line. The red dashed lines show the position of spin operators (made up of two fermionic operators).

Baker-Campbell-Hausdorff's formula):

$$\langle 0 | e^{-\frac{\lambda}{\omega_0}(b^\dagger - b)} | 0 \rangle_b = \langle 0 | e^{-\frac{\lambda}{\omega_0} b^\dagger} \underbrace{\mathbf{1}}_{\sum_{n=0}^{\infty} |n\rangle_b \langle n|_b} e^{-\frac{\lambda}{\omega_0} b} \underbrace{\mathbf{1}}_{\sum_{n=0}^{\infty} |n\rangle_b \langle n|_b} e^{-\frac{\lambda^2}{2\omega_0^2}} | 0 \rangle_b = e^{-\frac{\lambda^2}{2\omega_0^2}}$$

Then, $-\langle T \tilde{c}_\tau \tilde{c}_0^\dagger \rangle_{n_b=0} = Z_B [-\langle T c_\tau c_0^\dagger \rangle_{n_b=0}]$ with

$$Z_B = e^{-\frac{\lambda^2}{\omega_0^2}} \quad (11.27)$$

Thus, the coupling to bosonic modes, within this approximation, reduces the bandwidth by a factor Z_B .

11.1.5 Monte-Carlo updates

As shown in section 11.1.3, the Metropolis-Hastings algorithm consists in sampling the phase space Ω by going from one configuration to the other. From a given configuration, the choice of the next configuration (or how to “update” the current configuration) is totally free, as long as the set of all updates guarantees ergodicity, and that the proposal probability associated with this update is computed correctly.

In our case, a configuration is given by a set of imaginary times located on various “lines” (and also of a permutation of the \mathcal{J}^\perp lines, q , and of the edge state ψ). The basic moves consist in adding or removing times (be they associated with c^\dagger - c or s^+ - s^- segments), changing the permutation, changing the edge state (in the case it is not already defined by the operators on the lines, namely when a line has no operators). An illustration of such a move is shown in Fig. 11.3: from the left to the right configuration, a segment $[\tau_1^{\downarrow}, \tau_1^{\uparrow}]$ is removed.

Each update (or “move” in phase space) is characterized by a Metropolis ratio (Eq. (11.15)). A detailed description of each move along with the corresponding Metropolis ratio will be given in the implementation notes, section 11.2.

11.1.6 Determinant

11.1.6.1 Fast updates

The determinant term $\det \Delta$ appearing in the weight of a configuration, Eq. (11.8), in principle requires a $O(N^3)$ computation (with N : number of segments). However, a critical speedup follows from the form of $\Delta(C_n)$ and $\Delta(C_{n+1})$, where C_n and C_{n+1} are two successive configurations for “local moves”, *i.e.* moves that do not imply “too large” changes of a given configuration.

For instance, if the Metropolis update consists in adding or removing imaginary-time segments $[u, v]$ (as pictured in Fig. 11.3), then the matrices $\Delta(C_n)$ and $\Delta(C_{n+1})$ differ only by one column and one line. In this case, the so-called Sherman-Morrison formulae allow to compute $\Delta(C_{n+1})$ from $\Delta(C_n)$ in $O(N^2)$ time. Likewise, computing the ratio of the determinants is a $O(N^2)$ operation. More details (including the formulae) can

be found for instance in Bieder (2013). A dedicated library for the manipulation of such determinants is included in TRIQS.

This crucial simplification explains the success of continuous-time Quantum Monte-Carlo algorithms. As mentioned before, there is no equivalent of the Sherman-Morrison formulae in the bosonic case, *i.e.* to compute the *permanent* of a matrix in an efficient way.

11.1.6.2 Diagonal vs. off-diagonal Δ

The determinant manipulation can be simplified if the hybridization matrix has a block structure, *e.g.*

$$\Delta_{ab}^{\sigma\sigma'}(\tau) = \begin{pmatrix} \underline{\Delta}_1(\tau) & 0 & 0 \\ 0 & \ddots & 0 \\ 0 & 0 & \underline{\Delta}_m(\tau) \end{pmatrix} \quad (11.28)$$

The most common simplification is the simplification in spin space ($m = \sigma$). If there is no offdiagonal hybridization in orbital space, then $m = (a, \sigma)$, *i.e.* there is one determinant per line or “color”. In either case,

$$\det\Delta = \prod_{i=1}^m \det \underline{\Delta}^i \quad (11.29)$$

with much smaller matrix sizes and thence much faster computations.

11.1.7 Measurements

In this section, I briefly show how various expectation values can be computed in the CTQMC algorithm.

11.1.7.1 One-particle Green’s function G

11.1.7.1.1 Time measurement From the functional-derivative form (11.2) of the Green’s function, and making use of Eq (11.6), one sees that $G_{uv} = \frac{1}{Z} \sum_C \frac{\delta w_C}{\delta \Delta_{vu}}$. The derivative is computed using $\frac{\delta w_C}{\delta \Delta_{vu}} = \frac{\delta \det \Delta}{\delta \Delta_{vu}} w_{\text{loc}}(C)$ and then, exponentiating the determinant:

$$\frac{\delta \det \Delta}{\delta \Delta_{vu}} = \frac{\delta}{\delta \Delta_{vu}} \int \mathcal{D} [\xi^* \xi] e^{-\xi_k^* \Delta_{kl} \xi_l} = \int \mathcal{D} [\xi^* \xi] \sum_{kl} \delta_{vk} \delta_{ul} \xi_k^* \xi_l e^{-\xi_k^* \Delta_{kl} \xi_l} = \det \Delta \sum_{kl} \delta_{vk} \delta_{ul} M_{kl} \quad (11.30)$$

where $\mathbf{M} \equiv \Delta^{-1}$. Finally, using the definition of the Monte-Carlo average (Eq. (11.17)):

$$\begin{aligned} G_{uv} &= \frac{1}{Z} \sum_C \det \Delta(C) \sum_{kl} \delta_{vk} \delta_{ul} M_{kl}(C) w_{\text{loc}}(C) = \frac{1}{Z} \sum_C \sum_{kl} \delta_{vk} \delta_{ul} M_{kl}(C) w(C) \\ &= \left\langle \sum_{kl} \delta_{vk} \delta_{ul} M_{kl} \right\rangle_{\text{MC}} \end{aligned} \quad (11.31)$$

Using (11.12), G is more explicitly expressed as ($i = (a\sigma)$):

$$G_{ij}(\tau) = \left\langle \sum_{k,l} \delta \left[\tau; \tau_k^j - (\tau')_l^i \right] M_{ji}(\tau_k, \tau_l) \right\rangle_{\text{MC}} \quad (11.32)$$

In practice, this measurement is done with the pseudo-code (if $\tau_i > \tau_j$ and for one single color $a\sigma$):

```

for i in annihilation_ops:
    for j in creation_ops:
        G(tau_i - tau_j) += sign * M_ij/beta
    
```

The complexity of the measurement is thus $O(N^2)$ where N is the perturbation order in Δ or number of segments. This measurement is implemented in a class **measure_gt**.

11.1.7.1.2 Frequency measurement One can also measure the Fourier transform of $G_{ij}(\tau)$, $G_{ij}(i\omega) = \int_{\tau} e^{i\tau\omega} G_{ij}(\tau) = \left\langle \sum_{k,l} e^{i\omega(\tau_k^j - (\tau')^i)} M_{ji}(\tau_k, \tau_l) \right\rangle_{\text{MC}}$, i.e, defining the function:

$$M_{ij}(i\omega) \equiv \sum_{k,l} e^{i\omega(\tau_k^i - (\tau')^j)} M_{ij}(\tau_k, \tau_l) \quad (11.33)$$

one obtains:

$$G_{ij}(i\omega) = \left\langle M_{ji}(i\omega) \right\rangle_{\text{MC}} \quad (11.34)$$

In practice, this measurement is done following the pseudo-code (for one line $a\sigma$):

```

for i in annihilation_ops:
    for j in creation_ops:
        for w in freq_mesh:
            G(w) += sign * M_ij * exp((tau_i - tau_j)*w)
    
```

The complexity of the measurement is thus $N^2 n_w$ where N is the perturbation order in Δ and n_w the number of Matsubara frequencies. This measurement is implemented in a class **measure_gw**.

11.1.7.2 Density-density correlation function χ

The density-density correlation function is defined as $\chi_{a\sigma, b\sigma'}^{\text{nc}}(\tau) = \langle T n_{a\sigma}(\tau) n_{b\sigma'}(0) \rangle$ in the time domain, $\chi_{a\sigma, b\sigma'}^{\text{nc}}(i\Omega) = \langle T n_{a\sigma}(i\Omega) n_{b\sigma'}^*(i\Omega) \rangle$ in the frequency domain. The latter correlator is easy to evaluate in the segment picture, where the Fourier transform of $n(\tau)$ (itself a piecewise constant function, given by Eq. (11.20)), is:

$$n_i(i\Omega) = \int_0^\beta d\tau e^{i\Omega\tau} \sum_{k_i} [\theta(\tau - \tau_{k_i}) - \theta(\tau - \tau'_{k_i})] = \sum_{k_i} \int_{\tau_{k_i}}^{\tau'_{k_i}} e^{i\Omega\tau} = \sum_{k_i} \frac{e^{i\Omega\tau'_{k_i}} - e^{i\Omega\tau_{k_i}}}{i\Omega} \{1 - \delta_{i\Omega}\} + l_i \delta_{i\Omega} \quad (11.35)$$

Thus

$$\chi_{ij}^{\text{nc}}(i\Omega) = \left\langle n_i(i\Omega) n_j^*(i\Omega) \right\rangle_{\text{MC}} \quad (11.36)$$

More details can be found in Hafermann (2014). The measure is implemented in a class **measure_nnw**.

11.1.7.3 Three-point functions

The three-point function is defined as:

$$\tilde{\chi}_{ijk}^{\text{nc}}(i\omega, i\Omega) = \int_0^\beta d\tau \int_0^\beta d\tau' e^{i\omega\tau} e^{i\Omega\tau'} \langle T c_i(\tau) c_j^\dagger(0) n_k(\tau') \rangle = \int_0^\beta d\tau e^{i\omega\tau} \langle T c_i(\tau) c_j^\dagger(0) n_k(i\Omega) \rangle$$

where $\langle c_u c_v^\dagger n_k(i\Omega) \rangle = \frac{\delta \langle n_k(i\Omega) \rangle}{\delta \Delta_{vu}} = \frac{\delta}{\delta \Delta_{vu}} \sum_C \det \Delta n_k(i\Omega)(C) w_{\text{loc}}(C)$. Performing the same steps as for the Green's function (Eq. (11.30)), one obtains:

$$\langle c_u c_v^\dagger n_k(i\Omega) \rangle = \sum_C \det \Delta \sum_{ml} \delta_{vm} \delta_{ul} M_{ml} n_k(i\Omega)(C) w_{\text{loc}}(C) = \left\langle \sum_{ml} \delta_{vm} \delta_{ul} M_{ml} n_c(i\Omega) \right\rangle_{\text{MC}}$$

Or more explicitly: $\langle c_i(\tau) c_j^\dagger(0) n_k(i\Omega) \rangle = \left\langle \sum_{ml} \delta(\tau_m - \tau_j) \delta(\tau_l - \tau_i') M_{ij}(\tau_m, \tau_l') n_k(i\Omega) \right\rangle_{\text{MC}}$. Fourier transforming yields:

$$\boxed{\tilde{\chi}_{ijk}^{\text{nc}}(i\omega, i\Omega) = \left\langle M_{ij}(i\omega) n_k(i\Omega) \right\rangle_{\text{MC}}} \quad (11.37)$$

where $M_{ij}(i\omega)$ is defined in Eq. (11.33). More details can be found in Hafermann (2014). The measure of $n_k(i\Omega)$ is implemented in a class `precompute_nw`. The total measure is implemented in a class `measure_g2w`.

11.1.7.4 Improved estimator for Σ

Usually, the self-energy associated with the impurity action is computed using Dyson's equation, $\Sigma(i\omega) = \mathcal{G}^{-1}(i\omega) - G^{-1}(i\omega)$. Yet, the inversion of G required by this step and the subsequent cancellation of the terms linear in $i\omega$ leads to a blowing up of the high-frequency noise in Σ . This can lead to instabilities in the DMFT loop as the high-frequency asymptotic behavior or "tails" of Σ are important for *e.g.* the adjustment of the chemical potential.

An alternative to Dyson's equation is provided to by the equation of motion of $G(\tau)$, which leads to the result:

$$\Sigma(i\omega) = F(i\omega) G^{-1}(i\omega)$$

The general $F_{a\sigma, b\sigma'}(\tau)$ is given by Eq. (11.38) in appendix F.3.3). In the normal phase ($\sigma = \sigma'$), it becomes:

$$F_{a\sigma, b\sigma'}(\tau) = - \int_0^\beta d\bar{\tau} \sum_{I, cd} \mathcal{U}_{cd}^I(\tau - \bar{\tau}) \langle T c_{a\bar{\sigma}}(\tau) \sigma_{\bar{\sigma}}^I c_{b\sigma'}^\dagger(0) n_d^I(\bar{\tau}) \rangle \quad (11.38)$$

In the case without \mathcal{J}^\pm interactions, the sum runs on $I = 0, z$ with $\mathcal{U}_{ab}^0 = (\mathcal{U}_{a\uparrow b\uparrow} + \mathcal{U}_{a\uparrow b\downarrow})/2$ and $\mathcal{U}_{ab}^z = (\mathcal{U}_{a\uparrow b\uparrow} - \mathcal{U}_{a\uparrow b\downarrow})/2$, leading to

$$\begin{aligned} F_{a\sigma, b\sigma'}(\tau) &= - \sum_{cd} \int_{\bar{\tau}} \frac{\mathcal{U}_{c\uparrow d\uparrow} + \mathcal{U}_{c\uparrow d\downarrow}}{2} (\tau - \bar{\tau}) \langle T c_{a\sigma}(\tau) c_{b\sigma'}^\dagger(0) (n_{d\uparrow} + n_{d\downarrow})(\bar{\tau}) \rangle \\ &\quad - (\pm) \sum_{cd} \int_{\bar{\tau}} \frac{\mathcal{U}_{c\uparrow d\uparrow} - \mathcal{U}_{c\uparrow d\downarrow}}{2} \langle T c_{a\sigma}(\tau) c_{b\sigma'}^\dagger(0) (n_{d\uparrow} - n_{d\downarrow})(\bar{\tau}) \rangle \\ &= - \int_0^\beta d\bar{\tau} \sum_{cd, \bar{\sigma}} \mathcal{U}_{c\sigma, d\sigma'}(\tau - \bar{\tau}) \langle T c_{a\sigma}(\tau) c_{b\sigma'}^\dagger(0) n_{d\bar{\sigma}}(\bar{\tau}) \rangle \end{aligned}$$

Using the compound "line" index $i = (a, \sigma)$, this reads:

$$F_{ij}(\tau) = - \int_0^\beta d\bar{\tau} \sum_k \mathcal{U}_{ik}(\tau - \bar{\tau}) \langle T c_i(\tau) c_j^\dagger(0) n_k(\bar{\tau}) \rangle = - \int_0^\beta d\bar{\tau} \sum_k \mathcal{U}_{ik}(\tau - \bar{\tau}) \left\langle \sum_{ml} \delta_{jm} \delta_{il} M_{ml} n_k(\bar{\tau}) \right\rangle_{\text{MC}}$$

Finally:

$$\boxed{F_{ij}(\tau) = - \left\langle \sum_{ml} \delta_{jm} \delta_{il} M_{ml} I_i(\tau) \right\rangle_{\text{MC}}} \quad (11.39)$$

where I have defined: $I_i(\tau) \equiv \int_0^\beta d\bar{\tau} \sum_k \mathcal{U}_{ik}(\tau - \bar{\tau}) n_k(\bar{\tau}) = \sum_k U_{ik} n_k(\tau) + \sum_k \int_0^\beta d\bar{\tau} \mathcal{D}_{ik}(\tau - \bar{\tau}) n_k(\bar{\tau})$. The second term can be evaluated as a function of the dynamical kernel $K_{ij}(\tau)$ (see Eq. (M.3) in the appendix):

$$\begin{aligned} \int_0^\beta d\bar{\tau} \mathcal{D}_{ik}(\tau - \bar{\tau}) n_k(\bar{\tau}) &= \sum_{p_k=1}^{N_k} \int_{\tau_{p_k}}^{\tau'_{p_k}} d\bar{\tau} \mathcal{D}_{ik}(\tau - \bar{\tau}) \\ &= \sum_{p_k=1}^{N_k} -2K'_{ij}(0^+) \left\{ \theta(\tau - \tau_{k_j}) - \theta(\tau - \tau'_{k_j}) \right\} + K'_{ij}(\tau - \tau_{k_j}) - K'_{ij}(\tau - \tau'_{k_j}) \end{aligned}$$

which leads to:

$$\begin{aligned} I_i(\tau) &= \sum_k U_{ik} n_k(\tau) - 2 \sum_k K'_{ik}(0^+) n_k(\tau) + \sum_{\text{ops } \alpha} s_\alpha K'_{ik(\alpha)}(\tau - \tau_\alpha) \\ &= \sum_k \tilde{U}_{ik} n_k(\tau) - \sum_{\text{ops } \alpha} s_\alpha K'_{ik(\alpha)}(\tau - \tau_\alpha) \end{aligned} \quad (11.40)$$

with $s_\alpha = 1$ for creation operators and -1 otherwise. If one splits the contributions from the charge and the spin channel, $K_{a\sigma, b\sigma'} = K_{ab}^0 + (-)^{\sigma\sigma'} K_{ab}^z$, this becomes

$$I_i(\tau) = \sum_k \tilde{U}_{ik} n_k(\tau) - \sum_{\text{ops } \alpha} s_\alpha \left[K_{a(i)b(\alpha)}^{0'}(\tau - \tau_\alpha) + (-)^{\sigma(i)\sigma'(\alpha)} K_{a(i)b(\alpha)}^{z'}(\tau - \tau_\alpha) \right] \quad (11.41)$$

In the presence of \mathcal{J}^\perp (we recall that $\mathcal{J}^\perp = \mathcal{J}^z$), Eq. (11.41) is modified to

$$I_i(\tau) = \sum_k \left\{ \tilde{U}_{ik} - 2 \cdot 2 (-)^{\sigma(i)\sigma'(k)} K_{a(i)b(k)}^{z'}(0^+) \right\} n_k(\tau) - \sum_{\text{ops } \alpha} s_\alpha \left[K_{a(i)b(\alpha)}^{0'}(\tau - \tau_\alpha) + 3 (-)^{\sigma(i)\sigma'(\alpha)} K_{a(i)b(\alpha)}^{z'}(\tau - \tau_\alpha) \right]$$

At the cost of measuring an additional correlator ($F(\tau)$), one obtains a smooth self-energy. This is why this method of computing Σ is called the ‘‘improved estimator’’ method (Hafermann *et al.* (2012)). The measure of $I_i(\tau)$ is implemented in a class `precompute_fprefactor`.

The measure of $F(\tau)$ is performed in `measure_gt`, while the measure of $F(i\omega)$ is done in `measure_gw`.

11.1.7.5 Legendre measurements

Instead of using the Fourier basis to encode the Green’s function, one can use the basis of Legendre polynomials. This is described in Boehnke *et al.* (2011). The advantage of this basis is that it is more compact than the Fourier basis; it thus requires less storage. This becomes important for correlators with multiple arguments. In the current, this is implemented only for the one-particle Green’s function.

11.2 Implementation notes

This section explains how the CTQMC algorithm described above is implemented. A first aim is to underline the reasoning behind the implementation choices, which reflect the balance to be struck between efficiency and clarity. A second aim is to provide a starting point for developers within the group. As a result, in the following text, I will refer explicitly to the names of some classes of the actual code, which is not directly useful for the general reader but is meant for potential developers of the code.

The corresponding code is not publicly available but its documentation is nonetheless available online at the url http://ipht.cea.fr/triqs/1.2/applications/cthyb_segment/. The code can be run from Python or from C++; the implementation is entirely in C++. The Python wrapper is generated automatically using

the tool `c++2py` of the TRIQS library. The implementation makes use of the Monte-Carlo library available in TRIQS (see above, section 10.2.3).

A Monte-Carlo code can be seen as a set of Monte-Carlo updates or “moves” together with a set of measures (whose principles are described in the previous section) acting on a configuration. In the case of the “segment solver”, as I will call the hybridization-expansion CTQMC solver in the segment picture, this configuration contains a set of ordered times for fermionic as well as spin operators, the information on the edge state ψ , the information about which spin operator is “linked” to which other spin operator by a \mathcal{J}^\perp line.

The main computational difficulty of the segment solver lies in the efficient computation of the overlaps needed to compute the Metropolis ratios (see Eq. (11.18)) and in the manipulation of operators of different types (orbital, spin...) on the imaginary timeline. More importantly, proposal probability ratios and acceptance ratios (and in particular limiting cases thereof) have to be computed with great care, as any error will not necessarily be obvious to the naked eye. Mistakes in the detailed balance are difficult to spot and may result in subtle biases or drifts. Worse, ergodicity issues – which are not intrinsically “bugs” – can only be elucidated by adding more Monte-Carlo updates. For all these reasons, the implementation has to be as simple and as readable as possible without compromises on the speed of the code. This section intends to illustrate these challenges.

11.2.1 Description of a configuration

Monte-Carlo (MC) updates and measures perform operations on Monte-Carlo configurations, defined in Eq. (11.7).

The internal implementation of MC configurations (by a class named **configuration**) reflects the structure of the Monte-Carlo weight (Eq. (11.8)). A first worker called **trace_c_ops** performs all the operations associated to the local trace factor w_{loc} ; a second worker called **hybridization_dets** takes care of the operators in the hybridization determinant term; a third worker called **bosonic_lines** takes care of the spin operators and of the attached bosonic lines. These workers manipulate the operators, which are described in the next subsection.

11.2.1.1 Operators, fermionic and spin segments

The implementation of operators requires extra care. Indeed, one has to cope with the following three difficulties:

1. for operations such as insertion/removal of a fermionic or spin segment on a given line, one needs to be able to compute quickly the neighbors of this segment on the given line;
2. for the computation of overlaps, one wants to be able to compute quickly the neighbors of a given operator irrespective of the line;
3. there are two types of segments: fermionic segments $[c, c^\dagger]$ and spin segments $[s^+, s^-]$; a spin operator consists in two fermionic operators.

To cope with these difficulties, each operator (characterized by the triplet (time, type [creation/annihilation], color)) is stored in two hash tables (“`std::map`” in C++, with a $\log(N)$ search time due to the implementation of the hash table as a binary tree). The first hash table, named **fullopmap**, contains all the operators of all colors. Iterating over all operators (with “`const_iterators`”) merely consists in traversing this map. This makes it easy to compute the overlaps (provided the information about the occupation of the lines is stored, which is done in a vector “`right_occupations`”), or to compute for instance the dynamical contribution to the trace, Eq. (11.22), where a loop on all operators is required). Then, a vector of hash tables named **ops_map** stores hash tables each containing the operators of a given color, or more precisely iterators (“`colored_const_iterators`”) to the operators contained in **fullopmap** with can be easily “decoupled” to become “`const_operators`”.

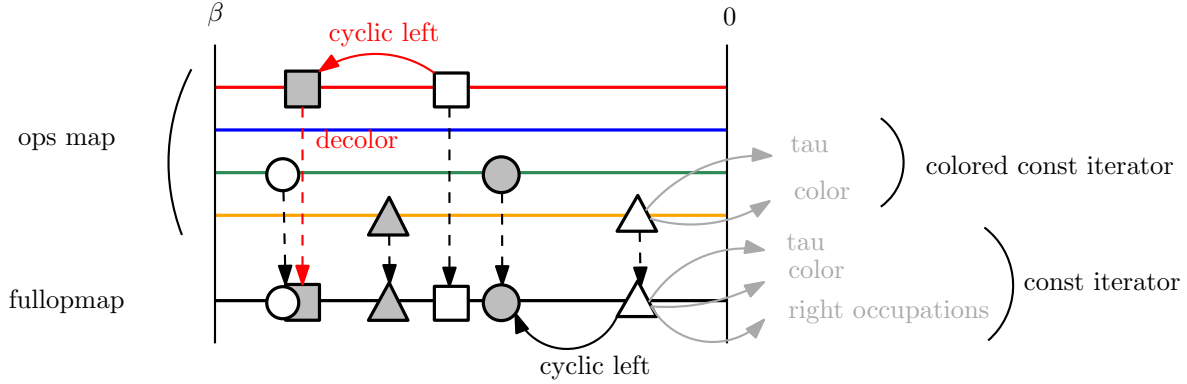


Figure 11.4: Graphical representation of the operator class, **t_ordered_colored_c_ops**. The colored lines represent the different colors and the corresponding operators, stored in **ops_map**. The black line and its operator represents **fullopmap**. The dashed vertical line represents the action of “decoloring” a colored_const_iterator into a const_iterator.

As a result, for a given operator on a given line, finding the neighbors on the same line is easy (through **ops_map**), and finding the “absolute” (irrespective of color) neighbors is easy (through **fullopmap**). These hash tables as well as the low-lying operations thereon are contained in a class **t_ordered_colored_operators**. This mechanism is illustrated in Fig. 11.4.

The imaginary time (“tau”) is not implemented as a double precision number (“double” in C++), but with a dedicated class which deals with the imaginary time periodicity and does not suffer from rounding errors inherent to double-precision numbers (each time is internally represented by an integer).

The information on which operator is “hybridized” (namely comes from the expansion of the hybridization term) or is part of a spin segment (namely comes from the expansion of the \mathcal{J}^\perp term) is contained in the workers **hybridization_dets** and **bosonic_lines**, which respectively contain maps of the corresponding colored_const_operators or vectors of “spin segments” (a small class containing two spin operators, each of which is made up of two colored_const_iterators). Note that: a segment is an ordered couple (order matters) $(O_l, O_r(\tau_r))$ where O_l and O_r are two operators (either creation or annihilation) of the same color. A spin segment is an unordered pair (order does not matter) $\{s^+(\tau_+), s^-(\tau_-)\}$ of a spin + operator and a spin - operator.

A word on notation: in the following,

- $\tau = \beta^-$ is placed on the left of $\tau = 0^+$. Thus, “left” means greater times (except when the operator is the first on the line)
- the letter c will denote a “color” or “line” (see e.g. Fig. 11.1), namely a given orbital-spin (a, σ) . n_c denotes the number of colors/lines
- at a given Monte-Carlo step, variables *without prime* refer to the state prior to the Monte-Carlo move while *primed* variables refer to the state if the Monte-Carlo update is accepted.
- n_{ops} stands for the total number of creation and annihilation operators (a spin operator is made up of two fermionic operators), $n_{\text{ops}}(c)$ stands for the number of operators on line c . $n_{\text{ops,hyb}}$ refers to the number of hybridized operators. l denotes the number of bosonic lines.

11.2.1.2 trace_c_ops

This worker performs all the operations related to the local trace factor, w_{loc} . In particular, it computes the contribution coming from w_{loc} to the Metropolis ratio corresponding to the addition or removal of a segment

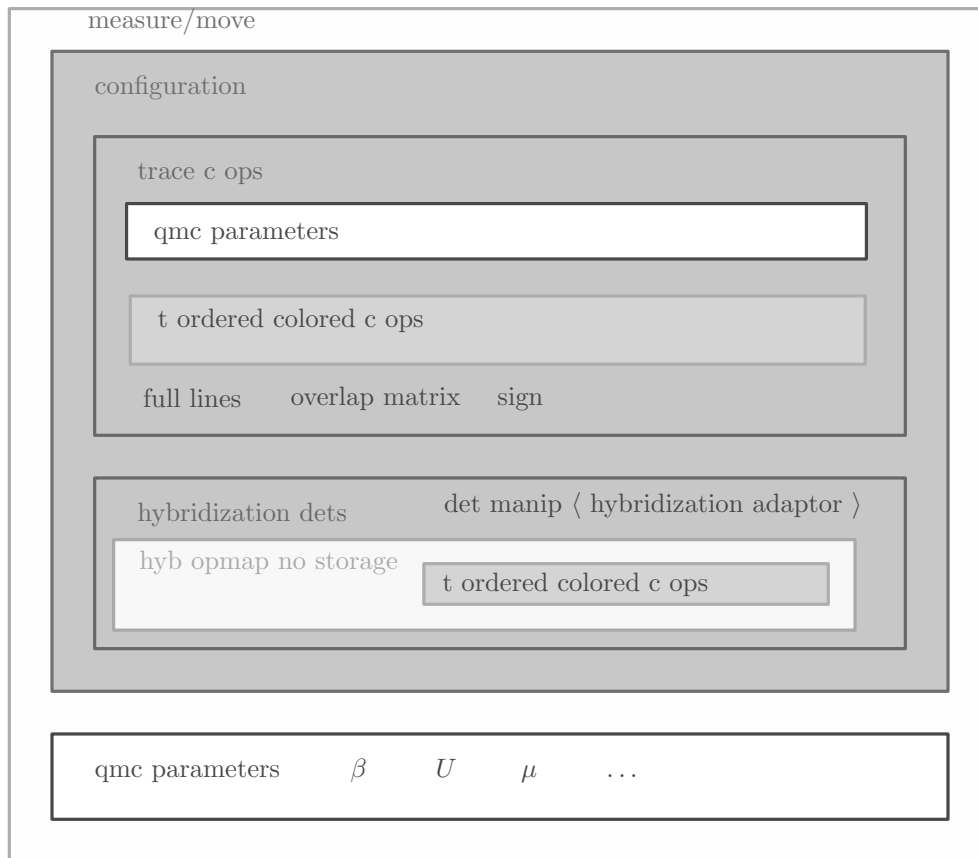


Figure 11.5: Class hierarchy: who contains whom?

(Eq. (11.22)). It contains the overlap computations. It also stores the state ψ in a vector “full_lines”, as well as the current signs of each line.

To increase speed, it also stores the current overlap matrix (O_{ij} of the previous section).

11.2.1.3 hybridization_dets

This worker performs all the operations related to the $\det\Delta$ factor of the Monte-Carlo weight. In particular, it computes the contribution coming from $\det\Delta$ to the Metropolis ratio upon inserting or removing a segment. It uses the TRIQS “det_manip” class to perform the low-lying operations on determinants (in particular, this is where the Sherman-Morrison formulae are implemented).

11.2.1.4 bosonic_lines

This worker performs all the operations related to the $\prod_{i=1}^k [-\mathcal{J}_{q(\alpha_i)\beta_i}^\perp]$ factor of the Monte-Carlo weight. In particular, it computes the contribution coming from this factor to the Metropolis ratio upon inserting or removing a spin segment.

11.2.1.5 Summary: dependencies

Figure 11.5 is a flow diagram showing which class contains which. The class **qmc_parameters** contains the relevant physical parameters of the simulation.

11.2.2 Monte-Carlo updates (or “moves”)

In this section, I describe each Monte-Carlo update. The proposal probability depends on the precise process of each update (including the order of the steps).

11.2.2.1 Move “insert” and “remove segment”

This is the basic move. It is illustrated in Fig. 11.3. This move is implemented in a class `move_insert_segment` and `move_remove_segment`. As a concrete example, the code of the insertion update is reproduced in appendix M.4.

11.2.2.1.1 Description of the insertion process The insertion of a segment consists in the following steps:

1. Choose a random color c ;
2. Choose a random time τ_1 between 0 and β ;
3. Determine the interval l_{\max} between the operator on the left of τ_1 on line c (time τ_l) and the one on the right of τ_1 on c (time τ_r);
4. Choose a random time τ_2 between and τ_l and τ_r ;
5. Swap both times as dictated by the occupation of line c if it already carries at least one segment. Otherwise (no operators before), τ_1 is the creation operator, τ_2 the annihilation operator;
6. Insert the segment $\{O(\tau_1), O(\tau_2)\}$, *i.e.* change occupation state of line c from the left of τ_1 to the right of τ_2 in `trace_c_ops`.

11.2.2.1.2 Description of the removal process The procedure is the following:

1. Choose a random color c ;
2. Choose a operator O_l among $n_{\text{ops,hyb}}(c)$. Find its right neighbor O_r . Compute δl , the space “around” the segment (*i.e.* to the neighboring operators);
3. Remove segment $\{O_l, O_r\}$, *i.e.* change occupation state of line c from the left of O_l to the right of O_r .

11.2.2.1.3 Proposition ratios Based on the insertion and removal processes, one finds the following proposition ratios:

| Insertion transition probabilities (case $n_{\text{ops}} > 0$) | Removal transition probabilities (case $n_{\text{ops}} > 0$) | Insertion transition probabilities (case $n_{\text{ops}} = 0$) | Removal transition probabilities (case $n_{\text{ops}} = 0$) |
|--|--|--|--|
| $P_{i \rightarrow f} = \frac{2}{n_c \beta l_{\max}}$ $P_{f \rightarrow i} = \frac{1}{n_c n'_{\text{ops,hyb}}(c)}$ $P_{\text{insertion}}^{\text{prop}} = \frac{\beta l_{\max}}{2 n'_{\text{ops,hyb}}(c)}$ | $P_{i \rightarrow f} = \frac{1}{n_c n_{\text{ops,hyb}}(c)}$ $P_{f \rightarrow i} = \frac{2}{n_c \beta \delta l}$ $P_{\text{insertion}}^{\text{prop}} = \frac{2 n_{\text{ops,hyb}}(c)}{\beta \delta l}$ | $P_{i \rightarrow f} = \frac{1}{\beta^2}$ $P_{f \rightarrow i} = \frac{1}{2}$ $P_{\text{insertion}}^{\text{prop}} = \frac{\beta^2}{2}$ | $P_{i \rightarrow f} = \frac{1}{2}$ $P_{f \rightarrow i} = \frac{1}{\beta^2}$ $P_{\text{insertion}}^{\text{prop}} = \frac{2}{\beta^2}$ |

11.2.2.2 Move “move segment”

This move consists in taking a segment (seg1) on one line c_1 and moving it on another line c_2 at the same position (Fig. 11.6). This move is important when spurious polarizations between identical lines appear (this often happens in insulating regimes). This move is implemented in a class `move_move_segment`.

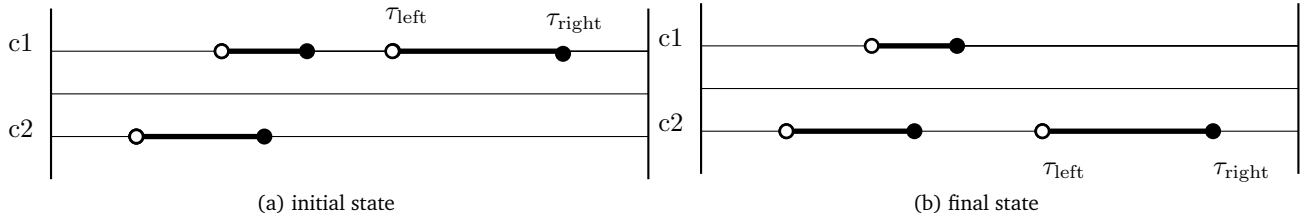


Figure 11.6: Move move segment

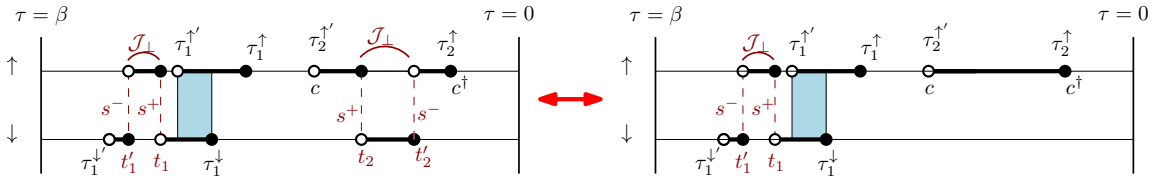


Figure 11.7: Move insert/remove spin segment

11.2.2.2.1 Description of the move The procedure is the following:

1. choose a color $c1$;
2. choose a color $c2$. If $c2==c1$, reject;
3. choose an operator on line $c1$. This determines
4. if $c2$ is unoccupied from the right of τ_left to the left of τ_right , propose the move to line $c2$;

11.2.2.2.2 Proposition ratios The corresponding proposition ratios are:

$$P_{i \rightarrow f} = \frac{1}{n_c} \frac{1}{n_c} \frac{1}{n_{ops}(c1)}$$

$$P_{f \rightarrow i} = \frac{1}{n_c} \frac{1}{n_c} \frac{1}{n'_{ops}(c2)}$$

$$P_{move}^{prop} = \frac{n_{ops}(c1)}{n'_{ops}(c2)}$$

11.2.2.2.3 Note In practice, the trace and determinant ratios are computed in the following way:

- Trace: $seg1$ is removed from the trace on $c1$ (completely) and try_add'ed to the trace on $c2$
- Determinant: in the diagonal- Δ case, $seg1$ is try_removed from the det on $c1$ and try_add'ed to the determinant on $c2$ (in this case, both determinants are independent of each other).

11.2.2.3 Move “insert” and “remove spin segment”

This move consists in adding/remove a spin segment $[s^+, s^-]$ to a configuration. It is illustrated in Fig. 11.7. This move is implemented in a class `move_insert_spin_segment` and `move_remove_spin_segment`.

11.2.2.3.1 Description of insertion process The procedure is the following:

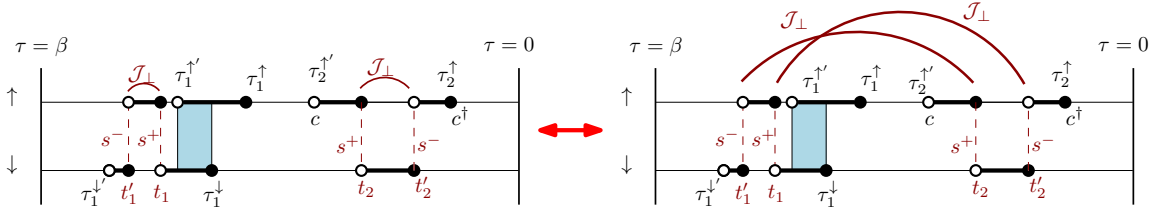


Figure 11.8: Move swap bosonic lines

1. Choose a random time τ_1 between 0 and β
2. Compute the interval l_{\max} between the first operator O_l on the left of τ_1 (on line 0 or 1) and the first operator O_r on the right of τ_1 , (on line 0 or 1)
3. Choose a random time τ_2 between O_r and O_l
4. If $n_{ops} > 0$, swap τ_1 and τ_2 as dictated by the state of both lines. Otherwise ($n_{ops} = 0$), do not swap.
5. Insert spin segment $\{s(\tau_1), s(\tau_2)\}$

11.2.2.3.2 Description of removal process

1. Randomly choose a bosonic line among the n_b lines.
2. If there are no operators between both spin operators, remove spin segment (ie modify occupation state of both lines on the side where there are no operators). Otherwise, reject. If $n_{ops} = 4$ (i.e. there is only one spin segment remaining), change occupation to the left of spin + with probability 1/2, to the right of spin + with probability 1/2.

11.2.2.3.3 Proposition ratios The corresponding proposition ratios are:

| Insertion transition probabilities (case $n_{ops} > 0$) | Removal transition probabilities (case $n_{ops} > 0$) | Insertion transition probabilities (case $n_{ops} = 0$) | Removal transition probabilities (case $n_{ops} = 0$) |
|--|---|--|--|
| $P_{i \rightarrow f} = \frac{2}{\beta l_{\max}}$ $P_{f \rightarrow i} = \frac{1}{n'_b(c)}$ $P_{\text{insertion}}^{\text{prop}} = \frac{\beta l_{\max}}{2n'_b}$ | $P_{i \rightarrow f} = \frac{1}{n_b}$ $P_{f \rightarrow i} = \frac{2}{\beta \delta l}$ $P_{\text{insertion}}^{\text{prop}} = \frac{2n_b}{\beta \delta l}$ | $P_{i \rightarrow f} = \frac{1}{\beta^2}$ $P_{f \rightarrow i} = \frac{1}{2}$ $P_{\text{insertion}}^{\text{prop}} = \frac{\beta^2}{2}$ | $P_{i \rightarrow f} = \frac{1}{2}$ $P_{f \rightarrow i} = \frac{1}{\beta^2}$ $P_{\text{insertion}}^{\text{prop}} = \frac{2}{\beta^2}$ |

11.2.2.4 Move “swap bosonic lines”

This move is aimed at sampling the permanent. It consists in changing the permutation q or graphically in swapping the bosonic lines between two spin segments. It is illustrated in Fig. 11.8. This move is implemented in a class `move_swap_bosonic_lines`.

11.2.2.4.1 Description of the move

1. Choose a random bosonic line index i_1
2. Choose a random bosonic line index i_2

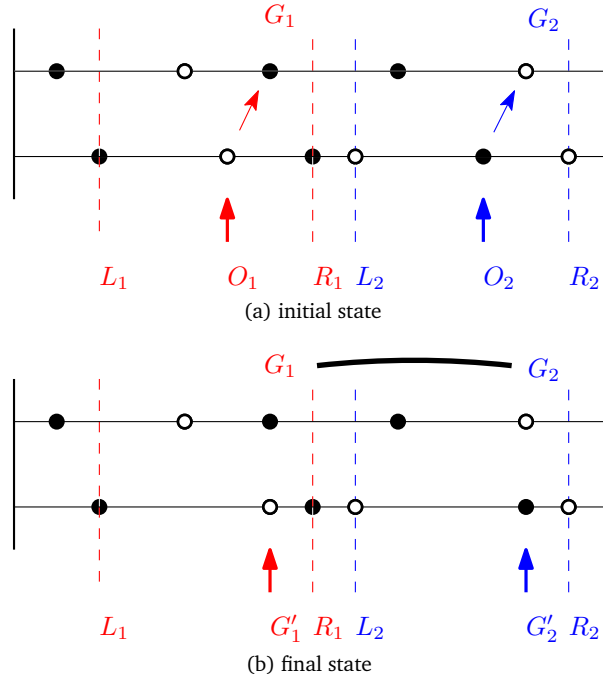


Figure 11.9: Regroup move.

3. If $i_1 = i_2$, reject. Else, remove the bosonic lines $(s_+(i_1), s_-(i_1))$ and $(s_+(i_2), s_-(i_2))$ and add the bosonic lines $(s_+(i_2), s_-(i_1))$ and $(s_+(i_1), s_-(i_2))$

11.2.2.5 Move group and split composite operators

This move consists in regrouping 4 fermionic operators into a spin segment, or conversely to split a spin segment into 4 fermionic operators. This move is implemented in a class `move_regroup_spin_segment` and `move_split_spin_segment`.

11.2.2.5.1 Regrouping four operators into a spin segment (Fig. 11.9) The procedure is the following:

- | | |
|---|---|
| <ol style="list-style-type: none"> 1. choose a line c ($1/l$) 2. choose two operators O_1 and O_2 of opposite type on this line ($1/n_{\text{ops}}(c)^2$) 3. find the left and right neighbors L_1 and R_1 (resp. L_2 and R_2) of O_1 and O_2 on the same line 4. find a candidate G_i to be grouped with O_i on | <p>the opposite line c', namely G_i is a left or right neighbor of O_i of the opposite type and on the opposite line and $L_i > G_i > R_i$. If cannot find candidate, reject.</p> <ol style="list-style-type: none"> 5. if there are no operators between O_1 and O_2 and between G_1 and G_2, reject; 6. otherwise, remove (O_1, O_2) and insert (G'_1, G'_2) on the line c. Insert a bosonic line. |
|---|---|

11.2.2.5.2 Splitting a spin segment into four operators (Fig. 11.10) The procedure is the following:

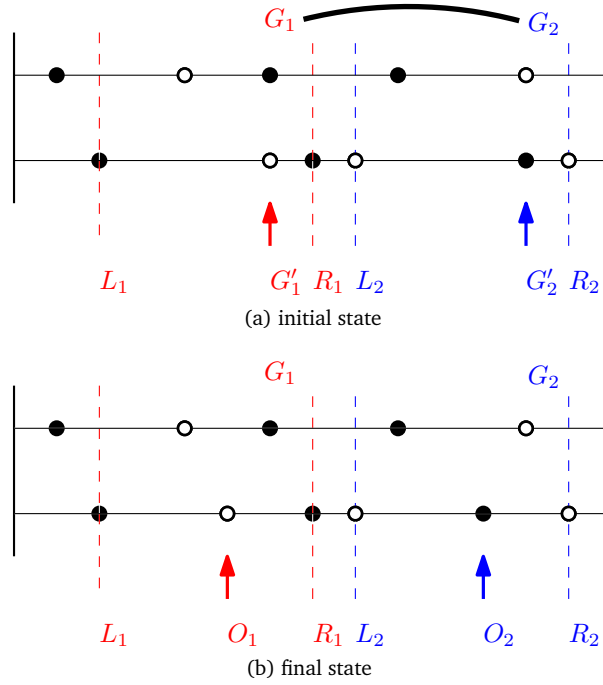


Figure 11.10: Split move.

1. choose a bosonic line ($1/l$)
2. if there are no operators between the segment's ends, reject
3. if there are no operators between the end points of either segment, choose the line where there are intercalated operators. Otherwise, choose either line ($1/2$), say c .
4. find the left and right neighbors L_1 and R_1 (resp. L_2 and R_2) of the end points G'_1 and G'_2 (check: $R_1 \neq L_2$) on c .
5. pick a time τ_i between L_i and R_i ($1/l_{\max,1}1/l_{\max,2}$)
6. remove segment (G'_1, G'_2) and add segment_desc($O_1(\tau_1), O_2(\tau_2)$) to c .

11.2.2.5.3 Proposition ratios The corresponding proposition ratios are:

| Regroup move (general case) | Split move (general case) | Regroup move (special case) | Split move (special case) |
|--|--|--|--|
| $P_{i \rightarrow f} = \frac{1}{n_c} \frac{1}{n_{\text{ops,hyb}}^2(c)}$ $P_{f \rightarrow i} = \frac{1}{l'} \frac{1}{2 l_{\max,1} l_{\max,2}}$ | $P_{i \rightarrow f} = \frac{1}{l} \frac{1}{2 l_{\max,1} l_{\max,2}}$ $P_{f \rightarrow i} = \frac{1}{n_c} \frac{1}{(n'_{\text{ops,hyb}}(c))^2}$ | $P_{i \rightarrow f} = \frac{1}{n_c} \frac{1}{n_{\text{ops,hyb}}^2(c)}$ $P_{f \rightarrow i} = \frac{1}{l'} \frac{1}{l_{\max,1} l_{\max,2}}$ | $P_{i \rightarrow f} = \frac{1}{l} \frac{1}{l_{\max,1} l_{\max,2}}$ $P_{f \rightarrow i} = \frac{1}{n_c} \frac{1}{(n'_{\text{ops,hyb}}(c))^2}$ |
| $P_{\text{prop}}^{\text{regroup}} = \frac{n_c n_{\text{ops,hyb}}^2(c)}{2l' \cdot l_{\max,1} l_{\max,2}} \quad (11.42)$ | $P_{\text{prop}}^{\text{split}} = \frac{2l \cdot l_{\max,1} l_{\max,2}}{n_c (n_{\text{ops,hyb}}(c))^2}$ | $P_{\text{prop}}^{\text{regroup}} = \frac{n_c n_{\text{ops,hyb}}^2(c)}{l' \cdot l_{\max,1} l_{\max,2}} \quad (11.43)$ | $P_{\text{prop}}^{\text{split}} = \frac{l \cdot l_{\max,1} l_{\max,2}}{n_c (n_{\text{ops,hyb}}(c))^2}$ |

Dynamical screening in solids: Combined Screened Exchange and dynamical DMFT

The quantum Monte-Carlo code that I have described in the previous chapter has been used by Ambroise van Roekeghem in the framework of electronic structure calculations.

In section 12.2, I give a brief overview of a new approach combining screened exchange and dynamical DMFT (SEx+DDMFT) developed in van Roekeghem (2014) and its application to the cobalt pnictide BaCo_2As_2 published as van Roekeghem *et al.* (2014) and included in section R.2. To put this method in context, I briefly describe one of the major methods used for the realistic description of correlated solids prior to this work (section 12.1).

12.1 Density functional theory combined to DMFT: LDA+DMFT in a nutshell

Density functional theory (DFT¹), the workhorse of *ab initio* electronic structure calculations, can be combined to dynamical mean-field theory to extend the scope of the theory to excitations and finite temperatures. The corresponding method, “LDA+DMFT” (Lichtenstein and Katsnelson (1997); Anisimov *et al.* (1997)), is discussed at greater length in appendix J.2. Here, I merely summarize its main principles.

In systems with narrow bands near the Fermi level, LDA+DMFT focuses on the degrees of freedom located in a low-energy window \mathcal{W} assumed to contain all relevant physical processes. A set of Wannier orbitals is constructed in this window. Then, the Kohn-Sham Hamiltonian – the main output of a DFT calculation,

¹More details are given about the principles of DFT in appendix J.1.

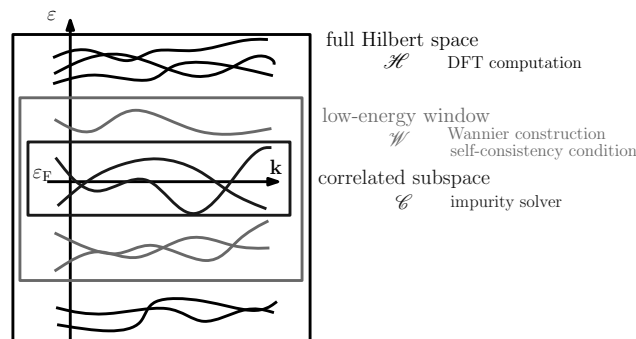


Figure 12.1: Definition of the various energy windows used in LDA+DMFT

parametrizing the band structure of the materials – is projected in this basis, yielding a Hamiltonian $\varepsilon_{\mathcal{W}}$ acting in \mathcal{W} . Among the Wannier orbitals, some are very localized and thus expected to be affected by correlation effects. For this subset, denoted \mathcal{C} , of orbitals, one performs a self-consistent DMFT calculation yielding a local self-energy $\Sigma_{mm'}(i\omega)$. The different energy windows are summarized in Fig. 12.1.

The LDA+DMFT self-consistency is similar to the single-site DMFT self-consistency condition, only it is performed in matrix form. The matrix inversion is performed in the low-energy window \mathcal{W} , but only the components of $G_{\text{loc}}(i\omega)$ belonging to the correlated subset \mathcal{C} (whose basis set is parametrized by indices m, m') are used to compute the Weiss field, namely G_{loc} is given by the expression:

$$[G_{\text{loc}}(i\omega)]_{mm'} = \sum_{\mathbf{k}} [(i\omega + \mu) \mathbf{1} - \varepsilon_{\mathcal{W}}(\mathbf{k}) - \Sigma_{\mathcal{W}}(i\omega)]_{mm'}^{-1} \quad (12.1)$$

with

$$\Sigma_{\mathcal{W}}(\mathbf{k}, i\omega) = \begin{pmatrix} \mathbf{0} & & \mathbf{0} & \\ & \Delta\Sigma_{m_1 m_1}(i\omega) & \cdots & \Delta\Sigma_{m_1 m_{N_{\mathcal{C}}}}(i\omega) \\ \mathbf{0} & \vdots & \ddots & \vdots \\ & \Delta\Sigma_{m_{N_{\mathcal{C}}} m_1}(i\omega) & \cdots & \Delta\Sigma_{m_{N_{\mathcal{C}}} m_{N_{\mathcal{C}}}}(i\omega) \end{pmatrix}$$

$\Delta\Sigma_{m_1 m_1}(i\omega)$ is the impurity self-energy corrected for the exchange and correlation effects already taken into account at the DFT level:

$$\Delta\Sigma_{mm'} = \Sigma_{mm'} - \Sigma_{mm'}^{\text{dc}}$$

The estimation of Σ^{dc} is, however, problematic since the precise diagrammatic content of DFT is difficult to assess; this is an important drawback of this method.

The Weiss field is given by the usual equation, in matrix form: $[\mathcal{G}^{-1}(i\omega)]_{mm'} = [G_{\text{loc}}^{-1}(i\omega)]_{mm'} + \Sigma_{mm'}$. The (static) interaction matrix $U_{m_1 m_2 m_3 m_4}$ can be computed from first principles by the constrained RPA method (see chapter J.3 for more details).

The corresponding multiorbital impurity problem is solved for $\Sigma_{mm'}(i\omega)$ as explained in the previous chapter, and plugged into 12.1 until convergence.

12.2 Beyond LDA+DMFT combined with cRPA: GW + DMFT and SEx+DDMFT

The combination of LDA+DMFT with constrained RPA can be improved on. Indeed,

- the double-counting problem of LDA+DMFT is a real issue and can probably not be solved owing to the different nature of the DFT approximation and many-body techniques. Realistic methods based only on Green's functions are needed;
- constrained RPA leads to a renormalization of the interactions via polarization effects coming from the high-energy electrons, leading to an effective low-energy Hamiltonian with partially screened interactions. However, self-energy effects coming from the high-energy electrons also in principle renormalize the one-body part of the low-energy Hamiltonian. In these effects, the long-range Coulomb tail is expected to play an important role.

12.2.1 GW + DMFT

The GW + (E)DMFT approximation as introduced by Biermann *et al.* (2003) aims at solving the above issues.

The full-fledged $GW+DMFT$ scheme is performed – at least in principle – in the full Hilbert space \mathcal{H} , namely: defining the screened interaction and full Green’s function as $W(\mathbf{q}, i\Omega) = v_{\mathbf{q}}^{\text{Coul}} (1 - v_{\mathbf{q}}^{\text{Coul}} P(\mathbf{q}, i\Omega))^{-1}$ and $G(\mathbf{k}, i\omega) = (G_0^{-1}(\mathbf{k}, i\omega) - \Sigma(\mathbf{k}, i\omega))^{-1}$ (where bold symbols denote operators acting in \mathcal{H}), the authors then define their local parts in the usual way ($W_{\text{loc}}(i\Omega) = \sum_{\mathbf{q}} W(\mathbf{q}, i\Omega)$ and $G_{\text{loc}}(i\omega) = \sum_{\mathbf{k}} G(\mathbf{k}, i\omega)$), which allows them to define the local “impurity” Weiss fields \mathcal{U} and \mathcal{G} as $\mathcal{U}^{-1}(i\Omega) = W_{\text{loc}}^{-1}(i\Omega) + P_{\text{imp}}(i\Omega)$ and $\mathcal{G}^{-1}(i\omega) = G_{\text{loc}}^{-1}(i\omega) + \Sigma_{\text{imp}}(i\omega)$. The corresponding “impurity” problem, defined as the generalization of Eq. (5.3) to several orbitals, $S_{\text{imp}}[\mathcal{U}, \mathcal{G}]$, is then in principle solved for $\Sigma_{\text{imp}}(i\omega)$ and $P_{\text{imp}}(i\omega)$, and the self-energy and polarization computed as the (now familiar) combination:

$$\begin{aligned}\Sigma(\mathbf{k}, i\omega) &= \Sigma_{\text{imp}}(i\omega) + [\Sigma^{GW}(\mathbf{k}, i\omega)]^{\text{nonloc}} \\ P(\mathbf{q}, i\omega) &= P_{\text{imp}}(i\omega) + [P^{GW}(\mathbf{q}, i\omega)]^{\text{nonloc}}\end{aligned}$$

with the GW self-energy and polarization:

$$\Sigma^{GW}(\mathbf{r}, \mathbf{r}', \tau) = -G(\mathbf{r}, \mathbf{r}', \tau)W(\mathbf{r}', \mathbf{r}, -\tau) \quad (12.2)$$

$$P^{GW}(\mathbf{r}, \mathbf{r}', \tau) = 2G(\mathbf{r}, \mathbf{r}', \tau)G(\mathbf{r}', \mathbf{r}, -\tau) \quad (12.3)$$

Σ and P are then plugged into G and P until convergence. Of course, this general formulation, where the impurity problem describes all orbitals in the solid, cannot be implemented in practice; in fact, since \mathcal{U} is expected to be relevant only for a subspace of correlated orbitals (\mathcal{C}), the algorithm can be simplified in the following way, as explained in Tomczak *et al.* (2014):

1. Start with given G and W (e.g. G^{LDA} and W^{RPA});
2. Compute the self-energy and polarization in the GW approximation (Eqs (12.2-12.3)): $\Sigma^{GW}(\mathbf{k}, i\omega)$ and $P^{GW}(\mathbf{q}, i\Omega)$;
3. Compute $\underline{\underline{U}}(\omega) \sim \langle \underline{\underline{w}}w | W_{\text{t}}(\omega) | \underline{\underline{w}}w \rangle$ (double-underlined quantities act in \mathcal{C}) (see Eq. (J.34)) from constrained RPA;
4. With $\underline{\underline{G}}_{\text{loc}}$ and $\underline{\underline{W}}_{\text{loc}}$ (computed with $v \rightarrow \underline{\underline{U}}(\omega)$), compute $\underline{\underline{\mathcal{U}}}$ and $\underline{\underline{\mathcal{G}}}$, and then $\underline{\underline{\Sigma}}^{\text{imp}}(i\omega)$ and $\underline{\underline{P}}^{\text{imp}}(i\Omega)$ from the impurity solver. Promote them to the full Hilbert space: Σ^{imp} and P^{imp} (see paragraph J.2.1 for more details about unfolding);
5. Combine Σ^{imp} and P^{imp} with $\Sigma^{GW}(\mathbf{k}, i\omega)$ and $P^{GG}(\mathbf{q}, i\Omega)$ (taking care of double-counting terms, which, contrary to LDA, can be determined unambiguously) into Σ and P . Compute the new G and W . Go back to step 2, until convergence.

This fully self-consistent scheme has to this date only been performed for one-particle quantities in Tomczak *et al.* (2012a, 2014), *i.e.* two-particle quantities were kept fixed.

12.2.2 SEx+DDMFT

To make the computations lighter, a simplified scheme, dubbed “Screened Exchange + dynamical DMFT” (SEx+DDMFT) has been introduced by van Roekeghem *et al.* (2014) (included in chapter R.2). It is based on the observation that the \mathbf{k} and ω dependences of Σ are separable (Tomczak *et al.* (2012b, 2014)).

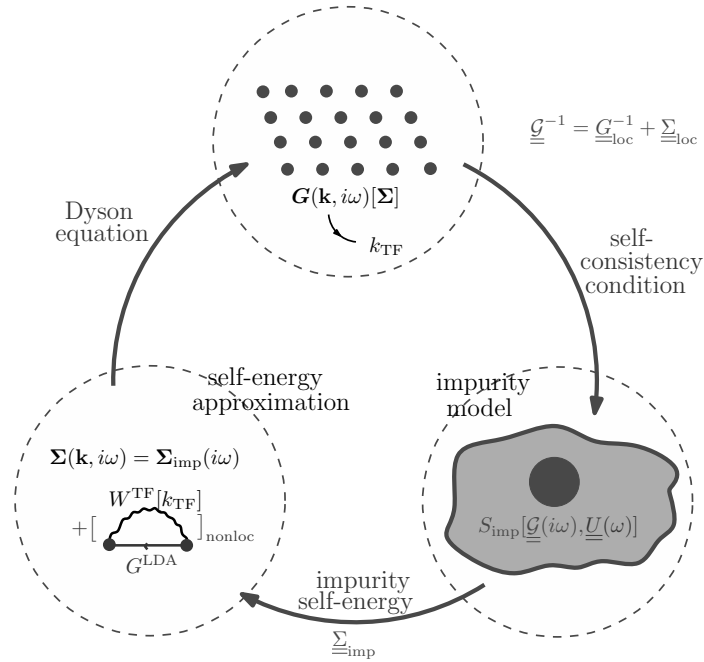


Figure 12.2: The SEx+DDMFT loop. Bold symbols operate in the full Hilbert space. Double-underlined symbols operate in the correlated subspace.

12.2.2.1 Algorithm

The SEx+DDMFT algorithm consists in the following steps:

1. Start with G^{LDA} and W^{TF} (W^{TF} is the fully screened interaction in the Thomas-Fermi approximation, namely $W^{\text{TF}} \sim e^2/\epsilon_0 / (\mathbf{q}^2 + \mathbf{k}_{\text{TF}}^2)$, with $\mathbf{k}_{\text{TF}}^2 = e^2 N(\epsilon_{\text{F}})/\epsilon_0$, see subsection J.3.1 for an intuitive picture; \mathbf{k}_{TF} is computed within LDA);
2. Compute $\underline{\underline{U}}(\omega) = \langle ww | W_{\text{rest}}(\omega) | ww \rangle$ (see Eq. (J.34)) from constrained RPA ($W_{\text{rest}} = v_{\text{Coul}}/(1 - v_{\text{Coul}}P_{\text{rest}})$);
3. Compute the self-energy in the screened Hartree-Fock approximation: $\Sigma^{\text{SEx}}(\mathbf{k}) = -G^{\text{LDA}}W^{\text{TF}}[\mathbf{k}_{\text{TF}}]$;
4. Perform a self-consistent “dynamical” DMFT computation (namely, with an impurity problem with *dynamical* interactions $U(\omega)$); at each step, instead of approximating the lattice self-energy by $\underline{\underline{\Sigma}}^{\text{imp}}(i\omega)$, unfold it to full Hilbert space ($\Sigma^{\text{imp}}(i\omega)$) and combine it to $\Sigma^{\text{SEx}}(\mathbf{k})$ (with an updated \mathbf{k}_{TF} , and taking care of double-counting terms) before recomputing G_{loc} . This step is illustrated in Fig. 12.2. Blue observables are kept fixed (in principle, G^{LDA} in Σ^{SEx} and $U(\omega)$ could be updated self-consistently but this has not been implemented so far)

The double-counting term (signalled by the subscript “nonloc” in Fig. 12.2) is computed as the mean-field Hartree contribution from the Hubbard model. More details can be found in van Roekeghem (2014).

The impurity model to be solved at step 4 is a multiorbital impurity model with dynamical interactions. This model is solved exactly, up to statistical noise, by the CTQMC algorithm described in the previous chapter.

12.2.2.2 Results

In van Roekeghem *et al.* (2014) (included in chapter R.2), this new method is applied to the BaCo_2As_2 compound, which is isostructural to BaFe_2As_2 , one of the recently discovered iron-based superconductors.

The effect of each contribution is, roughly speaking, the following:

1. the screened Hartree-Fock contribution, $\Sigma^{\text{SEx}}(\mathbf{k})$, increases the overall bandwidth compared to LDA
2. dynamical local correlations (encoded in $U(\omega)$ and then, after solving the impurity model, $\Sigma_{\text{imp}}(\omega)$) reduce the bandwidth

The second effect, namely the renormalization of the bandwidth due to dynamical interactions, can be understood intuitively by considering the dynamical interactions as stemming from the coupling to bosonic modes. The quasiparticles corresponding to the fermionic modes coupled to bosonic modes are “polarons”, whose effective mass is enhanced with respect to the original electrons (see paragraph 11.1.4.2.2 for a more rigorous derivation). The renormalization factor can be approximated by²

$$Z_{\text{B}} = \exp \left[- \int_0^{\infty} \frac{d\omega}{\pi} \frac{\text{Im}U(\omega)}{\omega^2} \right] \quad (12.4)$$

Both contributions to the total self-energy are important. The dynamical nature of Hubbard’s U computed from cRPA comes from high-energy electrons interacting via long-ranged Coulomb interactions. If the contribution of these electrons is taken into account at the level of interactions (in $U(\omega)$), it should also be taken into account at the self-energy level. Here, this is done in an approximate way via $\Sigma^{\text{SEx}}(\mathbf{k})$.

If only $\Sigma_{\text{imp}}(\omega)$ is included (in a “LDA + dynamical DMFT” calculation), the bandwidth reduction is overestimated. Conversely, only including the static and nonlocal self-energy $\Sigma^{\text{SEx}}(\mathbf{k})$ leads to an overestimation of the bandwidth.

Interestingly, the bandwidth found in SEx+DDMFT and LDA + (static) DMFT are similar: LDA+DMFT throws away the dynamical part of $U(\omega)$ (arising from high-energy electrons) and does not take into account nonlocal contribution of high-energy electrons to the self-energy. In the light of the previous discussion, these two simplifications are consistent with each other. Thus, SEx+DDMFT explains why the LDA+DMFT method suitably describes the overall bandwidth reduction of correlated materials. Compared to LDA+DMFT, SEx+DDMFT better captures finer details such as Fermi surface topology or the low-energy spectral function.

More importantly, SEx+DDMFT is much more lightweight than a full GW+DMFT computation. It has been recently applied to transition metal oxides (van Roekeghem and Biermann (2014)) and CaFe_2As_2 (van Roekeghem *et al.* (2015)).

The agreement of the spectrum obtained with SEx+DDMFT with ARPES in BaCo_2As_2 is illustrated in Fig. 12.3.

²This formula is the generalization of Eq. (11.27), valid for $\text{Im}U(\omega) = \lambda^2 (\delta(\omega - \omega_0) - \delta(\omega + \omega_0))$, to a continuum of bosonic modes.

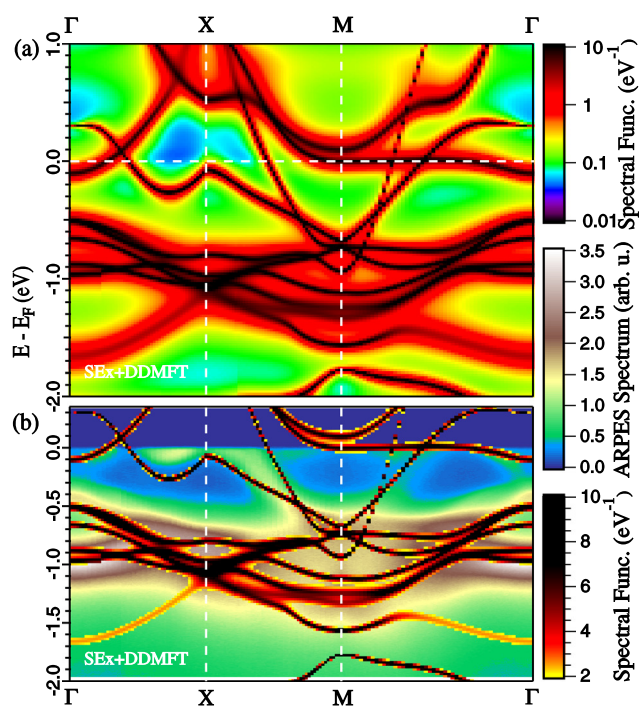


Figure 12.3: BaCo_2As_2 within screened exchange + DDMFT: (a) spectral function and (b) bands extracted from the maxima of panel (a) and superimposed on ARPES data.

Part V

Conclusions and perspectives

In this work, I have addressed several aspects of nonlocal correlations in solids.

First, the effect of nonlocal and even long-ranged interactions has been studied in the context of systems of atoms adsorbed on semiconducting surfaces. There, using the self-consistent combination of extended dynamical mean field theory with the diagrammatic GW method ($GW+EDMFT$), a materials trend has been proposed based on the first-principles determination of the interaction parameters of a family of compounds. In the Sn/Si compound, both the spatial and temporal information provided by $GW+EDMFT$ has been used to elucidate apparent contradictions from different experimental probes, based on the different timescales of each experiment.

Second, a novel approach to the description of nonlocal self-energy and polarization effects in strongly-correlated systems has been proposed. This method, called TRILEX, unifies two important points of view on high-temperature superconductors, the “doped Mott insulator” and the “spin fluctuation” viewpoints. In the spirit of dynamical mean field theory, it relies on a local approximation which reduces the description of the extended solid to a local effective description in terms of an impurity problem. In this method, however, not the self-energy, but the three-leg vertex, describing the interaction between the physical fermions and their bosonic fluctuations, is approximated by a local vertex. This vertex is computed by solving a single-site impurity problem with dynamical charge-charge and spin-spin interactions, and used to construct frequency- and momentum-dependent self-energies and polarizations that can capture the momentum differentiation effects observed in various experiments on cuprate materials.

Applied to the single-band Hubbard model in two dimensions, this method has been shown to reduce to the spin fluctuation approximation in the weak-interaction regime, and to describe isolated atoms in the strong-interaction regime. While featuring a first-order metal-to-Mott insulator transition at half-filling like DMFT and a strong momentum differentiation in the self-energy and polarizations at weak coupling like in spin fluctuation theory, it displays significant departures from either limit in the intermediate interaction regime. This is controlled by the frequency dependence of the central quantity of the approximation, the local three-leg vertex.

This new method, as well as the $GW+EDMFT$ method, relies on the development of recent algorithms such as the continuous-time quantum Monte-Carlo method in the hybridization expansion, whose generalization to retarded charge-charge and spin-spin interactions is also elaborated on in this work.

A lightweight method, TRILEX can be used to investigate many complex problems, like superconducting phases or multiorbital problems that are relevant, for instance, for the iron-based superconductors. Furthermore, many interesting aspects of TRILEX for single-band problems require further work, like the understanding of its low-temperature behavior or its cluster extension. The extension of TRILEX to study charge ordering phenomena – recently a subject of intense interest in the field of cuprate compounds – is also promising.

Acknowledgments

This work is the result of many fruitful interactions with many different people.

First and foremost, I would like to thank my advisors Olivier Parcollet and Silke Biermann for their supervision during these three years. I have learnt a great deal from them, taking advantage of their deep knowledge in physics and beyond. In particular, Olivier introduced to me to code design and helped me deal with the technical challenges of this field; Silke, always encouraging freewheeling and creative discussions, gave me the invaluable freedom to pursue new ideas.

I would like to warmly thank Massimo Capone and Andrew Millis for reviewing this manuscript in depth, as well as Benoît Douçot, Antonio Tejada and Simone Fratini for carefully examining my work and partaking in my defence.

My special thanks go to Philipp Hansmann for countless enriching discussions at and outside work, and to Michel Ferrero, who is always available for a piece of advice or just a chat, and makes our lab such a nice place to work at.

I would also like to thank Philipp Werner for valuable discussions in Fribourg, and before that in Zürich during my master's; Masatoshi Imada for a wonderful visit at Tokyo University; Sabine Andergassen for interesting discussions about the functional renormalization group and its combination with DMFT in Vienna, Stadt Schlaining and Tübingen.

I would like to thank Antoine Georges for his hospitality at Collège de France during my PhD work, and for introducing me to solid-state physics while I was a master student.

I also owe much to my past and present colleagues at CPhT and IPhT, Sophie, Pascal, Priyanka, Hartmut, Wenya, Yusuke, Jernej, Alaska, Zhenya as well as Leonid, Grégoire and Catherine; and also to the IT teams at CPhT and IPhT, Jean-Luc, Danh, François, Laurent, Patrick, and the team of secretaries at both laboratories for their availability and kindness; and last but not least, to the chef at the "Algorithmes" restaurant for making every lunch time a very pleasant moment!

I would also like to thank my former Chinese teacher Ms Bai for her trust and the opportunity she gave me to teach Chinese to second- and third-year students at Polytechnique. This was a very precious experience.

Un grand merci, aussi, à Alexandre et Ambroise pour tout plein de choses ! (dont la relecture des résumés, mais ce n'est que la partie émergée de l'iceberg !) Et à tous mes autres amis !

Merci à mes parents et mes sœurs !

Enfin, merci à toi, Géraldine, d'être à mes côtés !

This work has been supported by Ecole Polytechnique (Monge scholarship) and partially supported by the FP7/ERC, under Grant Agreement No. 278472 - MottMetals and by FP7/ERC under Grant Agreement No. 617196 - CorrelMat.

Part VI

Appendix: conventions

Unless otherwise stated, throughout the text,

- \equiv denotes a definition

A.1 Time and frequencies

- τ denotes the imaginary time variable, t the real time variable
- β denotes the inverse temperature
- T denotes the imaginary time ordering operator
- $\int d\tau$ denotes $\int_0^\beta d\tau$
- ω denotes the real-axis frequency variable, $i\omega$ and $i\nu$ fermionic Matsubara frequencies and $i\Omega$ bosonic Matsubara frequencies.
- $\sum_{i\omega} g(i\omega)$ denotes $\frac{1}{\beta} \sum_{n=-\infty}^{\infty} g(i\omega_n)$

A.2 Space and momentum

- \mathbf{k} and \mathbf{q} denote a (quasi) momentum variable
- $\sum_{\mathbf{k}} f(\mathbf{k})$ denotes $\frac{1}{N_{\mathbf{k}}} \sum_{n=1}^{N_{\mathbf{k}}} f(\mathbf{k}_n)$

A.3 Operators

- c^\dagger denotes a second-quantized creation operator, c an annihilation operator
- \bar{c} and c denote conjugate Grassmann variables
- H denotes a many-body Hamiltonian
- h denotes a one-body Hamiltonian
- S denotes an action
- Z denotes a partition function

- Ω denotes the free energy $-\log Z$
- Ψ denotes a many-body state
- ψ denotes a one-body state
- $\langle \dots \rangle$ denotes the thermal and quantal average $\frac{1}{Z} \sum_i e^{-\beta E_i} \langle \Psi_i | \dots | \Psi_i \rangle$ where (Ψ_i, E_i) are the eigenstates of H .

A.4 Indices

- σ denotes a spin \uparrow or \downarrow
- i denotes a Wannier site \mathbf{R}_i

A.5 Pauli matrices

The Pauli matrices are defined as: $\sigma^x = \begin{pmatrix} 0 & 1 \\ 1 & 0 \end{pmatrix}$, $\sigma^y = \begin{pmatrix} 0 & -i \\ i & 0 \end{pmatrix}$, $\sigma^z = \begin{pmatrix} 1 & 0 \\ 0 & -1 \end{pmatrix}$. Sometimes, I will denote the 2×2 identity matrix as σ^0 .

Fourier conventions

B.1 Fourier transforms in the imaginary time-frequency domain

B.1.1 Two-point functions

For any imaginary-time β -periodic or β -antiperiodic function $f(\tau)$, the direct and inverse Fourier transforms are defined as follows:

$$\begin{aligned} f(i\omega) &= \int_0^\beta d\tau f(\tau) e^{i\tau\omega} \\ f(\tau) &= \sum_{i\omega} e^{-i\omega\tau} f(i\omega) \end{aligned}$$

B.1.2 Three-point functions

I follow the following Fourier conventions, depending on whether I want to work with a fermionic and a bosonic Matsubara frequency $i\omega$ and $i\Omega$, or two fermionic frequencies $i\omega_1$ and $i\omega_2$:

$$\chi_{\alpha\beta\gamma}(i\omega, i\Omega) \equiv \iint_0^\beta d\tau d\tau' e^{i\omega\tau + i\Omega\tau'} \chi_{\alpha\beta\gamma}(\tau, 0, \tau') \quad (\text{B.1a})$$

$$\hat{\chi}_{\alpha\beta\gamma}(i\omega_1, i\omega_2) \equiv \iint_0^\beta d\tau d\tau' e^{i\omega_1\tau + i\omega_2\tau'} \chi_{\alpha\beta\gamma}(\tau, \tau', 0) \quad (\text{B.1b})$$

for any three-point function $A_{\alpha\beta\gamma}(\tau_1, \tau_2, \tau_3)$, e.g

$$\chi_{\alpha\beta\gamma}(\tau_1, \tau_2, \tau_3) \equiv \langle T c_\alpha(\tau_1) c_\beta^\dagger(\tau_2) \phi_\gamma(\tau_3) \rangle \quad (\text{B.2})$$

Both functions are related:

$$\chi_{\alpha\beta\gamma}(i\omega, i\Omega) = \hat{\chi}_{\alpha\beta\gamma}(i\omega, -i\omega - i\Omega) \quad (\text{B.3})$$

In the main text, I only use the first form $\chi_{\alpha\beta\gamma}(i\omega, i\Omega)$ but the form $\chi_{\alpha\beta\gamma}(i\omega_1, i\omega_2)$ is useful to derive certain results. These Fourier conventions are based on symmetry properties of three-point correlation functions such as $\chi_{\alpha\beta\gamma}(\tau_1, \tau_2, \tau_3)$. These properties are examined at greater length in appendix D.1.

The reciprocal transform reads:

$$\chi_{\alpha\beta\gamma}(\tau, 0, \tau') = \sum_{i\omega} \sum_{i\Omega} e^{-i\omega\tau - i\Omega\tau'} \chi_{\alpha\beta\gamma}(i\omega, i\Omega)$$

B.2 Fourier transform in the space-momentum domain

For any function $f(\mathbf{R})$ defined on a Bravais lattice “BL”, the direct and inverse Fourier transforms are defined as follows:

$$f(\mathbf{k}) = \sum_{\mathbf{R} \in \text{BL}} e^{-i\mathbf{k} \cdot \mathbf{R}} f(\mathbf{R}) \quad (\text{B.4})$$

$$f(\mathbf{R}) = \sum_{\mathbf{k} \in \text{BZ}} e^{i\mathbf{k} \cdot \mathbf{R}} f(\mathbf{k}) \quad (\text{B.5})$$

Part VII

Appendix: technical developments for TRILEX

This part contains important, but quite technical aspects necessary for the development of the TRILEX method presented in chapters 8 and 9.

H Experimental probes for condensed matter physics: a brief theoretical overview

- H.1 Surface probes: electron diffraction, electron energy loss spectroscopy, photoemission 195
- H.2 Bulk probes: neutron scattering, nuclear magnetic resonance, optics 203

I Reminder on many-body theory

- I.1 Correlation functions: general properties 211
- I.2 Time-dependent perturbation theory: the Golden Rule 217
- I.3 Analytical continuation techniques 220
- I.4 Around the Lindhard function and the random-phase approximation 222
- I.5 GW self-energy on the real axis 224
- I.6 Weak-coupling charge and spin density wave scenarios 226

J Reminder: realistic calculations for correlated materials

- J.1 Density functional theory 234
 - J.2 Density functional theory combined to many-body techniques: LDA+DMFT 238
 - J.3 The constrained random-phase approximation (cRPA) 240
-



Bosonic and fermionic correlation functions: relations

In this subsection, we prove the following relations between observables of the mixed fermion-boson action (8.15) and observables of the fermionic action:

$$\varphi^\eta = U^\eta \cdot \langle n^\eta \rangle \quad (\text{C.1a})$$

$$W^{\eta, \text{nc}} = U^\eta - U^\eta \cdot \chi^{\eta, \text{nc}} \cdot U^\eta \quad (\text{C.1b})$$

$$W^\eta = U^\eta - U^\eta \cdot \chi^\eta \cdot U^\eta \quad (\text{C.1c})$$

$$\chi^{3, \eta} = U^\eta \cdot \tilde{\chi}^{3, \eta} \quad (\text{C.1d})$$

W^η , χ^η and $\chi^{3, \eta}$ have been defined in Eqs (8.17b), (8.56) and (8.27), and

$$\chi_{u\nu\gamma} \equiv \langle c_u \bar{c}_\nu n_\gamma \rangle \quad (\text{C.2})$$

respectively. Latin indices denote $u \equiv (\mathbf{R}, \tau, \sigma, a \dots)$, Greek indices $\alpha \equiv (\mathbf{R}, \tau, I \dots)$. The dot denotes multiplication in frequency-momentum indices, convolution in time-space and Pauli indices, namely:

$$(A \cdot B)_{\alpha\beta} = A_{\alpha\gamma} B_{\gamma\beta} \quad (\text{C.3})$$

Let us recall the definition of the partition function in the presence of sources

$$Z[h, F] \equiv \int \mathcal{D}[\bar{c}, c, \phi] e^{-S_{\text{eb}} + h_\alpha \phi_\alpha - F_{uv} \bar{c}_u c_v - \frac{1}{2} \phi_\alpha B_{\alpha\beta} \phi_\beta} \quad (\text{C.4})$$

Integrating out the bosonic fields yields:

$$\begin{aligned} Z[h, F] &= \text{Det} [\bar{U}^{-1}]^{-1/2} \times \int \mathcal{D}[\bar{c}, c] e^{-\bar{c}_u \{-G_{0,uv}^{-1} + F_{uv}\} c_v + \frac{1}{2} \bar{U}_{\alpha\beta} (h_\alpha - \bar{c}_u \lambda_{uv\alpha} c_v)^2} \\ &= e^{\frac{1}{2} \text{Tr} \log [\bar{U}]} \times \int \mathcal{D}[\bar{c}, c] e^{-\bar{c}_u \{-G_{0,uv}^{-1} + F_{uv}\} c_v + \frac{1}{2} \bar{U}_{\alpha\beta} (h_\alpha - \bar{c}_u \lambda_{uv\alpha} c_v)^2} \end{aligned} \quad (\text{C.5})$$

with $\bar{U}_{\alpha\beta} = [(-U^{-1} + B)]_{\alpha\beta}^{-1}$. Hence

$$\Omega = \frac{1}{2} \text{Tr} \log [-U^{-1} + B] - \log \int \mathcal{D}[\bar{c}, c] \left[e^{-\bar{c}_u \{-G_{0,uv}^{-1} + F_{uv}\} c_v} \times e^{\frac{1}{2} \bar{U}_{\alpha\beta} (h_\alpha - \bar{c}_u \lambda_{uv\alpha} c_v) (h_\beta - \bar{c}_u \lambda_{uv\beta} c_v)} \right]$$

Relation (C.1a) follows from computing φ_α by successively using (C.4) and (C.5):

$$\varphi_\alpha = \frac{1}{Z} \frac{\partial Z}{\partial h_\alpha} = U_{\alpha\beta} \langle \bar{c}_u \lambda_{uv\beta} c_v \rangle$$

Similarly, one has:

$$\begin{aligned} W_{\alpha\beta}^{\text{nc}} &= -2 \frac{\partial \Omega}{\partial B_{\alpha\beta}} \\ &= -2 \left[\frac{1}{2} (-U_{\alpha\beta}) \right] \\ &\quad -2 \left[-\frac{1}{2} \left(\frac{\partial \bar{U}_{\gamma\delta}}{\partial B_{\alpha\beta}} \right) (h_\gamma - \bar{c}_u \lambda_{uv\gamma} c_v) (h_\delta - \bar{c}_u \lambda_{uv\delta} c_v) \right] \\ &= U_{\alpha\beta} - U_{\alpha\delta} \langle (\bar{c}_u \lambda_{uv\delta} c_v) (\bar{c}_u \lambda_{uv\gamma} c_v) \rangle U_{\gamma\beta} \\ &= U_{\alpha\beta} - U_{\alpha\delta} \langle n_\delta n_\gamma \rangle U_{\gamma\beta} \end{aligned}$$

which proves (C.1b-C.1c) and:

$$\chi_{uv\alpha}^{\text{nc}} = \frac{1}{Z} \frac{\partial^2 Z}{\partial F_{vu} \partial h_\alpha} \Big|_{h=0} = \frac{1}{Z} \frac{\partial}{\partial F_{vu}} \int \mathcal{D}[\bar{c}, c] (U_{\alpha\beta} (n_\beta - h_\beta)) e^{-S} = U_{\alpha\beta} \langle c_u \bar{c}_v n_\beta \rangle$$

which proves (C.1d).



Three-point correlation function: various properties

D.1 Time-translation symmetries and Fourier properties

This section is aimed at justifying the definition of the Fourier transforms Eqs (B.1a) and (B.1b) based on the symmetry properties of the three-leg correlation function.

D.1.1 Time-translation invariance and Fourier transform with three integration variables

Let us define a generic three-point function:

$$\chi_{ijk}(\tau_1, \tau_2, \tau_3) \equiv \langle T c_i(\tau_1) c_j^\dagger(\tau_2) \phi_k(\tau_3) \rangle$$

Using the definition of the Heisenberg representation and the cyclicity of the trace, one has:

$$\chi_{ijk}(\tau_1, \tau_2, \tau_3) = \langle T c_i(\tau_1 - \tau_3) c_j^\dagger(\tau_2 - \tau_3) \phi_k(0) \rangle \equiv A_{ijk}(\tau_1 - \tau_3, \tau_2 - \tau_3) \quad (\text{D.1})$$

$$\chi_{ijk}(\tau_1, \tau_2, \tau_3) = \langle T c_i(\tau_1 - \tau_2) c_j^\dagger(0) \phi_k(\tau_3 - \tau_2) \rangle \equiv B_{ijk}(\tau_1 - \tau_2, \tau_3 - \tau_2) \quad (\text{D.2})$$

As a result of the two time-translation invariances above, one can define the very general Fourier transforms:

$$A_{ijk}(i\omega_1, i\omega_2) = \frac{1}{3! \beta} \int_0^\beta d\tau_1 \int_0^\beta d\tau_2 \int_0^\beta d\tau_3 e^{i\omega_1(\tau_1 - \tau_3) + i\omega_2(\tau_2 - \tau_3)} A_{ijk}(\tau_1 - \tau_3, \tau_2 - \tau_3)$$

$$B_{ijk}(i\Omega_1, i\Omega_2) = \frac{1}{3! \beta} \int_0^\beta d\tau_1 \int_0^\beta d\tau_2 \int_0^\beta d\tau_3 e^{i\Omega_1(\tau_1 - \tau_2) + i\Omega_2(\tau_3 - \tau_2)} B_{ijk}(\tau_1 - \tau_2, \tau_3 - \tau_2)$$

From these definitions and the relation $i\Omega_1(\tau_1 - \tau_2) + i\Omega_2(\tau_3 - \tau_2) = i\Omega_1(\tau_1 - \tau_3) + (-i\Omega_1 - i\Omega_2)(\tau_2 - \tau_3)$, one can already see that:

$$B_{ijk}(i\Omega_1, i\Omega_2) = \frac{1}{3! \beta} \int_0^\beta d\tau_1 \int_0^\beta d\tau_2 \int_0^\beta d\tau_3 e^{i\Omega_1(\tau_1 - \tau_3) + (-i\Omega_1 - i\Omega_2)(\tau_2 - \tau_3)} A_{ijk}(\tau_1 - \tau_3, \tau_2 - \tau_3) = A_{ijk}(i\Omega_1, -i\Omega_1 - i\Omega_2) \quad (\text{D.3})$$

Note that $i\omega_1$ and $i\omega_2$ are fermionic frequencies, $i\Omega_1$ is a fermionic frequency, $i\Omega_2$ is a bosonic frequency. Let us define the two changes of variables $\tau = \tau_1 - \tau_3$, $\tau' = \tau_2 - \tau_3$ and $\tilde{\tau}_3 = \tau_3$ for A_{ijk} and $\tau = \tau_1 - \tau_2$, $\tau' = \tau_3 - \tau_2$ and $\tilde{\tau}_3 = \tau_3$ for B_{ijk} . In both cases the Jacobian is 1. The integration domain for the transformed variables τ and τ' is the union of all the orange and grey domains in Fig D.1. Since the integrand no longer depends on τ_3 , $\int_0^\beta d\tau_3$ just contributes a factor β . We now want to reduce the integration domain to the domains A and B using the symmetry properties of A_{ijk} and B_{ijk} .

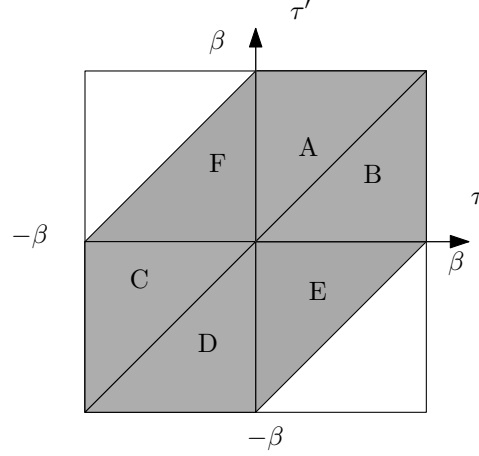


Figure D.1: Integration domain

D.1.2 Periodicities of the three-point functions

D.1.2.1 $A(\tau, \tau')$

Let us take $(\tau, \tau') \in C$, i.e. $0 > \tau' > \tau > -\beta$. Using the cyclicity of the trace and the properties of the time-ordering operator, we get:

$$\begin{aligned} A(\tau, \tau') &= \langle T c_i(\tau) c_j^\dagger(\tau') \phi_k(0) \rangle = -\langle \phi_k(0) c_j^\dagger(\tau') c_i(\tau) \rangle \\ A(\tau + \beta, \tau') &= \langle T c_i(\tau + \beta) c_j^\dagger(\tau') \phi_k(0) \rangle = \langle c_i(\tau + \beta) \phi_k(0) c_j^\dagger(\tau') \rangle = \langle \phi_k(0) c_j^\dagger(\tau') c_i(\tau) \rangle \\ A(\tau + \beta, \tau' + \beta) &= \langle T c_i(\tau + \beta) c_j^\dagger(\tau' + \beta) \phi_k(0) \rangle = -\langle c_j^\dagger(\tau' + \beta) c_i(\tau + \beta) \phi_k(0) \rangle = -\langle \phi_k(0) c_j^\dagger(\tau') c_i(\tau) \rangle \end{aligned}$$

i.e

$$\begin{aligned} A(\tau + \beta, \tau') &= -A(\tau, \tau') \\ A(\tau + \beta, \tau' + \beta) &= A(\tau, \tau') \end{aligned}$$

Let us now take $(\tau, \tau') \in D$, i.e. $0 > \tau > \tau' > -\beta$. Similarly:

$$\begin{aligned} A(\tau, \tau') &= \langle T c_i(\tau) c_j^\dagger(\tau') \phi_k(0) \rangle = \langle \phi_k(0) c_i(\tau) c_j^\dagger(\tau') \rangle \\ A(\tau, \tau' + \beta) &= \langle T c_i(\tau) c_j^\dagger(\tau' + \beta) \phi_k(0) \rangle = -\langle c_j^\dagger(\tau' + \beta) \phi_k(0) c_i(\tau) \rangle = -\langle \phi_k(0) c_i(\tau) c_j^\dagger(\tau') \rangle \\ A(\tau + \beta, \tau' + \beta) &= \langle T c_i(\tau + \beta) c_j^\dagger(\tau' + \beta) \phi_k(0) \rangle = \langle c_i(\tau + \beta) c_j^\dagger(\tau' + \beta) \phi_k(0) \rangle = \langle \phi_k(0) c_i(\tau) c_j^\dagger(\tau') \rangle \end{aligned}$$

i.e

$$\begin{aligned} A(\tau, \tau' + \beta) &= -A(\tau, \tau') \\ A(\tau + \beta, \tau' + \beta) &= A(\tau, \tau') \end{aligned}$$

D.1.2.2 $B(\tau, \tau')$

Let us take $(\tau, \tau') \in C$, i.e. $0 > \tau' > \tau > -\beta$.

$$\begin{aligned} B(\tau, \tau') &= \langle T c_i(\tau) c_j^\dagger(0) \phi_k(\tau') \rangle = -\langle c_j^\dagger(0) \phi_k(\tau') c_i(\tau) \rangle \\ B(\tau + \beta, \tau') &= \langle T c_i(\tau + \beta) c_j^\dagger(0) \phi_k(\tau') \rangle = \langle c_i(\tau + \beta) c_j^\dagger(0) \phi_k(\tau') \rangle = \langle c_j^\dagger(0) \phi_k(\tau') c_i(\tau) \rangle \\ B(\tau + \beta, \tau' + \beta) &= \langle T c_i(\tau + \beta) c_j^\dagger(0) \phi_k(\tau' + \beta) \rangle = \langle \phi_k(\tau' + \beta) c_i(\tau + \beta) c_j^\dagger(0) \rangle = \langle c_j^\dagger(0) \phi_k(\tau') c_i(\tau) \rangle \end{aligned}$$

i.e

$$B(\tau + \beta, \tau') = B(\tau, \tau') \quad (\text{D.4})$$

$$B(\tau + \beta, \tau' + \beta) = B(\tau, \tau') \quad (\text{D.5})$$

Note the absence of a minus sign. For $(\tau, \tau') \in D$, i.e. $0 > \tau > \tau' > -\beta$:

$$\begin{aligned} B(\tau, \tau') &= \langle T c_i(\tau) c_j^\dagger(0) \phi_k(\tau') \rangle = -\langle c_j^\dagger(0) c_i(\tau) \phi_k(\tau') \rangle \\ B(\tau, \tau' + \beta) &= \langle T c_i(\tau) c_j^\dagger(0) \phi_k(\tau' + \beta) \rangle = -\langle \phi_k(\tau' + \beta) c_j^\dagger(0) c_i(\tau) \rangle \\ B(\tau + \beta, \tau' + \beta) &= \langle T c_i(\tau + \beta) c_j^\dagger(0) \phi_k(\tau' + \beta) \rangle = \langle T c_i(\tau + \beta) \phi_k(\tau' + \beta) c_j^\dagger(0) \rangle \end{aligned}$$

i.e

$$B(\tau, \tau' + \beta) = B(\tau, \tau') \quad (\text{D.6})$$

$$B(\tau + \beta, \tau' + \beta) = -B(\tau, \tau') \quad (\text{D.7})$$

Note that in particular:

$$B(0^-, 0^-) = -B(\beta^-, \beta^-)$$

Since, on the other hand,

$$B_{ik}(0^-, 0^-) = \langle T c_i(0^-) c_i^\dagger(0) n_k(0^-) \rangle = -\langle c_i^\dagger(0) c_i(0^-) n_k(0^-) \rangle = -\langle n_i n_k \rangle$$

we obtain:

$$\langle n_i n_k \rangle = -B_{ik}(0^-, 0^-) = B_{ik}(\beta^-, \beta^-) \quad (\text{D.8})$$

D.1.3 Fourier transform on the reduced domain

D.1.3.0.1 $A(i\omega_1, i\omega_2)$ Once can write

$$\begin{aligned} A_{ijk}(i\omega_1, i\omega_2) &= \frac{1}{3!} \iint_{ABCDEF} d\tau d\tau' e^{i\omega_1 \tau + i\omega_2 \tau'} A_{ijk}(\tau, \tau') \\ &= \frac{1}{3!} \iint_{AB} d\tau d\tau' e^{i\omega_1 \tau + i\omega_2 \tau'} A_{ijk}(\tau, \tau') + \frac{1}{3!} \iint_{CD} d\tau d\tau' e^{i\omega_1 \tau + i\omega_2 \tau'} A_{ijk}(\tau, \tau') + \frac{1}{3!} \iint_{EF} d\tau d\tau' e^{i\omega_1 \tau + i\omega_2 \tau'} A_{ijk}(\tau, \tau') \end{aligned}$$

The integration domains A, B, \dots are defined in Fig. D.1. One has:

$$\begin{aligned} \iint_{CD} d\tau d\tau' e^{i\omega_1 \tau + i\omega_2 \tau'} A_{ijk}(\tau, \tau') &= \iint_{AB} d\tau d\tau' e^{i\omega_1(\tau-\beta) + i\omega_2(\tau'-\beta)} A_{ijk}(\tau - \beta, \tau' - \beta) \\ &= e^{-i\omega_1 \beta - i\omega_2 \beta} \iint_{AB} d\tau d\tau' e^{i\omega_1 \tau + i\omega_2 \tau'} A_{ijk}(\tau, \tau') \end{aligned}$$

and

$$\begin{aligned} \iint_{EF} d\tau d\tau' e^{i\omega_1 \tau + i\omega_2 \tau'} A_{ijk}(\tau, \tau') &= \iint_E d\tau d\tau' e^{i\omega_1 \tau + i\omega_2 \tau'} A_{ijk}(\tau, \tau') + \iint_F d\tau d\tau' e^{i\omega_1 \tau + i\omega_2 \tau'} A_{ijk}(\tau, \tau') \\ &= \iint_A d\tau d\tau' e^{i\omega_1 \tau + i\omega_2(\tau'-\beta)} A_{ijk}(\tau, \tau' - \beta) + \iint_B d\tau d\tau' e^{i\omega_1(\tau-\beta) + i\omega_2 \tau'} A_{ijk}(\tau - \beta, \tau') \\ &= -e^{-i\omega_2 \beta} \iint_A d\tau d\tau' e^{i\omega_1 \tau + i\omega_2 \tau'} A_{ijk}(\tau, \tau') - e^{-i\omega_1 \beta} \iint_B d\tau d\tau' e^{i\omega_1 \tau + i\omega_2 \tau'} A_{ijk}(\tau, \tau') \end{aligned}$$

so that:

$$\begin{aligned}
A_{ijk}(i\omega_1, i\omega_2) &= \frac{1}{3} \iint_{AB} d\tau d\tau' e^{i\omega_1\tau + i\omega_2\tau'} A_{ijk}(\tau, \tau') + \frac{1}{3} e^{-i\omega_1\beta - i\omega_2\beta} \iint_{AB} d\tau d\tau' e^{i\omega_1\tau + i\omega_2\tau'} A_{ijk}(\tau, \tau') \\
&\quad - \frac{1}{3} e^{-i\omega_2\beta} \iint_A d\tau d\tau' e^{i\omega_1\tau + i\omega_2\tau'} A_{ijk}(\tau, \tau') - \frac{1}{3} e^{-i\omega_1\beta} \iint_B d\tau d\tau' e^{i\omega_1\tau + i\omega_2\tau'} A_{ijk}(\tau, \tau') \\
&= \frac{1}{3} \iint_{AB} d\tau d\tau' e^{i\omega_1\tau + i\omega_2\tau'} A_{ijk}(\tau, \tau') \\
&\quad + \frac{1}{3} (e^{-i\omega_1\beta} - 1) e^{-i\omega_2\beta} \iint_A d\tau d\tau' e^{i\omega_1\tau + i\omega_2\tau'} A_{ijk}(\tau, \tau') + \frac{1}{3} (e^{-i\omega_2\beta} - 1) e^{-i\omega_1\beta} \iint_B d\tau d\tau' e^{i\omega_1\tau + i\omega_2\tau'} A_{ijk}(\tau, \tau') \\
&= \frac{1}{3} \iint_{AB} d\tau d\tau' e^{i\omega_1\tau + i\omega_2\tau'} A_{ijk}(\tau, \tau') + \frac{2}{3} \iint_A d\tau d\tau' e^{i\omega_1\tau + i\omega_2\tau'} A_{ijk}(\tau, \tau') + \frac{2}{3} \iint_B d\tau d\tau' e^{i\omega_1\tau + i\omega_2\tau'} A_{ijk}(\tau, \tau') \\
&= \iint_{AB} d\tau d\tau' e^{i\omega_1\tau + i\omega_2\tau'} A_{ijk}(\tau, \tau')
\end{aligned}$$

$i\omega_1$ and $i\omega_2$ being fermionic Matsubara frequencies,

$$A_{ijk}(i\omega_1, i\omega_2) = \int_0^\beta d\tau \int_0^\beta d\tau' e^{i\omega_1\tau + i\omega_2\tau'} A_{ijk}(\tau, \tau')$$

D.1.3.0.2 $B(i\Omega_1, i\Omega_2)$ The same calculation as for $A(i\omega_1, i\omega_2)$ carries over except for a few minus signs:

$$\begin{aligned}
B_{ijk}(i\omega_1, i\omega_2) &= \frac{1}{3} \iint_{AB} d\tau d\tau' e^{i\omega_1\tau + i\omega_2\tau'} B_{ijk}(\tau, \tau') - \frac{1}{3} e^{-i\omega_1\beta - i\omega_2\beta} \iint_{AB} d\tau d\tau' e^{i\omega_1\tau + i\omega_2\tau'} B_{ijk}(\tau, \tau') \\
&\quad + \frac{1}{3} e^{-i\omega_2\beta} \iint_A d\tau d\tau' e^{i\omega_1\tau + i\omega_2\tau'} B_{ijk}(\tau, \tau') - \frac{1}{3} e^{-i\omega_1\beta} \iint_B d\tau d\tau' e^{i\omega_1\tau + i\omega_2\tau'} B_{ijk}(\tau, \tau') \\
&= \frac{1}{3} \iint_{AB} d\tau d\tau' e^{i\omega_1\tau + i\omega_2\tau'} B_{ijk}(\tau, \tau') \\
&\quad + \frac{1}{3} (-e^{-i\omega_1\beta} + 1) e^{-i\omega_2\beta} \iint_A d\tau d\tau' e^{i\omega_1\tau + i\omega_2\tau'} B_{ijk}(\tau, \tau') + \frac{1}{3} (-e^{-i\omega_2\beta} - 1) e^{-i\omega_1\beta} \iint_B d\tau d\tau' e^{i\omega_1\tau + i\omega_2\tau'} B_{ijk}(\tau, \tau') \\
&= \frac{1}{3} \iint_{AB} d\tau d\tau' e^{i\omega_1\tau + i\omega_2\tau'} B_{ijk}(\tau, \tau') + \frac{2}{3} \iint_A d\tau d\tau' e^{i\omega_1\tau + i\omega_2\tau'} B_{ijk}(\tau, \tau') + \frac{2}{3} \iint_B d\tau d\tau' e^{i\omega_1\tau + i\omega_2\tau'} B_{ijk}(\tau, \tau') \\
&= \iint_{AB} d\tau d\tau' e^{i\omega_1\tau + i\omega_2\tau'} B_{ijk}(\tau, \tau')
\end{aligned}$$

$i\omega_1$ and $i\omega_2$ being fermionic Matsubara frequencies,

$$B_{ijk}(i\Omega_1, i\Omega_2) = \int_0^\beta d\tau \int_0^\beta d\tau' e^{i\Omega_1\tau + i\Omega_2\tau'} B_{ijk}(\tau, \tau')$$

Defining $\hat{\chi}_{ijk}(i\omega_1, i\omega_2) = A_{ijk}(i\omega_1, i\omega_2)$ and $\chi_{ijk}(i\omega, i\Omega) = B_{ijk}(i\omega, i\Omega)$, one obtains the Fourier conventions of section B.1.2.

D.2 Symmetries in the $(i\omega, i\Omega)$ plane

In this section, we derive the main symmetries of the three-point vertex for a simple limiting case. We consider the most simple fermionic model, namely a single fermionic level, $O_1 = c^\dagger$, $O_2 = c$. $O_1^\dagger = O_2$ (in the notations of Section I.1.3.3). The Hilbert space consists in two states: $|0\rangle$ and $|1\rangle$ with respective energies 0

and ϵ . Starting from I.13, we have:

$$\begin{aligned}\hat{\chi}(i\omega_1, i\omega_2) &= \frac{1}{Z} \sum_{ijk} \langle i|O_1|j\rangle \langle j|O_2|k\rangle \langle k|n|i\rangle f(\omega_1, \omega_2) + \underbrace{\sum_{ijk} \langle i|O_2|j\rangle \langle j|O_1|k\rangle \langle k|n|i\rangle f(\omega_2, \omega_1)}_{=0} \\ &= \frac{1}{Z} \langle 1|c^\dagger|0\rangle \langle 0|c|1\rangle \langle 1|n|1\rangle f(\omega_1, \omega_2) = \frac{1}{Z} f_{101}(\omega_1, \omega_2) \\ &= \frac{1}{Z} \frac{1}{i\omega_2 - \epsilon} \left(\frac{1 + e^{-\beta\epsilon}}{i\omega_1 + \epsilon} \right) + \frac{1}{Z} \frac{e^{-\beta\epsilon}}{i\omega_2 - \epsilon} \delta_{i\omega_1 + i\omega_2}\end{aligned}$$

Hence,

$$\tilde{\chi}(i\omega, i\Omega) \propto \frac{1}{-i\omega - i\Omega - \epsilon} \frac{1}{i\omega + \epsilon} + \frac{1}{-i\omega - \epsilon} \delta_{i\Omega} \propto \frac{1}{i\omega + i\Omega + \epsilon} \frac{1}{i\omega + \epsilon} + \frac{1}{i\omega + \epsilon} \delta_{i\Omega}$$

One can notice:

$$\tilde{\chi}(i\omega - i\Omega, i\Omega) \propto \frac{1}{i\omega + \epsilon} \frac{1}{i\omega - i\Omega + \epsilon} + \frac{1}{i\omega - i\Omega + \epsilon} \delta_{i\Omega} = \chi(i\omega, -i\Omega)$$

and:

$$\tilde{\chi}^*(i\omega, -i\Omega) \propto \left(\frac{1}{i\omega - i\Omega + \epsilon} \frac{1}{i\omega + \epsilon} + \frac{1}{i\omega + \epsilon} \delta_{i\Omega} \right)^* = \frac{1}{-i\omega + \epsilon} \frac{1}{i\Omega - i\omega + \epsilon} + \frac{1}{-i\omega + \epsilon} \delta_{i\Omega} = \tilde{\chi}(-i\omega, i\Omega)$$

To summarize, we obtain the following symmetry relations:

$$\tilde{\chi}(i\omega - i\Omega, i\Omega) = \tilde{\chi}(i\omega, -i\Omega) \quad (\text{D.9a})$$

$$\tilde{\chi}^*(i\omega, -i\Omega) = \tilde{\chi}(-i\omega, i\Omega) \quad (\text{D.9b})$$

One can check that these symmetry relations hold in the general case and carry over to the vertex $\Lambda(i\omega, i\Omega)$, see Eqs (8.69a-8.69b).

D.3 Partial sum on Matsubara frequencies

The three-point correlation function is defined as $\chi(i\omega, i\Omega) = \int_0^\beta d\tau \int_0^\beta d\tau' e^{i\omega\tau} e^{i\Omega\tau'} \langle T c_\sigma(\tau) c_\sigma^\dagger(0) n_{\sigma'}(\tau') \rangle$.

D.3.1 Sum on bosonic frequencies

Let us compute

$$\begin{aligned}\frac{1}{\beta} \sum_{i\Omega} \chi_{\sigma\sigma'}(i\omega, i\Omega) &= \int_0^\beta d\tau \int_0^\beta d\tau' e^{i\omega\tau} \underbrace{\frac{1}{\beta} \sum_{i\Omega} e^{i\Omega\tau'} \langle T c_\sigma(\tau) c_\sigma^\dagger(0) n_{\sigma'}(\tau') \rangle}_{\delta_{\tau'/2}} \\ &= \frac{1}{2} \int_0^\beta d\tau e^{i\omega\tau} \langle T c_\sigma(\tau) c_\sigma^\dagger(0) n_{\sigma'}(0^+) \rangle \\ &= -\frac{1}{2} \int_0^\beta d\tau e^{i\omega\tau} \langle T c_\sigma(\tau) n_{\sigma'}(0^+) c_\sigma^\dagger(0) \rangle\end{aligned}$$

If $\sigma = \sigma'$, $n_\sigma c_\sigma^\dagger = c_\sigma^\dagger$, i.e

$$\frac{1}{\beta} \sum_{i\Omega} \chi_{\sigma\sigma}(i\omega, i\Omega) = -\frac{1}{2} \int_0^\beta d\tau e^{i\omega\tau} \langle T c_\sigma(\tau) c_\sigma^\dagger(0) \rangle = \frac{1}{2} G_\sigma(i\omega) \quad (\text{D.10})$$

D.3.2 Sum on fermionic frequencies

Now

$$\begin{aligned}
\frac{1}{\beta} \sum_{i\omega} \chi_{\sigma\sigma'}(i\omega, i\Omega) &= \int_0^\beta d\tau \int_0^\beta d\tau' \underbrace{\frac{1}{\beta} \sum_{i\omega} e^{i\omega\tau} e^{i\Omega\tau'}}_{\delta_{\tau/2}} \langle T c_\sigma(\tau) c_\sigma^\dagger(0) n_{\sigma'}(\tau') \rangle \\
&= \frac{1}{2} \int_0^\beta d\tau' e^{i\Omega\tau'} \langle T c_\sigma(0^+) c_\sigma^\dagger(0) n_{\sigma'}(\tau') \rangle \\
&= \frac{1}{2} \int_0^\beta d\tau' e^{i\Omega\tau'} \langle T n_{\sigma'}(\tau') c_\sigma(0^+) c_\sigma^\dagger(0) \rangle \\
&= \frac{1}{2} \int_0^\beta d\tau' e^{i\Omega\tau'} \langle n_{\sigma'}(\tau') c_\sigma(0^+) c_\sigma^\dagger(0) \rangle \\
&= \frac{1}{2} \int_0^\beta d\tau' e^{i\Omega\tau'} \langle n_{\sigma'}(\tau') \{1 - n_\sigma\} \rangle \\
&= \frac{1}{2} \int_0^\beta d\tau' e^{i\Omega\tau'} \langle n_{\sigma'}(\tau') \rangle - \frac{1}{2} \int_0^\beta d\tau' e^{i\Omega\tau'} \langle n_{\sigma'}(\tau') n_\sigma \rangle \\
&= \frac{1}{2} \langle n_{\sigma'} \rangle \beta \delta_{i\Omega} - \frac{1}{2} \chi_{\sigma'\sigma}(i\Omega)
\end{aligned} \tag{D.11}$$

D.4 High-frequency expansion of the three-point correlation function

Let us consider the correlation function: $\chi(\tau_1, \tau_2, \tau_3) = \langle T c(\tau_1) c^\dagger(\tau_2) \phi(\tau_3) \rangle$ and its Fourier transform $\chi(i\omega, i\Omega)$. We want to study the asymptotic behavior of $\chi(i\omega, i\Omega)$ by counting the number of lines and vertices in the diagrams at each order of the perturbation expansion.

Let us consider the perturbation expansion of χ :

$$\chi(\tau_1, \tau_2, \tau_3) = \sum_{n=0}^{\infty} \frac{(-)^n}{n!} \int_0^\beta d\bar{\tau}_1 \dots \int_0^\beta d\bar{\tau}_n \lambda^n \underbrace{\langle T c(\tau_1) c^\dagger(\tau_2) \phi(\tau_3) \{ c(\bar{\tau}_1) c^\dagger(\bar{\tau}_1) \phi(\bar{\tau}_1) \dots c(\bar{\tau}_n) c^\dagger(\bar{\tau}_n) \phi(\bar{\tau}_n) \} \rangle_0}_{A_n}$$

where $\langle \dots \rangle_0$ corresponds to the average taken with the quadratic part of the action, the interacting part being $S_{\text{int}} = \lambda \int d\tau c(\tau) c^\dagger(\tau) \phi(\tau)$. The term denoted as A_n can be broken down in a product of non-interacting propagators $G_0(\tau) = -\langle T c(\tau) c^\dagger(0) \rangle_0$ and $W_0(\tau) = -\langle T \phi(\tau) \phi(0) \rangle_0$ via Wick's theorem. Pictorially, the term of order n contains n vertices λ . We are looking for the relation between the number of such vertices and the number of lines. Note that when n is even the average value vanishes, so that only odd terms remain.

First of all, note that as a consequence of the form of the interactions, $N_G = 2N_W$ where N_G (resp. N_W) is the number of G_0 (resp. W_0) propagators. Let us define $N \equiv N_G + N_W$. Let us already notice that for $n = 1$, there are $N_1 = 3$ lines. For $n = 3$, $N_3 = 6$, etc. One can notice that adding two vertices to a diagram leads to 3 additional lines, so that $N_{n+2} = N_n + 3$. This recurrence relation and the initial conditions lead to

$$N_n = \frac{3}{2} (n + 1) \tag{D.12}$$

Let us now find the relation between the number of internal summations on Matsubara frequencies, I , and the number of vertices n . We can notice that $I_{n=1} = 0$, $I_{n=3} = 1$, etc. Adding two vertices leads to one additional internal summation, namely $I_{n+2} = I_n + 1$, leading to

$$I_n = \frac{1}{2} (n - 1) \tag{D.13}$$

Let us now determine the asymptotic behavior of one diagram by first noting that G_0 lines behave as $1/i\omega$ while W_0 lines behave as constants, so that a given line behaves as $1/\omega^{2/3}$ on average. If a given diagram

behaves as $1/\omega^p$ we will call it of asymptotic order p . One line contributes $2/3$ to the asymptotic order, while one internal summation reduces the asymptotic order by 1: $p = \frac{2}{3}N - I$. Combining (D.12) and (D.13) leads to

$$p = n + 1 - \frac{1}{2}(n - 1) = \frac{n + 3}{2} \quad (\text{D.14})$$

One can thus see that as one could have expected, the dominant term at high Matsubara frequencies is the $n = 1$ term,

$$\lim_{\substack{i\Omega \rightarrow \infty \\ i\omega \rightarrow \infty}} \chi(i\omega, i\Omega) = \chi_{n=1}(i\omega, i\Omega) = \lambda G_0(i\omega + i\Omega)G_0(i\omega)W_0(i\Omega) \sim \lambda \frac{1}{i\omega + i\Omega} \frac{1}{i\omega}$$

If we construct the vertex as $\Lambda(i\omega, i\Omega) \equiv \chi(i\omega, i\Omega)/G(i\omega + i\Omega)G(i\omega)W(i\Omega)$, we see that asymptotically,

$$\Lambda(i\omega, i\Omega) \rightarrow \lambda$$

which is the non-interacting value, the bare vertex. This dictates the following definition for the ‘‘regular’’ part of the vertex:

$$\Lambda^{reg}(i\omega, i\Omega) = \frac{\chi(i\omega, i\Omega) - \lambda G(i\omega + i\Omega)G(i\omega)W(i\Omega)}{G(i\omega + i\Omega)G(i\omega)W(i\Omega)}$$

which vanishes for high frequencies.

D.5 Equations of motion for the three-point function, and Ward identity

Let us define

$$\chi_{k,q,k'}^{uvI}(\tau_1, \tau_2, \tau_3) \equiv \langle T_\tau A(\tau_1)B(\tau_2)C(\tau_3) \rangle \quad (\text{D.15})$$

with: $A = s_{k',q}^I = c_{w,k'-q}^\dagger \sigma_{wl}^I c_{l,k'}$, $B = c_{u,k+q}^\dagger$ and $C = c_{v,k}$ ($u, v = \uparrow, \downarrow$, $I = 0, x, y, z$).

D.5.1 Equation of motion

Differentiating χ with respect to τ_1 , one gets (see D.5.2 for details):

$$\partial_{\tau_1} \chi_{k,q,k'}^{uvI}(\tau_1, \tau_2, \tau_3) = \langle T_\tau [H, A](\tau_1)B(\tau_2)C(\tau_3) \rangle + \delta(\tau_1 - \tau_2) \langle T_\tau [A, B](\tau_1)C(\tau_3) \rangle + \delta(\tau_1 - \tau_3) \langle T_\tau B(\tau_2)[A, C](\tau_1) \rangle \quad (\text{D.16})$$

Hence, reinstating the momenta, summing over k' , and replacing by the commutators (see D.5.3 for details), one gets:

$$\begin{aligned} \sum_{k'} \partial_{\tau_1} \chi_{k,q,k'}^{uvI}(\tau_1, \tau_2, \tau_3) &= \sum_{k'} (\varepsilon_{k'-q} - \varepsilon_{k'}) \langle T_\tau \left(\mathbf{c}_{k'-q}^\dagger(\tau_1) \underline{\sigma}^I \mathbf{c}_{k'}(\tau_1) \right) c_{u,k+q}^\dagger(\tau_2) c_{v,k}(\tau_3) \rangle \\ &+ \delta(\tau_1 - \tau_2) \sigma_{wu}^I \delta_{k',k+q} \langle T_\tau c_{w,k'-q}^\dagger(\tau_1) c_{v,k}(\tau_3) \rangle \\ &- \delta(\tau_1 - \tau_3) \sigma_{vl}^I \delta_{k'+q,k} \langle T_\tau c_{u,k+q}^\dagger(\tau_2) c_{l,k'}(\tau_1) \rangle \end{aligned}$$

Replacing by the definition of G and rearranging terms:

$$\sum_{k'} \left[\partial_{\tau_1} - (\varepsilon_{k'-q} - \varepsilon_{k'}) \right] \chi_{k,q,k'}^{uvI}(\tau_1, \tau_2, \tau_3) = \delta(\tau_1 - \tau_2) \sigma_{wu}^I G_{vw}(k, \tau_3 - \tau_1) - \delta(\tau_1 - \tau_3) \sigma_{vl}^I G_{lu}(k + q, \tau_1 - \tau_2) \quad (\text{D.17})$$

Transforming to momentum/frequency space, one obtains Eq. (8.71) of the main text. In the zero-bandwidth limit,

$$i\Omega \chi^{uvI}(i\omega, i\Omega) = \sigma_{vu}^I \left[G_u^{\text{at}}(i\omega + i\Omega) - G_v^{\text{at}}(i\omega) \right] \quad (\text{D.18})$$

and the vertex reads (for $i\Omega \neq 0$):

$$\Lambda^{uvI}(i\omega, i\Omega) = \sigma_{vu}^I \frac{\chi^{uvI}(i\omega, i\Omega)}{G_u^{\text{at}}(i\omega + i\Omega)G_v^{\text{at}}(i\omega)} = \sigma_{vu}^I \frac{G_v^{-1}(i\omega) - G_u^{-1}(i\omega + i\Omega)}{i\Omega} = 1 + \frac{\Sigma^{\text{at}}(i\omega) - \Sigma^{\text{at}}(i\omega + i\Omega)}{i\Omega} = 1 + \frac{U^2}{4} \frac{1}{i\omega(i\omega + i\Omega)}$$

D.5.2 Differentiating the time-ordered product

Explicitly writing the time-ordering operator (dropping the momentum indices), one gets:

$$\begin{aligned} \chi^{uvI}(\tau_1, \tau_2, \tau_3) &= \theta(\tau_1 > \tau_2 > \tau_3) \langle A(\tau_1)B(\tau_2)C(\tau_3) \rangle \\ &- \theta(\tau_1 > \tau_3 > \tau_2) \langle A(\tau_1)C(\tau_3)B(\tau_2) \rangle \\ &+ \theta(\tau_2 > \tau_1 > \tau_3) \langle B(\tau_2)A(\tau_1)C(\tau_3) \rangle \\ &+ \theta(\tau_2 > \tau_3 > \tau_1) \langle B(\tau_2)C(\tau_3)A(\tau_1) \rangle \\ &- \theta(\tau_3 > \tau_1 > \tau_2) \langle C(\tau_3)A(\tau_1)B(\tau_2) \rangle \\ &- \theta(\tau_3 > \tau_2 > \tau_1) \langle C(\tau_3)B(\tau_2)A(\tau_1) \rangle \end{aligned}$$

The signs come from the fact that A commutes with B and C , B and C anticommute with each other. We note that: $\theta(\tau_i > \tau_j > \tau_k) = \theta(\tau_i - \tau_j)\theta(\tau_j - \tau_k)$. Differentiation with respect to τ_1 yields:

$$\begin{aligned} \partial_{\tau_1} \chi^{uvI}(\tau_1, \tau_2, \tau_3) &= \langle T_\tau [\partial_{\tau_1} A(\tau_1)] B(\tau_2)C(\tau_3) \rangle \\ &+ \delta(\tau_1 - \tau_2)\theta(\tau_2 - \tau_3) \langle A(\tau_1)B(\tau_2)C(\tau_3) \rangle \\ &- \delta(\tau_1 - \tau_3)\theta(\tau_3 - \tau_2) \langle A(\tau_1)C(\tau_3)B(\tau_2) \rangle \\ &+ (-)\delta(\tau_2 - \tau_1)\theta(\tau_1 - \tau_3) \langle B(\tau_2)A(\tau_1)C(\tau_3) \rangle \\ &+ \theta(\tau_2 - \tau_1)\delta(\tau_1 - \tau_3) \langle B(\tau_2)A(\tau_1)C(\tau_3) \rangle \\ &+ \theta(\tau_2 - \tau_3)(-)\delta(\tau_3 - \tau_1) \langle B(\tau_2)C(\tau_3)A(\tau_1) \rangle \\ &- (-)\delta(\tau_3 - \tau_1)\theta(\tau_1 - \tau_2) \langle C(\tau_3)A(\tau_1)B(\tau_2) \rangle \\ &- \theta(\tau_3 - \tau_1)\delta(\tau_1 - \tau_2) \langle C(\tau_3)A(\tau_1)B(\tau_2) \rangle \\ &- \theta(\tau_3 - \tau_2)(-)\delta(\tau_2 - \tau_1) \langle C(\tau_3)B(\tau_2)A(\tau_1) \rangle \end{aligned}$$

Regrouping terms:

$$\begin{aligned} \partial_{\tau_1} \chi^{uvI}(\tau_1, \tau_2, \tau_3) &= \langle T_\tau [\partial_{\tau_1} A(\tau_1)] B(\tau_2)C(\tau_3) \rangle \\ &+ \delta(\tau_1 - \tau_2)\theta(\tau_2 - \tau_3) \langle [A(\tau_1), B(\tau_2)]C(\tau_3) \rangle \\ &- \delta(\tau_1 - \tau_3)\theta(\tau_3 - \tau_2) \langle [A(\tau_1), C(\tau_3)]B(\tau_2) \rangle \\ &+ \theta(\tau_2 - \tau_1)\delta(\tau_1 - \tau_3) \langle B(\tau_2)[A(\tau_1), C(\tau_3)] \rangle \\ &- \theta(\tau_3 - \tau_1)\delta(\tau_1 - \tau_2) \langle C(\tau_3)[A(\tau_1), B(\tau_2)] \rangle \end{aligned}$$

This yields (D.16).

D.5.3 Computation of the commutators

D.5.3.1 Commutation rules

I recall

$$\begin{aligned}
[c_a^\dagger, c_b^\dagger] &= c_a^\dagger c_b^\dagger - c_b^\dagger c_a^\dagger = c_a^\dagger c_b^\dagger + c_a^\dagger c_b^\dagger = 2c_a^\dagger c_b^\dagger \\
[c_a^\dagger, c_b] &= c_a^\dagger c_b - c_b c_a^\dagger = c_a^\dagger c_b - (\delta_{ab} - c_a^\dagger c_b) = 2c_a^\dagger c_b - \delta_{ab} \\
\{c_a^\dagger, c_b\} &= \delta_{ab} \\
\{c_a^\dagger, c_b^\dagger\} &= 0
\end{aligned}$$

D.5.3.2 $[A, B]$ and $[A, C]$

Let us compute the anticommutators:

$$\begin{aligned}
[A, B] &= [c_{w, k'-q}^\dagger \sigma_{wl}^I c_{l, k'}, c_{u, k+q}^\dagger] \\
&= \sigma_{wl}^I \left(c_{w, k'-q}^\dagger [c_{l, k'}, c_{u, k+q}^\dagger] + [c_{w, k'-q}^\dagger, c_{u, k+q}^\dagger] c_{l, k'} \right) \\
&= \sigma_{wl}^I \left(-2c_{w, k'-q}^\dagger c_{u, k+q}^\dagger c_{l, k'} + c_{w, k'-q}^\dagger \delta_{lu} \delta_{k', k+q} + 2c_{w, k'+q}^\dagger c_{u, k+q}^\dagger c_{l, k'} \right) \\
&= c_{w, k'-q}^\dagger \sigma_{wu}^I \delta_{k', k+q}
\end{aligned}$$

and:

$$\begin{aligned}
[A, C] &= [c_{w, k'-q}^\dagger \sigma_{wl}^I c_{l, k'}, c_{v, k}] \\
&= \sigma_{wl}^I (c_{w, k'-q}^\dagger [c_{l, k'}, c_{v, k}] + [c_{w, k'-q}^\dagger, c_{v, k}] c_{l, k'}) \\
&= \sigma_{wl}^I (c_{w, k'-q}^\dagger [2c_{l, k'} c_{v, k}] + [2c_{w, k'-q}^\dagger c_{v, k} - \delta_{wv} \delta_{k'-q, k}] c_{l, k'}) \\
&= \sigma_{wl}^I \left(\underbrace{2c_{w, k'-q}^\dagger c_{l, k'} c_{v, k} + 2c_{w, k'-q}^\dagger c_{l, k'} c_{v, k} - \delta_{wv} c_{l, k'} \delta_{k'-q, k}}_{=0} \right) \\
&= -\sigma_{vl}^I c_{l, k'} \delta_{k'-q, k}
\end{aligned}$$

D.5.4 $[H, s^I]$

Let us define: $H = \sum_{kw} \varepsilon_k c_{w, k}^\dagger c_{w, k} + \frac{1}{2} U^I \sum_{q'} n_{q'}^I n_{-q'}^I \equiv H_{\text{kin}} + H_{\text{int}}$. Let us compute:

$$[H_{\text{kin}}, s_{k', q}^I] = \sum_{kw} \varepsilon_k \left[c_{w, k}^\dagger c_{w, k}, c_{u, k'-q}^\dagger \sigma_{uv}^I c_{v, k'} \right] = \sum_{kw} \varepsilon_k \sigma_{uv}^I \left[c_{w, k}^\dagger c_{w, k}, c_{u, k'-q}^\dagger c_{v, k'} \right]$$

with:

$$\begin{aligned}
\left[c_{w,k}^\dagger c_{w,k}, c_{u,k'-q}^\dagger c_{v,k'} \right] &= c_{w,k}^\dagger \left[c_{w,k}, c_{u,k'-q}^\dagger c_{v,k'} \right] + \left[c_{w,k}^\dagger, c_{u,k'-q}^\dagger c_{v,k'} \right] c_{w,k} \\
&= c_{w,k}^\dagger c_{u,k'-q}^\dagger \left[c_{w,k}, c_{v,k'} \right] + c_{u,k'-q}^\dagger \left[c_{w,k}^\dagger, c_{v,k'} \right] c_{w,k} \\
&\quad + c_{w,k}^\dagger \left[c_{w,k}, c_{u,k'-q}^\dagger \right] c_{v,k'} + \left[c_{w,k}^\dagger, c_{u,k'-q}^\dagger \right] c_{v,k'} c_{w,k} \\
&= c_{u,k'-q}^\dagger \left[2c_{w,k}^\dagger c_{v,k'} - \delta_{wv} \delta_{kk'} \right] c_{w,k} + c_{w,k}^\dagger \left[2c_{w,k} c_{u,k'-q}^\dagger - \delta_{wu} \delta_{k,k'-q} \right] c_{v,k'} \\
&\quad + \underbrace{2c_{w,k}^\dagger c_{u,k'-q}^\dagger c_{w,k} c_{v,k'} + 2c_{w,k}^\dagger c_{u,k'-q}^\dagger c_{v,k'} c_{w,k}}_{=0} \\
&= 2c_{u,k'-q}^\dagger c_{w,k}^\dagger c_{v,k'} c_{w,k} + 2c_{w,k}^\dagger c_{w,k} c_{u,k'-q}^\dagger c_{v,k'} - \delta_{wv} \delta_{kk'} c_{u,k'-q}^\dagger c_{w,k} - \delta_{wu} \delta_{k,k'-q} c_{w,k}^\dagger c_{v,k'} \\
&= 2c_{u,k'-q}^\dagger c_{w,k}^\dagger c_{v,k'} c_{w,k} + 2\delta_{wu} \delta_{k,k'-q} c_{w,k}^\dagger c_{v,k'} - 2c_{w,k}^\dagger c_{u,k'-q}^\dagger c_{w,k} c_{v,k'} \\
&\quad - \delta_{wv} \delta_{kk'} c_{u,k'-q}^\dagger c_{w,k} - \delta_{wu} \delta_{k,k'-q} c_{w,k}^\dagger c_{v,k'} \\
&= \delta_{wu} \delta_{k,k'-q} c_{w,k}^\dagger c_{v,k'} - \delta_{wv} \delta_{kk'} c_{u,k'-q}^\dagger c_{w,k}
\end{aligned}$$

Hence:

$$\begin{aligned}
[H_{\text{kin}}, s_{k',q}^I] &= \sum_{k w u v} \left(\varepsilon_k \sigma_{uv}^I \delta_{wu} \delta_{k,k'-q} c_{w,k}^\dagger c_{v,k'} - \varepsilon_k \sigma_{uv}^I \delta_{wv} \delta_{kk'} c_{u,k'-q}^\dagger c_{w,k} \right) \\
&= \sum_{uv} \left(\varepsilon_{k'-q} c_{u,k'-q}^\dagger \sigma_{uv}^I c_{v,k'} - \varepsilon_{k'} c_{u,k'-q}^\dagger \sigma_{uv}^I c_{v,k'} \right) \\
&= \left(\varepsilon_{k'-q} - \varepsilon_{k'} \right) \left(\mathbf{c}_{k'-q}^\dagger \underline{\underline{\sigma}}^I \mathbf{c}_{k'} \right)
\end{aligned} \tag{D.19}$$

The commutator of H_{int} with $s_{k',q}^I$ is a priori non-vanishing:

$$[H_{\text{int}}, c_{w,k'-q}^\dagger \sigma_{wl}^J c_{l,k'}] = \frac{1}{2} U^I \sum_{q'} \underbrace{\left[n_{q'}^I n_{-q'}^I, c_{w,k'-q}^\dagger \sigma_{wl}^J c_{l,k'} \right]}_{\neq 0}$$

But $[H_{\text{int}}, n_q^J]$ is. Indeed:

$$[H_{\text{int}}, \sum_{k'} s_{k',q}^I] = [H_{\text{int}}, n_q^J] = \frac{1}{2} \sum_{q'I} U^I [n_{q'}^I n_{-q'}^I, n_q^J] = \frac{1}{2} \sum_{q'I} U^I \{ n_{q'}^I [n_{-q'}^I, n_q^J] + [n_{q'}^I, n_q^J] n_{-q'}^I \}$$

Using the properties: $[n_{q'}^I, n_q^J] = 2i\varepsilon_{IJK} n_q^K \delta_{q,q'}$ and $\{n_{q'}^I, n_q^J\} = 2\delta_{IJ} \delta_{q',q}$, we get:

$$[H_{\text{int}}, n_q^J] = \frac{1}{2} \sum_I U^I 2i\varepsilon_{IJK} \{ n_{-q}^I n_q^K + n_q^K n_{-q}^I \} = \frac{1}{2} \sum_I U^I 2i\varepsilon_{IJK} \{ 2\delta_{IK} \} = 0$$

Thus

$$[H, n_q^I] = \sum_{k'} \left(\varepsilon_{k'-q} - \varepsilon_{k'} \right) \left(\mathbf{c}_{k'-q}^\dagger \underline{\underline{\sigma}}^I \mathbf{c}_{k'} \right) \tag{D.20}$$

Atomic limit

In this chapter, I derive a few exact results in the “atomic limit”, namely the problem defined by the Hamiltonian

$$H^{\text{at}} = U n_{\uparrow} n_{\downarrow} - \mu (n_{\uparrow} + n_{\downarrow}) \quad (\text{E.1})$$

The four eigenstates are the states $|0\rangle$, $|\uparrow\rangle$, $|\downarrow\rangle$ and $|\uparrow\downarrow\rangle$ with respective energies 0 , $-\mu$, $-\mu$, $U - 2\mu$. Half-filling corresponds to $\mu = U/2$. We call $\varepsilon = -\mu$ the energy of a single electron on a level.

E.1 Simple observables: Z , $\langle n_{\sigma} \rangle$, $\chi(i\Omega)$, $G(i\omega)$, $\Sigma(i\omega)$

The partition function in the atomic limit is:

$$Z = 1 + 2e^{\beta\mu} + e^{-\beta(U-2\mu)} = 2 \left(1 + e^{\beta U/2} \right) \quad (\text{E.2})$$

The second equality holds for half-filling. The filling per spin is:

$$\langle n_{\sigma} \rangle = \frac{1}{Z} \text{Tr} \left[e^{-\beta H} n_{\sigma} \right] = \frac{1}{Z} \left(0 + e^{\beta\mu} + e^{-\beta(U-2\mu)} \right) = \frac{1}{2}$$

The last equality holds for half-filling. Let us now turn to the density-density correlation function. The up-down component (at half-filling) is given by $\chi_{\uparrow\downarrow}(\tau) = \langle n_{\uparrow}(\tau) n_{\downarrow} \rangle = \frac{1}{Z} \text{Tr} \left[e^{-\beta H} n_{\uparrow}(\tau) n_{\downarrow} \right] = \frac{1}{2(1+e^{-\beta\varepsilon})}$. The connected component is thus, after Fourier transformation:

$$\chi_{\uparrow\downarrow}^{\text{conn}}(i\Omega) = \left[\frac{1}{2(1+e^{\beta U/2})} - \frac{1}{4} \right] \beta \delta_{i\Omega} \quad (\text{E.3})$$

By convention, $\delta_{i\Omega}$ should be understood as δ_n where n is the index of the bosonic Matsubara frequency. Similarly, $\chi_{\uparrow\uparrow}(\tau) = \langle n_{\uparrow}(\tau) n_{\uparrow} \rangle = \frac{1}{Z} (e^{-\beta\varepsilon} + 1) = \frac{1}{2}$, and hence: $\chi_{\uparrow\uparrow}^{\text{conn}}(i\Omega) = \left[\frac{1}{2} - \frac{1}{4} \right] \beta \delta_{i\Omega}$, i.e:

$$\chi_{\uparrow\uparrow}^{\text{conn}}(i\Omega) = \frac{\beta}{4} \delta_{i\Omega} \quad (\text{E.4})$$

Transposing these results for the charge and spin channels, one gets $\chi_{\text{ch}}^{\text{conn}}(i\Omega) = \frac{1}{2} \frac{1}{1+e^{\beta U/2}} \beta \delta_{i\Omega}$ and $\chi_{\text{sp}}^{\text{conn}}(i\Omega) = \left[\frac{1}{2} - \frac{1}{2(1+e^{\beta U/2})} \right] \beta \delta_{i\Omega} = \frac{1}{2} \frac{e^{\beta U/2}}{1+e^{\beta U/2}} \beta \delta_{i\Omega}$ and finally:

$$\begin{aligned} \chi_{\text{ch}}^{\text{conn}}(i\Omega) &= \frac{\beta}{4} \frac{e^{-\beta U/4}}{\cosh(\beta U/4)} \delta_{i\Omega} \\ \chi_{\text{sp}}^{\text{conn}}(i\Omega) &= \frac{\beta}{4} \frac{e^{\beta U/4}}{\cosh(\beta U/4)} \delta_{i\Omega} \end{aligned}$$

In the large- U limit, $\chi_{\text{ch}}^{\text{conn}}(i\Omega)$ vanishes exponentially (the charge sector is gapped), whereas $\chi_{\text{sp}}^{\text{conn}}(i\Omega) \rightarrow \frac{1}{2T} \delta_{i\Omega}$ becomes the Curie susceptibility of an isolated spin.

I now turn to the one-particle Green's function. Starting from the Lehmann representation, one gets:

$$G_{\sigma}^{\text{at}}(i\omega) = \frac{1}{Z} \sum_{ij} |\langle i|c_{\sigma}|j\rangle|^2 \frac{e^{-\beta\epsilon_i} + e^{-\beta\epsilon_j}}{i\omega + \epsilon_i - \epsilon_j} = \frac{1}{Z} \left(\frac{1 + e^{\beta\mu}}{i\omega + \mu} + \frac{e^{\beta\mu} + e^{-\beta(U-2\mu)}}{i\omega - \mu - U + 2\mu} \right) = \frac{1}{Z} \left(\frac{1 + e^{\beta U/2}}{i\omega + U/2} + \frac{e^{\beta U/2} + 1}{i\omega - U/2} \right)$$

Plugging in the expression for Z yields:

$$G_{\sigma}^{\text{at}}(i\omega) = \frac{1}{2} \left(\frac{1}{i\omega + U/2} + \frac{1}{i\omega - U/2} \right) = \frac{1}{i\omega - \frac{U^2}{4i\omega}} \quad (\text{E.5})$$

Since the non-interacting function is $G_0^{\text{at}}(i\omega) = (i\omega + \mu)^{-1}$, at half-filling, one gets:

$$\Sigma^{\text{at}}(i\omega) = U/2 + \frac{U^2}{4i\omega} \quad (\text{E.6})$$

E.2 Three-point correlation function $\tilde{\chi}(i\omega, i\Omega)$

In this section, I derive the expression for the three-point correlation function in the atomic limit.

I proceed in two steps. First, I use the Lehmann representation of the three-point correlation function $\langle c\bar{c}n \rangle$ in the case of a single atomic site to compute the expression for the three-point correlation function in the atomic limit. I then amputate the legs to find the expression of the vertex function.

E.2.1 Full correlator $\tilde{\chi}$

I use Lehmann's representation (Eq (I.13)). If n_3 is n or s_z , then the matrix element $\langle k|n_3|i\rangle$ selects states with the same occupation and same spin, so one can simplify the expression:

$$\begin{aligned} \hat{\chi}_{\sigma_1\sigma_2\sigma_3}(i\omega_1, i\omega_2) &= \frac{1}{Z} \sum_{ij} \sum_p \sigma(p) \langle i|O_{p\sigma_1}|j\rangle \langle j|O_{p\sigma_2}|i\rangle \langle i|n_{\sigma_3}|i\rangle f_{iji}(\omega_{p1}, \omega_{p2}) \\ &= \frac{1}{Z} \sum_{ij} \langle i|c_{\sigma_1}|j\rangle \langle j|c_{\sigma_2}^{\dagger}|i\rangle \langle i|n_{\sigma_3}|i\rangle f_{iji}(\omega_1, \omega_2) - \sum_{ij} \langle i|c_{\sigma_2}^{\dagger}|j\rangle \langle j|c_{\sigma_1}|i\rangle \langle i|n_{\sigma_3}|i\rangle f_{iji}(\omega_2, \omega_1) \end{aligned}$$

Furthermore,

$$\begin{aligned} f_{iji}(\omega_2, \omega_1) &= \frac{1}{i\omega_1 + \epsilon_j - \epsilon_i} \frac{e^{-\beta\epsilon_j} + e^{-\beta\epsilon_i}}{i\omega_2 + \epsilon_i - \epsilon_j} + \beta \frac{e^{-\beta\epsilon_i}}{i\omega_1 + \epsilon_j - \epsilon_i} \delta_{i\omega_1+i\omega_2} \\ f_{jij}(\omega_1, \omega_2) &= \frac{1}{i\omega_2 + \epsilon_i - \epsilon_j} \frac{e^{-\beta\epsilon_j} + e^{-\beta\epsilon_i}}{i\omega_1 + \epsilon_j - \epsilon_i} + \beta \frac{e^{-\beta\epsilon_j}}{-i\omega_1 + \epsilon_i - \epsilon_j} \delta_{i\omega_1+i\omega_2} \end{aligned}$$

i.e. the following relation holds:

$$f_{iji}(\omega_2, \omega_1) = f_{jij}(\omega_1, \omega_2) + \beta \frac{e^{-\beta\epsilon_i} + e^{-\beta\epsilon_j}}{i\omega_1 + \epsilon_j - \epsilon_i} \delta_{i\omega_1+i\omega_2}$$

Using this identity and swapping the dummy indices in the second term, one gets:

$$\begin{aligned} \hat{\chi}_{\sigma_1\sigma_2\sigma_3}(i\omega_1, i\omega_2) &= \frac{1}{Z} \sum_{ij} \langle i|c_{\sigma_1}|j\rangle \langle j|c_{\sigma_2}^{\dagger}|i\rangle \{ \langle i|n_{\sigma_3}|i\rangle - \langle j|n_{\sigma_3}|j\rangle \} f_{iji}(\omega_1, \omega_2) \\ &\quad - \beta \sum_{ij} \langle j|c_{\sigma_2}^{\dagger}|i\rangle \langle i|c_{\sigma_1}|j\rangle \langle j|n_{\sigma_3}|j\rangle \frac{e^{-\beta\epsilon_i} + e^{-\beta\epsilon_j}}{i\omega_1 + \epsilon_i - \epsilon_j} \delta_{i\omega_1+i\omega_2} \end{aligned}$$

Obviously, $\sigma_1 = \sigma_2$, and $i = |\uparrow\downarrow\rangle$ and $j = |0\rangle$ do not contribute, i.e., after defining $\hat{\chi}_{\sigma\sigma'} \equiv \hat{\chi}_{\sigma\sigma\sigma'}$ and $f_{ij} \equiv f_{iji} = f_{ij}^{reg} + \beta \frac{e^{-\beta\epsilon_i}}{i\omega_2 + \epsilon_j - \epsilon_i} \delta_{i\omega_1 + i\omega_2}$:

$$\hat{\chi}_{\sigma\sigma'}(i\omega_1, i\omega_2) = \hat{\chi}_{\sigma\sigma'}^1(i\omega_1, i\omega_2) + \hat{\chi}_{\sigma\sigma'}^2(i\omega_1, i\omega_2)$$

with

$$\begin{aligned} \hat{\chi}_{\sigma\sigma'}^1(i\omega_1, i\omega_2) &\equiv \frac{1}{Z} \sum_{i=|0\rangle, |\uparrow\rangle, |\downarrow\rangle} \sum_{j=|\uparrow\rangle, |\downarrow\rangle, |0\rangle} | \langle i | c_\sigma | j \rangle |^2 \{ \langle i | n_{\sigma'} | i \rangle - \langle j | n_{\sigma'} | j \rangle \} f_{ij}(\omega_1, \omega_2) \\ \hat{\chi}_{\sigma\sigma'}^2(i\omega_1, i\omega_2) &\equiv -\beta \frac{1}{Z} \sum_{ij} | \langle i | c_\sigma | j \rangle |^2 \langle j | n_{\sigma'} | j \rangle \frac{e^{-\beta\epsilon_i} + e^{-\beta\epsilon_j}}{i\omega_1 + \epsilon_i - \epsilon_j} \delta_{i\omega_1 + i\omega_2} \end{aligned}$$

One also sees that: $\hat{\chi}_{\uparrow\downarrow} = \hat{\chi}_{\downarrow\uparrow}$ and $\hat{\chi}_{\uparrow\uparrow} = \hat{\chi}_{\downarrow\downarrow}$. Out of the nine remaining terms, one can see that only the terms where i and j are states with a difference of occupation of one electron are nonzero:

$$\begin{aligned} Z \hat{\chi}_{\sigma\sigma'}^1(i\omega_1, i\omega_2) &= | \langle 0 | c_\sigma | \uparrow \rangle |^2 \{ \langle 0 | n_{\sigma'} | 0 \rangle - \langle \uparrow | n_{\sigma'} | \uparrow \rangle \} f_{0\uparrow}(\omega_1, \omega_2) \\ &+ | \langle 0 | c_\sigma | \downarrow \rangle |^2 \{ \langle 0 | n_{\sigma'} | 0 \rangle - \langle \downarrow | n_{\sigma'} | \downarrow \rangle \} f_{0\downarrow}(\omega_1, \omega_2) \\ &+ | \langle \uparrow | c_\sigma | \uparrow \downarrow \rangle |^2 \{ \langle \uparrow | n_{\sigma'} | \uparrow \rangle - \langle \uparrow \downarrow | n_{\sigma'} | \uparrow \downarrow \rangle \} f_{\uparrow, \uparrow \downarrow}(\omega_1, \omega_2) \\ &+ | \langle \downarrow | c_\sigma | \uparrow \downarrow \rangle |^2 \{ \langle \downarrow | n_{\sigma'} | \downarrow \rangle - \langle \uparrow \downarrow | n_{\sigma'} | \uparrow \downarrow \rangle \} f_{\downarrow, \uparrow \downarrow}(\omega_1, \omega_2) \end{aligned}$$

and (now specializing to the half-filled case)

$$\begin{aligned} Z \hat{\chi}_{\sigma\sigma'}^2(i\omega_1, i\omega_2) &= -\beta | \langle 0 | c_\sigma | \uparrow \rangle |^2 \langle \uparrow | n_{\sigma'} | \uparrow \rangle \frac{1 + e^{-\beta\epsilon}}{i\omega_1 - \epsilon} \delta_{i\omega_1 + i\omega_2} \\ &- \beta | \langle 0 | c_\sigma | \downarrow \rangle |^2 \langle \downarrow | n_{\sigma'} | \downarrow \rangle \frac{1 + e^{-\beta\epsilon}}{i\omega_1 - \epsilon} \delta_{i\omega_1 + i\omega_2} \\ &- \beta | \langle \uparrow | c_\sigma | \uparrow \downarrow \rangle |^2 \langle \uparrow \downarrow | n_{\sigma'} | \uparrow \downarrow \rangle \frac{1 + e^{-\beta\epsilon}}{i\omega_1 + \epsilon} \delta_{i\omega_1 + i\omega_2} \\ &- \beta | \langle \downarrow | c_\sigma | \uparrow \downarrow \rangle |^2 \langle \uparrow \downarrow | n_{\sigma'} | \uparrow \downarrow \rangle \frac{1 + e^{-\beta\epsilon}}{i\omega_1 + \epsilon} \delta_{i\omega_1 + i\omega_2} \end{aligned}$$

Thus, for the opposite spin component:

$$Z \hat{\chi}_{\uparrow\downarrow}^1(i\omega_1, i\omega_2) = 0 \quad (\text{E.7})$$

$$Z \hat{\chi}_{\uparrow\downarrow}^2(i\omega_1, i\omega_2) = -\beta (1 + e^{-\beta\epsilon}) \delta_{i\omega_1 + i\omega_2} \frac{1}{i\omega_1 + \epsilon} \quad (\text{E.8})$$

i.e., switching back from $\hat{\chi}(i\omega_1, i\omega_2)$ to $\tilde{\chi}(i\omega, i\Omega)$ (see section B.1.2):

$$\boxed{\chi_{\uparrow\downarrow}(i\omega, i\Omega) = -\beta \langle n_\sigma \rangle \frac{1}{i\omega - U/2} \delta_{i\Omega}} \quad (\text{E.9})$$

For the same spin component:

$$\begin{aligned} Z \hat{\chi}_{\uparrow\uparrow}^1(i\omega_1, i\omega_2) &= -f_{0\uparrow}(\omega_1, \omega_2) - f_{\downarrow, \uparrow \downarrow}(\omega_1, \omega_2) \\ &= -\frac{e^{-\beta\epsilon_0} + e^{-\beta\epsilon_\uparrow}}{(i\omega_1 + \epsilon_\uparrow - \epsilon_0)(i\omega_2 + \epsilon_0 - \epsilon_\uparrow)} - \beta \frac{1}{i\omega_2 + \epsilon} \delta_{i\omega_1 + i\omega_2} \\ &\quad - \frac{e^{-\beta\epsilon_\downarrow} + e^{-\beta\epsilon_\uparrow \downarrow}}{(i\omega_1 + \epsilon_\uparrow \downarrow - \epsilon_\downarrow)(i\omega_2 + \epsilon_\downarrow - \epsilon_\uparrow \downarrow)} - \beta \frac{e^{-\beta\epsilon}}{i\omega_2 - \epsilon} \delta_{i\omega_1 + i\omega_2} \\ &= -\frac{1 + e^{\beta U/2}}{(i\omega_1 - U/2)(i\omega_2 + U/2)} - \frac{1 + e^{\beta U/2}}{(i\omega_1 + U/2)(i\omega_2 - U/2)} - \left[\frac{1}{i\omega_2 + \epsilon} + \frac{e^{-\beta\epsilon}}{i\omega_2 - \epsilon} \right] \beta \delta_{i\omega_1 + i\omega_2} \\ &\quad \equiv Z \tilde{\chi}_{\uparrow\uparrow}^{1, reg} \end{aligned}$$

i.e.

$$\begin{aligned}\hat{\chi}_{\uparrow\uparrow}^{1reg}(i\omega_1, i\omega_2) &= -\frac{1}{2} \frac{(i\omega_1 + U/2)(i\omega_2 - U/2) + (i\omega_1 - U/2)(i\omega_2 + U/2)}{((i\omega_1)^2 - U^2/4)((i\omega_2)^2 - U^2/4)} \\ &= -\frac{i\omega_1 i\omega_2 - U^2/4}{((i\omega_1)^2 - U^2/4)((i\omega_2)^2 - U^2/4)}\end{aligned}$$

and $\hat{\chi}_{\uparrow\uparrow}^2(i\omega_1, i\omega_2) = -\frac{\beta}{2} \left(\frac{1}{i\omega_1 + U/2} + \frac{1}{i\omega_1 - U/2} \right) \delta_\Omega$. Thus, gathering both terms:

$$\begin{aligned}\hat{\chi}_{\uparrow\uparrow}(i\omega_1, i\omega_2) &= -\frac{i\omega_1 i\omega_2 - U^2/4}{((i\omega_1)^2 - \frac{U^2}{4})((i\omega_2)^2 - \frac{U^2}{4})} - \frac{\beta}{2} \left(\frac{1}{i\omega_1 + U/2} + \frac{1}{i\omega_1 - U/2} \right) \delta_\Omega \\ &\quad + \frac{1}{2(1 + e^{-\beta\epsilon})} \left[\frac{1}{i\omega_1 + U/2} + \frac{e^{-\beta\epsilon}}{i\omega_1 - U/2} \right] \beta \delta_{i\Omega} \\ &= -\frac{i\omega_1 i\omega_2 - U^2/4}{((i\omega_1)^2 - \frac{U^2}{4})((i\omega_2)^2 - \frac{U^2}{4})} - \frac{\beta}{2(1 + e^{-\beta\epsilon})} \left[\frac{e^{-\beta\epsilon}}{i\omega_1 + U/2} + \frac{1}{i\omega_1 - U/2} \right] \delta_{i\Omega}\end{aligned}$$

Hence, using the expression of G^{at} :

$$\boxed{\hat{\chi}_{\uparrow\uparrow}(i\omega_1, i\omega_2) = -G^{\text{at}}(i\omega_1)G^{\text{at}}(i\omega_2) + \frac{U^2/4}{((i\omega_1)^2 - \frac{U^2}{4})((i\omega_2)^2 - \frac{U^2}{4})} - \frac{\beta}{2(1 + e^{-\beta\epsilon})} \left[\frac{e^{-\beta\epsilon}}{i\omega_1 + \frac{U}{2}} + \frac{1}{i\omega_1 - \frac{U}{2}} \right] \delta_{i\Omega}} \quad (\text{E.10})$$

E.2.2 Connected part $\chi_{\sigma\sigma'}^c$

The connected part is defined as: $\tilde{\chi}_{\sigma\sigma'}^c(\tau, \tau') \equiv \tilde{\chi}_{\sigma\sigma'}(\tau, \tau') - \langle c_\sigma(\tau)c_\sigma^\dagger(\tau') \rangle \langle n_{\sigma'} \rangle = \tilde{\chi}_{\sigma\sigma'}(\tau, \tau') + G^{\text{at}}(\tau - \tau') \langle n_{\sigma'} \rangle$, whence:

$$\tilde{\chi}_{\sigma\sigma'}^c(i\omega, i\Omega) = \tilde{\chi}_{\sigma\sigma'}(i\omega, i\Omega) + \beta G^{\text{at}}(i\omega) \langle n_{\sigma'} \rangle \delta_{i\Omega} \quad (\text{E.11})$$

This yields:

$$\tilde{\chi}_{\uparrow\downarrow}^c(i\omega, i\Omega) = \frac{\beta}{4} \left[\frac{1}{i\omega + U/2} - \frac{1}{i\omega - U/2} \right] \delta_{i\Omega} \quad (\text{E.12a})$$

$$\hat{\chi}_{\uparrow\uparrow}^c(i\omega_1, i\omega_2) = -G^{\text{at}}(i\omega_1)G^{\text{at}}(i\omega_2) + \frac{U^2/4}{\{(i\omega_1)^2 - \frac{U^2}{4}\} \{(i\omega_2)^2 - \frac{U^2}{4}\}} + A(\omega_1) \delta_{i\Omega} \quad (\text{E.12b})$$

with:

$$\begin{aligned}A(\omega_1) &\equiv \frac{\beta}{2} \left\{ G^{\text{at}}(i\omega_1) - \frac{1}{1 + e^{\beta U/2}} \left[\frac{e^{\beta U/2}}{i\omega_1 + U/2} + \frac{1}{i\omega_1 - U/2} \right] \right\} \\ &= \frac{\beta}{2} \left\{ \frac{1}{i\omega_1 - U/2} \left\{ \frac{1}{2} - \frac{1}{1 + e^{\beta U/2}} \right\} + \frac{1}{i\omega_1 + U/2} \left\{ \frac{1}{2} - \frac{e^{\beta U/2}}{1 + e^{\beta U/2}} \right\} \right\} \\ &= \frac{\beta}{4} \tanh(\beta U/4) \left[\frac{1}{i\omega_1 - U/2} - \frac{1}{i\omega_1 + U/2} \right] \\ &= \frac{\beta}{4} \tanh(\beta U/4) \frac{U}{(i\omega_1)^2 - \frac{U^2}{4}}\end{aligned}$$

One can check expression (E.12a) and get some physical intuition by computing the self-energy from the equation of motion for G (i.e. Eq. (F.6a) specialized for the atomic limit). For the $\tilde{\chi}_{\uparrow\downarrow}$ term, one can check that:

$$\Sigma^{\text{at}}(i\omega)G^{\text{at}}(i\omega) = -U \sum_{i\Omega} \tilde{\chi}_{\uparrow\downarrow}^{\text{at}}(i\omega, i\Omega) \quad (\text{E.13})$$

Considering the contribution beyond Hartree, $\Sigma_{\text{bH}}(i\omega) \equiv -U \frac{1}{\beta} \sum_{\Omega} \frac{\tilde{\chi}_{\uparrow\downarrow}(\omega, \Omega)}{G(i\omega)} - U \langle n_{\sigma} \rangle = -U \frac{1}{\beta} \sum_{\Omega} \left\{ \frac{\tilde{\chi}_{\uparrow\downarrow}(\omega, \Omega) + G(i\omega) \langle n_{\sigma} \rangle \beta \delta_{\Omega}}{G(i\omega)} \right\}$, i.e.:

$$\Sigma_{\text{bH}}^{\text{at}}(i\omega)G^{\text{at}}(i\omega) = -U \sum_{i\Omega} \tilde{\chi}_{\uparrow\downarrow}^{\text{c,at}}(i\omega, i\Omega) \quad (\text{E.14})$$

which is to be contrasted with (E.13). For the $\tilde{\chi}_{\uparrow\uparrow}$ term, in the non-interacting case, using Wick's theorem, one can write:

$$\chi_{\uparrow\uparrow, \text{c}}^{U=0}(\tau, \tau') = \langle T c_{\uparrow}(\tau) c_{\uparrow}^{\dagger}(\tau') (c_{\uparrow}^{\dagger} c_{\uparrow} - \langle n_{\uparrow} \rangle) \rangle_0 = \langle T c_{\uparrow}(\tau) c_{\uparrow}^{\dagger} \rangle \langle T c_{\uparrow} c_{\uparrow}^{\dagger}(\tau') \rangle_0 = G_{0\uparrow}^{\text{at}}(\tau) G_{0\uparrow}^{\text{at}}(-\tau')$$

Fourier-transformed, this becomes $\chi_{\uparrow\uparrow}(i\omega, i\Omega) = G_{0\uparrow}(i\omega)G_{0\uparrow}(i\omega + i\Omega)$, to be compared to Eq (E.12b):

$$\tilde{\chi}_{\uparrow\uparrow}^{U=0}(i\omega, i\Omega) = -G_0^{\text{at}}(i\omega)G_0^{\text{at}}(-i\omega - i\Omega)$$

E.2.3 Expressions in charge and spin channels

Let us now transform from the (\uparrow, \downarrow) space to the (ch,sp) space:

$$\begin{aligned} \tilde{\chi}^{\text{ch,c}}(i\omega_1, i\omega_2) &\equiv \tilde{\chi}_{\uparrow\uparrow}^{\text{c}} + \tilde{\chi}_{\uparrow\downarrow}^{\text{c}} \\ &= -G^{\text{at}}(i\omega_1)G^{\text{at}}(i\omega_2) + \frac{U^2/4}{\{(i\omega_1)^2 - \frac{U^2}{4}\} \{(i\omega_2)^2 - \frac{U^2}{4}\}} \\ &\quad + \frac{\beta}{4} \left\{ \tanh(\beta U/4) \left[\frac{1}{i\omega_1 - \frac{U}{2}} - \frac{1}{i\omega_1 + \frac{U}{2}} \right] + \left[\frac{1}{i\omega_1 + \frac{U}{2}} - \frac{1}{i\omega_1 - \frac{U}{2}} \right] \right\} \delta_{i\Omega} \\ \tilde{\chi}^{\text{sp,c}}(i\omega_1, i\omega_2) &\equiv \tilde{\chi}_{\uparrow\uparrow}^{\text{c}} - \tilde{\chi}_{\uparrow\downarrow}^{\text{c}} \\ &= -G^{\text{at}}(i\omega_1)G^{\text{at}}(i\omega_2) + \frac{U^2/4}{\{(i\omega_1)^2 - \frac{U^2}{4}\} \{(i\omega_2)^2 - \frac{U^2}{4}\}} \\ &\quad + \frac{\beta}{4} \left\{ \tanh(\beta U/4) \left[\frac{1}{i\omega_1 - \frac{U}{2}} - \frac{1}{i\omega_1 + \frac{U}{2}} \right] - \left[\frac{1}{i\omega_1 + \frac{U}{2}} - \frac{1}{i\omega_1 - \frac{U}{2}} \right] \right\} \delta_{i\Omega} \end{aligned}$$

Simplifying and transposing to $i\omega, i\Omega$ variables, one gets (using $G^{\text{at}}(-i\omega) = -G^{\text{at}}(i\omega)$):

$$\begin{aligned} \tilde{\chi}^{\text{ch,c}}(i\omega, i\Omega) &= G^{\text{at}}(i\omega)G^{\text{at}}(i\omega + i\Omega) + \frac{U^2/4}{\{(i\omega)^2 - \frac{U^2}{4}\} \{(i\omega + i\Omega)^2 - \frac{U^2}{4}\}} \\ &\quad + \frac{\beta}{4} \frac{U}{(i\omega)^2 - U^2/4} \{ \tanh(\beta U/4) - 1 \} \delta_{i\Omega} \end{aligned} \quad (\text{E.15a})$$

$$\begin{aligned} \tilde{\chi}^{\text{sp,c}}(i\omega, i\Omega) &= G^{\text{at}}(i\omega)G^{\text{at}}(i\omega + i\Omega) + \frac{U^2/4}{\{(i\omega)^2 - \frac{U^2}{4}\} \{(i\omega + i\Omega)^2 - \frac{U^2}{4}\}} \\ &\quad + \frac{\beta}{4} \frac{U}{(i\omega)^2 - U^2/4} \{ \tanh(\beta U/4) + 1 \} \delta_{i\Omega} \end{aligned} \quad (\text{E.15b})$$

E.3 Three-leg vertex $\Lambda(i\omega, i\Omega)$

The vertex is defined as the amputated connected correlation function (see Eq. 8.29). One can easily compute the “legs” in the atomic limit:

$$G^{\text{at}}(i\omega)G^{\text{at}}(i\omega + i\Omega) (1 - U^{\text{ch}}\chi^{\text{ch,conn}}(i\Omega)) = \frac{i\omega (i\omega + i\Omega)}{((i\omega)^2 - U^2/4)((i\omega + i\Omega)^2 - U^2/4)} (1 - U^{\text{ch}}\chi^{\text{ch,conn}}(i\Omega))$$

$$G^{\text{at}}(i\omega)G^{\text{at}}(i\omega + i\Omega) (1 - U^{\text{sp}}\chi^{\text{sp,conn}}(i\Omega)) = \frac{i\omega (i\omega + i\Omega)}{((i\omega)^2 - U^2/4)((i\omega + i\Omega)^2 - U^2/4)} (1 - U^{\text{sp}}\chi^{\text{sp,conn}}(i\Omega))$$

Hence, for the charge channel:

$$\begin{aligned} \Lambda^{\text{ch}}(i\omega, i\Omega) &= \frac{\frac{U^2/4}{\{(i\omega)^2 - U^2/4\}\{(i\omega + i\Omega)^2 - U^2/4\}} + \frac{\beta}{4} \frac{U}{(i\omega)^2 - U^2/4} \left\{ \tanh\left(\frac{\beta U}{4}\right) - 1 \right\} \delta_{i\Omega}}{\frac{i\omega(i\omega + i\Omega)}{((i\omega)^2 - U^2/4)((i\omega + i\Omega)^2 - U^2/4)} (1 - U^{\text{ch}}\chi^{\text{ch,conn}}(i\Omega))} + \frac{1}{1 - U^{\text{ch}}\chi^{\text{ch,conn}}(i\Omega)} \\ &= \frac{U^2/4}{i\omega (i\omega + i\Omega) (1 - U^{\text{ch}}\chi^{\text{ch,conn}}\delta_{i\Omega})} + \frac{\beta}{4} \left\{ \frac{(i\omega)^2 - U^2/4}{i\omega} \right\}^2 \frac{U}{(i\omega)^2 - U^2/4} \frac{\tanh\left(\frac{\beta U}{4}\right) - 1}{(1 - U^{\text{ch}}\chi^{\text{ch,conn}})} \delta_{i\Omega} \\ &\quad + \frac{1}{1 - U^{\text{ch}}\chi^{\text{ch,conn}}\delta_{i\Omega}} \end{aligned}$$

and a similar result for the spin channel. Simplifying, one finds the final result, Eq. (8.72).

Equations of motion

In this chapter, I present an alternative derivation of the TRILEX equations for the self-energy and polarization in terms of the three-leg vertex.

F.1 Prerequisite: Schwinger-Dyson equations

F.1.1 Bosonic fields

For any bosonic field ϕ_α , matrix $U_{\alpha\beta}$ and function f , let us define:

$$A \equiv \int \mathcal{D} [\phi] e^{\frac{1}{2}\phi_\alpha [U^{-1}]_{\alpha\beta} \phi_\beta} \frac{\partial f[\phi]}{\partial \phi_\gamma}$$

By integration by parts, one obtains

$$A = - \int \mathcal{D} [\phi] \frac{\partial}{\partial \phi_\gamma} e^{\frac{1}{2}\phi_\alpha [U^{-1}]_{\alpha\beta} \phi_\beta} f[\phi] = - [U^{-1}]_{\gamma\beta} \int \mathcal{D} [\phi] \phi_\beta e^{\frac{1}{2}\phi_\alpha [U^{-1}]_{\alpha\beta} \phi_\beta} f[\phi]$$

and taking $f[\phi] \equiv h[\phi] e^{-\lambda_{uv\delta} \phi_\delta \bar{c}_u c_v}$, one has:

$$\begin{aligned} A &= \int \mathcal{D} [\phi] \left[e^{\frac{1}{2}\phi_\alpha [U^{-1}]_{\alpha\beta} \phi_\beta} \left\{ \frac{\partial h[\phi]}{\partial \phi_\gamma} - \lambda_{uv\delta} \bar{c}_u c_v h[\phi] \right\} e^{-\lambda_{uv\delta} \phi_\delta \bar{c}_u c_v} \right] \\ &= - [U^{-1}]_{\gamma\beta} \int \mathcal{D} [\phi] \phi_\beta e^{\frac{1}{2}\phi_\alpha [U^{-1}]_{\alpha\beta} \phi_\beta} h[\phi] e^{-\lambda_{uv\delta} \phi_\delta \bar{c}_u c_v} \end{aligned}$$

i.e., for any function h :

$$\left\langle \frac{\partial h[\phi]}{\partial \phi_\gamma} - \lambda_{uv\delta} \bar{c}_u c_v h[\phi] \right\rangle = - [U^{-1}]_{\gamma\beta} \langle \phi_\beta h[\phi] \rangle \quad (\text{F.1})$$

F.1.2 Fermionic fields

Similarly to the previous section, for any conjugate Grassmann fields c_i and \bar{c}_i , matrix $[G_0]_{ij}$ and function f , one can define:

$$A \equiv \int \mathcal{D} [\bar{c}c] e^{\bar{c}_k [G_0^{-1}]_{kl} c_l} \frac{\partial f[\bar{c}c]}{\partial \bar{c}_i}$$

Then, by integration by parts:

$$A = - \int \mathcal{D} [\bar{c}c] \frac{\partial}{\partial \bar{c}_i} e^{\bar{c}_k [G_0^{-1}]_{kl} c_l} f[\bar{c}c] = - [G^{-1}]_{il} \int \mathcal{D} [\bar{c}c] c_l e^{\bar{c}_k [G_0^{-1}]_{kl} c_l} f[\bar{c}c]$$

For $f[\bar{c}c] \equiv h[\bar{c}c]e^{-V}$:

$$A = \int \mathcal{D}[\bar{c}c] e^{\bar{c}_k [G_0^{-1}]_{kl} c_l} \left(\frac{\partial h[\bar{c}c]}{\partial \bar{c}_i} + \frac{\partial V}{\partial \bar{c}_i} \right) e^{-V} = - [G_0^{-1}]_{il} \int \mathcal{D}[\bar{c}c] c_l e^{\bar{c}_k [G_0^{-1}]_{kl} c_l} h[\bar{c}c] e^{-V}$$

i.e.

$$\left\langle \frac{\partial h[\bar{c}c]}{\partial \bar{c}_i} + h[\bar{c}c] \frac{\partial V}{\partial \bar{c}_i} \right\rangle = - [G_0^{-1}]_{il} \langle c_l h[\bar{c}c] \rangle \quad (\text{F.2})$$

F.2 Equations of motion for G and W

F.2.1 Fermionic propagator G

Specializing Eq (F.2) for $h[\bar{c}c] \equiv \bar{c}_p$ and $V = \frac{1}{2} n_\alpha U_{\alpha\beta} n_\beta = \frac{1}{2} U_{\alpha\beta} \bar{c}_u \lambda_{uv\alpha} c_v \bar{c}_w \lambda_{wl\beta} c_l$, and noting that:

$$\begin{aligned} \frac{\partial V}{\partial \bar{c}_i} &= \frac{1}{2} U_{\alpha\beta} \lambda_{iv\alpha} c_v \bar{c}_w \lambda_{wl\beta} c_l + \frac{1}{2} U_{\alpha\beta} \bar{c}_u \lambda_{uv\alpha} c_v \lambda_{il\beta} c_l \\ &= U_{\alpha\beta} \lambda_{iv\alpha} \lambda_{wl\beta} c_v \bar{c}_w c_l \end{aligned}$$

(I have used $U_{\alpha\beta} = U_{\beta\alpha}$), one has:

$$- [G_0^{-1}]_{il} \langle c_l \bar{c}_p \rangle = \delta_{ip} + U_{\alpha\beta} \lambda_{iv\alpha} \lambda_{wl\beta} \langle \bar{c}_p c_v \bar{c}_w c_l \rangle$$

i.e., multiplying by $[G_0]_{mi}^{zx}$ and using definitions (8.17c) and (C.2):

$$G_{mp} = [G_0]_{mp} - [G_0]_{mi} U_{\alpha\beta} \lambda_{iv\alpha} \tilde{\chi}_{vp\beta} \quad (\text{F.3})$$

Using (C.1d), we can rewrite this as:

$$G_{mp} = [G_0]_{mp} - [G_0]_{mi} \lambda_{iv\alpha} \chi_{vp\alpha} \quad (\text{F.4})$$

F.2.2 Bosonic propagator W

Specializing Eq. (F.1) for $h[\phi] \equiv \phi_\alpha$, we find:

$$\langle \delta_{\gamma\alpha} - \lambda_{uv\gamma} \bar{c}_u c_v \phi_\alpha \rangle = - [U^{-1}]_{\gamma\beta} \langle \phi_\beta \phi_\alpha \rangle$$

whence:

$$-\langle \phi_\delta \phi_\alpha \rangle = U_{\delta\alpha} - U_{\delta\gamma} \lambda_{uv\gamma} \langle \bar{c}_u c_v \phi_\alpha \rangle$$

i.e., using definitions (8.17b-8.27):

$$W_{\delta\alpha} = U_{\delta\alpha} + U_{\delta\gamma} \lambda_{uv\gamma} \chi_{v\alpha} \quad (\text{F.5})$$

F.3 General formulae for the self-energy and polarization

Identifying Σ and P from the Dyson equations (8.24a-8.24b) and (F.4-F.5) yields:

$$\Sigma_{ij} G_{jp} = -\lambda_{iv\alpha} \chi_{vp\alpha} \quad (\text{F.6a})$$

$$P_{\gamma\beta} W_{\beta\alpha} = \lambda_{uv\gamma} \chi_{v\alpha} \quad (\text{F.6b})$$

whence:

$$\Sigma_{ik} = -\lambda_{iv\alpha} \chi_{vp\alpha} [G^{-1}]_{pk} \quad (\text{F.7a})$$

$$P_{\gamma\delta} = \lambda_{uv\gamma} \chi_{v\alpha} [W^{-1}]_{\alpha\delta} \quad (\text{F.7b})$$

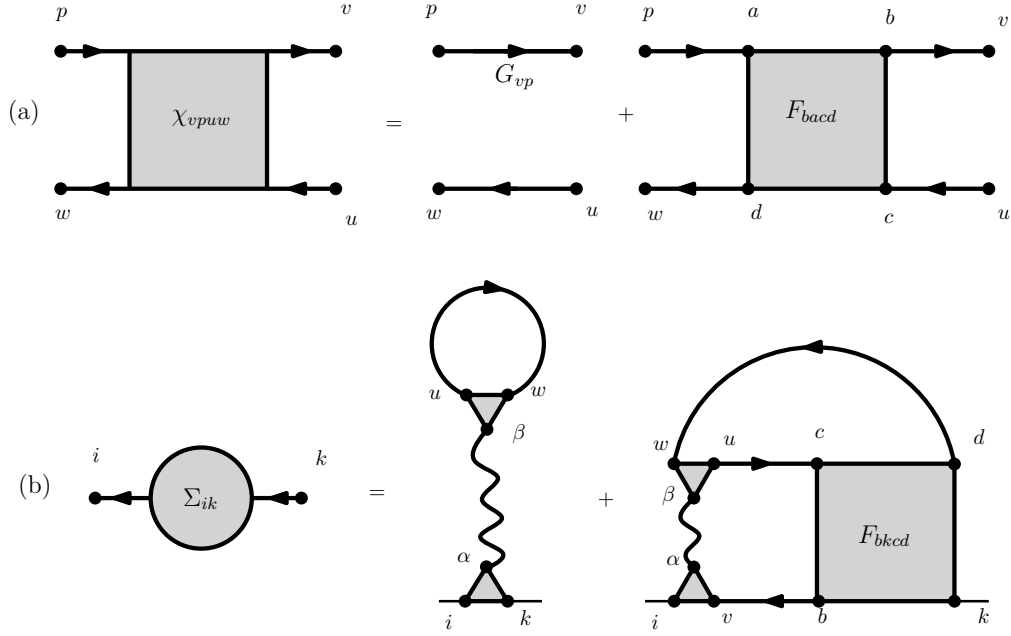


Figure F.1: (a) Generalized susceptibility: relation to the fully reducible vertex F . (b) Schwinger-Dyson equation. The grey triangle is the bare vertex $\lambda_{ij\alpha}$.

F.3.1 With a three-leg vertex

Using the definition of the three-leg vertex, Eq. (8.28), we find:

$$\Sigma_{ij} = -\lambda_{ik\alpha} G_{kl} W_{\alpha\beta} \Lambda_{lj\beta}$$

and similarly:

$$P_{\alpha\beta} = \lambda_{ik\alpha} G_{ji} G_{kl} \Lambda_{lj\beta}$$

which are the formulae (8.36a-8.36b) we derived using functionals in section 8.3.

F.3.2 With a four-leg vertex

Start from

$$\Sigma_{ij} G_{jp} = -\lambda_{iv\alpha} U_{\alpha\beta} \tilde{\chi}_{vp\beta} = -\lambda_{iv\alpha} \lambda_{uw\beta} U_{\alpha\beta} \langle c_v \bar{c}_p \bar{c}_u c_w \rangle$$

Define the generalized susceptibility:

$$\chi_{vpuw} = \langle c_v \bar{c}_p \bar{c}_u c_w \rangle \quad (\text{F.8})$$

As shown in panel (a) of Fig. F.1,

$$\chi_{vpuw} = G_{vp} G_{wu} + G_{ap} G_{wd} F_{bacd} G_{vb} G_{cu}$$

Hence,

$$\Sigma_{ij} G_{jp} = -\lambda_{iv\alpha} \lambda_{uw\beta} U_{\alpha\beta} [G_{vp} G_{wu} + G_{ap} G_{wd} F_{bacd} G_{vb} G_{cu}]$$

Multiplying by G_{pk}^{-1} yields the general Schwinger-Dyson equation for the self-energy (illustrated in panel (b)):

$$\Sigma_{ik} = -\lambda_{ik\alpha} \lambda_{uw\beta} U_{\alpha\beta} [G_{wu} + G_{wd} F_{bkcd} G_{vb} G_{cu}] \quad (\text{F.9})$$

F.3.3 Transcription to simple cases

F.3.3.1 Product Σ_G

F.3.3.1.1 Local version Let us rewrite Eq. (F.6a) in terms of $\tilde{\chi}$:

$$\Sigma_{ij}G_{jp} = -\lambda_{i\nu\alpha}U_{\alpha\beta}\tilde{\chi}_{\nu p\beta}$$

and then replace λ by $\lambda_{i\nu\alpha} = \sigma_{\sigma\bar{\sigma}}^I \delta_{\tau-\tau'} \delta_{\tau'-\bar{\tau}} \delta_{ab}$, $U_{\alpha\beta} = U_{ab}^I(\tau - \bar{\tau})\delta_{IJ}$, and $\Sigma_{ij} = \Sigma_{a\sigma, c\bar{\sigma}}(\tau - \bar{\tau})$. We get:

$$F_{a\sigma, b\sigma'}(\tau) \equiv \int_{\bar{\tau}} \sum_c \Sigma_{a\sigma, c\bar{\sigma}}(\tau - \bar{\tau}) G_{c\bar{\sigma}, b\sigma'}(\bar{\tau}) = - \sum_I \int_0^\beta d\bar{\tau} \sum_{cd\bar{\sigma}} U_{cd}^I(\tau - \bar{\tau}) \langle T c_{a\bar{\sigma}}(\tau) \sigma_{\sigma\bar{\sigma}}^I c_{b\sigma'}^\dagger(0) n_d^I(\bar{\tau}) \rangle \quad (\text{F.10})$$

(a, b, c, d are orbital indices). In frequency, this becomes:

$$\begin{aligned} F_{a\sigma, b\sigma'}(i\omega) &= - \sum_{i\Omega_1} \sum_{i\Omega_2} \sum_{i\omega_1} \sum_I \sum_{cd\bar{\sigma}} \int_0^\beta d\bar{\tau} \int_0^\beta d\tau e^{i\omega\tau - i\Omega_1(\tau - \bar{\tau}) - i\Omega_2\bar{\tau} - i\omega_1\tau} U_{cd}^I(i\Omega_1) \sigma_{\sigma\bar{\sigma}}^I \chi_{a\bar{\sigma}, b\sigma, dI}(i\omega_1, i\Omega_2) \\ &= \sum_{i\Omega} \sum_{cd\bar{\sigma}} U_{cd}^I(i\Omega) \sigma_{\sigma\bar{\sigma}}^I \chi_{a\bar{\sigma}, b\sigma, dI}(i\omega - i\Omega, i\Omega) \\ &= \sum_{i\Omega} \sum_{cd\bar{\sigma}} U_{cd}^I(i\Omega) \sigma_{\sigma\bar{\sigma}}^I \chi_{a\bar{\sigma}, b\sigma, dI}(i\omega, -i\Omega) \\ &= \sum_{i\Omega} \sum_{cd\bar{\sigma}} U_{cd}^I(i\Omega) \sigma_{\sigma\bar{\sigma}}^I \chi_{a\bar{\sigma}, b\sigma, dI}(i\omega, i\Omega) \end{aligned}$$

where I used $U^I(-i\Omega) = U^I(i\Omega)$.

F.3.3.1.2 Nonlocal version In the homogeneous phase for a static U , $\Sigma_{ij} = \Sigma_{\mathbf{R}\tau, \mathbf{R}'\tau'\sigma} \delta_{\sigma\sigma'}$,

$$\Sigma_{\mathbf{R}\tau, \mathbf{R}'\tau'\sigma} G_{\mathbf{R}'\tau', \mathbf{R}''\tau''\sigma} = -\sigma_{\sigma\sigma'}^I U^I \langle c_{\mathbf{R}\tau\sigma} \bar{c}_{\mathbf{R}''\tau''\sigma} n_{\mathbf{R}\tau}^I \rangle$$

For $I = 0, z$

$$\Sigma_{\mathbf{R}\tau, \mathbf{R}'\tau'\sigma} G_{\mathbf{R}'\tau', \mathbf{R}''\tau''\sigma} = -U \langle c_{\mathbf{R}\tau\sigma} \bar{c}_{\mathbf{R}''\tau''\sigma} \bar{c}_{\mathbf{R}\tau\bar{\sigma}} c_{\mathbf{R}\tau\bar{\sigma}} \rangle \quad (\text{F.11})$$

A selection of many-body methods seen from a “parquet” perspective

In this chapter, I present various approximate many-body methods which can be regarded as different approximations to the parquet equations. These methods can be compared to TRILEX. The relation is briefly mentioned in the main text (section 8.6).

G.1 Prerequisite: four-leg observables and parquet equations

In this section, I summarize the so-called “parquet” formalism. I voluntarily use somewhat loose notations for expressions (*i.e.* without frequency, momentum nor spin indices) to underline the structure of equations. The starting point is the generalized susceptibility or four-leg correlator $G_2(i, j, k, l, \tau_1, \tau_2, \tau_3, \tau_4)$ (sometimes denoted as χ when unambiguous) defined as:

$$G_2(i, j, k, l, \tau_1, \tau_2, \tau_3, \tau_4) \equiv -\langle T c_i^\dagger(\tau_1) c_j(\tau_2) c_k^\dagger(\tau_3) c_l(\tau_4) \rangle$$

where i, j, k, l are combined site, spin and orbital indices, and τ_i denotes the imaginary-time variable. G_2 can be decomposed in the following way (for an illustration, see Fig. F.1 in the appendix):

$$G_2 = -GG + GGFGG \tag{G.1}$$

where F is the fully reducible vertex function (sometimes also denoted Γ). It contains all connected, four-leg diagrams. F can be further decomposed in contributions defined by the topology of the Feynman graphs used to represent them:

The **irreducible vertex in channel** r , Γ_r (sometimes also denoted $\Gamma_{r,ir}$), contains all diagrams that cannot be split in two by cutting:

- $r = ph$: two horizontal lines with opposite directions
- $r = \overline{ph}$: two vertical lines with opposite directions
- $r = pp$: two lines with same directions

In the SU(2) symmetric case, the set of r and spin indices can be reduced to four indices, d (density), m (magnetic), s (singlet) and t (triplet). One further defines Φ_r as the complementary set of diagrams with respect to Γ_r in F , namely:

$$F = \Gamma_r + \Phi_r \quad (\text{G.2})$$

By definition, Φ_r is reducible in channel r , namely:

$$\Phi_r = FGG\Gamma_r \quad (\text{G.3})$$

The **fully irreducible function** Λ (sometimes denoted Γ_{fir}) contains all diagrams that cannot be split in two by cutting any two lines. Hence,

$$F = \Lambda + \sum_r \Phi_r \quad (\text{G.4})$$

Finally, by definition of Γ_r , the following relation holds:

$$\Gamma_r = \Lambda + \sum_{r' \neq r} \Phi_{r'} \quad (\text{G.5})$$

G.1.1 Bethe-Salpether equation

Combining Eqs. (G.2) and (G.3), one gets the Bethe-Salpether equations (BSE):

$$F = \Gamma_r + FGG\Gamma_r \quad (\text{G.6})$$

I will note symbolically:

$$\Gamma_r \begin{array}{c} \text{BSE} \\ \rightleftharpoons \\ \text{BSE}^{-1} \end{array} F \quad (\text{G.7})$$

Both the direct and the inverse equations require matrix inversions, e.g. for the direct BSE:

$$F = (1 - GG\Gamma_r)^{-1} \Gamma_r \quad (\text{G.8})$$

G.1.2 Parquet (and inverse parquet) equations

Replacing F using (G.4) and Γ_r using (G.5) in (G.3), one gets the parquet equations:

$$\Phi_r = \left(\Lambda + \sum_{r'} \Phi_{r'} \right) GG \left(\Lambda + \sum_{r' \neq r} \Phi_{r'} \right) \quad (\text{G.9})$$

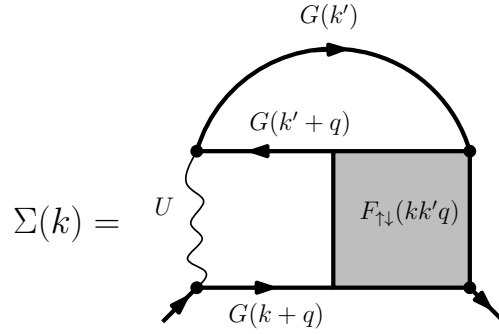
They allow to go from Λ to Φ_r , and hence from Λ to F . They are very involved nonlinear equations coupling the three channels. One names “parquet” the process of computing F from Λ :

$$\Lambda \xrightarrow[\text{(G.9)}]{\text{Parquet}} \Phi_r \xrightarrow[\text{(G.4)}]{} F \quad (\text{G.10})$$

Similarly, one calls “inverse parquet” (parquet^{-1}) the process of computing Λ from F :

$$F \xrightarrow[\text{(BSE}^{-1})]{\text{Parquet}^{-1}} \Gamma_r \xrightarrow[\text{(G.2)}]{} \Phi_r \xrightarrow[\text{(G.4)}]{} \Lambda \quad (\text{G.11})$$

Although it requires using BSE^{-1} , the inverse parquet is much easier to solve than the parquet (there is no coupling between the different channels).

Figure G.1: Schwinger Dyson equation for Σ

| Vertex | Approximation | Name |
|------------|-------------------|--|
| U | $U = 0$ | Free electrons |
| F | $F = 0$ | Self-consistent Hartree-Fock |
| | $F = U$ | Self-consistent second-order perturbation theory |
| Γ_r | $\Gamma_{ph} = U$ | Self-consistent RPA |
| | $\Gamma_r = U_r$ | Fluctuation-exchange approximation (FLEX, see section G.2) |
| Λ | $\Lambda = U$ | Self-consistent parquet approximation |

Table G.1: Various approximation strategies for two-particle vertex functions

G.1.3 Relation between F and Σ : Schwinger-Dyson equation

The fully reducible vertex $F(\mathbf{k}, \mathbf{k}', \mathbf{q}, i\omega, i\nu, i\Omega)$ and the self-energy (beyond Hartree-Fock) $\Sigma(\mathbf{k}, i\omega)$ are related by Schwinger-Dyson’s equation (derived in Appendix F.3.2). For the Hubbard model, it reads:

$$\Sigma(k) = U \sum_{k', q} G(k' + q)G(k')G(k + q)F_{\uparrow\downarrow}(k, k', q) \quad (\text{G.12})$$

with $k \equiv (\mathbf{k}, i\omega)$ etc. The corresponding diagram is shown in Fig. G.1.

G.1.4 Approximation strategies of the parquet equations

If the exact Λ were known for a given system, and if one were able to solve the parquet equations, one could in principle compute the exact self-energy. In practice, however, one has to perform approximations on Λ or on the other vertices introduced in the previous subsections. In Table G.1, I summarize various approximation strategies for the two-particle vertex functions. The “parquet approximation”, which consists in approximating the fully irreducible vertex by the bare interaction U , is limited to very small cluster sizes (4×4 Hubbard model, Yang *et al.* (2009); Tam *et al.* (2013)).

In the next subsection, I present various many-body approximation strategies which can be viewed as approximations to the full parquet equations.

G.2 The fluctuation-exchange (FLEX) approximation

The fluctuation-exchange (FLEX) approximation was introduced by Bickers and Scalapino (1989); Bickers *et al.* (1989); Bickers and White (1991). In essence, it constructs the self-energy as a sum of contributions

by all fluctuation channels, as if the fermionic variables of the Hubbard model were coupled to several bosonic modes each representing a possible instability. If we denote the propagator of these bosonic modes as $-U_r \tilde{\chi}_r(\mathbf{q}) U_r$ ($r = \text{ch, sp, singlet, triplet}$ for “density” (charge), “magnetic” (spin), “singlet” and “triplet” channels¹), then the FLEX self-energy for the single-band Hubbard model is given by the expression:

$$\Sigma^{\text{FLEX}}(k) = - \sum_r \eta_r \sum_q G(\pm(k-q)) \left[-U_r \chi_r^{\text{RPA}}(q) U_r \right] + \Sigma^{(2)}(k) \quad (\text{G.13})$$

where $k \equiv (\mathbf{k}, i\omega)$; the + sign is used for particle-hole channels (sp and ch), the – sign for the the particle-particle channels (singlet and triplet). The prefactors are $\eta_{\text{ch}} = 1$, $\eta_{\text{sp}} = 3$, $\eta_{\text{singlet}} = -1$, $\eta_{\text{triplet}} = 0$. Contrary to the spin fluctuation approach, the susceptibilities used in FLEX are the RPA susceptibilities, made up of rings of bubbles (particle-hole channels) or ladders (particle-particle channels):

$$\chi_r^{\text{RPA}}(q) = \frac{-P_r(q)}{1 - U_r P_r(q)} \quad (\text{G.14})$$

with $P_{\text{ch}}(q) = P_{\text{sp}}(q) = 2 \sum_k G(k+q)G(k)$ and $P_{\text{singlet}}(q) = -\sum_k G(k+q)G(-k)$. The interactions in the different channels are: $U_{\text{ch}} = U/2$, $U_{\text{sp}} = -U/2$ and $U_{\text{singlet}} = U$. The term $\Sigma^{(2)}$ avoids double counting some second-order terms. It is given by: $\Sigma^{(2)}(k) = \frac{1}{2} \sum_q G(k-q) U_{\text{ch}}^2 P_{\text{ch}}(q) + \frac{3}{2} \sum_q G(k-q) U_{\text{sp}}^2 P_{\text{sp}}(q) - \sum_q G(k-q) U_{\text{singlet}}^2 P_{\text{singlet}}(q)$.

For a given G , the self-energy $\Sigma^{\text{FLEX}}(k)$ is plugged in Dyson’s equation to determine a new G , and so forth until convergence. One can see that FLEX amounts to the self-consistent random-phase approximation generalized to all channels. Diagrammatically, the FLEX approximation to the self-energy corresponds to the approximation

$$\Gamma_r(k, k', q) = \Lambda_r(k, k', q) = U_r \quad (\text{G.15})$$

of the parquet equations.²

In some versions of FLEX, a pseudogap is observed (see e.g. Manske (2004)), but the parameter space where it appears is different from the next method, TPSC, for instance.

FLEX can be regarded as improving on spin fluctuation theory insofar as all fluctuations are now treated on the same footing, and their form is no longer phenomenological, thus removing a degree of arbitrariness. Yet, as in spin fluctuation theory, the FLEX self-energy is computed at one-loop order, namely without vertex corrections. The susceptibilities are infinite rings of “bubbles” or ladders with full propagators U_r in between, namely there are no vertex corrections in the susceptibilities either. As such, FLEX is at the same time analogous to spin fluctuation theory – in the sense that it stresses the importance of fluctuations in a weak-coupling scenario – and quite different in spirit, since it does not have a knob to go far or close to the quantum critical point.

G.3 The two-particle self-consistent theory (TPSC)

The two-particle self-consistent theory (TPSC) was introduced in Vilk *et al.* (1994); Vilk and Tremblay (1997). It also stresses the importance of two-particle fluctuations which it computes in a similar way as FLEX, with

¹The usual notation for these channels is $r = \text{d, m, s, t}$.

²Indeed, starting from the general definition of F , Eq. (G.4), one obtains, after a few reshufflings of integration variables and using the crossing symmetry, in loose notation:

$$\begin{aligned} GGGF &= -\frac{1}{2} G [GG]_{\text{ph}} \Lambda_{\text{ph}} - G [GG]_{\text{ph}} \Phi_{\text{ph}} \\ &\quad + G [GG]_{\text{pp}} \Lambda_{\text{pp}} - G [GG]_{\text{pp}} \Phi_{\text{pp}} \end{aligned}$$

In the SU(2) case, one can rewrite this equation in the $r = \text{ch, sp, singlet, triplet}$ channels, and use the BSE equation to write $\Phi_r = \Gamma_r [1 - \Gamma_r [GG]_r]^{-1}$. Making the approximation $\Gamma_r = \Lambda_r = U_r$ and plugging these relations into the Schwinger-Dyson equation (Eq. (G.12)), yields Eq. (G.13). More details can be found e.g. in chapter 6 of S en echal *et al.* (2003).

an additional degree of control given by the enforcement of sum rules. For a review, I refer the reader to Tremblay (2011).

Like FLEX, TPSC can be derived from the parquet formalism. In the SU(2) invariant case, the fully reducible four-leg vertex $F_{\uparrow\downarrow}$ of the Schwinger-Dyson equation (Eq. G.12) can be written as: $F_{\uparrow\downarrow}(k, k', q) = \frac{1}{2} (F_{\text{ch}}(k, k', q) - F_{\text{sp}}(k, k', q)) = -F_{\text{sp}}(k, k + q, k' - k)$, with $k \equiv (\mathbf{k}, i\omega)$. Using this property and reshuffling integration variables in the Schwinger-Dyson equation, one can rewrite the self-energy as

$$\Sigma_{\alpha}(k) = U \sum_{k', q} G(k' + q)G(k')G(k + q) \left\{ \alpha \left[\frac{F_{\text{ch}}(k, k', q) - F_{\text{sp}}(k, k', q)}{2} \right] + (1 - \alpha) [-F_{\text{sp}}(k, k', q)] \right\}$$

where α is an undetermined parameter. F can be obtained by solving the Bethe-Salpether equations (Eq.(G.6)): $F_r(kk'q) = \Gamma_r(kk_1q) (1 - \Gamma_r GG)_{kk'q}^{-1}$ (where inversion is done in k, k' space). The TPSC approximation consists in approximating the irreducible vertex in channel r , Γ_r , as $\Gamma_r(kk'q) \approx U_r$ in the numerator, and

$$\Gamma_r(kk'q) \approx g_r U_r \quad (\text{G.16})$$

in the denominator of F_r . Due to the locality of U_r , F_r depends only on q , yielding:

$$\Sigma_{\alpha}^{\text{TPSC}}(k) = -U \sum_q G_{q+k} \left(\frac{\alpha}{2} \chi_{\text{ch}}^{\text{TPSC}}(q) U_{\text{ch}} + \left(\frac{\alpha}{2} - 1 \right) \chi_{\text{sp}}^{\text{TPSC}}(q) U_{\text{sp}} \right) \quad (\text{G.17})$$

with:

$$\chi_r^{\text{TPSC}}(q) = \frac{-P_0(q)}{1 - g_r U_r P_0(q)} \quad (\text{G.18})$$

with $P_0(q) = 2 \sum_k G_0(k + q)G_0(k)$, $U_d = U/2$ and $U_m = -U/2$. (I am using slightly different conventions from the usual TPSC conventions: here U_r denotes the bare interaction in channel $r = \text{ch}, \text{sp}$, whereas in the TPSC literature it denotes the interaction renormalized by g_r).

The number g_r is akin to a local, static vertex correction; it is related to the double occupancy $\langle n_{\uparrow} n_{\downarrow} \rangle$. This can be seen by using the definition of $\Gamma_{\text{sp}} = \Gamma_{\uparrow\uparrow} - \Gamma_{\uparrow\downarrow}$, with

$$\Gamma_{\sigma\sigma'}(i, j, k, l) = \frac{\delta \Sigma_{\sigma}(ij)}{\delta G_{\sigma'}(kl)} \quad (\text{G.19})$$

(with $i \equiv (\tau, \mathbf{R})$). One can decompose $\Sigma_{\sigma}(ij) = \Sigma_{\sigma}(im)G_{\sigma}(mn)G_{\sigma}^{-1}(nj)$, evaluate the product ΣG using the equation of motion (Eq. (F.11) in Appendix F.3.3), and perform the following approximation: $\Sigma_{\sigma}(ik)G_{\sigma}(kl) = -U \langle c_{i\sigma} \bar{c}_{l\sigma} \bar{c}_{i\bar{\sigma}} c_{i\bar{\sigma}} \rangle \approx U \frac{\langle n_{i\sigma} n_{i\bar{\sigma}} \rangle}{\langle n_{i\sigma} \rangle \langle n_{i\bar{\sigma}} \rangle} G_{\sigma}(il)G_{\bar{\sigma}}(ii^+)$. One can now define

$$g_{\text{sp}} \equiv \frac{\langle n_{i\sigma} n_{i\bar{\sigma}} \rangle}{\langle n_{i\sigma} \rangle \langle n_{i\bar{\sigma}} \rangle} \quad (\text{G.20})$$

Hence, $\Gamma_{\sigma\sigma'} = \frac{\partial [U g_{\text{sp}} G_{\bar{\sigma}}(ii^+) \delta_{ij}]}{\partial G_{\sigma'}(kl)} = \frac{\partial [U g_{\text{sp}}]}{\partial G_{\sigma'}(kl)} G_{\bar{\sigma}}(ii^+) \delta_{ij} + U g_{\text{sp}} \delta_{\sigma'\bar{\sigma}} \delta_{ij} \delta_{il} \delta_{ij}$, so that finally, noticing that the first term does not depend on the spin indices, we get Eq. (G.16) for $r = \text{sp}$. The equation for $r = \text{ch}$ can be considered as an ansatz for the form of Γ_{ch} .

At this point, one still has two unknowns g_{sp} and g_{ch} , the former being related to the double occupancy. They are fixed using sum rules on the exact susceptibilities χ_r , namely $\chi_{\text{sp}}(\tau = 0, i - j = 0) = \langle s_z s_z \rangle_{\text{conn}} = \langle n \rangle - 2 \langle n_{\uparrow} n_{\downarrow} \rangle$ and $\chi_{\text{ch}}(\tau = 0, i - j = 0) = \langle nn \rangle_{\text{conn}} = \langle n \rangle + 2 \langle n_{\uparrow} n_{\downarrow} \rangle - \langle n \rangle^2$. In momentum-frequency space and in the paramagnetic phase, these sum rules read, after eliminating $\langle n_{\uparrow} n_{\downarrow} \rangle$ using Eq. (G.20):

$$\sum_q \frac{-P_0(q)}{1 + g_{\text{sp}} \frac{U}{2} P_0(q)} = \langle n \rangle - 2g_{\text{sp}} \frac{\langle n \rangle^2}{4} \quad (\text{G.21})$$

$$\sum_q \frac{-P_0(q)}{1 - g_{\text{ch}} \frac{U}{2} P_0(q)} = \langle n \rangle + 2g_{\text{sp}} \frac{\langle n \rangle^2}{4} - \langle n \rangle^2 \quad (\text{G.22})$$

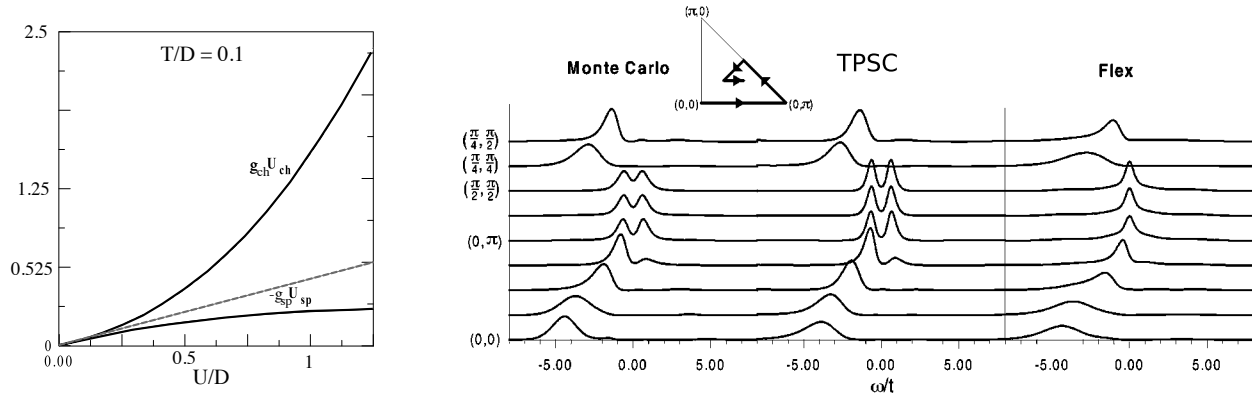


Figure G.2: *Left*: Evolution of $g_{\text{ch}}U_{\text{ch}}$ and $g_{\text{sp}}U_{\text{sp}}$ as a function of U at half-filling. The dashed line denotes the bare interaction $U/2$ (D : half-bandwidth) (adapted from Vilk and Tremblay (1997)). *Right*: Comparison of the spectral function $A(\mathbf{k}, \omega)$ obtained within TPSC and FLEX with determinantal QMC simulations at $U/D = 1$, $\beta D = 20$ and half-filling on a 8×8 lattice (from Moukouri *et al.* (2000)).

For a given filling $\langle n \rangle$ and bare interaction U , one can thus solve these equations for g_{sp} and g_{ch} , then compute $\chi_r^{\text{TPSC}}(q)$ and eventually $\Sigma(k)$ and $G(k)$. This is shown on the left panel of Fig. G.2: at half-filling, the effective irreducible interaction in the charge channel ($g_{\text{ch}}U_{\text{ch}}$) is larger than the bare interaction $U/2$ (red dashed line), whereas the irreducible spin interaction is lower than the bare interaction. This can be understood as a sign that the charge sector becomes gapped, while in the spin sector, the effective interaction is damped to enforce the Mermin-Wagner theorem: the Néel temperature is signalled by the divergence of χ_{sp} , *i.e.* when $1 + g_{\text{sp}} \frac{U}{2} P_0(q) = 0$. If the interaction is not renormalized, as in FLEX, this criterion is met for finite temperatures, leading to a violation of the Mermin-Wagner theorem. In TPSC, the sum rules lead to a preservation of the Mermin-Wagner theorem. This comes from the mere structure of Eq. (G.21): at fixed U and G_0 such that $g_{\text{sp}} \frac{U}{2} P_0(q) < 1$, let us suppose that g_{sp} increases. Then, the value of denominator decreases and the left-hand side, as a result, increases. Eq. (G.21) can only be fulfilled in the right-hand side also increases, which can only happen if g_{sp} decreases. Thus the sumrule enforces a negative feedback on the value of g_{sp} .

Note that the value α with which the self-energy is computed is in principle arbitrary. In the original papers, α was set to the value $\alpha = 1$, but it was later argued (Moukouri *et al.* (2000)) that choosing a value preserving SU(2) symmetry ($\alpha = 1/2$) was better.

As shown by Fig. G.2, TPSC applied to the Hubbard model in two dimensions is in good agreement with QMC simulations on a square lattice for quite moderate interactions. In particular, for the parameters under considerations, a pseudogap is visible in the TPSC spectrum, whereas it is absent in the FLEX spectrum. It would be hard to pinpoint the precise reason of this discrepancy and to tell which approach is “better” than the other.

The TPSC method – which can be viewed as consisting in introducing local, static vertex corrections controlled by sum rules on the susceptibilities – preserves the Mermin-Wagner theorem, describes the pseudogap phenomenon and is in good agreement with exact QMC results at weak-coupling.

G.4 The dynamical vertex approximation: an example of strong-coupling approach with long-range correlations

In the previous sections, I explained the need for methods taking into account long-range correlations while capturing local physics nonperturbatively. In recent years, a few methods have been developed to achieve

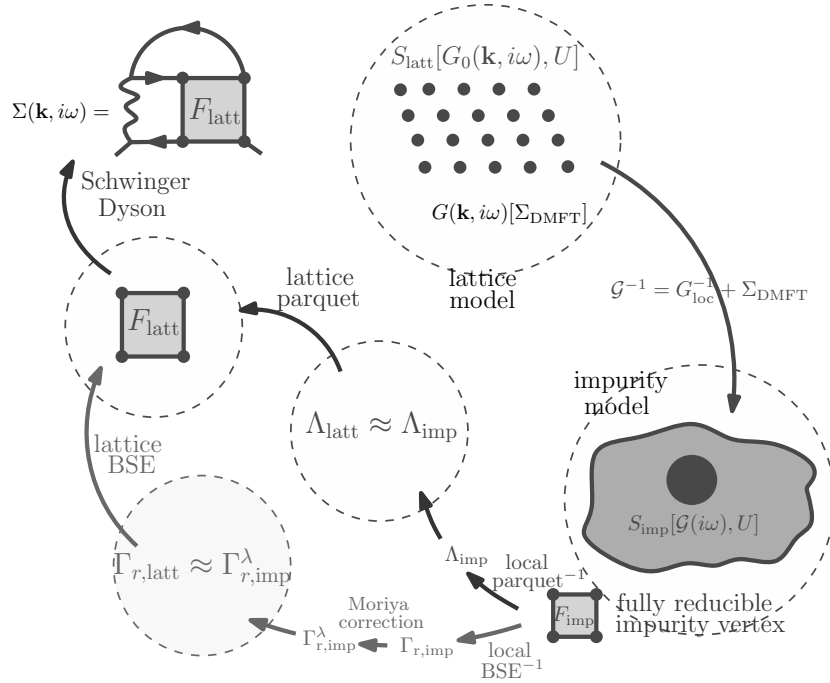


Figure G.3: The DFA method. F denotes the (4-leg) fully reducible vertex, Λ the (4-leg) fully irreducible vertex, Γ_r the irreducible vertex in channel r . Other variant (lower path): “ladder DFA”.

this goal. The GW +EDMFT method, introduced in chapter 6, is one of them. “Dual methods” (dual fermions (Rubtsov *et al.* (2008)) and dual bosons (Rubtsov *et al.* (2012))) and the very recent combination of functional renormalization group with DMFT, DMF²RG (Taranto *et al.* (2014)), are other examples.

In this section, I have chosen to focus on the dynamical vertex approximation (DFA), an approximation based on the approximation of two-particle quantities, namely observables which can be pictorially represented with four-leg diagrams. A pedagogical introduction to the two-particle formalism and DFA can be found in Held (2014); the interested reader will find more details in Rohringer *et al.* (2012).

G.4.1 DFA: A local approximation to the fully irreducible vertex

The dynamical vertex approximation (DFA, Toschi *et al.* (2007)) aims at constructing a momentum-dependent self-energy from the fully reducible vertex F using Schwinger-Dyson’s equation, Eq. (G.12).

The fully reducible vertex F is computed from an impurity 4-leg vertex. In the original formulation (Toschi *et al.* (2007)), called “parquet-DFA”, Λ is approximated by the impurity irreducible vertex:

$$\Lambda_{\text{latt}}(\mathbf{k}, \mathbf{k}', \mathbf{q}, i\omega, iv, i\Omega) \approx \Lambda_{\text{imp}}(i\omega, iv, i\Omega) \quad (\text{G.23})$$

This local approximation of Λ is directly inspired by the local approximation of the *self-energy* Σ performed in DMFT. While exact in the limit of infinite dimensions, this local approximation of the fully irreducible vertex is suspected to be valid also for low dimensions based on DCA calculations for the doped 2D Hubbard model ($U/D = 1$, $\delta = 15\%$, Maier *et al.* (2006), Fig. 4 (b)).

From this local irreducible vertex Λ , the parquet equations (Eq. G.10) – if one overcomes the task of solving them – yield a momentum-dependent $F(\mathbf{k}, \mathbf{k}', \mathbf{q}, i\omega, iv, i\Omega)$ function, and hence a momentum-dependent self-energy *via* (G.12). This is illustrated in Fig. G.3.

Due to the numerical complexity of solving the parquet equations, however:

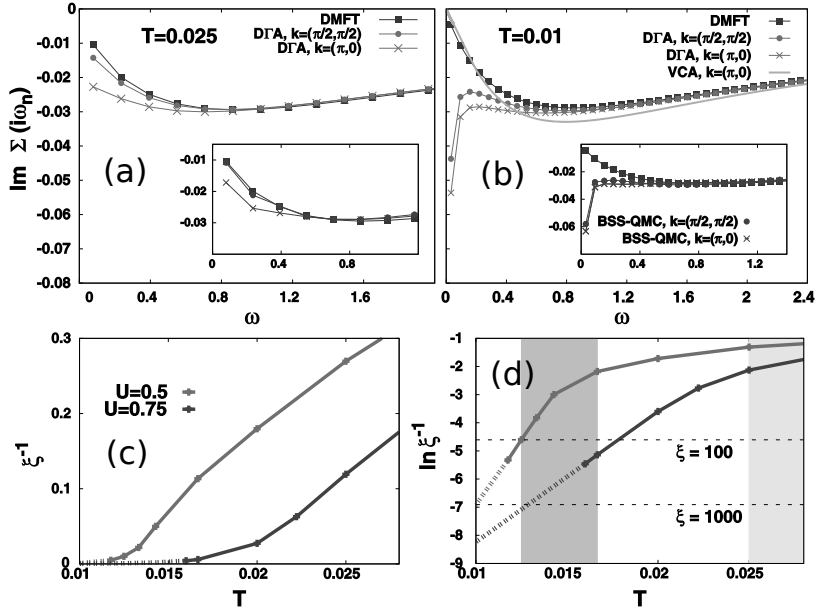


Figure G.4: DGA applied to the 2D Hubbard model. The energy unit is the half-bandwidth $D = 4t$. (a) $\text{Im} \Sigma_{\mathbf{k}}(i\omega)$ at $T = 0.025$ and $U/D = 0.5$ (b) same as (a), $T = 0.01$ (c) Dependence of the inverse AF correlation length ξ^{-1} on temperature (d) $\ln \xi^{-1}$ as a function of temperature. (from Schäfer *et al.* (2015a))

- the DGA method has only been performed in a one-shot way up to now (Held (2014)); $\Sigma(\mathbf{k}, i\omega)$ could in principle be fed back into $G(\mathbf{k}, i\omega)$ to compute a new Weiss field $\mathcal{G}(i\omega)$ and hence a new $\Lambda_{\text{imp}}(i\omega, iv, i\Omega)$ and so forth, but this has not been done ever since the original paper. Even if done in this way, it is unclear whether self-consistent DGA would be derivable from a functional.
- in this one-shot formulation, parquet-DGA has been restricted to small-size systems, namely at most an 8-site Hubbard ring (Valli *et al.* (2015)).
- a variant of DGA, coined “ladder-DGA”, has been introduced to circumvent the parquet hurdle (Toschi *et al.* (2007); Katanin *et al.* (2009)). I elaborate on this variant in the next subsection.

G.4.1.1 Ladder-DGA: A local approximation to the channel-wise irreducible vertex

“Ladder-DGA” has been introduced to avoid the daunting task of solving the parquet equations on the lattice (Toschi *et al.* (2007); Katanin *et al.* (2009)). It consists in making a local approximation not of the fully irreducible vertex Λ , but of the irreducible vertex in one given channel r , *viz.*

$$\Gamma_{r,\text{latt}}(\mathbf{k}, \mathbf{k}', \mathbf{q}, i\omega, iv, i\Omega) \approx \Gamma_{r,\text{imp}}(i\omega, iv, i\Omega) \quad (\text{G.24})$$

Directly resumming the ladders of the Bethe-Salpeter equation (G.6) to get F leads to divergences during the inversion process: the matrix $GG\Gamma_r$ in Eq. (G.8) starts having eigenvalues which are larger than unity, signalling instabilities in the given channel. Such instabilities are absent when solving the parquet equations where all channels are coupled with one another. To remove this artefact and mimic the full parquet equations in a less expensive way, a parameter λ is introduced and fixed by imposing the preservation of sum rules similar to those of TPSC (Toschi *et al.* (2007); Katanin *et al.* (2009)).

G.4.1.2 Selected results: effect of long-range correlations on the Mott transition in two dimensions

Ladder-DGA has been applied to the 2D Hubbard model (Schäfer *et al.* (2015a)) and the 3D Hubbard model (Schäfer *et al.* (2015b)). In Fig. G.4, results for the 2D Hubbard model are shown. While for intermediate

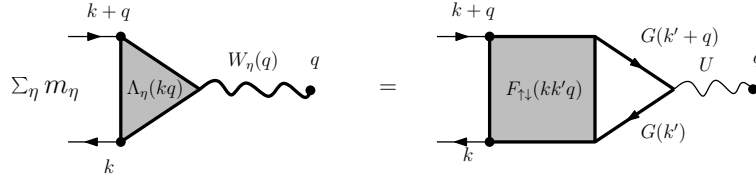


Figure G.5: Link between the three-leg vertex and the fully reducible four-leg vertex

(but low) temperatures, the self-energy is that of a correlated metal (panel (a)), for lower temperatures DΓA predicts the self-energy to acquire an insulating behavior at low energies (namely the insulating behavior is restricted to the three lowest Matsubara frequencies, panel (b)). This phenomenon is interpreted as a consequence of very large correlation lengths which would destroy coherence, as shown in panels (c) and (d). Interestingly, the high-temperature behavior of the inverse AF correlation length is linear and if extrapolated, would yield a finite Néel temperature, in violation of the Mermin-Wagner theorem. At very low temperatures, however, this behavior drastically changes as the correlation length acquires an exponential behavior approaching $T = 0$, in compliance with the Mermin-Wagner theorem. Thus, DΓA predicts the 2D Hubbard model to be insulating all the way down to $U = 0$ for low temperatures as a consequence of long-ranged spin fluctuations.

G.4.2 Link between the three-leg and the four-leg vertices

One can rewrite Eq. (G.12) in the following suggestive way:

$$\Sigma(k) = - \sum_q G(k+q) \left\{ \sum_{k'} U G(k'+q) G(k') F_{\uparrow\downarrow}(kk'q) \right\}$$

Remembering the TRILEX form of the self-energy

$$\Sigma(k) = - \sum_q G(k+q) \left\{ \sum_{\eta} \lambda_{\eta} m_{\eta} W_{\eta}(q) \Lambda_{\eta}(kq) \right\}$$

leads to the identification:

$$\sum_{\eta} \lambda_{\eta} m_{\eta} W_{\eta}(q) \Lambda_{\eta}(kq) = \sum_{k'} U G(k'+q) G(k') F_{\uparrow\downarrow}(kk'q)$$

which is depicted in Fig. G.5.

Part VIII

Appendix: general background

This part has mainly a pedagogical purposes. It gathers background information necessary to understand the main text.

K Appendix to chapter 6

L Appendix to chapter 8

| | |
|--|-----|
| L.1 Non-interacting free energy | 247 |
| L.2 Simplifications in the homogeneous phase | 248 |
| L.3 Spin rotation invariance: properties | 248 |

M Appendix to chapter 11

| | |
|--|-----|
| M.1 Dynamical trace factor in CTQMC | 249 |
| M.2 Hamiltonian formulation the impurity model | 250 |
| M.3 Computation of $K(\tau)$ from $U(iv)$ | 251 |
| M.4 A code example: the insert move | 252 |

N Appendix to chapter 10

| | |
|--|-----|
| N.1 Simple-minded estimates for $f(\langle X \rangle)$ | 254 |
| N.2 Relationship between the error estimate and the intrinsic variance | 255 |
| N.3 Relationship between empirical and intrinsic variance | 256 |
| N.4 Details for paragraph 10.3.4.1.2 | 257 |
| N.5 Autocorrelation time estimation from the autocorrelation function | 258 |

Index

Bibliography

Experimental probes for condensed matter physics: a brief theoretical overview

This part is devoted to experimental probes seen from a theoretical point of view. Its purpose is to understand what observables are accessible from a given probe.

H.1 Surface probes: electron diffraction, electron energy loss spectroscopy, photoemission

H.1.1 Low-energy electron diffraction and reflection high-energy electron diffraction (LEED and RHEED)

Low-energy electron diffraction (LEED) consists in shining electrons with energies of 20 to 200 eV on the surface of a solid, and then detecting the diffracted electrons, as illustrated in Fig. H.1a. The pattern observed on the screen of the detector is an image of the reciprocal lattice of the *surface* of the sample. Indeed, electrons have a very small penetration depth (as opposed to X-rays, which makes LEED better suited to study surfaces than X-ray diffraction, which is used to study bulk symmetries). LEED can thus detect changes in the symmetry of the surface.

Reflection high-energy electron diffraction (RHEED) is very similar to LEED, only the electrons are more energetic and shot almost parallel to the surface, as shown in Fig. H.1b. This probe also yields a diffraction pattern of the surface's symmetry.

H.1.2 Electron energy loss spectroscopy (EELS)

Electron energy loss spectroscopy (EELS) consists in focussing energetic electrons (in an energy range of 100-200 keV) on a sample and measuring the energy loss and momentum (scattering angle) of the *transmitted* electrons in an electron spectrometer (see Fig. H.1c). This is usually done in a transmission-emission microscope (TEM). Going through the material, the electron is scattered inelastically by various processes, including phonons, inter and intraband transitions, plasmons, etc. EELS was developed as early as the mid 1940s by Hillier and Baker but only in the 1990s did various technological advances allow to reach precisions of $\Delta E \sim 0.4$ eV nowadays. Compared to ARPES (explained later), EELS probes deeper states (~ 1000). Yet, it is limited to the investigation *thin samples* since it is a transmission probe and electrons, as charged particles, couple quite strongly to matter (compared to neutrons for instance, see section H.2.1 on neutron scattering).

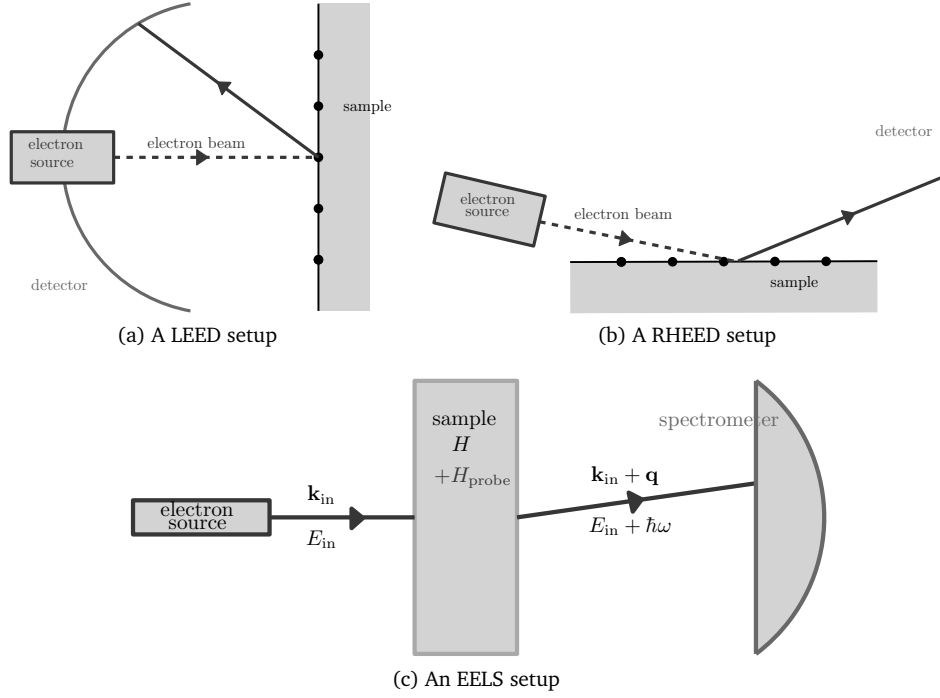


Figure H.1: Various electron scattering probes

In the following, I give a succinct description of the physical observables that are to be found in an EELS spectrum. More details about EELS in general can be found in Schnatterly (1979); Egerton (2008, 2011). Early works on the link between particle scattering and the charge-charge correlation or inverse dielectric function include van Hove (1954); Fano (1956); Nozières and Pines (1958).

H.1.2.1 Microscopic theory

As before, the sample is described by a Hamiltonian H with eigenstates $\Psi_n (E_n)$. An electron beam with energy E_{in} and momentum \mathbf{k}_{in} is focused on the sample. The spectrometer measures the outgoing electron beam with energy E_{out} and momentum \mathbf{k}_{out} . I note $\hbar\omega \equiv E_{out} - E_{in}$ and $\mathbf{q} \equiv \mathbf{k}_{out} - \mathbf{k}_{in}$. The electron interacts with the electrons in the solid via the Coulomb interaction:

$$H_{probe}^{q,\omega}(t) = v_{Coul}(\mathbf{q})n_{\mathbf{q}}e^{-i\omega t} \quad (\text{H.1})$$

with $n_{\mathbf{q}} = \sum_{\mathbf{k}} c_{\mathbf{k}+\mathbf{q}}^\dagger c_{\mathbf{k}}$ and $v_{Coul}(\mathbf{q})$ is the Fourier transform of the Coulomb interaction, $v_{Coul}(\mathbf{q}) = \frac{e^2}{\epsilon_0 q^2}$. Note that due to the high energy of the probing electrons, the Coulomb interaction is not screened. Since the probing electrons are highly energetic, one can assume the sample-probe coupling to be weak enough, and using the Golden Rule (derived in Appendix I.2.2, see Eq. (I.21) with $O_{\mathbf{q}} \equiv n_{\mathbf{q}}$ and $g \equiv v_{\mathbf{q}}$):

$$\Gamma(\mathbf{q}, i\omega) = 2v_{Coul}^2(\mathbf{q})(1 + n_B(\omega))\chi_{ch}''(\mathbf{q}, \omega) \quad (\text{H.2})$$

where $\chi_{ch}(\mathbf{q}, \omega)$ is the charge-charge correlation function. The $1 + n_B(\omega)$ factor comes from the fluctuation-dissipation theorem (see Appendix). This scattering rate can be expressed as a function of the dielectric function, defined as:

$$\epsilon(\mathbf{q}, \omega) \equiv 1 - v_{Coul}(\mathbf{q})P_{ch}(\mathbf{q}, \omega) \quad (\text{H.3})$$

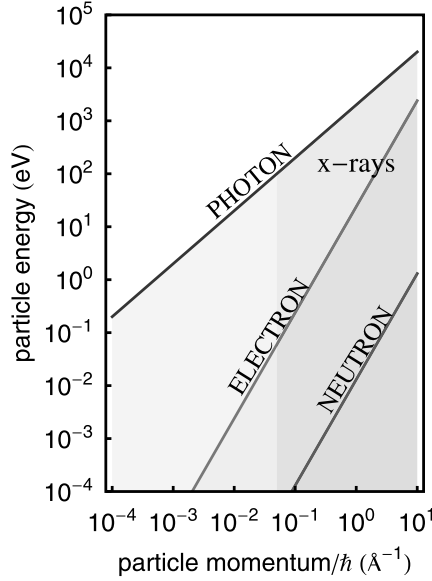


Figure H.2: Kinetic energy and momentum carried by particles used in inelastic scattering experiments (from Ament *et al.* (2011))

where the polarization P_{ch} is related to $\chi_{\text{ch}}(\mathbf{q}, \omega)$ via:

$$P_{\text{ch}}(\mathbf{q}, \omega) = \frac{-\chi_{\text{ch}}(\mathbf{q}, \omega)}{1 - v_{\text{Coul}}(\mathbf{q})\chi_{\text{ch}}(\mathbf{q}, \omega)}$$

so that: $\epsilon^{-1} = 1 - v_{\text{Coul}}\chi_{\text{ch}}$, and hence $-\text{Im}\epsilon^{-1}(\mathbf{q}, \omega) = v_{\text{Coul}}(\mathbf{q})\chi_{\text{ch}}''(\mathbf{q}, \omega)$. As a result,

$$\Gamma_{\text{EELS}}(\mathbf{q}, \omega) = 2(1 + n_{\text{B}}(\omega))v_{\text{Coul}}(\mathbf{q}) \left(-\text{Im} \left[\epsilon^{-1}(\mathbf{q}, \omega) \right] \right) \quad (\text{H.4})$$

H.1.2.2 Physical observables

As shown by Eq. (H.4),

EELS yields direct insights into the dielectric properties of a material, in particular collective modes in the charge sector such as plasmons. Indeed, in the $\mathbf{q} \rightarrow 0$ limit, the free (Lindhard) polarization for the electron gas is given by $P_{\text{ch}}(q \rightarrow 0, \omega) = \frac{n}{m} \frac{q^2}{\omega^2}$ (see Appendix I.4.1.2). Using (H.3), the zeros of the dielectric function are thus given by $0 = 1 - \frac{e^2}{\epsilon_0 q^2} \frac{n}{m} \frac{q^2}{\omega^2}$ i.e. $\omega = \sqrt{\frac{ne^2}{\epsilon_0 m}} \equiv \omega_{\text{P}}$, the plasmon frequency. More generally, it gives access to the charge correlation function (see Eq. (H.2)) and can thus be used to observe the opening of gaps.

EELS yields observables similar to inelastic X-ray scattering (RIXS/NIXS, see Ament *et al.* (2011) for a review), a probe where *photons* are scattered by the material. The main different lies in the energy scales, momenta and depths accessible by each method. This is summarized in Fig. H.2. Scattering with *neutrons* (inelastic neutron scattering) is elaborated on in section H.2.1.

H.1.3 Scanning tunneling microscopy (STM)

Scanning tunneling microscopy (STM) has been introduced by Binnig and Rohrer in 1982 to study surface states of $\text{CaIrSn}_4(110)$, $\text{Au}(110)$ and the 7×7 reconstruction of $\text{Si}(111)$ (Binnig *et al.* (1982b,a, 1983a); Binnig and Rohrer (1983); Binnig *et al.* (1983b)). It consists in approaching a metallic tip (typically tungsten or platinum-iridium) to the surface of a sample, and measure the tunneling current flowing from the sample

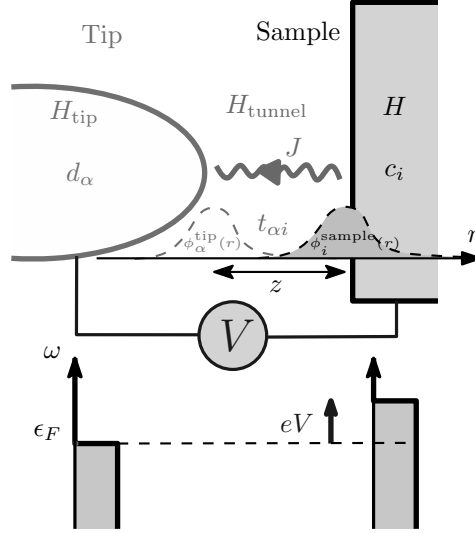


Figure H.3: A STM setup.

to the tip. Adjusting the tip-sample distance to keep the current fixed yields a topography of the surface with atomic resolution. A basic theoretical framework has been laid out by Bardeen as early as 1961 (Bardeen (1961)). Tersoff and Hamann (1985) proposed a more detailed description of the tip wavefunctions (in terms of s -waves) and showed the current to be proportional to the local density of states (LDOS) on the surface, while Chen (1990) extended the tip modelling to other orbital characters (especially d -waves, since W and Pt-Ir are d -wave metals). Since these approaches implicitly assume the sample to be described by weakly-interacting electrons, I give below a more general derivation of the STM current where no assumption is made on the Hamiltonian describing the sample.

H.1.3.1 Microscopic general derivation of the STM current

A schematic STM setup is shown in Fig. H.3. The tip, sample, and tip-sample interaction are modelled by the following Hamiltonians:

$$H_{\text{tip}} = \sum_{\alpha} \epsilon_{\alpha} d_{\alpha}^{\dagger} d_{\alpha} \quad (\text{H.5})$$

$$H = \sum_{ij} \epsilon_{ij} c_i^{\dagger} c_j + H_{\text{int}} \quad (\text{H.6})$$

$$H_{\text{tunnel}} = \sum_{\alpha i} t_{\alpha i} (d_{\alpha}^{\dagger} c_i + \text{h.c.}) \quad (\text{H.7})$$

Namely: the tip is described by a non-interacting or (for realistic calculations) Kohn-Sham Hamiltonian (d_{α}^{\dagger} creates *e.g.* a Bloch or Kohn-Sham state $\psi_{\alpha=n,\mathbf{k},\sigma}^{\text{tip}}(\mathbf{r})$), the sample by an interacting Hamiltonian (with annihilation and creation operators c_i and c_i^{\dagger} , i referring *e.g.* to a Wannier site \mathbf{R}_i), while the coupling between the tip and the sample is a simple hopping term, where the tunneling matrix element $t_{\alpha i}$ is given by:

$$t_{\alpha i} \equiv \langle \phi_{\alpha}^{\text{tip}} | h(\mathbf{r}) | \phi_i^{\text{sample}} \rangle = \iiint_V d\mathbf{r} (\phi_{\alpha}^{\text{tip}})^*(\mathbf{r}) \left(-\frac{\hbar^2 \Delta}{2m} + V_{\text{eff}}(\mathbf{r}) \right) \phi_i^{\text{sample}}(\mathbf{r}) \quad (\text{H.8})$$

A bias voltage $V > 0$ induces a potential difference between the tip and the sample: $n_{\text{F}}^{\text{sample}}(\omega) = n_{\text{F}}^{\text{tip}}(\omega - eV)$. The current flowing from the tip to the sample as a result of the bias voltage is given by

$$J_{\text{STM}} \equiv e \frac{d}{dt} \langle \hat{N}_{\text{tip}}(t) \rangle \quad (\text{H.9})$$

where $N_{\text{tip}} \equiv \sum_{\alpha} d_{\alpha}^{\dagger} d_{\alpha}$. $\hat{N}_{\text{tip}}(t)$ is written in the Heisenberg representation, so that $J = \frac{e}{\hbar} \langle [H_{\text{tot}}, N_{\text{tip}}](t) \rangle$. Since $[H_{\text{tot}}, N_{\text{tip}}] = [H_{\text{tunnel}}, N_{\text{tip}}] = \sum_{\alpha i} t_{\alpha i} (c_i^{\dagger} d_{\alpha} - d_{\alpha}^{\dagger} c_i)$, one obtains:

$$J_{\text{STM}} = \frac{e}{\hbar} \sum_{\alpha i} t_{\alpha i} (G_{\alpha i}^{<}(t, t) - G_{i \alpha}^{<}(t, t))$$

where I used the definition: $G_{i \alpha}^{<} \equiv i \langle d_{\alpha}^{\dagger} c_i \rangle$. Expanding to first order in t , we get: $G_{i \alpha} = G_i t_{i \alpha} G_{\alpha}$, where G denotes the Keldysh matrix $G \equiv \begin{pmatrix} G^R & G^K \\ 0 & G^A \end{pmatrix}$, $G^K \equiv G^> + G^<$, and we have used $G_{ij}^{<} \equiv G_i^{<} \delta_{ij}$ and $G_{\alpha \beta}^{<} \equiv G_{\alpha}^{<} \delta_{\alpha \beta}$. Hence, $G_{i \alpha}^{<}(\omega) = G_i^R(\omega) t_{i \alpha} G_{\alpha}^{<}(\omega) + G_i^{<}(\omega) t_{i \alpha} G_{\alpha}^A(\omega)$ so that, using $A(\omega) = i(G^R(\omega) - G^A(\omega))$ and $G^<(\omega) = i n_{\text{F}}(\omega) A(\omega)$:

$$\begin{aligned} G_{\alpha i}^{<}(\omega) - G_{i \alpha}^{<}(\omega) &= t_{i \alpha} (G_{\alpha}^R(\omega) G_i^{<}(\omega) + G_{\alpha}^{<}(\omega) G_i^A(\omega) - G_i^R(\omega) G_{\beta \alpha}^{<}(\omega) - G_i^{<}(\omega) G_{\alpha}^A(\omega)) \\ &= t_{i \alpha} (G_i^{<}(\omega) (G_{\alpha}^R(\omega) - G_{\alpha}^A(\omega)) + G_{\alpha}^{<}(\omega) (G_i^A(\omega) - G_i^R(\omega))) \\ &= t_{i \alpha} (i n_{\text{F}}^{\text{sample}}(\omega) A_i^{\text{sample}}(\omega) (-i A_{\alpha}^{\text{tip}}(\omega)) + i n_{\text{F}}^{\text{tip}}(\omega) A_{\alpha}^{\text{tip}}(\omega) (i A_i^{\text{sample}}(\omega))) \\ &= t_{i \alpha} (n_{\text{F}}^{\text{sample}}(\omega) - n_{\text{F}}^{\text{tip}}(\omega)) A_i^{\text{sample}}(\omega) A_{\alpha}^{\text{tip}}(\omega) \end{aligned}$$

Finally, one gets the general expression for the STM current:

$$J_{\text{STM}}(V) = \frac{4e}{\hbar} \int_{-\infty}^{\infty} d\omega \left[\{n_{\text{F}}(\omega) - n_{\text{F}}(\omega - eV)\} \sum_{i, n, \mathbf{k}} |t_{n\mathbf{k}, i}|^2 A_i^{\text{sample}}(\omega) A_{n\mathbf{k}}^{\text{tip}}(\omega) \right] \quad (\text{H.10})$$

The factor of 4 comes from the spin degree of freedom (note the *double* sum), and $n_{\text{F}}^{\text{sample}}(\omega) = n_{\text{F}}(\omega)$, $n_{\text{F}}^{\text{tip}}(\omega) = n_{\text{F}}(\omega - eV)$.

H.1.3.2 Expression in limiting cases and physical interpretation

Various approximations to the general result Eq.(H.10) can be made. At low bias voltage and low temperature, $n_{\text{F}}^{\text{tip}}(\omega - eV) \approx n_{\text{F}}^{\text{tip}}(\omega) - eV \delta(\omega - \varepsilon_{\text{F}})$, whence:

$$J_{\text{STM}} = -\frac{4e^2 V}{\hbar} \sum_{i, n\mathbf{k}} |t_{n\mathbf{k}, i}|^2 A_i^{\text{sample}}(\varepsilon_{\text{F}}) A_{n\mathbf{k}}^{\text{tip}}(\varepsilon_{\text{F}})$$

The current flows from right to left ($J_{\text{STM}} < 0$), as expected. Various approximations can be made to $t_{\alpha i}$, including those proposed in the conventional works of Bardeen (1961), Tersoff and Hamann (1985) and Chen (1990). Here, I focus on the crudest approximation ,

$$t_{n\mathbf{k}i} \propto e^{-\kappa z} \delta_{\mathbf{R}_i - \mathbf{r}_{\text{tip}}} \quad (\text{H.11})$$

where z is the tip-sample distance and $\delta_{\mathbf{R}_i - \mathbf{r}_{\text{tip}}}$ selects the sample region close to the tip. $t_{n\mathbf{k}i}$ amounts to the tunneling amplitude of the tip wavefunction into the sample.

Furthermore, if the tip is non-interacting: $A_{n\mathbf{k}}^{\text{tip}}(\omega) = \delta(\omega - \varepsilon_{n\mathbf{k}})$, and if we denote by $N^{\text{tip}}(\omega) \equiv A_{\text{loc}}^{\text{tip}}(\omega) = \sum_{n\mathbf{k}} \delta(\omega - \varepsilon_{n\mathbf{k}})$, we obtain the final simplified expression for the STM current:

$$J_{\text{STM}} \propto -\frac{4e^2 V}{\hbar} e^{-\kappa z} A_{\text{loc}, \mathbf{R}_{\text{tip}}}^{\text{sample}}(\varepsilon_{\text{F}}) N^{\text{tip}}(\varepsilon_{\text{F}}) \quad (\text{H.12})$$

Thus, STM measures the local spectral weight at the Fermi level in the vicinity of the tip, $A_{\text{loc}, \mathbf{R}_{\text{tip}}}^{\text{sample}}(\varepsilon_{\text{F}})$, which can be used to infer the insulating or metallic state of the sample. STM is of course used to measure the

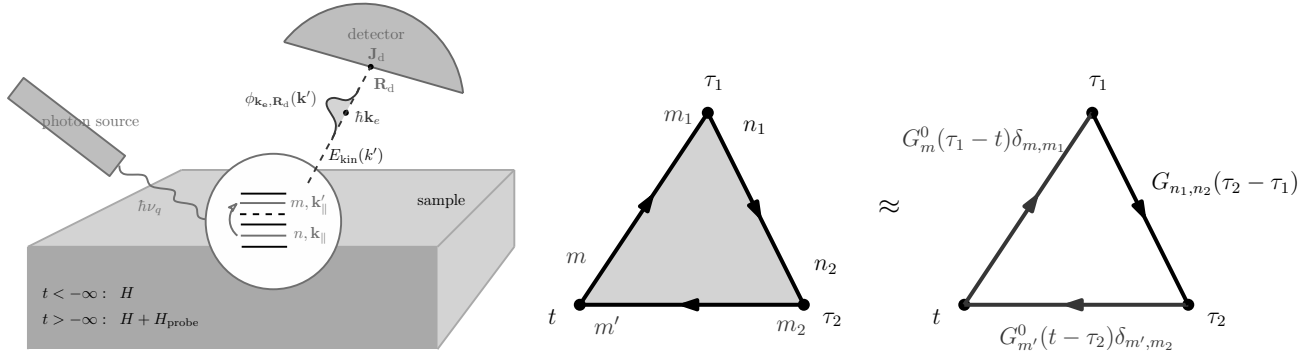


Figure H.4: Photoemission spectroscopy. Left: experimental setup. Right: sudden approximation

surface topography: keeping J_{STM} constant on a corrugated sample, the tip displacement z is a direct image of the real-space landscape.

The differential conductance at low temperature gives direct access to the frequency-dependence of $A^{\text{sample}}(\omega)$:

$$G_{\text{STM}}(V) \equiv \frac{dJ_{\text{STM}}}{dV} = \frac{4e^2}{\hbar} \int_{-\infty}^{\infty} d\omega \left(\frac{dn_F}{d\omega} \Big|_{\omega=eV} \right) \sum_{i,n,\mathbf{k}} |t_{n\mathbf{k},i}|^2 A_i^{\text{sample}}(\omega) A_{n\mathbf{k}}^{\text{tip}}(\omega) \text{ and thus}$$

$$G_{\text{STM}}(V) \approx -\frac{4e^2}{\hbar} \sum_{i,n,\mathbf{k}} |t_{n\mathbf{k},i}|^2 A_{n\mathbf{k}}^{\text{tip}}(eV) A_i^{\text{sample}}(eV) \quad (\text{H.13})$$

H.1.4 Photoemission spectroscopy (PES): ARPES and cPES

Photoemission spectroscopy (PES) is based on the photoelectric effect (discovered by Hertz in 1887 and explained by Einstein in 1905 by invoking the quantum nature of light), *i.e.* the photon-induced creation of electrical currents. PES consists in shining monochromatic light on the surface of a sample and then measuring the energy and momentum of the outgoing electrons in a detector, as illustrated in Fig. H.4. Depending on the incident photon energy $\hbar\nu$, one probes the core-level structure ($100 \text{ eV} < \hbar\nu < 1000 \text{ eV}$ for “soft X-rays” [SXPS, Soft X-ray Photoemission Spectroscopy], $\hbar\nu > 1000 \text{ eV}$ for X-rays [XPS]) or the valence structure ($5 \text{ eV} < \hbar\nu < 100 \text{ eV}$, ultraviolet light [ARPES, Angle-Resolved PES]) of the material. Thus, the typical timescales range from the femtosecond for ARPES to attoseconds for XPS. Since the escape depth of electrons from the solid is small (a few Angstroms), ARPES is a surface-sensitive probe (ARPES typically probes states with a maximum depth of 5-10 Å). It must be carried out in ultra-high vacuum conditions to keep the surface clean of adsorbed contaminants. Current experimental precisions for ARPES reach $\Delta E \sim 5\text{--}10 \text{ meV}$ and $\Delta\theta \sim 0.1^\circ$. XPS has a far coarser angle resolution.

H.1.4.1 Microscopic derivation of the photocurrent

In the following, I sketch a simplified microscopic theory of PES based on the Keldysh formalism to put the link between PES and the (interacting) spectral function $A(\mathbf{k}, i\omega)$ (introduced in Section 2.1) on a firm basis. I drew inspiration from recent works on pump-probe ARPES experiments (Freericks *et al.* (2009); Braun *et al.* (2015)). A similar derivation can also be found in Berthod (2012). More conventional ways of deriving the photocurrent as well as a general introduction on ARPES can be found *e.g.* in Hüfner (1995); Damascelli *et al.* (2003).

We model the sample and the probing field by the following Hamiltonians:

$$H = \sum_{n, \mathbf{k}_{\parallel}} \varepsilon_{n, \mathbf{k}_{\parallel}} c_{n, \mathbf{k}_{\parallel}}^{\dagger} c_{n, \mathbf{k}_{\parallel}} + H_{\text{int}} \quad (\text{H.14})$$

$$H_{\text{probe}, \tau} = \sum_{nm \mathbf{k}_{\parallel}} M_{n, m, \mathbf{k}_{\parallel}} c_{m, \mathbf{k}'_{\parallel}}^{\dagger} c_{n, \mathbf{k}_{\parallel}} a_{\mathbf{q}} e^{-i\omega_{\mathbf{q}} \tau} + \text{h.c.} \quad (\text{H.15})$$

The first term in H , which we will call H_0 , denotes the non-interacting (or Kohn-Sham) Hamiltonian. $c_{n, \mathbf{k}_{\parallel}}^{\dagger}$ creates a Bloch (or Kohn-Sham) state $\phi_{\mathbf{k}_{\parallel} n}(\mathbf{r})$ in band n with momentum \mathbf{k}_{\parallel} (since ARPES is a surface probe, only parallel momenta \mathbf{k}_{\parallel} are concerned). The many-body eigenstates (resp. eigenvalues) of H are denoted as $|\Psi_i\rangle$ (resp. E_i). $H_{\text{probe}, \tau}$ describes the coupling of the photon field of energy $\hbar\nu_{\mathbf{q}}$ with matter (time subscripts denote intrinsic time dependence, as opposed to the Heisenberg picture defined later with hats): the photon field, described by the operator $a_{\mathbf{q}}$, photoexcites low-energy electrons ($n, \mathbf{k}_{\parallel}$) into high-energy electrons ($m, \mathbf{k}'_{\parallel}$), with $\mathbf{k}'_{\parallel} = \mathbf{k}_{\parallel} + \mathbf{q} \approx \mathbf{k}_{\parallel}$. The matrix elements are given by:¹

$$M_{n, m, \mathbf{k}_{\parallel}} = \left\langle \phi_{\mathbf{k}_{\parallel} m} \left| -\frac{e}{m_e c} \mathbf{A}_{\mathbf{q}} \cdot \mathbf{p} \right| \phi_{\mathbf{k}_{\parallel} n} \right\rangle \quad (\text{H.16})$$

$\mathbf{A}_{\mathbf{q}}$ is the electromagnetic potential associated with the optical radiation, while \mathbf{p} is the momentum operator, $\mathbf{p} \equiv -i\hbar\nabla$. The matrix elements entail selection rules depending on the symmetries of the Bloch states.

The photon beam is switched on at time t_0 (which will be sent to $-\infty$). Neglecting detection noise, the detector measures the photocurrent of outgoing electrons, \mathbf{J}_d . After turning on the probe, the states of H evolve as $|\Psi_i(t)\rangle = U(t_0, t)|\Psi_i\rangle$, where the evolution operator is defined as $U(t_0, t) \equiv T \exp(-\frac{i}{\hbar} \int_{t_0}^t d\tau (H + H_{\text{probe}})_{\tau})$ (see Appendix I.2). The average photocurrent after turning on the probe is given by

$$\langle \mathbf{J}_d(t) \rangle = \sum_i p_i \langle \Psi_i(t) | \mathbf{J}_d | \Psi_i(t) \rangle \quad (\text{H.17})$$

where $p_i \equiv e^{-E_i/k_B T} / Z$ are the Boltzmann weights associated with H and Z is the partition function. Assuming that the probing optical field is a small perturbation, and noting that the first-order term will not contribute since the photon field has a vanishing expectation value, we have (see Appendix I.2.1) $U(t_0, t) \approx -\frac{i}{\hbar} \int_{t_0}^t d\tau U_H(t_0, \tau) H_{\text{probe}, \tau} U_H(\tau, t)$ where U_H is the evolution operator associated with H . Hence,

$$\langle \mathbf{J}_d(t) \rangle = \frac{1}{\hbar^2} \iint_{t_0}^t d\tau_1 d\tau_2 \langle \hat{H}_{\text{probe}}^{\dagger}(\tau_1) \hat{\mathbf{J}}_d(t) \hat{H}_{\text{probe}}(\tau_2) \rangle_H \quad (\text{H.18})$$

where for any operator O , $\langle O \rangle_H \equiv \sum_n p_n \langle \Psi_n | O | \Psi_n \rangle$, and hatted operators are written in the Heisenberg representation $\hat{O}(t) = U_H(t_0, t) O_t U_H(t, t_0)$.

If the energy of the excited electrons is higher than the work function of the solid, W^2 (namely if $\varepsilon_{m, \mathbf{k}'_{\parallel}} - \mu > W$), they can acquire a z component, *i.e.* their wavevector becomes $\mathbf{k}'(m) = (\mathbf{k}'_{\parallel}, k'_z(m))$ where k'_z is determined by the energy conservation rule: $\varepsilon_{m, \mathbf{k}'_{\parallel}} - \mu = \frac{\hbar k'^2}{2m_e} + W$. Finally, these outgoing electrons form wave packets that can in turn be detected by the detector. The wavepackets are described by the following creation operator:

$$c_{\mathbf{k}_e \mathbf{R}_d}^{\dagger} = \sum_{m \mathbf{k}'_{\parallel}} \phi_{\mathbf{k}_e \mathbf{R}_d}(\mathbf{k}'(m)) c_{m \mathbf{k}'_{\parallel}}^{\dagger} \quad (\text{H.19})$$

where $\phi_{\mathbf{k}_e \mathbf{R}_d}(\mathbf{k}'(m))$ is the envelope of the wavepacket, peaked around \mathbf{k}_e . The photocurrent is given by

$$\mathbf{J}_d = \mathbf{v}_e c_{\mathbf{k}_e \mathbf{R}_d}^{\dagger} c_{\mathbf{k}_e \mathbf{R}_d} \quad (\text{H.20})$$

¹This comes from the replacement $\hbar_0 = \frac{p^2}{2m_e}$ by $\hbar_0(A) = \frac{1}{2m_e} (\mathbf{p} - \frac{e}{c} \mathbf{A})^2$ in the presence of a magnetic field \mathbf{B} such that $\nabla \times \mathbf{A} = \mathbf{B}$. Neglecting bi-photon processes, one obtains $\delta \hbar_0 = -\frac{e}{m_e c} \mathbf{A} \cdot \mathbf{p}$.

²The work function is the minimal energy to remove an electron inside the solid to a position just outside the solid

with the velocity given by: $\mathbf{v}_e = \hbar \mathbf{k}_e / m_e$. Substituting Eqs (H.15-H.20) into (H.18) yields:

$$\begin{aligned} \langle \mathbf{J}_d(t) \rangle &= \frac{\mathbf{v}_e}{\hbar^2} \iint_{t_0}^t d\tau_1 d\tau_2 \sum_{n_1 m_1 \mathbf{k}_{\parallel 1}} \sum_{n_2 m_2 \mathbf{k}_{\parallel 2}} M_{n_1, m_1, \mathbf{k}_{\parallel 1}}^* M_{n_2, m_2, \mathbf{k}_{\parallel 2}} \sum_{m \mathbf{k}'_{\parallel}} \phi_{\mathbf{k}_e \mathbf{R}_d}(\mathbf{k}'(m)) \sum_{m \mathbf{k}_{\parallel}} \phi_{\mathbf{k}_e \mathbf{R}_d}^*(\mathbf{k}(m')) \\ &\quad e^{i\hbar v_q(\tau_1 - \tau_2)} \langle c_{n_1, \mathbf{k}_{\parallel 1}}^\dagger(\tau_1) c_{m_1, \mathbf{k}'_{\parallel 1}}(\tau_1) c_{m' \mathbf{k}'_{\parallel}}^\dagger(t) c_{m_2, \mathbf{k}_{\parallel 2}}(t) c_{m_2, \mathbf{k}_{\parallel 2}}^\dagger(\tau_2) c_{n_2, \mathbf{k}_{\parallel 2}}(\tau_2) \rangle_H \end{aligned}$$

where we have used: $\langle a_{\mathbf{q}}^\dagger(\tau_1) a_{\mathbf{q}}(\tau_2) \rangle_H = 1$.

Now, one can notice that in the three-body correlator of the second line, only the indices n_1 and n_2 refer to low-lying states, whereas all other indices (m) refer to high-energy states, the photoelectrons, which can be regarded as free electrons governed by H_0 (this is the ‘‘one-step’’ or ‘‘sudden’’ approximation first introduced by Pendry (1976)). Hence, we can approximate this three-body correlator as the product of three one-body correlators:

$$\begin{aligned} &\langle c_{n_1, \mathbf{k}_{\parallel 1}}^\dagger(\tau_1) c_{n_2, \mathbf{k}_{\parallel 2}}(\tau_2) \rangle_H \left\{ \langle c_{m_1, \mathbf{k}'_{\parallel 1}}(\tau_1) c_{m' \mathbf{k}'_{\parallel}}^\dagger(t) \rangle_{H_0} \langle c_{m' \mathbf{k}'_{\parallel}}(t) c_{m_2, \mathbf{k}_{\parallel 2}}^\dagger(\tau_2) \rangle_{H_0} \right\} \\ &= \langle c_{n_1, \mathbf{k}_{\parallel 1}}^\dagger(\tau_1) c_{n_2, \mathbf{k}_{\parallel 2}}(\tau_2) \rangle_H \left\{ \delta_{\mathbf{k}'_{\parallel 1}, \mathbf{k}'_{\parallel}} \delta_{m_1 m} e^{-i(\varepsilon_{n'} - \mu)(\tau_1 - t)} \delta_{\mathbf{k}'_{\parallel 2}, \mathbf{k}_{\parallel}} \delta_{m_2 m'} e^{-i(\varepsilon_n - \mu)(t - \tau_2)} \right\} \end{aligned} \quad (\text{H.21})$$

as illustrated in Fig.H.4 (right panel), so that we obtain:

$$\begin{aligned} \langle \mathbf{J}_d(t) \rangle &= \frac{\mathbf{v}_e}{\hbar^2} \iint_{t_0}^t d\tau_1 d\tau_2 \sum_{n_1 n_2} \sum_{m \mathbf{k}'_{\parallel}} \sum_{m' \mathbf{k}_{\parallel}} M_{n_1, m, \mathbf{k}'_{\parallel}}^* M_{n_2, m', \mathbf{k}_{\parallel}} \phi_{\mathbf{k}_e \mathbf{R}_d}(\mathbf{k}'(m)) \phi_{\mathbf{k}_e \mathbf{R}_d}^*(\mathbf{k}(m')) \\ &\quad \langle c_{n_1, \mathbf{k}_{\parallel}}^\dagger(\tau_1) c_{n_2, \mathbf{k}_{\parallel}}(\tau_2) \rangle_H \left\{ e^{i\hbar v_q(\tau_1 - \tau_2) - i(\varepsilon_m - \mu)(\tau_1 - t) - i(\varepsilon_{m'} - \mu)(t - \tau_2)} \right\} \end{aligned}$$

Then, we neglect the spread of the wavepacket ($\phi_{\mathbf{k}_e \mathbf{R}_d}^*(\mathbf{k}) \approx \delta_{\mathbf{k}, \mathbf{k}_e}$, and hence $m = m' \equiv n_e$), yielding:

$$\langle \mathbf{J}_d(t) \rangle = -i \frac{\mathbf{v}_e}{\hbar^2} \int_{t_0}^t d\tau_1 \int_{t_0}^t d\tau_2 \sum_{n_1 n_2} M_{n_1, n_e, \mathbf{k}_{e\parallel}}^* M_{n_2, n_e, \mathbf{k}_{e\parallel}} G_{n_2, \mathbf{k}_{\parallel}, n_1, \mathbf{k}_{\parallel}}^<(\tau_2, \tau_1) \left\{ e^{i\omega(\tau_1 - \tau_2)} \right\}$$

where we have defined: $\varepsilon_{n_e} - \mu \equiv \hbar v_q - \hbar \omega$ and the lesser Green's function $G_{n_2, \mathbf{k}_{\parallel}, n_1, \mathbf{k}_{\parallel}}^<(\tau_2, \tau_1) \equiv i \langle c_{n_1, \mathbf{k}_{\parallel}}^\dagger(\tau_1) c_{n_2, \mathbf{k}_{\parallel}}(\tau_2) \rangle_H$.

At equilibrium, $G^<(\tau_1, \tau_2)$ depends only on $\tau_1 - \tau_2$, and defining $I = \lim_{t \rightarrow \infty} \lim_{t_0 \rightarrow -\infty} \frac{\langle \mathbf{J}_d \rangle}{t - t_0}$, one recognizes the Fourier transform of $G^<$, namely

$$I(\mathbf{k}_e, \omega) = \frac{k_e}{\hbar m_e} \sum_{n_1 n_2} M_{n_1, n_e, \mathbf{k}_{e\parallel}}^* M_{n_2, n_e, \mathbf{k}_{e\parallel}} A_{v_2, \mathbf{k}_{e\parallel}, v_1, \mathbf{k}_{e\parallel}}(\omega) n_F(\omega) \quad (\text{H.22})$$

where we used the relation $-iG^<(\omega) = A(\omega) n_F(\omega)$. $A(\omega)$ is the spectral function associated with the many-body Hamiltonian H , and $n_F(\omega) = (1 + e^{\omega/k_B T})^{-1}$ is the Fermi-Dirac distribution. In the case of a single-band Hamiltonian H , one obtains:

$$I(\mathbf{k}, \omega) = \frac{|\mathbf{k}|}{\hbar m_e} |M_{n_e, \mathbf{k}_{\parallel}}|^2 A(\mathbf{k}, \omega) n_F(\omega) \quad (\text{H.23})$$

Expression (H.22) is the well-known relation between the spectral function A and the photocurrent $I(\mathbf{k}, \omega)$ in the one-step approximation of ARPES at equilibrium. There are three main ways of representing the ARPES current $I(\mathbf{k}, \omega)$: one can show $I_{\mathbf{k}}(\omega)$ for several \mathbf{k} points (the corresponding curves are called Energy Distribution Curves (EDC's)); one can plot a $I_{\omega}(\mathbf{k})$ with \mathbf{k} in the Brillouin zone (and usually $\omega = \varepsilon_F$ to show the shape of the Fermi surface; such plots are called Momentum Distribution Curves (MDC's) – an example can be seen in Fig. 7.7 in the context of cuprate materials); one may also show a color plot in the ω vs. \mathbf{k} plane where the \mathbf{k} 's follow paths of high symmetry in the Brillouin zone (see e.g. Fig. 6.9).

H.1.4.2 Core-level spectroscopy (cPES)

Core-level spectroscopy is a form of PES corresponding to photons in the X-ray range. It probes the core electronic levels. It is sensitive to the chemical bonding of the core electrons. As such, it yields information about the local electronic environment of atoms. Two atoms of a same species with different chemical environment will yield a different cPES spectrum. This will be illustrated in section 6.3.1.1.

H.2 Bulk probes: neutron scattering, nuclear magnetic resonance, optics

As I did for surface systems, I give a succinct theoretical description of a selection of experimental probes used to investigate the cuprate materials. Angle-resolved photoemission spectroscopy (ARPES) has already been dealt with in section H.1.4. In this section, I explain three additional important probes: neutron scattering, nuclear magnetic resonance (NMR) and optical measurements, with a focus on the observables they give access to. This is not intended to be an exhaustive review of experimental probes: probes such a Raman spectroscopy, consisting in inelastic scattering of light, are left out.

H.2.1 Neutron scattering

A standard reference on the subject is Squires (1997).

Neutron scattering experiments consist in shining a neutron beam with energy E_{in} and momentum \mathbf{k}_{in} onto the sample and measuring the energy $E_{\text{out}} \equiv E_{\text{in}} + \hbar\omega$ and momentum $\mathbf{k}_{\text{out}} \equiv \mathbf{k}_{\text{in}} + \mathbf{q}$ of the outgoing neutrons. As neutral particles, neutrons interact weakly with matter. Therefore, they have a long mean-free path and are thus well-suited to probe the *bulk* properties of matter. Their wavelength is of the order of the lattice spacing, making neutrons apt at studying the crystal structure by diffraction (this is *elastic* neutron scattering). Moreover, thanks to their magnetic moment (neutrons are spin 1/2 particles), neutrons “see” unpaired electron spins. The energy ranges (0.1 to 10 meV for “cold” neutrons, 5-100 meV for “thermal” neutrons and 100-500 eV for “hot” or “epithermal” neutrons) match those of low-energy excitations such as phonons (for instance, $\omega_{\text{D}}(\text{Cu}) \sim 30$ meV) and spin waves (typically, $J \sim 100$ meV). These energies are far larger than the characteristic NMR energies, but in general lower than those probed by ARPES. The main disadvantage of neutrons is the weakness of neutron sources whose corollaries are a low signal, and hence the need for large samples.

The interaction of neutrons with matter is twofold, namely

1. A *contact interaction* between the neutron and the ionic core:

$$H_{\text{probe},1} = g \iiint_{\mathcal{V}} d\mathbf{r} \psi_N^\dagger(\mathbf{r}) \psi_N(\mathbf{r}) \rho_{\text{ion}}(\mathbf{r}) \quad (\text{H.24})$$

where g is the interaction strength, $\psi_N(\mathbf{r})$ the neutron field operator and $\rho_{\text{ion}}(\mathbf{r})$ the density of ion cores/nuclei. Using the Golden Rule (appendix I.2.3), one obtains the scattering rate:

$$\Gamma_1(\mathbf{q}, \omega) = 2g^2 (1 + n_{\text{B}}(\omega)) \text{Im} \chi_{\text{ion}}(\mathbf{q}, \omega) \quad (\text{H.25})$$

where $\chi_{\text{ion}}(\mathbf{q}, \omega)$ is the analytical continuation of $\chi_{\text{ion}}(\mathbf{q}, i\omega)$, the Fourier transform of the correlation function: $\chi_{\text{ion}}(\mathbf{r}, \tau) = \langle T \rho_{\text{ion}}(\mathbf{r}, \tau) \rho_{\text{ion}}(0, 0) \rangle$. Since $\rho_{\text{ion}}(\mathbf{r}) \equiv \sum_{\mathbf{R} \in \text{BL}} \rho_{\text{ion}, \mathbf{R}}^0(\mathbf{r}) + u_{\mathbf{R}}(\mathbf{r})$, where $u_{\mathbf{R}}(r)$ is the displacement on the ion at site \mathbf{R} , and considering the relation of $u_{\mathbf{R}}$ to the phononic field ϕ (see Eq. (I.39) in the context of the Fröhlich Hamiltonian), we have:

$$\text{Im} \chi_{\text{ion}}(\mathbf{q}, \omega) \propto S(\mathbf{q}) \delta_\omega + \text{Im} D(\mathbf{q}, \omega) \sim S(\mathbf{q}) \delta_\omega + \delta(\omega - \tilde{\omega}_{\mathbf{q}}) \quad (\text{H.26})$$

where $S(\mathbf{q})$ is the static pair correlation function, with peaks at the reciprocal lattice sites \mathbf{K} (such that $e^{i\mathbf{K}\cdot\mathbf{R}} = 1$), and $D(\mathbf{q}, \omega)$ is the renormalized phonon propagator (with $\tilde{\omega}_{\mathbf{q}}$ the renormalized phonon frequency).

2. A magnetic interaction between the neutron's magnetic moment $\mathbf{M}_N = \gamma_N \frac{\hbar}{2} \boldsymbol{\sigma}_N$ ($\gamma_N = -1.91\gamma_n$ is the neutron's gyromagnetic factor³) and the internal magnetic field $\mathbf{B}(\mathbf{r})$:

$$H_{\text{probe},2} = \iiint_{\mathcal{V}} d\mathbf{r} \psi_N^\dagger(\mathbf{r}) \left(\gamma_N \frac{\hbar}{2} \boldsymbol{\sigma}_N \right) \psi_N(\mathbf{r}) \cdot \mathbf{B}(\mathbf{r})$$

The magnetic field is induced by the electrons' spin magnetic moment $\mathbf{m}_e(\mathbf{r}) = \psi^\dagger(\mathbf{r}) \left(\gamma_e \frac{\hbar}{2} \boldsymbol{\sigma} \right) \psi(\mathbf{r})$ via⁴ :

$$\mathbf{B}(\mathbf{r}) = \iiint_{\mathcal{V}} d\mathbf{r}' \underline{\underline{\mathbf{V}}}(\mathbf{r} - \mathbf{r}') \mathbf{m}_e(\mathbf{r}') \quad (\text{H.31})$$

with $\underline{\underline{\mathbf{V}}}(\mathbf{r} - \mathbf{r}') = -\nabla \times \nabla \frac{\mu_0}{4\pi|\mathbf{r} - \mathbf{r}'|} \times$. Fourier transformed, this is $\underline{\underline{\mathbf{V}}}(\mathbf{q}) = \mu_0 \hat{\mathbf{q}} \times \hat{\mathbf{q}} \times$, i.e. $V_{uv}(\mathbf{q}) = \mu_0 (\delta_{uv} - \hat{q}_u \hat{q}_v)$ (with $\hat{q}_u \equiv \mathbf{q} \cdot \mathbf{e}_u / |\mathbf{q}|$). The projection operator $P_{uv}^\perp = \delta_{uv} - \hat{q}_u \hat{q}_v$ removes the component of the dipole moment parallel to the field, e.g. $B_x(q\mathbf{e}_x) = 0$, $B_y(q\mathbf{e}_x) = \mu_0 m_y(q\mathbf{e}_x)$, $B_z(q\mathbf{e}_x) = \mu_0 m_z(q\mathbf{e}_x)$, so that we can note $\mathbf{B}(\mathbf{q}) = \mu_0 \underline{\underline{\mathbf{P}}}^\perp(\hat{\mathbf{q}}) \mathbf{m}_e(\mathbf{q}) = \mu_0 \mathbf{m}_e^\perp(\mathbf{q})$ and eventually:

$$H_{\text{probe},2} = \underbrace{\frac{\gamma_N \gamma_e \hbar^2}{4}}_{g_m} \int d\mathbf{q} \mathbf{s}_N(\mathbf{q}) \cdot \underline{\underline{\mathbf{P}}}^\perp(\hat{\mathbf{q}}) \mathbf{s}_e(\mathbf{q}) \quad (\text{H.32})$$

Using again the Golden Rule (Appendix I.2.3), one gets:

$$\Gamma_2(\mathbf{q}, \omega) = 2g_m^2 (1 + n_B(\omega)) \text{Im} \chi_{\text{sp},\perp}(\mathbf{q}, \omega) \quad (\text{H.33})$$

where $\chi_{\text{sp},\perp}$ is the transverse spin correlation function: $\chi_{\text{sp},\perp}(\mathbf{q}, \tau) \equiv \langle T s_e^\perp(\mathbf{q}, \tau) s_e(-\mathbf{q}, 0) \rangle$, for unpolarized neutrons (i.e. I have overaged over σ_N^z).

³Recall: the magnetic moment \mathbf{M} and the spin \mathbf{S} are related by the gyromagnetic ratio γ :

$$\mathbf{M} = \gamma \mathbf{S} \quad (\text{H.27})$$

The gyromagnetic ratio is given by

$$\gamma = g \frac{q}{2m} \quad (\text{H.28})$$

where g in the g -factor (called Landé factor for the electron), m the mass of the particle and q its charge. For a spin 1/2, \mathbf{S} is related to the Pauli matrices by

$$\mathbf{S} = \frac{\hbar}{2} \boldsymbol{\sigma}$$

In particular, for the electron, $g_e \approx -2$, ie:

$$\mathbf{M} = g_e \frac{-e}{2m_e} \frac{\hbar}{2} \boldsymbol{\sigma} = \frac{e\hbar}{2m_e} \frac{\boldsymbol{\sigma}}{2} = \mu_B \boldsymbol{\sigma}$$

where we have defined the Bohr magneton:

$$\mu_B \equiv \frac{e\hbar}{2m_e} \quad (\text{H.29})$$

⁴From Maxwell-Ampère law $\nabla \times \mathbf{B} = \mu_0 \mathbf{j}$ (in the absence of electric field) and with a vector potential defined by $\nabla \times \mathbf{A} = \mathbf{B}$, we have the analog of Poisson's law, $-\Delta \mathbf{A} = \mu_0 \mathbf{j}$, which gives the following expression for the vector potential induced by a magnetic dipole \mathbf{M} (represented by a current loop C centered in $\mathbf{r}' = \mathbf{r}_0$, of surface S and current I such that $M = IS$):

$$\mathbf{A}(\mathbf{r}) = \frac{\mu_0}{4\pi} \oint_C \frac{I}{|\mathbf{r} - \mathbf{r}'|} d\mathbf{l}(\mathbf{r}')$$

Now, using $\oint_C \lambda d\mathbf{l} = \iint_S d\mathbf{S} \times \nabla \lambda$, one gets $\mathbf{A}(\mathbf{r}) = \frac{\mu_0}{4\pi} \iint_S I d\mathbf{S} \times \nabla \frac{1}{|\mathbf{r} - \mathbf{r}'|}$. One now invokes the dipole approximation ($|\mathbf{r}| \gg |\mathbf{r}'|$) to neglect the variations around \mathbf{r}_0 and obtain

$$\mathbf{A}(\mathbf{r}) = \frac{\mu_0}{4\pi} \mathbf{M}(\mathbf{r}_0) \times \nabla \frac{1}{|\mathbf{r} - \mathbf{r}_0|}$$

with $\mathbf{M}(\mathbf{r}_0) = IS$, so that the magnetic field \mathbf{B} induced by a magnetic moment \mathbf{M} is given by the expression:

$$\mathbf{B}(\mathbf{r}) = -\frac{\mu_0}{4\pi} \nabla \times \nabla \frac{1}{|\mathbf{r} - \mathbf{r}_0|} \times \mathbf{M}(\mathbf{r}_0)$$

The generalization for several magnetic dipoles follows:

$$\mathbf{B}(\mathbf{r}) = -\frac{\mu_0}{4\pi} \iiint_{\mathcal{V}} \nabla \times \nabla \frac{1}{|\mathbf{r} - \mathbf{r}'|} \times \mathbf{m}(\mathbf{r}') \quad (\text{H.30})$$

where $\mathbf{m}(\mathbf{r}')$ is now the magnetic dipole density.

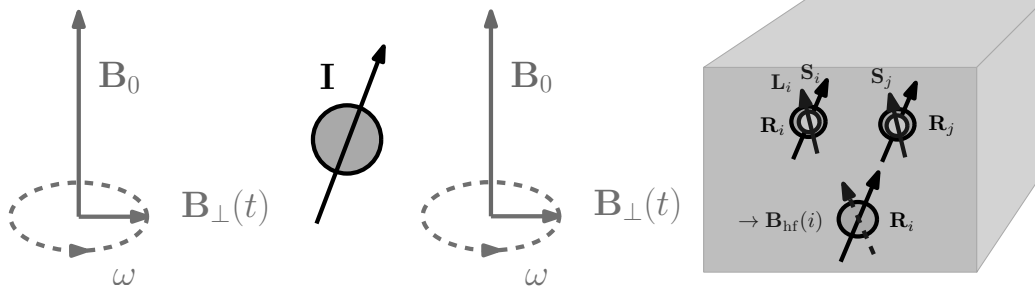


Figure H.5: Sketch of NMR. *Left*: single nucleus with magnetic moment \mathbf{I} in a magnetic field $\mathbf{B}_0 + \mathbf{B}_\perp(t)$. *Right*: solid in a magnetic field. \mathbf{L}_i is the orbital moment at site \mathbf{R}_i , \mathbf{S}_i the spin moment at site \mathbf{R}_i . This generates an overall magnetic field $\mathbf{B}_{\text{hf}}(i)$

Thus, neutron scattering gives information about:

- the **crystal structure** of the sample (elastic scattering, first term of Eq. (H.26))
- the **phonon dispersions** (inelastic scattering, second term of Eq. (H.26))
- the **spin correlation function** (inelastic magnetic scattering, Eq. (H.33))

H.2.2 Nuclear Magnetic Resonance (NMR)

In this section, I shortly present nuclear magnetic resonance (NMR) experiments from a theoretical point of view. A pedagogical introduction can be found in Alloul (2014) or Weller (2008). Standard textbooks include Abragam (1961) and Slichter (1989).

A single nuclear spin \mathbf{I} couples to an external magnetic field \mathbf{B}_0 via a Zeeman interaction term $h_{\text{Zeeman}} = -\gamma_n \hbar \mathbf{I} \cdot \mathbf{B}_0$, where γ_n is the gyromagnetic ratio of the species (here a nucleus) (see left panel of Fig. H.5). This term lifts the degeneracy of the nuclear states $|I, m\rangle$ ($m = -I, \dots, I$); the energy levels are: $\varepsilon_m = -\gamma_n \hbar m B_0$. If a perturbative perpendicular field $\mathbf{B}_\perp(t)$ rotating at frequency ω (and coupling to \mathbf{I} via a Zeeman term h_\perp) is switched on, the Golden Rule gives the transition rate as a function of ω :

$$\Gamma(\omega) = \frac{2\pi}{\hbar} \sum_m p_m |\langle I, m' | h_\perp | I, m \rangle|^2 \delta(\omega - (\varepsilon_{m'} - \varepsilon_m))$$

Since the perpendicular field acts as a spin raising or lowering operator, the matrix element yields the simple selection rule $m' = m \pm 1$, i.e. $\Gamma(\omega)$ has peaks at $|\omega| = \gamma_n \hbar B_0 \equiv \omega_L$, a frequency called the Larmor frequency. Alternatively, by keeping the magnetic field frequency ω fixed, $\Gamma(B_0)$ will be peaked at $B_0 = \frac{\omega}{\gamma_n \hbar}$. This phenomenon is called nuclear magnetic resonance (NMR). It was first described by Rabi *et al.* (1937) for LiCl molecules and generalized to solids by Bloch (1946) and Purcell *et al.* (1946), who benefited from advances in the generation of radio-frequency fields coming from radars. As different atomic species have different gyromagnetic ratios, the peak positions in the absorption rate $\Gamma(\omega)$ are signatures of the chemical composition of a material. This is used in magnetic resonance imaging (MRI) to map out the concentration of ^1H atoms in human tissues.

Nuclear spins are surrounded by electronic clouds (as illustrated in the right panel of Fig. H.5). With their spin and orbital degrees of freedom \mathbf{S}_i and \mathbf{L}_i , electrons generate a magnetic field \mathbf{B}_{hf} which couples to the spin through the so-called hyperfine Hamiltonian, h_{hf} , given by the following expression:

$$h_{\text{hf}} = -\gamma_n \hbar \mathbf{I}_i \cdot \mathbf{B}_{\text{hf}}(i)$$

Neglecting quadrupolar fields, the effective hyperfine magnetic field $\mathbf{B}_{\text{hf}}(i)$ is the sum of the following three contributions (see the right panel of Fig. H.5):

$$B_{\text{c}}(i) = \underline{V_{\text{c}}}(i)\mathbf{S}_i \quad (\text{H.34})$$

$$B_{\text{orb}}(i) = \underline{V_{\text{orb}}}(i)\mathbf{L}_i \quad (\text{H.35})$$

$$B_{\text{trans}}(i) = \sum_j \underline{V_{\text{trans}}}(i-j)\mathbf{S}_j \quad (\text{H.36})$$

which denote, respectively, a contact interaction between the electron spin and the nuclear spin, a contact interaction between the electron orbital momentum and the nuclear spin and dipole-dipole (or transferred hyperfine) interaction between the neighboring spins (at sites \mathbf{R}_j) and the nuclear spin (see Eq. (H.31) and note 4 for a derivation of $\underline{V_{\text{trans}}}$).

H.2.2.1 Knight shift

h_{hf} plays the role of a perturbation to h_{Zeeman} . In first-order perturbation theory, this induces a shift $\langle B_{\text{hf}} \rangle$ of the Zeeman energy levels ε_m defined above. In turn, this shift induces a shift in the resonance frequency: $\Delta\omega = \gamma_n \hbar \langle B_{\text{hf}} \rangle$. This effect was first discovered by Knight (1949) upon comparing the resonance frequencies of Cu and CuCl. The Knight shift is defined as the dimensionless ratio:

$$K \equiv \frac{\Delta\omega}{\omega_L} \quad (\text{H.37})$$

In paramagnetic phases, the average spin is related to the external field by the static, $\mathbf{q} = 0$ spin susceptibility (\mathbf{B}_0 being uniform in space): $\langle \mathbf{S}(i) \rangle = \sum_{\mathbf{q}} \langle \mathbf{S}(\mathbf{q}) \rangle = \sum_{\mathbf{q}} \chi_{\mathbf{q},\omega=0}^{\text{spin}} \mathbf{B}_0 \delta_{\mathbf{q}} = \chi_{\mathbf{q}=0,\omega=0}^{\text{spin}} \mathbf{B}_0$. Thus, restricting the hyperfine interaction to B_{c} only,

$$K_{\text{pm.}} = \frac{\gamma_n \hbar}{\omega_L} \underline{V_{\text{c}}}(i) \chi_{\mathbf{q}=0,\omega=0}^{\text{spin}} \mathbf{B}_0(i) = \underline{V_{\text{c}}}(i) \chi_{\mathbf{q}=0,\omega=0}^{\text{spin}} \quad (\text{H.38})$$

Thus, the Knight shift gives access to the static local spin susceptibility. In a non-interacting metal, $\chi_{\mathbf{q}=0,\omega=0}^{\text{spin}} = \mu_{\text{B}}^2 \chi_0(\mathbf{q} = 0, \omega = 0) \equiv \chi_{\text{Pauli}}$ where $\chi_0(\mathbf{q}, \omega)$ is Lindhard's function (Eq. (I.43))⁵ and χ_{Pauli} is the Pauli susceptibility (see Appendix I.4.1.1 for details):

$$\chi_{\text{Pauli}} = \mu_{\text{B}}^2 N(\varepsilon_{\text{F}}) \quad (\text{H.39})$$

Thus, in paramagnetic phases, the Knight shift directly measures the density of states at the Fermi level. Any depletion of $N(\varepsilon_{\text{F}})$ should be seen by NMR.

In contrast, the behavior of K in magnetically-ordered species, where $\langle \mathbf{S}(i) \rangle \equiv S \neq 0$ even for vanishing B_0 , is:

$$K_{\text{mag.}} = \frac{1}{B_0} V_{\text{c}} S \quad (\text{H.40})$$

H.2.2.2 Spin-lattice relaxation rate $1/T_1$

After switching off the rotating field $B_{\perp}(t)$, in the absence of any environment, the nuclear spin would endlessly precess around \mathbf{B}_0 at the Larmor frequency ω_L . In the presence of the electronic environment (described here by h_{hf}), however, the nuclear spin relaxes to thermal equilibrium with a rate given by the Golden Rule:

$$\frac{1}{T_1} = \frac{2\pi}{\hbar} \sum_m p_m |\langle I, m' | h_{\text{hf}} | I, m \rangle|^2 \delta(\omega - (\varepsilon_{m'} - \varepsilon_m))$$

⁵the μ_{B} factor comes from the fact that χ_0 is defined as the correlation functions of dimensionless spins σ whereas χ^{spin} is the correlation function of the magnetization, $\mathbf{m}_s = \gamma_e S = g_e \frac{e}{2m_e} \frac{\hbar}{2} \sigma \approx \mu_{\text{B}} \sigma$ since $g_e \approx -2$.

Here, note that only the perpendicular (spin flip) component of \mathbf{B}_{hf} (hence of the electronic spin \mathbf{S}_i via *e.g.* Eq. (H.34)) contributes to this rate (the parallel component does not mix states), so that as before, $\varepsilon_{m'} - \varepsilon_m = \omega_L$, and therefore: ⁶ $\frac{1}{T_1 T} = \frac{2\pi}{\hbar} \gamma_n^2 \hbar^2 |\mathbf{I}|^2 \sum_{\mathbf{q}} \underline{V}(\mathbf{q})^2 \langle S_+(\mathbf{q}) S_-(-\mathbf{q}) \rangle_{\omega=\omega_L}$, where $\underline{V}(\mathbf{q})$ is the Fourier transform of $\underline{V}(i-j) \equiv \underline{V}_{\text{c}}(i) + \underline{V}_{\text{trans}}(i-j)$. The sum over \mathbf{q} comes from the fact that we are dealing with *local* observables. Using the fluctuation-dissipation theorem (Eq. (I.7)), this yields, remembering that $\beta\omega_L \ll 1$:

$$\frac{1}{T_1 T} = -4\pi |\mathbf{I}|^2 \gamma_n^2 \hbar^2 \sum_{\mathbf{q}} \underline{V}(\mathbf{q})^2 \frac{\text{Im} \chi_{\perp}(\mathbf{q}, \omega_L)}{\omega_L} \quad (\text{H.41})$$

If we take $\chi_{\perp}(\mathbf{q}, \omega) \approx \mu_B^2 \chi_0(\mathbf{q}, \omega)$ and $V(\mathbf{q}) \approx V$, we obtain, after a few steps (detailed in Appendix I.4.1.3):

$$\sum_{\mathbf{q}} \frac{\text{Im} \chi_0(\mathbf{q}, \omega)}{\omega} = 2\pi \int_{-\infty}^{\infty} d\varepsilon N(\varepsilon)^2 \left[\frac{\partial n_{\text{F}}}{\partial \varepsilon} \right] \quad (\text{H.42})$$

and hence:

$$\frac{1}{T_1 T} = 8\pi^2 |\mathbf{I}|^2 \underline{V}^2 \mu_B^2 k_B \gamma_n^2 \hbar^2 \int_{-\infty}^{\infty} d\varepsilon N(\varepsilon)^2 \left[-\frac{\partial n_{\text{F}}}{\partial \varepsilon} \right] \quad (\text{H.43})$$

H.2.2.3 Korringa relation (and limitations)

In the low temperature regime, Eq. (H.43) becomes:

$$\frac{1}{T_1 T} = 8\pi^2 |\mathbf{I}|^2 \underline{V}^2 \mu_B^2 k_B \gamma_n^2 \hbar^2 N(\varepsilon_{\text{F}})^2$$

Putting this result together with Eq. (H.38), we see that the product $K^2 T_1 T$ is a constant (this is Korringa's relation):

$$K^2 T_1 T = \frac{\left[\underline{V}_{\text{c}} \mu_B^2 N(\varepsilon_{\text{F}}) \right]^2}{8\pi^2 |\mathbf{I}|^2 \underline{V}^2 \mu_B^2 k_B N(\varepsilon_{\text{F}})^2 \gamma_n^2 \hbar^2} = \frac{\mu_B^2}{8\pi^2 k_B |\mathbf{I}|^2 \gamma_n^2 \hbar^2} = \text{const.} \equiv \mathcal{S} \quad (\text{H.44})$$

This relation breaks down when going away from this simple limit. For instance:

- in unconventional superconductors with lines of nodes on the gap, $N(\varepsilon) \propto \varepsilon$ (see *e.g.* section III.A.1 of Sigrist and Ueda (1991)), so that using Eq. (H.43), we obtain

$$\frac{1}{T_1 T} \propto \int_{-\infty}^{\infty} d\varepsilon \varepsilon^2 \left[-\frac{\partial n_{\text{F}}}{\partial \varepsilon} \right] \propto (k_B T)^2$$

so that $\mathcal{S} \propto T^{-2}$

- close to ferromagnetic instabilities, $\chi_{\perp}(\mathbf{q}, \omega = 0)$ is enhanced at $\mathbf{q} = 0$, while $\sum_{\mathbf{q}} \chi_{\perp}(\mathbf{q}, \omega = 0)$ is not, so that K is more enhanced than $1/T_1 T$: $\Delta \mathcal{S} > 0$
- close to antiferromagnetic instabilities, $\chi_{\perp}(\mathbf{q}, \omega = 0)$ is enhanced at $\mathbf{q} = \mathbf{q}_{\text{AF}}$, so that $\sum_{\mathbf{q}} \chi_{\perp}(\mathbf{q}, \omega = 0)$ is more enhanced than $\chi_{\perp}(\mathbf{q} = 0, \omega = 0)$: $\Delta \mathcal{S} < 0$
- if transferred hyperfine fields (B_{trans}) are taken into account, namely if the \mathbf{q} dependence of V is reinstated, new T -dependences appear in $1/T_1 T$. For instance, this can lead to different $1/T_1 T$ ratios for the copper and the oxygen in cuprate materials (see *e.g.* Mila and Rice (1989); Shastry (1989))

⁶I have (a) neglected the orbital field, (b) used the fact that $\beta\omega_L \ll 1$ to simplify $p_m \approx 1/Z$: indeed *e.g.* $\omega_L \approx 80 \text{ MHz} \approx 60 \text{ mK}$ for ⁶³Cu at 7 Tesla, and (c) neglected the anisotropic, *i.e.* nondiagonal character of \underline{V} .

H.2.2.4 Summary

For all practical purposes, one can remember that

the Knight shift and the spin-lattice relaxation give access to the following observables:

$$K \propto \chi_{\perp}^{\text{SP}}(\mathbf{q} = 0, \omega = 0) \quad (\text{H.45})$$

$$\frac{1}{T_1 T} \propto \lim_{\omega \rightarrow 0} \sum_{\mathbf{q}} \frac{\text{Im} \chi_{\perp}^{\text{SP}}(\mathbf{q}, \omega)}{\omega} \quad (\text{H.46})$$

In the last equation, I have replaced ω_L by $\lim_{\omega \rightarrow 0}$ since Larmor frequencies are very small compared with the other energy scales (for the ^{63}Cu example above, $\omega_L = 0.5 \mu\text{eV}$). Thus, NMR essentially gives information about the static ($\omega = 0$) spin susceptibility, either uniform (or $\mathbf{q} \rightarrow 0$, in the Knight shift) or local (in the spin-lattice relaxation rate).

H.2.3 Optical measurements

A pedagogical introduction to the optical response of correlated solids can be found in Millis (2004), or in Chapter 9 of Avella and Mancini (2012), or in Tomczak (2007), with a focus on DMFT. A review on the topic can be found in Basov and Timusk (2005) (cuprates) or Basov *et al.* (2011) (correlated electrons). A general textbook is Dressel and Gruener (2002).

Optical experiments usually measure the reflection $R(\omega)$ and transmission $T(\omega)$ intensity of solids exposed to light, a wave with energy $\hbar\omega$ and momentum \mathbf{q} (some more sophisticated probes also measure the phases). One can take the $\mathbf{q} \rightarrow 0$ limit: the two relevant lengthscales – the optical wavelength λ_{optics} (a few hundreds of nanometers for visible light) and the penetration or skin depth (coming from the diffusion equation obeyed by the electromagnetic field in the material⁷, $\delta \propto \sqrt{1/(\mu_0 \sigma \omega)}$, of the order of 100 nm for visible light (for copper)) – are much larger than the lattice spacing a . The (complex) transverse⁸ dielectric function $\epsilon_{\perp}(\omega)$ and the transverse conductivity σ_{\perp} ($\epsilon_{\perp} = \epsilon_0 + \frac{i}{\omega} \sigma_{\perp}$) are extracted from $R(\omega)$ or $T(\omega)$ (for instance, ϵ_{\perp} is related to R by $R = \left| \frac{\sqrt{\epsilon_{\perp} - 1}}{\sqrt{\epsilon_{\perp} + 1}} \right|^2$). Thus, the main observable of optical probes is the conductivity.

The conductivity tensor $\sigma(\mathbf{q}, \omega)$ gives the electrical current response $\mathbf{j}_e(\mathbf{r}, t) = -e \langle \mathbf{j}(\mathbf{r}, t) \rangle$ (\mathbf{j} is the current of electrons; \mathbf{j}_e is formally defined as $\mathbf{j}_e = -\frac{c}{\gamma} \frac{\delta H}{\delta \mathbf{A}}$) to an external electromagnetic field $\mathbf{E}_{\text{ext}}(\mathbf{r}, t) = -\nabla \phi_{\text{ext}}(\mathbf{r}, t) - \partial_t \mathbf{A}_{\text{ext}}(\mathbf{r}, t)$ (this is Ohm's law):

$$\mathbf{j}_e(\mathbf{q}, \omega) = \underline{\underline{\sigma}}(\mathbf{q}, \omega) \mathbf{E}_{\text{ext}}(\mathbf{q}, \omega) \quad (\text{H.47})$$

Let us now compute σ . The perturbation corresponding to the electromagnetic field is given by the Hamiltonian $H_{\text{probe}}(t) = -e \iiint_{\mathcal{V}} d\mathbf{r} \rho(\mathbf{r}) \phi_{\text{ext}}(\mathbf{r}, t) + e \iiint_{\mathcal{V}} d\mathbf{r} \mathbf{j}(\mathbf{r}) \cdot \mathbf{A}_{\text{ext}}(\mathbf{r}, t)$. In a gauge where $\phi_{\text{ext}} = 0$, this simplifies to:

$$H_{\text{probe}}(\omega) = \frac{e}{i\hbar\omega} \iiint_{\mathcal{V}} d\mathbf{r} \mathbf{j}(\mathbf{r}) \cdot \mathbf{E}_{\text{ext}}(\mathbf{r}, t)$$

One is interested in electron current response, $\delta \langle \mathbf{j} \rangle$ to this perturbation. The current can be split in the paramagnetic ($\equiv \frac{c}{\gamma} \frac{\delta H}{\delta \mathbf{A}} \Big|_{A=0}$) and diamagnetic terms (see *e.g.* Bruus and Flensberg (2004), chapter 1): $\mathbf{j} = \mathbf{j}_p + \frac{e}{m_e} \mathbf{A}_{\text{ext}}(\mathbf{r}) \rho(\mathbf{r})$. Within linear response, one can drop high order terms in the perturbation term, yielding

⁷Using Maxwell equations and Ohm's law (Eq. (H.47)), one finds that the magnetic field obeys the diffusion equation $D\Delta B = \partial_t B$, with the diffusion coefficient $D \equiv \mu_0 \sigma$. The characteristic diffusion lengthscale found by dimensional analysis is $\delta \sim 1/\sqrt{D\omega}$.

⁸The electromagnetic field is transverse to the wave propagation, hence the optical response is given by the transverse conductivity: $\mathbf{j} = (\sigma_{\perp} \mathbf{P}^{\perp} + \sigma_{\parallel} (1 - \mathbf{P}^{\perp})) \mathbf{E} = \sigma_{\perp} \mathbf{E}$, with $[\mathbf{P}^{\perp}]_{uv} \equiv \delta_{uv} - \hat{q}_u \hat{q}_v$. In the limit of $\mathbf{q} \rightarrow 0$, $\sigma_{\perp} = \sigma_{\parallel}$.

$H_{\text{probe}}(\omega) = \frac{e}{i\hbar\omega} \iiint_{\mathcal{V}} d\mathbf{r} \mathbf{j}_p(\mathbf{r}) \cdot \mathbf{E}_{\text{ext}}(\mathbf{r}, t) + O(A_{\text{ext}}^2)$. Thus,

$$\mathbf{j}_e = -e\langle \mathbf{j} \rangle = -e\langle \mathbf{j}_p \rangle - \frac{e^2}{m} A_{\text{ext}}(\mathbf{r}) \langle \rho(\mathbf{r}) \rangle = -e\delta\langle \mathbf{j}_p \rangle - \frac{e^2 n(\mathbf{r})}{i\hbar\omega m_e} E_{\text{ext}}(\mathbf{r}) \quad (\text{H.48})$$

where $n(\mathbf{r}) \equiv \langle \rho(\mathbf{r}) \rangle$ and I used $\langle \mathbf{j}_p \rangle = \delta\langle \mathbf{j}_p \rangle$ since there is no paramagnetic current in the absence of perturbing field. Next, I use Kubo's formula to compute $\delta\langle \mathbf{j}_p \rangle$ in response to H_{ext} :

$$\delta\langle \mathbf{j}_p \rangle(\omega) = \chi_{\mathbf{j}_p \mathbf{j}_p}(\mathbf{q} = 0, \omega) \left\{ \frac{e}{i\hbar\omega} \mathbf{E}_{\text{ext}}(\mathbf{q} = 0, \omega) \right\}$$

with $\chi_{\mathbf{j}_p \mathbf{j}_p}^{\alpha\beta}(\mathbf{r}, \mathbf{r}', t, t') = -i\theta(t - t') \langle [j_p^\alpha(\mathbf{r}, t), j_p^\beta(\mathbf{r}', t')] \rangle_H$. Putting this together with Eq. (H.48), one finds the Ohm's law (Eq. (H.47)) with

$$\sigma^{\alpha\beta}(\mathbf{r}, \mathbf{r}', \omega) = \underbrace{\frac{e^2}{\hbar\omega} \int_0^\infty dt e^{i\omega t} \langle [j_p^\alpha(\mathbf{r}, t), j_p^\beta(\mathbf{r}', t')] \rangle_H}_{\equiv \sigma_r^{\alpha\beta}} + \underbrace{\frac{ie^2 n(\mathbf{r})}{\hbar\omega m_e} \delta(\mathbf{r} - \mathbf{r}') \delta_{\alpha\beta}}_{\equiv \sigma_d^{\alpha\beta}}, \quad \alpha, \beta = x, y, z \quad (\text{H.49})$$

Assuming that (a) due to scattering processes, $\mathbf{j}(\mathbf{q}, t)$ relaxes to equilibrium with the characteristic time τ ($j_p(t) \approx j_p(0)e^{-t/\tau}$), (b) \mathbf{q} is small ($j \approx \sum_i p_i/m_e$, with p_i the momentum of particle i) and (c) the electrons are free ($p_i = m_e v_i = \hbar k_i$), one recovers the Drude formula from the ‘‘regular’’ contribution:⁹

$$\sigma_r^{\text{Drude}}(\omega) = \frac{ne^2\tau}{m_e} \frac{1}{1 - i\omega\tau} \equiv \frac{e^2 D}{\gamma - i\omega} \quad (\text{H.50})$$

where n is the density of electrons in the conduction band. In the second equality, I have defined the scattering rate $\gamma \equiv 1/\tau$ and ‘‘Drude weight’’ $D \equiv n/m_e$. Both a suppression of carrier density and an enhancement of the effective mass – two characteristics of the Mott transition – will impact the Drude weight D . More general parametrizations (extended Drude formulae) have been introduced to capture behaviors beyond the Drude assumptions. I give here two often used notations:

$$\sigma^{\text{gen. Drude}}(\omega) = \frac{e^2 D}{\gamma(\omega) - i[1 + \lambda(\omega)]\omega} = \frac{\omega_p^2}{1/\tau(\omega) - i\omega m^*(\omega)}$$

where $\lambda(\omega)$ is called ‘‘mass enhancement function’’, $m^*(\omega)$ the ‘‘optical mass’’, $\gamma(\omega)$ the ‘‘optical scattering rate’’ and $\tau(\omega)$ the (generalized) scattering rate; ω_p is the plasmon frequency). Indeed, the assumptions presiding to the derivation of the Drude formula are not valid for correlated systems, where the optical spectrum has additional structures. If the material is modelled by a single-band Hubbard model, the one-particle spectrum $A(\omega)$ has incoherent features, the Hubbard bands, as illustrated in Fig. H.6. In the corresponding optical conductivity $\text{Re}\sigma(\omega)$, three structures are visible: a Drude peak at low energies, a peak around $U/2$ (which has been argued to correspond to the experimental ‘‘mid-infrared’’ (MIR) peaks owing to its energy scale) corresponding to transitions between either Hubbard band and the quasiparticle peak, and a broad peak around U (corresponding to inter-Hubbard band transitions). In the Mott insulator, only the latter peak survives.

More generally, optical spectra are essentially made up of a Drude peak (for metals only) and peaks located at interband transitions. In addition to the incoherent features coming *e.g.* from Hubbard bands,

⁹Indeed, under assumptions (a-b-c):

$$\sigma_r(\omega) = \frac{e^2}{\hbar\omega} \int_0^\infty dt e^{i\omega t - t/\tau} \langle j^2 \rangle_H = \frac{1}{1 - i\omega\tau} \frac{e^2\tau}{m_e} \frac{Z^{-1} \sum_{ik k'} |\langle k|p_i|k' \rangle|^2}{\hbar m_e \omega}$$

where we used $\langle j^2 \rangle_H = \frac{1}{m_e^2} Z^{-1} \sum_{ik k'} |\langle k|p_i|k' \rangle|^2 = \frac{n}{m_e^2} \frac{(mv)^2}{2} = \frac{N}{2} \hbar^2 k^2$ and $\hbar\omega = \hbar^2 k^2 / 2m_e$. See *e.g.* Dressel and Gruener (2002) for more details.

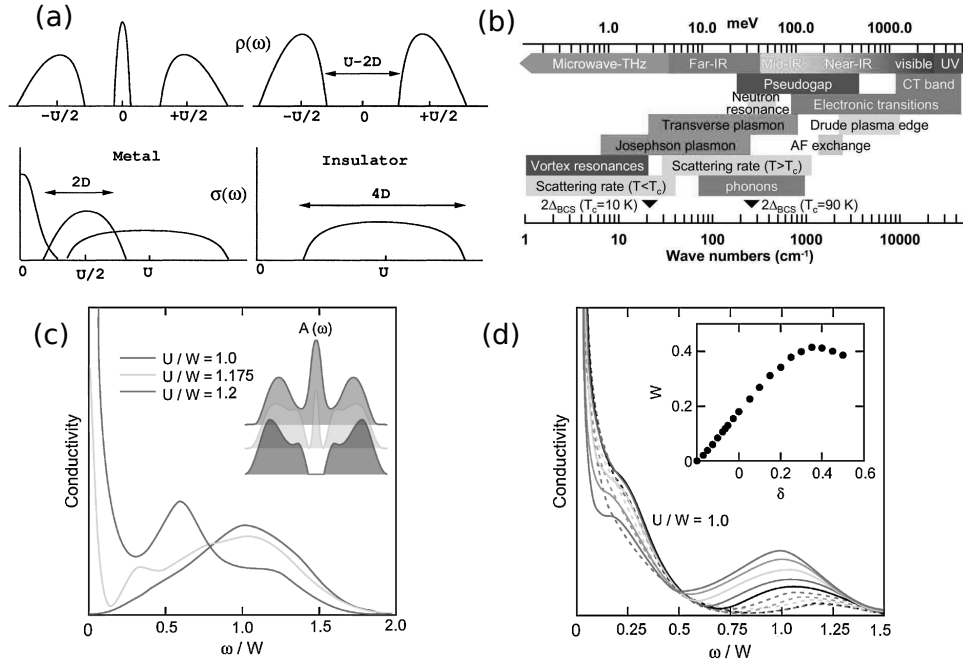


Figure H.6: (a) Top panels: generic one-particle spectra $\rho(\omega)$ (or $A(\omega)$) (left: correlated meta; right: Mott insulator). Bottom: corresponding optical spectra $\sigma(\omega)$ (from Rozenberg *et al.* (1995)). (b) Characteristic energy scales in high- T_c superconductors (from Basov and Timusk (2005)). (c) Optical spectrum for 3 values of U within DMFT applied to the single-band Hubbard model (d) Same as (c) for dopings $\delta = 0.068$ to 0.45 (solid lines $\delta < 0.25$, dashed lines $\delta > 0.25$) (from Basov *et al.* (2011))

the current-current correlation function has information about the collective modes in the solid. Indeed, its structure is close to that of the charge-charge correlation function of the solid. This can be seen by looking at its Lehmann representation, or by the following off-handed estimate for a single-band, tight-binding model: there, via the so-called Peierls substitution, the current is given in terms of creation and annihilation operators by: $j^\alpha(\tau) = 1/2 \sum_{\mathbf{k}\sigma} v_{\mathbf{k}}^\alpha c_{\mathbf{k}\sigma}^\dagger(\tau) c_{\mathbf{k}\sigma}(\tau)$ (with $\mathbf{v}_{\mathbf{k}}$ the group velocity, $v_{\mathbf{k}}^\alpha = \frac{1}{\hbar} \frac{\partial \epsilon(\mathbf{k})}{\partial k_\alpha}$), so that $\langle T j_{\mathbf{q}}^\alpha(\tau) j_{-\mathbf{q}}^\beta(0) \rangle = 1/4 \sum_{\mathbf{k}, \mathbf{k}', \sigma, \sigma'} v_{\mathbf{k}}^\alpha v_{\mathbf{k}'}^\beta \langle c_{\mathbf{k}\sigma}^\dagger(\tau) c_{\mathbf{k}\sigma}(\tau) c_{\mathbf{k}'\sigma'}^\dagger(0) c_{\mathbf{k}'\sigma'}(0) \rangle$. Hence, neglecting the momentum dependence of $v_{\mathbf{k}}$, $\langle T j_{\mathbf{q}}^\alpha(\tau) j_{-\mathbf{q}}^\beta(0) \rangle \propto v^\alpha v^\beta \chi_{\text{charge}}(\mathbf{q} = 0, \tau)$. Thus, optical measurements will see plasmon excitations¹⁰ – which is especially obvious by looking at the reflectivity $R(\omega)$, which, in simple metals, drops at the plasmon frequency, explaining the color of aluminum or gold.

The phenomena accessible by optical probes are summarized in the right panel of Fig. H.6. As one can see, optical probes cover a large range of energy scales, from the superconducting gap Δ_{BCS} (in the THz range) to the charge-transfer energy (in the visible/UV range).

¹⁰The relation between χ_{charge} and the plasmon energy is discussed in Section H.1.2.2

Reminder on many-body theory

The purpose of this chapter is mainly pedagogical. It introduces most of the background elements needed to understand the main text. Most of the material of this part can be found in scattered form in several good textbooks or lecture notes such as Coleman (2011), Berthod (2012), or Bruus and Flensberg (2004), or the references cited in the individual chapters.

I.1 Correlation functions: general properties

I.1.1 Linear response

I.1.1.1 Derivation in real time (Kubo formula)

For any operator O , $\langle B(t) \rangle_{H+H_{\text{probe}}} = \langle \Psi_0 | U(t_0 t) B U(t t_0) | \Psi_0 \rangle$. We expand the evolution operator using Eq. (I.17):

$$\begin{aligned}
 \langle B(t) \rangle_{H+H_{\text{probe}}} &= \langle \Psi_0 | B_H(t) - \frac{i}{\hbar} \int_t^{t_0} d\tau U_H(t_0 \tau) H_{\text{probe}}(\tau) U_H(\tau t) B U_H(t t_0) - \frac{i}{\hbar} \int_{t_0}^t d\tau U_H(t_0 t) B [U(\tau t) H_{\text{probe}}(\tau) U_H(\tau t_0)] | \Psi_0 \rangle \\
 &= \langle \Psi_0 | B_H(t) + \frac{i}{\hbar} \int_{t_0}^t d\tau \underbrace{U_H(t_0 \tau) H_{\text{probe}}(\tau) U_H(\tau t_0)}_{\hat{H}_{\text{probe}}(\tau)} \underbrace{U_H(t_0 t) B U_H(t t_0)}_{\hat{B}(t)} \\
 &\quad - \frac{i}{\hbar} \int_t^{t_0} d\tau \underbrace{U_H(t_0 t) B U_H(t t_0)}_{\hat{B}(t)} \underbrace{U(t_0 \tau) H_{\text{probe}}(\tau) U_H(\tau t_0)}_{\hat{H}_{\text{probe}}(\tau)} | \Psi_0 \rangle \\
 &= \langle B(t) \rangle_H - \frac{i}{\hbar} \int_{t_0}^t \underbrace{\langle [\hat{B}(t), \hat{H}_{\text{probe}}(\tau)] \rangle_H}_{\equiv \delta \langle B(t) \rangle} d\tau
 \end{aligned}$$

If, furthermore, one decomposes H_{probe} as $H_{\text{probe}}(t) = A(t)h(t)$, then $\delta \langle B(t) \rangle = - \int_{t_0}^t \frac{i}{\hbar} \langle [B(t), A(t')] \rangle_H h(t') dt'$, i.e

$$\delta \langle B(t) \rangle = \int_{t_0}^t \chi_{BA}(t, t') h(t') e^{-\eta(t-t')} dt' \quad (I.1)$$

with

$$\chi_{BA}(t, t') = -\frac{i}{\hbar} \theta(t-t') \langle [B(t), A(t')] \rangle_H \quad (I.2)$$

$\chi_{BA}(t, t')$ is called the (linear) response function. This formula is called the Kubo formula.

I.1.1.2 Spectral representations

I.1.1.2.1 Response function $\chi_{BA}(\omega)$ Introducing a complete set of states,

$$\begin{aligned}\chi_{BA}(t, t') &= -\frac{i}{\hbar}\theta(t-t')Z^{-1}\sum_{ij}e^{-\beta E_i}\left(\langle\Psi_i|B(t)|\Psi_j\rangle\langle\Psi_j|A(t')|\Psi_j\rangle - \langle\Psi_i|A(t')|\Psi_j\rangle\langle\Psi_j|B(t)|\Psi_j\rangle\right) \\ &= -\frac{i}{\hbar}\theta(t-t')Z^{-1}\sum_{ij}\left(e^{-\beta E_i}e^{-(t-t')(E_j-E_i)}\langle\Psi_i|B|\Psi_j\rangle\langle\Psi_j|A|\Psi_i\rangle - e^{-\beta E_i}e^{-(t-t')(E_j-E_i)}\langle\Psi_i|A|\Psi_j\rangle\langle\Psi_j|B|\Psi_j\rangle\right) \\ &= -\frac{i}{\hbar}Z^{-1}\sum_{ij}\left(e^{-\beta E_i} - e^{-\beta E_j}\right)\theta(t-t')e^{-(t-t')(E_j-E_i)}\langle\Psi_i|B|\Psi_j\rangle\langle\Psi_j|A|\Psi_i\rangle\end{aligned}$$

One can then notice $\chi_{BA}(t, t') = \chi_{BA}(t - t')$ and thus perform the Fourier transform:

$$\begin{aligned}\chi_{BA}(\omega) &= \int_{-\infty}^{\infty} dt e^{i(\omega-i\eta)t} \chi_{BA}(t) \\ &= -\frac{1}{\hbar}Z^{-1}\sum_{ij}\frac{e^{-\beta E_j} - e^{-\beta E_i}}{\omega - i\eta - (E_j - E_i)}\langle\Psi_i|B|\Psi_j\rangle\langle\Psi_j|A|\Psi_i\rangle\end{aligned}\quad (I.3)$$

We have used the identity: $\int_{-\infty}^{\infty} e^{i(\omega-i\eta)t}\theta(t) = \frac{i}{\omega-i\eta}$. Now, Using Dirac's relation $\text{Im}\frac{1}{\omega-i\eta} = \pi\delta(\omega)$, we can notice:

$$\begin{aligned}\text{Im}\chi_{BA}(\omega) &= -\frac{\pi}{\hbar}Z^{-1}\sum_{ij}\left(e^{-\beta E_j} - e^{-\beta E_i}\right)\delta\left(\omega + i\eta - (E_j - E_i)\right)\langle\Psi_i|B|\Psi_j\rangle\langle\Psi_j|A|\Psi_i\rangle \\ &= \frac{\pi}{\hbar}Z^{-1}(1 - e^{-\beta\omega})\sum_{ij}e^{-\beta E_i}\delta\left(\omega + i\eta - (E_j - E_i)\right)\langle\Psi_i|B|\Psi_j\rangle\langle\Psi_j|A|\Psi_i\rangle\end{aligned}\quad (I.4)$$

I.1.1.2.2 Imaginary-time correlation function $\chi_{BA}(i\omega)$ (**Lehmann representation**) Let us define the imaginary-time correlation function

$$\chi_{BA}(\tau) \equiv -\langle TB(\tau)A(0)\rangle$$

Then $\chi_{BA}(\tau) = -\frac{1}{Z}\sum_{ij}e^{-\beta E_i + \tau E_i}\langle\Psi_i|B|\Psi_j\rangle e^{-\tau E_j}\langle\Psi_j|A|\Psi_i\rangle$ and hence

$$\begin{aligned}\chi_{BA}(i\omega) &= -\frac{1}{Z}\sum_{ij}e^{-\beta E_i}\int_0^\beta d\tau e^{\tau(i\omega + E_i - E_j)}\langle\Psi_i|B|\Psi_j\rangle\langle\Psi_j|A|\Psi_i\rangle \\ &= -\frac{1}{Z}\sum_{ij}\frac{e^{-\beta E_j} - e^{-\beta E_i}}{i\omega - (E_j - E_i)}\langle\Psi_i|B|\Psi_j\rangle\langle\Psi_j|A|\Psi_i\rangle\end{aligned}\quad (I.5)$$

I.1.1.2.3 Analytical continuation $\chi_{BA}(z)$ Comparing Eq.(I.3) and (I.5), we introduce the analytical continuation of $\chi_{BA}(i\omega)$ to the complex plane, $\chi_{BA}(z)$:

$$\chi_{BA}(z) \equiv -\frac{1}{Z}\sum_{ij}\frac{e^{-\beta E_j} - e^{-\beta E_i}}{z - (E_j - E_i)}\langle\Psi_i|B|\Psi_j\rangle\langle\Psi_j|A|\Psi_i\rangle$$

I.1.1.2.4 Correlation function $S_{BA}(\omega)$ and fluctuation-dissipation theorem We define the correlation function:

$$\begin{aligned} S_{BA}(t, t') &\equiv \langle B(t)A(t') \rangle \\ &= Z^{-1} \sum_{ij} e^{-\beta E_i} \langle \Psi_i | B(t) | \Psi_j \rangle \langle \Psi_j | A(t') | \Psi_i \rangle \\ &= Z^{-1} \sum_{ij} e^{-\beta E_i + (E_i - E_j)(t - t')} \langle \Psi_i | B | \Psi_j \rangle \langle \Psi_j | A | \Psi_i \rangle \end{aligned}$$

where Ψ_i denotes an eigenstate of H with energy E_i . The Fourier transform is, using $\int_{-\infty}^{\infty} dt e^{i(\omega - E)t} = 2\pi\delta(E - \omega)$,

$$\begin{aligned} S_{BA}(\omega) &= \int_{-\infty}^{\infty} e^{i\omega t} S_{BA}(t - t') \\ &= 2\pi Z^{-1} \sum_{ij} e^{-\beta E_i} \delta(E_j - E_i - \omega) \langle \Psi_i | B | \Psi_j \rangle \langle \Psi_j | A | \Psi_i \rangle \end{aligned} \quad (I.6)$$

Comparing with (I.4), we obtain the relation:

$$S_{BA}(\omega) = \frac{2\hbar}{1 - e^{-\beta\omega}} \text{Im} \chi_{BA}(\omega) = 2\hbar(1 + n_B(\omega)) \text{Im} \chi_{BA}(\omega) \quad (I.7)$$

It links the fluctuation S_{BA} to the dissipation $\text{Im} \chi_{BA}$. It is referred to as the fluctuation-dissipation theorem.

I.1.1.2.5 Frequency domain In the frequency domain, the time convolution (Eq.(I.1)) becomes a product (with $t \rightarrow \infty$ and $t_0 \rightarrow -\infty$):

$$\delta \langle B(\omega) \rangle = \chi_{BA}(\omega) h(\omega) \quad (I.8)$$

I.1.2 Analyticity and causality: Kramers-Kronig relations and Matsubara sums

I.1.2.1 Cauchy's residue theorem

For any meromorphic function $f(z)$,

$$\oint_C \frac{dz}{2\pi i} f(z) = \sum_{\text{poles } \alpha \in C} \text{Res}(f, \alpha) \gamma(\alpha) \quad (I.9)$$

where C is a closed contour in the complex plane, $\text{Res}(f, \alpha)$ is the residue of f at pole α , and $\gamma(\alpha)$ the winding number of the pole.

I.1.2.2 Equivalence between causality and analyticity in the upper half-plane

Let $\chi(z)$ be function analytical in the upper half plane, namely with no poles in the upper half plane. Cauchy's residue theorem (Eq. I.9) applied to $\chi(z)e^{-izt}$ on a closed contour in the upper half plane, C^+ (shown in Fig I.1) implies:

$$I_{C^+} \equiv \int_{C^+} \frac{dz}{2\pi i} \chi(z) e^{-izt} = 0$$

C^+ has two portions $C^+ = C_1^+ + C_2^+$, which we use to split the integral:

$$\begin{aligned} I_{C^+} &= I_{C_1^+} + I_{C_2^+} \\ &= \int_{-\infty}^{\infty} \frac{d\omega}{2\pi i} \chi(\omega) e^{-i\omega t} + \int_{C_2^+} \frac{dz}{2\pi i} \chi(z) e^{-izt} \end{aligned}$$

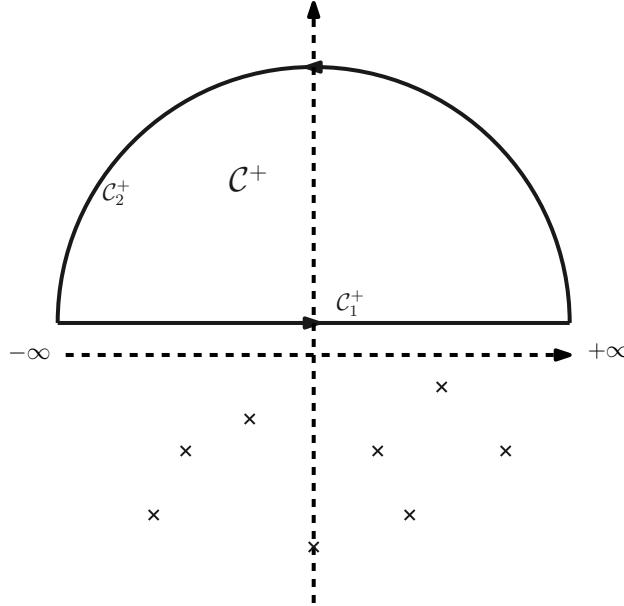


Figure I.1: Contours in the imaginary plane. The crosses denote poles.

If we suppose $t < 0$, since $\text{Im}(z) > 0$ on C_2^+ , the integrand of the first term decays quickly in absolute value: $|\chi(z)e^{-izt}| = |\chi(z)|e^{\text{Im}(z)t} \xrightarrow{|z| \rightarrow \infty} 0$, which implies that $I_{C_2^+} \rightarrow 0$ when we send to radius of C_2^+ to infinity. Thus,

$$\int_{-\infty}^{\infty} \frac{d\omega}{2\pi} \chi(\omega) e^{-i\omega t} = 0 \text{ for } t < 0$$

The left-hand side $\chi(t)$, ie we have proven that analyticity in the upper half plane is equivalent to

$$\boxed{\forall t < 0, \chi(t) = 0}$$

which is the definition of causality: for given perturbation at $t = 0$, the response function is non-zero only for subsequent (ie positive) times.

I.1.2.3 Spectral representation

Let $\chi(z)$ denote a causal response function. Cauchy's residue theorem allows us to write, for any \bar{z} in the lower half plane:

$$J_{C^+} \equiv \int_{C^+} \frac{dz}{2\pi i} \frac{\chi(z)}{z - \bar{z}} = 0$$

since $\frac{\chi(z)}{z - \bar{z}}$ has no pole in C^+ . The left-hand side can be decomposed on C_1^+ and C_2^+ ,

$$J_{C^+} = \frac{1}{2\pi i} \int_{-\infty}^{\infty} d\omega \frac{\chi(\omega)}{\omega - \bar{z}} + \int_{C_2^+} \frac{dz}{2\pi i} \frac{\chi(z)}{z - \bar{z}} \equiv J_{C_1^+} + J_{C_2^+}$$

For the same reasons as in the previous subsection, $J_{C_2^+}$ vanishes when the radius of C_2^+ is sent to infinity. Hence,

$$\forall \bar{z} \in i\mathbb{R}^-, 0 = \frac{1}{2\pi i} \int_{-\infty}^{\infty} d\omega \frac{\chi(\omega)}{\omega - \bar{z}}$$

I.1.2.4 Kramers-Kronig relations

We use the previous identity for a \bar{z} given by $\bar{z} = \omega - i\eta$: $0 = \int_{-\infty}^{\infty} d\bar{\omega} \frac{\chi(\bar{\omega})}{\bar{\omega} - (\omega - i\eta)}$ and let $\eta \rightarrow 0$, using $\lim_{\eta \rightarrow 0} \frac{1}{\bar{\omega} - \omega - i\eta} = \mathcal{P} \frac{1}{\bar{\omega} - \omega} + i\pi\delta(\bar{\omega} - \omega)$:

$$0 = \mathcal{P} \int_{-\infty}^{\infty} d\bar{\omega} \frac{\chi(\bar{\omega})}{\bar{\omega} - \omega} - i\pi\chi(\omega)$$

i.e

$$\chi(\omega) = \frac{1}{i\pi} \int_{-\infty}^{\infty} d\bar{\omega} \frac{\chi(\bar{\omega})}{\bar{\omega} - \omega}$$

Identifying the real and imaginary parts yields the Kramers-Kronig relations:

$$\begin{aligned} \chi'(\omega) &= \mathcal{P} \int_{-\infty}^{\infty} d\bar{\omega} \frac{\chi''(\bar{\omega})}{\pi(\bar{\omega} - \omega)} \\ \chi''(\omega) &= -\mathcal{P} \int_{-\infty}^{\infty} d\bar{\omega} \frac{\chi'(\bar{\omega})}{\pi(\bar{\omega} - \omega)} \end{aligned} \quad (\text{I.10})$$

where \mathcal{P} denotes the Cauchy principal value.

I.1.2.5 Matsubara sums

I.1.2.5.1 Fermionic sums

Derivation We want to compute

$$\bar{\mathcal{I}}_{\text{F}} = \sum_n \phi(i\omega_n)$$

where $i\omega_n$ is a fermionic Matsubara frequency.

Let us suppose that $\phi(z)$ decays faster than $1/|z|$ for $\text{Re}(z) \rightarrow +\infty$. In this case, let us define the function $g(z) \equiv n_{\text{F}}(-z)\phi(z)$. This function decays faster than $1/|z|$ both when $\text{Re}(z) \rightarrow +\infty$ and when $\text{Re}(z) \rightarrow -\infty$, hence, if we use a circular contour around the origin and send its radius to infinity, appealing to Jordan's lemma yields:

$$\oint_C n_{\text{F}}(-z)\phi(z) = 0$$

Now, using Cauchy's residue theorem, since $n_{\text{F}}(-z)$ has poles at $i\omega_n$ with residue $\gamma = \lim_{\epsilon \rightarrow 0} \epsilon n_{\text{F}}(i\omega + \epsilon) = \frac{\epsilon}{-e^{-\beta\epsilon} + 1} = 1/\beta$, we reexpress the right-hand side of the preceding equation:

$$\sum_n \phi(i\omega_n) \{1/\beta\} + \sum_{\text{poles } \alpha} \text{Res}(\phi, \alpha) n_{\text{F}}(-\alpha) = 0$$

i.e. we have

$$\frac{1}{\beta} \sum_n \phi(i\omega_n) = - \sum_{\text{poles } \alpha} \text{Res}(\phi, \alpha) n_{\text{F}}(-\alpha)$$

If $\phi(z)$ decays faster than $1/|z|$ for $\text{Re}(z) \rightarrow -\infty$, we use $g(z) \equiv n_{\text{F}}(z)\phi(z)$ and the fact that $n_{\text{F}}(z)$ has poles at $i\omega_n$ with residue $\gamma = \lim_{\epsilon \rightarrow 0} \epsilon n_{\text{F}}(i\omega + \epsilon) = \frac{\epsilon}{-e^{-\beta\epsilon} + 1} = -1/\beta$, to get:

$$\frac{1}{\beta} \sum_n \phi(i\omega_n) = \sum_{\text{poles } \alpha} \text{Res}(\phi, \alpha) n_{\text{F}}(\alpha)$$

Application 1: filling Suppose we want to compute the filling of a Green's function $G(i\omega) = 1/(i\omega - \varepsilon)$. Then,

$$n = G(0^-) = \frac{1}{\beta} \sum_n e^{-i\omega_n 0^-} \frac{1}{i\omega - \varepsilon}$$

In this case, $\phi(z) = \frac{e^{z\eta}}{z-\varepsilon}$ (with an infinitesimal $\eta > 0$) decays fast for negative z , hence

$$n = n_F(\varepsilon)$$

Application 2: relation between $A(\omega)$ and $G(\tau)$ Let us write the spectral representation of $G(i\omega)$:

$$G(i\omega) = \int_{-\infty}^{\infty} d\omega \frac{A(\omega)}{i\omega - \omega}$$

Hence, for $\tau > 0$, Fourier transforming yields

$$G(\tau) = \int_{-\infty}^{\infty} d\omega A(\omega) \frac{1}{\beta} \sum_n \frac{e^{-i\omega_n \tau}}{i\omega_n - \omega}$$

In this case, $\phi(z) = \frac{e^{-z\tau}}{z-\omega}$ decays fast for positive z , hence

$$\boxed{G(\tau) = - \int_{-\infty}^{\infty} d\omega A(\omega) \frac{e^{-\omega\tau}}{e^{-\beta\omega} + 1}} \quad (I.11)$$

One can rewrite this expression as

$$G(\tau) = - \int_{-\infty}^{\infty} d\omega A(\omega) \frac{e^{-(\frac{\beta}{2}-\tau)\omega}}{2 \cosh\left(\frac{\beta\omega}{2}\right)}$$

At $\tau = \beta/2$, in the low-temperature limit, the term $1/\cosh(\beta\omega/2)$ selects frequencies around $\beta/2$ ($\int_{-\infty}^{\infty} \frac{dx}{\pi \cosh(x)} \frac{1}{\cosh(x)} = 1$ and hence, $\frac{1}{\pi \cosh(x)} \approx \delta(x)$). Changing variables, one obtains $G\left(\tau = \frac{\beta}{2}\right) = -\frac{\pi}{\beta} \int_{-\infty}^{\infty} dx \frac{A(2x/\beta)}{\pi \cosh(x)}$ and finally:

$$\boxed{-\frac{\beta}{\pi} G\left(\tau = \frac{\beta}{2}\right) \approx A(\omega = 0) \quad (\beta \rightarrow \infty)} \quad (I.12)$$

I.1.3 Lehmann representations

I.1.3.1 Single-particle Green's function

Defining

$$G_{\alpha\beta}(\tau) \equiv -\langle T c_{\alpha}(\tau) c_{\beta}^{\dagger}(0) \rangle$$

One has:

$$G_{\alpha\beta}(\omega) = -\frac{1}{Z} \sum_{ij} \frac{(e^{-\beta E_i} + e^{-\beta E_j}) \langle \Psi_i | c_{\alpha} | \Psi_j \rangle \langle \Psi_j | c_{\beta}^{\dagger} | \Psi_i \rangle}{E_j - E_i - \omega}$$

I.1.3.2 Two-point correlation function

I.1.3.3 Three-point correlation

Using the identity $\int_0^\beta \int_0^\beta dt_1 dt_2 T f_1(t_1) f_2(t_2) = \int_0^\beta \int_0^{t_1} dt_1 dt_2 \sum_{p \in \mathfrak{E}_2} \sigma(p) f_{p1}(t_1) f_{p2}(t_2)$, we can write, using the definition of $\tilde{\chi}$ (Eq. C.2) and of its Fourier transform (Eq. B.1b)

$$\begin{aligned} \hat{\chi}_{123}(i\omega_1, i\omega_2) &\equiv \sum_{p \in \mathfrak{E}_2} \int_0^\beta d\tau \int_0^\tau d\tau' \sigma(p) \langle O_{p1}(\tau) O_{p2}(\tau') n_3(0) \rangle e^{i\omega_{p1}\tau} e^{i\omega_{p2}\tau'} \\ &= \frac{1}{Z} \sum_{ijk} \sum_{p \in \mathfrak{E}_2} \sigma(p) \langle i | O_{p1} | j \rangle \langle j | O_{p2} | k \rangle \langle k | n_3 | i \rangle f_{ijk}(\omega_{p1}, \omega_{p2}) \end{aligned} \quad (\text{I.13})$$

with $O_1 = c_1^\dagger$ and $O_2 = c_2$, and:

$$\begin{aligned} f_{ijk}(\omega_1, \omega_2) &= e^{-\beta\epsilon_i} \int_0^\beta d\tau e^{\tau(i\omega_1 + \epsilon_i - \epsilon_j)} \int_0^\tau d\tau' e^{\tau'(i\omega_2 + \epsilon_j - \epsilon_k)} \\ &= e^{-\beta\epsilon_i} \int_0^\beta d\tau e^{\tau(i\omega_1 + \epsilon_i - \epsilon_j)} \frac{e^{\tau(i\omega_2 + \epsilon_j - \epsilon_k)} - 1}{i\omega_2 + \epsilon_j - \epsilon_k} \\ &= \frac{e^{-\beta\epsilon_i}}{i\omega_2 + \epsilon_j - \epsilon_k} \int_0^\beta d\tau \left(e^{\tau(i\omega_1 + i\omega_2 + \epsilon_i - \epsilon_k)} - e^{\tau(i\omega_1 + \epsilon_i - \epsilon_j)} \right) \\ &= \frac{e^{-\beta\epsilon_i}}{i\omega_2 + \epsilon_j - \epsilon_k} \left(\frac{e^{\beta(i\omega_1 + i\omega_2 + \epsilon_i - \epsilon_k)} - 1}{i\omega_1 + i\omega_2 + \epsilon_i - \epsilon_k} (1 - \delta_{ik}) - \frac{e^{\beta(i\omega_1 + \epsilon_i - \epsilon_j)} - 1}{i\omega_1 + \epsilon_i - \epsilon_j} \right) + \frac{e^{-\beta\epsilon_i}}{i\omega_2 + \epsilon_j - \epsilon_i} \beta \delta_{i\omega_1 + i\omega_2} \delta_{ik} \\ &= \frac{1}{i\omega_2 + \epsilon_j - \epsilon_k} \left(\frac{e^{-\beta\epsilon_k} - e^{-\beta\epsilon_i}}{i\omega_1 + i\omega_2 + \epsilon_i - \epsilon_k} (1 - \delta_{ik}) + \frac{e^{-\beta\epsilon_j} + e^{-\beta\epsilon_i}}{i\omega_1 + \epsilon_i - \epsilon_j} \right) + \frac{e^{-\beta\epsilon_i}}{i\omega_2 + \epsilon_j - \epsilon_i} \beta \delta_{i\omega_1 + i\omega_2} \delta_{ik} \end{aligned}$$

We have used the fact that both $i\omega_1$ and $i\omega_2$ are fermionic Matsubara frequencies ($e^{\beta i\omega_1} = -1$).

I.2 Time-dependent perturbation theory: the Golden Rule

This chapter is used to derive the results experimental probes in part H.

Let us consider a time-independent many-body Hamiltonian H with (orthonormal) eigenstates $|\Psi_n\rangle$ and eigenvalues E_n , subject to a time-dependent perturbation $H_{\text{probe}}(t)$ for times $t > t_0$, i.e. the total Hamiltonian is

$$H_{\text{tot}} = H + H_{\text{probe}}(t) \quad (\text{I.14})$$

The time evolution of wavefunctions is given by the expression

$$|\Psi(t)\rangle = U(tt_0)|\Psi(t_0)\rangle$$

where the unitary time evolution operator is

$$U(tt_0) \equiv T \exp \left(-\frac{i}{\hbar} \int_{t_0}^t H_{\text{tot}}(\tau) d\tau \right) \quad (\text{I.15})$$

where T is the time-ordering operator. In particular, the unperturbed evolution operator simplifies to $U_H(tt_0) = e^{-iH(t-t_0)/\hbar}$. We define the Heisenberg representation of operators as follows:

$$\hat{O}(t) \equiv U_H(t_0 t) O_t U_H(tt_0) = e^{\frac{i}{\hbar} H(t-t_0)} O_t e^{-\frac{i}{\hbar} H(t-t_0)} \quad (\text{I.16})$$

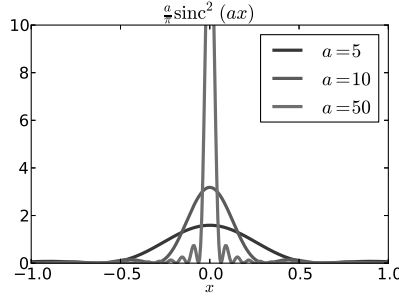


Figure I.2: Squared sinc function.

I.2.1 Evolution operator

Let us define $S(tt_0) \equiv U_H(t_0t)U(tt_0)$. Then,

$$\frac{dS(tt_0)}{dt} = \left(U_H(t_0t) \left[+\frac{i}{\hbar} H \right] \right) U(tt_0) + U_H(t_0t) \left(-\frac{i}{\hbar} (H + H_{\text{probe}}(t)) U(t_0t) \right) = -\frac{i}{\hbar} U_H(t_0t) H_{\text{probe}}(t) U(tt_0)$$

Integrating yields $S(tt_0) = 1 - \frac{i}{\hbar} \int_{t_0}^t U_H(t_0\tau) H_{\text{probe}}(\tau) U(\tau t_0) d\tau$ and finally the exact result:

$$U(tt_0) = U_H(tt_0) S(tt_0) = U_H(tt_0) - \frac{i}{\hbar} \int_{t_0}^t U(\tau t_0) H_{\text{probe}}(\tau) U_H(\tau t_0) d\tau \quad (I.17)$$

I.2.2 Fermi's Golden Rule

Let us suppose that H_{probe} is a monochromatic excitation, $H_{\text{probe}}(t) = H_{\text{probe}} e^{-i\omega t}$. Since the states evolve as $|\Psi_n(t)\rangle = U(t_0, t) |\Psi_n(t_0)\rangle$, the probability of transition between a state m at time t_0 and a state n at time t is given by:

$$P_{m \rightarrow n}(\omega) = |\langle \Psi_n(t) | \Psi_m(t_0) \rangle|^2 = \left| \langle \Psi_n | U(t_0, t) | \Psi_m \rangle \right|^2$$

Approximating Eq. (I.17) to first order in H_{probe} , we have:

$$\begin{aligned} \langle \Psi_n | U(t_0, t) | \Psi_m \rangle &= e^{-iE_m(t-t_0)/\hbar} \langle \Psi_n | \Psi_m \rangle - \frac{i}{\hbar} \int_{t_0}^t d\tau e^{-iE_n(\tau-t_0)/\hbar} e^{-i\omega\tau} e^{-iE_m(t-\tau)/\hbar} \langle \Psi_n | H_{\text{probe}} | \Psi_m \rangle \\ &= -\frac{i}{\hbar} e^{iE_n t_0/\hbar} e^{-iE_m t/\hbar} \int_{t_0}^t d\tau e^{-i\tau(E_n - E_m + \hbar\omega)/\hbar} \langle \Psi_n | H_{\text{probe}} | \Psi_m \rangle \end{aligned}$$

Using $\int_{t_0}^t e^{-i\tau E/\hbar} d\tau = \frac{e^{-it_0 E/\hbar} - e^{-it E/\hbar}}{-iE/\hbar} = -e^{-i\frac{E}{2\hbar}(t+t_0)} (t-t_0) \text{sinc} \left[\frac{t-t_0}{2\hbar} E \right]$, we obtain the transition rate between state m and state n :

$$\Gamma_{m \rightarrow n}(\omega) \equiv \lim_{t \rightarrow \infty} \frac{P_{m \rightarrow n}(\omega)}{t-t_0} = \frac{1}{\hbar^2} \left| \langle \Psi_n | H_{\text{probe}} | \Psi_m \rangle \right|^2 (t-t_0) \text{sinc}^2 \left[\frac{t-t_0}{2\hbar} (E_n - E_m + \hbar\omega) \right]$$

Using the property $\lim_{a \rightarrow \infty} \frac{a}{\pi} \cdot \text{sinc}^2(ax) = \delta(x)$ (see Fig. I.2), we obtain Fermi's Golden Rule:

$$\Gamma_{m \rightarrow n}(\omega) = \frac{2\pi}{\hbar} \left| \langle \Psi_n | H_{\text{probe}} | \Psi_m \rangle \right|^2 \delta(E_n - E_m + \hbar\omega) \quad (I.18)$$

This formula holds under the assumptions:

- long times ($t \rightarrow \infty$)

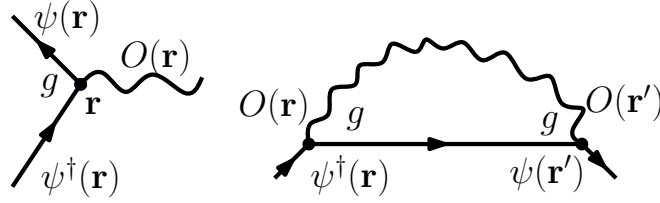


Figure I.3: Scattering diagrams. *Left*: Diagrammatic representation of H_{probe} . *Right*: Simplest self-energy diagram.

- weak perturbation ($H_{\text{probe}} \ll H$)

The total transition rate is:

$$\Gamma(\omega) = Z^{-1} \sum_{mn} e^{-\beta E_n} \Gamma_{m \rightarrow n}(\omega) = \frac{2\pi}{\hbar} \frac{1}{Z} \sum_n e^{-\beta E_n} \left| \langle \Psi_n | H_{\text{probe}} | \Psi_m \rangle \right|^2 \delta(E_n - E_m + \hbar\omega)$$

Comparing this expression to the structure factor $S_{BA}(\omega)$, one obtains:

$$\Gamma(\omega) = \frac{1}{\hbar} S_{H_{\text{probe}}, H_{\text{probe}}}(\omega) = 2(1 + n_B(\omega)) \text{Im} \chi_{H_{\text{probe}}, H_{\text{probe}}}(\omega) \quad (\text{I.19})$$

The second equality comes from the fluctuation dissipation theorem (Eq. (I.7)).

I.2.3 Application: scattering

$$H_{\text{probe}}(\mathbf{q}) \equiv g \iiint_{\mathcal{V}} d\mathbf{r} \rho_{\text{ext}, \mathbf{q}}(\mathbf{r}) O(\mathbf{r}) \quad (\text{I.20})$$

where $\rho_{\text{ext}}(\mathbf{r})$ is the density of the scattering particle, and $O(\mathbf{r})$ the observable to which it couples. Then,

$$\langle \Psi_n | H_{\text{probe}} | \Psi_m \rangle = g \iiint_{\mathcal{V}} d\mathbf{r} \rho_{\text{ext}, \mathbf{q}}(\mathbf{r}) \langle \Psi_n | O(\mathbf{r}) | \Psi_m \rangle = g \sum_{\mathbf{k}} \underbrace{\iiint_{\mathcal{V}} d\mathbf{r} e^{-i\mathbf{k} \cdot \mathbf{r}} \rho_{\text{ext}, \mathbf{q}}(\mathbf{r})}_{\equiv \rho_{\text{ext}, \mathbf{q}}(\mathbf{k})} \langle \Psi_n | O(\mathbf{k}) | \Psi_m \rangle$$

So that

$$\left| \langle \Psi_n | H_{\text{probe}} | \Psi_m \rangle \right|^2 = g^2 \sum_{\mathbf{k}, \mathbf{k}'} \rho_{\text{ext}, \mathbf{q}}(\mathbf{k}) \rho_{\text{ext}, \mathbf{q}}(-\mathbf{k}') \langle \Psi_n | O(\mathbf{k}) | \Psi_m \rangle \langle \Psi_m | O^\dagger(-\mathbf{k}') | \Psi_n \rangle$$

If the scattering particle is a plane wave with momentum \mathbf{q} , $\rho_{\text{ext}}(\mathbf{r}) \propto e^{i\mathbf{q} \cdot \mathbf{r}}$, $\rho_{\text{ext}}(\mathbf{k}) \propto \delta_{\mathbf{k}, \mathbf{q}}$, hence

$$\left| \langle \Psi_n | H_{\text{probe}} | \Psi_m \rangle \right|^2 = g^2 \langle \Psi_n | O(\mathbf{q}) | \Psi_m \rangle \langle \Psi_m | O^\dagger(-\mathbf{q}) | \Psi_n \rangle = g^2 \left| \langle \Psi_n | O(\mathbf{q}) | \Psi_m \rangle \right|^2$$

and hence, transposing Eq. (I.19), one gets:

$$\Gamma(\mathbf{q}, \omega) = \frac{g^2}{\hbar} S_{O_{\mathbf{q}}, O_{-\mathbf{q}}}(\omega) = 2g^2(1 + n_B(\omega)) \text{Im} \chi_{O_{\mathbf{q}}, O_{-\mathbf{q}}}(\omega) \quad (\text{I.21})$$

I.2.4 Diagrammatic variant

In this section, the goal is to recover the result of the previous section in a diagrammatic way. H_{probe} is shown diagrammatically in Fig. I.3. The simplest self-energy diagram reads:

$$\Sigma(\mathbf{r} - \mathbf{r}', \tau - \tau') = g^2 \langle O(\mathbf{r}\tau) O(\mathbf{r}'\tau') \rangle_H \langle \psi(\mathbf{r}'\tau') \psi^\dagger(\mathbf{r}\tau) \rangle$$

Transforming to momentum-energy space,

$$\begin{aligned} \Sigma(\mathbf{k}, i\omega) &= g^2 \sum_{\mathbf{q}, i\Omega} \chi_{OO}(\mathbf{q}, i\Omega) G_{\text{ext}}(\mathbf{k} + \mathbf{q}, i\omega + i\Omega) \\ &= g^2 \sum_{\mathbf{q}, i\Omega} \int_{-\infty}^{\infty} dv \frac{\chi''_{OO}(\mathbf{q}, \nu)}{i\Omega - \nu} \frac{1}{i\omega + i\Omega - E_{\mathbf{k}+\mathbf{q}}} \end{aligned}$$

Performing the Matsubara sum:

$$\sum_{i\Omega} \frac{1}{i\Omega - \nu} \frac{1}{i\omega + i\Omega - E_{\mathbf{k}+\mathbf{q}}} = \frac{1}{\nu - (E_{\mathbf{k}+\mathbf{q}} - i\omega)} (n_B(\nu) - n_B(E_{\mathbf{k}+\mathbf{q}} - i\omega)) = \frac{n_B(\nu) + n_F(E_{\mathbf{k}+\mathbf{q}})}{\nu - (E_{\mathbf{k}+\mathbf{q}} - i\omega)}$$

Hence, setting $n_F(E_{\mathbf{k}+\mathbf{q}}) = 1$,

$$\begin{aligned} \Sigma(\mathbf{k}, z) &= g^2 \sum_{\mathbf{q}} \int_{-\infty}^{\infty} dv \frac{1}{z + \nu - E_{\mathbf{k}+\mathbf{q}}} \chi''_{OO}(\mathbf{q}, \nu) (n_B(\nu) + 1) = g^2 \sum_{\mathbf{q}} \int_{-\infty}^{\infty} dv \frac{1}{z + \nu - E_{\mathbf{k}+\mathbf{q}}} \frac{S_{OO}(\mathbf{q}, \nu)}{2\hbar} \\ \Gamma &= 2\Sigma''(\mathbf{k}, E_{\mathbf{k}} + i\eta) = \frac{g^2}{\hbar} \sum_{\mathbf{q}} \int_{-\infty}^{\infty} dv \delta(\nu + E_{\mathbf{k}} - E_{\mathbf{k}+\mathbf{q}}) S_{OO}(\mathbf{q}, \nu) = \frac{g^2}{\hbar} S_{OO}(\mathbf{q}, E_{\mathbf{k}+\mathbf{q}} - E_{\mathbf{k}}) \end{aligned} \quad (I.22)$$

which is the same as Eq. (I.21).

I.3 Analytical continuation techniques

Analytically continuing $G(i\omega_n)$ or $G(\tau)$ from the imaginary to the real axis consists in the following task: One starts from a set of data $\bar{G}(\tau)$ or $\bar{G}(i\omega)$ (the bar indicates that this data are themselves possibly noisy estimates of $G(\tau)/G(i\omega)$) and one wants to find $A(\omega)$. For this, one must invert the following equation (Eq. (I.11)):

$$\bar{G}(\tau_i) = - \int_{-\infty}^{\infty} d\omega \frac{e^{-\tau\omega}}{e^{-\beta\omega} + 1} A(\omega) = \sum_{j=0}^{N_\omega} K_{ij} A(\omega_j) \quad (I.23)$$

with $K_{ij} \equiv -\Delta\omega \frac{e^{-\tau_i\omega_j}}{e^{-\beta\omega_j} + 1}$. Formally, one can write $A_j = \sum_i [K^{-1}]_{ji} \bar{G}_i$. The matrix K is, however, ill-conditioned.

I.3.1 Padé approximants

The Padé method consists in fitting the imaginary-frequency function $f(i\omega_n)$ with a rational function, namely a ratio of two polynomials (Padé (1892)). Equivalently, this corresponds to fitting $f(i\omega_n)$ with a continued fraction:

$$\tilde{f}(z) = \frac{a_1}{1 + \frac{a_2(z-z_1)}{1 + \frac{a_3(z-z_2)}{1 + \dots}}}$$

The $2N$ coefficients a_i and z_i ($i = 1 \dots N$) can be determined in a recursive way with the N conditions $\tilde{f}(z = i\omega_n) = f(i\omega_n)$, $n = 0 \dots N - 1$ (Vidberg and Serene (1977)). An estimate of the analytical continuation of $f(i\omega)$ on the real axis is thus given by

$$f(\omega) \approx \tilde{f}(\omega)$$

This procedure is particularly suited to data devoid of numerical noise. For noisy data, the maximum entropy method, presented in the next chapter, is in general better suited.

I.3.2 Maximum Entropy

In this short section, I describe the conceptual idea behind the MaxEnt algorithm rather than the technical implementation details of the algorithm. For details, I refer the reader to the standard reference on the topic, Jarrell and Gubernatis (1996). The implementation used in this thesis is that of Bryan (1990).

A standard way to circumvent the badly-conditioned matrix inversion of Eq. (I.23) is to perform a least-squares fit, namely to look for the “fit parameters” A_j minimizing the least squares distance between \bar{G} and KA , or “likelihood” function:

$$\chi^2[A] \equiv \sum_i \frac{\Delta\tau}{\sigma_i} \left\{ \sum_{j=0}^{N_\omega} K_{ij} A(\omega_j) - \bar{G}(\tau_i) \right\} \quad (\text{I.24})$$

Furthermore, it can be shown that:

$$P(\bar{G}|A) \propto e^{-\chi^2/2}$$

Thus, least squares fitting amounts to finding the A which maximizes the probability of the data \bar{G} for a given A , or in other words to find the most probable \bar{G} for a given spectrum A . In practice, this often leads to an overfitting of the noise in \bar{G} .

Instead of this, one may want to look for the most probable A for a given data set \bar{G} , or in other words to maximize the probability of A for given data \bar{G} and some information on the system, \mathcal{I} . Appealing to Bayes’ theorem, one gets:

$$P(A|\bar{G}, \mathcal{I}) = \frac{P(\bar{G}|A, \mathcal{I})P(A|\mathcal{I})}{P(\bar{G}, \mathcal{I})}$$

Here, $P(\bar{G}, \mathcal{I})$ is a normalization constant. It can be shown that $P(A|\mathcal{I})$ is related to the entropy (or information content) S of the spectrum A with respect to some prior knowledge on the system:

$$P(A|\mathcal{I}) \propto e^{\alpha S}$$

with $\mathcal{I} = (\alpha, M)$, α being a given parameter and M a “default model” which contains prior information about the system, and S the (Shannon) entropy:

$$S \equiv \sum_i A_i - M_i - A_i \log A_i/M_i$$

One can now find the spectrum \hat{A}_α which maximizes $P(A|\bar{G}, \mathcal{I}) = P(A|\bar{G}, \alpha, M) \propto e^Q$, where $Q \equiv \alpha S - \chi^2/2$ (it is defined as $\hat{A}_\alpha \approx \int \mathcal{D}[A] A P(A|\bar{G}, \alpha, M)$). This spectrum depends on the parameter α .

The final spectrum is given by: $\langle A \rangle = \int d\alpha \int \mathcal{D}[A] A P[A, \alpha|\bar{G}, M]$. Since $P[A, \alpha|\bar{G}, M] = P[A|\bar{G}, \alpha, M]P[\alpha|\bar{G}]$, one obtains the final formula:

$$\langle A \rangle = \int d\alpha \hat{A}_\alpha P[\alpha|\bar{G}] \quad (\text{I.25})$$

In some MaxEnt approaches (referred to a “classic MaxEnt”), the above integral is approximated by $\langle A \rangle \approx \hat{A}_{\alpha_{\max}}$ where α is the parameter which maximizes $P[\alpha|\bar{G}]$. $P[\alpha|\bar{G}]$ can be computed in the following way: using Bayes formula, $P(A, \alpha|\bar{G}) = \frac{P[A\alpha\bar{G}]}{P[\bar{G}]} = \frac{P[\bar{G}|A\alpha]P[A|\alpha]P[\alpha]}{P[\bar{G}]}$, and previous the relations ($P[\bar{G}] = Z$), one finds $P(A, \alpha|\bar{G}) = e^Q P[\alpha]/Z$ and finally:

$$P[\alpha|\bar{G}] = \int \mathcal{D}[A] P(A, \alpha|\bar{G}) = \frac{P[\alpha]}{Z} \int \mathcal{D}[A] e^Q$$

$P[\alpha]$ is often chosen to be equal to $1/\alpha$. Thus, $P[\alpha|\bar{G}]$ can be computed explicitly. The method introduced by Bryan (1990) consists in computing $P[\alpha|\bar{G}]$ and estimating A by $\langle A \rangle$ as given in Eq. I.25). Other approaches, such as “stochastic MaxEnt” (Beach (2004)), have been proposed.

I.4 Around the Lindhard function and the random-phase approximation

The Lindhard function is defined in Eq. (I.43).

I.4.1 Various limits of the Lindhard function

I.4.1.1 $\omega = 0, \mathbf{q} \rightarrow 0$ limit: Pauli susceptibility

In this limit, noting that $\xi_{\mathbf{k}+\mathbf{q}} - \xi_{\mathbf{k}} = \mathbf{q} \cdot \nabla \xi|_{\xi_{\mathbf{k}}}$ and $n_{\mathbf{F}}(\xi_{\mathbf{k}+\mathbf{q}}) - n_{\mathbf{F}}(\xi_{\mathbf{k}}) = \frac{\partial n_{\mathbf{F}}}{\partial \xi} \mathbf{q} \cdot \nabla \xi|_{\xi_{\mathbf{k}}}$, we obtain

$$\lim_{\mathbf{q} \rightarrow 0} \chi_0(\mathbf{q}, \omega = 0) = 2 \sum_{\mathbf{k}} \left(-\frac{\partial n_{\mathbf{F}}}{\partial \xi} \Big|_{\xi=\xi_{\mathbf{k}}} \right) = 2 \int_{-\infty}^{\infty} d\varepsilon N_{\sigma}(\varepsilon) \left(-\frac{\partial n_{\mathbf{F}}}{\partial \xi} \right)$$

which simplifies, for $T \rightarrow 0$ and up to a factor μ_B^2 , to the Pauli susceptibility defined in Eq. (H.39) (the factor 2 is absorbed in the total DOS $N(\varepsilon)$).

I.4.1.2 $\mathbf{q} \rightarrow 0, \text{finite } \omega$ limit: plasmon pole

Let us consider the case when $\mathbf{q} \rightarrow 0$. Then

$$\begin{aligned} \chi_0(\mathbf{q}, \omega) &= -2 \iiint \frac{d^3 \mathbf{k}}{(2\pi)^3} \frac{\mathbf{q} \cdot \nabla \xi_{\mathbf{k}} \frac{\partial n_{\mathbf{F}}}{\partial \varepsilon}}{\mathbf{q} \cdot \nabla \xi_{\mathbf{k}} - \omega} \\ &= -\frac{2}{\omega} \frac{2\pi}{(2\pi)^3} \int k^2 dk \frac{\delta(k - k_{\mathbf{F}})}{v_{\mathbf{F}}} \underbrace{\int_0^{\pi} \sin \theta d\theta \frac{q \cos(\theta) v_{\mathbf{F}}}{1 - \frac{q \cos(\theta) v_{\mathbf{F}}}{\omega}}}_{\equiv I} \end{aligned}$$

where I have used: $\frac{\partial n_{\mathbf{F}}}{\partial \varepsilon} = -\delta(\xi_{\mathbf{k}} - \varepsilon_{\mathbf{F}}) = -\frac{\delta(k - k_{\mathbf{F}})}{v_{\mathbf{F}}}$. I now evaluate the integral:

$$I = \int_{-1}^1 dx \frac{qxv_{\mathbf{F}}}{1 - \frac{qxv_{\mathbf{F}}}{\omega}} = \frac{\omega^2}{qv_{\mathbf{F}}} \int_{-qv_{\mathbf{F}}/\omega}^{qv_{\mathbf{F}}/\omega} dy \frac{y}{1 - y} \approx \frac{\omega^2}{qv_{\mathbf{F}}} \left[\frac{y^2}{2} + \frac{y^3}{3} \right]_{-qv_{\mathbf{F}}/\omega}^{qv_{\mathbf{F}}/\omega} = \frac{\omega^2}{qv_{\mathbf{F}}} \frac{2}{3} \left(\frac{qv_{\mathbf{F}}}{\omega} \right)^3 = \frac{2}{3} \frac{v_{\mathbf{F}}^2 q^2}{\omega}$$

Hence

$$\chi_0(\mathbf{q}, \omega) = -\frac{1}{\omega} \frac{1}{2\pi^2} \frac{k_{\mathbf{F}}^2}{v_{\mathbf{F}}} \left[\frac{2}{3} \frac{v_{\mathbf{F}}^2 q^2}{\omega} \right] = -\frac{v_{\mathbf{F}}^3 m^2 q^2}{3\pi^2 \omega^2} = -\frac{n}{m} \frac{q^2}{\omega^2} \quad (1.26)$$

where I have used $3\pi^2 n = k_{\mathbf{F}}^3 = m^3 v_{\mathbf{F}}^3$. When plugged into the dielectric function, this expression yields zeros at the plasmon energy (see section H.1.2.2).

I.4.1.3 \mathbf{q} -integration

$$\begin{aligned} \sum_{\mathbf{q}} \text{Im} \chi_0(\mathbf{q}, \omega) &= 2\pi \sum_{\mathbf{q}, \mathbf{k}} \left[n_{\mathbf{F}}(\xi_{\mathbf{k}+\mathbf{q}}) - n_{\mathbf{F}}(\xi_{\mathbf{k}}) \right] \delta(\omega - \{\xi_{\mathbf{k}+\mathbf{q}} - \xi_{\mathbf{k}}\}) \\ &= 2\pi \int_{-\infty}^{\infty} d\varepsilon \sum_{\mathbf{k}} N_{\mathbf{k}}(\varepsilon) \left[n_{\mathbf{F}}(\varepsilon) - n_{\mathbf{F}}(\xi_{\mathbf{k}}) \right] \delta(\omega - \{\varepsilon - \xi_{\mathbf{k}}\}) \end{aligned}$$

with $N_{\mathbf{k}}(\varepsilon) \equiv \sum_{\mathbf{q}} \delta(\varepsilon - \xi_{\mathbf{k}+\mathbf{q}})$. If one approximates $N_{\mathbf{k}}(\varepsilon) \approx N(\varepsilon)$ (which is true for a periodic lattice),

$$\begin{aligned} \sum_{\mathbf{q}} \text{Im} \chi_0(\mathbf{q}, \omega) &= 2\pi \int_{-\infty}^{\infty} d\epsilon \int_{-\infty}^{\infty} d\bar{\epsilon} N(\epsilon) N(\bar{\epsilon}) [n_{\text{F}}(\epsilon) - n_{\text{F}}(\bar{\epsilon})] \delta(\omega - \{\epsilon - \bar{\epsilon}\}) \\ &= 2\pi \int_{-\infty}^{\infty} d\epsilon N(\epsilon + \omega) N(\epsilon) [n_{\text{F}}(\epsilon + \omega) - n_{\text{F}}(\epsilon)] \end{aligned}$$

If furthermore, $\epsilon \gg \omega$ (which is true since $N(\epsilon)$ is concentrated around ϵ_{F} , which is $\gg \omega$), we then obtain Eq. (H.42).

I.4.2 Exact results within the Random-phase approximation

I.4.2.1 RPA susceptibilities: exactness up to second order

Our starting point is the bubble diagram of Eq. (I.42), which I rewrite here explicitly as (setting $\lambda_{\mathbf{q}} = 1$):

$$P_0(q, i\Omega) \equiv 2 \sum_{k, i\omega} G_0(k + q, i\omega + i\Omega) G_0(k, i\omega) \quad (\text{I.27})$$

I want to show that $\chi_{\text{ch}}^{\text{RPA}}$ and $\chi_{\text{sp}}^{\text{RPA}}$, defined by:

$$\begin{aligned} \chi_{\text{ch}}^{\text{RPA}} &= \frac{-P_0}{1 - \frac{U}{2} P_0} = -P_0 \left(1 + \frac{U}{2} P_0 \right) = -P_0 - \frac{U}{2} P_0^2 + O(U^2) \\ \chi_{\text{sp}}^{\text{RPA}} &= \frac{-P_0}{1 + \frac{U}{2} P_0} = -P_0 + \frac{U}{2} P_0^2 + O(U^2) \end{aligned}$$

are equal up to second order in U to the charge and spin correlation functions, defined as:

$$\begin{aligned} \chi_{\text{ch}} &= \langle T n(\tau) n(0) \rangle = 2 (\chi_{\uparrow\uparrow} + \chi_{\uparrow\downarrow}) \\ \chi_{\text{sp}} &= \langle T n^z(\tau) n^z(0) \rangle = 2 (\chi_{\uparrow\uparrow} - \chi_{\uparrow\downarrow}) \end{aligned}$$

with $\chi_{\sigma\sigma'} \equiv \langle T n_{\sigma}(\tau) n_{\sigma'}(0) \rangle$. Let us expand $\chi_{\sigma\sigma'}$ in powers of U :

$$\begin{aligned} \langle T n_{\sigma}(\tau) n_{\sigma'}(0) \rangle &= \int \mathcal{D}[c^* c] e^{\int c^* G_0^{-1} c - \int_{\tau} U n_{\uparrow} n_{\downarrow}} n_{\sigma}(\tau) n_{\sigma'}(0) \\ &= \langle T n_{\sigma}(\tau) n_{\sigma'}(0) \rangle_0 - U \int_{\tau_1} \langle T n_{\uparrow}(\tau_1) n_{\downarrow}(\tau_1) n_{\sigma}(\tau) n_{\sigma'}(0) \rangle_0 + O(U^3) \end{aligned}$$

I now use Wick's theorem:

$$\begin{aligned} \langle n_{\uparrow}(\tau) n_{\uparrow}(0) \rangle_0 &= \langle c_{\uparrow}^*(\tau) c_{\uparrow}(\tau) c_{\uparrow}^*(0) c_{\uparrow}(0) \rangle_0 \\ &= -\langle c_{\uparrow} c_{\uparrow}^*(\tau) \rangle_0 \langle c_{\uparrow}(\tau) c_{\uparrow}^*(0) \rangle_0 \\ &= -G_0(-\tau) G_0(\tau) \\ &= -\frac{1}{2} P_0(\tau) \end{aligned}$$

Thus:

$$\begin{aligned} \chi_{\uparrow\uparrow}(\tau) &= -P_0(\tau)/2 + O(U^2) \\ \chi_{\uparrow\downarrow}(\tau) &= -\frac{U}{4} \int_{\tau_1} P_0(\tau - \tau_1) P_0(\tau_1) + O(U^3) \end{aligned}$$

$$\chi_{\text{ch}}(i\Omega) = 2 \left(-P_0/2 - U P_0^2/4 + O(U^2) \right) = -P_0 - \frac{U}{2} P_0^2 + O(U^2) \quad (\text{I.28})$$

$$\chi_{\text{sp}}(i\Omega) = 2 \left(-P_0/2 + U P_0^2/4 + O(U^2) \right) = -P_0 + \frac{U}{2} P_0^2 + O(U^2) \quad (\text{I.29})$$

which ends the proof.

I.4.2.2 Ornstein-Zernicke form of the susceptibility

Let us consider the spin susceptibility in the random-phase approximation:

$$\chi_{\text{sp}}^{\text{RPA}}(\mathbf{q}, \omega) = \frac{\chi_0(\mathbf{q}, \omega)}{1 - U_{\text{sp}}\chi_0(\mathbf{q}, \omega)}$$

Let us take \mathbf{q} and ω such that the denominator is vanishing, namely $\mathbf{q} \approx \mathbf{Q}$ and $\omega \approx 0$. Let us define

$$\xi_0^2 \equiv -\frac{1}{2\chi_0(\mathbf{Q})} \left. \frac{\partial^2 \chi_0}{\partial q^2} \right|_{\mathbf{q}=\mathbf{Q}} \quad (1.30)$$

$$\frac{\xi_0^2}{D} = -i \left. \frac{1}{\chi_0(\mathbf{Q})} \frac{\partial \chi_0}{\partial \omega} \right|_{\omega=0} \quad (1.31)$$

and expand the denominator:

$$\chi_0(\mathbf{Q} + \mathbf{q}, \omega) = \chi_0(\mathbf{Q}) - \xi_0^2 q^2 \chi_0(\mathbf{Q}) + i\omega \frac{\xi_0^2}{D} \chi_0(\mathbf{Q}) = \chi_0(\mathbf{Q}) \left[1 - \xi_0^2 q^2 + i\omega \frac{\xi_0^2}{D} \right]$$

Hence: $\chi_{\text{sp}}^{\text{RPA}}(\mathbf{q} + \mathbf{Q}, \omega) = \frac{\chi_0(\mathbf{Q})}{1 - U_{\text{sp}}\chi_0(\mathbf{Q}) \left[1 - \xi_0^2 q^2 + i\omega \frac{\xi_0^2}{D} \right]}$. Let us now define

$$\delta U \equiv \chi_0(\mathbf{Q})^{-1} - U_{\text{sp}} \quad (1.32)$$

, i.e. $1 - U_{\text{sp}}\chi_0(\mathbf{Q}) = \delta U \chi_0(\mathbf{Q})$. Hence:

$$\chi_{\text{sp}}^{\text{RPA}}(\mathbf{q} + \mathbf{Q}, \omega) = \frac{\chi_0(\mathbf{Q})}{\delta U \chi_0(\mathbf{Q}) + U_{\text{sp}}\chi_0(\mathbf{Q}) \left[\xi_0^2 q^2 - i\omega \frac{\xi_0^2}{D} \right]} = \frac{1}{\delta U} \frac{1}{1 + \frac{U_{\text{sp}}}{\delta U} \left[\xi_0^2 q^2 - i\omega \frac{\xi_0^2}{D} \right]}$$

This expression prompts us to define

$$\xi^2 = \frac{U_{\text{sp}}}{\delta U} \xi_0^2$$

so that one finally obtains:

$$\chi_{\text{sp}}^{\text{RPA}}(\mathbf{q}, \omega) = \frac{1}{U_{\text{sp}}} \frac{\xi^2 / \xi_0^2}{1 + \xi^2 (\mathbf{q} - \mathbf{Q})^2 - i\omega \frac{\xi^2}{D}} \quad (1.33)$$

I.5 GW self-energy on the real axis

We want to analytically continue the “one-loop” or GW self-energy:

$$\Sigma(\mathbf{k}, i\omega) = -\frac{1}{\beta} \sum_{\mathbf{q}, i\Omega_m} W(\mathbf{q}, i\Omega_m) G(\mathbf{k} - \mathbf{q}, i\omega - i\Omega_m)$$

I.5.1 General G and W

Let us consider the integral

$$\mathcal{I}_{\mathbf{qk}, i\omega} \equiv \oint_C W_{\mathbf{q}}(z) G_{\mathbf{k}-\mathbf{q}}(i\omega - z) n_{\text{B}}(z) \frac{dz}{2\pi i}$$

for fixed \mathbf{q} , \mathbf{k} and $i\omega$. C is a circular contour with radius R . If we send $R \rightarrow \infty$, $\mathcal{I}_{\mathbf{qk}, i\omega} \rightarrow 0$. On the other hand, given that

- $n_{\text{B}}(z)$ has poles $i\Omega_m$ of residue $1/\beta$,

- $W_{\mathbf{q}}(z)$ has poles ω of residue $-\frac{1}{\pi}W_{\mathbf{q}}''(\omega)$ (using the spectral representation of W),
- $G_{\mathbf{k}-\mathbf{q}}(i\omega - z)$ has poles $i\omega - \omega$ of residue $\frac{1}{\pi}G_{\mathbf{k}-\mathbf{q}}''(\omega)$ (using the spectral representation of G),

Cauchy's residue theorem states that:

$$\begin{aligned} \mathcal{I}_{\mathbf{q}\mathbf{k},i\omega} &= \frac{1}{\beta} \sum_m W_{\mathbf{q}}(i\Omega_m) G_{\mathbf{k}-\mathbf{q}}(i\omega - i\Omega_m) + \int_{-\infty}^{\infty} d\omega \left(-\frac{1}{\pi} W_{\mathbf{q}}''(\omega) \right) G_{\mathbf{k}-\mathbf{q}}(i\omega - \omega) n_{\text{B}}(\omega) \\ &\quad + \int_{-\infty}^{\infty} d\omega W_{\mathbf{q}}(i\omega - \omega) \left(\frac{1}{\pi} G_{\mathbf{k}-\mathbf{q}}''(\omega) \right) n_{\text{B}}(i\omega - \omega) \end{aligned}$$

Hence:

$$\begin{aligned} \frac{1}{\beta} \sum_m W_{\mathbf{q}}(i\Omega_m) G_{\mathbf{k}-\mathbf{q}}(i\omega - i\Omega_m) &= - \int_{-\infty}^{\infty} d\omega \left(-\frac{1}{\pi} W_{\mathbf{q}}''(\omega) \right) \left\{ \int_{-\infty}^{\infty} \frac{-d\tilde{\omega}}{\pi} \frac{G_{\mathbf{k}-\mathbf{q}}''(\tilde{\omega})}{i\omega - \omega - \tilde{\omega}} \right\} n_{\text{B}}(\omega) \\ &\quad - \int_{-\infty}^{\infty} d\omega \left\{ \int_{-\infty}^{\infty} \frac{-d\tilde{\omega}}{\pi} \frac{W_{\mathbf{q}}''(\tilde{\omega})}{i\omega - \omega - \tilde{\omega}} \right\} \left(\frac{1}{\pi} G_{\mathbf{k}-\mathbf{q}}''(\omega) \right) (-n_{\text{F}}(-\omega)) \\ &= - \int_{-\infty}^{\infty} \int_{-\infty}^{\infty} \frac{d\omega}{\pi} \frac{d\tilde{\omega}}{\pi} \left(\frac{W_{\mathbf{q}}''(\omega) G_{\mathbf{k}-\mathbf{q}}''(\tilde{\omega}) (n_{\text{B}}(\omega) + n_{\text{F}}(-\tilde{\omega}))}{i\omega - \omega - \tilde{\omega}} \right) \\ &= - \int_{-\infty}^{\infty} \int_{-\infty}^{\infty} \frac{d\omega}{\pi} \frac{d\tilde{\omega}}{\pi} \left(\frac{W_{\mathbf{q}}''(\omega) G_{\mathbf{k}-\mathbf{q}}''(\tilde{\omega}) (n_{\text{B}}(\omega) + n_{\text{F}}(\tilde{\omega}))}{i\omega + \omega - \tilde{\omega}} \right) \end{aligned}$$

where we have used $n_{\text{B}}(-\Omega) = -1 - n_{\text{B}}(\Omega)$ and $n_{\text{F}}(-\omega) = 1 - n_{\text{F}}(\omega)$. The final result is

$$\boxed{\Sigma(\mathbf{k}, i\omega) = - \sum_{\mathbf{q}} \int_{-\infty}^{\infty} \frac{d\Omega}{\pi} W_{\mathbf{q}}''(\Omega) \int_{-\infty}^{\infty} \frac{d\epsilon}{\pi} G_{\mathbf{k}-\mathbf{q}}''(\epsilon) \frac{n_{\text{B}}(\Omega) + n_{\text{F}}(\epsilon)}{i\omega + \Omega - \epsilon}} \quad (\text{I.34})$$

I.5.2 Special cases

I.5.2.1 Non-interacting case: $G = G_0$

Let us now suppose that $G_{\mathbf{k}-\mathbf{q}}''(\omega) = G_0''(\mathbf{k} - \mathbf{q}, \omega) = -\pi\delta(\omega - \epsilon_{\mathbf{k}-\mathbf{q}})$. Then:

$$\Sigma(\mathbf{k}, i\omega) = \sum_{\mathbf{q}} \int_{-\infty}^{\infty} \frac{d\omega}{\pi} W_{\mathbf{q}}''(\omega) \frac{n_{\text{B}}(\omega) + n_{\text{F}}(\epsilon_{\mathbf{k}-\mathbf{q}})}{i\omega + \omega - \epsilon_{\mathbf{k}-\mathbf{q}}} \quad (\text{I.35})$$

Eq (I.35) can be further simplified by noticing that: $W_{\mathbf{q}}''(-\omega) = -W_{\mathbf{q}}''(\omega)$:

$$\begin{aligned} \Sigma(\mathbf{k}, i\omega) &= \sum_{\mathbf{q}} \left(\int_{-\infty}^0 \frac{d\omega}{\pi} W_{\mathbf{q}}''(\omega) \frac{n_{\text{B}}(\omega) + n_{\text{F}}(\epsilon_{\mathbf{k}-\mathbf{q}})}{i\omega + \omega - \epsilon_{\mathbf{k}-\mathbf{q}}} + \int_0^{\infty} \frac{d\omega}{\pi} W_{\mathbf{q}}''(\omega) \frac{n_{\text{B}}(\omega) + n_{\text{F}}(\epsilon_{\mathbf{k}-\mathbf{q}})}{i\omega + \omega - \epsilon_{\mathbf{k}-\mathbf{q}}} \right) \\ &= \sum_{\mathbf{q}} \left(\int_0^{\infty} \frac{d\omega}{\pi} W_{\mathbf{q}}''(\omega) \left[\frac{n_{\text{B}}(\omega) + n_{\text{F}}(\epsilon_{\mathbf{k}-\mathbf{q}})}{i\omega + \omega - \epsilon_{\mathbf{k}-\mathbf{q}}} - \frac{n_{\text{B}}(-\omega) + n_{\text{F}}(\epsilon_{\mathbf{k}-\mathbf{q}})}{i\omega - \omega - \epsilon_{\mathbf{k}-\mathbf{q}}} \right] \right) \\ &= \sum_{\mathbf{q}} \left(\int_0^{\infty} \frac{d\omega}{\pi} W_{\mathbf{q}}''(\omega) \left[\frac{n_{\text{B}}(\omega) + n_{\text{F}}(\epsilon_{\mathbf{k}-\mathbf{q}})}{i\omega + \omega - \epsilon_{\mathbf{k}-\mathbf{q}}} + \frac{n_{\text{B}}(\omega) + n_{\text{F}}(-\epsilon_{\mathbf{k}-\mathbf{q}})}{i\omega - \omega - \epsilon_{\mathbf{k}-\mathbf{q}}} \right] \right) \\ &= \sum_{\mathbf{q}, \pm} \int_0^{\infty} \frac{d\omega}{\pi} W_{\mathbf{q}}''(\omega) \frac{n_{\text{B}}(\omega) + n_{\text{F}}(\pm\epsilon_{\mathbf{k}-\mathbf{q}})}{i\omega \pm \omega - \epsilon_{\mathbf{k}-\mathbf{q}}} \end{aligned}$$

Hence

$$\Sigma(\mathbf{k}, \omega) = \sum_{\mathbf{q}, \pm} \int_0^\infty \frac{d\bar{\omega}}{\pi} W_{\mathbf{q}}''(\bar{\omega}) \frac{n_B(\bar{\omega}) + n_F(\pm \epsilon_{\mathbf{k}-\mathbf{q}})}{\omega + i\eta \pm \bar{\omega} - \epsilon_{\mathbf{k}-\mathbf{q}}} \quad (I.36)$$

I.5.2.2 Single phonon mode ω_q

Suppose $W_{\mathbf{q}}''(\omega) = -\pi (\delta(\omega - \omega_q) - \delta(\omega + \omega_q))$, then:

$$\Sigma(k, i\omega) = - \sum_q \frac{n_B(\omega_q) + n_F(\epsilon_{k-q})}{i\omega + \omega_q - \epsilon_{k-q}} - \sum_q \frac{n_B(\omega_q) + n_F(-\epsilon_{k-q})}{i\omega - \omega_q - \epsilon_{k-q}}$$

Using the relation: $n_F(-\omega_q) = 1 - n_F(\omega_q)$ again,

$$\Sigma(k, \omega) = - \sum_q \left[\frac{n_B(\omega_q) + n_F(\epsilon_{k-q})}{\omega + \omega_q - \epsilon_{k-q}} + \frac{1 + n_B(\omega_q) - n_F(\epsilon_{k-q})}{\omega - \omega_q - \epsilon_{k-q}} \right] \quad (I.37)$$

This result can be understood in the following way. From second-order perturbation theory the shift in energy of state ϵ_k due to the emission or absorption of a phonon at energy ω_q . The final state is in both cases ϵ_{k-q} . The corresponding term is:

$$\Delta E^2(\epsilon_k \rightarrow \epsilon_{k-q}) = \sum_q \underbrace{\frac{(1 - n_F(\epsilon_{k-q})) (1 + n_B(\omega_q))}{(\epsilon_{k-q} + \omega_q) - \epsilon_k}}_{\text{emission}} + \underbrace{\frac{(1 - n_F(\epsilon_{k-q})) (n_B(\omega_q))}{\epsilon_{k-q} - (\epsilon_k + \omega_q)}}_{\text{absorption}}$$

To this term, one must subtract the scattering possibilities from ϵ_{k-q} to ϵ_k (they are forbidden since ϵ_k is occupied). Such a term is

$$\Delta E^2(\epsilon_{k-q} \rightarrow \epsilon_k) = \sum_q \frac{n_F(\epsilon_{k-q}) (1 + n_B(\omega_q))}{(\epsilon_k + \omega_q) - \epsilon_{k-q}} + \frac{n_F(\epsilon_{k-q}) (n_B(\omega_q))}{\epsilon_k - (\epsilon_{k+q} + \omega_q)}$$

Thus:

$$\begin{aligned} \Delta E(\epsilon_k) &= \Delta E^2(\epsilon_k \rightarrow \epsilon_{k-q}) - \Delta E^2(\epsilon_{k-q} \rightarrow \epsilon_k) \\ &= \sum_q \frac{(1 - n_F(\epsilon_{k-q})) (1 + n_B(\omega_q)) + n_F(\epsilon_{k-q}) (n_B(\omega_q))}{(\epsilon_{k-q} + \omega_q) - \epsilon_k} + \frac{(1 - n_F(\epsilon_{k-q})) (n_B(\omega_q)) + n_F(\epsilon_{k-q}) (1 + n_B(\omega_q))}{\epsilon_{k-q} - (\epsilon_k + \omega_q)} \\ &= \sum_q \frac{1 - n_F(\epsilon_{k-q}) + n_B(\omega_q)}{(\epsilon_{k-q} + \omega_q) - \epsilon_k} + \frac{n_B(\omega_q) + n_F(\epsilon_{k-q})}{\epsilon_{k-q} - (\epsilon_k + \omega_q)} \end{aligned}$$

ie

$$\Delta E(\omega) = - \sum_q \frac{1 + n_B(\omega_q) - n_F(\epsilon_{k-q})}{\omega - (\epsilon_{k-q} + \omega_q)} + \frac{n_B(\omega_q) + n_F(\epsilon_{k-q})}{\omega - (\epsilon_{k-q} - \omega_q)}$$

Thus

$$\Sigma(\omega) = \Delta E(\omega)$$

I.6 Weak-coupling charge and spin density wave scenarios

In this chapter, I give an overview of weak-coupling mean-field approaches to charge and spin density waves. This focus is voluntarily on the coupling of the physical fermions with bosonic modes representing their collective excitations, as this coupling is central to the main text.

A standard reference on this topic is ?; see also [Tosatti and Anderson \(1974\)](#) in the context of surface systems.

I.6.1 Weak-interaction, phonon-driven charge density wave (CDW) theory

Our starting point is the Fröhlich action (Fröhlich (1950, 1952)) describing the coupling of phonons (denoted by the field ϕ_q) with electrons (described by the fields \bar{c}_k and c_k) :

$$S_{\text{eb}} = \frac{1}{2} \sum_q \phi_q^* [-D_0(q)^{-1}] \phi_q + \sum_{k\sigma} \bar{c}_{k\sigma} [-G_0(k)^{-1}] c_{k\sigma} + \sum_{kq\sigma} \lambda_{\mathbf{q}} \phi_q \bar{c}_{k+q,\sigma} c_{k\sigma} \quad (\text{I.38})$$

with $k \equiv (\mathbf{k}, i\omega)$ and $q \equiv (\mathbf{q}, i\Omega)$, $\Sigma_q \equiv \frac{1}{\beta} \sum_{\mathbf{q}} \sum_{i\Omega}$ and $D_0(q)$ and $G_0(k)$ denote the unperturbed phononic and electronic propagators:

$$D_0(q) = \frac{2\omega_{\mathbf{q}}}{(i\Omega)^2 - \omega_{\mathbf{q}}^2}$$

$$G_0(k) = \frac{1}{i\omega - \xi_{\mathbf{k}}}$$

$\omega_{\mathbf{q}}$ is the bare phonon dispersion (e.g. $\omega_{\mathbf{q}} = \frac{2c}{a} |\sin(\frac{qa}{2})|$ for acoustic phonons in 1D [c is the sound velocity], $\omega_{\mathbf{q}} = \omega_0$ for Einstein/Holstein phonons), $\xi_{\mathbf{k}}$ is the electronic dispersion including the chemical potential, and $\lambda_{\mathbf{q}}$ is the electron-phonon coupling constant. The phononic field ϕ is related to the ionic displacement $\mathbf{u}(\mathbf{R}_i)$ by the relation:

$$\mathbf{u}(\mathbf{R}_i) = \sum_{\mathbf{q}s} e^{i\mathbf{q}\cdot\mathbf{R}_i} L_{\mathbf{q}s} \epsilon_{\mathbf{q}s} \phi_{\mathbf{q}s} \quad (\text{I.39})$$

$$\lambda_{\mathbf{q}s} \equiv \iiint_{\mathcal{V}} d\mathbf{r} (-en(\mathbf{r})) (-\mathbf{u}(\mathbf{R}_i) \nabla V_{\text{ion}}(\mathbf{r} - \mathbf{R}_i)) = \frac{ie}{\mathcal{V}} L_{\mathbf{q}s} \epsilon_{\mathbf{q}s} \cdot \mathbf{q} V_{\text{ion}}(\mathbf{q}) \quad (\text{I.40})$$

where $L_{\mathbf{q}s} \equiv \sqrt{\frac{\hbar}{2M\omega_{\mathbf{q}s}}}$ is the harmonic oscillator length (M is the ionic mass), $\epsilon_{\mathbf{q}s}$ is the (unit) *polarization vector* of the phonon branch s and $V_{\text{ion}}(\mathbf{r})$ is the ionic potential. In Eq. (I.38), we have restricted ourselves to the case with a single phonon branch, dropping the branch index s for simplicity. We define the usual imaginary-time correlators: $G_{ij}(\tau) = -\langle T c_i(\tau) c_j^\dagger(0) \rangle$ and $D_{ij}(\tau) = -\langle T \phi_i(\tau) \phi_j(0) \rangle$ (where i and j denote lattice sites \mathbf{R}_i and \mathbf{R}_j) and the fermionic and bosonic self-energies:

$$\Sigma(k) \equiv G_0^{-1}(k) - G^{-1}(k)$$

$$P(q) \equiv D_0^{-1}(q) - D^{-1}(q)$$

$P(q)$ is also called the polarization.

I.6.1.1 Kohn anomaly, charge density wave and phonon softening: Lindhard function in the triangular lattice

We are interested in the influence of the electronic system on the phonon dispersion $\tilde{\omega}_{\mathbf{q}}$, given by the poles of $D(\mathbf{q}, \omega)$, i.e:

$$\tilde{\omega}_{\mathbf{q}}^2 = \omega_{\mathbf{q}}^2 \left(1 - \frac{2P(\mathbf{q}, \tilde{\omega}_{\mathbf{q}})}{\omega_{\mathbf{q}}} \right) \quad (\text{I.41})$$

To lowest order in λ , the phononic self-energy $P(q)$ is given by the bubble diagram:

$$P_0(q) = \lambda_{\mathbf{q}}^2 \sum_{k\sigma} G_0(k+q) G_0(k) \quad (\text{I.42})$$

One can perform the Matsubara summation and get $P_0(\mathbf{q}, i\Omega) = -\lambda_{\mathbf{q}}^2 \chi_0(\mathbf{q}, i\Omega)$, where $\chi_0(\mathbf{q}, i\Omega)$ denotes the Lindhard function (Lindhard (1954)):

$$\chi_0(\mathbf{q}, i\Omega) = -2 \sum_{\mathbf{k} \in \text{BZ}} \frac{n_{\text{F}}(\xi_{\mathbf{k}+\mathbf{q}}) - n_{\text{F}}(\xi_{\mathbf{k}})}{\xi_{\mathbf{k}+\mathbf{q}} - \xi_{\mathbf{k}} - i\Omega} \quad (\text{I.43})$$

χ_0 is the lowest order contribution to the electronic charge-charge correlation function $\chi_{ij}(\tau) = \langle T n_i(\tau) n_j(0) \rangle$ (as proven in Appendix I.4.2.1, see Eq. (I.28)), which is measured for instance by EELS (see section H.1.2).

If the Fermi surface has large portions which can be joined by the same wavevector \mathbf{Q} (“nested” Fermi surface), then $\chi_0(\mathbf{Q}, i\Omega)$ will be large. This effect is particularly relevant in low dimensions (for instance, nested portions in 2D correspond to infinite planes in 3D due to the integration along the z coordinate). For the electron gas ($\xi_{\mathbf{k}} = \hbar^2 k^2 / 2m$), where the Fermi surface is a sphere of radius k_F , the enhancement of $\chi_0(\mathbf{q}, i\Omega = 0)$ occurs at $|\mathbf{Q}| = 2k_F$.

The nesting at \mathbf{Q} thus induces a large electronic response $\delta\langle n_{\mathbf{q}} \rangle$ at the \mathbf{Q} wavevector. Indeed, in the presence of a coupling term $n_{\mathbf{q}} h_{\mathbf{q}} e^{i\omega t}$, the Kubo formula (derived in Appendix I.1.1) gives:

$$\delta\langle n_{\mathbf{q}} \rangle = \chi_0(\mathbf{q}, \omega) h_{\mathbf{q}}$$

If $\chi_0(\mathbf{Q}, \omega = 0)$ diverges, then a static charge modulation (a charge density wave) $\delta\langle n_{\mathbf{Q}} \rangle$ will settle in even for vanishing field $h_{\mathbf{Q}}$.

On a triangular lattice, there are several possible nesting vectors \mathbf{Q} . In Fig. 3.4, we show the density modulations $\delta n(\mathbf{r})$ resulting from a charge response peaked at either the K or the M point. The K point corresponds to a 3×3 unit cell (with 3 atoms per unit cell), while the M point corresponds to a $2\sqrt{3} \times 2\sqrt{3}$ unit cell (4 atoms per unit cell).

Another consequence of a large $\chi_0(\mathbf{Q}, \omega)$ is the reduction and eventual vanishing of the phonon energy at $\mathbf{q} = \mathbf{Q}$ (Eq. (I.41)). This strong reduction is called the *Kohn anomaly* (Kohn (1959)). If $\tilde{\omega}_{\mathbf{Q}}$ eventually vanishes, the phonon mode is said to become “soft” or to “freeze in”, signalling a finite static distortion of the lattice known as the *Peierls instability* (Peierls (1955)): $u(\mathbf{R}_i)$ becomes nonzero on average, Eq. (I.39). Peierls has predicted the instability of any metallic phase in one dimension due to this instability. This instability is seen *e.g.* by nuclear magnetic resonance (see section H.2.2 for an explanation of this probe) in the one-dimensional compound $\text{K}_2\text{Pt}(\text{CN})_4\text{Br}_{0.3}$ (Niedoba *et al.* (1973) do not observe any Knight shift) or one-dimensional TTF-TCNQ salts (see section 3.2 of Jérôme and Schulz (1982)).

In the next section, we substantiate the link between phonon softening and a finite phononic field expectation value.

I.6.1.2 Consequence of phonon softening: phonon condensation

Rewriting Eq. (I.38) as:

$$S_{\text{eb}} = \frac{1}{2} \sum_{\mathbf{q}} \phi_{\mathbf{q}}^* [-D_0(\mathbf{q})^{-1}] \phi_{\mathbf{q}} + \sum_{\mathbf{k}\mathbf{k}'\sigma} \bar{c}_{\mathbf{k}\sigma} [M_{\mathbf{k}\mathbf{k}'}] c_{\mathbf{k}'\sigma}$$

with $M_{\mathbf{k}\mathbf{k}'} \equiv -G_0(\mathbf{k})^{-1} \delta_{\mathbf{k},\mathbf{k}'} + \lambda_{\mathbf{k}-\mathbf{k}'} \phi_{\mathbf{k}-\mathbf{k}'}$, and integrating out the fermionic variables, we obtain:

$$Z = \int \mathcal{D}[\phi] \text{Det}[\mathbf{M}] e^{-\frac{1}{2} \sum_{\mathbf{q}} \phi_{\mathbf{q}}^* [-D_0(\mathbf{q})^{-1}] \phi_{\mathbf{q}}}$$

Reexponentiating the determinant yields: $\log \text{Det}[\mathbf{M}] = \text{Tr} \log[\mathbf{M}] = \text{Tr} \log[-G_0^{-1}(\mathbf{1} + G_0(\lambda\phi))] = \text{Tr} \log[\mathbf{1} + G_0(\lambda\phi)] + \text{const.}$, with: $[G_0^{-1}]_{\mathbf{k}\mathbf{k}'} = G_0^{-1}(\mathbf{k}) \delta_{\mathbf{k}\mathbf{k}'}$ and $[\lambda\phi]_{\mathbf{k}\mathbf{k}'} = \lambda_{\mathbf{k}''-\mathbf{k}'} \phi_{\mathbf{k}''-\mathbf{k}'}$. We expand the logarithm in powers of λ : $\text{Tr} \log[\mathbf{1} + G_0(\lambda\phi)] = \text{Tr}[G_0(\lambda\phi)] + \frac{1}{2} \text{Tr}[G_0(\lambda\phi) G_0(\lambda\phi)] + O(\lambda^3)$, and compute both terms:

$$\text{Tr}[G_0(\lambda\phi)] = \sum_{\mathbf{k}\bar{\mathbf{k}}} G_0(\mathbf{k}) \delta_{\mathbf{k}\bar{\mathbf{k}}} (\lambda_{\bar{\mathbf{k}}-\mathbf{k}} \phi_{\bar{\mathbf{k}}-\mathbf{k}}) = \sum_{\mathbf{k}} G_0(\mathbf{k}) \lambda_0 \phi_0 = 0$$

and

$$\begin{aligned} \text{Tr} [G_0(\lambda\phi)G_0(\lambda\phi)] &= \sum_k \sum_{\bar{k}} G_0(k)\lambda_{k-\bar{k}}\phi_{k-\bar{k}}G_0(\bar{k})\lambda_{\bar{k}-k}\phi_{\bar{k}-k} = \sum_q \phi_{-q} \left\{ \sum_k \lambda_{-q}\lambda_q G_0(k)G_0(k+q) \right\} \phi_q \\ &= \sum_q \phi_{-q} P_0(q)\phi_q \end{aligned}$$

Hence, the effective bosonic action reads: $S_b = \frac{1}{2} \sum_q \phi_q^* [-D_0(q)^{-1} + P_0(q)] \phi_q + O(\lambda^3)$. Let us define $\Omega[h] \equiv -\log \int \mathcal{D}[\bar{c}c\phi] e^{-S_{\text{eb}} - h_q \phi_q}$, so that:

$$\langle \phi_{\mathbf{q}} \rangle = \frac{\delta \Omega}{\delta h_{\mathbf{q}}} \quad (\text{I.44})$$

(with $h_q = h_{\mathbf{q}}$). Hence:

$$\langle \phi_{\mathbf{q}} \rangle = -\frac{1}{Z} \frac{\delta}{\delta h_{\mathbf{q}}} \int \mathcal{D}[\phi] \frac{1}{2} \sum_q \phi_q^* D(q)^{-1} \phi_q - h_q \phi_q = -\frac{\delta}{\delta h_{\mathbf{q}}} \langle e^{-\frac{1}{2} D(q) h_q^2} \rangle = D(q, i\Omega) h_{\mathbf{q}}$$

Recalling that $D(q) = \frac{2\omega_{\mathbf{q}}}{\omega_{\mathbf{q}}^2}$, we see that if a mode softens at $\mathbf{q} = \mathbf{Q}$ ($\tilde{\omega}_{\mathbf{Q}} = 0$), $D(\mathbf{Q}, i\Omega = 0)$ becomes infinite, and hence $\langle \phi_{\mathbf{Q}}(i\Omega = 0) \rangle \neq 0$ even for a vanishing probe field $h_{\mathbf{Q}}$. This motivates us to adopt a mean-field approach.

I.6.1.3 Mean-field theory: BCS-like gap equation

Inspired by the previous discussion, we define the mean field $\Delta_{\mathbf{Q}} \equiv \lambda_{\mathbf{Q}} \langle \phi_{\mathbf{Q}}(i\Omega = 0) \rangle$ and replace $\phi_q \approx \Delta_{\mathbf{Q}} \delta_{\mathbf{q}-\mathbf{Q}} \delta_{i\Omega}$ to obtain the mean-field action:

$$S_{\text{eb}}[\Delta_{\mathbf{Q}}] = \frac{1}{2\beta} \Delta_{\mathbf{Q}}^* \frac{\omega_{\mathbf{Q}}^2}{2\lambda_{\mathbf{Q}}^2} \Delta_{\mathbf{Q}} + \sum_{k\sigma} \bar{c}_{k\sigma} [-G_0(k)^{-1}] c_{k\sigma} + \sum_{k\sigma} \Delta_{\mathbf{Q}} \bar{c}_{\mathbf{k}+\mathbf{Q}, i\omega, \sigma} c_{\mathbf{k}, i\omega \sigma}$$

We now define the spinor: $\Psi_{k\mathbf{Q}}^\dagger \equiv [\bar{c}_{\mathbf{k}+\mathbf{Q}, i\omega}, \bar{c}_{\mathbf{k}, i\omega}]$. Hence,

$$S_{\text{eb}}[\Delta_{\mathbf{Q}}] = \frac{1}{2\beta} \Delta_{\mathbf{Q}}^* \frac{\omega_{\mathbf{Q}}^2}{2\lambda_{\mathbf{Q}}^2} \Delta_{\mathbf{Q}} + \sum_{\mathbf{k} \in \text{RBZ}, i\omega, \sigma} \Psi_{k\mathbf{Q}}^\dagger \begin{bmatrix} -G_0(k+Q)^{-1} & \Delta_{\mathbf{Q}} \\ \Delta_{\mathbf{Q}}^* & -G_0(k)^{-1} \end{bmatrix} \Psi_{k\mathbf{Q}}$$

This Gaussian action makes for an easy determination of the Green's function, defined as:

$$G_{\mathbf{k}} \equiv -\langle \Psi_{k\mathbf{Q}} \Psi_{k\mathbf{Q}}^\dagger \rangle = \begin{bmatrix} -\langle c_{\mathbf{k}+\mathbf{Q}, i\omega} c_{\mathbf{k}+\mathbf{Q}, i\omega}^\dagger \rangle & -\langle c_{\mathbf{k}+\mathbf{Q}, i\omega} c_{\mathbf{k}, i\omega}^\dagger \rangle \\ -\langle c_{\mathbf{k}, i\omega} c_{\mathbf{k}+\mathbf{Q}, i\omega}^\dagger \rangle & -\langle c_{\mathbf{k}, i\omega} c_{\mathbf{k}, i\omega}^\dagger \rangle \end{bmatrix}$$

i.e. we have:

$$G_{\mathbf{k}} = \frac{1}{G_0(k+Q)^{-1} G_0(k)^{-1} - |\Delta_{\mathbf{Q}}|^2} \begin{bmatrix} G_0(k)^{-1} & \Delta_{\mathbf{Q}} \\ \Delta_{\mathbf{Q}}^* & G_0(k+Q)^{-1} \end{bmatrix} \quad (\text{I.45})$$

The anomalous components of this Green's function are related to the expectation value of ϕ :¹

$$\langle \phi_{\mathbf{q}} \rangle = D_0(q) \sum_{k\sigma} \lambda_{\mathbf{k}\mathbf{q}} \langle \bar{c}_{\mathbf{k}+\mathbf{q}, \sigma} c_{k\sigma} \rangle \quad (\text{I.46})$$

¹Indeed, integrating out the phonon modes, and defining $\tilde{h}_{\mathbf{q}} \equiv h_{\mathbf{q}} + \sum_{k\sigma} \lambda_{\mathbf{k}\mathbf{q}} \bar{c}_{\mathbf{k}+\mathbf{q}, \sigma} c_{k\sigma}$, we have:

$$\begin{aligned} S[h] &= \sum_q \frac{1}{2} \phi_q^* [-D_0(q)^{-1}] \phi_q + \phi_q \tilde{h}_q = \sum_q -\frac{1}{2D_0(q)} [\phi_q^2 - 2D_0(q) \tilde{h}_q] \\ &= \sum_q -\frac{1}{2D_0(q)} [(\phi_q - D_0(q) \tilde{h}_q)^2 - (D_0(q) \tilde{h}_q)^2] = \sum_q \left\{ -\frac{1}{2D_0(q)} [(\tilde{\phi}_q)^2] + \frac{1}{2} D_0(q) \tilde{h}_q^2 \right\} \end{aligned}$$

Hence, $\Omega[h] = -\log \int \mathcal{D}[\bar{c}c] e^{-\sum_{k\sigma} \bar{c}_{k\sigma} [-G_0(k)^{-1}] c_{k\sigma} - \frac{1}{2} \sum_q D_0(q) \tilde{h}_q^2}$, so that using Eq. (I.44) one obtains Eq. (I.46).

The mean field $\Delta_{\mathbf{Q}}$ is thus related to the anomalous Green's function by the relation:

$$\Delta_{\mathbf{Q}} = \lambda_{\mathbf{Q}}^2 D_0(\mathbf{Q}, i\Omega = 0) \sum_{k\sigma} \langle \bar{c}_{\mathbf{k}+\mathbf{Q}, i\omega, \sigma} c_{\mathbf{k}, i\omega, \sigma} \rangle = \frac{2\lambda_{\mathbf{Q}}^2}{\omega_{\mathbf{Q}}} \sum_{k\sigma} \langle c_{\mathbf{k}, i\omega, \sigma} \bar{c}_{\mathbf{k}+\mathbf{Q}, i\omega, \sigma} \rangle$$

Finally, using Eq. (I.45), and noticing that $\Delta_{\mathbf{Q}} = \Delta_{\mathbf{Q}}^*$, one obtains the mean-field gap equation:

$$-\frac{\omega_{\mathbf{Q}}}{4\lambda_{\mathbf{Q}}^2} = \sum_{\mathbf{k}, i\omega} \frac{1}{(i\omega - \xi_{\mathbf{k}+\mathbf{Q}})(i\omega - \xi_{\mathbf{k}}) - \Delta_{\mathbf{Q}}^2} \quad (\text{I.47})$$

The similarity of the right-hand side with the bubble diagram (Eq. (I.42)) will be elaborated on in paragraph I.6.2.2. Using $\xi_{\mathbf{k}+\mathbf{Q}} \approx -\xi_{\mathbf{k}}$ (which is valid for momenta \mathbf{k} close to the Fermi surface), defining the effective coupling constant g and the Bogoliubov or CDW dispersion $E_{\mathbf{k}}$:

$$g \equiv \frac{2\lambda_{\mathbf{Q}}^2}{\omega_{\mathbf{Q}}} \quad (\text{I.48})$$

$$E_{\mathbf{k}}^2 \equiv \xi_{\mathbf{k}}^2 + \Delta_{\mathbf{Q}}^2 \quad (\text{I.49})$$

as well as the non-interacting DOS $N(\varepsilon) \equiv \sum_{\mathbf{k}} \delta(\varepsilon - \xi_{\mathbf{k}})$, and performing the Matsubara sums, one obtains the gap equation (which is analogous to the BCS gap equation):

$$\frac{1}{g} = 2 \sum_{\mathbf{k}, n} \frac{1}{\omega_n^2 + E_{\mathbf{k}}^2} = \sum_{\mathbf{k}} \frac{1}{E_{\mathbf{k}}} \tanh\left(\frac{\beta E_{\mathbf{k}}}{2}\right) = \int_{-\infty}^{\infty} d\varepsilon N(\varepsilon) \frac{1}{\sqrt{\varepsilon^2 + \Delta^2}} \tanh\left(\frac{\beta \sqrt{\varepsilon^2 + \Delta^2}}{2}\right) \quad (\text{I.50})$$

I now restrict the energy integral to the $[-\omega_{\text{D}}, \omega_{\text{D}}]$ range, where ω_{D} is the Debye frequency ($\omega_{\text{D}} \propto c_{\text{sound}} n^{1/3}$, where $c_{\text{sound}} = \sqrt{K/\rho} \propto 1/\sqrt{M}$, K : bulk modulus, ρ : massic density and M : atomic mass): at higher energies, the electrons decouple from the phonons and behave like free electrons. I further assume that $N(\varepsilon)$ is a constant in the vicinity of the Fermi level, leading to

$$\frac{1}{2gN(\varepsilon_{\text{F}})} = \int_0^{\omega_{\text{D}}} d\varepsilon \frac{\tanh\left(\frac{\sqrt{\varepsilon^2 + \Delta^2}}{2T}\right)}{\sqrt{\varepsilon^2 + \Delta^2}}$$

Let us now find T_{c} and $\Delta(T=0)$. When $T \rightarrow 0$, the hyperbolic tangent term is close to unity, leading to $\frac{1}{2gN(\varepsilon_{\text{F}})} = \int_0^{\omega_{\text{D}}/\Delta} \frac{dx}{\sqrt{x^2+1}} = \text{arsinh}\left(\frac{\omega_{\text{D}}}{\Delta}\right)$. When $T \rightarrow T_{\text{c}}$, by definition $\Delta \rightarrow 0$, so that $\frac{1}{2gN(\varepsilon_{\text{F}})} = \int_0^{\omega_{\text{D}}/2T_{\text{c}}} dx \frac{\tanh(x)}{x} \approx \log\left(\frac{4}{\kappa} \frac{\omega_{\text{D}}}{2T_{\text{c}}}\right)$, with $\kappa = \pi e^{-\gamma} \approx 1.76$.² Hence, one obtains the well-known mean-field results:

$$\Delta(T=0) = \omega_{\text{D}} \sinh\left(1/2gN(\varepsilon_{\text{F}})\right)^{-1} \approx 2\omega_{\text{D}} e^{-\frac{1}{2gN(\varepsilon_{\text{F}})}} \quad (\text{I.51a})$$

$$T_{\text{c}} = \frac{2\omega_{\text{D}}}{\kappa} e^{-\frac{1}{2gN(\varepsilon_{\text{F}})}} \quad (\text{I.51b})$$

In particular the ratio of the gap to the critical temperature is constant:

$$\frac{2\Delta}{k_{\text{B}}T_{\text{c}}} = 2\kappa \approx 3.53 \quad (\text{I.52})$$

I.6.2 Spin density waves with Hubbard interactions at weak coupling

Our starting point is the Hubbard model written here in an action form:

$$S_H = \sum_{k\sigma} \bar{c}_{k\sigma} \left[-G_0(k)^{-1}\right] c_{k\sigma} + \frac{1}{2} U^{\text{ch}} \sum_q n_q n_{-q} + \frac{1}{2} U^{\text{sp}} \sum_q s_q^z s_{-q}^z \quad (\text{I.53})$$

² γ is the Euler constant

Here, we rewrote the usual Hubbard term $H_{\text{int}} = U \sum_i n_{i\uparrow} n_{i\downarrow}$ with charge and spin operators and the corresponding interactions $U^{\text{sp}} = -U/2$ and $U^{\text{ch}} = U/2$. This rewriting is exact and will be elaborated on later, in Chapter 8.

As for the CDW case investigated in the previous section, the spin density change in response to an external magnetic probe field is given by Kubo's formula,

$$\delta\langle s_{\mathbf{q}}^z \rangle = \chi_0(\mathbf{q}, \omega) h_{\mathbf{q}}$$

where $\chi_0(\mathbf{q}, \omega) = \langle s_{\mathbf{q}}^z s_{-\mathbf{q}}^z \rangle_0$ turns out to be the Lindhard function (defined in Eq. (I.43)) owing to the property that the charge and spin correlation functions are equal to each other at lowest order (see Eqs. (I.28) and (I.29) in Appendix I.4.2.1). Thus, the nesting features that enhance the charge response at wavevector \mathbf{Q} , can enhance the spin response at the same wavevector.

I.6.2.1 Analogy to electron-phonon problem via a Hubbard-Stratonovich decoupling

At this stage, we could use this piece of information and proceed with a direct mean-field decoupling of the interaction term with the mean field

$$\Delta_{\mathbf{Q}} \propto U^{\text{sp}} \langle s_{\mathbf{Q}}^z \rangle \quad (\text{I.54})$$

Yet, in order to underline the formal analogy with the electron-phonon coupling model (Eq.(I.38)), we instead decouple the interaction term using a Hubbard-Stratonovich bosonic field ϕ using the identity:

$$e^{-\frac{1}{2} U^{\text{sp}} \sum_q s_q^z s_q^z} = \int \mathcal{D}[\phi] e^{-\frac{1}{2} \sum_q \phi_q [-(U^{\text{sp}})^{-1}] \phi_q - \sum_q \lambda_q \phi_q s_q^z} \quad (\text{I.55})$$

provided $\lambda_q = 1$. Thus, Eq. (I.53) becomes:

$$S_{H\phi} = \sum_{k\sigma} \bar{c}_{k\sigma} [-G_0(k)^{-1}] c_{k\sigma} + \frac{1}{2} \sum_q \phi_q [-(U^{\text{sp}})^{-1}] \phi_q + \sum_q \lambda_q \phi_q s_q^z \quad (\text{I.56})$$

Thus, we can identify the electron-phonon model described by Eq.(I.38) and the above equation provided

$$D_0^{-1}(q) = (U^{\text{sp}})^{-1}$$

Thus, the whole mean-field analysis carried out in section I.6.1.3 carries over with a coupling constant

$$g = -D_0(\mathbf{Q}, \omega = 0) \lambda_{\mathbf{Q}} = -U^{\text{sp}} \quad (\text{I.57})$$

and the mean-field results:

$$\Delta(T = 0) \approx 2\omega_c e^{-\frac{1}{2gN(\epsilon_{\text{F}})}} \quad (\text{I.58})$$

$$T_c \approx \frac{2\omega_c}{\kappa} e^{-\frac{1}{2gN(\epsilon_{\text{F}})}} \quad (\text{I.59})$$

Here, the cutoff frequency is no longer the Debye frequency ω_{D} but a cutoff frequency of the order of the spin-wave energy $\omega_c \sim J$.

I.6.2.2 Link to the random-phase approximation (RPA): Stoner criteria

With the replacement (I.57), the gap equation Eq. (I.47) becomes, when $\Delta_{\mathbf{Q}} = 0$:

$$1 = U^{\text{sp}} P_0(\mathbf{Q}, i\Omega = 0) \quad (\text{I.60})$$

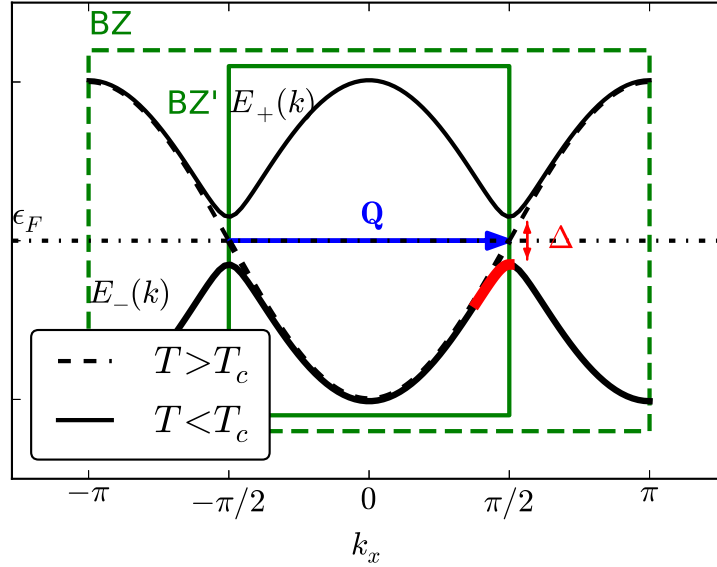


Figure I.4: Slater mechanism (1D case). BZ denotes the original Brillouin zone, BZ' the Brillouin zone after symmetry-breaking.

This is a Stoner criterion for the onset of antiferromagnetism (if \mathbf{Q} is commensurate) or more generally spin-density wave order. Indeed, the fulfillment of equation (I.60) signals the appearance of a pole in the spin susceptibility computed in the random-phase approximation (RPA):

$$\chi_{\text{RPA}}^{\text{sp}}(\mathbf{q}, i\Omega) \equiv \frac{-P_0(\mathbf{q}, i\Omega)}{1 - U^{\text{sp}} P_0(\mathbf{q}, i\Omega)} \quad (\text{I.61})$$

This corresponds to an infinite resummation of bubble diagrams. Viewing the gap equation in this light allows for straightforward generalizations of the mean-field approach sketched above, namely by writing a generalized Stoner criterion $1 = U^{\text{sp}} P_{\text{approx}}^{\text{sp}}(\mathbf{Q}, i\Omega = 0)$, where $P_{\text{approx}}^{\text{sp}}$ is an approximate spin polarization (for instance computed with renormalized or “full” propagators: $P_{\text{approx}}^{\text{sp}} \sim 2GG$ instead of $2G_0G_0\dots$).

Moreover, the same criterion can be formulated for the charge channel: after adding nonlocal interactions (in the form of a term $\frac{1}{2} \sum_q V_q n_q n_{-q}$) to the Hubbard model (I.53) – which thus becomes the extended Hubbard model (introduced in section 5.1), the RPA charge susceptibility is

$$\chi_{\text{RPA}}^{\text{ch}}(\mathbf{q}, i\Omega) \equiv \frac{-P_0(\mathbf{q}, i\Omega)}{1 - \left(\frac{U}{2} + V(\mathbf{q})\right) P_0(\mathbf{q}, i\Omega)} \quad (\text{I.62})$$

Eqs (I.61-I.62), when generalized to the ordered phase ($\Delta \neq 0$), correspond to the Hartree-Fock approximation used e.g. in Santoro *et al.* (1998) to study the influence of local and nonlocal interactions in surface systems.

I.6.2.3 Energetic conclusion: Slater mechanism vs. Mott mechanism

To conclude this subsection on the weak-interaction CDW and SDW scenarios, let us emphasize three important points:

- the scenarios put forth above are driven by a lowering of the electronic *kinetic* energy due to the symmetry breaking: the opening of the CDW or SDW gap Δ at the boundaries of the new Brillouin zone allows the electrons to lower their energy (see *e.g.* the red portion in Fig. I.4, to be compared to the original dashed dispersion). Thus, the CDW and SDW transitions are kinetic-energy-driven metal-insulator transitions, a simple mechanism first proposed by Slater (1951). This is in stark opposition to the metal-insulator transition mechanism put forth by Mott, where electrons lower their *potential* energy by becoming localized.
- these scenarios rely on nonzero but *infinitesimally weak* interactions (whether electron-electron in the SDW case or electron-phonon in the CDW case), as one can see by looking at the analytical forms of the gap or critical temperatures (see *e.g.* Eqs (I.51a) and (I.51b)). The charge-charge and spin-spin correlation functions have been treated at zeroth order in the interaction strength.
- the *nonlocal* interactions, whose magnitude can be sizable in some systems (see *e.g.* section 3.3.1), have been neglected altogether in the above mean-field treatment

Reminder: realistic calculations for correlated materials

In this chapter, I give background information on realistic calculations for correlated materials.

J.1 Density functional theory

The physics of electrons in a solid at equilibrium is determined by the electronic-structure Hamiltonian H_{ES} , written below in a second-quantized form in the Born-Oppenheimer approximation (the ionic cores are assumed to be fixed due to their much larger mass):

$$H_{\text{ES}} \equiv \iiint_{\mathcal{V}} d\mathbf{r} \psi^\dagger(\mathbf{r}) \left(-\frac{\hbar^2 \nabla^2}{2m} + V_{\text{ext}}(\mathbf{r}) \right) \psi(\mathbf{r}) + \frac{1}{2} \iiint_{\mathcal{V}} d\mathbf{r} \iiint_{\mathcal{V}} d\mathbf{r}' \psi^\dagger(\mathbf{r}) \psi^\dagger(\mathbf{r}') v_{\text{Coul}}(\mathbf{r} - \mathbf{r}') \psi(\mathbf{r}') \psi(\mathbf{r}) \quad (\text{J.1})$$

$V_{\text{ext}}(\mathbf{r})$ contains the ionic potential and (optionally) external driving fields, m is the electron mass, \mathcal{V} denotes the solid's volume, $v_{\text{Coul}}(\mathbf{r} - \mathbf{r}') = \frac{e^2}{|\mathbf{r} - \mathbf{r}'|}$ is the (bare) Coulomb interaction, and $\psi^\dagger(\mathbf{r})$ and $\psi(\mathbf{r})$ are fermionic field operators. \mathbf{r} denotes the continuous real-space coordinate. From the knowledge of the many-body eigenstates Ψ_ν and eigenenergies E_ν of H_{ES} :

$$H_{\text{ES}} \Psi_\nu(\mathbf{r}_1, \dots, \mathbf{r}_N) = E_\nu \Psi_\nu(\mathbf{r}_1, \dots, \mathbf{r}_N) \quad (\text{J.2})$$

where $\mathbf{r}_1, \dots, \mathbf{r}_N$ denotes the coordinates of the N electrons, one can in principle derive the electronic contribution to the thermodynamic properties of the solid. For instance, the thermodynamic expectation value of any observable O can be computed as:

$$\langle O \rangle = \frac{\sum_\nu e^{-\beta(E_\nu - \mu N)} \langle \Psi_\nu(\mathbf{r}_1, \dots, \mathbf{r}_N) | O | \Psi_\nu(\mathbf{r}_1, \dots, \mathbf{r}_N) \rangle}{\sum_\nu e^{-\beta(E_\nu - \mu N)}}$$

Of course, due to the huge number $-N \sim 10^{23}$ – of *interacting* electrons in a solid, this problem is in general intractable. Conversely, in the absence of the second term of Eq. (J.1), solving Eq. (J.2) becomes rather easy.

J.1.1 Free electrons: Bloch and Wannier functions

Defining the one-particle Hamiltonian

$$h(\mathbf{r}) \equiv -\frac{\hbar^2 \nabla^2}{2m} + V_{\text{ext}}(\mathbf{r}) \quad (\text{J.3})$$

we can solve it for its eigenvalues ε_i and (orthonormalized) eigenvectors $\phi_\alpha(\mathbf{r})$ ($\alpha = 1 \dots \mathcal{N}$):

$$h(\mathbf{r}) \phi_\alpha(\mathbf{r}) = \varepsilon_\alpha \phi_\alpha(\mathbf{r}) \quad (\text{J.4})$$

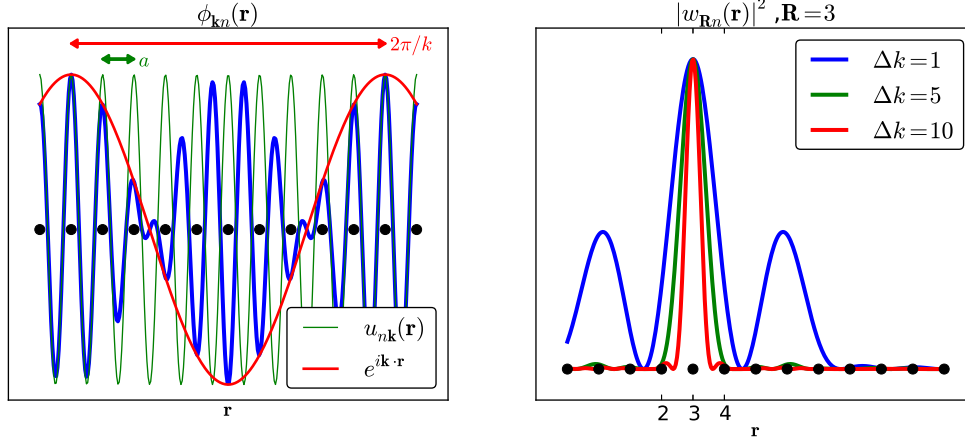


Figure J.1: Bloch (left) and Wannier (right) functions in 1D

In crystalline solids, $\hat{h}(\mathbf{r})$ is invariant by any translation by a Bravais lattice vector \mathbf{R} , and thus the eigenelements can be labelled by a *quasimomentum* index \mathbf{k} and a *band* index n , and can be decomposed as the product of a plane-wave by an envelope function $u_{n\mathbf{k}}(\mathbf{r})$ (see Fig.J.1), i.e. $\phi_{\mathbf{k}n}(\mathbf{r}) = u_{n\mathbf{k}}(\mathbf{r})e^{i\mathbf{k}\cdot\mathbf{r}}$ where for any Bravais lattice vector \mathbf{R} , $u_{n\mathbf{k}}(\mathbf{r} + \mathbf{R}) = u_{n\mathbf{k}}(\mathbf{r})$ (this is Bloch's theorem (Bloch (1929)) – $\phi_{\mathbf{k}n}(\mathbf{r})$ is called a “Bloch wavefunction”). The associated Wannier function can be defined as (a more general definition will be given in paragraph J.2.3):

$$w_{\mathbf{R}n}(\mathbf{r}) \equiv \sum_{\mathbf{k}} \phi_{\mathbf{k}n}(\mathbf{r})e^{-i\mathbf{k}\cdot\mathbf{R}} = \sum_{\mathbf{k}} u_{n\mathbf{k}}(\mathbf{r})e^{i\mathbf{k}\cdot(\mathbf{r}-\mathbf{R})} \quad (\text{J.5})$$

It is localized around $\mathbf{r} = \mathbf{R}$, as we can see from the following simple calculation in 1D. If $u_{n\mathbf{k}}$ is a vanishing everywhere except for a range $[k_0 - \frac{\Delta k}{2}, k_0 + \frac{\Delta k}{2}]$ where it equals 1, then $w_{\mathbf{R}n}(\mathbf{r}) = e^{i(k_0 - \frac{\Delta k}{2})(r-R)} M^{-1} \sum_{i=0}^M \left(e^{i\frac{\Delta k}{M}(r-R)} \right)^i = e^{ik_0(r-R)} \text{sinc}\left(\frac{\Delta k}{2}(r-R)\right)$. As Δk becomes larger, $w_{\mathbf{R}n}(\mathbf{r})$ becomes more localized around \mathbf{R} (see Fig. J.1). The Wannier basis is thus best suited to describe *localized states*.

The previous discussion shows that the Bloch basis diagonalizes the Hamiltonian h describing free electrons in a periodic potential V_{ext} . Expanding the field operator in this eigenbasis: $\psi(\mathbf{r}) = \sum_{\mathbf{k}n} \phi_{\mathbf{k}n}(\mathbf{r})c_{\mathbf{k}n}$, the many-body Hamiltonian H_{ES}^0 becomes:

$$H_{\text{ES}}^0 = \sum_{n\mathbf{k}} \varepsilon_{n\mathbf{k}} c_{n\mathbf{k}}^\dagger c_{n\mathbf{k}} \quad (\text{J.6})$$

where $\varepsilon_{n\mathbf{k}}$ is the “bare dispersion”, $\varepsilon_{n\mathbf{k}} \equiv \iiint_{\mathcal{V}} d\mathbf{r} \phi_{n\mathbf{k}}^*(\mathbf{r}) \hat{h}(\mathbf{r}) \phi_{n\mathbf{k}}(\mathbf{r})$.¹ The eigenfunctions of a many-body Hamiltonian such as (J.6) are

$$\Psi_{v=(n_1 \dots n_N)} = |n_1, n_2, \dots, n_N\rangle \equiv \prod_{\alpha=1}^N (c_{\alpha}^\dagger)^{n_{\alpha}} |0\rangle$$

with $n_{\alpha} = 0, 1$. There are 2^N of them. In terms of wavefunctions, if $N = \sum_{\alpha=1}^N n_{\alpha}$, and if we reorder the α 's so that the first N one-body states are occupied, the many-body wavefunction is given by *Slater determinants* of the one-body wavefunctions $\phi_{n\mathbf{k}}(\mathbf{r})$, namely

$$\Psi(\mathbf{r}_1, \dots, \mathbf{r}_N) = \frac{1}{\sqrt{N!}} \sum_{p \in \mathfrak{S}_N} \text{sign}(p) \prod_{i=1}^N \phi_{p(\alpha_i)}(\mathbf{r}_i)$$

¹Note that the same Hamiltonian can be written in the Wannier basis:

$$H_{\text{ES}}^0 = \sum_{n\mathbf{R}} t_{n\mathbf{R}\mathbf{R}'} c_{n\mathbf{R}}^\dagger c_{n\mathbf{R}'}$$

where $t_{n\mathbf{R}\mathbf{R}'}$ is the tight-binding hopping integral, $t_{n\mathbf{R}\mathbf{R}'} \equiv \iiint_{\mathcal{V}} d\mathbf{r} \phi_{n\mathbf{R}}^*(\mathbf{r}) \hat{h}(\mathbf{r}) \phi_{n\mathbf{R}'}(\mathbf{r})$.

where \mathfrak{S}_N is the symmetric group of order N .

J.1.2 Density-functional theory (DFT) in a nutshell

A modern textbook on the topic is Martin (2004). There are also multiple reviews, see *e.g.* Jones and Gunnarsson (1989) or Kohn (1999).

J.1.2.1 Basic principles

Let us define the electronic density

$$n(\mathbf{r}) \equiv N \iiint_{\mathcal{V}} \prod_{i=2}^N d\mathbf{r}_i |\Psi(\mathbf{r}, \mathbf{r}_2, \dots, \mathbf{r}_N)|^2 \quad (\text{J.7})$$

Hohenberg and Kohn (1964) have proven two important theorems about $n(\mathbf{r})$:

1. The equation giving $n(\mathbf{r})$ as a function of $\Psi(\mathbf{r}_1, \mathbf{r}_2, \dots, \mathbf{r}_N)$, Eq. (J.7), can be formally inverted for the ground-state Ψ_0 , namely Ψ_0 is a functional of the ground-state density $n_0(\mathbf{r})$:

$$\Psi_0 = \Psi_0[n_0] \quad (\text{J.8})$$

Consequently, all ground-state observables are functionals of the density: $O_0 = \langle \Psi_0[n_0] | O | \Psi_0[n_0] \rangle = O_0[n_0]$.

2. The total energy, $E \equiv \langle \Psi | H_{\text{ES}} | \Psi \rangle$, is a universal functional of the density $n(\mathbf{r})$ and obeys a variational principle:

$$E = E[n] \geq E_0[n_0] \quad (\text{J.9})$$

On the other hand, remembering the form of H_{ES} (Eq. J.1), the total energy can be split up as the sum $E = E_{\text{kin}} + E_{\text{ext}} + E_{\text{Coul}}$, and defining the exchange and correlation energy as $E_{\text{xc}} \equiv E_{\text{Coul}} - E_{\text{Hartree}}$, where $E_{\text{Hartree}} \equiv \iiint_{\mathcal{V}} d\mathbf{r}' n(\mathbf{r}) v_{\text{Coul}}(\mathbf{r} - \mathbf{r}') n(\mathbf{r}')$, we see, using (J.9), that $E_{\text{xc}} = E[n] - (E_{\text{kin}}[n] + E_{\text{ext}}[n] + E_{\text{Hartree}}[n])$ is itself (at least formally) a functional of n , *i.e.* $E_{\text{xc}} = E_{\text{xc}}[n]$.

The next step consists in finding a procedure to compute the ground state density n_0 . This procedure has first been described by Kohn and Sham (1965). Following Eq. (J.9), one looks for the ground-state density n_0 by solving the equation $\left. \frac{\delta E[n]}{\delta n} \right|_{n=n_0} = 0$, which can be rewritten as $\int \delta n(\mathbf{r}) \hat{h}_{\text{KS}}(\mathbf{r}) = 0$, where the Kohn-Sham Hamiltonian $\hat{h}_{\text{KS}}(\mathbf{r})$ is defined as:

$$h_{\text{KS}}(\mathbf{r}) \equiv -\frac{\hbar^2 \nabla^2}{2m} + V_{\text{ext}}(\mathbf{r})[n] + V_{\text{Hartree}}(\mathbf{r})[n] + V_{\text{xc}}(\mathbf{r})[n] \quad (\text{J.10})$$

with $V_{\text{Hartree}}(\mathbf{r}) \equiv \frac{\delta E_{\text{Hartree}}[n]}{\delta n(\mathbf{r})}$ and $V_{\text{xc}}(\mathbf{r}) \equiv \frac{\delta E_{\text{xc}}[n]}{\delta n(\mathbf{r})}$. Note the analogy with the ‘‘Bloch’’ Hamiltonian, Eq. (J.3). This minimization problem is solved by solving for the eigenelements of the Kohn-Sham Hamiltonian:

$$h_{\text{KS}}(\mathbf{r}) \phi_{\mathbf{k}\alpha}^{\text{KS}}(\mathbf{r}) = \varepsilon_{\mathbf{k}\alpha}^{\text{KS}} \phi_{\mathbf{k}\alpha}^{\text{KS}}(\mathbf{r}) \quad (\text{J.11})$$

The ground-state density is then reconstructed as:

$$n_0(\mathbf{r}) = \sum_{\substack{\mathbf{k}\alpha, \\ \varepsilon_{\mathbf{k}\alpha}^{\text{KS}} \leq \varepsilon_F}} |\phi_{\mathbf{k}\alpha}^{\text{KS}}(\mathbf{r})|^2 \quad (\text{J.12})$$

Equations (J.10-J.11-J.12) can be solved self-consistently, provided one can specify the relation between $n(\mathbf{r})$ and $V_{\text{xc}}(\mathbf{r})$.

In practice, the eigenvalue problem Eq. (J.11) has to be solved on a finite basis set which we will denote $\{|B_{\mathbf{k}\alpha}\rangle\}$: \mathbf{k} is the quasi-momentum (from Bloch's theorem), and the other label α depends on the choice of basis sets. There are three main classes of basis sets:

1. delocalized basis sets (such as plane waves, $\alpha \equiv \mathbf{G}$ [with \mathbf{G} a reciprocal lattice vector] or Bloch waves, $\alpha \equiv n$ [the band index];
2. localized basis sets (e.g. Gaussian wavefunctions or Linearized Muffin-Tin Orbitals [LMTO], $\alpha = L = (\mathbf{u}, l, m)$ [\mathbf{u} : label of atom in unit cell, l, m : orbital angular momentum numbers];
3. mixed basis sets such as Linearized Augmented Plane Waves [LAPW]. More details can be found e.g. in ?;
4. numerical basis sets.

J.1.2.2 Approximating the exchange-correlation energy: the local-density approximation (LDA), and its limitations

If the exact exchange-correlation potential were known, then the $n_0(\mathbf{r})$ computed using the above procedure would be the exact many-body ground-state density of the system. In practice, however, one has to resort to approximate forms for $E_{xc}[n]$. The earliest and most simple form is the so-called local density approximation (LDA), where one approximates E_{xc} as:

$$E_{xc}^{\text{LDA}}[n] \equiv \iiint_{\mathcal{V}} d\mathbf{r} n(\mathbf{r}) \varepsilon_{xc}(n(\mathbf{r})) \quad (\text{J.13})$$

where $\varepsilon_{xc}(n)$ is the exact exchange-correlation energy density as a function of the electronic density for the homogeneous electron gas. Despite the fact that DFT is rigorously defined only for ground-state observables, the Kohn-Sham eigenvalues $\varepsilon_{\alpha}^{\text{KS}}$ of the auxiliary Kohn-Sham problem are nonetheless routinely interpreted as the band structure of the material. LDA can readily be extended to magnetic materials by introducing the spin-resolved density $n_{\sigma}(\mathbf{r})$ instead of $n(\mathbf{r})$. This is called the local spin density approximation (LSDA).

Numerous more sophisticated functionals than LDA have been developed over time, including functionals with gradient corrections to LDA ("GGA", where ε_{xc} depends on $n(\mathbf{r})$ and $\nabla n(\mathbf{r})$), and "hybrid functionals" which can be seen as combinations of the Hartree-Fock approximation and DFT.

Computationally, DFT is a lightweight method implemented in a number of well-optimized codes. Its main limitation comes from its approximate treatment of exchange and correlation: since the many-body problem is mapped onto a one-body problem where exchange and correlation effects are lumped into an effective *one-body* potential, DFT is quite close in essence to mean-field theory (which corresponds to taking $V_{xc} = 0$). Many-body effects in spectral properties are treated only in an average way.

This leads to limitations of LDA when applied to materials with localized electrons. We list here but a few (more examples can be found in e.g. Aryasetiawan and Gunnarsson (1998) or section 5.1 of Georges (2008)):

- The unit cell volume of f -electron systems (such as δ -plutonium) is underestimated
- The Kohn-Sham spectra of many transition-metal oxides are metallic in DFT: this is the case for CoO, which is seen to be magnetic and insulating experimentally. With an odd number of electrons in the unit cell, it should be metallic in a simple paramagnetic band theory; with an antiferromagnetic unit cell, a Slater gap could be opened (see section I.6.2.3), but LSDA still predicts it to be metallic. Another well-known example is the La_2CuO_4 undoped cuprate, which is predicted to be metallic despite its actual (Mott) insulating state. A more thorough discussion can be found in section 7.1.1 or in sections VIII.A/B of Pickett (1989);
- The magnetic moment is systematically underestimated.

Efforts to better incorporate the effects of local interactions (Hubbard's U) into DFT include the “LDA+ U ” approximation to V_{xc} (Anisimov *et al.* (1991); for a recent review, see Himmetoglu *et al.* (2014)). Within LDA+ U , the exchange-correlation potential is written:

$$V_{xc,\sigma}^{\text{LDA}+U} = V_{xc,\sigma}^{\text{LDA}} + \sum_{\mathbf{R}, m \in \mathcal{C}} U_m \left(\frac{1}{2} - \langle n_{\mathbf{R}m\sigma} \rangle |w_{\mathbf{R}m}\rangle \langle w_{\mathbf{R}m}| \right) \quad (\text{J.14})$$

where \mathcal{C} denotes a subset of correlated bands, $w_{\mathbf{R}m}$ localized (Wannier-like) orbitals, and U_m the Hubbard interaction on this site. $|w_{\mathbf{R}m}\rangle \langle w_{\mathbf{R}m}|$ merely projects states on the localized bands. This approximation corrects the too small antiferromagnetic band gaps found in many transition-metal oxides. Yet, this method still amounts to a Hartree-like treatment of U (as can be seen from the form of the last term of Eq. (J.14)): while it can open “Slater” gaps with the right magnitude, it cannot open “Mott” gaps, *i.e.* gaps merely coming from the freezing of the charge degree of freedom. It can lead to unphysical spin polarizations.

J.2 Density functional theory combined to many-body techniques: LDA+DMFT

This chapter gives background details to chapter 12 of the main text.

In the previous chapter, we have seen that DFT does not treat correlations in a satisfactory manner, even when incorporating Hubbard's U in the Kohn-Sham Hamiltonian for “correlated orbitals”. The idea of treating a correlated subset of orbitals \mathcal{C} with dynamical mean-field theory is implemented by the LDA+DMFT method, introduced by Anisimov *et al.* (1997) and Lichtenstein and Katsnelson (1997). Here, we take inspiration from a more recent formulation (Lechermann *et al.* (2006)).

The starting point is the (imaginary-time) one-body Green's function associated with the field operators introduced in Eq. (J.1):

$$G(\mathbf{r}, \mathbf{r}', \tau) \equiv -\langle T\psi(\mathbf{r}, \tau)\psi^\dagger(\mathbf{r}, 0) \rangle \quad (\text{J.15})$$

We use bold letters to denote operators acting on the full Hilbert space \mathcal{H} and to emphasize the fact that G is written irrespective of any basis. Its Fourier transform $G(\mathbf{r}, \mathbf{r}', i\omega)$ is related to the one-particle Hamiltonian $h(\mathbf{r})$ and self-energy $\Sigma(\mathbf{r}, \mathbf{r}', i\omega)$ by Dyson's equation:

$$G(\mathbf{r}, \mathbf{r}', i\omega) = [(i\omega + \mu) \mathbf{1} - h(\mathbf{r}) - \Sigma(\mathbf{r}, \mathbf{r}', i\omega)]_{\mathbf{r}, \mathbf{r}'}^{-1} \quad (\text{J.16})$$

Here, inversion refers to defined in continuous space, namely the inverse $g(\mathbf{r}, \mathbf{r}')$ of $f(\mathbf{r}, \mathbf{r}')$ is defined as: $\int d\mathbf{r}'' f(\mathbf{r}, \mathbf{r}'')g(\mathbf{r}'', \mathbf{r}') = \delta(\mathbf{r} - \mathbf{r}')$. If working in the DFT context, this can be rewritten as

$$G(\mathbf{r}, \mathbf{r}', i\omega) = [(i\omega + \mu) \mathbf{1} - h_{\text{KS}}(\mathbf{r}) - \Delta\Sigma(\mathbf{r}, \mathbf{r}', i\omega)]_{\mathbf{r}, \mathbf{r}'}^{-1} \quad (\text{J.17})$$

where $\Delta\Sigma(\mathbf{r}, \mathbf{r}', i\omega)$ encodes self-energy effects beyond DFT.

J.2.1 DMFT treatment of a correlated subset of orbitals, \mathcal{C}

The idea of LDA+DMFT consists in correcting DFT for only a subset of “correlated orbitals” \mathcal{C} for which the self-energy is computed in a self-consistent DMFT cycle. More specifically, if one identifies a set of correlated orbitals $|\chi_{\mathbf{R}m}\rangle$ and defines a projector on \mathcal{C} : $P_{\mathbf{R}} \equiv \sum_m |\chi_{\mathbf{R}m}\rangle \langle \chi_{\mathbf{R}m}|$, the Green function operator of eq. (J.17) can be projected onto the correlated subset by the following operation:

$$\underline{\underline{G}}_{\mathbf{R}\mathbf{R}'}(i\omega) = P_{\mathbf{R}} G(\mathbf{r}, \mathbf{r}', i\omega) P_{\mathbf{R}'} \quad (\text{J.18})$$

Operators with double underbar act in the correlated subspace \mathcal{C} (indices m, m'). The local component is, as always, $\underline{\underline{G}}_{\text{loc}}(i\omega) = \underline{\underline{G}}_{\mathbf{R}\mathbf{R}}(i\omega)$. Given a local self-energy $\underline{\underline{\Sigma}}^{\text{imp}}(i\omega)$, one can then compute the Weiss field $\underline{\underline{G}}(i\omega)$, and solve the impurity model for a new $\underline{\underline{\Sigma}}^{\text{imp}}(i\omega)$ and approximate

$$\underline{\underline{\Sigma}}_{\mathbf{R}\mathbf{R}'}(i\omega) \approx \underline{\underline{\Sigma}}^{\text{imp}}(i\omega) \delta_{\mathbf{R}\mathbf{R}'} \quad (\text{J.19})$$

In the following, I keep the generic form $\underline{\Sigma}_{\underline{\mathbf{R}\mathbf{R}'}}(i\omega)$ for later purposes. One then removes contributions to $\underline{\Sigma}$ that have already been taken into account in DFT, gathered in a double-counting term $\underline{\Sigma}_{\text{dc}}$:

$$\Delta\underline{\Sigma}_{\underline{\mathbf{R}\mathbf{R}'}}(i\omega) = \underline{\Sigma}_{\underline{\mathbf{R}\mathbf{R}'}}(i\omega) - \underline{\Sigma}_{\text{dc}}$$

Evaluating the double-counting term is subject to intense debates because the self-energy contributions coming from DFT are difficult to cast in a diagrammatic form. For a discussion of this issue, I refer the reader to *e.g.* section 3.3 of van Roekeghem (2014). To compute the new Green's function $G(\mathbf{r}, \mathbf{r}', i\omega)$, one then promotes $\Delta\underline{\Sigma}_{\underline{\mathbf{R}\mathbf{R}'}}(i\omega)$ to the full Hilbert space \mathcal{H} by “upfolding” it in the following way:

$$\Delta\Sigma(\mathbf{r}, \mathbf{r}', i\omega) = \sum_{mm', \mathbf{R}\mathbf{R}'} \Delta\Sigma_{mm', \mathbf{R}\mathbf{R}'}(\omega) |\chi_{\mathbf{R}m}(\mathbf{r})\rangle \langle \chi_{\mathbf{R}'m'}(\mathbf{r}')| \quad (\text{J.20})$$

J.2.2 Specifying the basis set

The equations of the previous section are written independently of the basis set used at the DFT level, *i.e.* for solving Eq. (J.11). One now writes Eqs (J.18) and (J.20) explicitly in terms of the two basis sets, namely $\{|B_{\mathbf{k}\alpha}\rangle\}$ and $\{|\chi_{\mathbf{R}m}\rangle\}$:

$$\begin{aligned} G_{mm', \mathbf{R}\mathbf{R}'}(i\omega) &= \sum_{\mathbf{k}\alpha\alpha'} \langle \chi_{\mathbf{R}m} | B_{\mathbf{k}\alpha} \rangle \langle B_{\mathbf{k}\alpha'} | \chi_{\mathbf{R}'m'} \rangle G_{\alpha\alpha'}(\mathbf{k}, i\omega) \\ \Delta\Sigma_{\alpha\alpha'}(\mathbf{k}, i\omega) &= \sum_{mm', \mathbf{R}\mathbf{R}'} \langle B_{\mathbf{k}\alpha} | \chi_{\mathbf{R}m} \rangle \langle \chi_{\mathbf{R}'m'} | B_{\mathbf{k}\alpha'} \rangle \Delta\Sigma_{mm', \mathbf{R}\mathbf{R}'}(i\omega) \end{aligned}$$

Fourier transforming $\mathbf{R} \leftrightarrow \mathbf{k}$, one obtains the more conventional formulae:

$$G_{mm'}(\mathbf{k}, i\omega) = \sum_{\alpha\alpha'} \langle \chi_{\mathbf{k}m} | B_{\mathbf{k}\alpha} \rangle \langle B_{\mathbf{k}\alpha'} | \chi_{\mathbf{k}m'} \rangle G_{\alpha\alpha'}(\mathbf{k}, i\omega) \quad (\text{J.21})$$

$$\Delta\Sigma_{\alpha\alpha'}(\mathbf{k}, i\omega) = \sum_{mm'} \langle B_{\mathbf{k}\alpha} | \chi_{\mathbf{k}m} \rangle \langle \chi_{\mathbf{k}m'} | B_{\mathbf{k}\alpha'} \rangle \Delta\Sigma_{mm'}(\mathbf{k}, i\omega) \quad (\text{J.22})$$

If $\Delta\Sigma_{mm'}$ is approximated by the impurity self-energy (Eq. (J.19)), the \mathbf{k} -dependence of the upfolded self-energy stems only from the \mathbf{k} -dependence of the matrix elements $\langle B_{\mathbf{k}\alpha} | \chi_{\mathbf{k}m} \rangle$. The Green's function reads:

$$G_{\alpha\alpha'}(\mathbf{k}, i\omega) = \left[(i\omega + \mu) \delta_{\alpha\alpha'} - \varepsilon_{\alpha\alpha'}^{\text{KS}}(\mathbf{k}) - \Delta\Sigma_{\alpha\alpha'}(\mathbf{k}, i\omega) \right]_{\alpha\alpha'}^{-1} \quad (\text{J.23})$$

I recall that m, m' are indices referring to the correlated subspace \mathcal{C} , while α, α' refer to the full Hilbert space \mathcal{H} . The DMFT equation thus involves, in Eq. (J.23), the costly inversion of a large matrix for each \mathbf{k} and $i\omega$. A drastic simplification appears when carefully choosing the basis set $B_{\mathbf{k}\alpha}$ and the correlated orbitals, $\chi_{\mathbf{R}m}$.

J.2.3 Using Wannier functions

In the following, I show that by using suitably defined Wannier functions $w_{\mathbf{R}L}$ to specify the basis set $B_{\mathbf{k}\alpha}$ as well as the correlated orbitals $\chi_{\mathbf{R}m}$, one can reduce the computational cost of the matrix inversion. Let us to this effect select the states within an energy window around the Fermi energy containing at least the correlated bands \mathcal{C} ; this defines a subspace \mathcal{W} of the full Hilbert space \mathcal{H} such that

$$\mathcal{C} \subseteq \mathcal{W} \subseteq \mathcal{H}$$

This is illustrated in Fig.12.1. Given the Bloch or Kohn-Sham eigenfunctions $\psi_{\mathbf{k}n}(\mathbf{r})$, let us define the following Wannier functions:

$$w_{\mathbf{R}L}(\mathbf{r}) = \sum_{\mathbf{k}} e^{-i\mathbf{k}\cdot\mathbf{R}} \sum_{n \in \mathcal{W}} U_{Ln}(\mathbf{k}) \psi_{\mathbf{k}n}(\mathbf{r}) \quad (\text{J.24})$$

J.3.1 Screening in a solid: heuristic derivation of RPA and simple screening models

In a solid, the bare Coulomb interactions between electrons are screened: to compute the effective repulsion felt by two electrons, one must take into account the combined effect of the Coulomb interaction and of the electric field induced by charges. Before giving a formal definition of the screened interaction – which will be denoted as W – I give here a simple back-of-the-envelope estimate. Suppose we apply a probe field described by $H_{\text{probe}} = V_0(\mathbf{r})e^{i\omega t}(-en(\mathbf{r}))$, the Kubo formula (Eq. (I.8)) gives the response of the charge $\rho(\mathbf{r}) = -e\langle n(\mathbf{r}) \rangle$:

$$\delta\rho_1(\mathbf{q}, \omega) = e^2 P_0(\mathbf{q}, \omega) V_0(\mathbf{q}) \quad (\text{J.27})$$

with $P_0(\mathbf{r}, \mathbf{r}', \tau) \equiv -\langle n(\mathbf{r}\tau)n(\mathbf{r}'0) \rangle_0$. This induced charge fluctuation leads to an induced potential via Poisson's equation ($\frac{d^2V}{dx^2} = -\frac{\rho}{\epsilon_0}$) written in Fourier space: $V_1 = \frac{\rho_1}{\epsilon_0 q^2}$, and so forth. Summing up all contributions, we obtain for the total charge:

$$\begin{aligned} \rho_{\text{tot}} &= \rho_0 + e^2 P_0(\mathbf{q}, \omega) V_0 + e^2 P_0(\mathbf{q}, \omega) V_1 + \dots \\ &= \rho_0 + e^2 P_0(\mathbf{q}, \omega) \left(\frac{1}{\epsilon_0 q^2} \right) \rho_0 + e^2 P_0(\mathbf{q}, \omega) \left(\frac{1}{\epsilon_0 q^2} \right) e^2 P_0(\mathbf{q}, \omega) \left(\frac{1}{\epsilon_0 q^2} \right) \rho_0 + \dots \\ &= \frac{\rho_0}{1 - v_{\text{Coul}}(\mathbf{q}) P_0(\mathbf{q}, \omega)} \end{aligned}$$

with $v_{\text{Coul}}(\mathbf{q}) \equiv \frac{e^2}{\epsilon_0 q^2}$. Finally, the total effective electrostatic potential is: $V_{\text{tot}} = \frac{\rho_{\text{tot}}}{\epsilon q^2} = \frac{V_0}{1 - v_{\text{Coul}}(\mathbf{q}) P_0(\mathbf{q}, \omega)}$. We see that the initial potential is *screened* by a term called the dielectric function $\epsilon(\mathbf{q})$, here written in the ‘‘RPA’’ approximation:

$$\epsilon_{\text{RPA}}(\mathbf{q}, \omega) \equiv 1 - v_{\text{Coul}}(\mathbf{q}) P_0(\mathbf{q}, \omega) \quad (\text{J.28})$$

Likewise, the Coulomb potential is screened:

$$W = \frac{v_{\text{Coul}}(\mathbf{q})}{\epsilon(\mathbf{q}, \omega)} \quad (\text{J.29})$$

Starting from this general equation, several approximations on the dielectric function $\epsilon(\mathbf{q}, \omega)$ can be devised:

- the *Thomas-Fermi approximation* consists in approximating the charge response (Eq. (J.27)) by assuming a slowly-varying $V_0(\mathbf{r})$, so that it locally displaces the energy levels $\epsilon(\mathbf{k}) \rightarrow \epsilon(\mathbf{k}) - eV_0(\mathbf{r})$, i.e. $\delta\rho(\mathbf{r}) \approx -e \sum_{\mathbf{k}} \{n_{\text{F}}(\epsilon(\mathbf{k}) - eV_0(\mathbf{r})) - \sum_{\mathbf{k}} n_{\text{F}}(\epsilon(\mathbf{k}))\} = e^2 V_0(\mathbf{r}) \sum_{\mathbf{k}} \left. \frac{\partial n_{\text{F}}}{\partial \epsilon} \right|_{\epsilon=\epsilon_{\mathbf{k}}} = e^2 V_0(\mathbf{r}) \int d\epsilon N(\epsilon) \frac{\partial n_{\text{F}}}{\partial \epsilon} \equiv e^2 V_0(\mathbf{r}) \frac{\partial n_0}{\partial \epsilon}$, so that

$$\epsilon_{\text{TF}}(\mathbf{q}, \omega) = 1 - v_{\text{Coul}}(\mathbf{q}) \frac{\partial n_0}{\partial \epsilon}$$

At low temperature, $\epsilon_{\text{TF}}(\mathbf{q}, \omega) = 1 + v_{\text{Coul}}(\mathbf{q}) N(\epsilon_{\text{F}}) = 1 + \frac{e^2}{\epsilon_0 q^2} N(\epsilon_{\text{F}}) \equiv 1 + \frac{k_{\text{TF}}^2}{q^2}$, so that $W_{\text{TF}}(\mathbf{q}) = e^2/\epsilon_0 / (q^2 + k_{\text{TF}}^2)$, leading to the a short-range (Yukawa) screened potential:

$$W_{\text{TF}}(\mathbf{r}) \propto \frac{1}{|\mathbf{r}|} e^{-|\mathbf{r}|/\xi_{\text{TF}}}, \quad \xi_{\text{TF}} \propto 1/k_{\text{TF}}$$

- the *Lindhard approximation* consists in approximating $\epsilon(\mathbf{q}, \omega)$ by $\epsilon_{\text{RPA}}(\mathbf{q}, \omega)$ (Eq.(J.28)), i.e. by taking:

$$P_0(\mathbf{r}, \mathbf{r}', \tau) = 2G_0(\mathbf{r}, \mathbf{r}', t)G_0(\mathbf{r}', \mathbf{r}, -t) \quad (\text{J.30})$$

where G_0 is the non-interacting Green's function or, in the DFT context, $G_0(\mathbf{r}, \mathbf{r}', i\omega) = [i\omega + \mu - \hat{h}_{\text{KS}}(\mathbf{r})]_{\mathbf{r}, \mathbf{r}'}^{-1}$.

J.3.2 More formally: introducing a bosonic Hubbard-Stratonovich field

The partition function associated with H_{ES} (Eq. (J.1)) is $Z = \int \mathcal{D} [\bar{\psi}\psi] e^{-S[\bar{\psi}\psi]}$, with

$$S[\bar{\psi}\psi] = - \int_0^\beta d\tau \int d\mathbf{r} \bar{\psi}(\mathbf{r}\tau) G_0^{-1}(\mathbf{r}, \tau) \psi(\mathbf{r}\tau) + \frac{1}{2} \int_0^\beta d\tau \int \int d\mathbf{r} d\mathbf{r}' \bar{\psi}(\mathbf{r}\tau) \psi(\mathbf{r}\tau) v_{\text{Coul}}(\mathbf{r} - \mathbf{r}') \bar{\psi}(\mathbf{r}'\tau) \psi(\mathbf{r}'\tau)$$

The interaction term can be decoupled by a Hubbard-Stratonovich transformation (we do not write integration symbols explicitly here): $e^{-\frac{1}{2} \bar{\psi}(\mathbf{r}\tau) \psi(\mathbf{r}\tau) v_{\text{Coul}}(\mathbf{r} - \mathbf{r}') \bar{\psi}(\mathbf{r}'\tau) \psi(\mathbf{r}'\tau)} = \int \mathcal{D} [\phi] e^{\frac{1}{2} \phi(\mathbf{r}\tau) [v_{\text{Coul}}^{-1}](\mathbf{r} - \mathbf{r}') \phi(\mathbf{r}'\tau) + \lambda \bar{\psi}(\mathbf{r}\tau) \psi(\mathbf{r}\tau) \phi(\mathbf{r}\tau)}$, with $\lambda = 1$. In this context, we define the screened interaction to be the correlator of this new field:

$$W(\mathbf{r}, \mathbf{r}', \tau) \equiv -\langle \phi(\mathbf{r}\tau) \phi(\mathbf{r}'0) \rangle \quad (\text{J.31})$$

In the absence of the fermionic term, one can check that $W_0(\mathbf{r}, \mathbf{r}', \tau) = v_{\text{Coul}}(\mathbf{r} - \mathbf{r}')$. We define P as the bosonic self-energy, $P(\mathbf{r}, \mathbf{r}', \omega) \equiv [v_{\text{Coul}}^{-1}]_{\mathbf{r}, \mathbf{r}'} - [W^{-1}]_{\mathbf{r}, \mathbf{r}', \omega}$, so that after Fourier transformation, we have the familiar form (see Eq. (J.29))

$$W(\mathbf{r}, \mathbf{r}', \omega) = \int_{\bar{\mathbf{r}}} v_{\text{Coul}}(\mathbf{r}, \bar{\mathbf{r}}, \omega) \left\{ 1 - \int_{\mathbf{r}''} v_{\text{Coul}}(\mathbf{r}, \mathbf{r}'') P(\mathbf{r}'', \mathbf{r}', \omega) \right\}_{\bar{\mathbf{r}}, \mathbf{r}'}^{-1} \quad (\text{J.32})$$

With this construction, one sees that the random-phase approximation, Eq. (J.30), amounts to the zeroth order approximation of P .

J.3.3 Partial screening: Constrained RPA

Screening in a solid is caused by polarization effects, as shown by Eq. (J.32). We have already encountered the RPA polarization in the context of the single-band Fröhlich and Hubbard Hamiltonians, see paragraph I.6.1.1. There, $P_0(\mathbf{q}, i\omega)$ (or χ_0) was shown to consist in (intra-band) transitions between occupied and unoccupied states, with large contributions from momenta located on parallel portions of the Fermi surface. In other words, the screening processes captured at the RPA level for a single band are the creation of particle-hole pairs on the Fermi surface. Similarly, in a multiband context, RPA consists in approximating screening by all intra-band and inter-band particle-hole pair creation processes. In the same way as a correlated subspace \mathcal{C} was introduced to deal with correlations beyond the DFT level, one can also distinguish between particle-hole pair processes coming from a low-energy “target” window (e.g. the \mathcal{W} defined in Fig. 12.1) – they will contribute to a partial polarization P_{target} , and the rest (contributing to $P_{\text{rest}} \equiv P_0 - P_{\text{target}}$). If the bare Coulomb interaction is screened only by P_{rest} , the corresponding partially screened interaction merely amounts to the effective interaction in the target subspace:

$$W_{\text{rest}}(\mathbf{r}, \mathbf{r}', \omega) \equiv \int_{\bar{\mathbf{r}}} v_{\text{Coul}}(\mathbf{r}, \bar{\mathbf{r}}, \omega) \left\{ 1 - \int_{\mathbf{r}''} v_{\text{Coul}}(\mathbf{r}, \mathbf{r}'') P_{\text{rest}}(\mathbf{r}'', \mathbf{r}', \omega) \right\}_{\bar{\mathbf{r}}, \mathbf{r}'}^{-1} \quad (\text{J.33})$$

The screening coming from high-energy pair-hole creation processes are all taken into account into P_{rest} . In this sense, this way of computing the partially screened interaction, dubbed constrained RPA (Aryasetiawan *et al.* (2004)), is akin to a Wilson renormalization group downfolding procedure where the integration of high-energy degrees of freedom renormalizes the bare interaction parameters (v_{Coul}) into screened interaction parameters W_{rest} . This is summarized in Fig.4.3.

Importantly, the resulting interaction $W_{\text{rest}}(\mathbf{r}, \mathbf{r}', \omega)$ is

1. **frequency dependent**, *i.e.* it includes retardation effects coming from high-energy modes;
2. in general, **shorter-ranged** than v_{Coul} , see the discussion on the Thomas-Fermi approximation (subsection J.3.1).

While the second point is an *a posteriori* justification for restraining the description of correlations in the correlated subspace to *local* interactions (as done in the Hubbard model), the first one points to an intrinsic limitation of the *static* Hubbard model. This indeed indicates that in a generic case, Hubbard's U should be *dynamical*.

Importantly, cRPA includes only particle-hole bubble diagrams to screen the bare Coulomb interaction. Several recent works point to the importance of other classes of diagram (e.g. particle-particle diagrams) for the determination of the low-energy effective interactions (Honerkamp (2012); Shinaoka *et al.* (2014); Kinza and Honerkamp (2015)). These additional diagrams can be added in a functional renormalization group framework, for instance.

J.3.4 How to compute U (and V) in practice

The above formulation of cRPA does not make any reference to a basis set. In practice, however, the DMFT or LDA+DMFT equations are solved in the low-energy subspace \mathcal{C} with a localized basis $\{|w_{\mathbf{k}m}\rangle\}$ (see e.g. Eq. (J.26)). The connection of this basis set to the above discussion is made by expanding the field operators of the interaction term:

$$S_{\text{int}}^{\mathcal{C}} \equiv \frac{1}{2} \iint_0^\beta d\tau d\tau' \iiint_{\mathcal{V}} d\mathbf{r} \iiint_{\mathcal{V}} d\mathbf{r}' \bar{\psi}(\mathbf{r}\tau) \bar{\psi}(\mathbf{r}'\tau') W_{\text{rest}}(\mathbf{r}, \mathbf{r}', \tau - \tau') \psi(\mathbf{r}'\tau') \psi(\mathbf{r}\tau)$$

on the localized basis: $\psi(\mathbf{r}\tau) = \sum_{\mathbf{R}m} w_{\mathbf{R}m}(\mathbf{r}) c_{\mathbf{R}m}(\tau)$, yielding: $S_{\text{int}}^{\mathcal{C}} = \frac{1}{2} \iint_0^\beta d\tau d\tau' \sum_{m_1 m_2 m_3 m_4} U_{\mathbf{R}_1 \mathbf{R}_2 \mathbf{R}_3 \mathbf{R}_4}^{m_1 m_2 m_3 m_4} \bar{c}_{\mathbf{R}_1 m_1} \bar{c}_{\mathbf{R}_2 m_2} c_{\mathbf{R}_3 m_3} c_{\mathbf{R}_4 m_4}$, with

$$U_{\mathbf{R}_1 \mathbf{R}_2 \mathbf{R}_3 \mathbf{R}_4}^{m_1 m_2 m_3 m_4}(\tau - \tau') \equiv \langle w_{\mathbf{R}_1 m_1} w_{\mathbf{R}_2 m_2} | W_{\text{rest}}(\mathbf{r}, \mathbf{r}', \tau - \tau') | w_{\mathbf{R}_3 m_3} w_{\mathbf{R}_4 m_4} \rangle \quad (\text{J.34})$$

Using symmetries, these general matrix elements can be parametrized, in the case of a local interaction ($\mathbf{R}_1 = \mathbf{R}_2 = \mathbf{R}_3 = \mathbf{R}_4$) by a small number of *Slater integrals* F^k (3 for a d -shell, 4 for an f -shell) (see e.g. Vaugier *et al.* (2012)).

The approximation leading to the single-band, extended Hubbard model is, in this language:

$$U_{\mathbf{R}_1 \mathbf{R}_2 \mathbf{R}_3 \mathbf{R}_4}(\tau - \tau') \approx \left(U \delta_{\mathbf{R}_1 - \mathbf{R}_2} \delta_{\mathbf{R}_2 - \mathbf{R}_3} \delta_{\mathbf{R}_3 - \mathbf{R}_4} + V \delta_{\mathbf{R}_1 - \mathbf{R}_4} \delta_{\mathbf{R}_2 - \mathbf{R}_3} \delta_{\langle \mathbf{R}_1 \mathbf{R}_2 \rangle} \right) \delta_{\tau - \tau'}$$

where $\delta_{\langle \mathbf{R} \mathbf{R}' \rangle}$ vanishes except if \mathbf{R} and \mathbf{R}' are nearest neighbors.

Part IX

Appendix: details of some derivations

In this part, the reader will find details of some derivations mentioned in the main text.

Appendix to chapter 6

Let f be a function, $[a, b]$ a segment in \mathbb{R} and R_i a set of discrete equally spaced points with spacing δR . Then:

$$\begin{aligned}
 \Delta &= \int_a^b f(r)dr - \sum_i f(R_i)\delta R \\
 &= \sum_{i=1}^N \int_{R_i}^{R_{i+1}} [f(r) - f(R_i)] dr \\
 &\approx \sum_{i=1}^N \int_{R_i}^{R_{i+1}} (r - R_i) f'(R_i) dr \\
 &= \sum_{i=1}^N \frac{(R_{i+1} - R_i)^2}{2} f'(R_i)
 \end{aligned}$$

In going from the second to the third line, we have performed a Taylor expansion. Using the triangle equality, we obtain

$$\begin{aligned}
 |\Delta| &\leq \sum_{i=1}^N \frac{(\delta R)^2}{2} \max_r |f'(r)| \\
 &= \frac{(a - b)\delta R}{2} \max_r |f'(r)|
 \end{aligned} \tag{K.1}$$

Let us now quantify the error made in Eq. (6.2) for the one-dimensional case by defining

$$\Delta = \int_{-Na}^{Na} dr \frac{\text{erf}(r/\eta)}{r} e^{iqr} - \sum_{R \in BL} a \frac{\text{erf}(R/\eta)}{R} e^{iqR}$$

This problem is the same as finding the error $\Delta = \int_a^b f(r)dr - \sum_i f(R_i)\delta R$ with $f(r) = \frac{\text{erf}(r/\eta)}{r} e^{iqr}$. We apply Eq. (K.1) with $a - b = 2Na$, $\delta R = a$, and

$$\begin{aligned}
 \max \left| \frac{df}{dr} \right| &= \max_r \left[\left| \left(\frac{\text{erf}(r/\eta)}{r} \right)' e^{iqr} + \frac{\text{erf}(r/\eta)}{r} iq \cdot e^{iqr} \right| \right] \\
 &= \max \left[\max_r \left\{ \left(\frac{\text{erf}(r/\eta)}{r} \right)' \right\}; \max_r \left\{ \frac{\text{erf}(r/\eta)}{r} q \right\} \right] \\
 &= \max \left[\frac{0.42}{\eta^2}; \frac{2}{\sqrt{\pi}} \frac{q}{\eta} \right]
 \end{aligned} \tag{K.2}$$

Now, considering that the Fourier transform of f , expressed by \tilde{v}^{cont} , is short-ranged of range $1/\eta$, we need only look at $q \lesssim \frac{1}{\eta}$. Thus, $\max \left| \frac{df}{dr} \right| \sim \frac{1}{\eta^2} \left(\frac{2}{\sqrt{\pi}} \approx 1.12 \right)$ and the error $|\Delta|$ is bounded:

$$|\Delta| < \frac{2Na \cdot a}{2} \cdot \frac{1}{\eta^2}$$

This error is vanishing if $\frac{Na^2}{\eta^2} \ll 1$, which proves (6.3).



Appendix to chapter 8

L.1 Non-interacting free energy

The non-interacting free energy in the presence of sources reads:

$$\begin{aligned}
 \Omega[h, B, F, \lambda = 0] &= -\log \int \mathcal{D}[\bar{c}, c, \phi] e^{-S_{\text{cb}} - \bar{c}_u F_{uv} c_v + h_\alpha \phi_\alpha - \frac{1}{2} \phi_\alpha B_{\alpha\beta} \phi_\beta} \\
 &= -\log \left\{ \text{Det}(-G_0^{-1} + F) \text{Det}(-U^{-1} + B)^{-1/2} \right\} \\
 &\quad - \frac{1}{2} \frac{h^2}{-U^{-1} + B} \\
 &= -\text{Tr} \log(G_0^{-1} - F) + \frac{1}{2} \text{Tr} \log(U^{-1} - B) \\
 &\quad + \frac{1}{2} \frac{h^2}{U^{-1} - B}
 \end{aligned}$$

Hence, applying Eqs (8.17a-8.17c-8.17b) in the case $\lambda = 0$ lead to

$$\begin{aligned}
 \varphi &= -\frac{h}{U^{-1} - B} \\
 W^{\text{nc}} &= (U^{-1} - B)^{-1} - \frac{h^2}{(U^{-1} - B)^2} \\
 G &= (G_0^{-1} - F)^{-1}
 \end{aligned}$$

yielding the following inversion relations:

$$\begin{aligned}
 h &= -\varphi(U^{-1} - B) \\
 F &= G_0^{-1} - G^{-1} \\
 B &= U^{-1} - W^{-1}
 \end{aligned}$$

and the final expression:

$$\begin{aligned}
 \Omega[h, B, F, \lambda = 0] &= -\text{Tr} \log[G^{-1}] \\
 &\quad + \frac{1}{2} \text{Tr} \log[W^{-1}] + \frac{1}{2} W^{-1} \varphi^2
 \end{aligned} \tag{L.1}$$

L.2 Simplifications in the homogeneous phase

L.2.1 Simplification of Σ and P in the homogeneous phase

Under the assumptions of subsection 8.3.2.4, Eqs (8.36a-8.36b) can be simplified, namely

$$\begin{aligned}
\Sigma_{uv} &= -(\sigma_{\sigma\sigma_1}^I \delta_{ik} \delta_{km}) (G_{kl} \delta_{\sigma_1\sigma_2}) W_{mn}^{\eta(I)} \Lambda_{ljn}^{\eta(I)} \sigma_{\sigma_2\sigma'}^I \\
&\quad + (\sigma_{\sigma\sigma'}^I \delta_{ij} \delta_{jm}) \varphi_{m\eta(I)} \\
&= -(\sigma_{\sigma\sigma_1}^I \sigma_{\sigma_1\sigma'}^I) G_{il} W_{in}^{\eta(I)} \Lambda_{ljn}^{\eta(I)} + \sigma_{\sigma\sigma'}^I \varphi_{j\eta(I)} \delta_{ij} \\
&= -(\delta_{\sigma\sigma_1} \delta_{\sigma_1\sigma'}) G_{il} W_{in}^{\text{ch}} \Lambda_{ljn}^{\text{ch}} + \delta_{\sigma\sigma'} \varphi_{j,\text{ch}} \delta_{ij} \\
&\quad - (2\delta_{\sigma\sigma'} \delta_{\sigma_1\sigma_1} - \delta_{\sigma\sigma_1} \delta_{\sigma_1\sigma'}) G_{il} W_{in}^{\text{sp}} \Lambda_{ljn}^{\text{sp}} \\
&\quad + \sigma_{\sigma\sigma'}^I \varphi_{j,\text{sp}} \delta_{ij} \\
&= \Sigma_{ij} \delta_{\sigma\sigma'}
\end{aligned}$$

which yields Eq. (8.38a). Similarly:

$$\begin{aligned}
P_{mn}^{IJ} &= \sigma_{\sigma\sigma_1}^I \delta_{ik} \delta_{km} G_{kl} \delta_{\sigma_1\sigma_2} G_{ji} \delta_{\sigma'\sigma} \sigma_{\sigma_2\sigma'}^I \Lambda_{ljn}^{\eta(I)} \\
&= \text{tr} \left[(\sigma^I)^2 \right] G_{ml} G_{jm} \Lambda_{ljn}^{\eta(I)} \delta_{IJ} \\
&= P_{mn}^{\eta} \delta_{IJ}
\end{aligned}$$

which yields Eq. (8.38b).

L.2.2 Decomposition of Σ and P

Starting from (8.60a), one can rewrite:

$$\begin{aligned}
\Sigma(\mathbf{k}, i\omega) &= -\sum_{\eta} m_{\eta} \sum_{\mathbf{q}, i\Omega} \left(\tilde{G}(\mathbf{k} + \mathbf{q}, i\omega + i\Omega) + G_{\text{loc}}(i\omega) \right) \left(\tilde{W}^{\eta}(\mathbf{q}, i\Omega) + W_{\text{loc}}^{\eta}(i\Omega) \right) \Lambda_{\text{imp}}^{\eta}(i\omega, i\Omega) \\
&= -\sum_{\eta} m_{\eta} \sum_{\mathbf{q}, i\Omega} \tilde{G}(\mathbf{k} + \mathbf{q}, i\omega + i\Omega) \tilde{W}^{\eta}(\mathbf{q}, i\Omega) \Lambda_{\text{imp}}^{\eta}(i\omega, i\Omega) - \sum_{\eta} m_{\eta} \sum_{i\Omega} G_{\text{loc}}(i\omega + i\Omega) W_{\text{loc}}^{\eta}(i\Omega) \Lambda_{\text{imp}}^{\eta}(i\omega, i\Omega) \\
&= -\sum_{\eta} m_{\eta} \sum_{\mathbf{q}, i\Omega} \tilde{G}(\mathbf{k} + \mathbf{q}, i\omega + i\Omega) \tilde{W}^{\eta}(\mathbf{q}, i\Omega) \Lambda_{\text{imp}}^{\eta}(i\omega, i\Omega) + \Sigma_{\text{imp}}(i\omega)
\end{aligned}$$

This yields (8.63a). An analogous calculation yields (8.63b).

L.3 Spin rotation invariance: properties

All the following identities are equivalent:

$$\begin{aligned}
\langle n^I \phi^J \rangle &\propto \delta_{IJ} \\
\sigma_{wl}^I \sigma_{uv}^J \langle \bar{c}^u c^v \phi^J \rangle &\propto \sigma_{wl}^I \delta_{IJ} \\
(2\delta_{wv} \delta_{lu} - \delta_{wl} \delta_{uv}) \langle \bar{c}^u c^v \phi^J \rangle &\propto \sigma_{wl}^J \\
\left(2\langle \bar{c}^l c^w \phi^J \rangle - \langle \bar{c}^v c^v \phi^J \rangle \delta_{wl} \right) &\propto \sigma_{wl}^J \\
\langle \bar{c}^l c^w \phi^J \rangle &\propto \sigma_{wl}^J
\end{aligned}$$

We have used the fact that under rotation invariance, $\langle \bar{c}^v c^v \phi^x \rangle = \langle n\phi^x \rangle = 0 = \langle n\phi^y \rangle = \langle n\phi^z \rangle$.

Appendix to chapter 11

In this appendix, I present details of calculations for the CTQMC solver presented in chapter 11.

M.1 Dynamical trace factor in CTQMC

Let us perform the integration of

$$f(\tau) \equiv \int_{\tau_{k_j}}^{\tau'_{k_j}} d\tau' \mathcal{D}_{ij}(\tau - \tau') = - \int_{\tau - \tau_{k_j}}^{\tau - \tau'_{k_j}} d\bar{\tau} \mathcal{D}_{ij}(\bar{\tau}) \quad (\text{M.1})$$

One must now distinguish two cases: if $\tau \in [\tau_{k_j}, \tau'_{k_j}]$, $\mathcal{D}_{ij}(\bar{\tau})$ is discontinuous in the interval $[\tau - \tau_{k_j}, \tau - \tau'_{k_j}]$, forcing one to split the integral:

$$\begin{aligned} f(\tau) &= \int_{\tau - \tau'_{k_j}}^{0^-} d\bar{\tau} \mathcal{D}_{ij}(\bar{\tau}) + \int_{0^+}^{\tau - \tau_{k_j}} d\bar{\tau} \mathcal{D}_{ij}(\bar{\tau}) \\ &= K'_{ij}(0^-) - K'_{ij}(\tau - \tau'_{k_j}) + K'_{ij}(\tau - \tau_{k_j}) - K'_{ij}(0^+) \\ &= -2K'_{ij}(0^+) + K'_{ij}(\tau - \tau_{k_j}) - K'_{ij}(\tau - \tau'_{k_j}) \end{aligned} \quad (\text{M.2})$$

$K(\tau)$ is defined in Eq. (11.21a). Otherwise (if $\tau \notin [\tau_{k_j}, \tau'_{k_j}]$), one can directly integrate and get $f(\tau) = K'_{ij}(\tau - \tau_{k_j}) - K'_{ij}(\tau - \tau'_{k_j})$. Both cases are taken into account by the expression:

$$f(\tau) = -2K'_{ij}(0^+) \left\{ \theta(\tau - \tau_{k_j}) - \theta(\tau - \tau'_{k_j}) \right\} + K'_{ij}(\tau - \tau_{k_j}) - K'_{ij}(\tau - \tau'_{k_j}) \quad (\text{M.3})$$

Then:

$$\begin{aligned} \ln w_{\text{dyn}} &= -\frac{1}{2} \sum_{ij} \sum_{k_i k_j} \int_{\tau_{k_i}}^{\tau'_{k_i}} d\tau \left[-2K'_{ij}(0^+) \left\{ \theta(\tau - \tau_{k_j}) - \theta(\tau - \tau'_{k_j}) \right\} + K'_{ij}(\tau - \tau_{k_j}) - K'_{ij}(\tau - \tau'_{k_j}) \right] \\ &= K'_{ij}(0^+) \sum_{ij} \sum_{k_i k_j} \int_{\tau_{k_i}}^{\tau'_{k_i}} d\tau \left\{ \theta(\tau - \tau_{k_j}) - \theta(\tau - \tau'_{k_j}) \right\} - \frac{1}{2} \sum_{ij} \sum_{k_i k_j} \left[\int_{\tau_{k_i} - \tau_{k_j}}^{\tau'_{k_i} - \tau_{k_j}} K'_{ij}(\bar{\tau}) d\bar{\tau} - \int_{\tau_{k_i} - \tau'_{k_j}}^{\tau'_{k_i} - \tau'_{k_j}} K'_{ij}(\bar{\tau}) d\bar{\tau} \right] \\ &= K'_{ij}(0^+) \sum_{ij} \sum_{k_i k_j} l_{k_i k_j} - \frac{1}{2} \sum_{ij} \sum_{k_i k_j} \left[K_{ij}(\tau'_{k_i} - \tau_{k_j}) - K_{ij}(\tau_{k_i} - \tau_{k_j}) - K_{ij}(\tau'_{k_i} - \tau'_{k_j}) + K_{ij}(\tau_{k_i} - \tau'_{k_j}) \right] \end{aligned}$$

$l_{k_i k_j}$ denotes the overlap of segment k_i with k_j . Finally, one gets:

$$\ln w_{\text{dyn}} = \sum_{ij} K'_{ij}(0^+) O_{ij} - \underbrace{\frac{1}{2} \sum_{ij} \sum_{k_i k_j} [K_{ij}(\tau'_{k_i} - \tau_{k_j}) - K_{ij}(\tau_{k_i} - \tau_{k_j}) - K_{ij}(\tau'_{k_i} - \tau'_{k_j}) + K_{ij}(\tau_{k_i} - \tau'_{k_j})]}_{\equiv A}$$

where O_{ij} is the total overlap of line i with line j . I recall that τ_i (resp. τ'_i) label creation (resp. annihilation) operators. Splitting the sum (

$\sum_{k_i k_j} = 2 \sum_{k_i < k_j} + \sum_{k_i = k_j}$), the second term can be rewritten

$$\begin{aligned} A &= \sum_{ij} \sum_{k_i < k_j} [-K_{ij}(\tau'_{k_i} - \tau_{k_j}) - K_{ij}(\tau_{k_i} - \tau'_{k_j}) + K_{ij}(\tau_{k_i} - \tau_{k_j}) + K_{ij}(\tau'_{k_i} - \tau'_{k_j})] + \sum_i \sum_{k_i} [-K_{ij}(\tau'_{k_i} - \tau_{k_i}) + K_{ij}(0)] \\ &= \sum_{\text{pairs}(\alpha, \beta)} s_\alpha s_\beta K_{i(\alpha)j(\beta)}(\tilde{\tau}_\alpha - \tilde{\tau}_\beta) + N \sum_\alpha K_{\alpha\alpha}(0) \end{aligned}$$

where N is the total number of operators. Thus, A is given by a sum over distinct pairs of creation or annihilation operators (denoted by indices α, β) of $K(\tilde{\tau}_\alpha - \tilde{\tau}_\beta)$ times a factor which is 1 if it is a pair of distinct operators, -1 if it is a pair of identical operators (i.e. $s_\alpha = 1$ for creation operators and -1 for annihilation operators). Noticing that $\sum_{\text{pairs}(\alpha, \beta)} s_\alpha s_\beta = \frac{1}{2} \sum_{\alpha\beta} s_\alpha s_\beta - \sum_\alpha s_\alpha^2 = -N$, A simplifies to

$$A = \sum_{\text{pairs}(\alpha, \beta)} s_\alpha s_\beta [K_{i(\alpha)j(\beta)}(\tilde{\tau}_\alpha - \tilde{\tau}_\beta) - K_{i(\alpha)j(\beta)}(0)] \quad (\text{M.4})$$

Thus:

$$\ln w_{\text{dyn}} = \sum_{\text{pairs}(\alpha, \beta)} s_\alpha s_\beta [K_{i(\alpha)j(\beta)}(\tilde{\tau}_\alpha - \tilde{\tau}_\beta) - K_{i(\alpha)j(\beta)}(0)] + \sum_i l_i K'_{ii}(0) + 2 \sum_{\substack{i,j \\ i \neq j}} K'_{ij}(0^+) O_{ij} \quad (\text{M.5})$$

One thus obtains Eq. (11.22).

M.2 Hamiltonian formulation the impurity model

The action of Eq (11.3) can be obtained from a Hamiltonian formulation describing the coupling of a correlated fermionic level $\varepsilon_{a\sigma}$ (with Hubbard interactions $\frac{1}{2}U_{ij}n_i n_j$) with

- a free fermionic bath described by the operators d_α^\dagger and d_α ; the coupling strength is $V_{\alpha i}$ and the energy levels $\tilde{\varepsilon}_{\alpha\beta}$;
- a free bosonic bath described by the operators $b_{\alpha\xi}^\dagger$ and $b_{\alpha\xi}$ with three components $\xi = x, y, z$; the coupling strength is $g_{\alpha\xi}$;

namely:

$$\begin{aligned} H_{\text{imp}} &= \sum_i \varepsilon_i n_i + \frac{1}{2} \sum_{ij} U_{ij} n_i n_j \\ &+ \sum_{\alpha\beta\sigma} \tilde{\varepsilon}_\alpha d_\alpha^\dagger d_\alpha + \sum_{\alpha,i} V_{\alpha i} \{d_\alpha^\dagger c_i + c_i^\dagger d_\alpha\} \\ &+ \sum_{\alpha\xi} \omega_{\alpha\xi} b_{\alpha\xi}^\dagger b_{\alpha\xi} + \sum_{\alpha\xi} g_{\alpha\xi}^\xi \sum_q (b_{\alpha\xi} + b_{\alpha\xi}^\dagger) \end{aligned} \quad (\text{M.6})$$

Here, $i \equiv (a, \sigma)$, where a is an orbital index. Greek indices denote the bath degrees of freedom.

Let us define the hybridization function $\Delta(i\omega_n)$ and the effective retarded spin-spin interaction $\mathcal{J}_{ab}^{\xi\xi'}(i\nu_n)$:

$$\begin{aligned}\Delta_{ij}(i\omega_n) &\equiv \sum_{\alpha} V_{i\alpha} \frac{1}{i\omega_n - \tilde{\epsilon}_{\alpha}} V_{\alpha j} \\ \mathcal{J}_{ab}^{\xi\xi'}(i\nu_n) &\equiv \sum_{\alpha} g_{a\alpha}^{\xi} \frac{2\omega_{\alpha\xi}}{\nu_n^2 + \omega_{\alpha\xi}^2} g_{\alpha b}^{\xi'}\end{aligned}$$

Integrating out d and ϕ fields yields:

$$\begin{aligned}S_{\text{imp}} &= \iint_0^{\beta} d\tau d\tau' \sum_{ij} \{ \tilde{c}_i(\tau) ((\partial_{\tau} + \epsilon_i) \delta_{ij} \delta_{\tau-\tau'} + \Delta_{ij}(\tau - \tau')) c_j(\tau') \} + \int_0^{\beta} d\tau \frac{1}{2} \sum_{ij} U_{ijn} c_i(\tau) c_j(\tau) \quad (\text{M.7}) \\ &+ \iint_0^{\beta} d\tau d\tau' \frac{1}{2} \sum_{ab} \sum_{\xi\xi'} s_a^{\xi}(\tau) \mathcal{J}_{ab}^{\xi\xi'}(\tau - \tau') s_b^{\xi'}(\tau')\end{aligned}$$

M.3 Computation of $K(\tau)$ from $U(i\nu)$

Let $U(i\nu_n)$ denote the frequency-dependent interaction. In particular, $\lim_{n \rightarrow \infty} U(i\nu_n) = U_{\infty}$. Let us define

$$\mathcal{D}(i\nu_n) \equiv U(i\nu_n) - U_{\infty}$$

The dynamical kernel $K(\tau)$ is partially defined in Eq. (??). To fully define $K(\tau)$, one needs to define two boundary conditions. Inspired by the form of the dynamical contribution to the weight (Eq. (??)), we choose $K(0) = K(\beta) = 0$.

By definition of the Fourier transform,¹

$$\mathcal{D}(\tau) = \frac{\mathcal{D}(i\nu_n = 0)}{\beta} + \frac{2}{\beta} \sum_{n>0} \mathcal{D}(i\nu_n) \cos(\nu_n \tau)$$

The cosine comes from the fact that $\mathcal{D}(i\nu_n)$ is real. Upon a double τ -integration, we get

$$K(\tau) = \frac{\mathcal{D}(i\nu_n = 0)}{\beta} \frac{\tau^2}{2} + \frac{2}{\beta} \sum_{n>0} \mathcal{D}(i\nu_n) \frac{\cos(\nu_n \tau)}{-\nu_n^2} + A\tau + B$$

Using the initial conditions yields $0 = K(0) = \sum_{n>0} \mathcal{D}(i\nu_n) / (-\nu_n^2) + B$, and $0 = K(\beta) = \frac{\mathcal{D}(i\nu_n=0)}{\beta} \frac{\beta^2}{2} + \frac{2}{\beta} \sum_{n>0} \mathcal{D}(i\nu_n) \frac{1}{-\nu_n^2} + A\beta + B = \frac{\mathcal{D}(i\nu_n=0)}{2} \beta + A\beta$, i.e

$$\begin{aligned}A &= -\frac{\mathcal{D}(i\nu_n = 0)}{2} \\ B &= \frac{2}{\beta} \sum_{n>0} \frac{\mathcal{D}(i\nu_n)}{\nu_n^2}\end{aligned}$$

Thus

$$\begin{aligned}K(\tau) &= \frac{\mathcal{D}(i\nu_n = 0)}{2} \tau \left(\frac{\tau}{\beta} - 1 \right) + \frac{2}{\beta} \sum_{n>0} \frac{\mathcal{D}(i\nu_n)}{\nu_n^2} (1 - \cos(\nu_n \tau)) \quad (\text{M.8}) \\ K'(0) &= -\frac{\mathcal{D}(i\nu_n = 0)}{2}\end{aligned}$$

¹ $f(i\omega_n) = \int d\tau e^{i\tau\omega_n} f(\tau)$ and $f(\tau) = \frac{1}{\beta} \sum_{n=-\infty}^{\infty} e^{-i\tau\omega_n} f(i\omega_n)$

and:

$$K'(\tau) = \mathcal{D}(iv_n = 0) \left(\frac{\tau}{\beta} - \frac{1}{2} \right) + \frac{2}{\beta} \sum_{n>0} \mathcal{D}(iv_n) \frac{\sin(v_n \tau)}{v_n}$$

Going back to the original interaction $U(iv_n)$, this reads

$$\begin{aligned} K(\tau) &= \frac{U_0 - U_\infty}{2} \tau \left(\frac{\tau}{\beta} - 1 \right) + \frac{2}{\beta} \sum_{n>0} \frac{U(iv_n) - U_\infty}{v_n^2} (1 - \cos(v_n \tau)) \\ K'(0) &= \frac{U_\infty - U_0}{2} \end{aligned}$$

Using the Fourier transform of $1/(iv_n)^2$,² one finally finds the simplified formulae:

$$K(\tau) = \frac{2}{\beta} \sum_{n>0} \frac{U(iv_n) - U_0}{v_n^2} (1 - \cos(v_n \tau)) \quad (\text{M.9})$$

$$K'(\tau) = (U_0 - U_\infty) \left(\frac{\tau}{\beta} - \frac{1}{2} \right) + \frac{2}{\beta} \sum_{n>0} (U(iv_n) - U_\infty) \frac{\sin(v_n \tau)}{v_n} \quad (\text{M.10})$$

In particular, $K'(0) = \frac{U_\infty - U_0}{2}$. Hence, the renormalized parameters \tilde{U} and $\tilde{\mu}$ are:

$$\begin{aligned} \tilde{U} &= U_\infty - 2K'(0) = U_0 \\ \tilde{\mu} &= \mu + K'(0) = \mu + \frac{U_\infty - U_0}{2} \end{aligned}$$

M.3.1 Holstein case

If $D(i\Omega) = \frac{2g^2\omega_0}{(i\Omega)^2 - \omega_0^2}$ then³

$$K(\tau) = - \left(\frac{g}{\omega_0} \right)^2 \frac{\cosh\left(\left(\frac{\beta}{2} - \tau\right)\omega_0\right) - \cosh\left(\frac{\beta\omega_0}{2}\right)}{\sinh\left(\frac{\beta\omega_0}{2}\right)}$$

M.4 A code example: the insert move

Here, I give a full working example of Monte-Carlo update as implemented in the code. While without the full code, one cannot understand all the details, the general structure can be seen to directly follow the update procedure described in paragraph 11.2.2.1.1.

```
#pragma once
#include "../configuration.hpp"
#include "../qmc_parameters.hpp"
#include <triqs/mc_tools/random_generator.hpp>
namespace triqs { namespace applications { namespace impurity_solvers { namespace ctqmc_seg {
  class move_insert_segment{
  const qmc_parameters * params; configuration * config;
  mc_tools::random_generator &RND; int color;
  public:
  move_insert_segment(const qmc_parameters * params_, configuration * config_, mc_tools::
    random_generator &RND_):params(params_), config(config_),RND(RND_){};
```

2

$$\text{TF} \left[\frac{1}{(iv_n)^2} \right] = -\frac{\tau^2}{2\beta} + \frac{\tau}{2} - \frac{\beta}{12}$$

³Note: $D(i\Omega) < 0$, $D(\tau) < 0$

```

//-----
double attempt(){
  // ----- Selection of the times and color for the segment insertion -----
  //pick up color and first time
  color = RND(params->n_color);
  auto tau_1 = qmc_time_t::random(RND,params->beta,params->beta); //choose tau between 0 and beta
  qmc_time_t lmax, tau_2; bool need_swap;
  // pick up second time:
  if (config->ops_map().op_number(color)==0) { //no operators
    lmax = (params->beta);
    tau_2 = qmc_time_t::random(RND,lmax,params->beta);
    need_swap = !(config->trace.full_lines(color)); //by convention, if empty/full line: tau_1 is
      creation, tau_2 is annihilation
  }
  else {
    auto R = config->ops_map().right_neighbor(tau_1, color); //point at right of tau_1
    assert(config->ops_map().cyclic_left(R)->tau != R->tau);
    lmax = (config->ops_map().cyclic_left(R)->tau - R->tau);
    tau_2 = qmc_time_t::random (RND,lmax,params->beta) + R->tau;
    need_swap = on_same_side(tau_1,tau_2,R->tau) ? !(tau_1 > tau_2) : (tau_1 > tau_2);
  }
  if (need_swap) std::swap(tau_1,tau_2);
  auto sd = segment_desc {tau_1,tau_2, color};
  // ---- compute ratio of trace and det -----
  segment seg; double ln_trace_ratio;
  try { std::tie(ln_trace_ratio,seg) = config->trace.try_insert_segment(sd);}
  catch (insertion_error const & e) { std::cerr << "insert_error_--_move_insert"<< std::endl;
    return 0;}
  double trace_ratio = std::exp(ln_trace_ratio);
  double det_ratio = config->hyb_dets.try_add(seg.l,seg.r);
  int n_ops_after = 2*config->hyb_dets.seg_number(color); //try_insert updates hyb op map size
  // ---- compute proposition ratio -----
  double prop_ratio = config->ops_map().seg_number(color)==1?
    params->beta*params->beta/ 2.0:
    params->beta*lmax / ( 2*n_ops_after ); //compute proposal probability ratio
  double s = (det_ratio > 0.0 ? 1.0 : -1.0 );
  double prod = trace_ratio * det_ratio * prop_ratio;
  return (std::isfinite(prod) ? prod : s);
}
//-----
double accept(){
  config->id++; config->hyb_dets.complete_add();
  double sign_ratio = config->trace.complete_insert_segment();
  return sign_ratio;
}
//-----
void reject(){
  config->id++; config->hyb_dets.reject_add();
  config->trace.reject_insert_segment();
}
};
}}}}

```

Listing M.1: Listing of the move "insert segment"



Appendix to chapter 10

The mathematical definitions of the objects manipulated in this appendix are given in section 10.3.2.

N.1 Simple-minded estimates for $f(\langle X \rangle)$

In the limit $N \rightarrow \infty$, one expects that

$$f(\langle X \rangle) \approx f(\bar{x}) \quad (\text{N.1})$$

In the simple case $f(x) = x$. Eq. (N.1) is easy to prove since, by definition of the samples x_i , $\langle x_i \rangle = \langle X \rangle$, and hence:

$$\langle \bar{x} \rangle = \langle X \rangle$$

so that a good estimate for $\langle X \rangle$ is \bar{x} .

N.1.1 Unbiased estimate $f(\bar{x})$

$f(\bar{x})$ is called an *unbiased estimate* since the expectation value $\langle f(\bar{x}) - f(\langle X \rangle) \rangle$ vanishes for large sample sizes. Indeed,

$$\begin{aligned} \langle f(\bar{x}) - f(\langle X \rangle) \rangle &= \langle f(\bar{x} - \langle X \rangle) - f(\langle X \rangle) \rangle \\ &= \left\langle \frac{1}{2} (\bar{x} - \langle X \rangle)^2 f''(\langle X \rangle) + \dots \right\rangle \\ &= \frac{1}{2} f''(\langle X \rangle) \langle (\bar{x} - \langle X \rangle)^2 \rangle + \dots \\ &= \frac{1}{2} f''(\langle X \rangle) (\langle \bar{x}^2 \rangle - \langle \bar{x} \rangle^2) + \dots \end{aligned}$$

If the variables are independent,

$$\langle \bar{x}^2 \rangle - \langle \bar{x} \rangle^2 = \frac{1}{N^2} \sum_{ij} \langle x_i x_j \rangle - \langle x_i \rangle \langle x_j \rangle = \frac{1}{N^2} \sum_i \langle x_i^2 \rangle - \langle x_i \rangle^2 = \frac{\text{Var}(X)}{N}$$

where $\text{Var}(X) \equiv \langle (X - \langle X \rangle)^2 \rangle$ denotes the intrinsic variance of the random variable X . Finally,

$$\langle f(\bar{x}) - f(\langle X \rangle) \rangle = \frac{1}{2N} f''(\langle X \rangle) \text{Var}(X) + O\left(\frac{1}{N^2}\right) \quad (\text{N.2})$$

The error vanishes for large N . This still holds for correlated samples ($\text{Var}(X)$ is just replaced by $\text{Var}(X)(1 + 2\tau_c)$, see later). We have thus seen that to obtain an estimate for $f(\langle X \rangle)$, one should compute $f(\bar{x})$. Eq. (N.2) is not surprising: this is what one would have guessed without calculation.

N.1.2 Biased estimate $\overline{f(x)}$

Were one to use $\overline{f(x)}$ instead of $f(\bar{x})$, one would make, on average, the following error:

$$\begin{aligned} \langle \overline{f(x)} - f(\langle X \rangle) \rangle &= \frac{1}{N} \sum_i \langle f(x_i) \rangle - \langle f(\langle X \rangle) \rangle \\ &= \langle f(x) - f(\langle X \rangle) \rangle \\ &= \int dx P(x) (f(x) - f(\langle X \rangle)) \\ &= \int dx P(x) \left[(x - \langle X \rangle) f'(\langle X \rangle) + \frac{(x - \langle X \rangle)^2}{2} f''(\langle X \rangle) + \dots \right] \\ &= \frac{1}{2} f''(\langle X \rangle) \text{Var}(X) + \dots \end{aligned}$$

To go from the third to the fourth line, I have used the fact that \bar{x} is a good estimate for $\langle X \rangle$, so that we can make a Taylor expansion of f in powers of $(\bar{x} - \langle X \rangle)$.

This error remains finite in the limit of large N . This is called *bias* and is directly related to the non-linearity of f . This generalizes to the multi-variable case, and holds for independent as well as for correlated samples. The above results do not tell us, however, what the uncertainty on this estimate is. The next subsection will address the issue of assessing this uncertainty.

N.2 Relationship between the error estimate and the intrinsic variance

In the following subsection, I first deal with the simplified case, $f = 1$, namely, I shall find an estimate for

$$\Delta \langle X \rangle^2 \equiv \langle [\bar{x} - \langle X \rangle]^2 \rangle \quad (\text{N.3})$$

One can write

$$\begin{aligned} \Delta \langle X \rangle^2 &= \left\langle \left(\frac{1}{N} \sum_i x_i - \langle X \rangle \right)^2 \right\rangle \\ &= \left\langle \frac{1}{N^2} \sum_{i,j} x_i x_j - 2 \frac{\langle X \rangle}{N} \sum_i x_i + \langle X \rangle^2 \right\rangle \\ &= \frac{1}{N^2} \sum_{i,j} \langle x_i x_j \rangle - \langle X \rangle^2 \\ &= \frac{1}{N^2} \sum_i \langle x_i^2 \rangle - \frac{1}{N} \langle X \rangle^2 + \frac{1}{N^2} \sum_{i,j,i \neq j} \langle x_i x_j \rangle - \left(1 - \frac{1}{N} \right) \langle X \rangle^2 \\ &= \frac{\text{Var}(X)}{N} + \frac{1}{N^2} \left(\sum_{i,j,i \neq j} \langle x_i x_j \rangle - N(N-1) \langle X \rangle^2 \right) \end{aligned} \quad (\text{N.4})$$

N.2.1 Independent samples

If the samples are independent, $\langle x_i x_j \rangle = \langle x_i \rangle \langle x_j \rangle$ for $i \neq j$. Therefore, the second term vanishes in the limit $N \rightarrow \infty$. Therefore, an unbiased estimate for $\Delta \langle X \rangle^2$ is:

$$\Delta \langle X \rangle^2 \underset{\text{indep}}{=} \frac{\text{Var}(X)}{N} \quad (\text{N.5})$$

N.2.2 Correlated samples

If the samples are not independent, one can write

$$\sum_{i,j,i \neq j} \langle x_i x_j \rangle = 2 \sum_{i < j} \langle x_i x_j \rangle = 2 \sum_{i=1}^N \sum_{t=1}^{N-i} \langle x_i x_{i+t} \rangle$$

Noticing that $\sum_{i=1}^N \sum_{t=1}^{N-i} 1 = \frac{N(N-1)}{2}$, one arrives at

$$\frac{1}{N^2} \left(\sum_{i,j,i \neq j} \langle x_i x_j \rangle - N(N-1) \langle X \rangle^2 \right) = \frac{2}{N^2} \sum_{i=1}^N \sum_{t=1}^{N-i} (\langle x_i x_{i+t} \rangle - \langle X \rangle^2)$$

Hence, Eq. (N.4) becomes:

$$\Delta \langle X \rangle^2 = \frac{\text{Var}(X)}{N} \left(1 + \frac{2 \sum_{i=1}^N \sum_{t=1}^{N-i} (\langle x_i x_{i+t} \rangle - \langle X \rangle^2)}{\text{Var}(X)} \right) \quad (\text{N.6})$$

Defining an integrated autocorrelation time

$$\tau_X^{\text{int}} \equiv \frac{\sum_{t=1}^{\infty} (\langle x_i x_{i+t} \rangle - \langle X \rangle^2)}{\text{Var}(X)} = \sum_{t=1}^{\infty} A(t) \quad (\text{N.7})$$

The autocorrelation function $A(t)$ is defined in Eq. 10.12.

Taking the limit $N \rightarrow \infty$ in the second summation of Eq. (N.6), one thus obtains:

$$\Delta \langle X \rangle^2 = \frac{\text{Var}(X)}{N} (1 + 2\tau_X^{\text{int}}) \quad (\text{N.8})$$

Eqs. (N.5) and N.8) give a relation between the error estimate and the intrinsic variance $\text{Var}X$ of the random variable X , which is in general unknown. We shall hereafter derive a relation between the sample mean deviation and the true variance.

N.3 Relationship between empirical and intrinsic variance

The empirical variance is given by

$$\sigma_x^2 \equiv \frac{1}{N} \sum_{i=1}^N (x_i - \bar{x}_i)^2 = \frac{1}{N} \sum_{i=1}^N \left(x_i - \frac{1}{N} \sum_j x_j \right)^2 = \frac{1}{N} \sum_{i=1}^N \left(x_i^2 - \frac{2}{N} \sum_j x_i x_j + \frac{1}{N^2} \sum_{jk} x_j x_k \right)$$

Hence:

$$\begin{aligned} \langle \sigma_x^2 \rangle &= \langle X^2 \rangle + \frac{1}{N^2} \sum_{i=1}^N \left(-2 \left(\langle X^2 \rangle + \sum_{j \neq i} \langle x_i x_j \rangle \right) + \frac{1}{N} \sum_{jk} \langle x_j x_k \rangle \right) \\ &= \left(1 - \frac{2}{N} \right) \langle X^2 \rangle + \frac{1}{N^2} \sum_{i=1}^N \left(-2 \sum_{j \neq i} \langle x_i x_j \rangle + \frac{1}{N} \sum_{jk} \langle x_j x_k \rangle \right) \\ &= \left(1 - \frac{2}{N} \right) \langle X^2 \rangle + \frac{1}{N^2} \sum_{i=1}^N \left(-2 \sum_{j \neq i} \langle x_i x_j \rangle + \frac{1}{N} \left[N \langle X^2 \rangle + \sum_{jk, j \neq k} \langle x_j x_k \rangle \right] \right) \\ &= \left(1 - \frac{1}{N} \right) \langle X^2 \rangle + \frac{1}{N^2} \sum_{i=1}^N \left(-2 \sum_{j \neq i} \langle x_i x_j \rangle + \frac{1}{N} \sum_{jk, j \neq k} \langle x_j x_k \rangle \right) \end{aligned}$$

N.3.1 Independent samples

If the variables are independent,

$$\begin{aligned}\langle \sigma^2 \rangle &= \left(1 - \frac{1}{N}\right) \langle X^2 \rangle + \frac{1}{N^2} \sum_{i=1}^N \left(-2 \sum_{j \neq i} \langle X \rangle^2 + \frac{1}{N} \sum_{jk, j \neq k} \langle X \rangle^2 \right) \\ &= \left(1 - \frac{1}{N}\right) \langle X^2 \rangle + \frac{1}{N^2} N \left(-2(N-1) \langle X \rangle^2 + \frac{N(N-1)}{N} \langle X \rangle^2 \right)\end{aligned}$$

so that

$$\boxed{\langle \sigma^2 \rangle_{\text{indep}} = \frac{N-1}{N} \text{Var}(X)} \quad (\text{N.9})$$

The variance of the samples, in the limit of large sample size, is equal to the intrinsic variance. Thus, for independent variables, one can extract the error estimate from the sample mean deviation via Eq. (??).

The uncertainty on the estimate decreases as the inverse of the sample size. Equation (N.9) only holds

- for independent samples and
- for $f = 1$

N.3.2 Correlated samples

For correlated variables, using (N.8), one finds

$$\boxed{\langle \sigma^2 \rangle_{\text{correl}} = \frac{N-1}{N} \text{Var}(X)(1 + 2\tau_{\text{int}})} \quad (\text{N.10})$$

N.4 Details for paragraph 10.3.4.1.2

We have:

$$\begin{aligned}(N-1) \langle \sigma_{f^J}^2 \rangle &= (N-1) \frac{1}{N} \sum_i \left\langle \left(f_i^J - \bar{f}^J \right)^2 \right\rangle \\ &= \frac{N-1}{N} \sum_i \left\langle \left(\left[\frac{1}{N-1} \sum_{j=1, j \neq i}^N (x_j - \langle X \rangle) f'(\langle X \rangle) + \dots \right] \right. \right. \\ &\quad \left. \left. - \frac{1}{N} \sum_{k=1}^N \left[\frac{1}{N-1} \sum_{j=1, j \neq k}^N (x_j - \langle X \rangle) f'(\langle X \rangle) + \dots \right] \right)^2 \right\rangle \\ &= \frac{f'(\langle X \rangle)^2}{N(N-1)} \sum_i \left\langle \left(\left(\sum_{j=1, j \neq i}^N (x_j - \langle X \rangle) - \frac{1}{N} \sum_{k=1}^N \sum_{j=1, j \neq k}^N (x_j - \langle X \rangle) \right) \right)^2 \right\rangle + \dots \\ &= \frac{f'(\langle X \rangle)^2}{N(N-1)} \sum_i \left\langle \left(-(x_i - \langle X \rangle) + \frac{1}{N} \sum_{k=1}^N (x_k - \langle X \rangle) \right)^2 \right\rangle + \dots \\ &= \frac{f'(\langle X \rangle)^2}{N(N-1)} \sum_i \langle (x_i - \bar{x})^2 \rangle + \dots \\ &= f'(\langle X \rangle)^2 \frac{\sigma^2}{N-1} + \dots \\ &= f'(\langle X \rangle)^2 \langle (\bar{x} - \langle X \rangle)^2 \rangle + \dots\end{aligned}$$

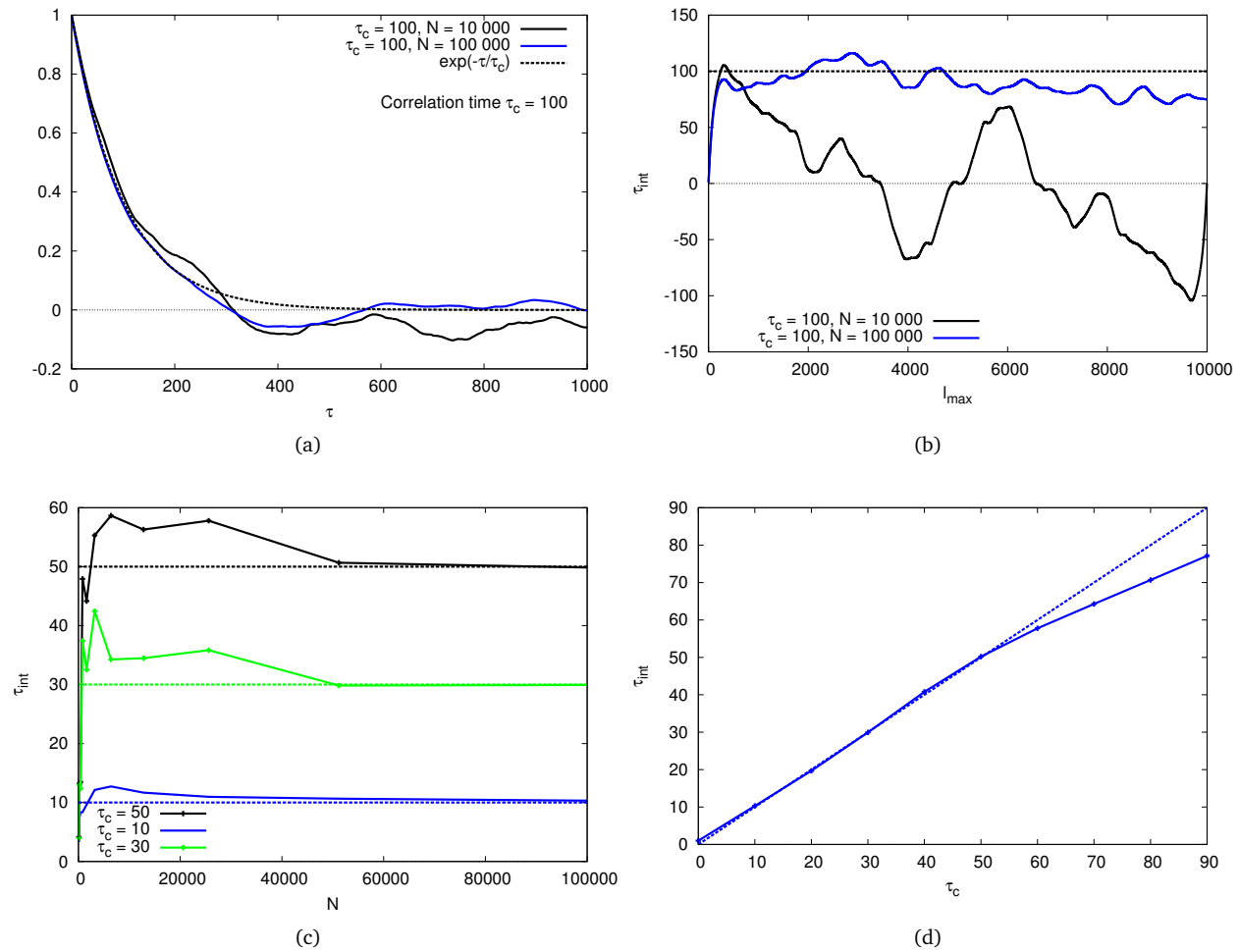


Figure N.1: Autocorrelation time estimation. (a) **Autocorrelation function** $A(t)$. It follows the law e^{-t/τ_c} . (b) **Integrated autocorrelation time**: influence of N on the autocorrelation time estimate. N has to be large enough, and l_{max} neither too small nor too large. The rule of thumb is usually $l_{\text{max}} = 6\tau_{\text{int}}(l_{\text{max}})$. (c) **Influence of the sample size N on the autocorrelation time estimate** $\tau_{\text{int}}(l_{\text{max}})$. For a given τ_c , the larger N , the better the estimate. For a given N , the lower τ_c , the better the estimate. Indeed, the effective sample size is $N_{\text{eff}} \approx N/(1 + 2\tau_c)$. (d) **Autocorrelation time estimation at fixed $N = 100,000$** . The estimate is reliable for low τ_c (as τ_c grows, N_{eff} decreases). One needs at least $N = 2000\tau_c$ to get a reliable estimate.

To derive the last line, I used Eqs. (10.7-10.8).

N.5 Autocorrelation time estimation from the autocorrelation function

In Fig. N.1a, one can check that the autocorrelation function of $\{x_i\}$ (defined in Eq. (10.12)), verifies:

$$A(t) \approx e^{-t/\tau_c} \quad (\text{N.11})$$

The autocorrelation time can be estimated by computing the integrated autocorrelation time defined in Eq. N.7). With this form, one has: $\int_0^t d\bar{t} A(\bar{t}) = \tau_c (1 - e^{-t/\tau_c})$. This explains the definition of the autocorrelation time Eq. (10.11). In practice, the series contains a finite number of samples, so that the integrated correlation time estimate becomes:

$$\tau_{\text{int}}[t_{\text{max}}] = \sum_{t=1}^{t_{\text{max}}} A(t)$$

As one can see in Figure N.1b, the estimate of the autocorrelation time is correct only (i) for a large enough sample size N and (ii) for a not too large t_{max} (compared to N). One can self-consistently estimate τ_{int} by choosing t_{max} such that the following rule of thumb is satisfied:

$$t_{\text{max}} = 6\tau_{\text{int}}[t_{\text{max}}] \quad (\text{N.12})$$

which corresponds to a precision of 0.25% if the autocorrelation function were exactly modelled by a decaying exponential (Eq.(N.11)). The corresponding estimate for the autocorrelation time, $\tau_{\text{int}}(t_{\text{max}})$ is accurate provided the sample size is large enough. This is illustrated by Figure N.1c.

Albeit a precise estimate of the autocorrelation time, this estimate is slow because the computation of τ_{int} is a $O(N^2)$ computation.

Index

A

ARPES, 199
atomic limit approximation, 17

B

BCS gap equation, 229
Bethe-Salpeter equation, 185
Bloch state, 197, 199

C

constrained random-phase approximation (cRPA),
239
cPES, 199

D

Density functional theory, 235
Dirac relation, 211
Dyson equation, 237

E

EDMFT, 40
EELS, 227
electron energy loss spectroscopy (EELS), 194
Extended Hubbard model, 39

F

Fermi Golden Rule, 217
Fierz ambiguity, 89
fluctuation-dissipation theorem, 212
Fröhlich model, 226

G

GW+EDMFT, 42

H

Hartree mean field theory, 19

hot spots, 79

Hubbard model, 18, 229
Hubbard-Stratonovich transformation, 230, 241

K

Knight shift, 205
Kohn anomaly, 226
Kohn-Sham Hamiltonian, 235
Kramers-Kronig, 214
Kubo formula, 210, 240

L

Landau Fermi liquid theory, 15
Larmor frequency, 204
LDA+DMFT, 237
LEED (low-energy electron diffraction), 194
Legendre transform, 90
Lindhard function, 226, 240
Local Density Approximation (LDA), 236

M

Migdal theorem, 86
Mott insulator, 15

N

nesting, 227
Neutron scattering, 202

O

Ornstein-Zernicke, 71
Ornstein-Zernicke susceptibility, 75

P

Parquet equations, 185
Pauli susceptibility, 205

Peierls instability, 227
pseudo gap, 71

Q

quasiparticle residue (Z), 16

S

selection rules, 200
Self-energy, 16
Slater mechanism, 232
Spin fluctuation theory, 75
spin-fermion model, 75
STM, 196

T

Thomas-Fermi approximation, 240
two-particle irreducible graphs, 22

W

Wannier function, 31, 234, 239

Bibliography

- Abragam A.** *The principles of nuclear magnetism* (Oxford University Press, London, 1961) H.2.2
- Abrikosov A.A., Gor'kov L.P., and Dzyaloshinskii I.** *Quantum field theoretical methods in statistical physics* (1965) 2.1.1.1
- Aeppli G., Hayden S.M., Mook H.A., Fisk Z., Cheong S.W., Rytz D., Remeika J.P., Espinosa G.P., and Cooper A.S.** “Magnetic dynamics of La_2CuO_4 and $\text{La}_{2-x}\text{Ba}_x\text{CuO}_4$ ”. *Physical Review Letters* **62**, 2052 (1989) 7.1.2.1
- Allais A., Bauer J., and Sachdev S.** “Density wave instabilities in a correlated two-dimensional metal”. *Physical Review B* **90**, 155114 (2014) 7.1.1
- Alloul H.** “NMR studies of electronic properties of solids”. *Scholarpedia* (2014). 1504.06992v1 H.2.2
- Alloul H., Ohno T., and Mendels P.** “ ^{89}Y NMR evidence for a fermi-liquid behavior in $\text{YBa}_2\text{Cu}_3\text{O}_{6+x}$ ”. *Physical Review Letters* **63**, 1700 (1989) 7.5
- Almbladh C., Barth U., and Leeuwen R.** “Variational total energies from ϕ - and ψ - derivable theories”. *International Journal of Modern Physics B* **13**, 535 (1999) 8.3.2.1
- Ament L.J.P., van Veenendaal M., Devereaux T.P., Hill J.P., and van Den Brink J.** “Resonant inelastic x-ray scattering studies of elementary excitations”. *Reviews of Modern Physics* **83**, 705 (2011). 1009.3630 H.2, H.1.2.2
- Anderson P.W.** “Localized Magnetic States in Metals”. *Physical Review* **124**, 41 (1961) 2.2.2.2
- Anderson P.W.** “More is different.” *Science* **177**, 393 (1972) 2
- Anderson P.W.** “Resonating valence bonds : a new kind of insulator ?” *Materials Research Bulletin* **8**, 153 (1973) 7.2.2.1
- Anderson P.W.** “The resonating valence bond state in La_2CuO_4 and superconductivity”. *Science* **235**, 1196 (1987) 2.1.2, 7.2, 7.2.2.1
- Anderson P.W.** “Physics. Is there glue in cuprate superconductors?” *Science (New York, N.Y.)* **316**, 1705 (2007) 7.2.2.1
- Anisimov V.I., Poteryaev A.I., Korotin M.A., Anokhin A.O., and Kotliar G.** “First-principles calculations of the electronic structure and spectra of strongly correlated First-principles calculations of the electronic structure and spectra of strongly correlated systems : the LDA + U method”. *J. Phys.: Condens. Matter* **9**, 767 (1997) 12.1, J.2
- Anisimov V.I., Zaanen J., and Andersen O.K.** “Band theory and Mott insulators: Hubbard U instead of Stoner I”. *Physical Review B* **44**, 943 (1991) J.1.2.2
- Aryasetiawan F. and Biermann S.** “Generalized Hedin’s Equations for Quantum Many-Body Systems with Spin-Dependent Interactions”. *Physical Review Letters* **100**, 116402 (2008) 8.3.2.3

- Aryasetiawan F. and Gunnarsson O.** “The GW method”. *Rep. Prog. Phys.* **61**, 237 (1998) 5.3.2, 8.3.2.2, J.1.2.2
- Aryasetiawan F., Imada M., Georges A., Kotliar G., Biermann S., and Lichtenstein A.** “Frequency-dependent local interactions and low-energy effective models from electronic structure calculations”. *Physical Review B* **70**, 195104 (2004) 4.3.1, J.3.3
- Atkinson W.a., Kampf a.P., and Bulut S.** “Charge Order in the Pseudogap Phase of Cuprate Superconductors”. *ArXiv 1404.1335* 17, 13025 (2014). 1404.1335 7.1.1
- Auerbach A.** *Interacting electrons and quantum magnetism* (Springer Verlag, 1994) 4, 7.2.2.1
- Avella A. and Mancini F., editors.** *Strongly Correlated Systems: Experimental Techniques*, volume 171 (Springer Verlag, 2012). 1108.2183 H.2.3
- Avila J., Mascaraque A., Michel E., Asensio M., LeLay G., Ortega J., Pérez R., and Flores F.** “Dynamical Fluctuations as the Origin of a Surface Phase Transition in Sn/Ge(111)”. *Physical Review Letters* **82**, 442 (1999) 3.2, ??
- Ayral T., Biermann S., and Werner P.** “Screening and nonlocal correlations in the extended Hubbard model from self-consistent combined GW and dynamical mean field theory”. *Physical Review B* **87**, 125149 (2013) (document), 1.3, 5, 5.1.1, 5.3, 5.3.2, 8.3.2.1, O.2
- Ayral T. and Parcollet O.** “Mott physics and spin fluctuations: a unified framework”. *Physical Review B* **92**, 115109 (2015). 1503.07724v1 (document), 1.3, 9, Q.1
- Ayral T., Werner P., and Biermann S.** “Spectral Properties of Correlated Materials: Local Vertex and Nonlocal Two-Particle Correlations from Combined GW and Dynamical Mean Field Theory”. *Physical Review Letters* **109**, 226401 (2012) (document), 1.3, 5, 5.3, 8.2, O.1
- Baier T., Bick E., and Wetterich C.** “Temperature dependence of antiferromagnetic order in the Hubbard model”. *Physical Review B* **70**, 125111 (2004) 8.3.1.3
- Bardeen J.** “Tunnelling from a many-particle point of view”. *Physical Review Letters* **6**, 57 (1961) H.1.3, H.1.3.2
- Bartosch L., Freire H., Cardenas J.J.R., and Kopietz P.** “A functional renormalization group approach to the Anderson impurity model.” *Journal of physics. Condensed matter : an Institute of Physics journal* **21**, 305602 (2009) 8.3.1.3
- Basov D. and Timusk T.** “Electrodynamics of high-T_c superconductors”. *Reviews of modern physics* **77**, 721 (2005) H.2.3, H.6
- Basov D.N., Averitt R.D., van Der Marel D., Dressel M., and Haule K.** “Electrodynamics of correlated electron materials”. *Reviews of Modern Physics* **83**, 471 (2011). 1106.2309 H.2.3, H.6
- Baym G.** “Self-Consistent Approximations in Many-Body Systems”. *Physical review* (1962) 8.3.2.1, 8.3.2.1
- Baym G. and Kadanoff L.** “Conservation Laws and Correlation Functions”. *Physical Review* (1961) 8.3.2.1, 8.3.2.1
- Beach K.S.D.** “Identifying the maximum entropy method as a special limit of stochastic analytic continuation” (pages 1–10) (2004). 0403055v1 I.3.2
- Béal-Monod M.T., Bourbonnais C., and Emery V.J.** “Possible superconductivity in nearly antiferromagnetic itinerant fermion systems”. *Physical Review B* **34**, 7716 (1986) 7.2.1.2
- Bednorz J. and Muller K.** “Possible High T_c Superconductivity in the Ba - La - Cu - O System”. *Zeitschrift für Physik B: Condensed Matter* **64**, 189 (1986) 7.1.1
- Berthod C.** “Applications of the Many-Body Formalism in Condensed-Matter Physics”. In “Lecture Notes”, chapter 7, (pages 95–112) (2012) H.1.4.1, I
- Bickers N. and Scalapino D.** “Conserving approximations for strongly fluctuating electron systems. I. Formalism and calculational approach”. *Annals of Physics* **206251**, 206 (1989) G.2
- Bickers N., Scalapino D., and White S.** “Conserving approximations for strongly correlated electron systems: Bethe-Salpeter equations and dynamics

- for the two-dimensional Hubbard model". *Physical review letters* **62**, 961 (1989) G.2
- Bickers N.** and **White S.** "Conserving approximations for strongly fluctuating electron systems. II. Numerical results and parquet extension". *Physical Review B* **43**, 8044 (1991) G.2
- Bieder J.** *Etude théorique de la transition de phase $\alpha - \gamma$ du cérium : prise en compte des fortes corrélations en DFT + DMFT.* Ph.D. thesis, Université Paris XI (2013) 11.1.6.1
- Biermann S., Aryasetiawan F., and Georges A.** "First-Principles Approach to the Electronic Structure of Strongly Correlated Systems: Combining the GW Approximation and Dynamical Mean-Field Theory". *Physical Review Letters* **90**, 086402 (2003) 1.2, 5.2, 12.2.1
- Binnig G.** and **Rohrer H.** "Scanning tunneling microscopy". *Surface Science* **126**, 236 (1983) H.1.3
- Binnig G., Rohrer H., Gerber C., and Weibel E.** "Surface studies by scanning tunneling microscopy". *Physical review letters* **49**, 57 (1982a) H.1.3
- Binnig G., Rohrer H., Gerber C., and Weibel E.** "Tunneling through a controllable vacuum gap". *Applied Physics Letters* **40**, 178 (1982b) H.1.3
- Binnig G., Rohrer H., Gerber C., and Weibel E.** "(111) facets as the origin of reconstructed Au(110) surfaces". *Surface Science Letters* **131**, L379 (1983a) H.1.3
- Binnig G., Rohrer H., Gerber C., and Weibel E.** "7x7 Reconstruction on Si(111) Resolved in Real Space". *Physical Review Letters* **50**, 120 (1983b) 3.1, H.1.3
- Bloch F.** "Über die Quantenmechanik der Elektronen in Kristallgittern". *Zeitschrift für Physik* **52**, 555 (1929) J.1.1
- Bloch F.** "Nuclear induction". *Physical Review* **70**, 460 (1946) H.2.2
- Boehnke L., Hafermann H., Ferrero M., Lechermann F., and Parcollet O.** "Orthogonal Polynomial Representation of Imaginary-Time Green's Functions" (page 14) (2011). 1104.3215 11.1.7.5
- Borejsza K.** and **Dupuis N.** "Antiferromagnetism and single-particle properties in the two-dimensional half-filled Hubbard model: Slater vs. Mott-Heisenberg". *EPL (Europhysics Letters)* (2003). 0212411v2 8.3.1.3
- Borejsza K.** and **Dupuis N.** "Antiferromagnetism and single-particle properties in the two-dimensional half-filled Hubbard model: A nonlinear sigma model approach". *Physical Review B* **69**, 085119 (2004) 8.3.1.3
- Bourges P., Regnault L.P., Sidis Y., Bossy J., Burlet P., Vettier C., Henry J.Y., and Couach M.** "Spin dynamics by inelastic neutron scattering in YBCO". *Journal of Low Temperature Physics* **105**, 377 (1996) 7.1.2.1, 7.4
- Braun J., Rausch R., Potthoff M., Minár J., and Ebert H.** "One-step theory of pump-probe photoemission". *Physical Review B* **91**, 1 (2015) H.1.4.1
- Brinkman W.F.** and **Rice T.M.** "Single-particle excitations in magnetic insulators". *Physical Review B* **2**, 1324 (1970) 2
- Bruus H.** and **Flensberg K.** *Introduction to Many-body quantum theory in condensed matter physics* (Oxford Graduate Texts, 2004) H.2.3, I
- Bryan R.K.** "Maximum entropy analysis of oversampled data problems". *European Biophysics Journal* (pages 165–174) (1990) I.3.2, I.3.2
- Capone M., Civelli M., Kancharla S.S., Castellani C., and Kotliar G.** "Cluster-dynamical mean-field theory of the density-driven Mott transition in the one-dimensional Hubbard model". *Physical Review B* **69**, 195105 (2004). 0401060 7.2.2.2.3
- Capone M.** and **Kotliar G.** "Competition between d-wave superconductivity and antiferromagnetism in the two-dimensional Hubbard model". *Physical Review B* **74**, 054513 (2006) 7.2.2.2.2
- Carpinelli J.M., Weitering H.H., Bartkowiak M., Stumpf R., and Plummer E.W.** "Surface Charge Ordering Transition: a Phase of Sn/Ge(111)". *Physical Review Letters* (pages 2859–2862) (1997) 3.2, ??
- Carpinelli J.M., Weitering H.H., Plummer E.W., and Stumpf R.** "Direct observation of a surface charge density wave" (1996) 3.2, ??, 3.3.2

- Castellani C.** and **Castro C.D.** “Arbitrariness and symmetry properties of the functional formulation of the Hubbard hamiltonian”. *Physics Letters A* **70**, 37 (1979) 8.3.1.3
- Casula M., Rubtsov A., and Biermann S.** “Dynamical screening effects in correlated materials: Plasmon satellites and spectral weight transfers from a Green’s function ansatz to extended dynamical mean field theory”. *Physical Review B* **85**, 035115 (2012). 1107.3123 5.3.2, 11.1.4.2.2
- Chen C.J.** “Tunneling matrix elements in three-dimensional space: The derivative rule and the sum rule”. *Physical Review B* **42**, 8841 (1990) H.1.3, H.1.3.2
- Chowdhury D.** and **Sachdev S.** “Density-wave instabilities of fractionalized Fermi liquids”. *Physical Review B* **90**, 245136 (2014) 7.1.1
- Chubukov A.V., Pines D., and Schmalian J.** “A Spin Fluctuation Model for D-wave Superconductivity” (page 50) (2002). 0201140 7.2.1.1, 7.2.1.2
- Ciuchi S., de Pasquale F., Fratini S., and Feinberg D.** “Dynamical mean-field theory of the small polaron”. *Physical Review B* **56**, 4494 (1997) 11.1.4.2.2
- Civelli M.** “Evolution of the dynamical pairing across the phase diagram of a strongly correlated high-temperature superconductor”. *Physical Review Letters* **103**, 136402 (2009). 0812.1201 7.2.2.2.2
- Civelli M., Capone M., Georges A., Haule K., Parcollet O., Stanescu T.D., and Kotliar G.** “Nodal-antinodal dichotomy and the two gaps of a superconducting doped mott insulator”. *Physical Review Letters* **100**, 046402 (2008). 0704.1486 7.2.2.2.2
- Civelli M., Capone M., Kancharla S.S., Parcollet O., and Kotliar G.** “Dynamical breakup of the fermi surface in a doped mott insulator”. *Physical Review Letters* **95**, 106402 (2005). 0411696 7.2.2.2.2
- Coleman P.** “New approach to the mixed-valence problem”. *Physical Review B* **29**, 3035 (1984) 7.2.2.1
- Coleman P.** *Introduction to Many-Body Physics* (2011) 2.1.1.1, I
- Comanac A., de Medici L., Capone M., and Millis A.J.** “Optical conductivity and the correlation strength of high temperature copper-oxide superconductors”. *Nature Physics* (pages 287–290) (2007). 0712.2392 9.3
- Corboz P., Rice T.M., and Troyer M.** “Competing states in the t - J model: Uniform d -wave state versus stripe state”. *Physical Review Letters* **113**, 046402 (2014). 1402.2859 7.1.1
- Cornwall J., Jackiw R., and Tomboulis E.** “Effective action for composite operators”. *Physical Review D* **10** (1974) 8.3.1.3
- Croft T.P., Lester C., Senn M.S., Bombardi A., and Hayden S.M.** “Charge density wave fluctuations in LaSrCuO4 and their competition with superconductivity”. *Physical Review B* **89**, 224513 (2014) 7.2
- Custance O., Gomez-Rodriguez J., Baro A., Juré L., Mallet P., and Veuillen J.Y.** “Low temperature phases of Pb/Si(111)”. *Surface Science* **485**, 1399 (2001) ??, 3.2
- Cyr-Choinière O., Grissonnanche G., Badoux S., Day J., Bonn D.A., Hardy W.N., Liang R., and Taillefer L.** “Onset of nematicity and its link with charge order and the pseudogap in the cuprate superconductor”. *arXiv preprint arXiv:1504.06972* (2015) 7.1.1
- Dahm T., Hinkov V., Borisenko S.V., Kordyuk a.a., Zabolotnyy V.B., Fink J., Büchner B., Scalapino D.J., Hanke W., and Keimer B.** “Strength of the Spin-Fluctuation-Mediated Pairing Interaction in a High-Temperature Superconductor”. *Nature Physics* **5**, 25 (2008). 0812.3860 7.2.1.3
- Damascelli A., Hussain Z., and Shen Z.** “Angle-resolved photoemission studies of the cuprate superconductors”. *Reviews of Modern Physics* **75**, 473 (2003) 7.2, 7.3, H.1.4.1
- De Carvalho V.S. and Freire H.** “Evidence of a short-range incommensurate d-wave charge order from a fermionic two-loop renormalization group calculation of a 2D model with hot spots”. *Annals of Physics* **348**, 32 (2014). 1402.4820 7.1.1
- de Dominicis C. and Martin P.** “Stationary Entropy Principle and Renormalization in Normal and Su-

- perfluid Systems. I. Algebraic Formulation”. *Journal of Mathematical Physics* **5**, 14 (1964a) 8.3.2
- de Dominicis C.** and **Martin P.** “Stationary Entropy Principle and Renormalization in Normal and Superfluid Systems. II. Diagrammatic Formulation”. *Journal of Mathematical Physics* **5**, 31 (1964b) 8.3.2, 8.3.2.2
- Ding H., Yokoya T., Campuzano J.C., Takahashi T., Randeria M., Norman M.R., Mochiku T., Kadowaki K., and Giapintzakis J.** “Spectroscopic evidence for a pseudogap in the normal state of underdoped high-Tc superconductors” (1996) 7.1.2.3
- Doiron-Leyraud N., Proust C., LeBoeuf D., Levallois J., Bonnemaïson J.B., Liang R., Bonn D.a., Hardy W.N., and Taillefer L.** “Quantum oscillations and the Fermi surface in an underdoped high-Tc superconductor.” *Nature* **447**, 565 (2007). 0801.1281 7.1.1
- Dressel M.** and **Gruener G.** *Electrodynamics of Solids: Optical Properties of Electrons in Matter* (Cambridge University Press, 2002) H.2.3, 9
- Dupuis N.** “Spin fluctuations and pseudogap in the two-dimensional half-filled Hubbard model at weak coupling”. *Physical Review B* **65**, 245118 (2002) 8.3.1.3
- Efetov K.B., Meier H., and Pépin C.** “Pseudogap state near a quantum critical point”. *Nature Physics* **9**, 442 (2013). 1210.3276 7.1.1
- Egerton R.F.** “Electron energy-loss spectroscopy in the TEM”. *Reports on Progress in Physics* **72**, 016502 (2008) H.1.2
- Egerton R.F.** *Electron energy-loss spectroscopy in the electron microscope* (2011), 3rd editio edition H.1.2
- Eliashberg G.M.** “Interactions between electrons and lattice vibrations in a superconductor” (1960) 7.2.1.2
- Fano U.** “Atomic theory of electromagnetic interactions in dense materials”. *Physical Review* **103**, 1202 (1956) H.1.2
- Fauqué B., Sidis Y., Hinkov V., Pailhès S., Lin C.T., Chaud X., and Bourges P.** “Magnetic order in the pseudogap phase of high-TC superconductors”. *Physical Review Letters* **96**, 1 (2006). 0805.0319 7.2
- Ferrero M., Cornaglia P., De Leo L., Parcollet O., Kotliar G., and Georges A.** “Pseudogap opening and formation of Fermi arcs as an orbital-selective Mott transition in momentum space”. *Physical Review B* **80**, 064501 (2009) 7.2.2.2.2
- Ferrero M., Cornaglia P.S., De Leo L., Parcollet O., Kotliar G., and Georges A.** “Valence-Bond Dynamical Mean-Field Theory of Doped Mott Insulators with Nodal/Antinodal Differentiation”. *Europhysics Letters* **85**, 57009 (2008). 0806.4383 7.2.2.2.2, 9.3
- Fink J., Nücker N., Pellegrin E., Romberg H., Alexander M., and Knupfer M.** “Electron energy-loss and x-ray absorption spectroscopy of cuprate superconductors and related compounds”. *Journal of Electron Spectroscopy and Related Phenomena* **66**, 395 (1994) 7.3
- Florens S.** *Cohérence et Localisation dans les systèmes d’électrons fortement corrélés*. Ph.D. thesis, Université Paris 6 (2003) 5.3.2
- Freericks J.K., Krishnamurthy H.R., and Pruschke T.** “Theoretical description of time-resolved photoemission spectroscopy: Application to pump-probe experiments”. *Physical Review Letters* **102**, 3 (2009). 0806.4781 H.1.4.1
- Fröhlich H.** “Theory of the Superconducting State. I. the ground state at the absolute zero of temperature”. *Phys. Rev.* **79**, 845 (1950) I.6.1
- Fröhlich H.** “Interaction of Electrons with Lattice Vibrations”. *Proceedings of the Royal Society A: Mathematical, Physical and Engineering Sciences* **215**, 291 (1952) I.6.1
- Fujita K., Kim C.K., Lee I., Lee J., Hamidian M.H., Fermo I.a., Mukhopadhyay S., Eisaki H., Uchida S., Lawler M.J., Kim E., and Davis J.C.** “Simultaneous Transitions in Cuprate”. *Science (New York, N.Y.)* **344**, 612 (2014) 7.1.1
- Georges A.** “Strongly Correlated Electron Materials : Dynamical Mean-Field Theory and Electronic Structure”. *Arxiv preprint condmat0403123* **715**, 1 (2008). 0403123v1 J.1.2.2
- Georges A., Kotliar G., Krauth W., and Rozenberg M.J.** “Dynamical mean-field theory of strongly correlated fermion systems and the limit of infinite dimensions”. *Reviews of Modern Physics* **68**, 13 (1996) 1.1, 2.2.2, 2.2.2.1, 2.2.3, 2.2.5

- Ghiringhelli G., Tacon M.L., Minola M., Mazzoli C., Brookes B., Luca G.M.D., Frano A., Hawthorn D.G., He F., Loew T., Sala M., Peets D.C., Salluzzo M., Schierle E., Sutarto R., Weschke E., Keimer B., and Braicovich L.** “Long-Range Incommensurate Charge Fluctuations in $(Y,Nd)Ba_2Cu_3O_{6+x}$ ”. *Science (New York, N.Y.)* **8**, 6 (2012) 7.1.1
- Gomes A. and Lederer P.** “Remarks on coupled spin and charge fields in the Hubbard Hamiltonian”. *Journal de Physique* (pages 231–239) (1977) 8.3.1.3
- Göthelid M., Björkqvist M., Grehk T.M., Le Lay G., and Karlsson U.O.** “Metal-semiconductor fluctuation in the Sn adatoms in the Si(111)-Sn and Ge(111)-Sn(3x3)R30° reconstructions”. *Physical Review B* **52**, 352 (1995) 3.2, ??, ??, 6.3
- Gull E.** *Continuous-time quantum Monte Carlo algorithms for fermions*. Ph.D. thesis, ETH Zürich (2008) 11
- Gull E., Ferrero M., Parcollet O., Georges A., and Millis A.J.** “Momentum-space anisotropy and pseudogaps: A comparative cluster dynamical mean-field analysis of the doping-driven metal-insulator transition in the two-dimensional Hubbard model”. *Physical Review B* **82**, 155101 (2010) 7.14, 7.2.2.2.2, 7.2.2.2.3
- Gull E., Millis A.J., Lichtenstein A.I., Rubtsov A.N., Troyer M., and Werner P.** “Continuous-time Monte Carlo methods for quantum impurity models”. *Reviews of Modern Physics* **83**, 349 (2011) 11, 11.1.3.2
- Gull E., Parcollet O., and Millis A.J.** “Superconductivity and the pseudogap in the two-dimensional Hubbard model”. *Physical Review Letters* **110**, 216405 (2013). 1207.2490 7.2.2.2.2
- Gull E., Parcollet O., Werner P., and Millis A.J.** “Momentum-sector-selective metal-insulator transition in the eight-site dynamical mean-field approximation to the Hubbard model in two dimensions”. *Physical Review B* **80**, 245102 (2009). 0909.1795 7.2.2.2.2
- Gull E., Werner P., Millis A., and Troyer M.** “Performance analysis of continuous-time solvers for quantum impurity models”. *Physical Review B* **76**, 1 (2007) 11
- Gutzwiller M.C.** “Effect of Correlation on the Ferromagnetism of Transition Metals”. *Physical Review Letters* **10**, 159 (1963) 2.1.2
- Hafermann H.** “Self-energy and vertex functions from hybridization expansion continuous-time quantum Monte Carlo for impurity models with retarded interaction”. *Physical Review B* **89**, 235128 (2014). arXiv:1311.5801v1 11.1.7.2, 11.1.7.3
- Hafermann H., Patton K.R., and Werner P.** “Improved estimators for the self-energy and vertex function in hybridization-expansion continuous-time quantum Monte Carlo simulations”. *Physical Review B* **85**, 205106 (2012). 1108.1936 11.1.7.4
- Hamann D.** “Fluctuation theory of dilute magnetic alloys”. *Physical Review Letters* **2** (1969) 8.3.1.3
- Hansmann P., Ayrat T., Tejada A., and Biermann S.** “Uncertainty principle for experimental probes : Fast spectroscopy vs . slow microscopy”. *in preparation* (2014) 1.3
- Hansmann P., Ayrat T., Tejada A., and Biermann S.** “Uncertainty principle for experimental probes: Fast spectroscopy vs . slow microscopy”. *in preparation* (pages 1–9) (2015) (document), 6, 6.3, P.2
- Hansmann P., Ayrat T., Vaugier L., Werner P., and Biermann S.** “Long-Range Coulomb Interactions in Surface Systems: A First-Principles Description within Self-Consistently Combined GW and Dynamical Mean-Field Theory”. *Physical Review Letters* **110**, 166401 (2013a) (document), 1.3, 4.2, 4.3.2, 6, P.1
- Hansmann P., Vaugier L., Jiang H., and Biermann S.** “What about U on surfaces? Extended Hubbard models for adatom systems from first principles.” *Journal of physics. Condensed matter : an Institute of Physics journal* **25**, 094005 (2013b) 4.1, 4.2, 4.3, 4.3.2
- Hassing R. and Esterling D.** “Functional-Integral Approaches to the Anderson Model: A Comparison of Results in Limiting Cases”. *Physical Review B* **7** (1973) 8.3.1.3
- Hastings W.K.** “Monte Carlo sampling methods using Markov chains and their applications”. *Biometrika* **57**, 97 (1970) 10.2.3, 11.1.3.1

- Hedin L.** “New method for calculating the one-particle Green’s function with Application to the Electron-Gas problem”. *Physical Review* **139**, 796 (1965) 5.2.1, 8.3.2.3
- Held K.** “Dynamical Vertex Approximation”. In E. Pavarini, E. Koch, D. Vollhardt, and A.I. Lichtenstein, editors, “Autumn School on Correlated Electrons. DMFT at 25: Infinite Dimensions”, volume 4, chapter 10 (Forschungszentrum Julich, 2014) G.4, G.4.1
- Hellberg C. and Erwin S.** “Strongly Correlated Electrons on a Silicon Surface: Theory of a Mott Insulator”. *Physical Review Letters* **83**, 1003 (1999) 3.3.2, 3.2
- Hettler M.H., Mukherjee M., Jarrell M., and Krishnamurthy H.R.** “The Dynamical Cluster Approximation: Non-Local Dynamics of Correlated Electron Systems”. *Physical Review B* **61**, 12739 (1999). 9903273 7.2.2.2.1
- Hettler M.H., Tahvildar-Zadeh A.N., Jarrell M., Pruschke T., and Krishnamurthy H.R.** “Nonlocal Dynamical Correlations of Strongly Interacting Electron Systems”. *Physical Review B* **58**, R7475 (1998). 9803295 7.2.2.2.1
- Himmetoglu B., Floris A., De Gironcoli S., and Coccioni M.** “Hubbard-corrected DFT energy functionals: The LDA+U description of correlated systems”. *International Journal of Quantum Chemistry* **114**, 14 (2014). arXiv:1309.3355v1 J.1.2.2
- Hoffman J.E., McElroy K., Lee D.H., Lang K.M., Eisaki H., Uchida S., and Davis J.C.** “Imaging quasiparticle interference in Bi₂Sr₂CaCu₂O₈+ δ .” *Science (New York, N.Y.)* **297**, 1148 (2002). 0209276 7.1.1
- Hohenberg P. and Kohn W.** “The Inhomogeneous Electron Gas”. *Phys. Rev.* **136**, B864 (1964) J.1.2.1
- Holstein T.** “Studies of polaron motion: Part I. The molecular-crystal model”. *Annals of Physics* **8**, 325 (1959) 11.1.4.2.2
- Honerkamp C.** “Effective interactions in multiband systems from constrained summations”. *Physical Review B* **85**, 195129 (2012) J.3.3
- Horikoshi K., Tong X., Nagao T., and Hasegawa S.** “Structural phase transitions of Pb-adsorbed Si (111) surfaces at low temperatures”. *Phys. Rev. B* **60**, 287 (1999) ??, 3.2
- Huang L., Ayrat T., Biermann S., and Werner P.** “Extended dynamical mean-field study of the Hubbard model with long range interactions”. *Physical Review B* **90**, 195114 (2014). 1404.7047 (document), 1.3, 5, 5.3, O.3
- Hubbard J.** “Calculation of partition functions”. *Physical Review Letters* (1959) 5.1.1
- Hubbard J.** “Electron Correlations in Narrow Energy Bands”. *Proceedings of the Royal Society A: Mathematical, Physical and Engineering Sciences* **276**, 238 (1963) 2.1.2
- Hüfner S.** *Photoelectron spectroscopy: principles and applications* (Springer Verlag, Berlin, 1995) H.1.4.1
- Huscroft C., Jarrell M., Maier T.A., Moukouri S., and Tahvildarzadeh A.N.** “Pseudogaps in the 2D Hubbard model”. *Physical Review Letters* **86**, 139 (2001) 7.2.2.2.2
- Imada M., Fujimori A., and Tokura Y.** “Metal-insulator transitions”. *Reviews of Modern Physics* **70**, 1039 (1998) 7.1.1
- Jarrell M. and Gubernatis J.** “Bayesian inference and the analytic continuation of imaginary-time quantum Monte Carlo data”. *Physics Reports* **269**, 133 (1996) I.3.2
- Jarrell M., Maier T.A., Huscroft C., and Moukouri S.** “A Quantum Monte Carlo algorithm for non-local corrections to the Dynamical Mean-Field Approximation”. *Physical Review B* **64**, 195130 (2001). 0108140 7.14
- J erome D. and Schulz H.** “Organic conductors and superconductors”. *Advances in Physics* **31**, 299 (1982) I.6.1.1
- Jones R.O. and Gunnarsson O.** “The density functional formalism, its applications and prospects”. *Reviews of Modern Physics* **61**, 689 (1989) J.1.2
- Kajueter H.** *Interpolating Perturbation Scheme for Correlated Electron Systems*. Ph.D. thesis, Rutgers University (1996) 1.2, 5.1, 5.1.1
- Kanamori J.** “Electron correlation and ferromagnetism of Transition Metals”. *Progress of Theoretical Physics* (1963) 2.1.2

- Kancharla S.S., Kyung B., Sénéchal D., Civelli M., Capone M., Kotliar G., and Tremblay A.M.S.** “Anomalous superconductivity and its competition with antiferromagnetism in doped Mott insulators”. *Physical Review B* **77**, 184516 (2008). 0508205 7.2.2.2.2
- Katanin A., Toschi A., and Held K.** “Comparing pertinent effects of antiferromagnetic fluctuations in the two- and three-dimensional Hubbard model”. *Physical Review B* **80**, 075104 (2009) 9.5, G.4.1, G.4.1.1, G.4.1.1
- Keimer B., Belk N., Birgeneau R.J., Cassanho A., Chen C.Y., Greven M., Kastner M.A., Aharony A., Endoh Y., Erwin R.W., and Shirane G.** “Magnetic excitations in pure, lightly doped, and weakly metallic La₂CuO₄”. *Physical Review B* **46**, 14034 (1992) 7.4
- Kinza M. and Honerkamp C.** “Low-energy effective interactions beyond cRPA by the functional renormalization group” (pages 16–18) (2015). 1504.00232v1 J.3.3
- Knight W.** “Nuclear Magnetic Resonance Shift in Metals”. *Physical Review* **76**, 1259 (1949) H.2.2.1
- Kohn W.** “Image of the fermi surface in the vibration spectrum of a metal”. *Physical Review Letters* **2**, 393 (1959) I.6.1.1
- Kohn W.** “Nobel Lecture: Electronic structure of matter-wave functions and density functionals”. *Reviews of Modern Physics* **71**, 1253 (1999) J.1.2
- Kohn W. and Luttinger J.M.** “New Mechanism for Superconductivity”. *Phys. Rev. Lett.* **15**, 524 (1965) 7.2.1.2
- Kohn W. and Sham L.J.** “Self-consistent equations including exchange and correlation effects”. *Physical Review* **385**, 1133 (1965) J.1.2.1
- Kotani T., van Schilfhaarde M., and Faleev S.V.** “Quasiparticle self-consistent GW method: A basis for the independent-particle approximation”. *Physical Review B* **76**, 165106 (2007). 0611002 5.3.2
- Kotliar G.** “Resonating valence bonds and d-wave superconductivity”. *Physical Review B* **37**, 3664 (1988) 7.2.2.1
- Kotliar G. and Liu J.** “Superconducting Instabilities in the Large-U Limit of a Generalized Hubbard Model”. *Physical review letters* **61**, 1784 (1988a) 7.2.2.1
- Kotliar G. and Liu J.** “Superexchange mechanism and d-wave superconductivity”. *Physical Review B* **38**, 5142 (1988b) 7.2.2.1
- Kotliar G., Savrasov S., Pálsson G., and Biroli G.** “Cellular Dynamical Mean Field Approach to Strongly Correlated Systems”. *Physical Review Letters* **87**, 186401 (2001) 7.2.2.2.1
- Krauth W.** “Introduction to Monte Carlo algorithms” (1996) 11.1.3.1
- Krauth W.** “Statistical mechanics: Algorithms and computations” (2006) 10.3.3
- Kuneš J.** “Efficient treatment of two-particle vertices in dynamical mean-field theory”. *Physical Review B* **83**, 085102 (2011). 1010.3809 9.1, 9.8
- Kyung B., Kancharla S.S., Sénéchal D., Tremblay A.M.S., Civelli M., and Kotliar G.** “Pseudogap induced by short-range spin correlations in a doped Mott insulator”. *Physical Review B* **73**, 165114 (2006) 7.2.2.2.2
- Kyung B., Sénéchal D., and Tremblay A.M.S.** “Pairing dynamics in strongly correlated superconductivity”. *Physical Review B* **80**, 205109 (2009). 0812.1228 7.2.2.2.2
- Lang I.G. and Firsov Y.A.** “Calculation of the activation probability for a jump of a small-radius polaron”. *Soviet Physics JETP* **27**, 1301 (1968) 11.1.4.2.2
- Le Tacon M.** “High T_c cuprates: Recent insights from X-ray scattering”. In “Collège de France”, (Paris, 2015) 7.8
- LeBoeuf D., Krämer S., Hardy W.N., Liang R., Bonn D.a., and Proust C.** “Thermodynamic phase diagram of static charge order in underdoped YBa₂Cu₃O_y”. *Nature Physics* **9**, 79 (2012). 1211.2724 7.1.1
- Lechermann F., Georges A., Poteryaev A., Biermann S., Posternak M., Yamasaki A., and Andersen O.K.** “Dynamical mean-field theory using Wannier functions: A flexible route to electronic struc-

- ture calculations of strongly correlated materials". *Physical Review B* **74**, 125120 (2006). 0605539 J.2
- Li G., Höpfner P., Schäfer J., Blumenstein C., Meyer S., Bostwick A., Rotenberg E., Claessen R., and Hanke W.** "Magnetic order in a frustrated two-dimensional atom lattice at a semiconductor surface". *Nature Communications* **4**, 1620 (2013). 1112.5062 ??, 3.2, 3.3.2, 3.2, 6.2.1, 6.3
- Li G., Laubach M., Fleszar A., and Hanke W.** "Geometrical frustration and the competing phases of the Sn/Si(111) $\sqrt{3}\times\sqrt{3}$ R30 surface systems". *Physical Review B* **83**, 041104(R) (2011) 3.3.2, 3.2
- Lichtenstein A.I. and Katsnelson M.I.** "Ab initio calculations of quasiparticle band structure in correlated systems: LDA++ approach". *Physical Review B* **57**, 6884 (1997). 9707127 12.1, J.2
- Lichtenstein A.I. and Katsnelson M.I.** "Antiferromagnetism and d-wave superconductivity in cuprates: A cluster dynamical mean-field theory". *Physical Review B* **62**, R9283 (2000) 7.2.2.2.1
- Limelette P., Wzietek P., Florens S., Georges A., Costi T.A., Pasquier C., Jérôme D., Mézière C., and Batail P.** "Mott transition and transport crossovers in the organic compound kappa-(BEDT-TTF)₂Cu[N(CN)₂Cl]". *Physical review letters* **91**, 016401 (2003) 2.2
- Lindhard J.** "On the properties of a gas of charged particles". *Kongelige Danske Videnskabernes Selskab Matematisk-fysiske Meddelelser* **28**, 1 (1954) I.6.1.1
- Lobo J., Tejada A., Mugarza A., and Michel E.** "Electronic structure of Sn/Si(111)-(3x3)R30° as a function of Sn coverage". *Physical Review B* **68**, 235332 (2003) ??, 3.2, 6.3
- Loeser A.G., Shen Z.X., Dessau D.S., Marshall D.S., Park C.H., Fournier P., and Kapitulnik A.** "Excitation Gap in the Normal State of Underdoped Bi₂Sr₂CaCu₂O₈+delta". *Science* **273**, 325 (1996) 7.1.2.3
- Luttinger J. and Ward J.** "Ground-State Energy of a Many-Fermion System. II". *Physical Review* (1960) 2.2.3, 8.3.2.1
- Macêdo C. and Coutinho-Filho M.** "Hubbard model: Functional-integral approach and diagrammatic perturbation theory". *Physical Review B* **43** (1991) 8.3.1.3
- Macêdo C., Coutinho-Filho M., and de Moura M.** "Critical study of the functional-integral method applied to the itinerant magnetism". *Physical Review B* **25** (1982) 8.3.1.3
- Maier T., Jarrell M., and Scalapino D.** "Structure of the Pairing Interaction in the Two-Dimensional Hubbard Model". *Physical Review Letters* **96**, 047005 (2006) 7.2.2.2.2, G.4.1
- Maier T.A., Jarrell M., Macridin A., and Slezak C.** "Kinetic energy driven pairing in cuprate superconductors." *Physical Review Letters* **92**, 027005 (2004). 0211298 7.2.2.2.2
- Maier T.A., Jarrell M., Pruschke T., and Hettler M.H.** "Quantum cluster theories". *Reviews of Modern Physics* **77**, 1027 (2005a). 0404055 7.2.2.2.1
- Maier T.A., Jarrell M., Pruschke T., and Keller J.** "A Non-Crossing Approximation for the Study of Intersite Correlations". *The European Physical Journal B - Condensed Matter* **13**, 613 (2000). 9906253 7.2.2.2.2
- Maier T.A., Jarrell M., Schulthess T.C., Kent P.R.C., and White J.B.** "Systematic study of d-wave superconductivity in the 2D repulsive Hubbard model". *Physical Review Letters* **95**, 237001 (2005b). 0504529 7.2.2.2.2
- Maier T.A., Poilblanc D., and Scalapino D.J.** "Dynamics of the pairing interaction in the hubbard and t-J models of high-temperature superconductors". *Physical Review Letters* **100**, 237001 (2008) 7.2.2.1
- Manske D.** *Theory of Unconventional Superconductors*, volume 202 of *Springer Tracts in Modern Physics* (Springer Berlin Heidelberg, Berlin, Heidelberg, 2004) 7, G.2
- Manske D., Eremin I., and Bennemann K.H.** "Renormalization of the elementary excitations in hole- and electron-doped cuprates due to spin fluctuations". *Physical Review B* **67**, 134520 (2002). 0210299 7.2.1.3

- Marshall D., Dessau D., Loeser A., Park C.H., Matsuura A., Eckstein J., Bozovic I., Fournier P., Kapitulnik A., Spicer W., and Shen Z.X.** “Unconventional Electronic Structure Evolution with Hole Doping in $\text{Bi}_2\text{Sr}_2\text{CaCu}_2\text{O}_{8+\delta}$: Angle-Resolved Photoemission Results”. *Physical Review Letters* **76**, 4841 (1996) 7.1.2.3
- Marshall D.S., Dessau D.S., King D.M., Park C., Matsuura A.Y., Shen Z., Spicer W.E., Eckstein J.N., and Bozovic I.** “Angle-resolved photoemission spectroscopy study of $\text{Bi}_2\text{Sr}_2\text{CaCu}_2\text{O}_{8+\delta}$ thin films.” *Physical review. B* **52**, 12548 (1995) 7.1.2.3
- Martin R.M.** *Electronic Structure* (2004) J.1.2
- Metropolis N., Rosenbluth A.W., Rosenbluth M.N., Teller A.H., and Teller E.** “Equation of State Calculations by Fast Computing Machines”. *The Journal of Chemical Physics* **21**, 1087 (1953) 10.2.3, 11.1.3.1
- Metzner W., Salmhofer M., Honerkamp C., Meden V., and Schönhammer K.** “Functional renormalization group approach to correlated fermion systems”. *Reviews of Modern Physics* **84**, 299 (2012) 7.2.1.1
- Metzner W. and Vollhardt D.** “Correlated Lattice Fermions in $d=\infty$ dimensions”. *Physical Review Letters* **62**, 324 (1989) 2.2.2.1
- Migdal A.B.** “Interaction Between Electrons and Lattice Vibrations in a normal metal” (1958) 7.2.1.2
- Mila F. and Rice T.** “Analysis of magnetic resonance experiments in $\text{YBa}_2\text{Cu}_3\text{O}_7$ ”. *Physica C: Superconductivity* **157**, 561 (1989) H.2.2.3
- Millis A.J.** “Optical conductivity and Correlated electron physics”. In D. Beariswyl and L. Degiorgi, editors, “Strong Interactions in Low Dimensions”, chapter 7, (pages 146–155) (Kluwer Academic Publishers, 2004) H.2.3
- Millis A.J., Monien H., and Pines D.** “Phenomenological model of nuclear relaxation in the normal state of $\text{YBa}_2\text{Cu}_3\text{O}_7$ ”. *Physical Review B* **42**, 167 (1990) 7.2.1.1
- Modesti S., Petaccia L., Ceballos G., Vobornik I., Panaccione G., Rossi G., Ottaviano L., Larciprete R., Lizzit S., and Goldoni A.** “Insulating ground state of $\text{Sn}/\text{Si}(111)$ ”. *Physical Review Letters* **98**, 126401 (2007) ??, 3.2, 6.3
- Monthoux P., Balatsky A., and Pines D.** “Toward a theory of high-temperature superconductivity in the antiferromagnetically correlated cuprate oxides”. *Physical review letters* **67**, 3448 (1991) 7.2, 7.2.1, 7.2.1.1
- Morikawa H., Matsuda I., and Hasegawa S.** “STM observation of $\text{Si}(111)\text{-}\alpha\text{-sq}_3\text{xsq}_3\text{-Sn}$ at low temperature”. *Physical Review B* **65**, 201308 (2002) ??, 3.2, 6.3
- Mott N.F. and Peierls R.** “Discussion of the paper by de Boer and Verwey”. *Proceedings of the Physical Society* **49**, 72 (1937) 2.1.1
- Moukouri S., Allen S., Lemay F., Kyung B., Poulin D., Vilk Y., and Tremblay A.M.** “Many-body theory versus simulations for the pseudogap in the Hubbard model”. *Physical Review B* **61**, 7887 (2000) G.2, G.3
- Moukouri S. and Jarrell M.** “Absence of a Slater Transition in the Two-Dimensional Hubbard Model”. *Physical Review Letters* **87**, 167010 (2001) 7.14
- Müller-Hartmann E.** “Correlated fermions on a lattice in high dimensions”. *Zeitschrift für Physik B Condensed Matter* **74**, 507 (1989) 2.2.2.1
- Nambu Y.** “Quasi-Particles and Gauge Invariance in the Theory of Superconductivity”. *Physical Review* (1960) 7.2.1.2
- Negele J.W. and Orland H.** *Quantum Many-Particle Systems* (1988) 2.2.2.1
- Nie L., Tarjus G., and Kivelson S.a.** “Quenched disorder and vestigial nematicity in the pseudogap regime of the cuprates”. *Proceedings of the National Academy of Sciences* **111**, 7980 (2014). 1311.5580 7.1.1
- Niedoba H., Launois H., Brinkmann D., Brugger R., and Zeller H.R.** “NMR Study of the Low-Temperature Insulating State in the One-Dimensional “Conductor” $\text{K}_2\text{Pt}(\text{CN})_4\text{Br}_0.3\text{-3H}_2\text{O}$ ”. *Physica Status Solidi (b)* **58**, 309 (1973) I.6.1.1
- Norman M.R. and Pépin C.** “The Electronic Nature of High Temperature Cuprate Superconductors”.

- Reports on Progress in Physics* **66**, 1547 (2003). 0302347 7.9
- Nozières P.** and **Pines D.** “A dielectric formulation of the many body problem: Application to the free electron gas”. *Il Nuovo Cimento Series 10* **9**, 470 (1958) H.1.2
- Onnes K.** “Further Experiments with liquid Helium”. *Proceedings of the Koninklijke Akademie van Wetenschappen te Amsterdam* **120b**, 1479 (1911) III
- Onufrieva F.** and **Pfeuty P.** “SC state in the underdoped high- T_c cuprates as a quantum spin liquid. A microscopic theory”. *Physical Review Letters* **82**, 3136 (1999). 9903097 7.2.1.3
- Onufrieva F.** and **Pfeuty P.** “Low-doping anomalies in high- T_c cuprate superconductors as evidence of a spin-fluctuation-mediated superconducting state”. *Physical Review Letters* **109**, 257001 (2012) 7.2.1.3
- Onufrieva F.**, **Pfeuty P.**, and **Kiselev M.** “New scenario for high- T_c cuprates: electronic topological transition as a motor for anomalies in the underdoped regime”. *Physical Review Letters* **82**, 2370 (1998). 9804189 7.2.1.3
- Otsuki J.** “Spin-boson coupling in continuous-time quantum Monte Carlo”. *Physical Review B* **87**, 125102 (2013). 1211.5935 8.3.3.2, 11.1.1
- Padé H.** “Sur la représentation approchée d’une fonction par des fractions rationnelles”. *Annales Scientifiques de l’É.N.S.* **9**, 3 (1892) I.3.1
- Parcollet O.**, **Biroli G.**, and **Kotliar G.** “Cluster dynamical mean field analysis of the Mott transition”. *Physical Review Letters* **92**, 226402 (2004). 0308577 7.2.2.2.2
- Parcollet O.**, **Ferrero M.**, **Ayral T.**, **Hafermann H.**, **Seth P.**, and **Krivenko I.S.** “TRIQS: The Toolbox for Research in Interacting Quantum Systems”. *Computer Physics Communications* **196**, 398 (2015). 1504.01952 (document), 1.3, 2, 10, 10.1, 10.2.3, 10.2, R.1
- Peierls R.** *Quantum Theory of Solids* (Clarendon Press - Oxford University Press, Oxford, 1955), 2001 edition I.6.1.1
- Pendry J.B.** “Theory of photoemission”. *Surface Science* **57**, 679 (1976) H.1.4.1
- Perfetti L.**, **Loukakos P.A.**, **Lisowski M.**, **Bovensiepen U.**, **Eisaki H.**, and **Wolf M.** “Ultrafast electron relaxation in superconducting $\text{Bi}_2\text{Sr}_2\text{CaCu}_2\text{O}_{8+d}$ by time-resolved photoelectron spectroscopy”. *Physical Review Letters* **99**, 197001 (2007) 7.1.3
- Pickett W.E.** “Electronic structure of the high-temperature oxide superconductors”. *Reviews of Modern Physics* **61**, 433 (1989) J.1.2.2
- Pietig R.**, **Bulla R.**, and **Blawid S.** “Reentrant Charge Order Transition in the Extended Hubbard Model” **2** (1999) 5.1
- Pignedoli C.**, **Catellani A.**, **Castrucci P.**, **Sgarlata A.**, **Scarselli M.**, **De Crescenzi M.**, and **Bertoni C.** “Carbon induced restructuring of the $\text{Si}(111)$ surface”. *Physical Review B* **69**, 113313 (2004) 3.3, ??, 3.2
- Plakida N.** *High-Temperature Cuprate Superconductors: Experiment, Theory, and Applications* (Springer Verlag, 2010) 7
- Potthoff M.** “Two-site dynamical mean-field theory”. *Physical Review B* **64**, 165114 (2001). 0107502 5.3.3
- Profeta G.**, **Continenza A.**, **Ottaviano L.**, **Mannstadt W.**, and **Freeman A.J.** “Structural and electronic properties of the $\text{Sn}/\text{Si}(111)\text{sq}(3)\text{xsq}(3)\text{R}30^\circ$ surface”. *Physical Review B* **62**, 1556 (2000) 3.3.2, 3.2
- Profeta G.** and **Tosatti E.** “Novel electronically driven surface phase predicted in $\text{C}/\text{Si}(111)$ ”. *Physical Review Letters* **95**, 1 (2005) 3.2
- Profeta G.** and **Tosatti E.** “Triangular Mott-Hubbard insulator phases of $\text{Sn}/\text{Si}(111)$ and $\text{Sn}/\text{Ge}(111)$ surfaces”. *Physical Review Letters* **98**, 1 (2007). 0703181 3.3.2, 3.2
- Punk M.**, **Allais A.**, and **Sachdev S.** “A quantum dimer model for the pseudogap metal” (pages 1–12) (2015). arXiv:1501.00978v1 7.2.2.1
- Purcell E.**, **Torrey H.**, and **Pound R.** “Resonance Absorption by Nuclear Magnetic Moments in a Solid”. *Physical Review* **69**, 37 (1946) H.2.2
- Quenouille M.H.** “Problems in plane sampling”. *The Annals of Mathematical Statistics* **20**, 355 (1949) 10.3.1.1, 10.3.4

- Rabi I., Zacharias J., Millman S., and Kusch P.** “A New Method of Measuring Nuclear magnetic Moment”. *Physical Review* **53**, 318 (1937) H.2.2
- Rech J., Pépin C., and Chubukov A.** “Quantum critical behavior in itinerant electron systems: Eliashberg theory and instability of a ferromagnetic quantum critical point”. *Physical Review B* **74**, 195126 (2006) 7.2.1.1
- Rohringer G., Valli A., and Toschi A.** “Local electronic correlation at the two-particle level”. *Physical Review B* **86**, 125114 (2012) G.4
- Rossat-Mignod J., Regnault L.P., Vettier C., Bourges P., Burllet P., Bossy J., Henry J.Y., and Lapertot G.** “Neutron scattering study of the YBa₂Cu₃O_{6+x} system”. *Physica C: Superconductivity* **189**, 86 (1991) 7.4
- Rozenberg M.J., Kotliar G., Kajueter H., Thomas G.A., Rapkine D.H., Honig J.M., and Metcalf P.** “Optical conductivity in Mott-Hubbard systems”. *Physical Review Letters* **75**, 105 (1995). 9507002 H.6
- Rubtsov A.N., Katsnelson M.I., and Lichtenstein A.I.** “Dual fermion approach to nonlocal correlations in the Hubbard model”. *Physical Review B* **77**, 033101 (2008). 0612196 7.2.3, 8.1.1, G.4
- Rubtsov A.N., Katsnelson M.I., and Lichtenstein A.I.** “Dual boson approach to collective excitations in correlated fermionic systems”. *Annals of Physics* **327**, 1320 (2012). 1105.6158 7.2.3, 8.1.1, G.4
- Rubtsov A.N., Savkin V.V., and Lichtenstein A.I.** “Continuous Time Quantum Monte Carlo method for fermions”. *Physical Review B* **72**, 035122 (2005). 0411344 11
- Santoro G., Scandolo S., and Tosatti E.** “Charge density waves and surface Mott insulators for ad-layer structures on semiconductors: extended Hubbard modeling”. *Physical Review B* **59**, 1891 (1998). 9809016 3.3.2, 3.2, I.6.2.2
- Scalapino D.J., Loh E., and Hirsch J.E.** “D-wave pairing near a spin-density-wave instability”. *Physical Review B* **34**, 8190 (1986) 7.2.1, 7.2.1.2
- Scalapino D.J., Loh E., and Hirsch J.E.** “Fermi-surface instabilities and superconducting d-wave pairing”. *Physical Review B* **35**, 6694 (1987) 7.2.1, 7.2.1.2
- Schäfer T., Geles F., Rost D., Rohringer G., Arrigoni E., Held K., Blümer N., Aichhorn M., and Toschi A.** “Fate of the false Mott-Hubbard transition in two dimensions”. *Physical Review B* **91**, 125109 (2015a). 1405.7250 7.14, G.4, G.4.1.2
- Schäfer T., Toschi A., and Tomczak J.M.** “Separability of dynamical and nonlocal correlations in three dimensions”. *Physical Review B* **91**, 1 (2015b) G.4.1.2
- Schmalian J., Pines D., and Stojković B.** “Weak pseudogap behavior in the underdoped cuprate superconductors”. *Physical Review Letters* **80**, 3839 (1998) 7.2.1.1
- Schnatterly S.E.** “Inelastic Electron Scattering Spectroscopy”. In H. Ehrenreich, F. Seitz, and D. Turnbull, editors, “Solid State Physics, Advances in Research and Applications”, (pages 275–340) (Academic Press, New York, 1979) H.1.2
- Schrieffer J.R., Wen X.G., and Zhang S.C.** “Dynamic spin fluctuations and the bag mechanism of high-T_c superconductivity”. *Physical Review B* **39**, 11663 (1989) 7.2.1
- Schrieffer J.R. and Wolff P.A.** “Relation between the Anderson and Kondo Hamiltonians”. *Physical Review* **149**, 491 (1966) 11.1.4.2.2
- Schulz H.** “Effective action for strongly correlated fermions from functional integrals”. *Physical review letters* **65**, 2462 (1990) 8.3.1.3
- Schumann R. and Heiner E.** “Transformations of the Hubbard interaction to quadratic forms”. *Physics Letters A* **134**, 202 (1988) 8.3.1.3
- Schuwalow S., Grieger D., and Lechermann F.** “Realistic modeling of the electronic structure and the effect of correlations for Sn/Si(111) and Sn/Ge(111) surfaces”. *Physical Review B* **82**, 035116 (2010) 3.3.2, 3.2, 4.2
- Sénéchal D., Tremblay A.M.S., and Bourbonnais C.** *Theoretical Methods for Strongly Correlated Electrons* (Springer Verlag, 2003) 2
- Sengupta A.M. and Georges A.** “Non-Fermi-liquid behavior near a T=0 spin-glass transition”. *Physical Review B* **52**, 10295 (1995) 1.2, 5.1, 5.1.1

- Shao J. and Tu D.** *The Jackknife and Bootstrap* (Springer Verlag, 1995) 10.3.4
- Shastry B.S.** “t-J model and nuclear magnetic relaxation in high- T_c materials”. *Physical Review Letters* **63**, 1288 (1989) H.2.2.3
- Shen K.M., Ronning F., Lu D.H., Baumberger F., Ingle N.J.C., Lee W.S., Meevasana W., Kohsaka Y., Azuma M., Takano M., Takagi H., and Shen Z.X.** “Nodal quasiparticles and antinodal charge ordering in $\text{Ca}_{2-x}\text{NaxCuO}_2\text{Cl}_2$.” *Science* **307**, 901 (2005) 7.7
- Shinaoka H., Sakuma R., Troyer M., and Werner P.** “Accuracy of downfolding based on the constrained random phase approximation” (pages 1–13) (2014). arXiv:1410.1276v1 J.3.3
- Si Q. and Smith J.L.** “Kosterlitz-Thouless Transition and Short Range Spatial Correlations in an Extended Hubbard Model”. *Physical Review Letters* **77**, 3391 (1996). 9606087 1.2, 5.1, 5.1.1
- Sigrist M. and Ueda K.** “Phenomenological theory of unconventional superconductivity”. *Reviews of Modern Physics* **63**, 239 (1991) H.2.2.3
- Slater J.C.** “Magnetic effects and the Hartree-Fock equation”. *Physical Review* **82**, 538 (1951) I.6.2.3
- Slezak J., Mutombo P., and Cha V.** “STM study of a Pb/Si(111) interface at room and low temperatures”. *Physical Review B* **60**, 328 (1999) ??, 3.2
- Slichter C.P.** *Principles of magnetic resonance* (Springer Verlag, Berlin Heidelberg, 1989), 3rd edition H.2.2
- Squires G.L.** *the Theory of Thermal Neutron Scattering Thermal Neutron* (Dover, Mineola, New York, 1997) H.2.1
- Sun P. and Kotliar G.** “Extended dynamical mean-field theory and GW method”. *Physical Review B* **66**, 085120 (2002) 5.1.2, 5.2, 5.2.2
- Sun P. and Kotliar G.** “Many-body approximation scheme beyond GW”. *Physical Review Letters* **92**, 196402 (2004). 0312303v2 1.2, 5.2
- Tam K.M., Fotso H., Yang S.X., Lee T.W., Moreno J., Ramanujam J., and Jarrell M.** “Solving the parquet equations for the Hubbard model beyond weak coupling”. *Physical Review E* **87**, 1 (2013). 1108.4926 G.1.4
- Taranto C., Andergassen S., Bauer J., Held K., Katanin A., Metzner W., Rohringer G., and Toschi A.** “From Infinite to Two Dimensions through the Functional Renormalization Group”. *Physical Review Letters* **112**, 196402 (2014) G.4
- Tersoff J. and Hamann D.R.** “Theory of the scanning tunneling microscope”. *Physical Review B* **31**, 805 (1985) H.1.3, H.1.3.2
- Tomczak J.M.** *Spectral and Optical Properties of Correlated Materials*. Ph.D. thesis, Ecole Polytechnique (2007) H.2.3
- Tomczak J.M., Casula M., Miyake T., Aryasetiawan F., and Biermann S.** “Combined GW and dynamical mean-field theory: Dynamical screening effects in transition metal oxides”. *EPL (Europhysics Letters)* **100**, 67001 (2012a) 12.2.1
- Tomczak J.M., Casula M., Miyake T., and Biermann S.** “Asymmetry in band widening and quasiparticle lifetimes in SrVO_3 : Competition between screened exchange and local correlations from combined GW and dynamical mean-field theory GW+DMFT”. *Physical Review B* **90**, 165138 (2014) 12.2.1, 12.2.1, 12.2.2
- Tomczak J.M., van Schilfgaarde M., and Kotliar G.** “Many-body effects in iron pnictides and chalcogenides: Nonlocal versus dynamic origin of effective masses”. *Physical Review Letters* **109**, 1 (2012b). 1209.2213 12.2.2
- Tosatti E. and Anderson P.W.** “Charge and Spin Density Waves on Semiconductor Surfaces”. *Japanese Journal of Applied Physics Supplement* **2**, 381 (1974) 3.1, I.6
- Toschi A., Katanin A., and Held K.** “Dynamical vertex approximation: A step beyond dynamical mean-field theory”. *Physical Review B* **75**, 045118 (2007) 8.1.1, G.4.1, G.4.1, G.4.1.1, G.4.1.1
- Tranquada J.M., Sternlieb B.J., Axe J.D., Nakamura Y., and Uchida S.** “Evidence for stripe correlations of spins and holes in copper oxide superconductors” (1995) 7.1.1, 7.1.2.4
- Tremblay A.M.S.** “Two-Particle-Self-Consistent Approach for the Hubbard Model”. In “Theoretical

- methods for Strongly Correlated Systems”, (2011). arXiv:1107.1534v2 G.3
- Uchida S., Ido T., Takagi H., Arima T., Tokura Y., and Tajima S.** “Optical spectra of $\text{La}_{2-x}\text{Sr}_x\text{CuO}_4$: Effect of carrier doping on the electronic structure of the CuO_2 plane”. *Physical Review B* **43**, 7942 (1991) 7.6
- Uhrberg R. and Balasubramanian T.** “Electronic Structure of the $\sqrt{3} \times \sqrt{3}$ and 3×3 Periodicities of $\text{Sn/Ge}(111)$ ”. *Physical Review Letters* **81**, 2108 (1998) 3.2, ??
- Uhrberg R., Zhang H., Balasubramanian T., Jemander S., Lin N., and Hansson G.** “Electronic structure of $\text{Sn/Si}(111)$ $\sqrt{3} \times \sqrt{3}$: Indications of a low-temperature phase”. *Physical Review B* **62**, 8082 (2000a) ??, 3.2, 6.3
- Uhrberg R.I.G., Zhang H.M., and Balasubramanian T.** “Determination of the Sn 4d line shape of the $\text{Sn/Ge}(111)$ $\sqrt{3} \times \sqrt{3}$ and 3×3 surfaces”. *Physical Review Letters* **85**, 1036 (2000b) 3.2, ??
- Vaknin D., Sinha S.K., Moncton D.E., Johnston D.C., Newsam J.M., Safinya C.R., and King H.E.** “Antiferromagnetism in $\text{La}_2\text{CuO}_{4-y}$ ”. *Physical Review Letters* **58**, 2802 (1987) 7.1.2.1, 7.4
- Valli A., Schäfer T., Thunström P., Rohringer G., Andergassen S., Sangiovanni G., Held K., and Toschi A.** “Dynamical vertex approximation in its parquet implementation: Application to Hubbard nanorings”. *Physical Review B* **91**, 115115 (2015). arXiv:1410.4733v1 8.1.3, G.4.1
- van Hove L.** “Correlations in Space and Time and Born Approximation in Systems of Interacting Particles”. *Phys. Rev.* **93**, 249 (1954) H.1.2
- van Roekeghem A.** *Electronic Coulomb Correlations in Transition Metal Pnictides*. Ph.D. thesis, Ecole Polytechnique (2014) 12, 12.2.2.1, J.2.1
- van Roekeghem A., Ayrat T., Tomczak J.M., Casula M., Xu N., Ding H., Ferrero M., Parcollet O., Jiang H., and Biermann S.** “Dynamical Correlations and Screened Exchange on the Experimental Bench: Spectral Properties of the Cobalt Pnictide BaCo_2As_2 ”. *Physical Review Letters* **113**, 266403 (2014). 1408.3136 (document), 1.3, 12, 12.2.2, 12.2.2.2, R.2
- van Roekeghem A. and Biermann S.** “Screened exchange dynamical mean-field theory and its relation to density functional theory: SrVO_3 and SrTiO_3 ”. *EPL (Europhysics Letters)* **108**, 57003 (2014) 12.2.2.2
- van Roekeghem A., Richard P., Shi X., Wu S., Zeng L., Ohtsubo Y., Qian T., Sefat A.S., Biermann S., and Ding H.** “Tetragonal and collapsed-tetragonal phases of CaFe_2As_2 - a view from angle-resolved photoemission and dynamical mean field theory”. arXiv (2015). 1505.00753v1 12.2.2.2
- Varma C.M.** “Pseudogap Phase and the Quantum-Critical Point in Copper-Oxide Metals”. *Physical Review Letters* **83**, 3538 (1999). 9905100 7.2
- Varma C.M., Littlewood P.B., Schmitt-Rink S., Abrahams E., and Ruckenstein A.E.** “Phenomenology of the normal state of Cu-O high-temperature superconductors”. *Physical Review Letters* **63**, 1996 (1989) 7.2
- Vaugier L.** *Electronic Structure of Correlated Materials from First Principles: Hubbard interaction and Hund’s exchange*. Ph.D. thesis, Ecole Polytechnique (2011) J.3
- Vaugier L., Jiang H., and Biermann S.** “Hubbard U and Hund exchange J in transition metal oxides: Screening versus localization trends from constrained random phase approximation”. *Physical Review B* **86**, 165105 (2012) J.3.4
- Verwey E.J.W. and de Boer J.H.** “Cation arrangement in a few oxides with crystal structures of the spinel type”. *Recueil des Travaux Chimiques des Pays-Bas* **55**, 531 (1936) 2.1.1
- Vidberg H.J. and Serene J.W.** “Solving the Eliashberg equations by means of N-point Padé approximants”. *Journal of Low Temperature Physics* **29**, 179 (1977) I.3.1
- Vilk Y., Chen L., and Tremblay A.M.S.** “Theory of spin and charge fluctuations in the Hubbard model”. *Physical Review B* **49**, 0 (1994) G.3
- Vilk Y. and Tremblay A.M.S.** “Non-perturbative many-body approach to the hubbard model and single-particle pseudogap”. *Journal de Physique I* (pages 1–49) (1997). 9702188v3 9.5, G.3, G.2

- Vučičević J., Terletska H., Tanasković D., and Dobrosavljević V.** “Finite-temperature crossover and the quantum Widom line near the Mott transition”. *Physical Review B* **88**, 075143 (2013) 2.2
- Wang Y., Agterberg D.F., and Chubukov A.** “Interplay between pair- and charge-density-wave orders in underdoped cuprates”. *Physical Review B* **91**, 115103 (2015) 7.1.1
- Weiss P.** “L’hypothèse du champ moléculaire et la propriété ferromagnétique”. *Journal de Physique Théorique et Appliquée* **6**, 661 (1907) 2.2.1
- Weller M.** *NMR / NQR studies at very low temperatures and high pressures in strongly correlated*. Ph.D. thesis, ETH Zürich (2008) H.2.2
- Werner P., Comanac A., de’ Medici L., Troyer M., and Millis A.** “Continuous-Time Solver for Quantum Impurity Models”. *Physical Review Letters* **97**, 076405 (2006) 11
- Werner P., Gull E., Parcollet O., and Millis A.J.** “Momentum-selective metal-insulator transition in the two-dimensional Hubbard model: An 8-site dynamical cluster approximation study”. *Physical Review B* **80**, 045120 (2009) 7.2.2.2.2
- Werner P. and Millis A.** “Efficient Dynamical Mean Field Simulation of the Holstein-Hubbard Model”. *Physical Review Letters* **99**, 146404 (2007) 11.1.1
- Wood E.A.** “Vocabulary of surface crystallography”. *Journal of Applied Physics* **35**, 1306 (1964) 3.1
- Wu M.K., Ashburn J.R., Torng C.J., Hor P.H., Meng R.L., Gao L., Huang Z.J., Wang Y.Q., and Chu C.W.** “Superconductivity at 93 K in a new mixed-phase Yb-Ba-Cu-O compound system at ambient pressure”. *Physical Review Letters* **58**, 908 (1987) 7.1.1
- Wu T., Mayaffre H., Mer S.K.A., Cacute M.H., Berthier C., Kuhns P.L., Reyes A.P., Liang R., Hardy W.N., Bonn D.A., and Julien M.H.** “Emergence of charge order from the vortex state of a high-temperature superconductor”. *Nature Communications* **4**, 1 (2013). 1307.2049 7.1.1
- Yamada K., Kakurai K., Endoh Y., Thurston T., Kastner M., Birgeneau R., Shirane G., Hidaka Y., and Murakami T.** “Spin dynamics in the two-dimensional quantum antiferromagnet La₂CuO₄”. *Physical Review B* **40**, 4557 (1989) 7.1.2.1, 7.4
- Yang S.X., Fotso H., Liu J., Maier T.A., Tomko K., D’Azevedo E.F., Scalettar R.T., Pruschke T., and Jarrell M.** “Parquet approximation for the 4x4 Hubbard cluster”. *Physical Review E* **80**, 2 (2009). 0906.4736 G.1.4
- Yoo J., Chandrasekharan S., Kaul R.K., Ullmo D., and Baranger H.U.** “On the Sign Problem in the Hirsch-Fye Algorithm for Impurity Problems”. *Journal of Physics A: Mathematical and General* **38**, 10307 (2005). 0412771 11.1.3.2
- Zaanen J., Sawatzky G.A., and Allen J.W.** “Band gaps and electronic structure of transition-metal compounds”. *Physical Review Letters* **55**, 418 (1985) 7.1.1
- Zhang F.C., Gros C., Rice T.M., and Shiba H.** “A renormalised hamiltonian approach for a resonant valence bond wavefunction”. *Supercond. Sci. Technol.* (pages 36–46) (1988). 0311604 7.2.2.1
- Zhang F.C. and Rice T.M.** “Effective Hamiltonian for the superconducting Cu oxides”. *Physical Review B* **37**, 3759 (1988) 7.1.1

Part X

Publications



EDMDT and $GW + \text{EDMFT}$ applied to the
extended Hubbard model on the square and cubic
lattices

O.1 Paper 1: Ayrat *et al.* (2012)

Spectral Properties of Correlated Materials: Local Vertex and Nonlocal Two-Particle Correlations from Combined *GW* and Dynamical Mean Field Theory

Thomas Ayrál,^{1,2,3} Philipp Werner,^{4,1} and Silke Biermann^{2,5}

¹*Theoretical Physics, ETH Zurich, 8093 Zürich, Switzerland*

²*Centre de Physique Théorique, Ecole Polytechnique, CNRS UMR7644, 91128 Palaiseau Cedex, France*

³*Institut de Physique Théorique (IPhT), CEA, CNRS, URA 2306, 91191 Gif-sur-Yvette, France*

⁴*Department of Physics, University of Fribourg, 1700 Fribourg, Switzerland*

⁵*Japan Science and Technology Agency, CREST, Kawaguchi 332-0012, Japan*

(Received 21 May 2012; published 28 November 2012)

We present a fully self-consistent combined *GW* and dynamical mean field (DMFT) study of the extended two-dimensional Hubbard model. The inclusion of the local dynamical vertex stemming from the DMFT self-energy and polarization is shown to cure the known problems of self-consistent *GW*. We calculate momentum-resolved spectral functions, two-particle polarizations, and electron-loss spectra, as well as the effective dynamical interaction induced by nonlocal screening. The momentum-dependence introduced by *GW* into the extended DMFT description leads to a narrowing of the quasiparticle width and more pronounced Hubbard bands in the metallic regime as one approaches the charge-ordering transition. It further affects the shape of collective modes, giving rise to dispersive plasmon-like long-wavelength and stripe modes.

DOI: 10.1103/PhysRevLett.109.226401

PACS numbers: 71.27.+a, 72.15.Qm, 75.20.Hr

Modern spectroscopic techniques are able to measure one- and two-particle spectra of condensed matter systems with remarkable precision, characterizing not only quasiparticle excitations but unveiling also satellite structures. Examples include Hubbard bands in photoemission spectroscopy, stemming from the atomic-like behavior of the electrons in partially filled narrow *d* or *f* shells [1], or collective excitations such as plasmonic features. Addressing such effects requires an accurate description of one- and two-particle spectral functions within the framework of many-body theory. The quantitative prediction of satellite features has even been used as a quality marker for many-body techniques. The failure of self-consistent perturbation theory in the screened Coulomb interaction, the self-consistent *GW* approximation, to describe plasmon satellites in the electron gas, for example, has provided arguments in favor of a non-self-consistent (“one-shot *GW*”) treatment [2–4]. For real solids, few fully self-consistent calculations are available [5,6], and no consensus concerning the virtues of self-consistency has been reached so far. A popular scheme, dubbed quasiparticle self-consistent (QPSC) *GW* [7] yields reasonable estimates both for total energies and spectra. Yet, most of the calculations within this scheme were applied to semiconductors, and applications to correlated metals only start to appear [8]. The inclusion of an appropriate vertex correction is expected to resolve the ambiguities around the self-consistency question, and it has been in particular proposed that a combined *GW* and dynamical mean field scheme [9] would enable self-consistent calculations even for spectral properties. Early pioneering calculations on a three-dimensional extended Hubbard model [10,11] have

benchmarked several flavors of combined schemes along these lines. However, the numerical difficulty of solving the DMFT equations with frequency-dependent interactions has until now prevented the direct investigation of spectral properties.

Implementing the *GW* + DMFT scheme in a fully self-consistent manner for the two-dimensional extended Hubbard model, we here demonstrate that this technique indeed successfully overcomes the deficiencies of *GW*. The implicit inclusion of a nonperturbative local vertex enables fully self-consistent calculations for spectral properties. In the correlated metal regime, the *GW* + DMFT self-energy encodes both band renormalization effects and Hubbard satellite features. The theory also describes the Mott insulating state for strong local Coulomb interaction, which is inaccessible in *GW* alone, as well as the charge-ordered state driven by intersite interactions, absent from standard DMFT. We calculate the effective local interaction, containing the dynamical screening from nonlocal processes, and demonstrate how these give rise to plasmonic features in the local spectral function. Close to the charge-ordering transition, the nonlocal self-energy contributions stemming from *GW* lead to a considerable enhancement of quasiparticle weights. We analyze momentum-resolved two-particle spectra and show that the self-consistent combination of *GW* and *extended* dynamical mean field theory (EDMFT) strongly affects the shape of collective modes, giving rise to dispersive plasmon-like long-wavelength modes and stripe modes.

We consider the half-filled extended Hubbard model on a two-dimensional square lattice,

$$H = -t \sum_{i \neq j, \sigma} c_{i\sigma}^\dagger c_{j\sigma} + \sum_i (U n_{i\uparrow} n_{i\downarrow} - \mu n_i) + \frac{V}{2} \sum_{i \neq j} n_i n_j,$$

where $c_{i\sigma}$ and $c_{i\sigma}^\dagger$ denote the annihilation and creation operators of a particle of spin $\sigma = \uparrow, \downarrow$ at the lattice site i , $n_{i\sigma} = c_{i\sigma}^\dagger c_{i\sigma}$, and $n_i = n_{i\uparrow} + n_{i\downarrow}$. $\sum_{i \neq j}$ is the sum over all nearest-neighbor sites, $t > 0$ is the hopping amplitude between two neighboring sites, μ is the chemical potential, U the on-site repulsion between electrons of opposite spin and V the repulsion between two electrons on neighboring sites. The Fourier-transformed bare interaction term thus reads $v_k = U + 2V[\cos(k_x) + \cos(k_y)]$. All energies are given in units of the half-bandwidth $D = 4t$. We show results for inverse temperature $\beta D = 100$, restricting our study to the paramagnetic phase.

The $GW + DMFT$ approach is derivable from a free energy functional [12]. The Legendre transform of the free energy with respect to the Green's function G and the screened interaction W [13] can be expressed as a sum of the Hartree-Fock part and a Luttinger-Ward-like correlation functional $\Psi[G, W]$, which sums up all skeleton diagrams built from G and W [14]. The $GW + DMFT$ scheme consists in approximating Ψ as $\Psi \approx \Psi^{\text{EDMFT}}[G_{ii}, W_{ii}] + \Psi_{\text{nonloc}}^{\text{GW}}[G_{ij}, W_{ij}]$, where the first term is calculated from a (dynamical) impurity problem as in EDMFT [15–17] and the second term is the nonlocal ($i \neq j$) part of the GW functional $\Psi_{\text{nonloc}}^{\text{GW}}[G_{ij}, W_{ij}] = -\sum_{i,j} G_{ij} W_{ij} G_{ji} + \sum_i G_{ii} W_{ii} G_{ii}$.

The $GW + DMFT$ scheme self-consistently constructs the Green's function G and the screened interaction W of the system as a stationary point of the free energy functional. The self-energy Σ and polarization P are formally obtained by functional differentiation of Ψ with respect to G and W , leading to the expressions $\Sigma(k, i\omega) = \Sigma_{\text{imp}}(i\omega_n) + \Sigma_{\text{nonloc}}^{\text{GW}}(k, i\omega)$ and $P(k, i\nu_n) = P_{\text{imp}}(i\nu_n) + P_{\text{nonloc}}^{\text{GW}}(k, i\nu_n)$ (ω_n and ν_n are fermionic and bosonic Matsubara frequencies, respectively). This endows $GW + DMFT$ with conserving properties [18]. The momentum-dependent G and W are then calculated from the one- and two-particle Dyson equations and used as inputs for a GW calculation, yielding $\Sigma^{\text{GW}} = -G \cdot W$ and $P^{\text{GW}} = 2G \cdot G$ (the dot denotes a convolution in frequency-momentum space and the factor 2 comes from the spin degeneracy). Their local parts are extracted to compute the local Weiss fields \mathcal{G} and \mathcal{U} : $\mathcal{G}^{-1}(i\omega_n) = G_{\text{loc}}^{-1}(i\omega_n) + \Sigma_{\text{imp}}(i\omega_n)$ and $\mathcal{U}^{-1}(i\nu_n) = W_{\text{loc}}^{-1}(i\nu_n) + P_{\text{imp}}(i\nu_n)$. These, in turn, are used as inputs to a dynamical impurity model, which we solve using a continuous-time Monte Carlo algorithm [19,20] to obtain updated local self-energies. The whole scheme, summarized in Fig. 1, is iterated until convergence. The calculations have been performed on a 64×64 momentum grid, while the analytical continuation of the imaginary-time data has been performed using the maximum entropy method [21] in the spirit of Ref. [22]. We monitor the following quantities:

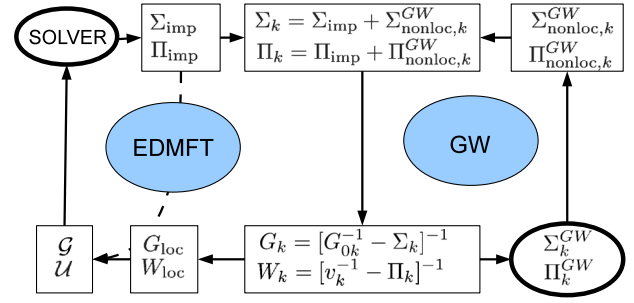


FIG. 1 (color online). Flow chart of the $GW + DMFT$ scheme.

(i) the local spectral function $A_{\text{loc}}(\omega) = -\frac{1}{\pi} \text{Im} G_{\text{loc}}(\omega)$, (ii) the momentum-resolved spectral function, (iii) the electron energy-loss spectrum (EELS) $\text{Im}[-\epsilon(k, \omega)^{-1}]$ [where $\epsilon(k, \omega) = 1 - v_k P(k, \omega)$ is the dielectric function], and (iv) the effective dynamical interaction \mathcal{U} , which takes into account screening processes induced by V .

Within extended DMFT and $GW + DMFT$, in the absence of intersite repulsion, the Mott transition takes place at $U_c \approx 2.5$. This value is slightly modified by intersite repulsions $V < V_c = 0.8$. At V_c a transition to a charge-ordered phase occurs [23]. In the following we study the local spectral properties in the metallic phase with weak ($U = 0.5$, $V = 0.1$) and intermediate ($U = 2$, $V = 0.4$) interactions, as well as in the Mott insulator at $U = 3.5$ and $V = 3$. Figure 2 shows the local spectral function $A_{\text{loc}}(\omega)$ obtained within (i) (self-consistent) EDMFT, (ii) self-consistent $GW + DMFT$ (iii) self-consistent GW , and (iv) QPSC GW . The latter scheme was implemented by computing the lattice Green's function from the GW self-energy via $G(k, i\omega_n)^{-1} = i\omega_n - Z_k[\epsilon_k - \text{Re}\Sigma_{\text{GW}}(k, i\omega_0)]$, where $Z_k \approx (1 - \text{Im}\Sigma_{\text{GW}}(k, i\omega_0)/\omega_0)^{-1}$ is the quasiparticle weight as estimated from the value of the self-energy at the first

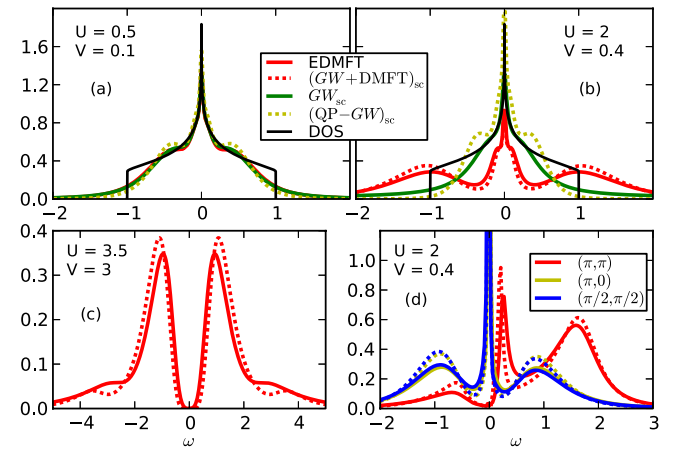


FIG. 2 (color online). Panels (a) to (c): spectral function $A_{\text{loc}}(\omega)$ obtained within different self-consistent schemes (see text). Panel (d): spectral function at selected k points (solid line: EDMFT; dotted line: $GW + DMFT$).

Matsubara frequency. For small interactions [panel 2(a)], correlation effects are negligible, and the four schemes result in indistinguishable spectra within the numerical accuracy. As the local interaction U becomes significant [panel 2(b)], the width of the coherent central peak shrinks, and the corresponding spectral weight is transferred to higher energies. This (physically expected) behavior is realized by the EDMFT and $GW + DMFT$ spectra, which exhibit higher-energy structures at $\omega \approx \pm U/2$. These Hubbard bands gain spectral weight as U increases further. The (integrated) quasiparticle weight Z goes from 0.44 (0.32) at $U = 1.5$, $V = 0.4$ for EDMFT ($GW + DMFT$) to 0.21 (0.12) at $U = 2$, $V = 0.4$. At $U = 3.5$, a Mott gap has opened, and the EDMFT and $GW + DMFT$ spectra are similar [panel 2(c)]. In addition to the two Hubbard bands, the EDMFT and $GW + DMFT$ spectra display two symmetric high-energy satellites, whose spectral weight depends on the intersite interaction V . The QPSC GW spectra display only a weak renormalization of the bandwidth as U increases from the weak to the strong coupling limit, and at all correlation levels the spectra remain metallic. The same is true within the self-consistent GW method (where the quasiparticle weight goes from 0.74 at $U = 1.5$, $V = 0.4$ to 0.67 at $U = 2$, $V = 0.4$). Here, with increasing correlations, some spectral weight is shifted to higher frequencies, albeit in a featureless way.

These observations show that both self-consistent GW approaches yield a correct result only in the weak-correlation regime. As correlations increase, GW fails to describe the shift of spectral weight to high-energy incoherent bands, present in DMFT. We note that in the local $GW + DMFT$ spectra the Hubbard bands are enhanced compared to the EDMFT or GW spectra. This effect can be ascribed to the self-consistency, which allows the local quantities to readjust to the nonlocal self-energies Σ_{GW} and P_{GW} .

EDMFT and $GW + DMFT$ spectra exhibit high-energy satellites in the Mott phase, which reflect the frequency dependence of the local interaction $\mathcal{U}(\omega)$ induced by the nearest-neighbor repulsion term V . The real part of this interaction is shown for the metallic phase in panel (c) of Figure 3. A sharp pole in $\mathcal{U}(\omega)$ (such as a plasmon pole) leads to multiple satellites in the local spectral function [22]. In our case, the $\mathcal{U}(\omega)$ are characterized by a broad continuum of poles centered at some energy ω_d , resulting in only two symmetric satellites in the Mott spectra [see Fig. 2(c)]. In the metallic phase, these satellites are present, but they are broad and merged with the Hubbard bands, making them hardly distinguishable.

The failure of both self-consistent GW schemes to capture Hubbard bands or high-energy satellites is consistent with the well-known observation that self-consistency in GW for the homogeneous electron gas results in a smearing out and displacement of high energy satellite features [3]. In light of this observation, most modern GW schemes

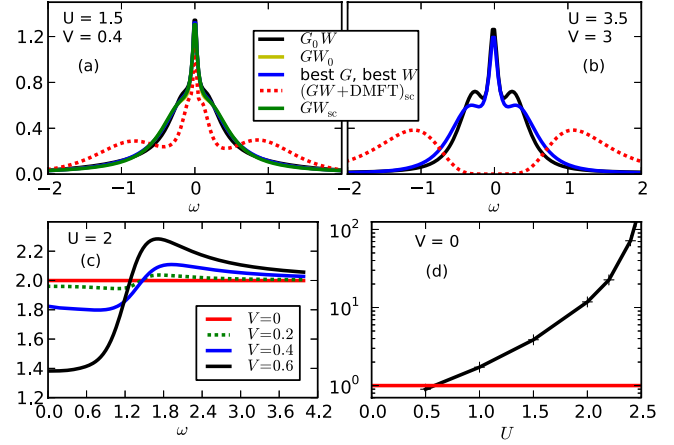


FIG. 3 (color online). Panels (a) and (b): Spectral function $A_{\text{loc}}(\omega)$ obtained using 3 different one-shot GW schemes (see text). Panel (c): $\text{Re}\mathcal{U}(\omega)$ obtained from EDMFT for different values of V . Panel (d): vertex estimate $\Lambda(\omega = 0)$ as a function of U .

therefore adopt a “best- G -best- W ” strategy, rather than aiming at full self-consistency. Figure 3 illustrates the virtues and limitations of this strategy by displaying the spectra obtained in different one-shot GW schemes: (i) in “ G_0W ,” the noninteracting Green’s function G_0 and the converged $GW + DMFT$ W are taken as inputs to a one-shot GW calculation, (ii) “ GW_0 ” takes the converged $GW + DMFT$ G and $W_0 = v(1 - vG_0G_0)^{-1}$ evaluated within the random-phase approximation as inputs and (iii) “best G , best W ” takes the converged $GW + DMFT$ G and W as inputs. At all correlation levels ($U = 1.5$ to $U = 3.5$), these three GW schemes produce results very similar to self-consistent GW . In particular, they remain metallic [at $U = 0.5$ (not shown), they are completely identical]. In the Mott phase ($U = 3.5$), even the “best G , best W ” scheme yields a metallic self-energy, despite the Mott-like character of the input G and W . This phenomenon is due to the lack of Hedin’s three-legged vertex Λ in GW schemes, as shown in Fig. 3(d). There, an estimate of the local part of Λ is computed from EDMFT results at $V = 0$. Remembering that, schematically, the irreducible vertex function Λ appears in the self-energy as $\Sigma = G\mathcal{W}\Lambda$ [2], a rough estimate—neglecting the true frequency structure—is computed as follows: one computes an effectively vertex-corrected screened interaction $\tilde{W}(\tau) = \Sigma_{\text{imp}}(\tau)/G_{\text{imp}}(\tau)$ from EDMFT, then Fourier transforms it to $\tilde{W}(i\nu_n)$; finally, the static vertex estimate is obtained as $\Lambda(0) \approx \tilde{W}(i\nu_0)/W_{\text{loc}}(i\nu_0)$. Crude as it is (the full vertex depends on two independent frequencies), this estimate nonetheless clearly demonstrates the role of vertex corrections for the Mott transition: from unity in the weakly correlated regime, it increases with U until it diverges at the Mott transition. This indicates that within the language of Hedin’s equations, the divergence of the local vertex is the driving force of the Mott

phenomenon, making any vertexless approximation unfit to capture it.

The effect of the nonlocal GW contributions on EDMFT are illustrated by the momentum-resolved spectral functions, displayed in Fig. 2(d). In the presence of a strong intersite interaction, the nonlocal self-energy and polarization lead to a k -dependent modulation of the linewidth and weights. Compared to EDMFT, the $GW + DMFT$ spectra display a strong sharpening of the quasiparticle peak along with an enhanced weight of the Hubbard bands. The impact of the GW diagrams becomes very strong on the brink of the charge-ordering transition.

We now turn to a study of two-particle quantities. Figure 4 shows the momentum-resolved imaginary part of the polarization and the electron energy-loss (EELS) spectrum $\text{Im}[-\epsilon^{-1}(k, \omega)]$ in the metallic regime. Within EDMFT, the polarization displays a broad mode which reflects the particle-hole excitations of the system. They are centered at $U/2$, reflecting the emergence of the Hubbard bands and the corresponding excitations between Hubbard bands and the quasiparticle peak. In contrast, the polarization spectrum within $GW + DMFT$ is dispersive. While displaying sharper features close to the $\Gamma \equiv (0, 0)$ point, it captures particle-hole excitations due to Fermi-surface nesting at wave vector (π, π) , as well as the zero-sound mode at long wavelengths and low energies. The EELS spectrum contains the particle-hole excitations (poles of the polarization) of the system and its collective modes, which correspond to the solutions of $\text{Re}P(k, \omega) = 1/v_k$. These collective modes are damped out close to particle-hole excitations [when $\text{Im}P(k, \omega)$ is large]. This analogue of the free-electron-gas Landau damping occurs at the (π, π) point in EDMFT and $GW + DMFT$. It can be directly ascribed to the nearest-neighbor repulsion, which

induces scattering along this direction. The energy and lifetime of this collective excitation differs from EDMFT to $GW + DMFT$. In $GW + DMFT$ it is lower in energy, more dispersive and with a larger lifetime. In $GW + DMFT$, two modes are visible above the $(\pi, 0)$ point, indicating the existence of two stripe modes at energies $\omega = 1$ and $\omega = 2$ corresponding to stripe-like modulations, where the sign of the density fluctuation varies from row to row in the x direction. For obvious reasons, they are not captured by EDMFT. These two-particle excitations are directly related to the screening in the system as the screened interaction, W , is given by $W(k, \omega) = \epsilon^{-1}(k, \omega)v_k$. In particular, they explain the retardation effects in the local interactions $\mathcal{U}(\omega)$ and the corresponding satellites in the local spectra.

In conclusion, based on a fully self-consistent implementation of the combined $GW + DMFT$ scheme, we have analyzed one- and two-particle satellite features in correlated materials. While we confirm the well-known “washing out” of satellite features in self-consistent GW calculations, self-consistent $GW + DMFT$ does not suffer from this deficiency. Plasma- and zero-sound-like oscillations involving itinerant carriers as in the electron gas survive only in the regime of small local Coulomb interactions, but are quickly suppressed in the correlated metal. In this regime, excitations related to the creation of doublons become dominant. The momentum-dependence self-consistently introduced by the GW part becomes crucial when assessing dispersions of two-particle spectral properties, differentiating in particular the nature of the collective modes in the $(0, 0)$, $(0, \pi)$, and (π, π) regions [24]. Our findings have implications for the nature of satellite features in correlated materials. In particular, it becomes obvious that electron-gas-like plasmons in materials stem dominantly from the charge contained in completely filled shells (that is from multiorbital effects), while partially filled shells give rise to doublon excitations of the kind we describe. Concerning the long-term goal of $GW + DMFT$ calculations for realistic systems, the importance of this study is to demonstrate the ability to *calculate* the effective dynamical Coulomb interactions (rather than assuming a Hubbard U parameter) fully from first principles, in a self-consistent manner. Last but not least, the interplay of local correlations and charge-ordering phenomena and their intriguing wave-vector dependence that we evidence in this simple but generic model may already have been observed in two-dimensional materials: recent experimental findings of charge ordering in cuprates [25], cobaltates [26] or in systems of adatoms on surfaces [27] are prominent examples.

We acknowledge useful discussions with F. Aryasetiawan, M. Casula, A. Georges, P. Hansmann, M. Imada, M. Katsnelson, A. Millis, and T. Miyake. This work was supported by the French ANR under project SURMOTT, GENCI/IDRIS Orsay under Project

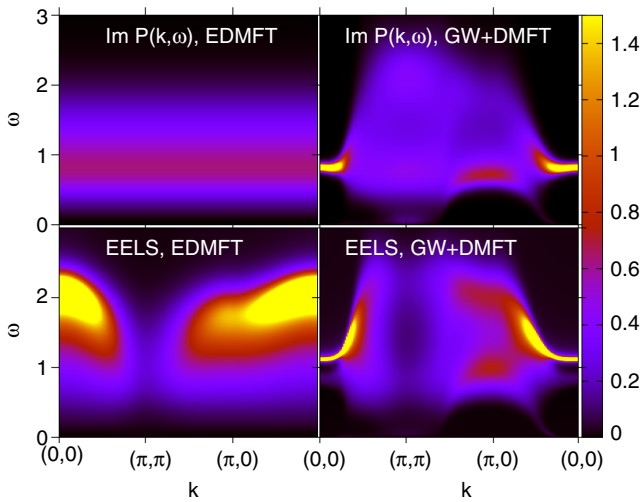


FIG. 4 (color online). $U = 2$, $V = 0.4$. Upper panels: $\text{Im}P(k, \omega)$ within EDMFT (left) and $GW + DMFT$ (right). Lower panels: $-\text{Im}\epsilon^{-1}(k, \omega)$ within EDMFT (left) and $GW + DMFT$ (right).

No. 1393, by DFG FOR 1346 and by the Swiss National Science Foundation (Grant No. PP0022-118866). Most of the calculations have been performed on the Brutus cluster at ETH Zurich, using a code based on ALPS [28]. We thank L. Boehnke for allowing us to use his MaxEnt code.

-
- [1] M. Imada, A. Fujimori, and Y. Tokura, *Rev. Mod. Phys.* **70**, 1039 (1998).
- [2] L. Hedin, *Phys. Rev.* **139**, A796 (1965).
- [3] U. von Barth and B. Holm, *Phys. Rev. B* **54**, 8411 (1996).
- [4] B. Holm and U. von Barth, *Phys. Rev. B* **57**, 2108 (1998).
- [5] W. Ku and A. G. Eguiluz, *Phys. Rev. Lett.* **89**, 126401 (2002).
- [6] A. Kutepov, K. Haule, S. Y. Savrasov, and G. Kotliar, *Phys. Rev. B* **82**, 045105 (2010).
- [7] T. Kotani, M. van Schilfhaarde, and S. V. Faleev, *Phys. Rev. B* **76**, 165106 (2007).
- [8] A. Kutepov, K. Haule, S. Y. Savrasov, and G. Kotliar, *Phys. Rev. B* **85**, 155129 (2012).
- [9] S. Biermann, F. Aryasetiawan, and A. Georges, *Phys. Rev. Lett.* **90**, 086402 (2003).
- [10] P. Sun and G. Kotliar, *Phys. Rev. B* **66**, 085120 (2002).
- [11] P. Sun and G. Kotliar, *Phys. Rev. Lett.* **92**, 196402 (2004).
- [12] S. Biermann, F. Aryasetiawan, and A. Georges, *Physics of Spin in Solids: Materials, Methods, and Applications*, NATO Science Series II (Kluwer Academic Publishers B. V, Dordrecht, Boston, London, 2004), pp. 43–65.
- [13] This bosonic propagator, defined after a Hubbard-Stratonovich decoupling of the whole interaction term, is different from the one discussed in Ref. [10], which stems from the decoupling of the intersite interaction term only. The formulation in terms of W allows us to treat the on-site and the intersite interaction on the same footing.
- [14] C. Almladh, U. von Barth, and R. van Leeuwen, *Int. J. Mod. Phys. B* **13**, 535 (1999).
- [15] A. M. Sengupta and A. Georges, *Phys. Rev. B* **52**, 10295 (1995).
- [16] Q. Si and J. L. Smith, *Phys. Rev. Lett.* **77**, 3391 (1996).
- [17] H. Kajueter, Ph.D. thesis, Rutgers University, New Brunswick, 1996.
- [18] G. Baym, *Phys. Rev.* **127**, 1391 (1962).
- [19] P. Werner and A. J. Millis, *Phys. Rev. Lett.* **99**, 146404 (2007).
- [20] P. Werner and A. J. Millis, *Phys. Rev. Lett.* **104**, 146401 (2010).
- [21] M. Jarrell and J. Gubernatis, *Phys. Rep.* **269**, 133 (1996).
- [22] M. Casula, A. Rubtsov, and S. Biermann, *Phys. Rev. B* **85**, 035115 (2012).
- [23] T. Ayrál, S. Biermann, and P. Werner, arXiv:1210.2712.
- [24] Interestingly, the self-consistency matters: we checked explicitly that a one-shot computation of the momentum-dependent polarization function based on a converged EDMFT Green's function G leads to a notably different result than the self-consistent one.
- [25] T. Wu, H. Mayaffre, S. Kramer, M. Horvatic, W. N. Berthier, Claude and-Hardy, R. Liang, D. A. Bonn, and M.-H. Julien, *Nature (London)* **477**, 191 (2011).
- [26] I. R. Mukhamedshin, H. Alloul, G. Collin, and N. Blanchard, *Phys. Rev. Lett.* **94**, 247602 (2005).
- [27] P. Hansmann, L. Vaugier, and S. Biermann, *J. Phys. Cond. Matt.* (to be published).
- [28] B. Bauer *et al.*, *J. Stat. Mech.* (2011), P05001.

O.2 Paper 2: Ayrat *et al.* (2013)



Screening and nonlocal correlations in the extended Hubbard model from self-consistent combined GW and dynamical mean field theory

Thomas Ayal,^{1,2,3} Silke Biermann,^{2,4} and Philipp Werner^{1,5}

¹*Theoretische Physik, ETH Zurich, 8093 Zürich, Switzerland*

²*Centre de Physique Théorique, Ecole Polytechnique, CNRS-UMR7644, 91128 Palaiseau, France*

³*Institut de Physique Théorique (IPhT), CEA, CNRS, URA 2306, 91191 Gif-sur-Yvette, France*

⁴*Japan Science and Technology Agency, CREST, Kawaguchi 332-0012, Japan*

⁵*Department of Physics, University of Fribourg, 1700 Fribourg, Switzerland*

(Received 25 September 2012; published 29 March 2013)

We describe a recent implementation of the combined GW and dynamical mean field method ($GW + DMFT$) for the two-dimensional Hubbard model with onsite and nearest-neighbor repulsion. We clarify the relation of the $GW + DMFT$ scheme to alternative approaches in the literature, and discuss the corresponding approximations to the free-energy functional of the model. Furthermore, we describe a numerically exact technique for the solution of the $GW + DMFT$ equations, namely, the hybridization expansion continuous-time algorithm for impurity models with retarded interactions. We compute the low-temperature phase diagram of the half-filled extended Hubbard model, addressing the metal-insulator transition at small intersite interactions and the transition to a charge-ordered state for stronger intersite repulsions. $GW + DMFT$ introduces a nontrivial momentum dependence into the many-body self-energy and polarization. We find that the charge fluctuations included in the present approach have a larger impact on the latter than on the former. Finally, within the $GW + DMFT$ framework, as in extended DMFT, the intersite repulsion translates into a frequency dependence of the local effective interaction. We analyze this dependence and show how it affects the local spectral function.

DOI: 10.1103/PhysRevB.87.125149

PACS number(s): 71.10.Fd

I. INTRODUCTION

Understanding the effects of strong electronic correlations in lattice systems remains a challenge in condensed matter physics. The competition between the tendency of electrons to delocalize due to the resulting gain in kinetic energy and localization by the Coulomb interaction gives rise to a panoply of interesting phenomena, ranging from simple mass enhancements in the sense of Landau theory to charge-, spin-, or orbital-ordering phenomena. To reduce the complexity of the problem, while still keeping the main qualitative effects, e.g., of the delocalization-localization transition, one resorts to low-energy effective models such as the Hubbard or Anderson lattice models. The two-dimensional single-band Hubbard Hamiltonian with a static onsite repulsive interaction U , for example, is believed to describe the physics of the high-temperature superconducting cuprates.¹ Charge-ordering transitions can be captured when an additional intersite interaction term, mimicking the longer-range Coulomb interactions, is retained. This motivates the study of the extended Hubbard model, where charge-ordering effects and screening of the local interactions due to the nonlocal ones are included in addition to the pure Hubbard model physics.

In the paramagnetic phase at half-filling, the Hubbard model exhibits a Mott transition from a metal to a Mott insulator whose spectral function is characterized by a gap at the Fermi energy and Hubbard bands corresponding to atomic-like excitations. This behavior is captured by computational schemes such as the dynamical mean field theory (DMFT) (see Refs. 2 and 3 for reviews) and its extensions [C-DMFT,^{4,5} dynamical cluster approximation (DCA),⁶ dual fermions,⁷ dual bosons,⁸ $D\Gamma A$,⁹ DMFT + Σ_k ¹⁰]. A formalism which allows one to treat screening by nonlocal interactions is

extended DMFT (EDMFT).^{11–15} Its combination with the *ab initio* GW approach^{16–18} introduces some momentum dependence into the self-energy, thereby capturing the interplay of screening and nonlocal correlations. This scheme allows for a self-consistent computation of the effective “Hubbard U ” in a solid and in principle a fully parameter-free *ab initio* simulation approach for correlated materials. The idea is to take the local part of the self-energy from the EDMFT calculation and supplement it by the nonlocal component of the GW self-energy. A rigorous functional formulation, which is detailed in Sec. II, puts this theory on the same level of mathematical rigor as, e.g., the functional formulation of Hohenberg-Kohn density functional theory.

Despite these promising perspectives, the technical difficulties associated with the numerical treatment of the frequency-dependent effective interaction have for a long time prevented a self-consistent calculation of spectral properties within $GW + DMFT$, even at the model level. Recent progress, both within approximate schemes¹⁹ and numerically exact Monte Carlo techniques,^{20,21} is currently giving a new impact to the field.^{22–26} In particular, the development of efficient continuous-time Monte Carlo techniques,^{27,28} generalized to dynamical interactions in Refs. 20 and 21, now allows for the fully self-consistent solution of the $GW + DMFT$ equations, with high enough accuracy to also extract spectral properties.

In this paper, we use these state-of-the-art techniques to study an extended Hubbard model with onsite interaction U and nearest-neighbor repulsive interaction V , and explore the interplay of screening and nonlocal correlations. We show that this model, if solved within the EDMFT framework, captures dynamical screening effects related to the nonlocal interaction V , high-energy satellite features in the one-particle spectra

and, for large V , a transition to a charge-ordered state. We then proceed to study how diagrammatic corrections to EDMFT in the form of momentum-dependent GW contributions to the self-energy modify this picture, and compare the results of self-consistent and non-self-consistent implementations.

The paper is organized as follows: In Sec. II, we discuss the model. In particular, we will show how the Hamiltonian formulation of the problem can be recast into an action or functional formulation. We will explicitly construct two flavors of free-energy functionals whose stationary points would give the exact solution of the model, the first one due to Almladh *et al.*²⁹ (see also Ref. 30), the second one constructed by Sun *et al.*¹⁴ In Sec. III, we present different methods of solution: extended DMFT, GW , and combined schemes. We argue that the $GW + DMFT$ formalism can be derived from the Almladh free-energy functional, and discuss the differences to the scheme proposed in Ref. 14. The latter stems from another energy functional, which would correspond to a “GD + SOPT + DMFT” method, where D is the boson propagator associated with screening of the nonlocal interaction only, used in a GW -like fashion, supplemented by second-order perturbation theory (SOPT) for the nonlocal effects of the local interaction and dynamical mean field theory for the local ones. Numerical techniques for the solution of the equations are described in Sec. IV and the computational scheme used in this work is summarized in Sec. V. The results of our study are presented in Sec. VI. Section VII contains a summary of our most important findings, and provides perspectives as to how our work inserts itself into the field.

II. MODEL

A. Hamiltonian formulation

We consider the single-band U - V Hubbard model on a two-dimensional square lattice, defined by the grand-canonical Hamiltonian

$$H = -t \sum_{\langle ij \rangle \sigma} (c_{i\sigma}^\dagger c_{j\sigma} + \text{H.c.}) - \mu \sum_i n_i + U \sum_i n_{i\uparrow} n_{i\downarrow} + V \sum_{\langle ij \rangle} n_i n_j, \quad (1)$$

where $c_{i\sigma}$ and $c_{i\sigma}^\dagger$ denote the annihilation and creation operators of a particle of spin $\sigma = \uparrow, \downarrow$ at the lattice site i , $n_{i\sigma} = c_{i\sigma}^\dagger c_{i\sigma}$, and $n_i = n_{i\uparrow} + n_{i\downarrow}$. $\sum_{\langle ij \rangle}$ denotes the sum over nearest-neighbor bonds, $t > 0$ is the hopping integral between two neighboring sites, μ is the chemical potential, U the onsite interaction between electrons of opposite spin, and V the interaction between two electrons on neighboring sites, irrespective of their spin. The number of nearest neighbors is $z = 2d = 4$, where d is the dimension.

With certain approximations, this model can be derived from first principles, as discussed in Appendix A. The limiting case $V = 0$ corresponds to the conventional Hubbard model.^{31–33} In this study, we will limit ourselves to the paramagnetic phase at half-filling with repulsive interactions $U > 0$ and $V > 0$.

In the limit of large V , the extended Hubbard model has been shown to display a transition to a charge-ordered state characterized by a freezing of charge carriers and a

spatial modulation of the charge density [charge-density wave (CDW)]. This can be explained by a simple energetical argument³⁴ in the strongly correlated regime ($U \gg t$) at half-filling: while for U much larger than V , electrons will lower their energy by arranging themselves one per site to minimize the onsite repulsion, for V much larger than U , electrons will minimize their off-site repulsion by choosing an arrangement such that one sublattice is occupied by two electrons per site while the other is empty, leading to a commensurate charge order. In the metallic phase ($U \ll t$), the effect of V is more easily understood in terms of screening: the charge fluctuations induced by the V term lead to a reduction of the local effective interaction.

The U - V Hubbard model has been studied in a variety of approximations. An early study in the zero-overlap limit ($U/t \gg 1$) has predicted a phase transition between a Mott insulator and a charge-ordered (CO) insulator at $V_c = U/z$ at zero temperature,³⁵ while weak-coupling mean field studies have predicted a transition between antiferromagnetic order (AFM, i.e., commensurate SDW) and charge order (i.e., commensurate CDW) at the same boundary.^{36,37} This has been confirmed by Monte Carlo calculations in two dimensions.³⁸ The $V_c = U/z$ boundary has been shown to hold in the $U/V \rightarrow 0$ limit as well as in the $U/V \rightarrow \infty$ limit by a study at half-filling in the infinite-dimensional limit.³⁹ Higher-order corrections have been considered in Refs. 40 and 41, leading to a renormalization of the critical temperature and order parameter, as well as the prediction of phase separation in the zero-temperature limit. More recently, variational cluster⁴² and two-particle self-consistent approaches⁴³ have been applied to the U - V Hubbard model.

A first DMFT treatment described the opening of a “pseudo-gap” and the reentrant behavior of the critical V_c as a function of temperature.⁴⁴ In this scheme, the V term only contributed at the Hartree level by shifting the chemical potential since in the limit of infinite dimensions, the contributions beyond Hartree of nonlocal terms vanish, while fluctuations due to local terms such as the onsite Hubbard U do not vanish under rescaling.^{45,46} The screening effects contained in the V term are not captured by standard single-site DMFT. Therefore, an extended DMFT (EDMFT) scheme has been proposed to remedy this shortcoming.^{11–15} Within this scheme, the nonlocal interactions induce a frequency dependence of the effective local interaction and lead to a sizable *reduction* of the static value of U . In addition, Refs. 14 and 15 showed that one of the consequences of adding a spatially nonlocal contribution to the self-energy is to make the system more insulating.

In this work, we give a precise account of how U and V affect the properties of the local frequency-dependent interactions, and how the latter in turn modify the spectral properties of the system, while systematically investigating the effect of nonlocal GW contributions. We restrict ourselves to the paramagnetic phase at half-filling and will give all energies in units of the half-bandwidth ($4t$). The inverse temperature will be denoted by $\beta = 1/T$ ($k_B = 1$).

B. Action formulation

The solution of model (1) amounts to computing the Green’s functions and other correlation functions. For this

purpose, it is convenient to write the grand-canonical partition function $Z = \text{Tr}e^{-\beta H}$ as a coherent-state path integral⁴⁷ $Z = \int \mathcal{D}[c_i^*, c_i] e^{-S}$ where

$$S[c^*, c] = \int_0^\beta d\tau \left\{ \sum_{ij\sigma} c_{i\sigma}^*(\tau) [(\partial_\tau - \mu)\delta_{ij} + t_{ij}] c_{j\sigma}(\tau) + U \sum_i n_{i\uparrow}(\tau) n_{i\downarrow}(\tau) + \frac{1}{2} \sum_{ij} v_{ij}^{nl} n_i(\tau) n_j(\tau) \right\}. \quad (2)$$

c_i^* and c_i denote conjugate anticommuting Grassmann fields for site i [$c_i(\tau + \beta) = -c_i(\tau)$], $t_{ij} = -t\delta_{(ij)}$, $v_{ij}^{nl} = V\delta_{(ij)}$, and $\delta_{(ij)} = 1$ if i and j are nearest neighbors and 0 otherwise. τ is the imaginary-time variable. We will denote by $\omega_n = (2n + 1)\pi/\beta$ ($\nu_n = 2n\pi/\beta$) the corresponding fermionic (bosonic) Matsubara frequencies. The Fourier transforms of t_{ij} and v_{ij}^{nl} on the lattice are

$$\epsilon_k = -2t[\cos(k_x) + \cos(k_y)], \quad (3)$$

$$v_k^{nl} = 2V[\cos(k_x) + \cos(k_y)]. \quad (4)$$

Using the identity $n_i n_i = 2n_{i\uparrow} n_{i\downarrow} + n_i$, we can rewrite the interaction terms of Eq. (2) as $\frac{1}{2} \sum_{ij} v_{ij} n_i(\tau) n_j(\tau)$ with $v_{ij} = U\delta_{ij} + V\delta_{(ij)}$, or

$$v_k = U + v_k^{nl}, \quad (5)$$

provided that we shift the chemical potential $\mu \rightarrow \tilde{\mu} = \mu + U/2$. The action hence becomes

$$S[c^*, c] = \int_0^\beta d\tau \left\{ \sum_{ij\sigma} c_{i\sigma}^*(\tau) [(\partial_\tau - \tilde{\mu})\delta_{ij} + t_{ij}] c_{j\sigma}(\tau) + \frac{1}{2} \sum_{ij} v_{ij} n_i(\tau) n_j(\tau) \right\}. \quad (6)$$

C. Functional formulation

The problem of finding the solution to the Hamiltonian model (1) or calculating the Green's function corresponding to the action (6) can also be formulated in a functional language. The familiar Luttinger-Ward or Baym-Kadanoff functionals provide examples of such a construction. In the present context, a formulation in terms of the free energy written as a functional of both the Green's function G and the screened Coulomb interaction W is the method of choice since the combined GW + DMFT method can naturally be viewed as a specific approximation to such a functional. Indeed, the GW + DMFT solution as formulated in Refs. 16 and 17 can be derived as a stationary point (G, W) of the free-energy functional introduced by Almladh *et al.*,²⁹ after approximating the correlation part of this functional by a combination of local and nonlocal terms stemming from DMFT and GW , respectively. To draw an illustrative analogy, GW + DMFT provides an approximation to the correlation part of the Almladh free-energy functional, on the same footing as the local density approximation of density functional theory⁴⁸ is an approximation to the exchange-correlation part of the Hohenberg-Kohn functional of the energy.

In the literature, several variants of functionals of G and W have been discussed,^{14,17,30} and different derivations given. Using a Hubbard-Stratonovich (HS) decoupling as in Ref. 16, we discuss two flavors of free-energy functionals which differ by the choice of the part of the interaction that is decoupled by the HS transformation. The first one reproduces the Ψ functional introduced by Almladh on which the GW + DMFT construction of Ref. 16 is based. The second one is a variant that was used in the study of the extended Hubbard model in Ref. 14.

The Hubbard-Stratonovich transformation⁴⁹ relies on the following identity:

$$\exp\left(\frac{1}{2} \int_0^\beta d\tau b_i(\tau) A_{ij} b_j(\tau)\right) = \int \frac{\mathcal{D}[x_1(\tau), x_2(\tau), \dots]}{\sqrt{(2\pi)^N \det A}} \times \exp\left(\int_0^\beta d\tau \left\{ -\frac{1}{2} x_i(\tau) [A^{-1}]_{ij} x_j(\tau) \mp x_i(\tau) b_i(\tau) \right\}\right), \quad (7)$$

where A is a real symmetric positive-definite matrix, $b_i(\tau)$ is a periodic field [$b_i(\tau + \beta) = b_i(\tau)$], $x_i(\tau)$ a real periodic field, and summation over repeated indices is assumed. In the following, we will choose the upper sign for the last term.

Decoupling the whole (local and nonlocal) interaction $\frac{1}{2} \sum_{ij} v_{ij} n_i(\tau) n_j(\tau)$ by the HS transformation corresponds to applying the above formula (7) to the interaction term in Eq. (6), that is, to the choice $b_i \equiv in_i$, $A_{ij} \equiv v_{ij}$, and $x_i \equiv \phi_i$. This choice, denoted as HS- UV in the following, leads to the construction of the Ψ functional as in Almladh *et al.*²⁹ and the formalism of Ref. 17. Within the approximation introduced in the next section, this corresponds to the GW + DMFT scheme as introduced in Ref. 16. This approach (which was also used in Ref. 15) relies on the argument that the two terms, which represent different matrix elements of the same interaction, should be treated on the same footing.

In Ref. 14, on the other hand, the HS transform has been applied only to the nonlocal interaction term $\frac{1}{2} \sum_{ij} v_{ij}^{nl} n_i(\tau) n_j(\tau)$ in the action (2). This approach, dubbed HS- V in the following, leads to a modified free-energy functional, which we denote by Ψ_V . It was motivated by the aforementioned fact that in the limit of infinite dimensions, with the nonlocal interaction rescaled as $V \rightarrow V/z$, the nonlocal term results in a trivial shift of the chemical potential, while the onsite interaction remains nontrivial, justifying a separate treatment for the nonlocal term.

We will first explicitly derive the two functionals Ψ and Ψ_V and, in Sec. VIA, we will compare the results from both decoupling strategies. The results in the remainder of the section, finally, are based on the HS- UV decoupling, that is, on the Ψ functional and the GW + DMFT formalism of Ref. 16.

1. “ UV decoupling”: The Ψ functional

In the HS- UV decoupling scheme, the full interaction term is decoupled via an auxiliary bosonic field ϕ_i . Choosing $b_i \equiv in_i$, $A_{ij} \equiv v_{ij}$, and $x_i \equiv \phi_i$, the transformation (7) applied to

the action (2) leads to

$$\begin{aligned}
 S[c^*, c, \phi] &= \int_0^\beta d\tau \left\{ - \sum_{ij\sigma} c_{i\sigma}^*(\tau) [(G_0^H)^{-1}]_{ij} c_{j\sigma}(\tau) \right\} + \int_0^\beta d\tau \\
 &\quad \times \left\{ \frac{1}{2} \sum_{ij} \phi_i(\tau) [v^{-1}]_{ij} \phi_j(\tau) + i\alpha \sum_i \phi_i(\tau) n_i(\tau) \right\}, \quad (8)
 \end{aligned}$$

where we introduced the fermionic lattice Hartree Green's function G_0^H defined by $[G_0^H]_{ij} \equiv [(-\partial_\tau + \mu + \frac{U}{2})\delta_{ij} - t_{ij}]$. For later use, we have moreover inserted a coupling constant α in front of the fermion-boson coupling term. The physically relevant case corresponds to $\alpha = 1$.

The HS transformation replaces an electron-electron interaction by an electron-boson interaction, and introduces a new variable: the auxiliary real boson field ϕ . This has an important consequence: even a first-order diagram in this new interaction contains diagrams of infinite order in the electron-electron interaction. Making even simple approximations on the new action can thus lead to nontrivial diagrams for the original action. Moreover, the electron-boson vertex $i\phi_i n_i$ is *local*. This locality ensures that in the limit of infinite dimensions, the interactions (and in particular V) will contribute beyond the Hartree level.

The generating functional of correlation functions is obtained by introducing the bilinear sources J_f and J_b , coupling to the fermionic and bosonic operators, respectively, so that the action becomes $S[c^*, c, \phi] - S[J_f, J_b]$, with

$$\begin{aligned}
 S[J_f, J_b] &= \int_0^\beta d\tau d\tau' \sum_{ij} \left\{ J_{f,ij}(\tau, \tau') c_i^*(\tau) c_j(\tau') \right. \\
 &\quad \left. + \frac{1}{2} J_{b,ij}(\tau, \tau') \phi_i(\tau) \phi_j(\tau') \right\}. \quad (9)
 \end{aligned}$$

The fermionic and bosonic Green's functions for this action are $G_{ij}(\tau - \tau') = -\langle T c_i(\tau) c_j^*(\tau') \rangle = \delta\Omega / \delta J_{f,ij}(\tau, \tau')$ and $W_{ij}(\tau - \tau') = \langle T \phi_i(\tau) \phi_j(\tau') \rangle = -2\delta\Omega / \delta J_{b,ij}(\tau, \tau')$, where we have defined

$$\Omega \equiv -\ln Z[J_f, J_b] = -\ln \text{Tr} e^{-S[c^*, c, \phi] + S[J_f, J_b]}. \quad (10)$$

The noninteracting Green's functions (obtained by setting $i\phi_i n_i = 0$) are, respectively, $G|_{\alpha=0} = G_0^H$ and $W(k, i\nu_n)|_{\alpha=0} = [v_k^{-1}]^{-1} = v_k$. This gives a first hint as to the physical meaning of W : without renormalization by the auxiliary bosons, it corresponds to the bare interaction. Coupling to the bosons, which represent density fluctuations of the system, introduces screening into the physical description.

We next perform a Legendre transformation with respect to the sources J_f and J_b ,

$$\Gamma[G, W] = \Omega[J_f[G], J_b[W]] - \text{Tr} J_f G + \frac{1}{2} \text{Tr} J_b W, \quad (11)$$

with the reciprocity relations $J_f = -\frac{\delta\Gamma}{\delta G}$ and $J_b = 2\frac{\delta\Gamma}{\delta W}$. The physical Green's functions will be obtained by setting $J_f = 0$ and $J_b = 0$ or, equivalently, by requiring the stationarity of Γ with respect to G and W .

The free-energy functional Γ can be written as

$$\Gamma_{\alpha=1} = \Gamma_{\alpha=0} + \Psi, \quad (12)$$

where we have defined

$$\Psi \equiv \int_0^\beta d\alpha \frac{d\Gamma}{d\alpha}. \quad (13)$$

Γ is the well-known Baym-Kadanoff functional,⁵⁰ while Ψ is the extension of the Luttinger-Ward functional $\Phi[G]$ to one- and two-particle propagators.⁵¹

The noninteracting ($\alpha = 0$) part of the Γ functional is readily evaluated as

$$\begin{aligned}
 \Gamma_{\alpha=0} &= \text{Tr} \ln(-G) - \text{Tr}(G_0^{-1} - G^{-1})G \\
 &\quad - \frac{1}{2} \text{Tr} \ln W + \frac{1}{2} \text{Tr}(v^{-1} - W^{-1})W. \quad (14)
 \end{aligned}$$

Indeed, when $\alpha = 0$, the action becomes Gaussian and thus explicitly integrable, namely, $\Omega_{\alpha=0} = -\ln \text{Det}[-G_0^{-1} + J_f] - \ln(\text{Det}[v^{-1} - J_b])^{1/2}$. The above definition $G = \delta\Omega / \delta J_f$ imposes $(G_0^{-1} - J_f)G = 1$ and similarly $(v^{-1} - J_b)W = 1$, yielding Eq. (14). Finally, stationarity of the full Γ implies $\frac{\delta\Gamma}{\delta G} = 0 = \frac{\delta\Gamma_{\alpha=0}}{\delta G} + \frac{\delta\Psi}{\delta G} = G^{-1} - G_0^{-1} + \frac{\delta\Psi}{\delta G}$ for G and $0 = -\frac{1}{2}(W^{-1} - v^{-1}) + \frac{\delta\Psi}{\delta W}$ for W . Defining the self-energies as

$$\Sigma = \frac{\delta\Psi}{\delta G}, \quad \Pi = -2\frac{\delta\Psi}{\delta W} \quad (15)$$

yields Dyson's equations for G and W :

$$G^{-1} = G_0^{-1} - \Sigma, \quad W^{-1} = v^{-1} - \Pi. \quad (16)$$

Being “ Ψ derivable,” these self-energies will obey global conservation rules.⁵²

The above formulation shows that, formally, solving the lattice problem defined by Eq. (2) amounts to evaluating the corresponding Ψ functional, from which G and W can be derived. In Sec. III, we will describe two complementary ways of approximating this functional, EDMFT and GW , before showing how to merge the two approaches, thus arriving at the $GW + \text{DMFT}$ free-energy functional.

2. “ V decoupling”: The Ψ_V functional

In the HS- V scheme, proposed in Ref. 14, only the nonlocal interaction term is decoupled via an auxiliary bosonic field ϕ_i . Choosing $b_i \equiv i n_i$, $A_{ij} \equiv v_{ij}^n$, and $x_i \equiv \phi_i$, the transformation (7) applied to the action (2) leads to

$$\begin{aligned}
 S[c^*, c, \phi] &= \int_0^\beta d\tau \left\{ - \sum_{ij\sigma} c_{i\sigma}^*(\tau) [G_0^{-1}]_{ij} c_{j\sigma}(\tau) \right. \\
 &\quad \left. + \alpha U \sum_i n_{i\uparrow}(\tau) n_{i\downarrow}(\tau) \right\} \\
 &\quad + \int_0^\beta d\tau \left\{ \frac{1}{2} \sum_{ij} \phi_i(\tau) [(v^n)^{-1}]_{ij} \phi_j(\tau) \right. \\
 &\quad \left. + i\alpha \sum_i \phi_i(\tau) n_i(\tau) \right\}, \quad (17)
 \end{aligned}$$

where we used the noninteracting fermionic lattice Green's function G_0 defined by $[G_0^{-1}]_{ij} \equiv [(-\partial_\tau + \mu)\delta_{ij} - t_{ij}]$. Again, a coupling constant α was introduced, and the physical case corresponds to $\alpha = 1$. Now, however, the coupling constant is not only a switch for turning on or off the

fermion-boson coupling but at the same time also the local Hubbard interaction.

In principle, the interaction should be a positive-definite matrix in order for the Gaussian integrals invoked in the HS transformation to converge. In contrast to the HS- UV decoupling, where U and V are matrix elements of the screened Coulomb interaction, which is positive definite, this is not the case for the interaction of HS- V , v_{ij}^{nl} . This issue can be dealt with by adding an auxiliary identity matrix multiplied by a large enough constant.¹⁴ In practice, however, the simulation results are not affected by the value of this constant.

As before, the generating functional of correlation functions is obtained by introducing source terms. The fermionic Green's function for this action is unchanged compared to the UV -decoupling case: $G_{ij}(\tau - \tau') = -\langle T c_i(\tau) c_j^*(\tau') \rangle = \delta\Omega/\delta J_{f,ij}(\tau, \tau')$. The bosonic propagator formally still reads $D_{ij}(\tau - \tau') = \langle T \phi_i(\tau) \phi_j(\tau') \rangle = -2\delta\Omega/\delta J_{b,ij}(\tau, \tau')$. It does not, however, correspond to the screened interaction, as in the HS- UV scheme: in the case of vanishing fermion-boson coupling, the bosonic propagator reduces by construction to only the nonlocal part of the bare interaction.

The construction of the free-energy functional Γ proceeds as before by Legendre transformation with respect to the sources J_f and J_b ,

$$\Gamma_V[G, D] = \Omega[J_f[G], J_b[D]] - \text{Tr} J_f G + \frac{1}{2} \text{Tr} J_b D, \quad (18)$$

with the reciprocity relations $J_f = -\frac{\delta\Gamma_V}{\delta G}$ and $J_b = 2\frac{\delta\Gamma_V}{\delta D}$. The physical Green's functions will be obtained by setting $J_f = 0$ and $J_b = 0$ or, equivalently, by requiring the stationarity of Γ_V with respect to G and D . Thanks to the choice of the coupling constant α in front of the interaction and boson-fermion coupling terms $\alpha(U \sum_i n_{i\uparrow} n_{i\downarrow} + i \sum_i \phi_i n_i)$, Γ_V acquires the same form as before, $\Gamma_{V, \alpha=1} = \Gamma_{V, \alpha=0} + \Psi_V$, with $\Psi_V \equiv \int_0^1 d\alpha \frac{d\Gamma_V}{d\alpha}$, but it is now a functional of G and D .

The noninteracting ($\alpha = 0$) part of the Γ functional reads

$$\Gamma_{V, \alpha=0} = \text{Tr} \ln(-G) - \text{Tr}(G_0^{-1} - G^{-1})G - \frac{1}{2} \text{Tr} \ln W + \frac{1}{2} \text{Tr}[(v^{nl})^{-1} - D^{-1}]D. \quad (19)$$

Finally, stationarity of the full Γ_V reproduces the fermionic Dyson equation for the Green's function and self-energy. For the bosonic part, however, we obtain $0 = -\frac{1}{2}[D^{-1} - (v^{nl})^{-1}] + \frac{\delta\Psi_V}{\delta D}$ for D . The bosonic self-energy

$$\Pi_V = -2 \frac{\delta\Psi_V}{\delta D} \quad (20)$$

is thus not equal to the physical polarization of the system.

Again, solving the lattice problem defined by Eq. (2) amounts to evaluating the corresponding Ψ_V functional, from which Σ and Π_V , and in turn G and D , can be derived. Compared to the previous case of the Ψ functional, however, the subtlety of D being the screened nonlocal interaction (not equal to the full W) requires additional care in the construction of a combined DMFT scheme.

III. METHODS OF SOLUTION

A. EDMFT

Ψ is a functional of the fermionic and bosonic Green's functions G_{ij} and W_{ij} . EDMFT replaces this functional by a

functional of the local components of the Green's function and screened interaction only. The numerical procedure outlined below thus corresponds to a numerically exact solution of the purely local but otherwise exact $\Phi[G_{ii}, W_{ii}]$. Similarly, the HS- V approach constructs a functional of the local parts of G and D , $\Psi_V[G_{ii}, D_{ii}]$. The local Green's functions can be obtained by solving an auxiliary effective local problem defined by the action

$$S_{\text{eff, HS-}UV}^{\text{EDMFT}} = - \int_0^\beta d\tau d\tau' \sum_\sigma c_\sigma^*(\tau) \mathcal{G}^{-1}(\tau - \tau') c_\sigma(\tau') + \frac{1}{2} \int_0^\beta d\tau d\tau' \phi(\tau) \mathcal{U}^{-1}(\tau - \tau') \phi(\tau') + i \int_0^\beta d\tau \phi(\tau) n(\tau), \quad (21)$$

$$S_{\text{eff, HS-}V}^{\text{EDMFT}} = - \int_0^\beta d\tau d\tau' \sum_\sigma c_\sigma^*(\tau) \mathcal{G}^{-1}(\tau - \tau') c_\sigma(\tau') + \int_0^\beta d\tau U n_\uparrow(\tau) n_\downarrow(\tau) + \frac{1}{2} \int_0^\beta d\tau d\tau' \phi(\tau) \mathcal{D}^{-1}(\tau - \tau') \phi(\tau') + i \int_0^\beta d\tau \phi(\tau) n(\tau). \quad (22)$$

These actions are very similar to the lattice actions [Eqs. (8) and (17)], with G_0^H and G_0 replaced by an appropriately defined dynamical \mathcal{G} describing the excursions of an electron in the lattice from a given site (the impurity) and back, and the bare and instantaneous interaction v (or v^{nl} in HS- V) replaced by the retarded interaction \mathcal{U} (or \mathcal{D}). The effective actions (21) and (22) are obtained by integrating out all sites but one in the lattice action and taking the infinite-dimensional limit. The derivation of the action for the HS- UV scheme, as well as the EDMFT loop sketched below, are presented in Appendix B.

Integrating out the ϕ field in Eqs. (21) and (22) yields the impurity actions

$$S_{\text{eff, HS-}UV}^{\text{EDMFT}} = - \int_0^\beta d\tau d\tau' \sum_\sigma c_\sigma^*(\tau) \mathcal{G}^{-1}(\tau - \tau') c_\sigma(\tau') + \frac{1}{2} \int_0^\beta d\tau d\tau' n(\tau) \mathcal{U}(\tau - \tau') n(\tau') - \frac{1}{2} \text{Tr} \ln \mathcal{U}, \quad (23)$$

$$S_{\text{eff, HS-}V}^{\text{EDMFT}} = - \int_0^\beta d\tau d\tau' \sum_\sigma c_\sigma^*(\tau) \mathcal{G}^{-1}(\tau - \tau') c_\sigma(\tau') + \int_0^\beta d\tau U n_\uparrow(\tau) n_\downarrow(\tau) + \frac{1}{2} \int_0^\beta d\tau d\tau' n(\tau) \mathcal{D}(\tau - \tau') n(\tau') - \frac{1}{2} \text{Tr} \ln \mathcal{D}, \quad (24)$$

which feature a retarded interaction $\mathcal{U}(\tau - \tau')$ (for HS- UV) or $\mathcal{D}(\tau - \tau')$ (for HS- V) between charges.

The solution of this impurity problem, described in detail in Sec. IV, requires the calculation of the one-particle Green's

functions $G_{\text{loc}} \equiv -\langle Tc(\tau)c^*(0) \rangle$ and $W_{\text{loc}} \equiv \langle T\phi(\tau)\phi(0) \rangle$ (or D_{loc} for HS-V). From G_{loc} and W_{loc} , one computes the corresponding self-energies $\Sigma_{\text{loc}} = \mathcal{G}^{-1} - G_{\text{loc}}^{-1}$ and $\Pi_{\text{loc}} = \mathcal{U}^{-1} - W_{\text{loc}}^{-1}$ [or $(\Pi_V)_{\text{loc}} = \mathcal{D}^{-1} - D_{\text{loc}}^{-1}$]. The EDMFT approximation identifies the impurity self-energies with the lattice self-energies: $\Sigma(k, i\omega_n) \approx \Sigma_{\text{loc}}(i\omega_n)$, $\Pi(k, i\nu_n) \approx \Pi_{\text{loc}}(i\nu_n)$ [or $(\Pi_V)_{\text{loc}}(i\nu_n)$]. This allows one to evaluate (approximate) lattice Green's functions $G(k, i\omega_n)$ and $W(k, i\nu_n)$ [or $D(k, i\nu_n)$] through Dyson's equation and estimates of the local lattice Green's functions by summation over k . Eventually, one obtains updated \mathcal{G} and \mathcal{U} (or \mathcal{D}) via

$$\mathcal{G}^{-1} = G_{\text{loc}}^{-1}[\Sigma_{\text{loc}}] + \Sigma_{\text{loc}}, \quad (25)$$

$$\mathcal{U}^{-1} = W_{\text{loc}}^{-1}[\Pi_{\text{loc}}] + \Pi_{\text{loc}}, \quad (26)$$

$$\mathcal{D}^{-1} = D_{\text{loc}}^{-1}[(\Pi_V)_{\text{loc}}] + (\Pi_V)_{\text{loc}}. \quad (27)$$

B. GW approximation

While EDMFT can treat strong local correlations, it completely neglects the nonlocal contributions to the self-energy. A complementary approach, which treats spatial fluctuations, but works reliably only in the weakly correlated regime, is the *GW* method.^{53–55} The *GW* approximation has been used extensively to investigate the properties of weakly correlated materials, such as the band gaps of semiconductors and is nowadays implemented in several different electronic structure codes (see, e.g., Refs. 56 and 57). In these materials, *GW* correctly accounts for the screening effects of the electrons at the random-phase approximation (RPA) level. Schematically, for a general Coulomb interaction $v(r) \sim 1/r$, one-shot *GW* replaces the bare interaction v of the Fock self-energy $\Sigma_F \sim G_0 v$ by the screened interaction $W = v/\epsilon_{\text{RPA}}$, where $\epsilon_{\text{RPA}} = 1 - vP_0$ and $P_0 \sim G_0 G_0$ is the dynamical Lindhard function. In a self-consistent scheme, G_0 is replaced by the interacting Green's function G .⁵⁸ The Fock self-energy thus becomes $\Sigma_{GW} \sim GW$, hence the name of the approximation. Formally, the *GW* approximation can be obtained by Hubbard-Stratonovich decoupling the Coulomb interaction v via an auxiliary bosonic field ϕ characterized by the propagator $W \sim \langle \phi\phi \rangle$. This amounts to replacing the electron-electron interaction by the indirect interaction of two electrons mediated by a boson described by ϕ . The first-order self-energy diagram in the expansion of this electron-boson interaction is $\Sigma \sim GW$.

The standard derivation of the *GW* approximation relies on a truncation of Hedin's equations,⁵³ where the three-legged vertex $\Lambda = 1 + \frac{\delta\Sigma}{\delta G} G G \Lambda$ is set to unity. In the following, we will derive the *GW* approximation for our lattice model in a diagrammatic way based on the four-legged vertices of standard perturbation theory for both free-energy functionals, that is, both choices of the HS decoupling. In the HS-V approach, the lattice action of Eq. (8) contains two interaction vertices: a local electron-electron interaction $U n_{i\uparrow} n_{i\downarrow}$ and a local electron-boson interaction $i\phi_i n_i$. Consequently, the perturbation expansion of the Green's function will contain two types of bare interaction vertices, namely, $\Gamma_{\text{ee}}^{(0)}(\tau_1, \tau_2, \tau_3, \tau_4)_{ijkl} = U \delta_{ijk} \delta_{i\uparrow} \delta_{j\downarrow} \delta_{k\uparrow} \delta_{l\downarrow} \delta(\tau_1 - \tau_2) \delta(\tau_3 - \tau_4) \delta(\tau_2 - \tau_3)$ and $\Gamma_{\text{eb}}^{(0)}(\tau_1, \tau_2, \tau_3)_{ijk} = i \delta_{ijk} \delta(\tau_1 -$

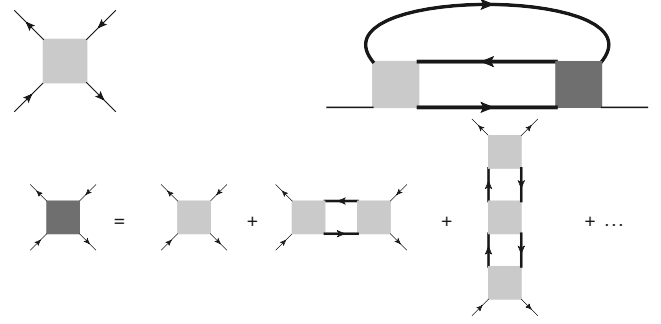


FIG. 1. Diagrammatic expansion of the electron-electron vertex. From left to right, top to bottom: Bare electron-electron interaction vertex $\Gamma_{\text{ee}}^{(0)}$. Fully boldfied Σ_{ee} . Expansion of the full electron-electron vertex Γ_{ee} .

$\tau_2) \delta(\tau_3 - \tau_2)$, which we will represent as shown in Figs. 1 and 2. We will suppose that we can perform the expansions separately and then sum the two results (which is an approximation since there could well be sequences of interactions with alternating $\Gamma_{\text{ee}}^{(0)}$ and $\Gamma_{\text{eb}}^{(0)}$). In the HS-UV approach, there is only the electron-boson vertex $\Gamma_{\text{eb}}^{(0)}$.

The vertex $\Gamma_{\text{ee}}^{(0)}$ will lead to contributions that are not present in the HS-UV decoupling scheme. The perturbation expansion in powers of $\Gamma_{\text{ee}}^{(0)}$ yields a series of self-energy diagrams, the lines of which are noninteracting Green's functions G_0 . Since some higher-order diagrams contain “self-energy insertions,” the number of diagrams can be reduced by “boldfying” the lines, namely, by replacing G_0 by the interacting Green's function G . Subsequently, the number of diagrams can be further reduced by regrouping the interaction vertices into a “boldfied” vertex Γ_{ee} pictured in Fig. 1. Thus, the electron-electron part of the self-energy (beyond the Hartree self-energy) can be described (Fig. 1) by the exact expression⁶⁰

$$\Sigma_{\text{ee}} = -\Gamma_{\text{ee}}^{(0)} G G G \Gamma_{\text{ee}}, \quad (28)$$

with bold propagators G and bold vertices Γ_{ee} . Note that only the right vertex is boldfied to avoid double counting. This

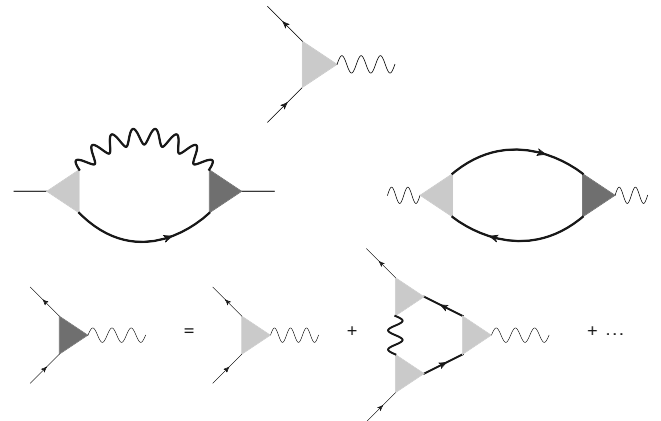


FIG. 2. Diagrammatic expansion of the electron-boson vertex. From left to right, top to bottom: Bare electron-boson interaction vertex $\Gamma_{\text{eb}}^{(0)}$. Fully boldfied Σ_{eb} . Fully boldfied Π . Expansion of the full electron-boson vertex Γ_{eb} .

vertex is also called the fully reducible vertex. We stress that this electron-electron contribution to the electronic self-energy is absent in the HS- UV approach since in this scheme there is no longer any electron-electron interaction vertex after the HS decoupling.

Similarly, the expansion of the partition function in powers of $\Gamma_{\text{eb}}^{(0)}$ can be simplified by boldfying the G_0 and W_0 ($=v$ or v^m) lines and the vertices, leading to graphs of the form displayed in Fig. 2, corresponding to the expressions

$$\Sigma_{\text{eb}} = \Gamma_{\text{eb}}^{(0)} G W \Gamma_{\text{eb}}, \quad (29)$$

$$\Pi_{\text{eb}} = -2\Gamma_{\text{eb}}^{(0)} G G \Gamma_{\text{eb}}. \quad (30)$$

The expansion for the bold electron-boson vertex Γ_{eb} is also pictured in Fig. 2.

The usual GW approximation truncates the expansion of the electron-boson vertex function Γ_{eb} after its first term, namely, by taking $\Gamma_{\text{eb}} \approx \Gamma_{\text{eb}}^{(0)} = i\delta$. This simplification, which amounts to neglecting the so-called vertex corrections, yields the familiar expressions $\Sigma_{\text{eb}}^{GW} = -GW$ and $\Pi^{GW} = 2GG$.⁶¹ For the HS- UV decoupling, $\Sigma = \Sigma_{\text{eb}}$ and thus

$$\Sigma_{\text{HS-UV}}^{GW} = -GW. \quad (31)$$

For the HS- V decoupling, there is a second contribution coming from the electron-electron vertex. If one approximates $\Gamma_{\text{ee}} \approx \Gamma_{\text{ee}}^{(0)}$ (as in Ref. 14), one gets $\Sigma_{\text{ee}}^{GW} = -U^2 G G G$, and hence

$$\Sigma_{\text{HS-V}}^{GW} = -GD - U^2 G G G. \quad (32)$$

At this point, a few remarks are in order: the two approximations (31) and (32) are not equivalent. Making the lowest-order approximation on the electron-electron vertex is a stronger assumption than truncating the electron-boson vertex. In the HS- V approach, the series of diagrams corresponding to Eq. (32) contains the ring of “bubbles” made up of G and v_{ij}^m (which contains only the off-site repulsion V), plus a second-order diagram in U . In contrast, the diagrams in $\Sigma_{\text{HS-UV}}^{GW}$ contain the ring of bubbles made up of G and v_{ij} (which contains U and V). Put differently, it not only comprises the off-site interaction V to all orders (at the RPA level), but also the onsite interaction U to all orders (at the RPA level). We thus expect the HS- UV scheme to be better poised to capture nonlocal effects arising from V and U , while the HS- V scheme will probably give nontrivial contributions only in parameter regimes where V plays the dominant role. Therefore, while benchmarking both approaches in the results section, we will focus on the formulation in terms of the Almladh functional in the following discussion of the combined $GW + \text{DMFT}$ scheme. A similar combination based on the Ψ_V functional is possible, leading to a combination of the GD plus self-consistent second-order perturbation theory expression of Eq. (32) with dynamical mean field theory, as described in Ref. 14. We refer to this combination in the following as “GD + SOPT + DMFT”.

C. $GW + \text{DMFT}$ approach

As already hinted at before, EDMFT and GW are complementary approximate schemes: EDMFT provides a good

description of local correlations, while GW captures longer-range correlations and in particular long-range screening. Therefore, combining both approximations appears promising. The $GW + \text{DMFT}$ approach^{16,17} makes an approximation on $\Psi[G_{ij}, W_{ij}]$ by decomposing it in the following way:

$$\Psi \approx \Psi^{\text{EDMFT}}[G_{ii}, W_{ii}] + \Psi_{\text{nonloc}}^{GW}[G_{ij}, W_{ij}], \quad (33)$$

where $\Psi_{\text{nonloc}}^{GW} = \Psi^{GW} - \Psi_{\text{loc}}^{GW}$.

While EDMFT will generate the series of local self-energy diagrams up to infinite order, the nonlocal contributions to Ψ will be generated in a perturbative way by the nonlocal part of the GW diagrams, thus avoiding double counting.

In the limit of infinite dimensions, nonlocal diagrams vanish. Thus, the effect (if any) of the nonlocal contributions is expected to manifest itself only as the dimension is lowered. The proximity to a phase transition should also enhance spatial fluctuations. In principle, the GW contribution should nonetheless remain a correction to the DMFT part, which justifies why $\Psi_{\text{nonloc}}[G_{ij}, W_{ij}]$ can be treated on a perturbative level, while $\Psi[G_{ii}, W_{ii}]$ is evaluated to all orders.

The approximate electronic self-energy will be given by $\Sigma_{ij} = \Sigma_{ij}^{\text{loc}} \delta_{ij} + (1 - \delta_{ij}) \Sigma_{ij}^{GW}$. The $1 - \delta_{ij}$ factor ensures that only the nonlocal part of the GW self-energy is added. Analogous expressions hold for Π_{ij} . This approach is very general. In the specific case of the extended Hubbard model, one can expect the GW contribution to become significant as one approaches an instability in the charge sector, namely, close to the charge-ordering transition. The GW diagrams can in principle be replaced by other perturbative diagrammatic corrections, corresponding to a decoupling of the interaction in other channels.

IV. NUMERICAL IMPLEMENTATION

A. Solution of the EDMFT impurity problem

The impurity models (23) and (24) can be solved efficiently using the hybridization-expansion continuous-time quantum Monte Carlo solver (CTQMC-hyb).²⁷ The formalism has been previously derived using a Hamiltonian representation of the impurity model.^{20,21} Here, we discuss an alternative derivation based on the effective action, focusing on the case of action (23). A CTQMC-hyb simulation samples configurations representing specific time sequences of “hybridization events,” with weight proportional to the determinant of a matrix of hybridization functions. The perturbation expansion of the partition function Z and the summation of diagrams with identical operator sequences leads to

$$\begin{aligned} Z &= \sum_{\{n_\sigma\}=0}^{\infty} \prod_{\sigma} \left[\frac{1}{(n_\sigma!)^2} \int_0^\beta d\tau_1^\sigma \int_0^\beta d\tau_1'^\sigma \dots \right. \\ &\times \int_0^\beta d\tau_{n_\sigma}^\sigma \int_0^\beta d\tau_{n_\sigma}'^\sigma \text{Det} \Delta_\sigma \left. \right] \int D[c^*, c] e^{-S_{\text{eff}} T} \\ &\times \prod_{\sigma} c_\sigma^*(\tau_1'^\sigma) c_\sigma(\tau_1^\sigma) \dots c_\sigma^*(\tau_{n_\sigma}'^\sigma) c_\sigma(\tau_{n_\sigma}^\sigma), \end{aligned} \quad (34)$$

where $(\Delta_\sigma)_{ij} = \Delta_\sigma(\tau_i - \tau_j')$ is the hybridization function evaluated for the time difference between annihilation operator

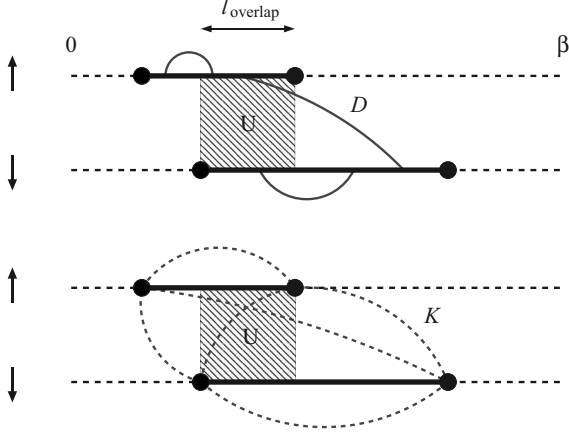


FIG. 3. (Color online) Illustration of a Monte Carlo configuration in the segment representation. The top figure corresponds to a configuration with one spin-up and one spin-down segment, each representing a time interval marked by a creation operator (empty circle) and an annihilation operator (full circle). The overlap of the segments, corresponding to the width of the hashed region, yields the weight due to the instantaneous interaction U . The retarded interaction $\mathcal{D}(\tau - \tau')$ is represented by the blue curved lines. The bottom panel represents the weight of this configuration after integration of the retarded interaction over the segments. The dashed blue lines correspond to the interaction $K(\tilde{\tau}_i - \tilde{\tau}_j)$ between creation and annihilation operators.

i and creation operator j and

$$S_{at} = \frac{1}{2} \sum_{\sigma\sigma'} \int \int d\tau d\tau' n_{\sigma}(\tau) \mathcal{U}_{\sigma\sigma'}(\tau - \tau') n_{\sigma'}(\tau') + \int d\tau \sum_{\sigma} c_{\sigma}(\tau)^* (\partial_{\tau} - \mu) c_{\sigma}(\tau) \quad (35)$$

represents the interaction and chemical potential contributions of action (23). The interaction \mathcal{U} can always be split into a delta-function contribution and a nonsingular contribution $\mathcal{U}(\tau)_{\sigma\sigma'} = U\delta(\tau)(1 - \delta_{\sigma\sigma'}) + \mathcal{D}(\tau)_{\sigma\sigma'}$. (In the HS-V scheme, this separation is already explicit.) The last factor of Eq. (34) can be easily evaluated since the time-evolution operators are diagonal in the occupation-number basis. In the segment representation,²⁷ each imaginary-time interval with occupation $n_{\sigma} = 1$ is marked by a segment, and the last factor can (up to a permutation sign) be written as $w_{\mu} w_U w_{\mathcal{D}}$ with $w_{\mu} = e^{\mu(l_{\uparrow} + l_{\downarrow})}$ and $w_U = e^{-U l_{\text{overlap}}}$. Here, l_{σ} stands for the total length of segments of spin σ , while l_{overlap} is the total overlap between segments of opposite spin (see illustration of a segment configuration in Fig. 3). The retarded interaction contributes a factor

$$w_{\mathcal{D}} = e^{-\frac{1}{2} \sum_{\sigma_1\sigma_2} \int_0^{\beta} d\tau_1 \int_0^{\beta} d\tau_2 \mathcal{D}(\tau_1 - \tau_2)_{\sigma_1\sigma_2} n_{\sigma_1}(\tau_1) n_{\sigma_2}(\tau_2)} = \exp \left(-\frac{1}{2} \sum_{\substack{\sigma_1\sigma_2 \\ k_{\sigma_1} k_{\sigma_2}}} \int_{\tau'_{k_{\sigma_1}}}^{\tau_{k_{\sigma_1}}} d\tau_1 \int_{\tau'_{k_{\sigma_2}}}^{\tau_{k_{\sigma_2}}} d\tau_2 \mathcal{D}(\tau_1 - \tau_2)_{\sigma_1\sigma_2} \right), \quad (36)$$

where $\{k_{\sigma}\}$ represents the collection of segments of spin σ .

Let us now define a function $K(\tau)$ such that $K''(\tau) = \mathcal{D}(\tau)$ for $0 < \tau < \beta$ and $K(0^+) = K(\beta^-) = 0$. K is β periodic and symmetric around $\tau = \beta/2$. It has a slope discontinuity at zero, so that the second derivative also gives a delta-function contribution. In the interval $[0, \beta]$,

$$K(\tau) = \frac{1}{\beta} \sum_{n \neq 0} \frac{\mathcal{D}(i\nu_n) - \mathcal{D}(0)}{(i\nu_n)^2} (e^{i\tau\nu_n} - 1). \quad (37)$$

Carrying out the integral in Eq. (36) thus yields

$$\ln w_{\mathcal{D}} = -\frac{1}{2} \sum_{\substack{\sigma_1\sigma_2 \\ k_{\sigma_1} k_{\sigma_2}}} [-K(\tau'_{k_{\sigma_1}} - \tau'_{k_{\sigma_2}}) + K(\tau_{k_{\sigma_1}} - \tau_{k_{\sigma_2}}) + K(\tau'_{k_{\sigma_1}} - \tau_{k_{\sigma_2}}) - K(\tau_{k_{\sigma_1}} - \tau_{k_{\sigma_2}})] + K'(0)(l_{\uparrow} + l_{\downarrow}) + 2K'(0)l_{\text{overlap}}. \quad (38)$$

Using the fact that $K(\tau)$ is an even function, we can write $\ln w_{\mathcal{D}} = \sum_{i>j} s_i s_j [K(\tilde{\tau}_i - \tilde{\tau}_j) - K(0)] + K'(0)(l_{\uparrow} + l_{\downarrow}) + 2K'(0)l_{\text{overlap}}$ where the time arguments of the hybridization events (creation and annihilation operators) are now ordered as $0 < \tilde{\tau}_1 < \tilde{\tau}_2 < \dots < \beta$ and s is +1 for a creation operator and -1 for an annihilation operator.

We conclude that the retarded part of the interaction, $\mathcal{D}(\tau - \tau')$, results in a retarded “interaction” between all pairs of impurity creation and annihilation operators, as well as a shift of the instantaneous interaction $U \rightarrow \tilde{U} = U - 2K'(0)$ and a shift of the chemical potential $\mu \rightarrow \tilde{\mu} = \mu + K'(0)$. If one writes the interaction term in terms of density fluctuations, $\frac{1}{2} \iint \tilde{n}(\tau) \mathcal{D}(\tau - \tau') \tilde{n}(\tau')$ with $\tilde{n} = n - \langle n \rangle$, the only change induced in the weight is yet another shift of the chemical potential $\tilde{\mu} = \mu + K'(0) - 2\langle n \rangle K'(0)$. The retarded interactions can be evaluated at negligible computational cost since the calculation of this contribution for a local update is $O(n)$ (where n is the number of operators), while the evaluation of a determinant ratio is $O(n^2)$.

In practice, the local bosonic propagator $W_{\text{loc}} = \langle T\phi(\tau)\phi(0) \rangle$ needed in Eq. (26) is deduced from the connected charge-charge correlation function $\chi_{\text{loc}} = \langle T\tilde{n}(\tau)\tilde{n}(0) \rangle$ via the relation

$$W_{\text{loc}}(i\nu_n) = \mathcal{U}(i\nu_n) - \mathcal{U}(i\nu_n)\chi_{\text{loc}}(i\nu_n)\mathcal{U}(i\nu_n). \quad (39)$$

Indeed, using Eq. (21), W_{loc} can be reexpressed as $W_{\text{loc}} = -2 \frac{\delta \ln Z}{\delta \mathcal{U}^{-1}}$. The chain rule $\frac{\delta \ln Z}{\delta \mathcal{U}^{-1}} = -\mathcal{U} \frac{\delta \ln Z}{\delta \mathcal{U}}$ and Eq. (23) give $\frac{\delta \ln Z}{\delta \mathcal{U}} = -\frac{1}{2} \chi_{\text{loc}} + \frac{1}{2} \mathcal{U}^{-1}$, and hence one arrives at Eq. (39). An analogous expression holds for D_{loc} .

B. Self-consistency

The GW + EDMFT scheme is generally expected to work well if the nonlocal GW contribution to the self-energy is a relatively small correction to the local self-energy computed by EDMFT. It thus makes sense to first obtain a reasonable guess of the final solution by applying EDMFT only, and then compute the nonlocal correction and study its effect on the properties of the system. Following this observation, we implemented the GW + EDMFT scheme as follows: for a given U and V , we (i) obtain a converged EDMFT solution, (ii) take the EDMFT solution as the starting point for a

self-consistent $GW + \text{EDMFT}$ calculation, and (iii) stop when local and nonlocal observables have converged.

This is not the only possible combination of EDMFT with GW , although the final result of the self-consistent scheme should not depend on the starting point, provided the scheme converges. For instance, one can choose to initialize the scheme by computing Σ^{GW} and Π^{GW} from the noninteracting propagators $G_0(k, i\omega_n) = [i\omega_n + \mu - \epsilon(k)]^{-1}$ and $W_0(k, i\nu_n) = v_k$. Yet, these propagators yield a very large GW polarization owing to their metallic character (they correspond to the $U = 0, V = 0$ case). Especially for the regions of interest here (V close to V_c and finite U), this large polarization is far from the expected solution. Indeed, one can observe that when taking an insulating G and, e.g., $W = v$ as inputs for GW , the resulting polarization is small compared to the local polarization Π_{loc} .

C. Analytical continuation

The nontrivial structures of the frequency-dependent interaction result in additional features in the local spectral function $A(\omega) = -\frac{1}{\pi} \text{Im}G(\omega + i\eta)$. For example, the case $\text{Im}\mathcal{D}(\omega) = -\lambda^2 [\delta(\omega - \omega_0) - \delta(\omega + \omega_0)]$, studied in Ref. 21, corresponds to the Holstein-Hubbard model, for which the local spectral function is expected to display plasmonic peaks at multiples of the ‘‘plasmon’’ frequency ω_0 .¹⁹ However, the commonly used maximum entropy (MaxEnt) analytical continuation⁶² tends to smooth out high-energy features and therefore a dedicated scheme must be implemented to recover the sought-after features. A solution to this problem has been proposed in Ref. 19, inspired from the exact expression of the Green’s function in the atomic limit.⁶³ We thus proceed as follows: (a) From $\mathcal{U}(i\nu_n)$ (or, equivalently, \mathcal{D}), we compute the bosonic function $B(\tau) = \exp[-K(\tau)]$, its Fourier transform $B(i\nu_n)$ and, using a Padé procedure,⁶⁴ its spectral function $B(\omega)$. (b) From $G(\tau)$, we compute an auxiliary function $G_{\text{aux}}(\tau) = G(\tau)/B(\tau)$ and use MaxEnt to obtain $A_{\text{aux}}(\omega)$. (c) Finally, we compute the spectral function as the convolution

$$A(\omega) = \int_{-\infty}^{\infty} d\epsilon B(\epsilon) \frac{1 + e^{-\beta\omega}}{(1 + e^{\beta(\epsilon-\omega)})(1 - e^{-\beta\epsilon})} A_{\text{aux}}(\omega - \epsilon). \quad (40)$$

V. SUMMARY OF THE COMPUTATIONAL SCHEME

The computational scheme can be summarized as follows for the HS- UV [resp. HS- V] decoupling:

(1) Start with an initial guess for $\Sigma(k, i\omega)$ and $\Pi(k, i\nu)$: for instance, $\Sigma = 0$ and $\Pi = 0$ (noninteracting limit).

(2) *Lattice Green’s functions.* Compute $G(k, i\omega)$ and $W(k, i\nu)$ [resp. $D(k, i\nu)$] via Dyson’s equation with v_k [resp. v_k^{nl}] as the bare interaction.

(3) *EDMFT self-consistency.* Extract $G_{\text{loc}}(i\omega) = \sum_k G(k, i\omega)$ and $W_{\text{loc}}(i\nu) = \sum_k W(k, i\nu)$ [resp. D_{loc}] and use Eqs. (25) and (26) to find $\mathcal{G}(i\omega)$ and $\mathcal{U}(i\nu)$ [resp. $\mathcal{D}(i\nu)$].

(4) *Impurity solver.* Compute $G_{\text{loc}}(\tau)$ and $\chi_{\text{loc}}(\tau)$ [resp. $\chi_{\text{loc}}^V(\tau)$], as well as $W_{\text{loc}} = \mathcal{U} - \mathcal{U}\chi_{\text{loc}}\mathcal{U}$ [resp. $D_{\text{loc}} = \mathcal{D} - \mathcal{D}\chi_{\text{loc}}^V\mathcal{D}$]. From these, extract the self-energies $\Sigma_{\text{loc}} = \mathcal{G}^{-1} - G_{\text{loc}}^{-1}$ and $\Pi_{\text{loc}} = \mathcal{U}^{-1} - W_{\text{loc}}^{-1}$ [resp. $(\Pi_V)_{\text{loc}} = \mathcal{D}^{-1} - D_{\text{loc}}^{-1}$].

(5) *GW + DMFT step (optional).*

(a) Compute

$$\begin{aligned} \Pi^{GW}(k, \tau) &= 2 \sum_q G(q, \tau) G(q - k, -\tau), \\ \Sigma^{GW}(k, \tau) &= - \sum_q G(q, \tau) W^c(k - q, \tau) \\ &\quad + \sum_q G(q, 0) v(k - q), \end{aligned}$$

where $W^c = W - v$ is the regular part of W . Respectively, for HS- V ,

$$\begin{aligned} \Sigma^{GW}(k, \tau) &= - \sum_q G(q, \tau) D(k - q, \tau), \\ &\quad - U^2 \sum_q G(q, \tau) \Pi^{GW}(q - k, \tau). \end{aligned}$$

(b) Extract nonlocal parts from GW :

$$\begin{aligned} \Sigma_{\text{nonloc}}^{GW}(k, i\omega) &= \Sigma^{GW}(k, i\omega) - \sum_k \Sigma(k, i\omega), \\ \Pi_{\text{nonloc}}^{GW}(k, i\nu) &= \Pi^{GW}(k, i\nu) - \sum_k \Pi(k, i\nu). \end{aligned}$$

(c) Combine $\Sigma_{\text{loc}}(i\omega)$ and $\Sigma_{\text{nonloc}}^{GW}(k, i\omega)$ into $\Sigma(k, i\omega)$, as well as $\Pi_{\text{loc}}(i\nu)$ and $\Pi_{\text{nonloc}}^{GW}(k, i\nu)$ into $\Pi(k, i\nu)$.

(6) Go back to step 2 until convergence.

In a pure EDMFT scheme, steps 5(a)–(c) are skipped. Note that the decomposition of W into W^c and v in 5(a) is aimed at suppressing the singular part of W , namely, in the limit of infinite frequency, W goes to a finite value v , whereas W^c vanishes, making the Fourier transform of the latter well defined. Figure 4 gives an overview of the implementation of the $GW + \text{DMFT}$ scheme.

VI. RESULTS

In this section, we present numerical results for the half-filled U - V Hubbard model on a two-dimensional square lattice using the different approximate formalisms discussed in the previous sections. We solve the impurity problems using the CTQMC-hyb method. Unless otherwise stated, the computations are performed at inverse temperature $\beta = 100$ (we use the half-bandwidth $4t$ as the unit of energy). The k sums are discretized in the irreducible Brillouin zone on a 80×80 grid, while the imaginary-time correlation functions are measured on a grid of $N = 1000$ equally spaced points. Up to 40 EDMFT steps are required to reach convergence close to the Mott transition.

A. Phase diagram

Figure 5 shows the phase diagram in the space of the parameters U and V for the two decoupling schemes HS- UV and HS- V . The top panel shows the EDMFT result, the bottom panel corresponds to $GW + \text{DMFT}$. There are three phases: (i) a Fermi liquid (FL) metal at small U and small V , (ii) a charge-ordered (CO) insulator at small U and large V , and (iii) a Mott insulating (MI) phase at large U and small V .

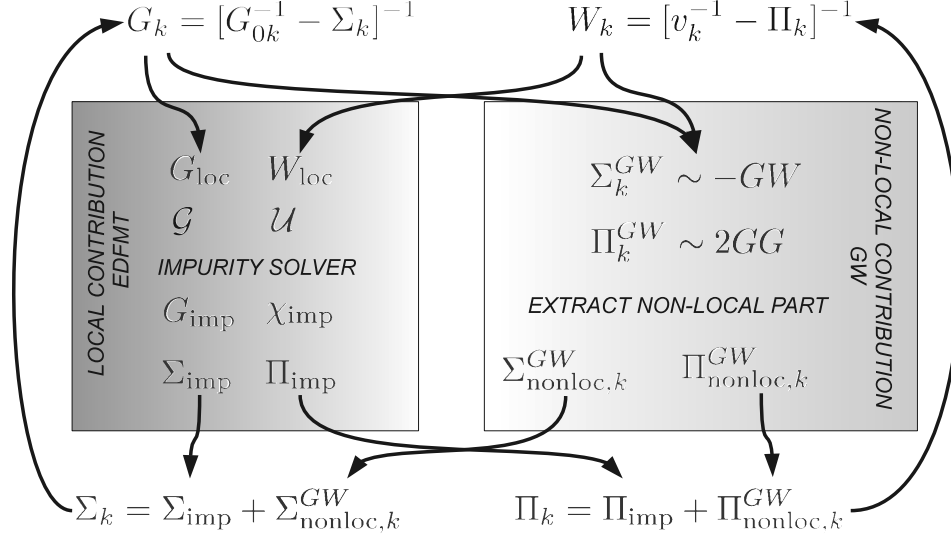


FIG. 4. Computational scheme (HS-UV decoupling).

The phase boundary to the charge-ordered phase has been located by approaching the phase transition from below V_c .

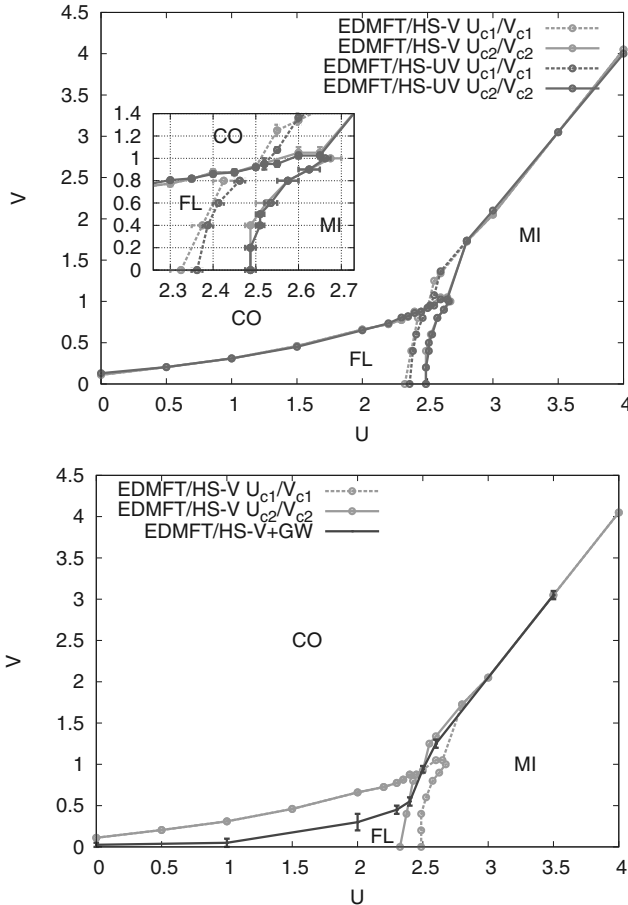


FIG. 5. (Color online) Phase diagram of the U - V Hubbard model for HS-UV (red), and HS-V (green) decoupling at $\beta = 100$. The top panel shows the EDMFT result, and the bottom panel compares the GW + EDMFT result for the HS-V scheme to EDMFT.

The phase transition corresponds to a diverging charge susceptibility, namely, to the formation of a pole in the Fourier transform $\chi(k, \omega)$ of $\chi_{ij}(t-t') \equiv \partial \langle n_i(t) \rangle / \partial h_j(t')$, where $h_j(t)$ is a probe field. Specifically, the charge-ordering transition will be signaled by a divergence at $Q = (\pi, \pi)$ and $\omega = 0$ since the probe field for this phase is $h_i(t) = h e^{iQR_i}$. Using the action (2), one can easily show that $\chi_{ij}(t-t') = \langle \bar{n}_i(t) \bar{n}_j(t') \rangle$. Recalling that $W = v - v\chi v$, we find the exact relation

$$\chi(k, \omega) = -\frac{\Pi(k, \omega)}{1 - v_k \Pi(k, \omega)} \quad (41)$$

for the HS-UV scheme. Similarly, for the HS-V scheme, χ_V can be computed from $D = v^{nl} - v^{nl} \chi_V v^{nl}$ or $\chi_V = -\Pi_V / (1 - v^{nl} \Pi_V)$. This shows that the transition also corresponds to the appearance of a pole in the fully screened interaction $W(k, i\nu_n)$, and provides a rigorous definition of V_c for HS-UV and HS-V, respectively:

$$1 - (U - 4V_c) \Pi[k = (\pi, \pi), \omega = 0] = 0, \quad (42)$$

$$1 + 4V_c \Pi_V[k = (\pi, \pi), \omega = 0] = 0. \quad (43)$$

On the other hand, the phase boundary between the metal and the Mott insulator is signaled by a vanishing spectral weight at the Fermi level, which is related to the imaginary-time Green's function by $A_{T \rightarrow 0}(\omega = 0) = \lim_{\beta \rightarrow \infty} \frac{\beta}{2} G(\frac{\beta}{2})$. The curvature of the FL-MI phase boundary shows that increasing the nearest-neighbor repulsion V makes the system more metallic.

Within EDMFT, both decoupling schemes yield very similar phase diagrams. In the temperature range $\beta \in [25, 100]$, the phase diagram also does not depend much on temperature. The boundary of the charge-ordered phase is characterized by two main regimes: for $U < U_c \approx 2.5$, $dV_c/dU \approx \frac{1}{4}$, which is the prediction of mean-field studies. For $U > U_c$, $dV_c/dU \approx 2$. The transition between the two regimes is marked by a kink. This kink also coincides with the point where the charge-ordered critical line meets the Mott critical line $U_c(V)$. The latter is only weakly dependent on V . The sudden change of

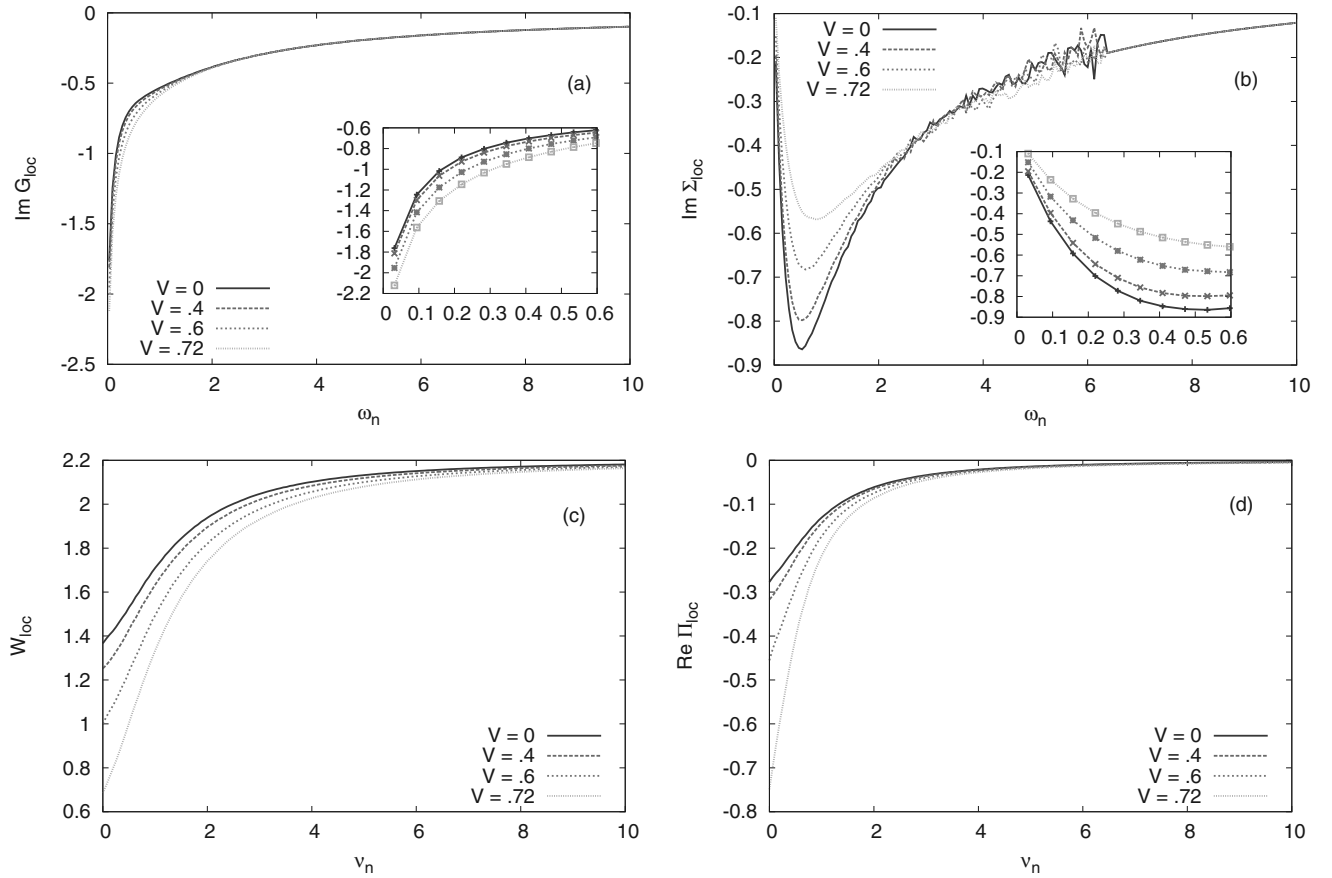


FIG. 6. (Color online) Imaginary-frequency data for the EDMFT calculations at $U = 2.2$ and indicated values of V (HS- UV scheme). (a) $\text{Im}G_{\text{loc}}(i\omega_n)$. (b) $\text{Im}\Sigma_{\text{loc}}(i\omega_n)$. (c) $\text{Re}W_{\text{loc}}(i\nu_n)$. (d) $\text{Re}\Pi_{\text{loc}}(i\nu_n)$.

slope in the critical line can be ascribed to the very nature of the two transitions at stake: one is a transition between a metal and a charge-ordered insulator, the other takes place between an incompressible Mott insulator and a charge-ordered insulator. The slope change is accompanied by a discontinuity of the V_c line at its junction with the Mott critical line: this is due to the first-order character of the Mott transition within DMFT. We note that the critical value $V_c(U)$ for $U > U_c$ is substantially larger than its naive mean field estimate. EDMFT may, however, overestimate the effect of the local interaction, so that the true value of V_c is lower.

The effect of the GW contribution to the phase diagram depends on the decoupling scheme. For HS- UV , GW does not have any influence on the phase boundaries, while in HS- V , GW substantially lowers the FL-CO phase boundary. This has the following origin: the HS- V scheme resums the diagrammatic series for V and for U separately (and treats U only to second order), whereas the HS- UV scheme resums both terms simultaneously. HS- UV is thus better poised to capture the competition between the localizing term U and the delocalizing term V . That GW in this scheme does not alter the phase boundaries should therefore come as no surprise: it merely shows that the local (EDMFT) physics alone fixes the critical value of the nonlocal interaction, and suggests that the HS- V decoupling underestimates V_c . For this reason, we will henceforth restrict most of our attention to the HS- UV scheme.

Figure 6 plots the results for $\text{Im}G_{\text{loc}}(i\omega_n)$, $\text{Re}W_{\text{loc}}(i\nu_n)$, $\text{Im}\Sigma_{\text{loc}}(i\omega_n)$, and $\text{Re}\Pi_{\text{loc}}(i\nu_n)$ corresponding to the EDMFT simulation at $U = 2.2$ and various values of V . As V grows, $|\text{Im}G(i\omega_0)|$ increases and $|\Sigma_{\text{loc}}(i\omega_0)|$ decreases, which indicates that the system becomes more metallic as a result of screening by V . Indeed, the screening effect can be quantified by the static values of the fully screened interaction $W(0) \equiv W_{\text{loc}}(i\nu_0)$ and of the partially screened interaction $U(0) \equiv \mathcal{U}(i\nu_0)$, which are plotted in Fig. 9. The nearest-neighbor repulsion V induces a screening of the onsite Hubbard U , which becomes $U(0)$. When V increases, $W(0)$ and $U(0)$ get smaller and smaller, resulting in a more metallic behavior. For U close to U_c , the transition to the charge-ordered insulator occurs close to the value of V for which the cost of doublon formation vanishes, i.e., when $W(0) = 0$.

The last panel of Fig. 6 shows the polarization $\Pi_{\text{loc}}(i\nu_n)$ (which is the local bosonic self-energy). $|\Pi_{\text{loc}}(i\nu_0)|$ gets larger as one approaches the phase boundary.

B. Screening in EDMFT

1. Screened interaction

The off-site interactions translate into an effective retarded interaction at the level of the impurity action, as made apparent in Eq. (23). The frequency-dependent local interactions in the HS- UV formalism are now described by $\mathcal{U}(\omega)$ [or $U + \mathcal{D}(\omega)$

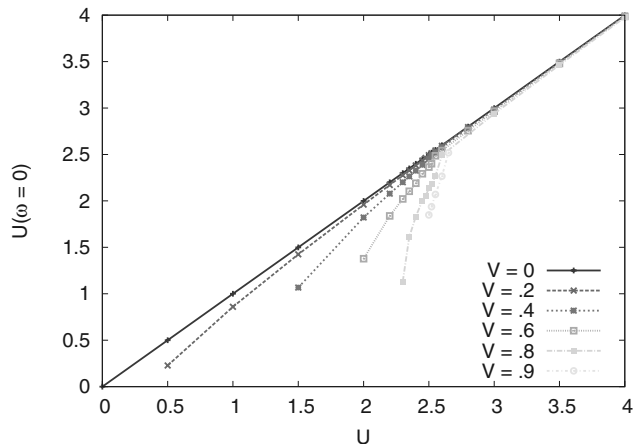


FIG. 7. (Color online) Partially screened $\mathcal{U}(\omega = 0)$ as a function of U (HS- UV scheme).

in the HS- V decoupling scheme]. They differ from the fully screened local interactions W_{loc} insofar as they only include nonlocal screening effects, at least in EDMFT. In particular, when the interactions become local ($V = 0$), \mathcal{U} becomes static and equal to the bare interaction U , and EDMFT becomes exactly equivalent to the usual single-site DMFT. This is shown in Fig. 7, where $\mathcal{U}(\omega = 0) = U$ for $V = 0$, and explains the location of the Mott transition for $V = 0$, which coincides with that found within single-site DMFT applied to the Hubbard model. Moreover, one should also emphasize that using a partially screened interaction (i.e., screened only by nonlocal processes) to solve the impurity model, one avoids double counting of the local screening effects, which are taken into account in the DMFT calculation.

In the following, we will focus more specifically on W_{loc} , which we have analytically continued to real frequencies using a Padé scheme.⁶⁴ The shape of $W_{\text{loc}}(\omega)$ at $U = 2.2$ and various V is displayed in Fig. 8. $W_{\text{loc}}(\omega)$ has the typical shape of a screened interaction: the real part features two distinct energy scales, a bare interaction $W_{\infty} = W_{\text{loc}}(\omega \rightarrow \infty) = U$ at high energies and a screened interaction $W(0) = W_{\text{loc}}(\omega = 0) < U$ at low energies, separated by a screening frequency ω_0 . Its Kramers-Kronig-conjugated imaginary part has most of its spectral weight concentrated around ω_0 . We note that $\mathcal{U}(\omega)$ has a very similar overall shape. Also noteworthy is the fact that $\text{Re}W_{\text{loc}}(\omega)$ can become negative at a nonzero frequency *before* its static value vanishes, that is, before the phase transition. This signals that charge-ordering fluctuations to charge-ordered configurations are already enhanced in the system before the phase transition occurs.

In order to characterize screening effects, we will mainly focus on the following three parameters: (i) the value of the local static screened interaction $W_{\text{loc}}(0)$, (ii) the screening frequency ω_0 , and (iii) the strength λ of this screening, which we will define later.

$W_{\text{loc}}(0)$ is the effective fully screened interaction between two electrons on the same lattice site. Its evolution across the U - V plane for the HS- UV scheme is illustrated in Fig. 9. $W_{\text{loc}}(0)$ decreases for increasing V , and drops to zero as V approaches V_c . This is intuitively easy to understand: the critical line corresponds to the locus where the cost

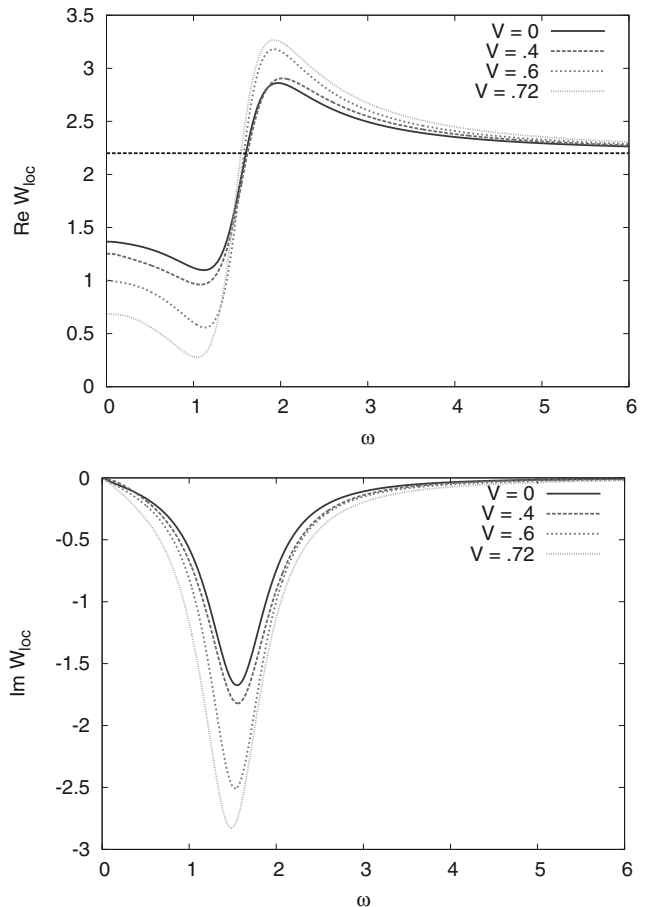


FIG. 8. (Color online) Influence of V on the effective local interaction for $U = 2.2$ (HS- UV scheme). Upper panel: $\text{Re}W_{\text{loc}}(\omega)$. Lower panel: $\text{Im}W_{\text{loc}}(\omega)$.

$W_{\text{loc}}(\omega = 0)$ for the formation of doublons vanishes. The lower panel of Fig. 9 shows that the screening of the local interaction is much more efficient and gradual in the metallic phase than in the Mott insulator. In the insulating phase, screening is weak and weakly V dependent, all the way up to V_c . Let us emphasize that there are screening effects even when $V = 0$ in the metallic phase (middle panel, red curve with crosses). This shows that in a EDMFT description of the simple Hubbard model ($V = 0$), there is a screening of the static U by the *local* polarization caused by U itself, provided one uses the HS- UV decoupling scheme. In the HS- V method, the screening comes only from V , as D originates from the HS decoupling of the nearest-neighbor interaction only. The local static interactions without polarization effects are shown in Fig. 9. As expected, $\mathcal{U}(\omega = 0) > W(0)$ since the local polarization further screens the local interaction.

2. Screening frequency

A relevant question is in which parameter regime a model with a static screened interaction provides a reasonable approximation. A useful quantity to investigate in this context is the screening frequency ω_0 , whose precise determination is a somewhat tricky task owing to the Padé procedure's inaccuracy. Instead of measuring ω_0 as the minimum of

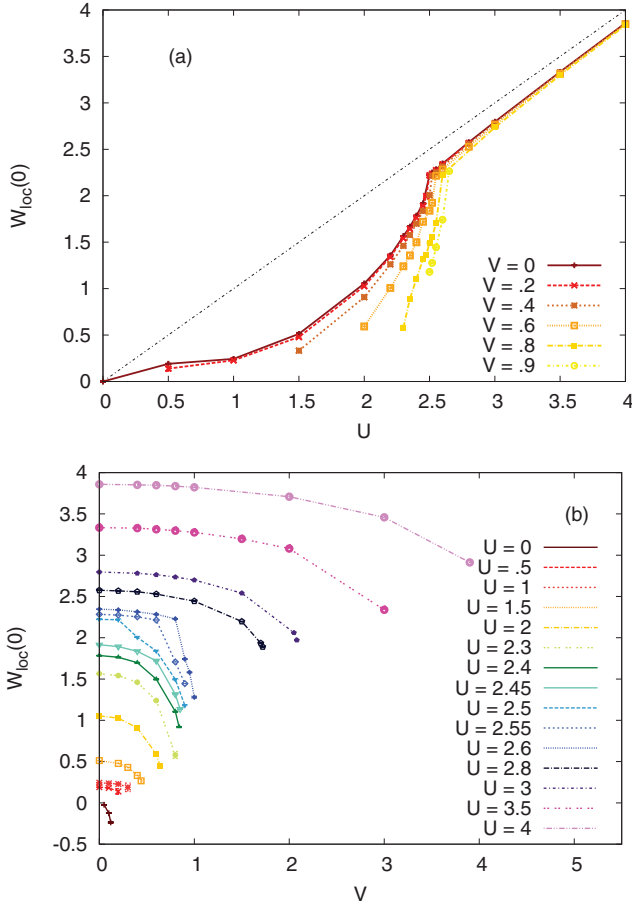


FIG. 9. (Color online) Static screened interactions in the HS- UV scheme. (a) Fully screened $W_{\text{loc}}(\omega = 0)$ as a function of U . (b) $W_{\text{loc}}(\omega = 0)$ as a function of V .

$\text{Im}W_{\text{loc}}(\omega)$, we have found it more meaningful to determine it from the first moment of $\text{Im}W_{\text{loc}}(\omega)$: $\omega_0 \approx \langle \omega \rangle \equiv \int_0^\infty d\omega \omega \text{Im}W_{\text{loc}}(\omega) / \int_0^\infty d\omega \text{Im}W_{\text{loc}}(\omega)$, whose dependence on U and V in the HS- UV scheme is presented in the upper panel of Fig. 10. This figure shows that the screening frequency is only weakly dependent on the nearest-neighbor interaction V . On the other hand, the larger the bare interaction $U = U_\infty$, the larger the screening frequency.

The U dependence of $\langle \omega \rangle$ (for $V = 0$) is discussed in Appendix D, where we also provide an interpretation of the two regimes, separated by a kink at $U = U_c$, based on the so-called linearized DMFT.⁶⁵

3. Electron-boson coupling

Motivated by the Hamiltonian representation of the impurity model with dynamically screened interaction (see Appendix C), we define the strength of the screening by the parameter $\lambda \equiv \sqrt{|\int_0^\infty d\omega \text{Im}\mathcal{U}(\omega)|}$. It follows from Eq. (C5) that $\lambda \propto \sqrt{\sum_p \lambda_p^2}$, where λ_p is the coupling of the harmonic oscillator with frequency ω_p to the charge on the impurity. Therefore, λ can be interpreted as the strength of the coupling to the charge fluctuations. Its dependence on U and V is presented in the lower panel of Fig. 10. Except in the vicinity of the

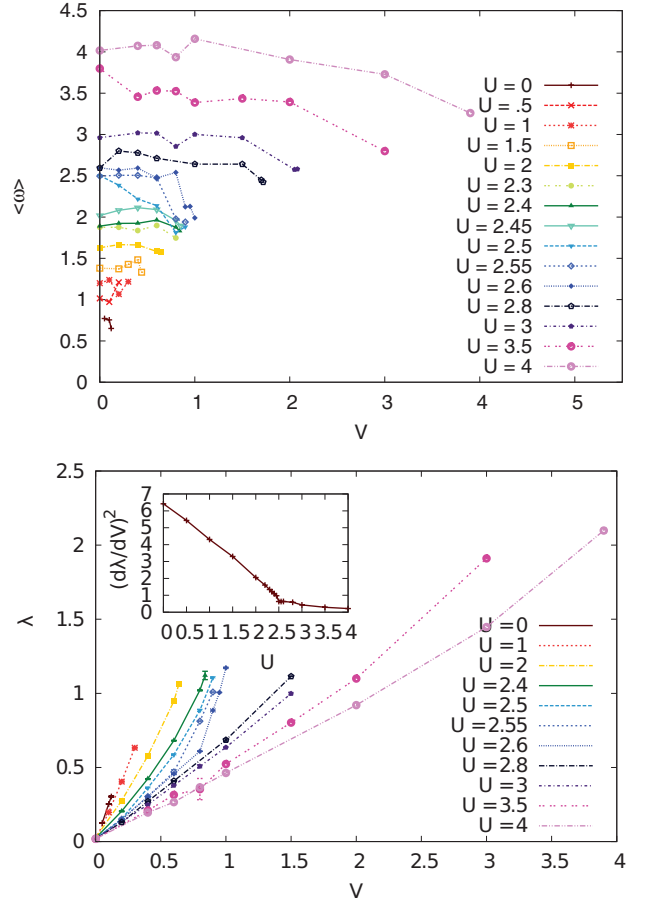


FIG. 10. (Color online) Screening parameters. Upper panel: $\langle \omega \rangle$ as a function of V . Lower panel: λ as a function of V (HS- UV scheme). Inset: $(\frac{d\lambda}{dV})^2$ as a function of U .

phase transition to the charge-ordered phase, λ is proportional to V . The square of the proportionality constant (see inset⁶⁶) decreases with increasing U , and exhibits two regimes separated by a kink at $U = U_c$: for $U \leq U_c$, $\frac{d}{dU}[(\frac{d\lambda}{dV})^2] \approx -2.2$, otherwise $\frac{d}{dU}[(\frac{d\lambda}{dV})^2] \approx -0.34$. Recalling that the effective dynamical interaction is, schematically, $\lambda^2 \mathcal{D}$, where \mathcal{D} is the propagator of the mediating boson (see Appendix C), one can observe that $[d\lambda/dV]^2$ is directly proportional to the effective interaction, since $\lambda \approx [d\lambda/dV]_{V=0} \cdot V$. The inset of the upper panel of Fig. 10 thus gives a direct indication of the strength of dynamical effects. In particular, it indicates once again that screening in the Mott insulator is radically different from screening in the Fermi-liquid metal.

4. Influence of screening on spectral properties

The screening effects coming from U and V have some impact on the local spectral function. In the weakly correlated regime ($U < U_c$), the nonlocal interactions V tend to smooth out the incoherent Hubbard bands and transfer some spectral weight to the quasiparticle peak and into the gap region between the quasiparticle peak and the Hubbard bands (Fig. 11, upper panel). This behavior is consistent with the imaginary-frequency data showing a more metallic behavior as V increases. The effects are more dramatic in the strongly

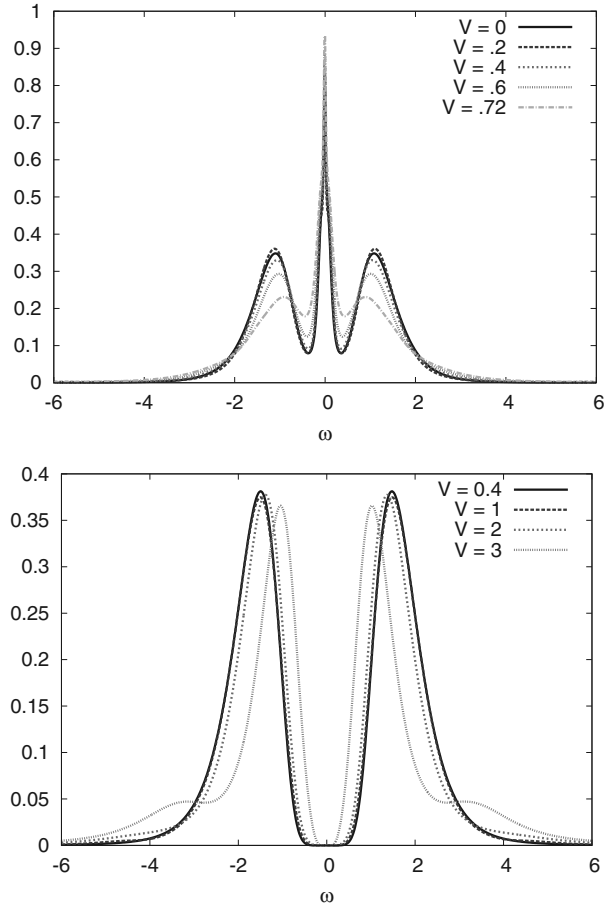


FIG. 11. (Color online) Local spectral function $A_{\text{loc}}(\omega)$ (HS-UV scheme).

correlated regime ($U > U_c$), where one observes new features in the local spectral function, as shown in the lower panel of Fig. 11. In addition to the two Hubbard bands located at $\omega = \pm U/2$, the spectral function has two symmetric satellites at $\omega = \pm(U/2 + \omega_0)$, whose spectral weight grows with V . The position of the peaks comes from the convolution in Eq. (40) since A_{aux} contains spectral weight at $\pm U/2$ and B contains weight at $\pm \omega_0$.

C. Momentum dependence in GW + DMFT

1. Nonlocal self-energy

Figure 12 displays $\Sigma_{\text{nonlocal}}^{GW}(k, i\omega_0)$ and $\Pi_{\text{nonlocal}}^{GW}(k, i\nu_0)$ in the metallic phase near the charge-ordering transition. These quantities vanish in the limit of large dimensions and are thus neglected in the EDMFT treatment. The GW contribution to the imaginary part of the electronic self-energy Σ is negligible with respect to the local self-energy [for instance, at $U = 2$ and $V = 0.6$, $\text{Im}\Sigma_{\text{loc}}(i\omega_0) = -0.18$, compared to a nonlocal GW self-energy < 0.001]. This holds across the Fermi-liquid phase and the Mott insulating phase. The real part of $\Sigma_{\text{nonlocal}}^{GW}$ is relatively large away from the EDMFT Fermi surface, but does not alter this Fermi surface. On the other hand, the nonlocal polarization is comparable to its local counterpart [$\Pi_{\text{loc}}(i\nu_0) = -0.39$ for $U = 2$, $V = 0.6$].

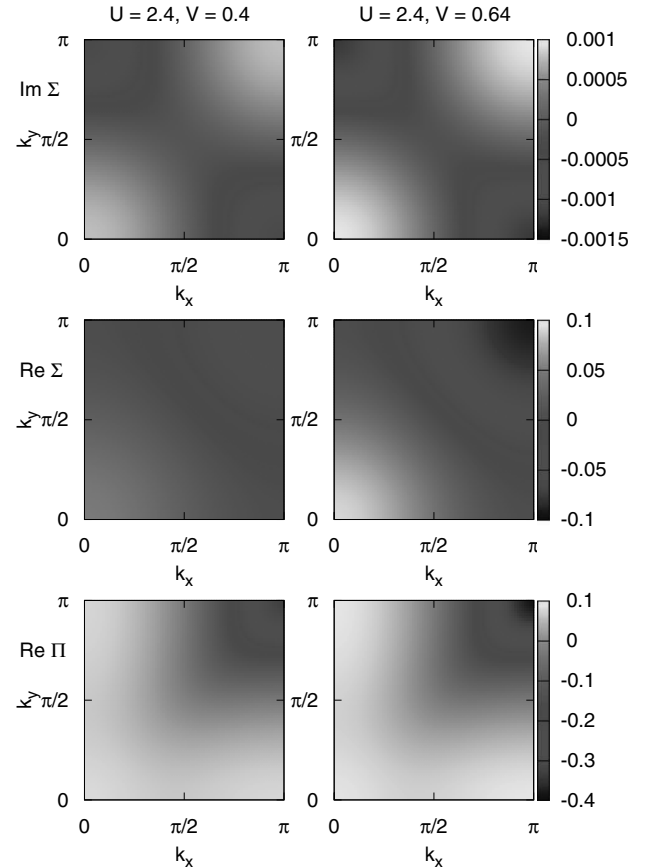


FIG. 12. (Color online) GW nonlocal contribution in the HS-UV scheme. Top: $\text{Im}\Sigma_{\text{nonlocal}}^{GW}(k, i\omega_{n=0})$. Middle: $\text{Re}\Sigma_{\text{nonlocal}}^{GW}(k, i\omega_{n=0})$. Bottom: $\text{Re}\Pi_{\text{nonlocal}}^{GW}(k, i\nu_{n=0})$.

This should have an impact on the phase diagram if one recalls the criterion of Eq. (42). However, the *local* observables are also modified in the self-consistent calculation, as will be described in the next section, which prevents a direct prediction of the effect of the nonlocal terms. As shown in Fig. 5, the effect of GW depends on the decoupling scheme. For the HS-UV scheme, the GW contribution has a negligible influence on the phase diagram. For the HS-V scheme, the GW contribution has a large effect on the phase boundary between the metallic phase and the charge-ordered phase. The nonlocal polarization, peaked at $k = (\pi, \pi)$, enhances nesting effects and leads to a substantially lower V_c compared to EDMFT.

2. Nonlocal polarization

Two-particle quantities such as the charge-charge correlation function or the electron energy-loss spectrum are quite strongly affected by the nonlocal GW contribution to the polarization, as discussed in Ref. 24. In particular, $GW + \text{DMFT}$ gives insights into the nature of the collective modes in the homogeneous system, which EDMFT cannot give due to the local nature of its polarization.

Figure 13 shows results for the polarization function. We note that within single-site DMFT, one could in principle obtain a nonlocal polarization function from the momentum-dependent one-particle Green's function $G(k, \omega)$ (evaluated

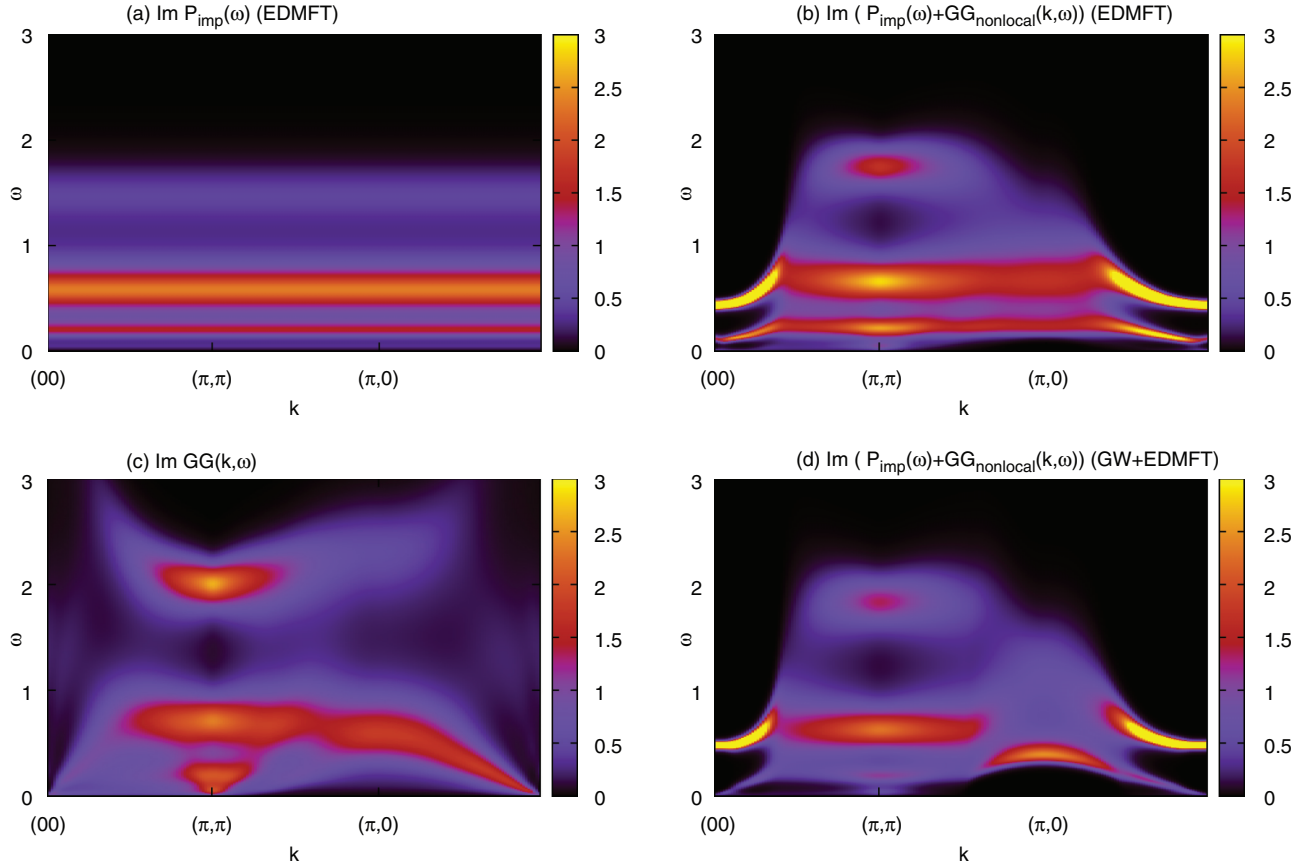


FIG. 13. (Color online) Comparison of various polarizations for $U = 1.5$, $V = 0.4$ (HS-UV scheme).

with the local EDMFT self-energy) by computing the polarization bubble GG . While this approximation to the polarization is momentum dependent, it nevertheless lacks any information about the local vertex other than through G itself. However, as was demonstrated in Ref. 24, the local vertex plays a major role when the strength U of local correlations grows. In EDMFT, on the other hand, the locality of the polarization function is assumed [see Fig. 13(a)], but the nonperturbative local vertex is taken into account since the local polarization is obtained from the nonperturbative local charge-charge correlation function. The $GW + DMFT$ scheme allows one to overcome both limitations by encompassing both the local vertex (through the local part of the polarization) *and* the momentum dependence (through the nonlocal part of the bubble). In other words, conceptually, $GW + DMFT$ contains more than just the bubble (through the local part of the polarization) and still yields a momentum-dependent polarization, which is more than both single-site DMFT and extended DMFT can achieve. To illustrate this point, we show in Fig. 13 the polarization bubble computed from a converged EDMFT calculation in Fig. 13(c), and the full, converged polarization of a $GW + DMFT$ calculation in Fig. 13(d) (for $U = 1.5$, $V = 0.4$).

Using the output of the converged EDMFT calculation, namely, the local self-energy Σ_{imp} and the polarization P_{imp} , one could again construct a momentum-dependent polarization in the following way: first, compute the one-particle Green's function $G(k, \omega)$ from Σ_{imp} through Dyson's equation; second, compute the bubble GG ; third,

combine it with P_{imp} to get the momentum-dependent polarization: $P(k, \omega) = P_{\text{imp}}(\omega) + (GG)_{\text{nonloc}}(k, \omega)$. This approach is similar to the $GW + DMFT$ method with the important difference that it is not self-consistent, namely, the computed momentum-dependent polarization is not in turn used as an input to the next computational step. Even if the momentum dependence is physically important, it will not in this scheme have a consequence on the local one-particle spectra, for example. In Fig. 13, we compare this polarization [Fig. 13(b)] to the $GW + DMFT$ polarization [Fig. 13(d)]. While being quite similar in certain regions of the Brillouin zone, the two functions are very different in others [above the $(\pi, 0)$ point for instance]. In particular, one notices that the structure of the polarization computed on top of EDMFT, albeit momentum dependent, is very similar to the local EDMFT polarization [Fig. 13(a)] away from the $(0, 0)$ point, while the $GW + DMFT$ polarization shows significant deviations from it throughout the Brillouin zone.

D. Influence of the self-consistency on local observables

The self-consistency condition leads to an “adjustment” of the local quantities to the nonlocal self-energies, as shown in Fig. 14, which illustrates the convergence from EDMFT to $GW + DMFT$: GW not only adds a nonlocal contribution to the self-energy and polarization, it also induces a change in the *local* observables (see also Fig. 15).

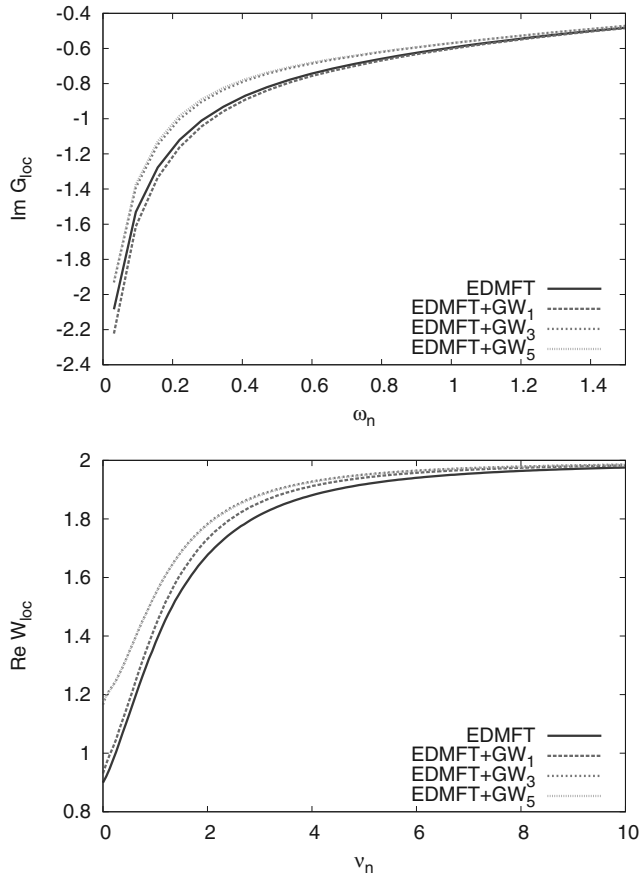


FIG. 14. (Color online) Convergence properties for $U = 2$, $V = 0.4$ (HS- UV scheme). EDMFT corresponds to the converged EDMFT result, EDMFT + GW_i denotes the observables corresponding to the i th iteration with nonlocal self-energies, with EDMFT as starting input. Upper panel: $\text{Im}G_{\text{loc}}(i\omega_n)$. Lower panel: $\text{Re}W_{\text{loc}}(i\nu_n)$.

The $GW + \text{DMFT}$ local spectral function features more pronounced Hubbard bands than the EDMFT spectrum. This is a sign of increased local correlations. Inspection of the imaginary frequency data corroborates this observation: $W_{\text{loc}}(\omega = 0)$ is enhanced with respect to the EDMFT result, indicating that the local interactions are stronger. Likewise, $|\text{Im}G_{\text{loc}}(i\omega_0)|$ is reduced in $GW + \text{DMFT}$.

These observations mean that the local quantities have become more “insulating” in character as a result of the addition of the nonlocal GW self-energy. This can be interpreted in the following way: contrary to the EDMFT case, where all the screening and correlation effects are absorbed into the local self-energy, in $GW + \text{DMFT}$ some of these effects are now carried by the nonlocal components. Specifically, GW nonlocal self-energies carry important screening effects owing to the very nature of the GW approximation. This leads to a redistribution of the screening between local and nonlocal observables: local observables become less screened, and thus more correlated.

We note that the convergence properties depend on the observable. For example, after the first iteration, $\text{Im}G_{\text{loc}}$ looks more metallic than the EDMFT result, while the converged solution is more strongly correlated. In the case of $\text{Re}W_{\text{loc}}$ already the first iteration leads to an increase in the interaction.

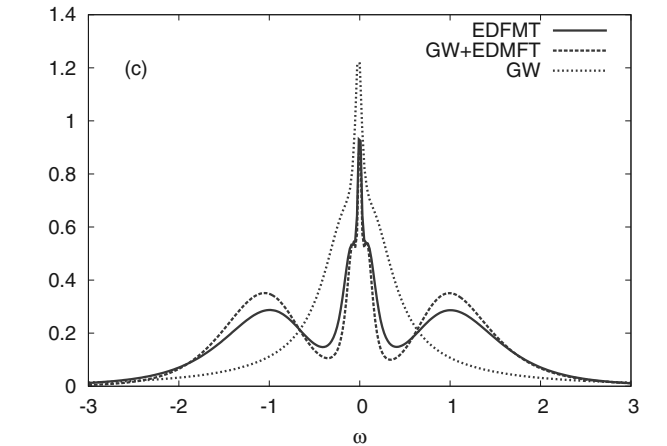
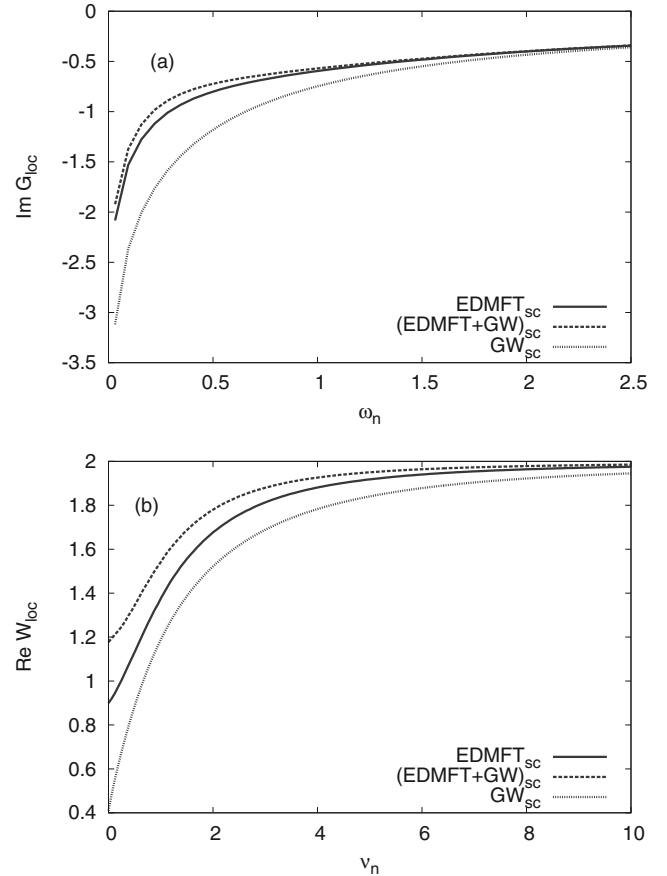


FIG. 15. (Color online) Influence of the self-consistency for $U = 2$, $V = 0.4$ (HS- UV scheme). (a) $\text{Im}G_{\text{loc}}(i\omega_n)$. (b) $\text{Re}W_{\text{loc}}(i\nu_n)$. (c) $A_{\text{loc}}(\omega)$ (obtained from MaxEnt continuation).

In both cases, the result is clearly not converged after one iteration, which casts some doubt on the validity of “one-shot” $GW + \text{DMFT}$ schemes.

Figure 15 shows the converged $\text{Im}G_{\text{loc}}$ and $\text{Re}W_{\text{loc}}$ for the three self-consistent schemes: EDMFT alone, $GW + \text{DMFT}$, and GW alone (with the $GW + \text{DMFT}$ result as a starting point). As expected, GW is the most metallic in character and the corresponding spectrum does not have Hubbard bands. Interestingly, $GW + \text{DMFT}$ is not a kind of “average” between

TABLE I. Summary of the different schemes.

| | HS- V | HS- UV |
|--------------------|--|--|
| Single-site DMFT | Accurate treatment of local interactions from weakly correlated limit to atomic limit. Cannot deal with long-range interactions beyond Hartree level. Local description of correlations through a local self-energy. Captures Mott transition. | |
| EDMFT | Accurately handles local interactions from weakly correlated limit to atomic limit. Captures Mott transition and charge-ordering transition. Deals with long-range interactions through dynamical interactions at the local level. Describes local one-particle correlations through the local self-energy. Captures local polarization processes. | Same as HS- V . Additionally, allows one to compute a fully screened interaction $W_{\text{loc}}(\omega)$, screened by a nontrivial local polarization, even when $V = 0$. |
| GW | Accurately handles local and nonlocal (including long-ranged) interactions in the weakly correlated regime. Captures local and nonlocal polarization processes, among which nesting effects. The self-energy sums up the subset of local and nonlocal diagrams to infinite order in V , to second order in U , possibly overestimating nonlocal processes. | Same as HS- V , but treats both local and nonlocal interaction terms at the same level of approximation, i.e., to infinite order. Hence, gives better account of competition between local and nonlocal processes. |
| $GW + \text{DMFT}$ | Accurate treatment of local and nonlocal (including long-ranged) interactions from weakly correlated regime to atomic limit. Captures local and nonlocal polarization processes, among which nesting effects. At a given iteration, the self-energy sums up all the local diagrams to infinite order in U and V , as well as a (RPA) subset of nonlocal diagrams to infinite order in V , to second order in U , thus overestimating nonlocal processes; in particular, underestimates the value of the critical V to the charge-ordered phase compared to HS- UV . Intersite antiferromagnetic fluctuations are not included. | Same as HS- UV , but the nonlocal diagrams treat U and V on the same footing, curing the deficiency of HS- V ; in particular, gives better estimate of critical V to the charge-ordered phase. |

GW and EDMFT. It exhibits stronger correlation effects than both GW and EDMFT.

E. Summary

Table I gives a general overview of the results presented above.

VII. CONCLUSIONS

We have implemented the EDMFT and $GW + \text{DMFT}$ methods and presented an application to the single-band extended Hubbard model. In a first step, the two formalisms have been reviewed in detail: we have discussed the construction of the free-energy functional, and compared two different flavors of such functionals that have been proposed in the literature, corresponding to two distinct decouplings of the interaction term, and leading, respectively, to the $GW + \text{DMFT}$ (Refs. 16–18) and $\text{GD} + \text{SOPT} + \text{DMFT}$ (Refs. 14 and 15) approaches. We have presented the details of our implementation of a fully self-consistent $GW + \text{DMFT}$ scheme based on a numerically exact continuous-time quantum Monte Carlo solver adapted for frequency-dependent local interactions. The investigation of the frequency dependence of these interactions for parameters ranging from weak to strong coupling shows that the U dependence of the local screening frequency reflects the form of the local one-particle spectrum. We have investigated the spectral properties of the extended Hubbard model within three self-consistent schemes, namely, EDMFT, GW , and $GW + \text{DMFT}$. The nearest-neighbor repulsion V leads, in the Mott insulator, to high-energy satellites in the local spectra.

The $GW + \text{DMFT}$ calculations demonstrate that the non-local contributions to the self-energy coming from the GW diagrams are quite small in the case of the extended Hubbard model. In view of the strong momentum dependence observed in self-energies obtained from cluster DMFT calculations for the two-dimensional Hubbard model as one approaches the Mott transition,^{67,68} our results confirm the importance of spin fluctuations, suggesting that further nonlocal diagrams have to be considered in order to capture the dominant fluctuations in the extended Hubbard model.

The model calculations presented in this paper can be straightforwardly extended to the multiorbital case and to additional, longer-range matrix elements of the screened interaction, paving the way for realistic first-principles material calculations.²⁶ It is worthwhile to note that the $GW + \text{DMFT}$ method and its variations are a computationally cheap way of incorporating the leading vertex contribution, in the form of the EDMFT self-energy, into the description of a solid, and to introduce some spatial fluctuations through a perturbative scheme. This contrasts with methods involving an explicit computation of the vertex functions^{7,9,69} whose implementation for simple model systems is already a formidable challenge.

In real materials, further degrees of freedom, stemming for example from the multiband nature and ligand orbitals, lead to a renormalization and/or frequency-dependence of the parameters in the low-energy description. Relatively weak, but nonlocal correlation effects are expected to play a dominant role in the case of extended ligand or higher-lying empty states, thus providing an additional motivation for a combination of GW and DMFT. Indeed, GW provides an accurate

and comparatively inexpensive description of the screening from “uncorrelated” bands, making the application of the $GW + DMFT$ method to electronic-structure calculations for realistic solids highly promising.

ACKNOWLEDGMENTS

We acknowledge useful discussions with F. Aryasetiawan, M. Casula, A. Georges, M. Imada, Y. Nomura, A. Millis, and T. Miyake, as well as computing time on the Brutus cluster at ETH Zurich. This work was supported by the Swiss National Science Foundation (Grants No. PP0022_118866, No. 200021_140648, and through NCCR MANEP), DFG FOR 1346, and by the French ANR under projects CORRELMAT and SURMOTT, GENCI/IDRIS Orsay under project 1393. The Monte-Carlo scheduler uses the ALPS library.⁷⁰

APPENDIX A: EXTENDED HUBBARD MODELS FROM FIRST PRINCIPLES

The Hamiltonian H of the extended Hubbard model is supposed to describe the low-energy physics of correlated materials. H can be regarded as an effective Hamiltonian resulting from a “downfolding procedure,” based on some localized Wannier basis. The downfolding procedure is akin to a renormalization group transformation which, starting from all the bands resulting from a LDA calculation, produces an effective model for the bands in a low-energy window by integrating out the remaining bands. In this process, the bare Coulomb interaction $v(r, r') = 4\pi e^2/|r - r'|$ is transformed into a frequency-dependent partially screened interaction $W_r(r, r', \omega)$,^{71–73} which acts in the low-energy subspace. In principle, W_r is computed as $W_r = v(1 - vP_r)^{-1}$, where P_r is the polarization obtained when transitions within the effective model are removed. The matrix elements of this interaction in the Wannier basis are

$$V_{ijkl}(\omega) = \int d^3r d^3r' \phi_i^*(r) \phi_j^*(r') W_r(r, r', \omega) \phi_k(r) \phi_l(r'), \quad (\text{A1})$$

where ϕ_i denotes a Wannier orbital centered at site i .

Model (1) involves three approximations on the above matrix elements: (i) the frequency dependence of $V_{ijkl}(\omega)$ is neglected: $V_{ijkl} \equiv V_{ijkl}(\omega = 0)$, (ii) the interaction is restricted to density-density terms $V_{ijkl} = V_{ijji} \delta_{ik} \delta_{jl} \equiv V_{ij}$, and (iii) only the onsite matrix element $U \equiv V_{ii}$ and the nearest-neighbor matrix element $V \equiv V_{ij}$ (with i and j nearest neighbors) are retained. The last assumption is valid only if $W_r(r - r', \omega = 0)$ decays rapidly in space.⁷⁴ The neglected non-site-diagonal parts of the electron-electron interactions such as, for instance, the bond-charge-bond-charge matrix elements $W \equiv V_{ijji}$, are believed to be small in usual solids.⁷⁵

We also mention that a “locally unscreened cRPA” approach has been recently implemented.^{76,77} It is geared at a direct construction of an impurity Hubbard interaction, akin to the one resulting from $GW + DMFT$, but computed from a single-shot RPA calculation.

APPENDIX B: DERIVATION OF THE SINGLE-SITE EDMFT ACTION USING THE CAVITY METHOD

In the following, we use the cavity method² to derive the EDMFT action (22) and the EDMFT self-consistency equations which fix \mathcal{G} and \mathcal{U} . To this end, let us focus on a given site (denoted by the index 0) and split the lattice action [Eq. (8)] into three parts: $S = S_0 + S^{(0)} + \Delta S$ where S_0 denotes the action of the site 0, $S^{(0)}$ the action of the lattice with site 0 removed (the lattice with a “cavity” at site 0), and ΔS the remaining part:

$$S_0 = \int_0^\beta d\tau \left\{ \sum_\sigma c_{0\sigma}^* (\partial_\tau - \mu) c_{0\sigma} + i\phi_0 n_0 + \frac{1}{2} \phi_0 [v^{-1}]_{00} \phi_0 \right\}, \quad (\text{B1})$$

$$\Delta S = \int_0^\beta d\tau \left\{ - \sum_{i \neq 0, \sigma} t_{i0} (c_{0\sigma}^* c_{i\sigma} + c_{i\sigma}^* c_{0\sigma}) + \sum_{i \neq 0} \phi_i [v^{-1}]_{i0} \phi_0 \right\}, \quad (\text{B2})$$

$$S^{(0)} = \int_0^\beta d\tau \left\{ \sum_{ij \neq 0, \sigma} c_{i\sigma}^* (\partial_\tau - \mu - t_{ij}) c_{j\sigma} + \frac{1}{2} \sum_{ij \neq 0} \phi_i [v^{-1}]_{ij} \phi_j + i \sum_{i \neq 0} \phi_i n_i \right\}. \quad (\text{B3})$$

Defining $\eta_{i\sigma} \equiv t_{i0} c_{0\sigma}$ and $j_i \equiv [v^{-1}]_{i0} \phi_0$, we can write $\Delta S = \int_0^\beta d\tau \{ - \sum_{i \neq 0, \sigma} (\eta_i^* c_{i\sigma} + c_{i\sigma}^* \eta_i) + \sum_{i \neq 0} j_i \phi_i \}$, such that $\eta_{i\sigma}$ and j_i can be regarded as sources of correlation functions for the effective action of the site 0, defined by $e^{-S_{\text{eff}}[c_0^*, c_0, \phi_0]} / Z_{\text{eff}} \equiv \int \mathcal{D}_{i \neq 0} [c_i^*, c_i, \phi_i] e^{-(S_0 + S^{(0)} + \Delta S)} / Z$. We can express the action as $S_{\text{eff}} = S_0 - \Omega[\eta_i^*, \eta_i, j_i] + \text{const}$, where $\Omega[\eta_i^*, \eta_i, j_i] \equiv \ln \int \mathcal{D}_{i \neq 0} [c_i^*, c_i, \phi_i] e^{-(S^{(0)} + \Delta S)}$ is the generating functional of connected correlation functions of the cavity,⁴⁷

$$G_{i_1 \dots i_n j_n \dots j_1}^{(0)}(\tau_1 \dots \tau_n, \tau'_1 \dots \tau'_n) = (-1)^n \frac{\delta^{2n} \Omega}{\delta \eta_{i_1}^*(\tau_1) \dots \delta \eta_{i_n}^*(\tau_n) \delta \eta_{j_n}(\tau'_n) \dots \delta \eta_{j_1}(\tau'_1)}, \quad (\text{B4})$$

$$W_{i_1 \dots i_n j_n \dots j_1}^{(0)}(\tau_1 \dots \tau_n, \tau'_1 \dots \tau'_n) = \frac{\delta^{2n} \Omega}{\delta j_{i_1}(\tau_1) \dots \delta j_{i_n}(\tau_n) \delta j_{j_n}(\tau'_n) \dots \delta j_{j_1}(\tau'_1)}. \quad (\text{B5})$$

An explicit expression for Ω is thus

$$\begin{aligned} \Omega[\eta_i^*, \eta_i, j_i] &= \sum_{n=1}^{\infty} \sum_{i_1 \dots i_n, j_1 \dots j_n} \int d\tau_1 \dots d\tau'_n \eta_{i_1}^*(\tau_1) \dots \eta_{j_1}(\tau'_n) \\ &\quad \times (-1)^n G_{i_1 \dots i_n j_n \dots j_1}^{(0)}(\tau_1 \dots \tau'_n) \\ &\quad + \sum_{n=1}^{\infty} \sum_{i_1 \dots i_n, j_1 \dots j_n} \int d\tau_1 \dots d\tau'_n j_{i_1}(\tau_1) \dots j_{j_n}(\tau'_n) \\ &\quad \times W_{i_1 \dots i_n j_n \dots j_1}^{(0)}(\tau_1 \dots \tau'_n). \end{aligned} \quad (\text{B6})$$

The DMFT approximates Ω by its infinite-dimensional limit. In this limit, the hopping t between sites must be scaled as t/\sqrt{z} (with $z = 2d$) in order to keep a finite kinetic energy, while V must be scaled as V/z in order to keep

the Hartree energy corresponding to the nearest-neighbor interaction finite.⁴⁶ As a consequence of taking this limit, all terms of order $n > 1$ in Eq. (B6) vanish, so that $\Omega^{\text{DMFT}} = \int d\tau d\tau' c_0^*(\tau) (-\sum_{ij} t_{i0} t_{j0} G_{ij}^{(0)}(\tau - \tau')) c_0(\tau') + \int d\tau d\tau' \phi_0(\tau) (\sum_{ij} v_{i0}^{-1} v_{j0}^{-1} W_{ij}^{(0)}(\tau - \tau')) \phi_0(\tau')$. We thus arrive at the DMFT effective action of Eq. (21) (where we have dropped the index 0 in order to simplify the notation) with

$$\mathcal{G}^{-1}(i\omega_n) \equiv i\omega_n + \mu - \sum_{ij} t_{i0} t_{j0} G_{ij}^{(0)}(i\omega_n), \quad (\text{B7})$$

$$\mathcal{U}^{-1}(i\nu_n) \equiv v_{00}^{-1} - \sum_{ij} v_{i0}^{-1} v_{j0}^{-1} W_{ij}^{(0)}(i\nu_n). \quad (\text{B8})$$

Furthermore, in the limit of infinite dimensions, the cavity Green's function is related to the lattice Green's function through $G_{ij}^{(0)} = G_{ij} - G_{i0} G_{0j} / G_{00}$ and $W_{ij}^{(0)} = W_{ij} - W_{i0} W_{0j} / W_{00}$, which is shown by considering the paths contributing to G_{ij} (W_{ij}) and not to $G_{ij}^{(0)}$ ($W_{ij}^{(0)}$) (see Ref. 2 for more details). This allows us to write $\sum_{ij} t_{i0} t_{j0} G_{ij}^{(0)}$, after Fourier transformation, as

$$\sum_k \epsilon_k^2 G_k(i\omega_n) - \left(\sum_k \epsilon_k G_k(i\omega_n) \right)^2 / \sum_k G_k(i\omega_n). \quad (\text{B9})$$

At this point, a second approximation is made: the self-energies are assumed to be k -independent, namely, $\Sigma(k, i\omega) \approx \Sigma_{\text{loc}}(i\omega)$ and $\Pi(k, i\nu) \approx \Pi_{\text{loc}}(i\nu)$. This also becomes exact in the $d \rightarrow \infty$ limit.⁷⁸ As a consequence, we can define the densities of states $\rho(\epsilon) = \sum_k \delta(\epsilon - \epsilon_k)$ and $\rho'(\epsilon) = \sum_k \delta(\epsilon - v_k^{-1})$, which allows us to rewrite (B9) as

$$\int \frac{d\epsilon \rho(\epsilon) \epsilon^2}{\zeta - \epsilon} - \left(\int \frac{d\epsilon \rho(\epsilon) \epsilon}{\zeta - \epsilon} \right)^2 / \int \frac{d\epsilon \rho(\epsilon)}{\zeta - \epsilon}, \quad (\text{B10})$$

where $\zeta \equiv i\omega_n + \mu - \Sigma_{\text{loc}}(i\omega_n)$. The same expression holds for the screened interaction, with $\rho \rightarrow \rho'$ and $\zeta \rightarrow \zeta' = [v^{-1}]_{00} - \Pi_{\text{loc}}(i\nu_n)$ [as can be seen by comparing Eqs. (B7) and (B8)].

Using the following identities for Hilbert transforms,

$$\int_{-\infty}^{\infty} \frac{d\epsilon \rho(\epsilon) \epsilon^2}{\zeta - \epsilon} = \zeta \int_{-\infty}^{\infty} \frac{d\epsilon \rho(\epsilon) \epsilon}{\zeta - \epsilon}, \quad (\text{B11})$$

$$\int_{-\infty}^{\infty} \frac{d\epsilon \rho(\epsilon) \epsilon}{\zeta - \epsilon} = -1 + \zeta \int_{-\infty}^{\infty} \frac{d\epsilon \rho(\epsilon)}{\zeta - \epsilon}, \quad (\text{B12})$$

we obtain the self-consistency relations (25) and (26).

Equations (21), (25), and (26) form a closed set of equations: $S_{\text{eff}}^{\text{DMFT}}$, once solved, yields Σ_{loc} and Π_{loc} , which gives updated \mathcal{G} and \mathcal{U} which can in turn be used to solve the effective local problem again until convergence is reached.

APPENDIX C: HAMILTONIAN FORMULATION OF THE IMPURITY PROBLEM

Some properties of action (24) are more easily understood in terms of its Hamiltonian representation. The first two terms correspond to an Anderson impurity model

$$H_{\text{AIM}} = \sum_p \varepsilon_p a_p^\dagger a_p + \sum_p (V_p^\sigma a_{p\sigma}^\dagger c_\sigma + \text{H.c.}) + U n_\uparrow n_\downarrow - \mu n, \quad (\text{C1})$$

describing an impurity (c , c^\dagger) coupled to a bath of noninteracting fermionic levels (a_p , a_p^\dagger , energy ε_p). Here, $n_\sigma = c_\sigma^\dagger c_\sigma$ and $n = n_\uparrow + n_\downarrow$. The connection between Eqs. (24) and (C1) is given by $\mathcal{G}^{-1}(i\omega_m) = i\omega_m + \mu - \Delta(i\omega_m)$ and the hybridization function $\Delta(i\omega_m) = \sum_p \frac{|V_p^\sigma|^2}{i\omega_m - \varepsilon_p}$. On the other hand, the retarded effective interaction can be generated by coupling the impurity to a bath of bosonic modes described by the Hamiltonian

$$H_{\text{boson}} = \sum_p \omega_p b_p^\dagger b_p + \sum_p \frac{\lambda_p}{\sqrt{2}} n (b_p + b_p^\dagger) = \sum_p \frac{\omega_p}{2} (\phi_p^2 + \Pi_p^2) + \sum_p \lambda_p n_0 \phi_p, \quad (\text{C2})$$

with $\phi_p \equiv \frac{1}{\sqrt{2}}(b_p + b_p^\dagger)$ and $\Pi_p \equiv \frac{1}{i\sqrt{2}}(b_p - b_p^\dagger)$.

Using the identity $\Pi_p^2(\tau) = -[\partial_\tau \phi_p(\tau)]^2 / \omega_p^2$, this can be written in an action formulation as

$$S_{\text{boson}} = \frac{1}{\beta} \sum_{m,p} \phi_p(i\nu_m) \left(\frac{-(i\nu_m)^2 + \omega_p^2}{2\omega_p} \right) \phi_p(-i\nu_m) + \lambda_p \phi_p(i\nu_m) n(-i\nu_m). \quad (\text{C3})$$

Integrating out the bosonic degrees of freedom leads to

$$S_{\text{boson}} = \frac{1}{\beta} \sum_m n(i\nu_m) \left\{ - \sum_p \lambda_p^2 \frac{2\omega_p}{(i\nu_m)^2 - \omega_p^2} \right\} n(-i\nu_m). \quad (\text{C4})$$

Defining $\mathcal{D}(i\nu_m) = \int \frac{d\omega}{\pi} \text{Im} \mathcal{D}(\omega) \frac{2\omega}{(i\nu_m)^2 - \omega^2}$ with

$$\text{Im} \mathcal{D}(\omega) \equiv -\pi \sum_p \lambda_p^2 \delta(\omega - \omega_p) \quad (\text{C5})$$

and Fourier transforming $\mathcal{D}(i\nu_n)$ yields the retarded interaction in Eq. (24).

The retarded interaction may thus be regarded as stemming from the coupling to a bath of harmonic oscillators labeled by the index p , with frequency ω_p and coupling strength λ_p (as already emphasized in Ref. 11). The effective interaction mediated by these auxiliary degrees of freedom is proportional to the squared coupling strength λ_p^2 times the free-phonon Green's function⁷⁹ $D_p^0(i\nu_n) \equiv -\int_0^\beta d\tau e^{i\nu_n \tau} \langle \phi_p(\tau) \phi_p(0) \rangle = \frac{2\omega_p}{(i\nu_n)^2 - \omega_p^2}$. Note that in complete analogy to the fermionic hybridization function $\Delta(\omega)$, the frequency-dependent interaction $\mathcal{D}(\omega)$ is determined self-consistently.

APPENDIX D: SCREENING FREQUENCY FROM LINEARIZED DMFT

The U -dependence of the screening frequency may be traced back to the form of the one-particle local spectrum. As can be seen from Eq. (39), for $V = 0$,⁸⁰ the frequency dependence of W_{loc} (and thus the value of ω_0) is inherited from the charge-charge correlation function χ_{loc} . An analytical estimate for the poles of this function can be calculated by means of a simple approximation named linearized DMFT.⁶⁵ In this method, the impurity problem is approximated by the coupling of the correlated impurity to a *single* uncorrelated bath level describing the hybridization of the impurity to the

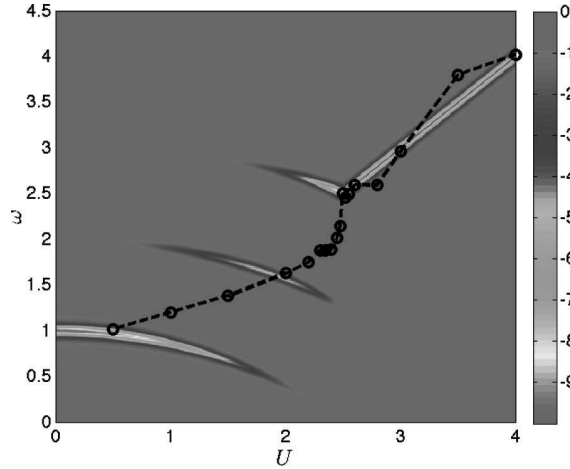


FIG. 16. (Color online) $\text{Im}\chi_{\text{loc}}^{I\text{-DMFT}}$ in the (ω, U) plane for $V = 0$. The poles have been artificially broadened by an imaginary factor $\eta = 0.01$. Black line: EDMFT result for $\langle\omega\rangle$ as a function of U (for $V = 0$).

lattice degrees of freedom. This simplified version of the impurity problem allows for the explicit calculation of the local Green's function⁸¹:

$$G_{\text{loc}}^{I\text{-DMFT}}(\omega) = \sum_{i=1}^2 a_i \left\{ \frac{1}{\omega - \bar{\epsilon}_i} + \frac{1}{\omega + \bar{\epsilon}_i} \right\} \quad (\text{D1})$$

with

$$\bar{\epsilon}_{1,2} = \frac{1}{4} \left(\sqrt{U^2 + 64V_{\text{hyb}}^2} \mp \sqrt{U^2 + 16V_{\text{hyb}}^2} \right), \quad (\text{D2})$$

$$a_1 = \frac{1}{4} \left(1 - \frac{U^2 - 32V_{\text{hyb}}^2}{\sqrt{U^2 + 64V_{\text{hyb}}^2} \sqrt{U^2 + 16V_{\text{hyb}}^2}} \right), \quad (\text{D3})$$

as well as $a_2 = \frac{1}{2} - a_1$. The hybridization strength's dependence on U is given by $V_{\text{hyb}} = t\sqrt{z}\sqrt{1 - U^2/U_c^2}$ (see Ref. 65 for details). U_c denotes the critical U for the Mott transition. In the estimate below, we will use the value computed within EDMFT, $U_c = 2.5$.

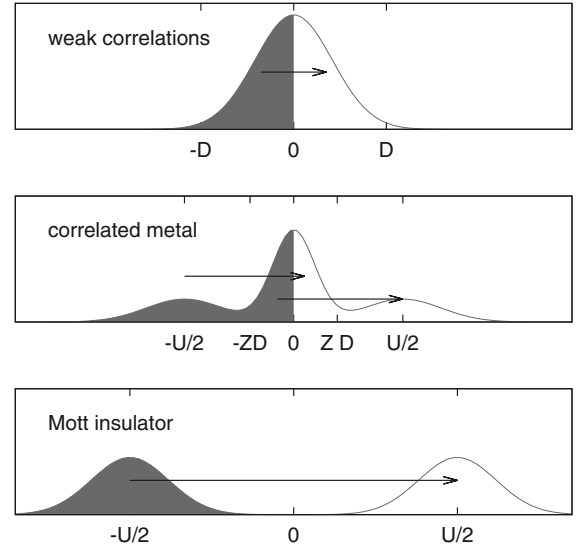


FIG. 17. (Color online) Sketch of transitions in generic spectra for the Hubbard model at various interaction strengths.

In the absence of vertex corrections, the corresponding charge-charge correlation function can be computed as $\chi_{\text{loc}} = -2G_{\text{loc}}G_{\text{loc}}$, leading to the expression

$$\chi_{\text{loc}}(\omega) = -2 \left\{ \frac{2a_1^2\epsilon_1}{\omega^2 - \epsilon_1^2} + \frac{2a_2^2\epsilon_2}{\omega^2 - \epsilon_2^2} + \frac{4a_1a_2\epsilon_3}{\omega^2 - \epsilon_3^2} \right\}. \quad (\text{D4})$$

The six (3×2) poles are defined as $\epsilon_1 = 2\bar{\epsilon}_1$, $\epsilon_2 = 2\bar{\epsilon}_2$, and $\epsilon_3 = \bar{\epsilon}_1 + \bar{\epsilon}_2$.

These poles, displayed in Fig. 16, correspond to the transitions allowed in the various correlation regimes, namely, in the low-correlation limit, only transitions within the quasiparticle peak are possible (see Fig. 17). As correlations increase, the appearance of Hubbard bands enable additional transitions from the lower Hubbard band to the unoccupied states of the quasiparticle peak, and from the occupied states of the quasiparticle peak to the upper Hubbard band. In the strong correlation regime, finally, the only possible transitions are those between the lower and the upper Hubbard bands.

¹F. C. Zhang and T. M. Rice, Phys. Rev. B **37**, 3759 (1988).

²A. Georges, G. Kotliar, W. Krauth, and M. J. Rozenberg, Rev. Mod. Phys. **68**, 13 (1996).

³G. Kotliar and D. Vollhardt, Phys. Today **57**(3), 53 (2004).

⁴A. I. Lichtenstein and M. I. Katsnelson, Phys. Rev. B **62**, R9283 (2000).

⁵G. Kotliar, S. Y. Savrasov, G. Pálsson, and G. Biroli, Phys. Rev. Lett. **87**, 186401 (2001).

⁶M. H. Hettler, A. N. Tahvildar-Zadeh, M. Jarrell, T. Pruschke, and H. R. Krishnamurthy, Phys. Rev. B **58**, R7475 (1998).

⁷A. N. Rubtsov, M. I. Katsnelson, and A. I. Lichtenstein, Phys. Rev. B **77**, 033101 (2008).

⁸A. Rubtsov, M. Katsnelson, and A. Lichtenstein, Ann. Phys. (NY) **327**, 1320 (2012).

⁹A. Toschi, A. A. Katanin, and K. Held, Phys. Rev. B **75**, 045118 (2007).

¹⁰E. Kuchinskii, I. Nekrasov, and M. Sadovsii, JETP Lett. **82**, 198 (2005) [Pis'ma Zh. Éksp. Teor. Fiz. **82**, 217 (2005)].

¹¹Q. Si and J. L. Smith, Phys. Rev. Lett. **77**, 3391 (1996).

¹²A. M. Sengupta and A. Georges, Phys. Rev. B **52**, 10295 (1995).

¹³H. Kajueter, Ph.D. thesis, Rutgers University, New Brunswick, 1996.

¹⁴P. Sun and G. Kotliar, Phys. Rev. B **66**, 085120 (2002).

¹⁵P. Sun and G. Kotliar, Phys. Rev. Lett. **92**, 196402 (2004).

¹⁶S. Biermann, F. Aryasetiawan, and A. Georges, Phys. Rev. Lett. **90**, 086402 (2003).

- ¹⁷F. Aryasetiawan, S. Biermann, and A. Georges, *Proceedings of the Conference on Coincidence Studies of Surfaces, Thin Films and Nanostructures, Ringberg castle, September 2003*, edited by J. Berakdar and J. Kirschner (Wiley-VCH Verlag GmbH & Co. KGaA, Weinheim, 2004), arXiv:cond-mat/0401626.
- ¹⁸S. Biermann, F. Aryasetiawan, and A. Georges, *Physics of Spin in Solids: Materials, Methods, and Applications* (Kluwer Academic, Dordrecht, 2004), pp. 43–65, arXiv:cond-mat/0401653.
- ¹⁹M. Casula, A. Rubtsov, and S. Biermann, *Phys. Rev. B* **85**, 035115 (2012).
- ²⁰P. Werner and A. J. Millis, *Phys. Rev. Lett.* **99**, 146404 (2007).
- ²¹P. Werner and A. J. Millis, *Phys. Rev. Lett.* **104**, 146401 (2010).
- ²²P. Werner, M. Casula, T. Miyake, F. Aryasetiawan, A. J. Millis, and S. Biermann, *Nat. Phys.* **8**, 331 (2012).
- ²³M. Casula, P. Werner, L. Vaugier, F. Aryasetiawan, A. J. Millis, and S. Biermann, *Phys. Rev. Lett.* **109**, 126408 (2012).
- ²⁴T. Ayrál, P. Werner, and S. Biermann, *Phys. Rev. Lett.* **109**, 226401 (2012).
- ²⁵J. M. Tomczak, M. Casula, T. Miyake, F. Aryasetiawan, and S. Biermann, *Europhys. Lett.* **100**, 67001 (2012).
- ²⁶P. Hansmann, T. Ayrál, L. Vaugier, P. Werner, and S. Biermann, arXiv:1301.4325.
- ²⁷P. Werner, A. Comanac, L. de' Medici, M. Troyer, and A. J. Millis, *Phys. Rev. Lett.* **97**, 076405 (2006).
- ²⁸A. N. Rubtsov, V. V. Savkin, and A. I. Lichtenstein, *Phys. Rev. B* **72**, 035122 (2005).
- ²⁹C. Almladh, U. von Barth, and R. van Leeuwen, *Int. J. Mod. Phys. B* **13**, 535 (1999).
- ³⁰R. Chitra and G. Kotliar, *Phys. Rev. B* **63**, 115110 (2001).
- ³¹M. C. Gutzwiller, *Phys. Rev. Lett.* **10**, 159 (1963).
- ³²J. Hubbard, *Proc. R. Soc. London, Ser. A* **276**, 238 (1963).
- ³³J. Kanamori, *Prog. Theor. Phys.* **30**, 275 (1963).
- ³⁴S. V. Vonsovsky and M. I. Katsnelson, *J. Phys. C: Solid State Phys.* **12**, 2043 (1979).
- ³⁵R. A. Bari, *Phys. Rev. B* **3**, 2662 (1971).
- ³⁶U. Wolff, *Nucl. Phys. B* **225**, 391 (1983).
- ³⁷X.-Z. Yan, *Phys. Rev. B* **48**, 7140 (1993).
- ³⁸Y. Zhang and J. Callaway, *Phys. Rev. B* **39**, 9397 (1989).
- ³⁹P. G. J. van Dongen, *Phys. Rev. Lett.* **67**, 757 (1991).
- ⁴⁰P. G. J. van Dongen, *Phys. Rev. B* **50**, 14016 (1994).
- ⁴¹P. G. J. van Dongen, *Phys. Rev. Lett.* **74**, 182 (1995).
- ⁴²M. Aichhorn, H. G. Evertz, W. von der Linden, and M. Potthoff, *Phys. Rev. B* **70**, 235107 (2004).
- ⁴³B. Davoudi and A.-M. S. Tremblay, *Phys. Rev. B* **76**, 085115 (2007).
- ⁴⁴R. Pietig, R. Bulla, and S. Blawid, *Phys. Rev. Lett.* **82**, 4046 (1999).
- ⁴⁵W. Metzner and D. Vollhardt, *Phys. Rev. Lett.* **62**, 324 (1989).
- ⁴⁶E. Müller-Hartmann, *Z. Phys. B* **74**, 507 (1989).
- ⁴⁷J. W. Negele and H. Orland, *Quantum Many-Particle Systems* (Westview Press, Boulder, CO, 1988).
- ⁴⁸W. Kohn, *Rev. Mod. Phys.* **71**, 1253 (1999).
- ⁴⁹J. Hubbard, *Phys. Rev. Lett.* **3**, 77 (1959).
- ⁵⁰G. Baym, *Phys. Rev.* **127**, 1391 (1962).
- ⁵¹J. M. Luttinger and J. C. Ward, *Phys. Rev.* **118**, 1417 (1960).
- ⁵²G. Baym and L. P. Kadanoff, *Phys. Rev.* **124**, 287 (1961).
- ⁵³L. Hedin, *Phys. Rev.* **139**, A796 (1965).
- ⁵⁴F. Aryasetiawan and O. Gunnarsson, *Rep. Prog. Phys.* **61**, 237 (1998).
- ⁵⁵G. Onida, L. Reining, and A. Rubio, *Rev. Mod. Phys.* **74**, 601 (2002).
- ⁵⁶M. Shishkin, M. Marsman, and G. Kresse, *Phys. Rev. Lett.* **99**, 246403 (2007).
- ⁵⁷H. Jiang, R. I. Gomez-Abal, P. Rinke, and M. Scheffler, *Phys. Rev. Lett.* **102**, 126403 (2009).
- ⁵⁸We do not enter here into a discussion of different levels of (partial or full) self-consistency, nor into a description of the quasiparticle self-consistent *GW* scheme by Kotani and Schilfgarde (Ref. 59). See, however, the benchmark calculations in Ref. 24.
- ⁵⁹T. Kotani, M. van Schilfgarde, and S. V. Faleev, *Phys. Rev. B* **76**, 165106 (2007).
- ⁶⁰A. Abrikosov, L. Gor'kov, and I. Dzyaloshinski, *Methods of Quantum Field Theory in Statistical Physics*, 2nd ed. (Pergamon, New York, 1965).
- ⁶¹The formula is written here in imaginary-time space.
- ⁶²M. Jarrell and J. Gubernatis, *Phys. Rep.* **269**, 133 (1996), ISSN 0370-1573.
- ⁶³S. Florens, Ph.D. thesis, Université Paris 6, Paris, 2003.
- ⁶⁴H. J. Vidberg and J. W. Serene, *J. Low Temp. Phys.* **29**, 179 (1977).
- ⁶⁵M. Potthoff, *Phys. Rev. B* **64**, 165114 (2001).
- ⁶⁶The slope at origin of $\lambda(V)$ has been used to compute $[d\lambda/dV]_{V=0}$.
- ⁶⁷P. Werner, E. Gull, O. Parcollet, and A. J. Millis, *Phys. Rev. B* **80**, 045120 (2009).
- ⁶⁸E. Gull, O. Parcollet, P. Werner, and A. J. Millis, *Phys. Rev. B* **80**, 245102 (2009).
- ⁶⁹G. Rohringer, A. Valli, and A. Toschi, *Phys. Rev. B* **86**, 125114 (2012).
- ⁷⁰B. Bauer, L. D. Carr, H. G. Evertz, A. Feiguin, J. Freire, S. Fuchs, L. Gamper, J. Gukelberger, E. Gull, S. Guertler *et al.*, *J. Stat. Mech.: Theor. Exp.* (2011) P05001.
- ⁷¹F. Aryasetiawan, M. Imada, A. Georges, G. Kotliar, S. Biermann, and A. I. Lichtenstein, *Phys. Rev. B* **70**, 195104 (2004).
- ⁷²T. Miyake and F. Aryasetiawan, *Phys. Rev. B* **77**, 085122 (2008).
- ⁷³L. Vaugier, H. Jiang, and S. Biermann, *Phys. Rev. B* **86**, 165105 (2012).
- ⁷⁴This assumption is not necessarily valid if low-energy metallic screening is due to particle-hole excitations within the low-energy window itself. However, extending the formalism from nearest-neighbor to even longer-range interactions is trivial, so we will not discuss this case explicitly.
- ⁷⁵D. K. Campbell, J. T. Gammel, and E. Y. Loh, *Phys. Rev. B* **42**, 475 (1990).
- ⁷⁶Y. Nomura, M. Kaltak, K. Nakamura, C. Taranto, S. Sakai, A. Toschi, R. Arita, K. Held, G. Kresse, and M. Imada, *Phys. Rev. B* **86**, 085117 (2012).
- ⁷⁷L. Vaugier, Ph.D. thesis, Ecole Polytechnique, Palaiseau, France, 2012.
- ⁷⁸W. Metzner and D. Vollhardt, *Phys. Rev. Lett.* **62**, 324 (1989).
- ⁷⁹G. D. Mahan, *Many-Particle Physics*, 2nd. ed (Plenum, New York, NY, 1993).
- ⁸⁰In this case, one can check that within EDMFT, $\mathcal{U} = U$.
- ⁸¹E. Lange, *Mod. Phys. Lett. B* **12**, 915 (1998).

O.3 Paper 3: Huang *et al.* (2014)

Extended dynamical mean-field study of the Hubbard model with long-range interactionsLi Huang,¹ Thomas Ayrál,^{2,3} Silke Biermann,^{2,4} and Philipp Werner¹¹*Department of Physics, University of Fribourg, 1700 Fribourg, Switzerland*²*Centre de Physique Théorique, Ecole Polytechnique, CNRS-UMR7644, 91128 Palaiseau, France*³*Institut de Physique Théorique (IPhT), CEA, CNRS, URA 2306, 91191 Gif-sur-Yvette, France*⁴*Collège de France, 11 place Marcelin Berthelot, 75005 Paris, France*

(Received 28 April 2014; revised manuscript received 17 October 2014; published 10 November 2014)

Using extended dynamical mean-field theory and its combination with the GW approximation, we compute the phase diagrams and local spectral functions of the single-band extended Hubbard model on the square and simple cubic lattices, considering long-range interactions up to the third nearest neighbors. The longer-range interactions shift the boundaries between the metallic, charge-ordered insulating, and Mott insulating phases, and lead to characteristic changes in the screening modes and local spectral functions. Momentum-dependent self-energy contributions enhance the correlation effects and thus compete with the additional screening effect from longer-range Coulomb interactions. Our results suggest that the influence of longer-range intersite interactions is significant, and that these effects deserve attention in realistic studies of correlated materials.

DOI: 10.1103/PhysRevB.90.195114

PACS number(s): 71.15.-m, 71.10.Fd, 71.30.+h

I. INTRODUCTION

In condensed matter physics, electron-electron correlations give rise to many intriguing phenomena ranging from simple energy band renormalization to complex phase diagrams with charge, spin, or orbital ordering [1]. The essential physics is the competition between electron localization and itinerancy. The Hubbard model is one of the simplest models which captures this competition, and it is therefore often used to investigate correlation effects in lattice systems [2,3]. For instance, it is generally believed that the two-dimensional single-band Hubbard model with static on-site Coulomb interaction U can be used to explain some underlying physics of cuprate high-temperature superconductors [4]. One widely accepted assumption in these studies is that the electron-electron interaction is local, i.e., that long-range intersite interactions are fully screened or may be ignored. When additional intersite Coulomb interactions are considered, the model becomes an extended Hubbard model, which can be used for example to explore charge-ordering and Wigner-Mott transitions [5]. This model also describes the screening of local interactions by the nonlocal interactions. Both the charge-ordering transition and the screening effect in the extended Hubbard model have been investigated in numerous theoretical studies [6–15].

The physical properties of the Hubbard model have been studied extensively using the dynamical mean-field theory (DMFT) [2,3]. This approximate scheme describes the generic behavior of high-dimensional lattice systems. In particular, at half-filling and low temperature, the DMFT solution for the hypercubic lattice will be an antiferromagnetically ordered insulator, whose character changes from a Slater-type antiferromagnet at weak interactions, to a Heisenberg-type antiferromagnet with local moments at large interaction. If the calculations are restricted to the paramagnetic phase, the DMFT method predicts a transition from a Fermi-liquid metal to a Mott insulator at a temperature-dependent critical value of the on-site interaction U (comparable to the bandwidth). This paramagnetic Mott transition can be considered as the generic physical situation in the magnetically frustrated case. The extended Hubbard model with strong nonlocal interactions (parametrized by V) exhibits a transition to a

charge-ordered state characterized by a freezing of charge carriers and a spatial modulation of the charge density [5]. To describe this transition, one may resort to the extended dynamical mean-field theory (EDMFT) framework [7,16–22]. The basic idea of EDMFT was originally developed in studies of heavy-fermion systems and spin glasses with nonlocal Coulomb interactions [16,17]. The physical effects induced by the nonlocal interaction V , including a frequency dependence of the effective local interaction and a sizable reduction of the static value of U , are well captured by the EDMFT scheme. Since EDMFT takes into account the spatially nonlocal interactions beyond the Hartree level, it is a sophisticated numerical tool for studying the extended Hubbard model. However, EDMFT is still based on a local approximation, i.e., it assumes a k -independent self-energy function and polarization function. To further incorporate spatially nonlocal contributions into these functions, one can combine the EDMFT approach with the GW approximation [6,7,14,15,22].

While the EDMFT and $GW + \text{EDMFT}$ schemes have been developed more than ten years ago, there has been a recent revival in interest in these approaches, due to methodological improvements which enable an efficient and accurate solution of the self-consistency equations. In the previous studies, phase diagrams in the space of on-site interaction U and the nearest-neighbor interaction V , fully screened and retarded interactions, and local spectral functions have been calculated for the extended Hubbard model on square and simple cubic lattices [7,14,15,20,22]. It has been found that the critical charge-ordering lines $V_c(U)$ between the Mott insulator phase and the charge-ordered insulator phase obtained by the EDMFT and $GW + \text{EDMFT}$ approaches are substantially steeper than the naive mean-field estimate $V_c = U/z$, where z is the number of nearest neighbors [15]. This may point to an overestimation of the local interactions in the EDMFT and $GW + \text{EDMFT}$ schemes or a nontrivial screening effect. Further issues left open in previous work concern the physical interpretation of the dominant screening processes, and their dependence on the parameters of the model. In Ref. [23], it was proposed that the effective local interaction incorporating screening by neighboring lattice sites can be well approximated

by simple estimates in terms of on-site and intersite interactions. The recent $GW + \text{EDMFT}$ study of Ref. [15] was consistent with this simple picture in the correlated metallic case in two dimensions with nearest-neighbor interactions. However, the usefulness and accuracy of these estimates in the higher dimensional case or with longer-range interactions remains an open question.

The early studies of the three-dimensional extended Hubbard model [7,22] used a modified Hirsch-Fye algorithm to solve the effective impurity problem and could not reach low temperatures. In these calculations, the fermionic part of the impurity model was handled by a standard Hirsch-Fye algorithm [2,3], while the statistical weight due to the continuous bosonic fields was obtained directly by computing the corresponding Boltzmann factor [24]. This algorithm is not as efficient and accurate as the recently developed continuous time quantum Monte Carlo (CT-QMC) solver [25–28], which can treat systems with a frequency-dependent retarded interaction without any approximations. Thus it is worthwhile to reinvestigate the model using the EDMFT and $GW + \text{EDMFT}$ approaches in combination with the state-of-the-art CT-QMC quantum impurity solver. This was done in Refs. [14,15] for the two-dimensional model with local and nearest-neighbor interactions. Here, we extend the investigation to the three-dimensional model and to interactions of longer range. Indeed, recent constrained random phase approximation calculations [29] and a recent $GW + \text{EDMFT}$ study [30] of adatom systems $\text{Si}(111):X$, with $X = \text{Sn}, \text{Si}, \text{C}, \text{Pb}$, suggest that taking into account substantially longer-range interactions is mandatory to understand experimentally observed trends from Mott physics toward charge-ordering physics along this series. In particular, it was shown that long-range interactions (for the surface systems, the full Coulomb tail was considered) can decrease the effective local interaction by up to a factor of two. Similar conclusions were drawn in Ref. [23] for other two-dimensional systems like graphene, silicene, and benzene. Other studies suggest that the superconducting T_c is generally suppressed in some pairing channels as the strength of longer-range interactions increases [13]. It thus appears that longer-range intersite interactions beyond the nearest neighbors may be important, at least for low-dimensional systems. So, it is worth investigating in a simple model context how longer-range intersite interactions modify the phase diagrams and various local and nonlocal observables.

The purpose of this paper is to gain qualitative and quantitative insights into the role of screening from nonlocal Coulomb interactions. For this, we study the extended Hubbard model on the square (2D) and simple cubic (3D) lattices using a modern EDMFT and $GW + \text{EDMFT}$ implementation with a numerically exact CT-QMC impurity solver. The calculations are restricted to repulsive interactions $U > 0$ and $V > 0$, and to the paramagnetic phase, so that we can investigate the particularly interesting screening effects in the correlated metal, close to the Mott or charge ordered insulator phase boundaries. In particular, we extract the dominant screening modes and analyze the effects of longer-range intersite interactions on local, but energy dependent observables, such as spectral functions. At first, we will perform self-consistent EDMFT calculations to map out the entire U - V phase diagram, and then compare to $GW + \text{EDMFT}$ results at some representative

points to gain insights into the effects of nonlocal self-energy and polarization contributions.

The rest of this paper is organized as follows. Section II defines the extended Hubbard model used in this study. The flowcharts for the EDMFT and $GW + \text{EDMFT}$ methods and the computational details are also briefly summarized in this section. Section III A shows the results obtained using the EDMFT approach. The phase diagrams, fully screened and retarded interactions induced by the V term, and local spectral functions are presented and discussed in detail. Especially, doping-dependent phase diagrams and related bosonic spectral functions are also presented in this section. Some representative results obtained with the $GW + \text{EDMFT}$ approach are discussed in Sec. III B. A brief summary and outlook are given in Sec. IV. Appendix A describes the long-range intersite interactions considered in the 2D and 3D extended Hubbard models, while Appendix B details the maximum entropy based analytical continuation method used to extract the spectral functions for the frequency-dependent fully screened and retarded interactions.

II. MODEL AND METHODS

A. Extended Hubbard model

In the present study, we consider the single-band extended Hubbard models on a two-dimensional square lattice and a three-dimensional simple cubic lattice, respectively (see schematic picture in Fig. 1). The grand-canonical Hamiltonian can be written as

$$H = - \sum_{(i,j),\sigma} t_{ij}(c_{i\sigma}^\dagger c_{j\sigma} + \text{H.c.}) - \mu \sum_i n_i + U \sum_i n_{i\uparrow} n_{i\downarrow} + \sum_{(i,j)} V_{ij} n_i n_j, \quad (1)$$

where i and j are site indices and (i, j) denotes a pair of sites i and j . $c_{i\sigma}$ and $c_{i\sigma}^\dagger$ are the annihilation and creation operators of an electron of spin σ at the lattice site i . $n_{i\sigma}$ is the orbital

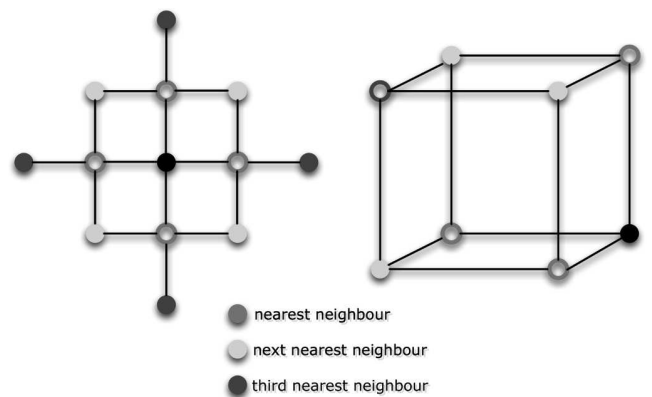


FIG. 1. (Color online) Schematic picture of the one-band half-filled extended Hubbard model in the charge-ordered state for the square lattice (left) and simple cubic lattice (right). The full dots represent doubly occupied sites and the open dots empty sites. The red, green, and purple dots denote the NN, NNN, and 3NN sites of the black dot, respectively.

occupation operator, and $n_i = n_{i\uparrow} + n_{i\downarrow}$. t_{ij} is the hopping matrix element between two different sites, μ is the chemical potential, U is the on-site interaction, and V_{ij} is the intersite interaction between sites i and j .

When $i = j$, both t_{ij} and V_{ij} must be zero. Only the hopping between the nearest-neighbor (NN) sites is allowed in this study, namely, $t_{ij} = t_{(ij)} = t > 0$. However, for the nonlocal repulsive interactions V_{ij} we also consider the next nearest-neighbor (NNN) and the third nearest-neighbor (3NN) sites. Our definitions for the NN, NNN, and 3NN sites are shown in Fig. 1. We further assume that V_{ij} can be calculated by scaling V with $a/|\vec{r}_i - \vec{r}_j|$, in other words, with the inverse distance in units of the NN distance a . In this sense, V is not only the NN interaction but also the parameter that determines the strength of all the long-range Coulomb interactions. The detailed formulas of the Fourier-transformed t_{ij} and V_{ij} are given in Appendix A.

B. EDMFT and $GW + EDMFT$

We solve the single-band extended Hubbard model [see Eq. (1)] with fully self-consistent EDMFT and $GW + EDMFT$ calculations. The EDMFT approach with the “ UV decoupling” scheme [15] formally treats the local interactions and nonlocal intersite interactions on the same footing. It can be used to describe the Mott transition and charge-ordering transition in the extended Hubbard model [16,17,20,21]. The idea of the combined $GW + EDMFT$ [6] scheme is the following: one takes the local part of the self-energy (or polarization) from the EDMFT calculation and adds to it the nonlocal component of the GW self-energy (or polarization). Thus a momentum dependence is introduced into the self-energy (or polarization), and the scheme captures the interplay of screening and nonlocal correlations at least to some extent. While the accuracy of the scheme has not been systematically tested, self-consistent $GW + EDMFT$ calculations can be obtained in the whole interaction range from the weakly correlated region to the atomic limit. A detailed derivation of the $GW + EDMFT$ formulation for the extended Hubbard model can be found in Ref. [15].

The $GW + EDMFT$ self-consistency loop involves the following steps [7,15]. One starts with an initial guess for the k -dependent fermionic self-energy $\Sigma(k, i\omega_n)$ and the bosonic self-energy (or polarization) $\Pi(k, iv_n)$, with Matsubara frequencies $\omega_n = (2n + 1)\pi/\beta$ and $v_n = 2n\pi/\beta$ for integer n . The initial $\Sigma(k, i\omega_n)$ and $\Pi(k, iv_n)$ can be obtained from previously calculated results, or chosen to be zero. Then one calculates the lattice Green’s function $G(k, i\omega_n)$ and fully screened interaction $W(k, iv_n)$ using the lattice Dyson equations

$$G(k, i\omega_n) = \frac{1}{i\omega_n + \mu - \epsilon_k - \Sigma(k, i\omega_n)} \quad (2)$$

and

$$W(k, iv_n) = \frac{1}{v_k^{-1} - \Pi(k, iv_n)}. \quad (3)$$

Here, ϵ_k is the band dispersion and v_k is the bare interaction in reciprocal space (see Appendix A for more details). Then the local counterparts of G , W , Σ , and Π are calculated by

averaging over the whole Brillouin zone, for instance (N_k is the number of k points),

$$G(i\omega_n) = \frac{1}{N_k} \sum_k G(k, i\omega_n). \quad (4)$$

Next, the local bath Green’s function $\mathcal{G}(i\omega_n)$ and frequency dependent retarded interaction $\mathcal{U}(iv_n)$ are calculated through the impurity Dyson equations, namely,

$$\mathcal{G}^{-1}(i\omega_n) = G^{-1}(i\omega) + \Sigma(i\omega_n) \quad (5)$$

and

$$\mathcal{U}^{-1}(iv_n) = W^{-1}(iv_n) + \Pi(iv_n). \quad (6)$$

Then the quantum impurity model defined by $\mathcal{G}(i\omega_n)$ and $\mathcal{U}(iv_n)$ is solved numerically. The impurity solver directly yields the new $G(i\omega_n)$. On the other hand, the calculation of the new $W(iv_n)$ involves as an intermediate step, the calculation of the connected charge-charge correlation function $\chi(\tau) = \langle \mathcal{T} \bar{n}(\tau) \bar{n}(0) \rangle$ with $\bar{n} = n - \langle n \rangle$. From the Fourier-transformed $\chi(iv_n)$ and $\mathcal{U}(iv_n)$, we finally obtain the new $W(iv_n)$ via

$$W(iv_n) = \mathcal{U}(iv_n) - \mathcal{U}(iv_n) \chi(iv_n) \mathcal{U}(iv_n). \quad (7)$$

Using these $G(i\omega_n)$ and $W(iv_n)$ as inputs, the new local self-energy functions $\Sigma(i\omega_n)$ and $\Pi(iv_n)$ are determined by using Eqs. (5) and (6) again. Within the GW approximation, one evaluates the momentum-dependent GW self-energy and polarization functions as $\Sigma^{\text{GW}} = -GW$ and $\Pi^{\text{GW}} = 2GG$ [6]. Here, the factor 2 comes from the contribution of the spin degree of freedom. Finally, one has to separate the local and nonlocal parts of these GW self-energies and polarizations:

$$\Sigma_{\text{loc}}^{\text{GW}}(i\omega_n) = \frac{1}{N_k} \sum_k \Sigma^{\text{GW}}(k, i\omega_n), \quad (8)$$

$$\Pi_{\text{loc}}^{\text{GW}}(iv_n) = \frac{1}{N_k} \sum_k \Pi^{\text{GW}}(k, iv_n), \quad (9)$$

$$\Sigma_{\text{nonloc}}^{\text{GW}}(k, i\omega_n) = \Sigma^{\text{GW}}(k, i\omega_n) - \Sigma_{\text{loc}}^{\text{GW}}(i\omega_n), \quad (10)$$

$$\Pi_{\text{nonloc}}^{\text{GW}}(k, iv_n) = \Pi^{\text{GW}}(k, iv_n) - \Pi_{\text{loc}}^{\text{GW}}(iv_n), \quad (11)$$

and then combine the nonlocal parts with the local contributions obtained from the impurity calculations, i.e.,

$$\Sigma(k, i\omega_n) = \Sigma_{\text{nonloc}}^{\text{GW}}(k, i\omega_n) + \Sigma(i\omega_n) \quad (12)$$

and

$$\Pi(k, iv_n) = \Pi_{\text{nonloc}}^{\text{GW}}(k, iv_n) + \Pi(iv_n). \quad (13)$$

The new self-energy and polarization functions, $\Sigma(k, i\omega_n)$ and $\Pi(k, iv_n)$, serve as the starting point of the next iteration. This completes the self-consistent loop.

The EDMFT self-consistency loop can be viewed as a simplification of the full $GW + EDMFT$ iteration, where one ignores the calculations of the GW self-energies $\Sigma^{\text{GW}}(k, i\omega_n)$ and polarizations $\Pi^{\text{GW}}(k, iv_n)$, and adopts the following local approximations:

$$\Sigma(k, i\omega_n) = \Sigma(i\omega_n) \quad (14)$$

and

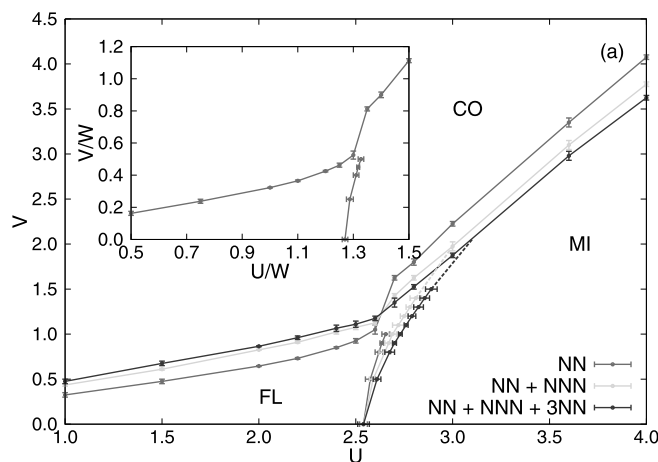
$$\Pi(k, i\nu_n) = \Pi(i\nu_n). \quad (15)$$

In the following calculations, we consider half-filled single-band extended Hubbard models on the square lattice and simple cubic lattice (some results for the 2D model away from half-filling can be found in Sec. III A). The k sums are discretized in the irreducible Brillouin zone on 81×81 and $19 \times 19 \times 19$ grid points, respectively. We used the hybridization expansion quantum impurity solver to solve the effective impurity problems [27,28]. The imaginary time Green's function $G(\tau)$ and charge-charge correlation function $\chi(\tau)$ are measured on $N = 1024$ equally spaced time points. We used $4t$ as the unit of energy and performed calculations at inverse temperature $\beta = 100$, restricting our study to the paramagnetic phase. Up to 40 EDMFT and $GW + \text{EDMFT}$ iterations are required to reach convergence when the system is close to the Mott or charge-ordering transition.

C. Analytical continuation

Since the self-consistency loop is implemented fully on the imaginary time/frequency axis, we have to analytically continue the converged $G(\tau)$, $\mathcal{U}(i\nu)$, and $W(i\nu)$ to obtain meaningful information about single particle excitations and screening modes. The frequency dependence of the retarded interaction $\mathcal{U}(i\nu)$ affects the single particle spectral function $A(\omega)$, and in particular induces satellites at energies which are determined by the dominant screening frequencies [27,31,32]. However, the classical maximum entropy method [33], which is commonly used to perform analytical continuations of $G(\tau)$, tends to smooth out these high-energy features. To overcome this obstacle, we adopted the algorithm proposed by Casula *et al.* [31] and proceed as follows. From the spectral function $\text{Im}\mathcal{U}(\nu)$ we calculate the bosonic function

$$B(\tau) = \exp[K(0) - K(\tau)], \quad (16)$$



where [34]

$$K(\tau) = \int_0^\infty d\nu \frac{\text{Im}\mathcal{U}(\nu) \cosh[\nu(\beta/2 - \tau)]}{\nu^2 \sinh(\nu\beta/2)} \quad (17)$$

and the corresponding spectral function $A_B(\nu)$. We then define the auxiliary fermionic Green's function $G_{\text{aux}}(\tau) = G(\tau)/B(\tau)$, which later is analytically continued using the conventional maximum entropy method to yield $A_{\text{aux}}(\omega)$. Finally, the spectral function for $G(\tau)$ is obtained from the convolution

$$A(\omega) = \int d\epsilon \frac{A_B(\epsilon) A_{\text{aux}}(\omega - \epsilon) (1 + e^{-\beta\omega})}{(1 + e^{\beta(\epsilon - \omega)})(1 - e^{-\beta\epsilon})}. \quad (18)$$

This procedure requires an accurate estimate of the spectral function $\text{Im}\mathcal{U}(\nu)$. In previous studies, the Padé approximation was used [15]. However, we found that the Padé results are very sensitive to the data quality of $\mathcal{U}(i\nu)$. Small fluctuations in $\mathcal{U}(i\nu)$, which are almost unavoidable [see Eq. (6)], can lead to drastic modifications in the Padé estimation of $\text{Im}\mathcal{U}(\nu)$. Thus a robust procedure with respect to the typical level of numerical noise is crucial. The maximum entropy method is superior in this respect, and we have adapted it to the problem of analytically continuing the retarded interaction $\mathcal{U}(i\nu)$ and fully screened interaction $W(i\nu)$. The details of this procedure are explained in Appendix B.

III. RESULTS AND DISCUSSION

A. EDMFT results

In this section, we present self-consistent EDMFT results for the paramagnetic, half-filled single-band U - V Hubbard model on the square lattice and simple cubic lattice. All results are for inverse temperature $\beta = 100$.

1. U - V phase diagrams

Figure 2 shows the phase diagrams in the space of the parameters U and V . In this figure, the left panel shows the result for the square lattice, and the right panel corresponds

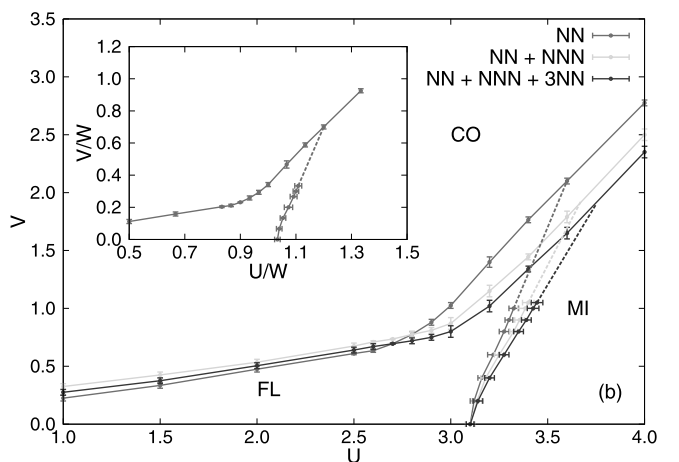


FIG. 2. (Color online) The paramagnetic U - V phase diagrams for the single-band half-filled extended Hubbard model determined by EDMFT calculations. (a) Phase diagram for the 2D square lattice. (b) Phase diagram for the 3D simple cubic lattice. Here CO denotes a charge-ordered insulating phase, FL the metallic state, and MI the Mott insulator. The dashed lines are extrapolated FL-MI phase boundaries. The insets in (a) and (b) show the phase diagrams with axes rescaled by the bandwidth.

to the simple cubic lattice. Both phase diagrams exhibit three phases: a metallic Fermi-liquid (FL) phase in which the kinetic energy dominates the interactions, the Mott insulating (MI) phase with one particle per site, where U is dominant, and the charge-ordered (CO) insulator with a charge density wave (CDW) when V prevails. The insets plot the phase diagrams with axes rescaled by the bandwidth ($8t$ for the square lattice and $12t$ for the simple cubic lattice), to emphasize the similarities and differences between the 2D and 3D cases.

The paramagnetic phase diagram for the extended Hubbard model with NN interactions on the square lattice is consistent with the result by Ayrál *et al.* [15]. The paramagnetic phase diagram for the simple cubic lattice with NN interactions has been calculated in the pioneering paper by Sun *et al.* [7]. Their calculations however were performed at a much higher temperature ($\beta = 5$), above the end-point of the FL-MI transition. Also, the quantum impurity solver used in that study was a modified Hirsch-Fye algorithm with Bose factor approximation [24], which is not as accurate as the numerically exact CT-QMC algorithm [27]. Taking into account these differences, the phase diagram presented in Fig. 2(b) appears to be qualitatively consistent with the previous result by Sun *et al.* [7]. When the temperature is increased, the $V_c(U)$ line shifts upwards, and the $U_c(V)$ line is shifted to the left. In contrast to the paramagnetic MI, the CO insulator does not have a large entropy of $\ln 2$ per site (the phase boundary is determined from the divergence in the charge susceptibility, see Sec. III A 2 for further details).

In the previous calculations, only the NN intersite interactions have been included. In the present work, we also consider the effects of longer-range interactions, more specifically the NNN and 3NN intersite interactions, as depicted in Fig. 1. In a future study, it would be interesting to consider the effect of an infinite range Coulomb $1/r$ -type tail. A proper treatment of it requires an Ewald lattice summation, as discussed by Hansmann *et al.* [30].

The modifications in the phase diagram for the square lattice are shown in Fig. 2(a). When U is small, the $V_c(U)$ line is shifted upward if the NNN and 3NN interactions are added, which means that these longer-range intersite interactions destabilize the CO state. This is not surprising, since the left panel of Fig. 1 shows that both the NN and 3NN interactions act between sites of the same sublattice, and hence penalize the CDW. In the strongly correlated region, the $V_c(U)$ line is shifted downward, which means that the MI state is suppressed by longer-range intersite interactions, which can be interpreted as the result of the enhanced screening of the on-site interaction. For the same reason, the $U_c(V)$ line is slightly shifted to the right. Finally, if only the NN intersite interaction is considered, the $V_c(U)$ line “jumps” in the region where the $V_c(U)$ and $U_c(V)$ lines intersect, and this jump is accompanied by a change of the slope. If longer-range interactions are included, the metallic phase extends to larger values of U , so that the transition between MI and CO phases is no longer a direct one, at least for $2.5 \lesssim U \lesssim 3.0$. As a result of this intermediate metallic phase, the jump in the $V_c(U)$ line disappears. We note that the shape of the metallic phase with longer-range interactions is qualitatively similar to the FL phase in the single-band Holstein-Hubbard model with large phonon frequency [27]. One difference is that the

phase diagram for the Holstein-Hubbard model does not have a sudden slope change in the phase boundary to the CO phase in the vicinity of the Mott transition. This suggests that the slope change in the extended Hubbard model originates from changes in the screening processes near U_c . We will investigate this issue in more detail in Sec. III A 3.

Next, let us turn to the simple cubic lattice case [see Fig. 2(b)]. Here, for small U , the $V_c(U)$ phase boundary is shifted upward when the NNN interaction is added, just as in the 2D case, but the 3NN interaction has the opposite effect. Therefore the shift is not monotonous any more. This can be understood by looking at the right-hand panel of Fig. 1. While the NNN interactions act between sites on the same sublattice, and hence frustrate the CDW, the 3NN interactions act between sites on different sub-lattices, and thus favor the CO phase. Another difference to the 2D case is that the metallic region between the MI and CO phases is larger, so that there is no obvious “kink” or sudden “jump” in the $V_c(U)$ line near the Mott transition. In fact, for the model with only the NN interactions, the slope change in the $V_c(U)$ line happens already quite a bit before the Mott transition ($U_c \sim 3.1$) at $V = 0$.

2. Charge-ordering and Mott metal-insulator transitions

The phase transition from the FL and MI phases to the CO phase is signaled by a diverging charge susceptibility $\chi(i\nu = 0)$ [7]. This divergence almost coincides with a sign change in the fully screened interaction $\text{Re}W(i\nu = 0)$ [see Eq. (7)]. When V increases, $\text{Re}W(i\nu = 0)$ gets smaller, and when it reaches zero, the cost for the formation of doublons vanishes [15]. In Fig. 3, the real parts of $W(i\nu = 0)$ and $\chi(i\nu = 0)$ are plotted against V for $U = 2.5$, which is still in the metallic state for the square and simple cubic lattices. The phase boundary to the CO state has been located by approaching the phase transition from below V_c . Actually, before $\text{Re}\chi(i\nu = 0)$ diverges or $\text{Re}W(i\nu = 0)$ reaches zero, we already encounter a numerical instability which prevents the convergence of the EDMFT self-consistency loop. Thus we extrapolate the curves using $(V - V_c)^{-1}$, as shown by the dashed lines in Fig. 3, to determine the critical V_c . While the extrapolation procedure is somewhat arbitrary, the trend is unambiguous; in the square lattice case, V_c increases as we add longer-range interactions, even though for $V \lesssim 0.9$, the trend is actually opposite (due to an increasing screening effect). For the simple cubic lattice, the screening effect leads to a reduction of $\text{Re}W(i\nu = 0)$ with increasing range of the interaction for $V \lesssim 0.6$, but then the drop to zero occurs in a nonmonotonic way, for reasons related to lattice geometry as discussed above. In the large- U region, close to the Mott transition, the $V_c(U)$ phase boundary shifts down with increasing range of the interaction, both for the square and the simple cubic lattice. This indicates that the interaction induced changes in the screening function should play the dominant role there.

The phase boundary between metal and Mott insulator is signaled by a vanishing spectral weight at the Fermi level. We increased the on-site interaction U step by step to approach the phase transition from the FL metallic side, so that our U_c values indicate the stability region of the metallic phase ($U < U_c$).

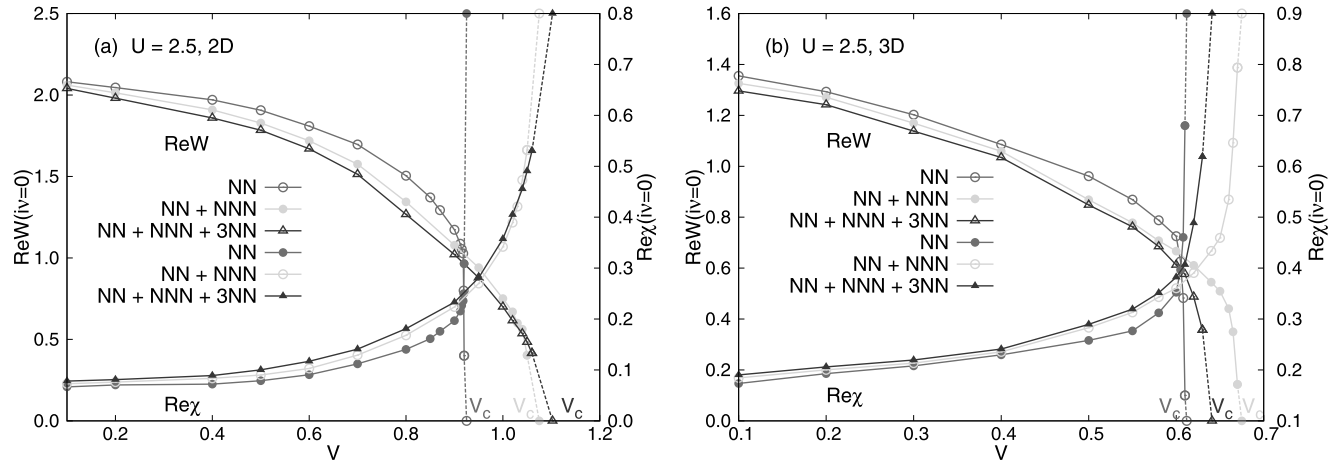


FIG. 3. (Color online) $\text{Re}W(i\nu=0)$ (left y axis) and $\text{Re}\chi(i\nu=0)$ (right y axis) as a function of V . $U = 2.5$. (a) Results for the square lattice. (b) Results for the simple cubic lattice. The dashed lines are used to determine V_c for the charge-ordering transition.

In our calculations, the Mott metal-insulator transition is determined by computing the quasiparticle weight Z [2]

$$Z = \left[1 - \frac{\text{Im}\Sigma(i\omega_0)}{\omega_0} \right]^{-1}, \quad (19)$$

where ω_0 is the first Matsubara frequency $\omega_0 = \pi/\beta$. Strictly speaking, this equation is only valid at zero temperature, but our temperature is low enough ($\beta = 100$) that it can be regarded as a good approximation. In Fig. 4, the calculated quasiparticle weights Z for the square and simple cubic lattices are plotted for selected V parameters. This figure shows that longer-range intersite interactions lead to a larger Z and hence to a larger U_c . The reason is again a larger screening effect.

3. Screened and retarded interactions

In the top panels of Fig. 5, we plot the real parts of $W(i\nu)$ and $\mathcal{U}(i\nu)$, and the imaginary parts of $W(i\nu)$ and $\mathcal{U}(i\nu)$ for the square lattice with selected U and V parameters. The counterparts for the simple cubic lattice are shown in the bottom panels of Fig. 5. We concentrate here on the FL region

for both the 2D and 3D lattices. When $\nu \rightarrow \infty$, both the fully screened interactions $\text{Re}W(i\nu)$ and partially screened interactions $\text{Re}\mathcal{U}(i\nu)$ [see Figs. 5(a) and 5(b)] asymptotically approach the bare interaction U . As the frequency ν is lowered, $\text{Re}W(i\nu)$ and $\text{Re}\mathcal{U}(i\nu)$ decrease monotonously. Longer-range intersite interactions produce a stronger screening effect, and lead to lower values of the static interactions $\text{Re}W(i\nu=0)$ and $\text{Re}\mathcal{U}(i\nu=0)$.

Let us take a closer look at the $\text{Im}W(i\nu)$ and $\text{Im}\mathcal{U}(i\nu)$ spectra, which we have obtained from a modified maximum entropy procedure [33] (see Appendix B). To analyze the spectra, we fit $\text{Im}W(i\nu)$ with multiple Gaussians. Each peak can be regarded as a screening mode (abbreviated as SM), and the position of the peak corresponds to the screening frequency. Figures 5(c) and 5(d) show that the $\text{Im}W(i\nu)$ spectra feature two prominent SMs, whose screening frequencies differ by about a factor of two. The insets of Figs. 5(a) and 5(b) show the contributions of these modes to the frequency dependence of $\text{Re}W(i\nu)$. In the $\text{Im}\mathcal{U}(i\nu)$ spectra, one can also distinguish two humps, and the locations and weights of these screening modes are similar to the $\text{Im}W(i\nu)$ counterparts. In both cases, the weight of the

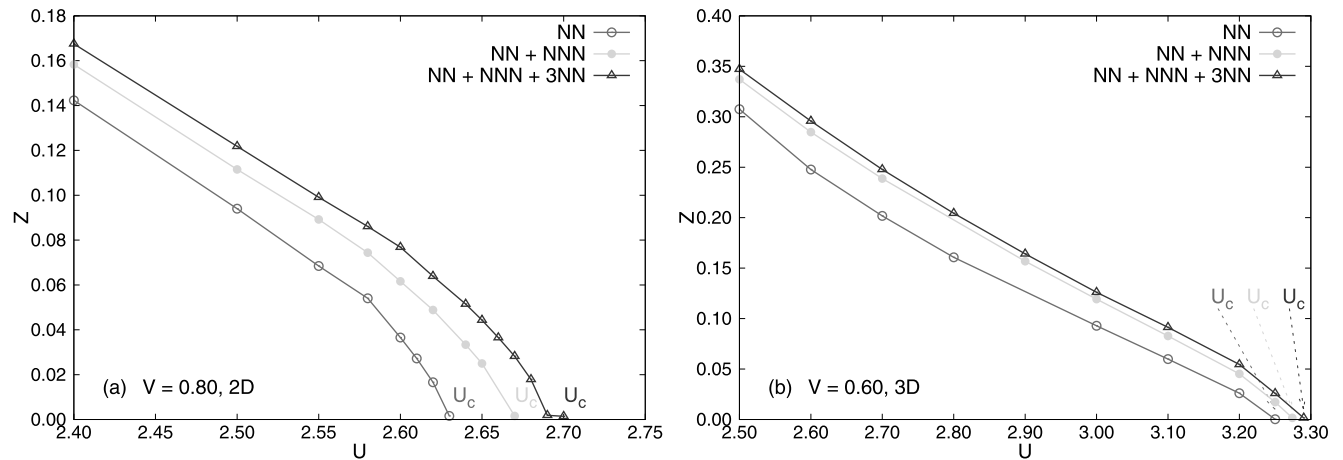


FIG. 4. (Color online) Quasiparticle weight Z as a function of U . (a) Results for the square lattice, $V = 0.80$. (b) Results for the simple cubic lattice, $V = 0.60$. When Z goes to zero, the Mott-Hubbard metal-insulator transition occurs. The corresponding U is U_c . In (b), the dashed lines are used to guide the eyes.

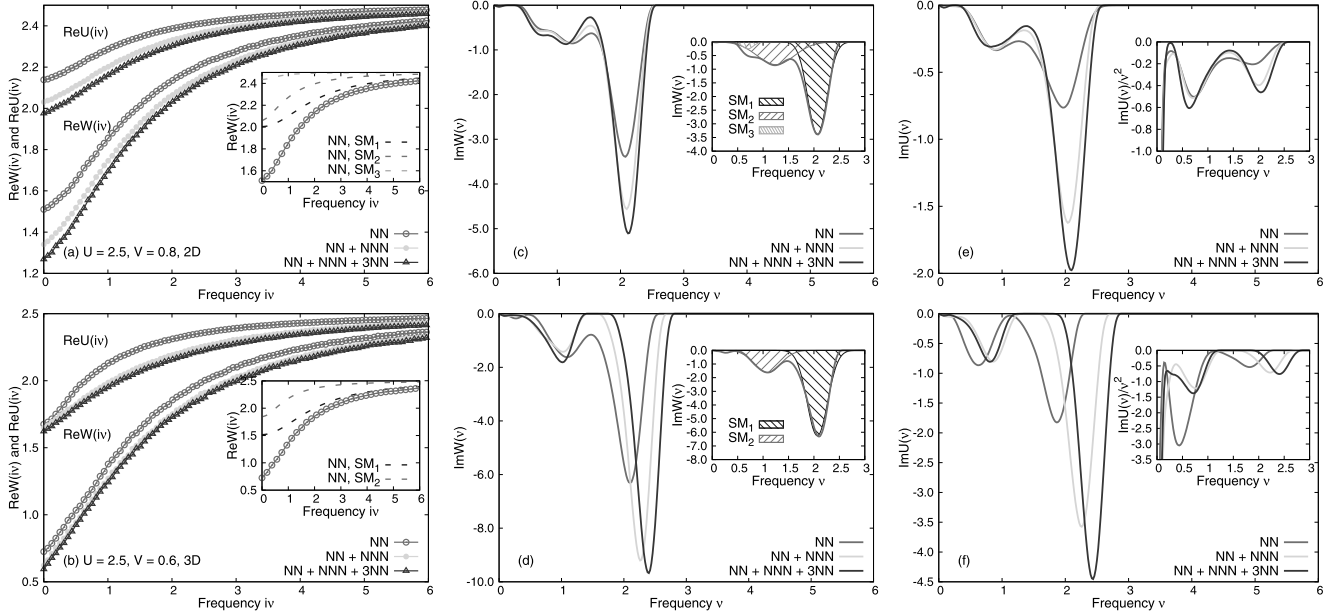


FIG. 5. (Color online) Real part of the fully screened interactions $\text{Re}W(i\nu)$ and partially screened interaction $\text{Re}U(i\nu)$, imaginary part of the real frequency fully screened interaction $\text{Im}W(\nu)$ and partially screened interactions $\text{Im}U(\nu)$ for the extended Hubbard model solved by EDMFT. (a), (c), and (e) Results for the square lattice, $U = 2.5$ and $V = 0.8$. (b), (d), and (e) Results for the simple cubic lattice, $U = 2.5$ and $V = 0.6$. In this figure, SM means screening mode. In the insets of (a) and (b), the SM-resolved $\text{Re}W(i\nu)$, together with the full $\text{Re}W(i\nu)$ are shown for the NN case. In (c) and (d), $\text{Im}W(\nu)$ for the NN case is approximated by Gaussian-type functions. The fitted results are shown in the insets. Each Gaussian peak denotes a SM. The insets in (e) and (f) show the $\text{Im}U(\nu)/\nu^2$ functions. Here $\text{Im}W(\nu)$ and $\text{Im}U(\nu)$ are extracted using a modified maximum entropy method. See Appendix B for more details.

high-energy screening mode depends on the range of the intersite interaction. In the 3D case, the high-energy mode also seems to shift in energy, as longer-range interactions are included.

The physical interpretation of the two screening modes is somewhat subtle. As we will see in the following section, the spectral function in the metallic phase essentially exhibits a three-peak structure consisting of two Hubbard bands and a renormalized quasiparticle band. One can therefore distinguish screening processes stemming from transitions between the Hubbard bands, between the quasiparticle peak and one of the Hubbard bands, and within the quasiparticle band [15]. It is natural to associate the high-energy screening mode with inter-Hubbard band transitions and the low-energy mode with transitions from the quasiparticle peak to either Hubbard band. Consistent with this interpretation is the fact that the energy difference between the two modes is roughly a factor of two. Even the energy values associated with the two modes are in good agreement with the energy separation between the two Hubbard bands and between the quasiparticle and the Hubbard bands, respectively (see Fig. 8 below). One may, however, wonder why the bosonic spectra do not exhibit a low-energy mode related to transitions within the renormalized quasiparticle band. There is in fact no necessity for this to happen: even in the metallic phase, where $\text{Im}\chi_{\text{imp}}(\omega)$ has a Drude-like contribution $\pi\alpha\delta(\omega)$ and hence, by the Kramers-Kronig relation, $\text{Re}\chi_{\text{imp}} = \alpha/\omega$, the polarization Π_{imp} does not have a pole at $\omega = 0$. Indeed, taking $\mathcal{U} = U$ for simplicity, we have $\Pi_{\text{imp}} = -\chi_{\text{imp}}/(1 - U\chi_{\text{imp}}) = -\alpha/(\omega - \alpha U)$. As a result, the screened interaction does not have a pole at $\omega = 0$

either: $W_{\text{loc}} = \sum_q v_q/(1 - v_q\Pi_{\text{imp}}) = \sum_q v_q(\omega - \alpha U)/[\omega - \alpha(U - v_q)]$.

It is worth noting that the structures in the $\text{Im}U(\nu)/\nu^2$ function, which are shown in the insets of Figs. 5(e) and 5(f), determine the most relevant screening modes and the associated energies of satellites in the local spectral function $A(\omega)$ [32]. Therefore, despite the smaller weight, the low-energy mode is equally or even more important than the high-energy mode. In order to quantify the evolution of the screening modes by a single number, we define the effective screening frequency ν_0 as follows [34]:

$$\nu_0 = \int_0^\infty d\nu \nu \text{Im}U(\nu) / \int_0^\infty d\nu \text{Im}U(\nu). \quad (20)$$

In Table I, the static retarded interaction $\text{Re}U(\nu = 0)$, fully screened interaction $\text{Re}W(\nu = 0)$, and the effective screening frequency ν_0 are listed for some representative regions in the phase diagrams (see Fig. 2). $\text{Re}U(\nu = 0)$ and $\text{Re}W(\nu = 0)$ are two key quantities that can be used to quantify the screening effect. They decrease for longer-range intersite interactions, irrespective of the strength of the bare interaction U , the strength of the intersite interaction V , and the lattice dimension. This is to be expected, since a longer-ranged interaction increases the number of sites which participate in the screening process. In addition, $\text{Re}W(\nu = 0)$ is always smaller than $\text{Re}U(\nu = 0)$, since the former incorporates the screening effects not only from the nonlocal processes, but also from the local processes. As is seen in Table I, the effective screening frequency increases with increasing range

TABLE I. Summary of $\text{Re}\mathcal{U}(\nu = 0)$, $\text{Re}W(\nu = 0)$ and effective screening frequency ν_0 for U and V parameters in the metallic and Mott insulating regime. The ν_0 is defined by Eq. (20). The results in parentheses are from fully self-consistent $GW + \text{EDMFT}$ calculations (see Sec. III B for further details), while the others are from self-consistent EDMFT calculations.

| Metallic state | | | | | | | | | | |
|-----------------------|----------------|------|---------------------------------|-----------------------|-------------|----------------------|------|---------------------------------|-----------------------|-------------|
| mode | Square lattice | | | | | Simple cubic lattice | | | | |
| | V | U | $\text{Re}\mathcal{U}(\nu = 0)$ | $\text{Re}W(\nu = 0)$ | ν_0 | V | U | $\text{Re}\mathcal{U}(\nu = 0)$ | $\text{Re}W(\nu = 0)$ | ν_0 |
| NN | 0.80 | 2.50 | 2.14 (2.36) | 1.51 (1.96) | 1.61 (1.11) | 0.60 | 2.50 | 1.68 (2.21) | 0.73 (1.23) | 1.44 (1.06) |
| NN + NNN | 0.80 | 2.50 | 2.03 (2.31) | 1.34 (1.91) | 1.77 (1.12) | 0.60 | 2.50 | 1.65 (2.06) | 0.62 (1.15) | 1.96 (1.12) |
| NN + NNN + 3NN | 0.80 | 2.50 | 1.98 (2.28) | 1.27 (1.86) | 1.84 (1.10) | 0.60 | 2.50 | 1.62 (2.03) | 0.59 (1.14) | 2.14 (1.16) |
| Mott insulating state | | | | | | | | | | |
| mode | Square lattice | | | | | Simple cubic lattice | | | | |
| | V | U | $\text{Re}\mathcal{U}(\nu = 0)$ | $\text{Re}W(\nu = 0)$ | ν_0 | V | U | $\text{Re}\mathcal{U}(\nu = 0)$ | $\text{Re}W(\nu = 0)$ | ν_0 |
| NN | 1.50 | 3.00 | 2.75 (2.82) | 2.54 (2.61) | 2.48 (1.75) | 1.50 | 3.60 | 3.24 (3.33) | 2.98 (3.08) | 2.88 (2.16) |
| NN + NNN | 1.50 | 3.00 | 2.63 (2.75) | 2.40 (2.55) | 2.52 (1.66) | 1.50 | 3.60 | 2.81 (3.04) | 2.50 (2.79) | 2.84 (2.00) |
| NN + NNN + 3NN | 1.50 | 3.00 | 2.56 (2.71) | 2.34 (2.51) | 2.54 (1.66) | 1.50 | 3.60 | 2.56 (2.98) | 2.27 (2.74) | 2.87 (2.00) |

of the intersite interaction in the metallic phase, while it is almost independent of the range of the interaction in the Mott insulating phase. The larger the bare interaction, the larger the effective screening frequency, which is consistent with previous EDMFT calculations [15].

It is instructive to look at the evolution of the SM along the metallic side of the $V_c(U)$ phase boundary, especially in the U region where this phase boundary exhibits a slope change. The results for the two- and three-dimensional lattices with the nearest-neighbor interactions are shown in Fig. 6. In the case of the simple cubic lattice [Fig. 6(d)], the slope change is smooth and occurs quite a bit before U reaches the $V = 0$ Mott transition value U_c . The slope change therefore occurs within the metallic phase, and is not directly associated with the Mott transition. Nevertheless, there is a sudden increase in the effective screening frequency at $U \approx 2.9$, originating from a simultaneous shift in the energy of both screening modes. In the square lattice case [Fig. 6(c)], where the slope change occurs simultaneously with the Mott transition, the effective screening frequency does not exhibit such a jump within the metallic phase. These results, and the comparison with the phase diagram of the Holstein-Hubbard model [27] show that the slope change, which cannot be understood within a simple mean-field picture, is related to correlation induced changes in the effective screening frequency.

4. Effective static interaction

EDMFT provides an elegant means of constructing a model with purely local—though dynamical—interactions incorporating the effects of the nonlocal interactions in an effective manner. Furthermore, Ref. [34] demonstrated that—at least in the antiadiabatic limit—a model with dynamical interactions can to a first approximation be thought of as a model with static interactions corresponding to the zero-frequency limit of the dynamical ones and a renormalized one-body Hamiltonian. These facts motivate a comparison of the zero-frequency limit of the effective dynamical interaction with attempts in the literature of constructing low-energy Hamiltonians with effective local static interactions, incorporating some of the

screening effects stemming from longer-range interactions. In Ref. [23], it was shown that the *best* Hubbard model with purely local interactions mimicking the physics of a model with long-range interactions is one with modified local interactions. “Best” is here defined in the sense of the Peierls-Feynman-Bogoliubov variational principle, leading to a free energy closest to the one of the original system. The result is an effective interaction where the bare interaction U is modified by a weighted average of the nonlocal interaction matrix elements V_{ij} :

$$U_{\text{eff}} = U + \frac{1}{2} \sum_{i \neq j, \sigma, \sigma'} V_{ij} \frac{\partial U_{\text{eff}} \langle n_{i\sigma} n_{j\sigma'} \rangle}{\sum_l \partial U_{\text{eff}} \langle n_{l\uparrow} n_{l\downarrow} \rangle}. \quad (21)$$

Here, the sums are over lattice sites and spins, and $\langle n_{i\sigma} n_{j\sigma'} \rangle$ denotes the density-density correlator between sites i and j . Assuming that a variation of U leads to a displacement of charge only to the nearest-neighbor sites, charge conservation leads to a further simplification. Eq. (21) then reduces to

$$U_{\text{eff}} = U - V_{01}, \quad (22)$$

that is, screening by nonlocal interactions results in a simple reduction of the on-site interaction by the nearest-neighbor one. Numerical calculations for graphene, silicene, and benzene in Ref. [23] indeed found values for the effective interactions close to the simple estimate given by Eq. (22). Inspection of the calculations of Ref. [15] for an extended Hubbard model in two dimensions with NN interactions reveals another interesting aspect: in these calculations screening was found to be strongly dependent on the regime, with barely any screening in the Mott phase (as expected) but a strong reduction of the effective local interaction in the correlated metal. Interestingly, however, the simple estimate of Eq. (22) was found to provide a lower bound with U_{eff} coming closer to $U - V_{01}$ or U depending on the proximity to the metallic or Mott phase, respectively.

Here, we address the question of the generic character of this observation. In Fig. 7, we plot the static part of the effective local interaction obtained from EDMFT as a function of V . As expected, this quantity is strongly reduced when approaching the phase boundary to the CO phase where strong charge

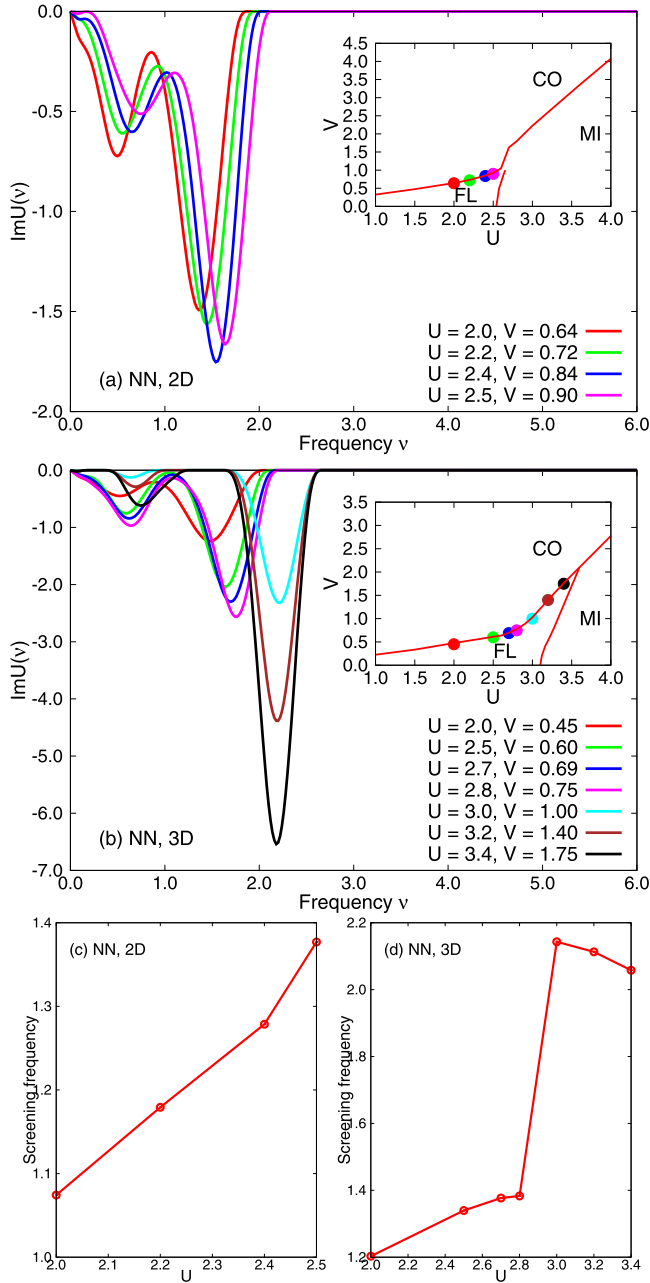


FIG. 6. (Color online) Imaginary part of real frequency partially screened interactions $\text{Im}\mathcal{U}(v)$ for the extended Hubbard model with the NN interactions solved by EDMFT. (a) Results for the square lattice. (b) Results for the simple cubic lattice. The U and V parameters are shown as color-filled circles in the insets. In (c) and (d), the corresponding effective screening frequencies ν_0 are shown.

fluctuations dominate. In the two-dimensional case with on-site and NN interactions, the effective interaction remains bounded by Eq. (22), while for longer-ranged interactions, $\mathcal{U}(0)$ drops below this bound as one approaches the phase boundary. In three dimensions, we find a drastic drop of the effective interaction even for the NN case, invalidating any simple estimate. Some of the differences between the 2D and 3D results are presumably due to the fact that the 2D system is closer to the Mott transition.

5. Local spectral properties

We focus on three characteristic regions in the phase diagrams: the FL metallic phase, the MI phase, and the metallic region between the CO and MI phases [or “triangle zone” in between the $V_c(U)$ and $U_c(V)$ lines]. We computed the local spectral functions in these zones via analytical continuation of the impurity Green’s function $G(\tau)$. For the calculations, we use the method described in Sec. II C, with the bosonic factor $B(\tau)$ obtained from the maximum entropy result for $\text{Im}\mathcal{U}(v)$ [31,33]. In the calculations of $B(\tau)$, we introduced a cutoff at small frequencies to prevent an unphysical divergence of $\text{Im}\mathcal{U}(v)/v^2$ [see insets in Figs. 5(e) and 5(f)]. The spectral functions $A(\omega)$ for the square lattice are displayed in the top panels of Fig. 8, while those for the simple cubic lattice are shown in the bottom panels.

We found that the screening effects resulting from long-range intersite interactions affect the impurity spectral functions in several ways. In the FL regime, the on-site interaction is weak. The major effect of longer-range intersite interactions is to transfer spectral weight from the Hubbard bands to the quasiparticle peak, and to small satellites, which are shifted from the Hubbard bands by roughly the effective screening frequency ν_0 . In the triangle zone, where the on-site interaction is moderate, the longer-range intersite interactions can trigger an insulator-metal phase transition. Let us look at Fig. 8(e), which illustrates the evolution of the spectral functions across such a metal-insulator transition. For the NN case, the system is an insulator with sharp Hubbard bands and sizable gap. However, for the NN + NNN case, spectral weight appears at the Fermi level, which indicates a strongly renormalized metallic state. While the Hubbard bands are smeared out, their position is almost unchanged. When the 3NN intersite interaction is added, the system turns into a good metal with a large quasiparticle peak and the Hubbard bands are shifted to higher energy. In the MI phase in which the on-site interaction is strong, the spectral functions are less affected by longer-range intersite interactions. It seems that the longer-range intersite interactions do not significantly shrink the gaps. The main effect is to redistribute the weight within the Hubbard bands. At the beginning, the upper and lower Hubbard bands are broad and smooth. When longer-range intersite interactions are included, the Hubbard bands turn sharper and thinner, and spectral weight is transferred to the edges of the gap and high-frequency features [see Fig. 8(d)].

As mentioned before, the structures in $\text{Im}\mathcal{U}(v)/v^2$ produce satellites in the local spectral functions $A(\omega)$. For example, the screening modes displayed in Figs. 5(e) and 5(f) explain the broad tails in the energy range $|\omega| \gtrsim 2$ in Figs. 8(a) and 8(b).

6. Away from half-filling

Having identified the dominant screening modes in the half-filled system and interpreted them in terms of the spectral function, it is interesting to look also at the evolution of these quantities away from half-filling. In this section, we present some results for the 2D and 3D lattices with on-site and NN intersite interactions. First, we show the phase diagrams for fixed U in the space of V and $\delta\mu = \mu - U/2$ (Fig. 9). In the 2D (3D) case, we choose $U = 2.4$ and 3.6 ($U = 2.5$ and 3.6).

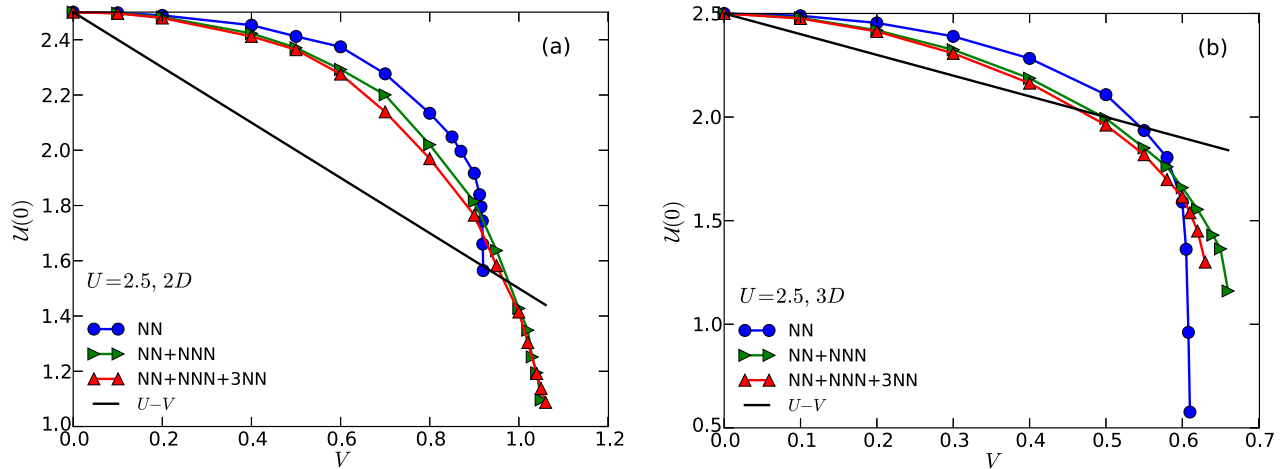


FIG. 7. (Color online) Comparison of the effective static interaction $\mathcal{U}(0)$ and the simple estimate $U - V$ [see Eq. (22)]. (a) Results for the 2D model with $U = 2.5$. (b) Results for the 3D model with $U = 2.5$.

For the smaller on-site interaction, the system at half-filling ($\delta\mu = 0$) and small enough V is metallic, while for the larger U it is Mott insulating. As the filling of the metallic system is increased, the phase boundary to the CO phase shifts to larger V , i.e., in the small- U regime, the CO instability is a nesting-type phenomenon. We also plot, as dashed lines, the location where the screened interaction $W(0)$ changes sign. We note that this $W(0) = 0$ line is very different from the FL-CO phase boundary. In the heavily doped region, one can still obtain a stable metallic solution even though $W(0) < 0$.

The situation is quite different for the larger U , where the half-filled solution is either MI or CO. Here, the MI solution is destabilized by doping. In the 3D case, one observes a

transition into a doped metal phase for $V \lesssim 1.0$, while in the 2D system, a similar transition occurs for $V \lesssim 2.0$. We note that these phase diagrams are qualitatively very similar to those of the Holstein-Hubbard model [25].

Both the electron spectral function and the screened interaction depend sensitively on $\delta\mu$. Some representative results are shown in Fig. 10. For $\delta\mu > 0$, the electron spectral function (left panels) becomes asymmetric. In the metallic phase, the quasiparticle peak grows and shifts closer to the upper Hubbard band, while in the insulating phase, the gap shrinks due to a broadening of the lower Hubbard band. These changes in the electron spectral function qualitatively explain the changes in the bosonic spectra (right panels). In the metallic

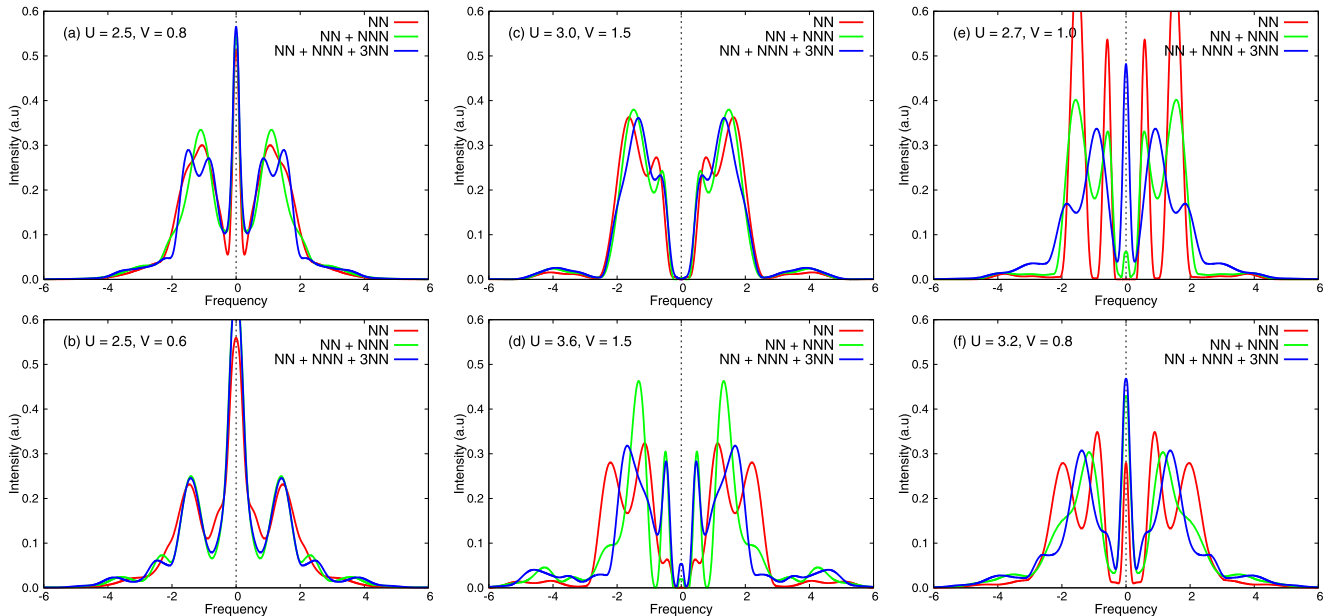


FIG. 8. (Color online) Spectral functions at selected points for the single-band half-filled extended Hubbard model solved by EDMFT. (a), (c), and (e) Results for the square lattice. (b), (d), and (f) Results for the simple cubic lattice. The parameters are as follows: (a) metallic region, $U = 2.5$ and $V = 0.8$; (b) metallic region, $U = 2.5$ and $V = 0.6$; (c) Mott insulating region, $U = 3.0$ and $V = 1.5$; (d) Mott insulating region, $U = 3.6$ and $V = 1.5$; (e) "triangle" zone, $U = 2.7$ and $V = 1.0$; (f) "triangle" zone, $U = 3.2$ and $V = 0.8$. The impurity spectral functions are obtained using the analytical continuation method proposed in Ref. [31].

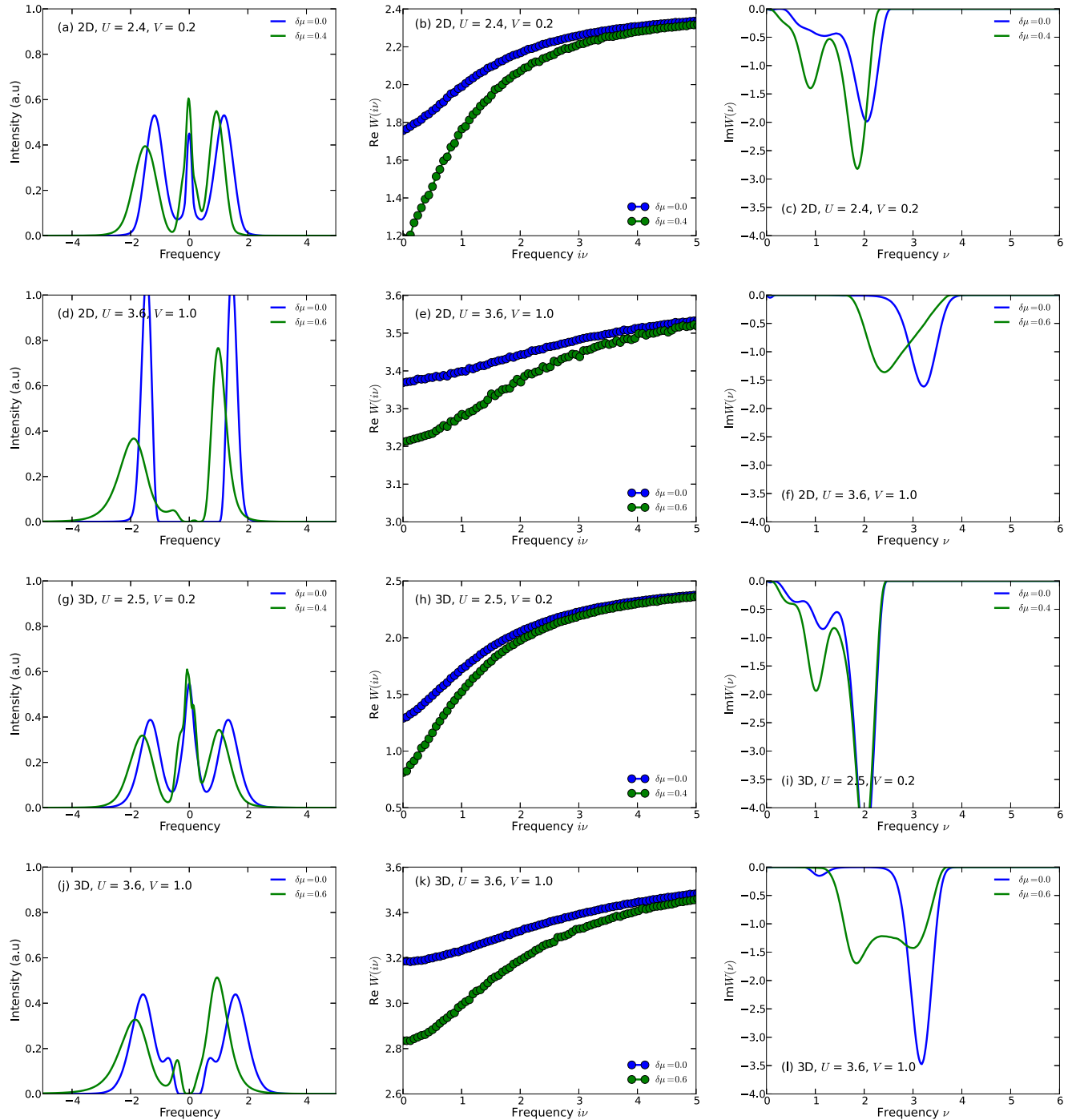


FIG. 9. (Color online) Spectral functions for the Hubbard model with NN interactions away from half-filling. (a)–(f) Results for the square lattice. (g)–(i) Results for the cubic lattice. In the left column, the impurity spectral functions $A(\omega)$ are shown. In the middle and right columns, we show the screened interaction $W(i\nu)$ and corresponding $\text{Im}W(\nu)$. The parameters are as follows: (a)–(c) $U = 2.4$, $V = 0.2$, 2D lattice. (d)–(f) $U = 3.6$, $V = 1.0$, 2D lattice. (g)–(i) $U = 2.5$, $V = 0.2$, 3D lattice. (j)–(l) $U = 3.6$, $V = 1.0$, 3D lattice.

case, the main effect of increasing $\delta\mu$ is a growing low-energy feature in $\text{Im}W(\nu)$. This can be explained by the larger number of states in the quasiparticle band. In the Mott insulating case, where the bosonic spectra for the half-filled system show a single peak at an energy given by the gap, the shrinking of the gap with increasing $\delta\mu$ leads to a broadening and shift of this peak to lower energies. In the 3D case, where the gap

size for $\delta\mu = 0.6$ is small and the electron spectral function has a peak at the lower gap edge, we also find a low-energy mode in $\text{Im}W(\nu)$, which is associated with transitions between this peak and the upper Hubbard band. Since the low-energy mode in $\text{Im}W(\nu)$ produces the largest screening effect, it is not surprising that increasing $\delta\mu$ has a large effect on the screened interaction (middle panels). As we saw in Fig. 9 (dashed line),

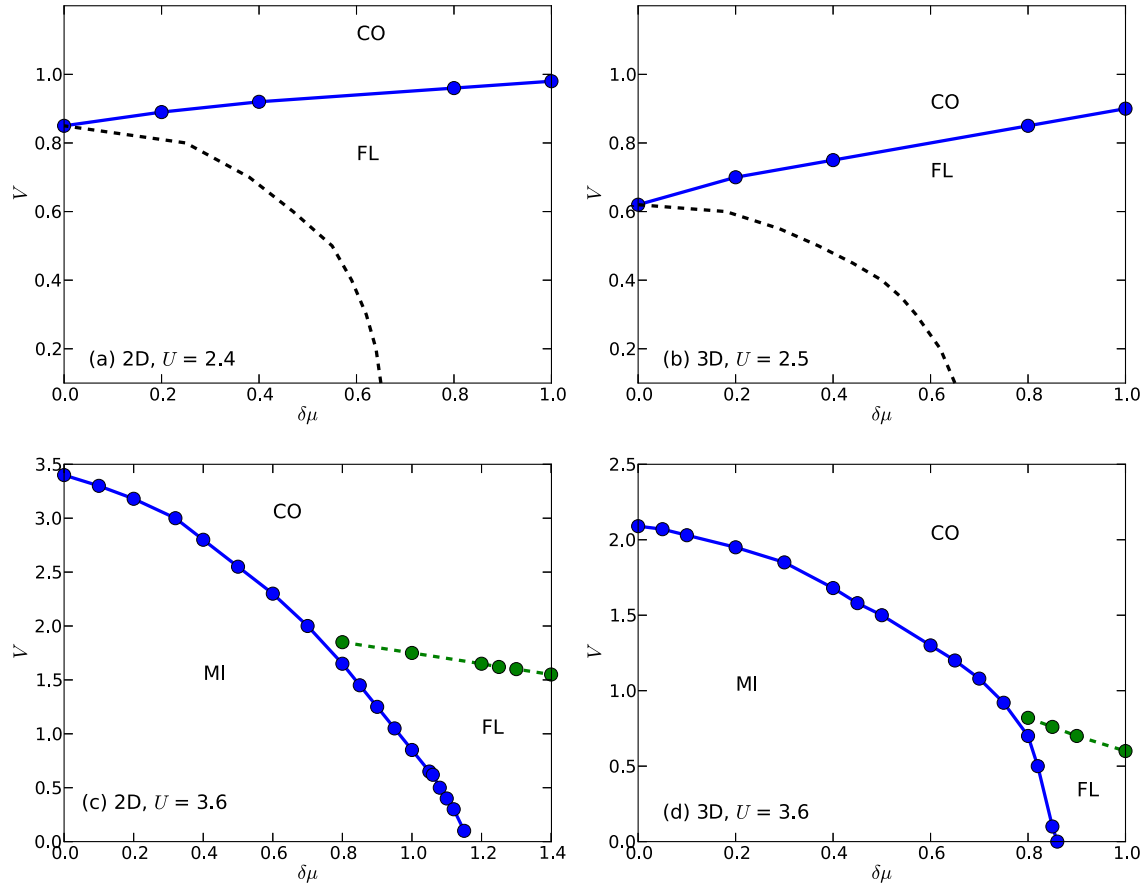


FIG. 10. (Color online) V - μ phase diagrams for the single-band extended Hubbard model with NN interactions, determined by EDMFT calculations. Here, $\delta\mu = \mu - U/2$. (a) and (c) show results for the 2D square lattice which at half-filling is in the FL or MI regime. (b) and (d) show similar results for the 3D simple cubic lattice. The black dashed lines in (a) and (b) show the location of $W(0) = 0$, i.e., on the right side of this boundary, the static screened interaction is negative.

in the metallic phase, doping quickly leads to an overscreening of the local interaction.

B. $GW + EDMFT$ results

In this section, we present the $GW + EDMFT$ results. Since the computational cost of fully self-consistent $GW + EDMFT$ calculations is much higher than in the case of EDMFT calculations, we do not map out the whole U - V phase diagram. Instead, we performed $GW + EDMFT$ calculations for selected U and V parameters. As a starting point for the self-consistent $GW + EDMFT$ calculation, we used the converged EDMFT results.

1. Nonlocal and local self-energy and polarization

The $GW + EDMFT$ method incorporates nonlocal correlations by adding the nonlocal components of the GW self-energy and polarization functions to the EDMFT result [6,7,14,15]. Hence the $GW + EDMFT$ self-energy and polarization functions are not only frequency-dependent but also momentum-dependent.

In Fig. 11, the nonlocal parts of the self-energy for the lowest Matsubara frequency ω_0 are shown. These data have been obtained using Eq. (10). For the square lattice, we plot $\Sigma_{\text{nonloc}}(k, i\omega_0)$ for k_x and $k_y \in [0, 2\pi]$. In the case of the simple

cubic lattice, we show a cut of $\Sigma_{\text{nonloc}}(k, i\omega_0)$ in the $k_z = 0$ plane. Consistent with previous $GW + EDMFT$ calculations for the square lattice with NN interactions [15], we find that the GW contribution to the imaginary part of the nonlocal self-energy is negligible with respect to the local self-energy. The real part of the nonlocal self-energy is relatively large away from the EDMFT Fermi surface, but does not alter this Fermi surface. Longer-range interactions do increase the k dependence, but they do not significantly affect the conclusion that the k dependence of the self-energy both for the 2D and 3D lattice models is not very strong in the $GW + EDMFT$ scheme. Even in the vicinity of the Mott transition (for instance, $U = 2.5$ and $V = 0.8$ for the square lattice is very close to the Mott transition, see Fig. 2), the momentum differentiation is weak. This result is in contrast to the strong momentum dependence observed in the self-energy functions obtained from dynamical cluster approximation (DCA) [35,36] and cellular dynamical mean-field theory (CDMFT) [37,38] calculations for the two-dimensional Hubbard model as one approaches the Mott transition. This discrepancy suggests that additional nonlocal diagrams, such as ladder diagrams, should be included to provide a better description of the momentum dependence of the self-energy functions (and other k -dependent quantities).

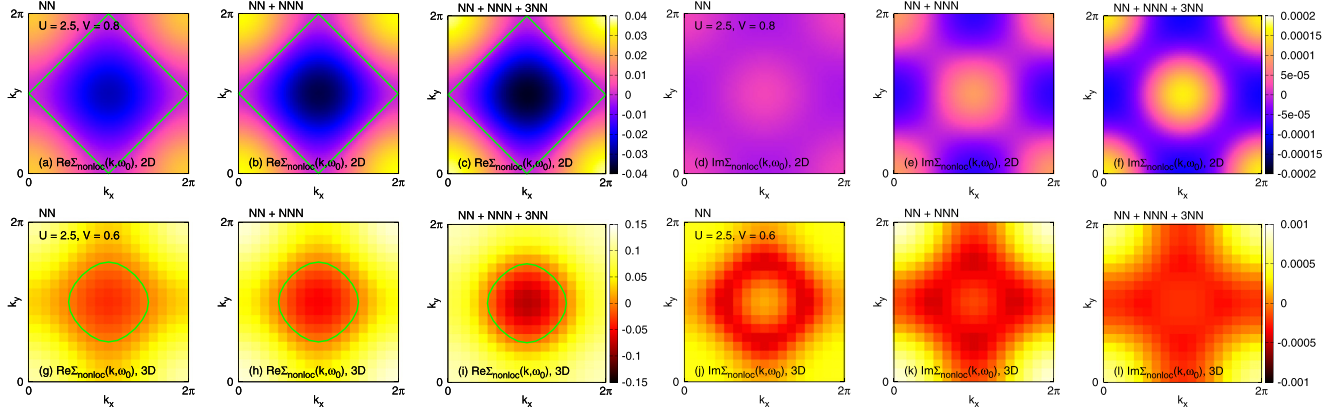


FIG. 11. (Color online) $\Sigma_{\text{nonloc}}(k, i\omega_0)$ for the extended Hubbard model from $GW + \text{EDMFT}$. (a)–(f) Results for the square lattice, $U = 2.5$, $V = 0.80$. (g)–(l) Results for the simple cubic lattice, $U = 2.5$, $V = 0.60$. We only show the $k_z = 0$ plane. (a)–(c) and (g)–(i) $\text{Re}\Sigma_{\text{nonloc}}(k, i\omega_0)$. (d)–(f) and (j)–(l) $\text{Im}\Sigma_{\text{nonloc}}(k, i\omega_0)$. The green curves in (a)–(c) and (g)–(i) denote the EDMFT Fermi surface.

As for the nonlocal polarization function for the first bosonic Matsubara frequency $\Pi_{\text{nonloc}}(k, i\nu = 0)$ (not shown in this figure), we observe a stronger momentum dependence, especially when one approaches the charge-ordering transition [15]. However, it seems that longer-range intersite interactions do not enhance this k dependence prominently, which is contrary to the trend found for the nonlocal self-energy.

Finally, we plot in Fig. 12 some typical local self-energies in the FL phase. $|\text{Im}\Sigma(i\omega_0)|$ is considerably enhanced in the $GW + \text{EDMFT}$ calculations, compared to the EDMFT result. These observations show that local correlations become stronger if the k -dependent GW contributions are added to the self-energy and polarization functions in the self-consistency loop. More evidence for this change will be presented in the following section. In Fig. 12, we also compare the local self-energies for intersite interactions of different range. The effect of the longer-ranged interactions is to reduce the self-energy. In the calculations with long-range interactions and nonlocal self-energies, we thus have a competition between the additional screening from long-range interactions, which leads to weaker correlation effects, and the momentum dependence, which enhances local correlations. The latter effect seems to be dominant.

2. Screened and retarded interactions

As we have seen in the previous subsection, the $GW + \text{EDMFT}$ scheme not only adds nonlocal contributions to the self-energy $\Sigma(k, i\omega_n)$ and polarization $\Pi(k, i\nu_n)$, but it also affects the local quantities through the self-consistency loop [15]. Figure 13 shows the fully screened local interaction $\text{Re}W(i\nu)$ and partially screened interaction $\text{Re}\mathcal{U}(i\nu)$, together with the corresponding spectral functions $\text{Im}W(\nu)$ and $\text{Im}\mathcal{U}(\nu)$, for the square lattice and simple cubic lattice in the FL metallic state. The related EDMFT data have been plotted in Fig. 5 and analyzed in Sec. III A. Again, our results are consistent with available $GW + \text{EDMFT}$ data for the 2D and 3D extended Hubbard model [7,15].

Compared to the EDMFT result, both $\text{Re}W(i\nu = 0)$ and $\text{Re}\mathcal{U}(i\nu = 0)$ are greatly enhanced [see Figs. 13(a) and 13(b)], while $|\text{Im}G(i\omega_0)|$ (not shown in these figures) is reduced. This indicates that the local interactions are stronger in $GW + \text{EDMFT}$ than in EDMFT, i.e., that the screening effect is weaker. This can be understood in the following way [15]: in the EDMFT approach, all of the screening and correlation effects are absorbed into the local self-energy. However, in the framework of $GW + \text{EDMFT}$, some of these effects are carried

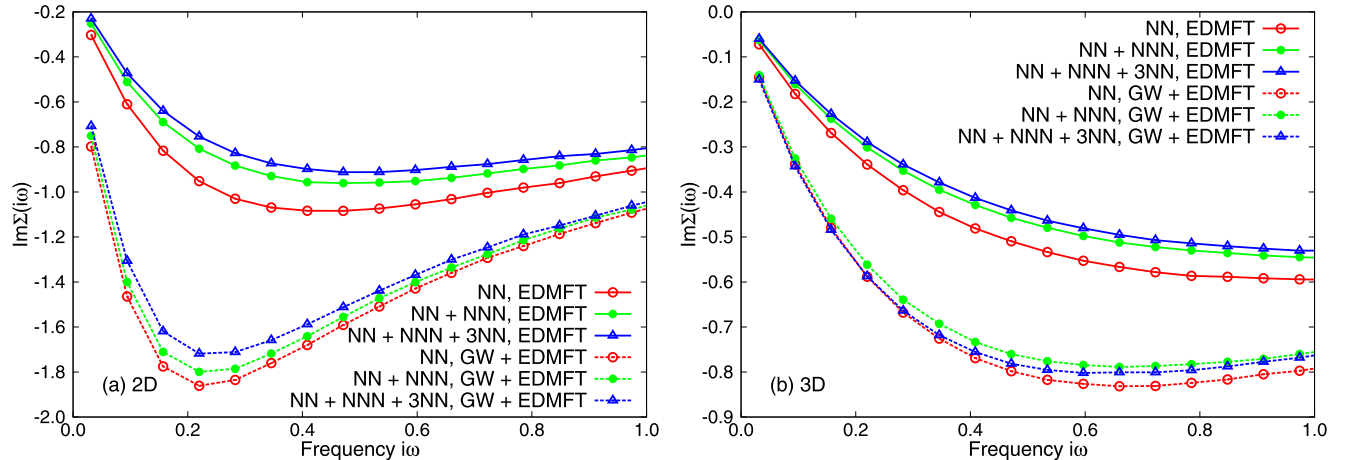


FIG. 12. (Color online) Imaginary part of the local self-energy function $\text{Im}\Sigma(i\omega)$ for the extended Hubbard model solved with EDMFT and $GW + \text{EDMFT}$. (a) Results for the square lattice, $U = 2.5$ and $V = 0.8$. (b) Results for the simple cubic lattice, $U = 2.5$ and $V = 0.6$.

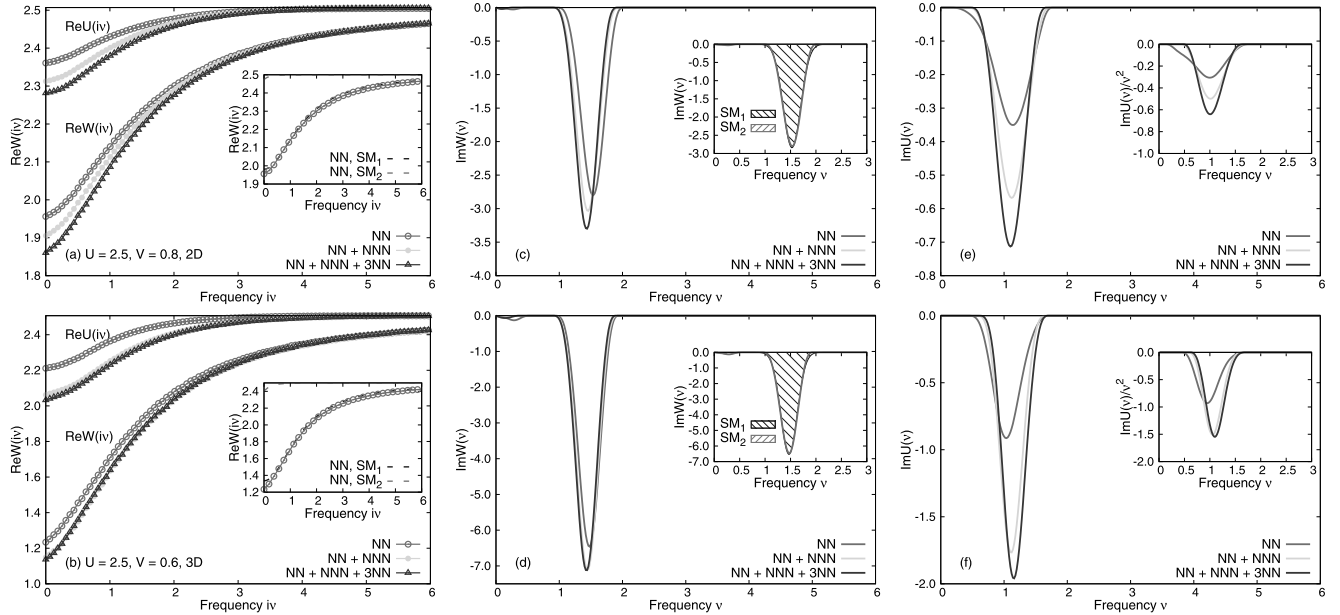


FIG. 13. (Color online) Real part of the fully screened interactions $\text{Re}W(i\nu)$ and partially screened interaction $\text{Re}\mathcal{U}(i\nu)$, and imaginary part of the real frequency fully screened interaction $\text{Im}W(\nu)$ and partially screened interactions $\text{Im}\mathcal{U}(\nu)$ for the extended Hubbard model solved by $GW + \text{EDMFT}$. (a), (c), and (e) Results for the square lattice, $U = 2.5$ and $V = 0.8$. (b), (d), and (f) Results for the simple cubic lattice, $U = 2.5$ and $V = 0.6$. In this figure, SM means screening mode. In the insets of (a) and (b), the SM-resolved $\text{Re}W(i\nu)$, together with the full $\text{Re}W(i\nu)$ are shown for the NN case. In (c) and (d), $\text{Im}W(\nu)$ for the NN case is approximated by Gaussian-type functions. The fitted results are shown in the insets. Each Gaussian peak corresponds to a SM. The insets in (e) and (f) show the $\text{Im}\mathcal{U}(\nu)/\nu^2$ functions. Here, $\text{Im}W(\nu)$ and $\text{Im}\mathcal{U}(\nu)$ are extracted using a modified maximum entropy method. See Appendix B for more details.

by the nonlocal self-energy. In other words, the screening between local and nonlocal quantities is redistributed in the $GW + \text{EDMFT}$ scheme, and the result of this is that the local interaction becomes less screened. Let us also mention that Nomura *et al.* [39] have shown that the nonlocal polarization induces an antiscreening effect, which competes with the screening effect caused by the long-range intersite interactions. Our results confirm that the interplay between the local and nonlocal self-energy and polarization in $GW + \text{EDMFT}$ leads, after self-consistency, to a weaker screening effect.

Another interesting observation is that the $\text{Im}W(\nu)$ and $\text{Im}\mathcal{U}(\nu)$ spectra extracted from the self-consistent $GW + \text{EDMFT}$ calculations [see Figs. 13(c)–13(f)] exhibit a single-hump structure, whereas the corresponding EDMFT results yield a two-hump structure [see Figs. 5(c)–5(f)]. Once again, we have fitted $\text{Im}W(\nu)$ with multiple Gaussians to extract the positions and weights of the dominant SMs. It seems that the $\text{Im}W(\nu)$ spectra obtained from the $GW + \text{EDMFT}$ calculations feature only one medium-frequency SM (~ 1.5 eV), while the low-frequency SMs (~ 0.5 eV) are extremely weak and the high-frequency SMs ($2\sim 3$ eV) previously identified in the EDMFT results have disappeared. As for the $\text{Im}\mathcal{U}(\nu)$ spectra, analogous characteristics are observed. Since the satellite structures of the local spectral function $A(\omega)$ are determined by the function $\text{Im}\mathcal{U}(\nu)/\nu^2$ [32], we conclude that the high-frequency features of $A(\omega)$ will be different in the $GW + \text{EDMFT}$ calculations, and more specifically that the satellites will be at lower energy. Though we only present results for the FL metallic phase in this figure, those for the Mott phase and the strongly correlated metal phase between the MI and CO states exhibit the same trend (see also Table I).

Next, we consider the influence of longer-range intersite interactions on the static screened and retarded interactions obtained with the $GW + \text{EDMFT}$ scheme. Table I also shows data collected from $GW + \text{EDMFT}$ calculations. Once more, we see that $\text{Re}\mathcal{U}(\nu = 0)$ and $\text{Re}W(\nu = 0)$ are reduced, and $|\text{Im}G(i\omega_0)|$ (not shown in the table) is enhanced if longer-range intersite interactions are present. The effects of longer-range interactions and nonlocal correlations compete with each other; the longer-range intersite interaction tends to enhance the screening and make the system less correlated, while including the GW nonlocal self-energies and polarizations has the opposite effect. The latter effect is dominant. From Figs. 13(e) and 13(f), we can see that the weight of the hump in the $\text{Im}\mathcal{U}(\nu)$ spectra increases if longer-range intersite interactions are added which means a larger screening effect. However, interestingly, the effective screening frequency ν_0 is only little affected by the range of the interaction within the $GW + \text{EDMFT}$ approach, which is also seen in Table I.

3. Local spectral properties

The top panels of Fig. 14 show some typical spectral functions for the square lattice obtained by $GW + \text{EDMFT}$. Similar results for the simple cubic lattice are shown in the bottom panels. Here, we consider the FL metallic state, MI state, and the “triangle” zone in the U - V phase diagrams. Since the parameter values are the same, one can directly compare these spectra to the EDMFT results as shown in Fig. 8. Consistent with the previous discussion, within the $GW + \text{EDMFT}$ scheme, the quasiparticle peak is greatly reduced, and the upper and lower Hubbard bands become more pronounced.

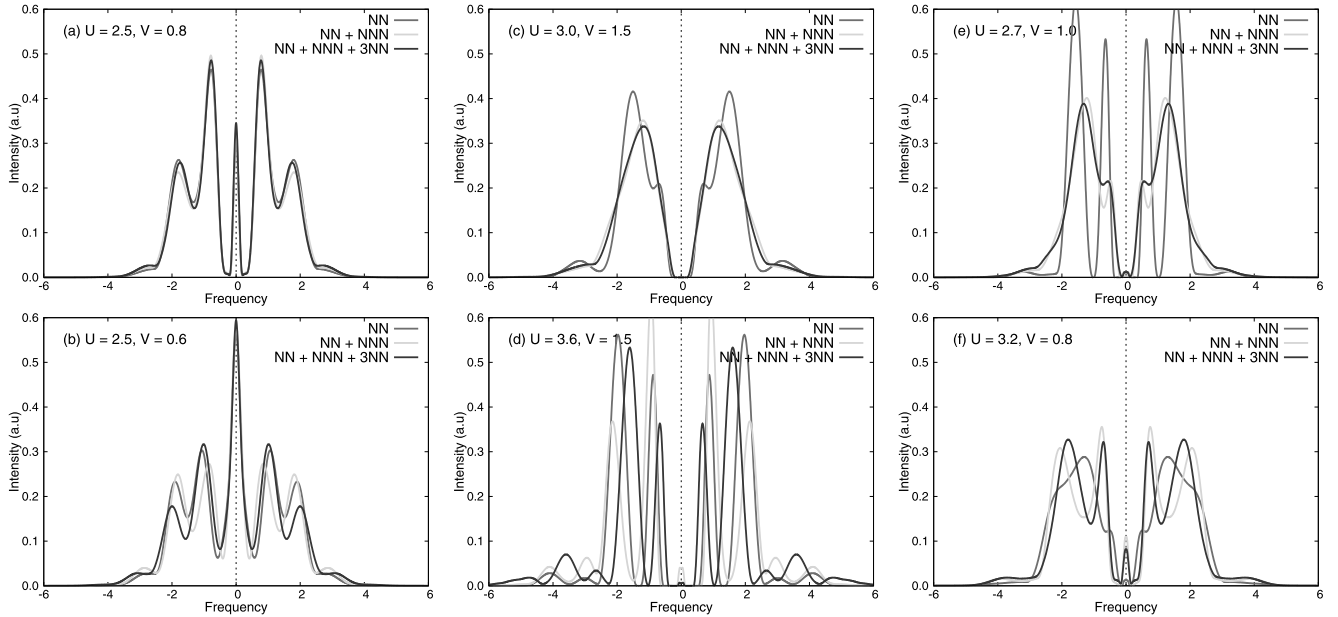


FIG. 14. (Color online) Spectral functions at selected points for the single-band half-filled extended Hubbard model solved by $GW + EDMFT$. (a), (c), and (e) Results for the square lattice. (b), (d), and (f) Results for the simple cubic lattice. The parameters are as follows: (a) metallic region, $U = 2.5$ and $V = 0.8$; (b) metallic region, $U = 2.5$ and $V = 0.6$; (c) Mott insulating region, $U = 3.0$ and $V = 1.5$; (d) Mott insulating region, $U = 3.6$ and $V = 1.5$; (e) “triangle” zone, $U = 2.7$ and $V = 1.0$; (f) “triangle” zone, $U = 3.2$ and $V = 0.8$. The impurity spectral functions are obtained using the analytical continuation method proposed in Ref. [31].

For instance, let us focus on the “triangle” zone for the square lattice (parameters $U = 2.7$ and $V = 1.0$). The EDMFT local spectral function shows considerable weight at the Fermi level, i.e., the system is metallic [see Fig. 8(e), for the NN + NNN case]. However, the corresponding $GW + EDMFT$ spectral function has almost no weight at $\omega = 0$, which means that it is close to or even in the MI phase [see Fig. 14(e), for the NN + NNN case]. From this fact, we conclude that there exists a small difference between the FL-MI phase boundaries calculated with EDMFT and $GW + EDMFT$, respectively, and that the MI region in the latter case should be larger.

The influence of longer-range intersite interactions on the local spectral functions $A(\omega)$ is very similar to the EDMFT case. Namely, longer-range intersite interactions enhance the quasiparticle peak and shift spectral weight to high-energy satellites. The local spectral function becomes more metallic in character as a result of the additional screening. Consistent with the lower energies of the SMs in the $GW + EDMFT$ case, the satellite features appear at lower energies. For example, in Fig. 13(c) (with $GW + EDMFT$) the satellites are at energy ± 3 – 3.5 eV, while in Fig. 5(c) (with EDMFT), they are at $\omega \approx \pm 4$ eV.

IV. CONCLUSIONS

We studied the paramagnetic solutions of the single-band half-filled extended Hubbard model on the square and simple cubic lattices by means of the EDMFT method. Longer-range intersite interactions introduce additional screening and lead to smaller effective local interactions. In the weakly correlated region, longer-range intersite interactions favor the metallic phase, whereas in the strongly correlated region, they stabilize the CO phase. The obvious “kink” in the $V_c(U)$ line near the Mott transition point in the square lattice model with NN

intersite interaction becomes a smooth slope change if longer-range interactions are included. At the same time, the metallic region extends to larger U values, so that the transition between MI and CO phases is via an intermediate metallic phase. We showed that the slope change in the $V_c(U)$ line, which cannot be explained by a simple mean-field picture, is associated with a sudden increase in the effective screening frequency near the critical U_c for the FL-MI transition.

Like DMFT, the EDMFT formalism is based on a local approximation [7,20]. To incorporate spatial correlations, we performed fully self-consistent $GW + EDMFT$ calculations for some selected U and V parameters. On the one hand, longer-range intersite interactions enhance the screening effect, just as in the EDMFT case. The screened and retarded interactions are strongly reduced. On the other hand, within the GW approximation the screening effect is weakened, which leads to a larger $U_{scr} [\equiv \text{Re}\mathcal{U}(i\nu = 0)]$ compared to the EDMFT result. In other words, considering the nonlocal GW self-energy and polarization makes the system more correlated. As a consequence, the $U_c(V)$ line (MI-FL phase boundary) will be modified slightly and shifted to smaller U . The results obtained from the $GW + EDMFT$ calculations confirm that the nonlocal contributions to the self-energy coming from the GW diagrams are quite small in the case of the extended Hubbard model, which agrees with previous $GW + EDMFT$ studies [15], but is not consistent with DCA [35,36] and CDMFT results [37,38]. The effect of longer-range intersite interactions is to enhance the nonlocal self-energy and polarization functions.

We have critically reexamined the possibility of finding simple rules of thumb for local interaction parameters incorporating screening by nonlocal interactions in an effective manner. While in the 2D case with NN interactions only, a

local interaction U reduced by the NN interaction V provides a lower bound for such an effective interaction, in all other cases the strong charge fluctuations in the proximity of the charge-ordered phase invalidate any simple estimate. This is consistent with a growing range of charge-charge correlations close to the transition.

The single-band extended Hubbard model calculations presented in this paper can be straightforwardly extended to the general multiorbital case, paving the way for realistic first-principles materials calculations. Low-dimensional sp -electron systems like graphene [40], silicene [23], aromatic molecules such as benzene [23], and systems of adatoms on semiconductor surfaces such as Si(111):X [30] feature simultaneously strong local and nonlocal Coulomb interactions. Obviously, these cannot be adequately addressed in the simple DMFT framework, which cannot handle nonlocal intersite interaction V beyond the Hartree level. The EDMFT and $GW + EDMFT$ approaches provide a relatively inexpensive treatment of local and (short-range or long-range) nonlocal interactions, making the application of them to electronic structure calculations of realistic materials worthwhile and promising.

ACKNOWLEDGMENTS

We acknowledge fruitful discussions with Junya Otsuki and Hiroshi Shinaoka. L.H. was supported by SNSF (Swiss National Science Foundation) Grant No. 200021-140648, P.W. by FP7/ERC starting Grant No. 278023, and S.B. by the European Research Council under project 617196. The calculations have been performed on the computer cluster at Fribourg University, using a code based on ALPS [41].

APPENDIX A: LONG-RANGE INTERSITE INTERACTIONS FOR THE EXTENDED HUBBARD MODEL

The partition function of the single-band extended Hubbard model [see Eq. (1)] is

$$Z = \text{Tr} e^{-\beta H}, \quad (\text{A1})$$

with inverse temperature β . It is more convenient to express it in the path-integral form

$$Z = \int \mathcal{D}[c_i^*, c_i] e^{-S}, \quad (\text{A2})$$

where the effective action S is

$$S[c^*, c] = \int_0^\beta d\tau \left\{ \sum_{ij,\sigma} c_{i\sigma}^*(\tau) [(\partial_\tau - \mu)\delta_{ij} - t_{ij}] c_{j\sigma}(\tau) + U \sum_i n_{i\uparrow}(\tau) n_{i\downarrow}(\tau) + \frac{1}{2} \sum_{ij} V_{ij} n_i(\tau) n_j(\tau) \right\}. \quad (\text{A3})$$

Using the identity $n_i n_i = (n_{i\uparrow} + n_{i\downarrow})^2 = n_i + 2n_{i\uparrow} n_{i\downarrow}$, we can rewrite the action as

$$S[c^*, c] = \int_0^\beta d\tau \left\{ \sum_{ij,\sigma} c_{i\sigma}^*(\tau) [(\partial_\tau - \tilde{\mu})\delta_{ij} - t_{ij}] c_{j\sigma}(\tau) + \frac{1}{2} \sum_{ij} v_{ij} n_i(\tau) n_j(\tau) \right\}, \quad (\text{A4})$$

where $\tilde{\mu} = \mu + U/2$, and $v_{ij} = U\delta_{ij} + V_{ij}$. Thus, in reciprocal space, we have the equation: $v_k = U + V_k$. Here, v_k is the k -dependent bare interaction, U is the static on-site interaction, and V_k is the k -dependent intersite interaction.

Since both the band dispersion ϵ_k and the bare interaction v_k enter the lattice Dyson equations [see Eqs. (2) and (3)], we will next give the explicit formulas for V_k . The formulas for ϵ_k are identical, with the interaction parameter V_{ij} replaced by the hopping parameter $-t_{ij}$. Unless explicitly stated otherwise, in the following the lattice constant $a_0 = 1$. In the present work, we only considered the following three cases (see Fig. 1).

(1) The nearest-neighbor (NN) case:

$$V_{ij} = V_0 \delta_{(ij)}, \quad (\text{A5})$$

where $\delta_{(ij)} = 1$ if i and j are the nearest neighbors and 0 otherwise. The Fourier transformation of V_{ij} on the square lattice is

$$V_k = 2V_0 [\cos(k_x) + \cos(k_y)]. \quad (\text{A6})$$

On the simple cubic lattice, we obtain

$$V_k = 2V_0 [\cos(k_x) + \cos(k_y) + \cos(k_z)]. \quad (\text{A7})$$

(2) The nearest-neighbor (NN) + the next nearest-neighbor (NNN) case:

$$V_{ij} = V_0 \delta_{(ij)} + V_1 \delta_{\langle\langle ij \rangle\rangle}, \quad (\text{A8})$$

where $\delta_{\langle\langle ij \rangle\rangle} = 1$ if i and j are next nearest neighbors and 0 otherwise. The Fourier transformation of V_{ij} on the square lattice is

$$V_k = +2V_0 [\cos(k_x) + \cos(k_y)] + 2V_1 [\cos(k_x + k_y) + \cos(k_x - k_y)]. \quad (\text{A9})$$

On the simple cubic lattice, we obtain

$$V_k = +2V_0 [\cos(k_x) + \cos(k_y) + \cos(k_z)] + 2V_1 [\cos(k_x + k_y) + \cos(k_x - k_y)] + 2V_1 [\cos(k_y + k_z) + \cos(k_y - k_z)] + 2V_1 [\cos(k_z + k_x) + \cos(k_z - k_x)]. \quad (\text{A10})$$

(3) The nearest-neighbor (NN) + the next nearest-neighbor (NNN) + the third nearest-neighbor (3NN) case:

$$V_{ij} = V_0 \delta_{(ij)} + V_1 \delta_{\langle\langle ij \rangle\rangle} + V_2 \delta_{\langle\langle\langle ij \rangle\rangle\rangle}, \quad (\text{A11})$$

where $\delta_{\langle\langle\langle ij \rangle\rangle\rangle} = 1$ if i and j are third nearest neighbors and 0 otherwise. The Fourier transformation of V_{ij} on the square lattice is

$$V_k = +2V_0 [\cos(k_x) + \cos(k_y)] + 2V_1 [\cos(k_x + k_y) + \cos(k_x - k_y)] + 2V_2 [\cos(2k_x) + \cos(2k_y)]. \quad (\text{A12})$$

On the simple cubic lattice, we obtain

$$V_k = +2V_0 [\cos(k_x) + \cos(k_y) + \cos(k_z)] + 2V_1 [\cos(k_x + k_y) + \cos(k_x - k_y)] + 2V_1 [\cos(k_y + k_z) + \cos(k_y - k_z)] + 2V_1 [\cos(k_z + k_x) + \cos(k_z - k_x)] + 2V_2 [\cos(k_x + k_y + k_z)] + 2V_2 [\cos(k_x + k_y - k_z)]$$

$$\begin{aligned}
& + 2V_2[\cos(k_x + k_z - k_y)] \\
& + 2V_2[\cos(k_y + k_z - k_x)]. \tag{A13}
\end{aligned}$$

Now the remaining issue is how to choose reasonable t_0, t_1, t_2, V_0, V_1 and V_2 parameters. For simplicity, we only retain the hoppings between the nearest neighbours, in other words, we set $t_0 = t$, and $t_1 = t_2 = 0$. On the other hand, we assume that the intersite interaction V_{ij} fulfills the following relation:

$$V_{ij} = \frac{V}{|\vec{r}_i - \vec{r}_j|/a}, \tag{A14}$$

where $i \neq j$, V is an adjustable parameter which controls the strength of nonlocal intersite interactions, and a is the shortest distance between two neighbors. By applying this restriction, we can easily determine V_0, V_1 and V_2 for the square and simple cubic lattices.

(1) The nearest-neighbor case: $|\vec{r}_i - \vec{r}_j| = a, V_0 = V$.

(2) The next nearest-neighbor case: $|\vec{r}_i - \vec{r}_j| = \sqrt{2}a, V_1 = V/\sqrt{2}$.

(3) The third nearest-neighbor case: The V_2 parameters for 2D and 3D lattices are different. For the square lattice, $|\vec{r}_i - \vec{r}_j| = 2a$ and $V_2 = V/2$, while for the simple cubic lattice, $|\vec{r}_i - \vec{r}_j| = \sqrt{3}a$ and $V_2 = V/\sqrt{3}$.

APPENDIX B: MAXIMUM ENTROPY METHOD FOR THE RETARDED INTERACTION $\mathcal{U}(i\nu)$ AND FULLY SCREENED INTERACTION $W(i\nu)$

In the self-consistent EDMFT and GW + EDMFT calculations, the frequency-dependent retarded interaction $\mathcal{U}(i\nu)$ can be calculated via the local Dyson equation [see Eq. (6)]. In order to determine the effective screening frequency ν_0 and reveal the high-energy plasmonic peaks in the local spectral function $A(\omega)$, we need $\mathcal{U}(\nu)$ [in fact, $\text{Im}\mathcal{U}(\nu)$]. However, the analytical continuation of $\mathcal{U}(i\nu)$ is not a trivial task due to the unavoidable numerical noise. In that case, the commonly used Padé procedure [42] is questionable, and is not the first choice any more. The maximum entropy method is widely used in the Monte Carlo community to extract real frequency data from imaginary time correlation functions [33]. In this appendix, we will extend it to support the analytical continuation of the retarded interaction $\mathcal{U}(i\nu)$.

First of all, the retarded interaction $\mathcal{U}(i\nu)$ obeys the following relation [27,32]:

$$U_{\text{scr}} = U + 2 \int_0^\infty \frac{d\nu}{\pi} \frac{\text{Im}\mathcal{U}(\nu)}{\nu}, \tag{B1}$$

with $U_{\text{scr}} = \text{Re}\mathcal{U}(i\nu = 0)$ and U the static on-site interaction. This equation can be rewritten as

$$\int_0^\infty \tilde{\mathcal{U}}(\nu) d\nu = 1, \tag{B2}$$

where

$$\tilde{\mathcal{U}}(\nu) = -\frac{\text{Im}\mathcal{U}(\nu)}{\pi} \frac{2}{\nu(U - U_{\text{scr}})}. \tag{B3}$$

Equations (B2) and (B3) can be viewed as the sum-rule for $\mathcal{U}(\nu)$, which is important for the maximum entropy algorithm. On the other hand, the kernel equation for the maximum

entropy method is [33]

$$\mathcal{U}(\tau) = \int_0^\infty d\nu \frac{e^{-\tau\nu}}{1 - e^{-\beta\nu}} \left[\frac{-\text{Im}\mathcal{U}(\nu)}{\pi} \right]. \tag{B4}$$

Using Eq. (B3), it is easy to rewrite Eq. (B4) as

$$\mathcal{U}(\tau) = \int_0^\infty d\nu K(\nu, \tau) \tilde{\mathcal{U}}(\nu), \tag{B5}$$

where $K(\nu, \tau)$ is the so-called bosonic Kernel function. The explicit definition of $K(\nu, \tau)$ is

$$K(\nu, \tau) = \frac{e^{-\tau\nu}}{1 - e^{-\beta\nu}} \frac{\nu(U - U_{\text{scr}})}{2}. \tag{B6}$$

Note that the $U - U_{\text{scr}} = U - \text{Re}\mathcal{U}(i\nu = 0)$ parameter is determined by the self-consistency equation [see Eq. (6)]. Now we can apply the standard maximum entropy algorithm [33] to solve Eqs. (B2), (B3), (B5), and (B6) to obtain the solutions $\tilde{\mathcal{U}}(\nu)$ and $\text{Im}\mathcal{U}(\nu)$.

Once we have determined $\text{Im}\mathcal{U}(\nu)$, the following equation can be used to verify its correctness [27,34]:

$$\mathcal{U}(\tau) = \int_0^\infty \frac{d\nu}{\pi} \text{Im}\mathcal{U}(\nu) B(\nu, \tau), \tag{B7}$$

with $B(\nu, \tau) = \cosh[(\tau - \frac{\beta}{2})\nu] / \sinh[\frac{\nu\beta}{2}]$ for $0 \leq \tau \leq \beta$. Additionally, with $\text{Im}\mathcal{U}(\nu)$, the corresponding real part of the retarded interaction $\text{Re}\mathcal{U}(\nu)$ can be easily calculated via the Kramers-Kronig relation

$$\text{Re}\mathcal{U}(\nu) = \frac{1}{\pi} \mathcal{P} \int_{-\infty}^\infty \frac{\text{Im}\mathcal{U}(\nu')}{\nu' - \nu} d\nu', \tag{B8}$$

where \mathcal{P} denotes the Cauchy principal value.

In summary, the procedure to apply the maximum entropy method for the analytical continuation of the retarded interaction $\mathcal{U}(i\nu)$ is as follows.

(i) Calculate $\mathcal{U}(\tau)$ from $\mathcal{U}(i\nu)$ by using the inverse Fourier transformation:

$$\mathcal{U}(\tau) = \frac{1}{\beta} \sum_{n=-\infty}^\infty e^{-i\nu_n\tau} \mathcal{U}(i\nu_n). \tag{B9}$$

(ii) Use the classic maximum entropy algorithm [33] to solve Eq. (B5). The normalization condition is Eq. (B2). In general, we have to specify the default model in the maximum entropy algorithm. According to our experience, the flat default model is sufficient.

(iii) With $\tilde{\mathcal{U}}(\nu)$, the $\text{Im}\mathcal{U}(\nu)$ can be determined by using Eq. (B3).

(iv) Apply Eq. (B7) to check the correctness of the spectral function $\text{Im}\mathcal{U}(\nu)$ if need.

(v) Apply Kramers-Kronig relation Eq. (B8) to evaluate $\text{Re}\mathcal{U}(\nu)$ if necessary.

Next, we will benchmark this modified maximum entropy method. At first, we will generate some exact spectra with a Gaussian distribution. Starting from an initial $\text{Im}\mathcal{U}(\nu)$, we calculate $\mathcal{U}(\tau)$ via Eq. (B7). Then, applying the maximum entropy method as introduced above to it, we can obtain a new estimate for $\text{Im}\mathcal{U}(\nu)$. At last, we should verify whether the new spectrum coincides with the exact one. Figure 15 shows some representative results. It is apparent that the extended

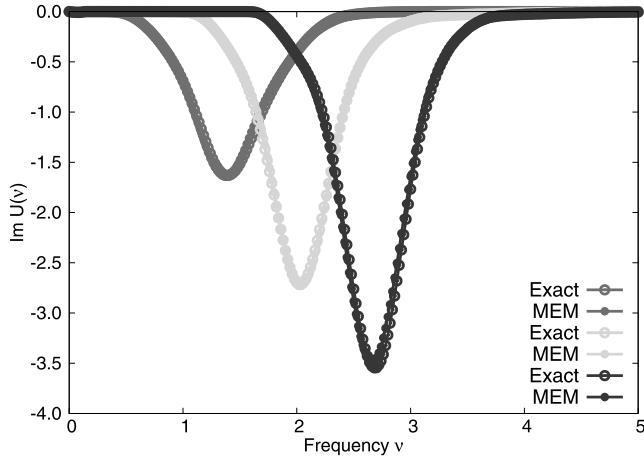


FIG. 15. (Color online) Benchmarks for the maximum entropy method for retarded interaction $\mathcal{U}(i\nu)$. The exact spectra for $\text{Im}\mathcal{U}(\nu)/\nu$ are generated using classic Gaussian model. They are converted into $\mathcal{U}(\tau)$, and then processed by the proposed maximum entropy method. In the simulations, we assume $\beta = 100$ and $U - U_{\text{scr}} = 2.0/\pi$.

maximum entropy method works well, and allows to reproduce the initial spectra accurately.

Finally, we will test the robustness of this maximum entropy method, i.e., benchmark its stability and ability to deal with the numerical noise contained in realistic $\mathcal{U}(i\nu)$ data. Let's start from an exact spectrum again. Here we consider a more complicated two-hump spectrum. We first convert it to $\mathcal{U}(\tau)$ and then calculate $\mathcal{U}(i\nu)$ by the Fourier transformation

$$\mathcal{U}(i\nu_n) = \int_0^\beta d\tau e^{i\nu_n\tau} \mathcal{U}(\tau). \quad (\text{B10})$$

Next, we use the following algorithm to introduce some random noise to the real part of $\mathcal{U}(i\nu)$. The strength of the numerical noise is controlled by a δ parameter:

$$\mathcal{U}(i\nu) \rightarrow \begin{cases} \mathcal{U}(i\nu) + \xi_1\delta/2, & \xi_2 < 0.5, \\ \mathcal{U}(i\nu) - \xi_1\delta/2, & \xi_2 \geq 0.5, \end{cases} \quad (\text{B11})$$

where ξ_1 and ξ_2 are two random numbers in the interval $[0,1]$. Then we transform it back to $\mathcal{U}(\tau)$ again using Eq. (B9), and apply the maximum entropy method to obtain the spectral

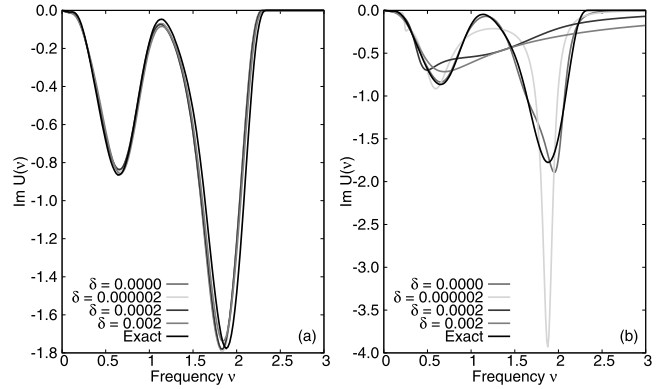


FIG. 16. (Color online) Benchmarks for the maximum entropy method and Padé approximation against numerical noise. (a) Results obtained by maximum entropy method. (b) Results obtained by Padé approximation. In the calculations, we set $\beta = 100$ and $\alpha = 1.288$. The δ parameter is used to control the strength of data noise. Please see the text for the details.

function $\text{Im}\mathcal{U}(\nu)$. Through this benchmark, we can assess the influence of numerical noise on the maximum entropy method. The benchmark results are shown in Fig. 16(a). In principle, the Padé approximation can also be used to extract $\text{Im}\mathcal{U}(\nu)$ from $\mathcal{U}(i\nu)$ directly [42]. The results from the Padé analytical continuation are shown in Fig. 16(b), to enable a direct comparison. We see that when δ is small, the two-hump structure can be roughly reproduced by the Padé approximation. But when δ is large, the Padé approximation fails: it gives a wrong single-peak spectrum with a very broad tail. On the other hand, it seems that the maximum entropy method is not sensitive to this level of numerical noise. The maximum entropy spectra agree well with the exact spectra, irrespective of the details of the numerical noise. For this reason, we believe that the maximum entropy method is superior to the Padé approximation for the analytical continuation of the retarded interaction computed within EDMFT or $GW + \text{EDMFT}$ schemes.

In this appendix, we have focused on the analytical continuation of the retarded interaction $\mathcal{U}(i\nu)$. However, the method is general and can be applied to the analytical continuation of the fully screened interaction $W(i\nu)$ as well. We merely need to replace \mathcal{U} with W in the above equations.

-
- [1] M. Imada, A. Fujimori, and Y. Tokura, *Rev. Mod. Phys.* **70**, 1039 (1998).
- [2] A. Georges, G. Kotliar, W. Krauth, and M. J. Rozenberg, *Rev. Mod. Phys.* **68**, 13 (1996).
- [3] G. Kotliar, S. Y. Savrasov, K. Haule, V. S. Oudovenko, O. Parcollet, and C. A. Marianetti, *Rev. Mod. Phys.* **78**, 865 (2006).
- [4] P. A. Lee, N. Nagaosa, and X.-G. Wen, *Rev. Mod. Phys.* **78**, 17 (2006).
- [5] A. Amaricci, A. Camjayi, K. Haule, G. Kotliar, D. Tanasković, and V. Dobrosavljević, *Phys. Rev. B* **82**, 155102 (2010).
- [6] S. Biermann, F. Aryasetiawan, and A. Georges, *Phys. Rev. Lett.* **90**, 086402 (2003).
- [7] P. Sun and G. Kotliar, *Phys. Rev. B* **66**, 085120 (2002).
- [8] K.-S. Chen, Z. Y. Meng, S.-X. Yang, T. Pruschke, J. Moreno, and M. Jarrell, *Phys. Rev. B* **88**, 245110 (2013).
- [9] W.-M. Huang, C.-Y. Lai, C. Shi, and S.-W. Tsai, *Phys. Rev. B* **88**, 054504 (2013).
- [10] K.-S. Chen, Z. Y. Meng, T. Pruschke, J. Moreno, and M. Jarrell, *Phys. Rev. B* **86**, 165136 (2012).
- [11] C. Husemann and W. Metzner, *Phys. Rev. B* **86**, 085113 (2012).

- [12] G. Sordi, K. Haule, and A.-M. S. Tremblay, *Phys. Rev. B* **84**, 075161 (2011).
- [13] S. Raghu, E. Berg, A. V. Chubukov, and S. A. Kivelson, *Phys. Rev. B* **85**, 024516 (2012).
- [14] T. Ayrál, P. Werner, and S. Biermann, *Phys. Rev. Lett.* **109**, 226401 (2012).
- [15] T. Ayrál, S. Biermann, and P. Werner, *Phys. Rev. B* **87**, 125149 (2013).
- [16] A. M. Sengupta and A. Georges, *Phys. Rev. B* **52**, 10295 (1995).
- [17] Q. Si and J. L. Smith, *Phys. Rev. Lett.* **77**, 3391 (1996).
- [18] O. Parcollet and A. Georges, *Phys. Rev. B* **59**, 5341 (1999).
- [19] R. Chitra and G. Kotliar, *Phys. Rev. B* **63**, 115110 (2001).
- [20] R. Chitra and G. Kotliar, *Phys. Rev. Lett.* **84**, 3678 (2000).
- [21] J. L. Smith and Q. Si, *Phys. Rev. B* **61**, 5184 (2000).
- [22] P. Sun and G. Kotliar, *Phys. Rev. Lett.* **92**, 196402 (2004).
- [23] M. Schüler, M. Rösner, T. O. Wehling, A. I. Lichtenstein, and M. I. Katsnelson, *Phys. Rev. Lett.* **111**, 036601 (2013).
- [24] Y. Motome and G. Kotliar, *Phys. Rev. B* **62**, 12800 (2000).
- [25] P. Werner and A. J. Millis, *Phys. Rev. Lett.* **99**, 146404 (2007).
- [26] P. Werner, A. Comanac, L. de' Medici, M. Troyer, and A. J. Millis, *Phys. Rev. Lett.* **97**, 076405 (2006).
- [27] P. Werner and A. J. Millis, *Phys. Rev. Lett.* **104**, 146401 (2010).
- [28] E. Gull, A. J. Millis, A. I. Lichtenstein, A. N. Rubtsov, M. Troyer, and P. Werner, *Rev. Mod. Phys.* **83**, 349 (2011).
- [29] P. Hansmann, L. Vaugier, H. Jiang, and S. Biermann, *J. Phys.: Cond. Matter* **25**, 094005 (2013).
- [30] P. Hansmann, T. Ayrál, L. Vaugier, P. Werner, and S. Biermann, *Phys. Rev. Lett.* **110**, 166401 (2013).
- [31] M. Casula, A. Rubtsov, and S. Biermann, *Phys. Rev. B* **85**, 035115 (2012).
- [32] P. Werner, M. Casula, T. Miyake, F. Aryasetiawan, A. J. Millis, and S. Biermann, *Nat. Phys.* **8**, 331 (2012).
- [33] M. Jarrell and J. Gubernatis, *Phys. Rep.* **269**, 133 (1996).
- [34] M. Casula, P. Werner, L. Vaugier, F. Aryasetiawan, T. Miyake, A. J. Millis, and S. Biermann, *Phys. Rev. Lett.* **109**, 126408 (2012).
- [35] P. Werner, E. Gull, O. Parcollet, and A. J. Millis, *Phys. Rev. B* **80**, 045120 (2009).
- [36] E. Gull, O. Parcollet, P. Werner, and A. J. Millis, *Phys. Rev. B* **80**, 245102 (2009).
- [37] B. Kyung, G. Kotliar, and A.-M. S. Tremblay, *Phys. Rev. B* **73**, 205106 (2006).
- [38] T. Maier, M. Jarrell, T. Pruschke, and M. H. Hettler, *Rev. Mod. Phys.* **77**, 1027 (2005).
- [39] Y. Nomura, M. Kaltak, K. Nakamura, C. Taranto, S. Sakai, A. Toschi, R. Arita, K. Held, G. Kresse, and M. Imada, *Phys. Rev. B* **86**, 085117 (2012).
- [40] T. O. Wehling, E. Şaşıoğlu, C. Friedrich, A. I. Lichtenstein, M. I. Katsnelson, and S. Blügel, *Phys. Rev. Lett.* **106**, 236805 (2011).
- [41] B. Bauer, L. D. Carr, H. G. Evertz, A. Feiguin, J. Freire, S. Fuchs, L. Gamper, J. Gukelberger, E. Gull, S. Guertler, A. Hehn, R. Igarashi, S. V. Isakov, D. Koop, P. N. Ma, P. Mates, H. Matsuo, O. Parcollet, G. Pawłowski, J. D. Picon, L. Pollet, E. Santos, V. W. Scarola, U. Schollwöck, C. Silva, B. Surer, S. Todo, S. Trebst, M. Troyer, M. L. Wall, P. Werner, and S. Wessel, *J. Stat. Mech.: Theory Exp.* (2011) P05001.
- [42] H. Vidberg and J. Serene, *J. Low Temp. Phys.* **29**, 179 (1977).

P

Adatoms on semiconducting surfaces

P.1 Paper 4: Hansmann *et al.* (2013a)

Long-Range Coulomb Interactions in Surface Systems: A First-Principles Description within Self-Consistently Combined *GW* and Dynamical Mean-Field Theory

P. Hansmann,¹ T. Ayrál,^{1,2} L. Vaugier,¹ P. Werner,³ and S. Biermann^{1,4}

¹*Centre de Physique Théorique, Ecole Polytechnique, CNRS UMR7644, 91128 Palaiseau, France*

²*Institut de Physique Théorique (IPhT), CEA, CNRS, URA 2306, 91191 Gif-sur-Yvette, France*

³*Department of Physics, University of Fribourg, 1700 Fribourg, Switzerland*

⁴*Japan Science and Technology Agency, CREST, Kawaguchi 332-0012, Japan*

(Received 17 January 2013; published 16 April 2013)

Systems of adatoms on semiconductor surfaces display competing ground states and exotic spectral properties typical of two-dimensional correlated electron materials which are dominated by a complex interplay of spin and charge degrees of freedom. We report a fully *ab initio* derivation of low-energy Hamiltonians for the adatom systems Si(111):*X*, with *X* = Sn, Si, C, Pb, that we solve within self-consistently combined *GW* and dynamical mean-field theory. Calculated photoemission spectra are in agreement with available experimental data. We rationalize experimentally observed trends from Mott physics toward charge ordering along the series as resulting from substantial long-range interactions.

DOI: 10.1103/PhysRevLett.110.166401

PACS numbers: 71.15.-m, 71.10.Fd, 71.30.+h, 73.20.At

Understanding the electronic properties of materials with strong electronic Coulomb correlations remains one of the biggest challenges of modern condensed matter physics. The interplay of delocalization and interactions is not only at the origin of exotic ground states, but also determines the excitation spectra of correlated materials. The “standard model” of correlated fermions, the Hubbard model, in principle captures these phenomena. Yet relating the model to the material on a microscopic footing remains a challenge. Even more importantly, the approximation of purely local Coulomb interactions can become severe in realistic materials, where long-range interactions and charge fluctuation physics cannot be neglected.

Systems of adatoms on semiconducting surfaces, such as Si(111):*X* with *X* = Sn, C, Si, Pb, have been suggested [1] to be good candidates for observing low-dimensional correlated physics. Commonly considered to be realizations of the one-band Hubbard model and toy systems for investigating many-body physics on the triangular lattice, such surfaces have been explored both experimentally [2–18] and theoretically [19–31]. These so-called α phases show a remarkable variety of interesting physics including commensurate charge density wave states [5,6,9] and isostructural metal to insulator transitions [14]. However, while specific systems and/or phenomena have been investigated also theoretically, a comprehensive understanding including materials trends is still lacking. A central goal of our work is to present a unified picture that relates, within a single framework, different materials (adatom systems), placing them in a common phase diagram.

We derive low-energy effective Hamiltonians *ab initio* from a combined density functional and constrained random phase approximation (cRPA) scheme [32] in the implementation of Ref. [33] (see also the extension to surface systems in Ref. [34]). While the first surprise is

the relatively large value of the on-site interactions, which we find to be of the order of the bandwidth (≈ 1 eV), most importantly we show that nonlocal interactions are large (nearest-neighbor interaction of ≈ 0.5 eV) and, hence, an essential part of the resulting many-body Hamiltonians. This result confirms previous speculations about the importance of nonlocal effects in these materials [21,29]. We solve these low-energy Hamiltonians within fully self-consistent combined *GW* and dynamical mean-field theory (*GW* + DMFT) [35], calculating in particular (single-particle) angular resolved photoemission spectra and the (two-particle) charge susceptibility. We identify a clear-cut materials trend starting from Si(111):C deep in a Mott phase to Si(111):Pb which shows tendencies toward metallicity and charge-ordered states driven by nonlocal interactions. Comparing our results to available experimental data yields encouraging insights: *Without adjustable parameters* we reproduce the experimentally measured gap size of insulating Si(111):Sn and its transition to a “bad insulator” at elevated temperatures. Moreover, based on the charge susceptibility, we identify the *electronic* tendency of Si(111):Pb toward charge ordering of the so-called 3×3 symmetry, which is indeed seen experimentally by scanning tunneling microscopy. Our work is the first one that addresses the electronic properties of real materials on the basis of fully self-consistent *GW* + DMFT calculations [36] (for a non-self-consistent calculation, see Ref. [37]; for self-consistent calculations for models, see Refs. [38–40]) [41].

The single-particle part of the Hamiltonian is calculated in the local density approximation of density functional theory. In Fig. 1, we present local density approximation band structures for the series Si(111):{C, Si, Sn, Pb}. For all considered systems, the surface state in the semiconducting gap is indeed responsible for a *well-separated*,

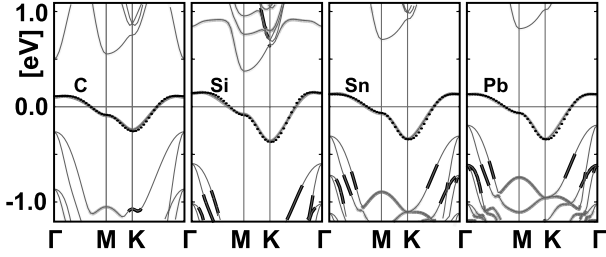


FIG. 1 (color online). Band structures of the $\alpha\text{-}\sqrt{3} \times \sqrt{3}$ phases of Si(111):X with $X = \text{Sn, Si, C, Pb}$ [53]. In red (gray) we plot the contributions stemming from the p_z orbital of the adatom, while the blue (dark gray) color denotes $p_{x,y}$ -like (i.e., planar) character. Even though the actual molecular orbital composition might be complicated, the half-filled surface band has a clear-cut “apical” (i.e., carrotlike) character. The black dots represent the tight binding relation Eq. (1) with hopping parameters from Table I. The quality of the fit supports the picture of Wannier-like orbitals with a fast decaying real space overlap on neighboring sites.

single band around the Fermi energy. The tight-binding dispersion of the half-filled surface band can be well fitted by using up to third-nearest-neighbor hopping (with t , t' , and t'' from Table I):

$$\begin{aligned} \varepsilon_{\mathbf{k}} = & 2t[\cos(k_x) + 2 \cos(k_x/2) \cos(\sqrt{3}/2k_y)] \\ & + 2t'[\cos(\sqrt{3}k_y) + 2 \cos(3k_x/2) \cos(\sqrt{3}/2k_y)] \\ & + 2t''[\cos(2k_x) + 2 \cos(k_x) \cos(\sqrt{3}k_y)]. \end{aligned} \quad (1)$$

In order to determine the interaction parameters as partially screened matrix elements of the Coulomb interaction within the cRPA, we chose an energy window around the Fermi energy encompassing the surface band. The bare interaction parameters are calculated by means of explicit evaluation of the radial (Slater) integrals of the Wannier functions. The local and nonlocal Hubbard interaction parameters are obtained as the corresponding matrix elements of the partially screened interaction within the cRPA [34]. The cRPA scheme provides us with the full frequency dependence of the interactions. Up to the energy scale of the plasma frequency of silicon, however, this frequency dependence is small and will be neglected in the following. The resulting static effective interactions are summarized in Table I.

The bare on-site interaction parameters (V_0) vary between 6.0 eV for Si(111):C and 4.3 eV for Si(111):Pb, decreasing monotonically within the series. The on-site U_0 is reduced roughly by a factor of 4–5 due to cRPA screening. At first glance the on-site U_0 of the order of 1 eV—about twice the size of the bandwidth—strongly points toward Mott physics. This is, however, a premature conclusion due to the effect of *nonlocal* interactions. The first nonlocal contribution (nearest-neighbor interaction) U_1 (bare V_1) is 0.5 eV (2.8 eV). Remarkably, the value is—in contrast to U_0 (V_0)—almost the same for all materials.

TABLE I. Values of the bare (effective) on-site V_0 (U_0) and intersite V_1 (U_1) interactions. Also reported are the values of the static component of the effective $\mathcal{U}(\omega = 0)$ calculated from GW + DMFT; see the text.

| | C | Si | Sn | Pb |
|---|-----------|-----------|-----------|----------------------------|
| t (meV) | 38.0 | 50.0 | 42.0 | 42.0 |
| $-t'$ (meV) | 15.0 | 23.0 | 20.0 | 20.0 |
| t'' (meV) | 0.5 | 5.0 | 10.0 | 10.0 |
| U_0 (eV) | 1.4 | 1.1 | 1.0 | 0.9 |
| U_1 (eV) | 0.5 | 0.5 | 0.5 | 0.5 |
| U_n | U_1/r_a | U_1/r_a | U_1/r_a | U_1/r_a |
| V_0 (eV) | 6.0 | 4.7 | 4.4 | 4.3 |
| V_1 (eV) | 2.8 | 2.8 | 2.7 | 2.8 |
| $V_1/\varepsilon_{\text{Si surf.}}^{\text{stat.}}$ (eV) | 0.47 | 0.47 | 0.45 | 0.47 |
| $\mathcal{U}(\omega = 0)$ (eV) | 1.3 | 0.94 | 0.84 | 0.67 (ins.) 0.54 (met.) |

The reason is that the intersite overlap of the orbitals is so small that the Coulomb energy corresponds to the electrostatic energy of two point charges. With the virial theorem $\langle E^{\text{tot.}} \rangle = 1/2\langle V \rangle$, we quantify this argument by a rescaled hydrogen problem with effective Bohr radius of 12 a.u. (\approx distance of adatom sites),

$$\left\langle \frac{e^2}{r_{\text{rel}}} \right\rangle = \frac{1}{12} |V_{\text{pot}}^{\text{H-atom}}| = \frac{1}{12} 2 |E_{\text{groundstate}}^{\text{H-atom}}| = 2.3 \text{ eV}, \quad (2)$$

which roughly matches the value of our bare intersite interaction parameters. The second, likewise remarkable, observation is that the screened values U_1 are extremely close to the value we get by assuming a static continuum approximation on the surface of a dielectric medium: $V_1/\varepsilon_{\text{Si}}^{\text{surf.}}$, where $\varepsilon_{\text{Si}}^{\text{surf.}} = \frac{1}{2}(\varepsilon_{\text{Si}} + 1)$ is the static dielectric constant of silicon on the surface. The reason is straightforward: The adatom distance (6 Å) is already large enough compared to the atomic structure of the silicon substrate (≈ 2 Å) so that *local field effects* (included in the cRPA) are negligible. Following this reasoning, we can calculate longer-range interaction terms by simply scaling U_1 with a/r , i.e., with the inverse distance in units of the nearest-neighbor distance a , i.e., $U_2 = U_1/\sqrt{3}$ and so on. In this respect, U_1 is not only the nearest-neighbor interaction, but the parameter that quantifies the strength of nonlocal interactions. The many-body Hamiltonian resulting from our *parameter-free* downfolding procedure thus reads

$$H = \sum_{\mathbf{k}, \sigma} \varepsilon_{\mathbf{k}} c_{\mathbf{k}, \sigma}^\dagger c_{\mathbf{k}, \sigma} + \sum_i U_0 n_{i, \uparrow} n_{i, \downarrow} + \sum_{i \neq j} U_{|i-j|} n_i n_j, \quad (3)$$

where $\varepsilon_{\mathbf{k}}$ is the dispersion relation (1), $c_{\mathbf{k}, \sigma}^\dagger$ ($c_{\mathbf{k}, \sigma}$) are fermionic creation (annihilation) operators, $n_{i, \sigma}$ is the number operator counting electrons in the p_z -like Wannier orbital centered at adatom i , and $n_i = n_{i, \uparrow} + n_{i, \downarrow}$.

To solve this Hamiltonian, we implement the combined GW + DMFT scheme [35,44] and calculate spectral

properties and charge-charge response functions. Fully self-consistent $GW + DMFT$ was applied to the extended Hubbard model in the seminal work by Sun and Kotliar [38,45], but only recently have numerical techniques for the solution of dynamical impurity models [47–49] been sufficiently advanced to extract real-frequency information from such calculations [39,40]. We employ the techniques of the latter two works (in particular, a continuous-time quantum Monte Carlo impurity solver based on the hybridization expansion [47]) but implement them for the realistic Hamiltonian derived above. Moreover, we go beyond the “standard” extended Hubbard model and do not restrict the range of the nonlocal interaction terms. Rather, we include the entire $1/r$ tail by means of an Ewald-type lattice sum. In Fig. 2, we show momentum-resolved spectral functions from $GW + DMFT$ for all compounds in our series: As expected from the large on-site interactions compared to the bandwidth, we obtain insulating spectra for all four compounds. Interestingly, however, for the Pb compound, in contrast to the other three systems, we find, depending on the initialization, two stable solutions at the temperature of our study ($T = 116$ K)—one metallic and one insulating. This indicates that we are in a coexistence region of a first-order phase transition similar to that seen in the extended Hubbard model [40].

In all compounds, the upper and lower Hubbard bands show a substantial dispersion following the bare band structure, as would be expected from an atomic limit estimate. The insulating gap decreases within the series, and we can estimate from the center of mass of the

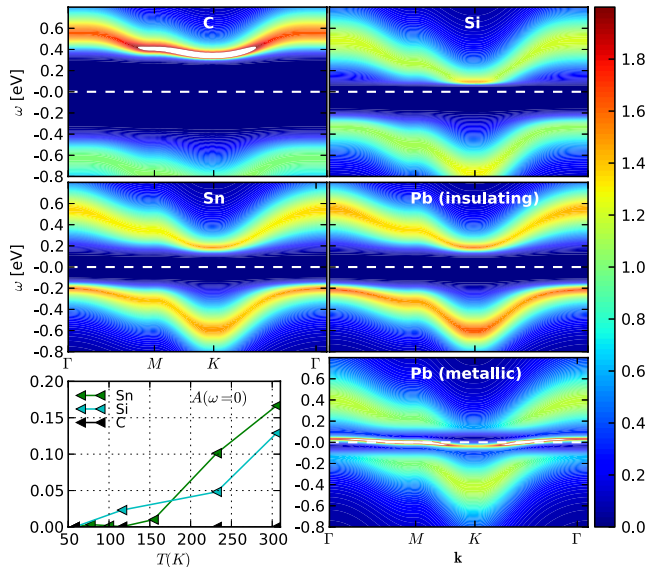


FIG. 2 (color online). Momentum-resolved spectral function at $T = 116$ K of $\text{Si}(111):X$ with $X = \text{Sn}, \text{Si}, \text{C}, \text{Pb}$ obtained by analytical continuation of $GW + DMFT$ imaginary-time data. The Fermi energy is set to $\varepsilon_F = 0$ and indicated by the white dashed line. On the bottom left, we show the spectral weight at the Fermi energy as a function of temperature.

Hubbard band values of 1.3 (C), 0.8 (Si), 0.7 (Sn), and 0.5 eV (Pb). However, specifically for the $\text{Si}(111):\{\text{Sn}, \text{Pb}\}$ we find substantial spectral weight already at ≥ -0.2 eV. Given this small gap, a sizable temperature dependence can be expected. We have extracted the value of the local (i.e., \mathbf{k} -integrated) spectral function at the Fermi level [50] (see Fig. 2, bottom left panel). While for $\text{Si}(111):\text{C}$ the spectral weight transfer to the Fermi energy with temperature is negligible as expected from the larger gap, specifically $\text{Si}(111):\text{Si}$ and most of all $\text{Si}(111):\text{Sn}$ display a significant transfer of spectral weight on a temperature scale from 50 K to room temperature 300 K.

Photoemission experiments for $\text{Si}(111):\text{Sn}$ [10,18] (and, possibly Ref. [51], for $\text{Si}(111):\text{Pb}$ [11]) observe, indeed, such a temperature dependence and agree well with our findings, both concerning the gap size and temperature scale. Our results—obtained *without any adjustable parameters*—also provide theoretical predictions for more extensive studies on $\text{Si}(111):\text{Pb}$ and the (experimentally so far not studied) $\text{Si}(111):\text{C}$ compound. Next, we analyze the spectral functions in view of the interaction strengths calculated by cRPA (see Table I). The gap sizes no longer reflect the energy scale of the on-site interaction U_0 but are reduced due to nonlocal interactions which *screen* the local interaction by nonlocal charge fluctuations. This physics is naturally present in the $GW + DMFT$ scheme, where nonlocal effects are incorporated into an effective retarded on-site interaction $\mathcal{U}(\omega)$ (plotted in the left panel of Fig. 3). The dynamical character of this quantity results from downfolding of nonlocal degrees of freedom and is not to be confused with the frequency dependence of effective interactions within cRPA [32] (neglected here—see above). The latter results from downfolding higher energy (orbital) degrees of freedom. The shape of the $GW + DMFT$ $\mathcal{U}(\omega)$ is reminiscent of the latter, but the energy scales are drastically reduced.

At large frequencies, screening is not efficient and, hence, $\mathcal{U}(\omega = \infty) = U_0$. On the other hand, the static value $\mathcal{U}(\omega = 0)$ can be significantly reduced [up to nearly a factor of 2 for $\text{Si}(111):\text{Pb}$]. The latter sets the energy scale for the gaps we observe in the spectral function. The

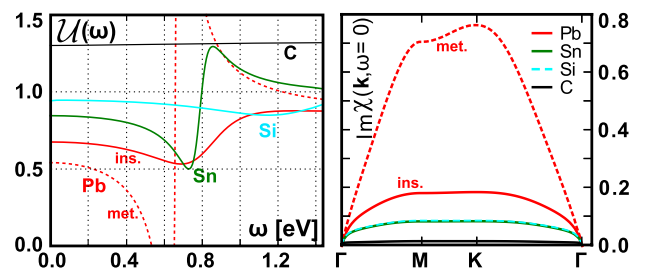


FIG. 3 (color online). Left: frequency-dependent $\mathcal{U}(\omega)$ (calculated from $GW + DMFT$) including both insulating and metallic cases for the Pb system. Right: imaginary part of the charge-charge susceptibility along the usual path in the Brillouin zone.

transition between unscreened high-frequency behavior and the static value takes place at an energy scale ω_0 characteristic of charge fluctuations driven by nonlocal interactions. The strikingly different behavior of the dynamical effective interactions $\mathcal{U}(\omega)$ reflects the observed materials trend: Si(111):C [Si(111):Si] is [nearly] unaffected by nonlocal interaction terms, and there is barely any screening. The remaining two compounds show, however, large effects. The static values $\mathcal{U}(\omega = 0)$ are reduced compared to the on-site interaction to 0.84 eV for Si(111):Sn and to 0.67 eV (0.54 eV) for the insulating (metallic) solution for Si(111):Pb, which leads to the reduced gap sizes. Moreover, resonances at energies between 0.6 and 0.8 eV stress the importance of nonlocal interactions and charge fluctuations for these systems.

Besides leading to a retarded, frequency-dependent interaction, the nonlocal charge fluctuations signal tendencies toward a charge-ordered state. Analyzing the momentum dependence of the imaginary part of the charge-charge response function $\text{Im}\chi(\mathbf{k}, \omega = 0)$ for the high-symmetry points of the Brillouin zone, shown in Fig. 3, we find for the different materials a very characteristic behavior. The local double occupancy, which corresponds to the integral of the plotted quantity over all momenta, becomes larger toward the end of the series. Most interesting is the case of metallic Si(111):Pb for which we find a distinct structure within the Brillouin zone: The maximum of $\text{Im}\chi(\mathbf{k}, \omega = 0)$ at the K symmetry point indicates strong charge fluctuations of the so-called 3×3 symmetry, sketched in Fig. 4. This order might eventually be frozen in to form a charge-ordered ground state which is actually seen in scanning tunneling microscopy for this material [8]. An insulating charge-ordered ground state of 3×3 symmetry is, in fact, also found in Ge(111):Sn [52], where a concomitant structural distortion (vertical displacement of adatoms) of the same symmetry is seen. Our results show that the instability in the correlated electronic response function may play a key role in this physics.

We can summarize our results by drawing a schematic phase diagram as a function of the strength of local and nonlocal interactions (represented by the value of U_1); see Fig. 4. For zero nonlocal interactions, our phase diagram describes the Mott-Hubbard metal to insulator transition. The adatom systems are placed at about 0.5 eV of nonlocal interaction strength. However, due to the difference in the on-site term U_0 their respective position in the phase diagram and, hence, their ground state character are different: Si(111):C is deep in the Mott phase with a charge localization with one electron per adatom site. The Si(111):Si compound [53] is also of Mott type with only small values for the double occupancy and little effect of charge fluctuations. However, Si(111):Sn and, most dramatic, Si(111):Pb (which is actually already in a coexistence region) are much closer to a phase boundary to a metallic phase. Even more peculiar is the obvious tendency

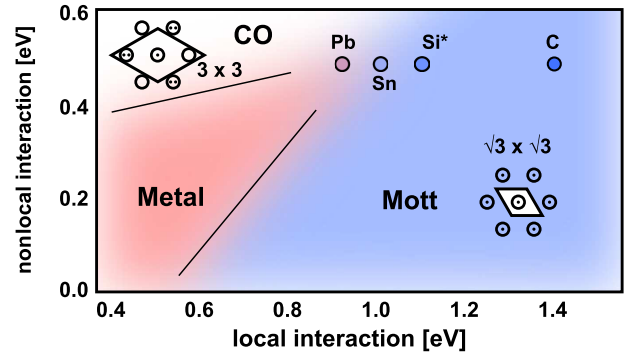


FIG. 4 (color online). Schematic local-nonlocal interaction phase diagram: The black-bordered circles mark the positions of the adatom systems of our study. Straight lines are guides to the eyes, and blurry color indicates coexistence regions. Within the localized (i.e., insulating) phases CO and Mott, small sketches indicate the shape of the surface unit cell.

of Si(111):Pb toward a charge-ordered phase of 3×3 symmetry indicated by the white region in our phase diagram.

In conclusion, we have set up a fully self-consistent $GW + \text{DMFT}$ scheme for the realistic treatment of correlated surface systems to address the electronic properties of the α phases of adatoms on the Si(111) surface. We have reported on the *ab initio* construction of the materials-specific low-energy Hamiltonians and, most importantly, on the respective interaction parameters including the long-range Coulomb tail. From these, it becomes clear that for the adatom systems, taking into account nonlocal interaction effects is mandatory. We have solved the derived many-body Hamiltonians and discussed our findings for momentum-resolved spectral functions, to be compared to angular resolved photoemission spectra. Without adjustable parameters we have reproduced experimental findings or, in cases where experiments are missing, made predictions. Specifically, the angular resolved photoemission spectra for the series, as well as the charge order instabilities in the case of Si(111):Pb, are key conclusions which can provide guidance for further experimental and theoretical studies of semiconductor adatom structures.

We acknowledge useful discussions with the authors of Refs. [17,18], as well as with M. Capone, M. Casula, H. Hafermann, H. Jiang, M. Katsnelson, O. Parcollet, and E. Tosatti. This work was supported by the French ANR under project SURMOTT and IDRIS/GENCI under Project No. 129313.

-
- [1] E. Tosatti and P. W. Anderson, Jpn. J. Appl. Phys. **2S2**, 381 (1974).
 - [2] R.I.G. Uhrberg, G.V. Hansson, J.M. Nicholls, P.E. S. Persson, and S.A. Flodström, Phys. Rev. B **31**, 3805 (1985).

- [3] T.M. Grehk, L.S.O. Johansson, U.O. Karlsson, and A.S. Flödstrom, *Phys. Rev. B* **47**, 13887 (1993).
- [4] H.H. Weitering, J. Chen, N.J. DiNardo, and E.W. Plummer, *Phys. Rev. B* **48**, 8119 (1993).
- [5] J.M. Carpinelli, H.H. Weitering, E.W. Plummer, and R. Stumpf, *Nature (London)* **381**, 398 (1996).
- [6] J.M. Carpinelli, H.H. Weitering, M. Bartkowiak, R. Stumpf, and E.W. Plummer, *Phys. Rev. Lett.* **79**, 2859 (1997).
- [7] H.H. Weitering, X. Shi, P.D. Johnson, J. Chen, N.J. DiNardo, and K. Kempa, *Phys. Rev. Lett.* **78**, 1331 (1997).
- [8] J. Slezák, P. Mutombo, and V. Cháb, *Phys. Rev. B* **60**, 13328 (1999).
- [9] G.L. Lay, M.G. Rad, M. Gthelid, U. Karlsson, J. Avila, and M. Asensio, *Appl. Surf. Sci.* **175–176**, 201 (2001).
- [10] J. Lobo, A. Tejada, A. Mugarza, and E.G. Michel, *Phys. Rev. B* **68**, 235332 (2003).
- [11] V. Dudr, N. Tsud, S. Fabík, B. Ressel, M. Vondráček, K.C. Prince, V. Matolín, and V. Cháb, *Surf. Sci.* **566–568**, 804 (2004).
- [12] C.A. Pignedoli, A. Catellani, P. Castrucci, A. Sgarlata, M. Scarselli, M. De Crescenzi, and C.M. Bertoni, *Phys. Rev. B* **69**, 113313 (2004).
- [13] M.H. Upton, T. Miller, and T.-C. Chiang, *Phys. Rev. B* **71**, 033403 (2005).
- [14] S. Modesti, L. Petaccia, G. Ceballos, I. Vobornik, G. Panaccione, G. Rossi, L. Ottaviano, R. Larciprete, S. Lizzit, and A. Goldoni, *Phys. Rev. Lett.* **98**, 126401 (2007).
- [15] L.A. Cardenas, Y. Fagot-Revurat, L. Moreau, B. Kierren, and D. Malterre, *Phys. Rev. Lett.* **103**, 046804 (2009).
- [16] T. Zhang, P. Cheng, W.-J. Li, Y.-J. Sun, G. Wang, X.-G. Zhu, K. He, L. Wang, X. Ma, X. Chen, Y. Wang, Y. Liu, H.-Q. Lin, J.-F. Jia, and Q.-K. Xue, *Nat. Phys.* **6**, 104 (2010).
- [17] C. Tournier-Colletta, L. Cardenas, Y. Fagot-Revurat, A. Tejada, B. Kierren, and D. Malterre, *Phys. Rev. B* **84**, 155443 (2011).
- [18] G. Li, P. Höpfner, J. Schäfer, C. Blumenstein, S. Meyer, A. Bostwick, E. Rotenberg, R. Claessen, and W. Hanke, *Nat. Commun.* **4**, 1620 (2013).
- [19] E. Kaxiras, K.C. Pandey, F.J. Himpsel, and R.M. Tromp, *Phys. Rev. B* **41**, 1262 (1990).
- [20] K.D. Brommer, M. Needels, B.E. Larson, and J.D. Joannopoulos, *Phys. Rev. Lett.* **68**, 1355 (1992).
- [21] G. Santoro, S. Scandolo, and E. Tosatti, *Phys. Rev. B* **59**, 1891 (1999).
- [22] C.S. Hellberg and S.C. Erwin, *Phys. Rev. Lett.* **83**, 1003 (1999).
- [23] H. Aizawa, M. Tsukada, N. Sato, and S. Hasegawa, *Surf. Sci.* **429**, L509 (1999).
- [24] G. Profeta, A. Continenza, L. Ottaviano, W. Mannstadt, and A.J. Freeman, *Phys. Rev. B* **62**, 1556 (2000).
- [25] H.Q. Shi, M.W. Radny, and P.V. Smith, *Phys. Rev. B* **66**, 085329 (2002).
- [26] H.Q. Shi, M.W. Radny, and P.V. Smith, *Phys. Rev. B* **70**, 235325 (2004).
- [27] G. Profeta and E. Tosatti, *Phys. Rev. Lett.* **95**, 206801 (2005).
- [28] G. Profeta and E. Tosatti, *Phys. Rev. Lett.* **98**, 086401 (2007).
- [29] S. Schuwalow, D. Grieger, and F. Lechermann, *Phys. Rev. B* **82**, 035116 (2010).
- [30] L. Chaput, C. Tournier-Colletta, L. Cardenas, A. Tejada, B. Kierren, D. Malterre, Y. Fagot-Revurat, P. Le Fèvre, F. Bertran, A. Taleb-Ibrahimi, D.G. Trabada, J. Ortega, and F. Flores, *Phys. Rev. Lett.* **107**, 187603 (2011).
- [31] G. Li, M. Laubach, A. Fleszar, and W. Hanke, *Phys. Rev. B* **83**, 041104 (2011).
- [32] F. Aryasetiawan, M. Imada, A. Georges, G. Kotliar, S. Biermann, and A.I. Lichtenstein, *Phys. Rev. B* **70**, 195104 (2004).
- [33] L. Vaugier, H. Jiang, and S. Biermann, *Phys. Rev. B* **86**, 165105 (2012).
- [34] P. Hansmann, L. Vaugier, H. Jiang, and S. Biermann, *J. Phys. Condens. Matter* **25**, 094005 (2013).
- [35] S. Biermann, F. Aryasetiawan, and A. Georges, *Phys. Rev. Lett.* **90**, 086402 (2003).
- [36] We stress again, however, that our calculations are performed for the low-energy effective Hamiltonian, not directly in the continuum.
- [37] J. Tomczak, M. Casula, T. Miyake, F. Aryasetiawan, and S. Biermann, *Europhys. Lett.* **100**, 67001 (2012).
- [38] P. Sun and G. Kotliar, *Phys. Rev. Lett.* **92**, 196402 (2004).
- [39] T. Ayrál, P. Werner, and S. Biermann, *Phys. Rev. Lett.* **109**, 226401 (2012).
- [40] T. Ayrál, S. Biermann, and P. Werner, *Phys. Rev. B* **87**, 125149 (2013).
- [41] We also mention attempts of simplified combined schemes using static screened interactions in Refs. [35,42,43].
- [42] K. Karlsson, *J. Phys. Condens. Matter* **17**, 7573 (2005).
- [43] C. Taranto, M. Kaltak, N. Parragh, G. Sangiovanni, G. Kresse, A. Toschi, and K. Held, arXiv:1211.1324.
- [44] S. Biermann, F. Aryasetiawan, and A. Georges, *Proceedings of the NATO Advanced Research Workshop on Physics of Spin in Solids: Materials, Methods, and Applications, Azerbaijan, 2003*, NATO Science Series II Vol. 156 (Kluwer, Dordrecht, 2004), p. 43.
- [45] See also Ref. [46] for a variant of the $GW + DMFT$ scheme.
- [46] P. Sun and G. Kotliar, *Phys. Rev. B* **66**, 085120 (2002).
- [47] P. Werner and A.J. Millis, *Phys. Rev. Lett.* **104**, 146401 (2010).
- [48] P. Werner, M. Casula, T. Miyake, F. Aryasetiawan, A. Millis, and S. Biermann, *Nat. Phys.* **8**, 331 (2012).
- [49] M. Casula, A. Rubtsov, and S. Biermann, *Phys. Rev. B* **85**, 035115 (2012).
- [50] From the imaginary-time Green's function at $G(\tau = \beta/2)$.
- [51] It is experimentally difficult to determine the symmetry of the Si(111):Pb ground state—this challenge can, in fact, be explained by our results of charge order instabilities.
- [52] J. Avila, A. Mascaraque, E.G. Michel, M.C. Asensio, G. LeLay, J. Ortega, R. Perez, and F. Flores, *Phys. Rev. Lett.* **82**, 442 (1999).
- [53] The structure Si(111):Si is a hypothetical structure—it is not stable in the $\sqrt{3} \times \sqrt{3}$ phase.

P.2 Preprint 1: Hansmann *et al.* (2015)

Uncertainty principle for experimental probes: Fast spectroscopy vs. slow microscopy

P. Hansmann,^{1,2} T. Ayrál,^{1,3} A. Tejada,⁴ and S. Biermann^{1,5,6}

¹*Centre de Physique Théorique, Ecole Polytechnique, CNRS-UMR7644, 91128 Palaiseau, France*

²*Max-Planck-Institut für Festkörperforschung, Heisenbergstrasse 1, 70569 Stuttgart, Germany*

³*Institut de Physique Théorique (IPhT), CEA, CNRS, URA 2306, 91191 Gif-sur-Yvette, France*

⁴*Laboratoire de Physique des Solides, CNRS, Univ. Paris Sud, Univ. Paris-Saclay, 91405 Orsay, France*

⁵*Collège de France, 11 place Marcelin Berthelot, 75005 Paris, France*

⁶*European Theoretical Synchrotron Facility, Europe*

(Dated: June 29, 2015)

PACS numbers: 71.30.+h, 78.30.-j, 62.50.+p

The result of a physical measurement depends on the timescale of the experimental probe. In solid-state systems, this simple quantum mechanical principle has far-reaching consequences: the interplay of several degrees of freedom close to charge, spin or orbital instabilities combined with the disparity of the time scales associated to their fluctuations can lead to seemingly contradictory experimental findings. A particularly striking example is provided by systems of adatoms adsorbed on semiconductor surfaces where different experiments – angle-resolved photoemission, scanning tunneling microscopy and core-level spectroscopy – suggest different ordering phenomena. Using most recent first principles many-body techniques, we develop a unified theoretical picture of these phenomena, based on an analysis of the fluctuations associated to the different probes. These findings should have implications for the interpretation of ordering phenomena and their fluctuations in a wide class of solid state systems ranging from organic materials to high-temperature superconducting cuprates.

Understanding the mechanisms of charge, spin or orbital ordering and the competition of different instabilities is a leitmotiv of modern solid-state physics. Charge ordering phenomena in (quasi-)two-dimensional transition metal oxides have recently attracted tremendous attention [1–5]. Indeed, competing ordering phenomena might pave the way to superconductivity and could be key to an understanding of the unusually high transition temperatures observed in high T_c cuprate superconductors. The competition of different instabilities also leads to surprisingly complex phase diagrams in a number of other materials, ranging from low-dimensional organics [6], heavy fermion materials [7] to even simple oxides [8, 9], iridates [21] or tellurides [22]. Here, we study a material that epitomizes this interplay of degrees of freedom, the timescales associated to their fluctuations and the subtleties involved when probing them experimentally. 1/3 of a monolayer of Sn atoms adsorbed on the Si(111) surface – a representative of the so-called Si α -phases – forms a two-dimensional triangular lattice, where three

of the four valence electrons of Sn are forming covalent bonds with the silicon substrate while the remaining dangling bond results in a narrow half-filled surface band. While the electronic structure at the band theory level is thus extremely simple, many-body Coulomb correlations are a source for complex phase diagrams which have been attracting considerable interest, both experimentally [24–32, 34–37] and theoretically [23, 38–51]. Interestingly, despite the appealing single-orbital nature of the physics of these compounds a simple model with purely local Hubbard interactions falls short [51–53] of describing the observed phase diagrams. In particular, charge ordering instabilities are driven by nonlocal interactions, and the closely related compounds Pb/Si(111) or Sn/Ge(111) are found to be in the symmetry-broken charge-ordered (CO) phase. For Sn/Si(111), experimental results seem contradictory: angle-resolved photoemission spectroscopy (ARPES) shows backfoldings of bands associated to a 3x3 reconstruction of the unit cell[?], while scanning tunneling microscopy (STM) does not yield any indication of static order.

In a recent study Li et al. [50] proposed a magnetically-ordered state to be at the origin of these contradictions. However, while the proposed spin order would indeed be a natural candidate and has justly deserved attention, no direct experimental evidence for such an order has been found yet. Moreover, as shown below, only charge fluctuations solve an equally important puzzle raised by core-level spectroscopies of Sn. There, local excitations of the Sn 4d core shell suggest that the ground state of the Sn/Si(111) system is composed of more than one Sn configuration (i.e. valence states). A similar contradiction between ARPES and low-energy electron diffraction (LEED) has led to speculations about inhomogenous phases [55], with thermally fluctuating Sn-positions [13–18].

A recent *ab initio* determination of the interaction parameters of the Si α -phases (X/Si(111) with X=C, Sn, and Pb) has found nonlocal interactions to be as large as 50% of the onsite ones and established a materials trend with the Sn compound being “half-way” between Mott insulating C/Si(111) and charge-ordered Pb/Si(111)[54]. Here, we will show that this intermediate position in the

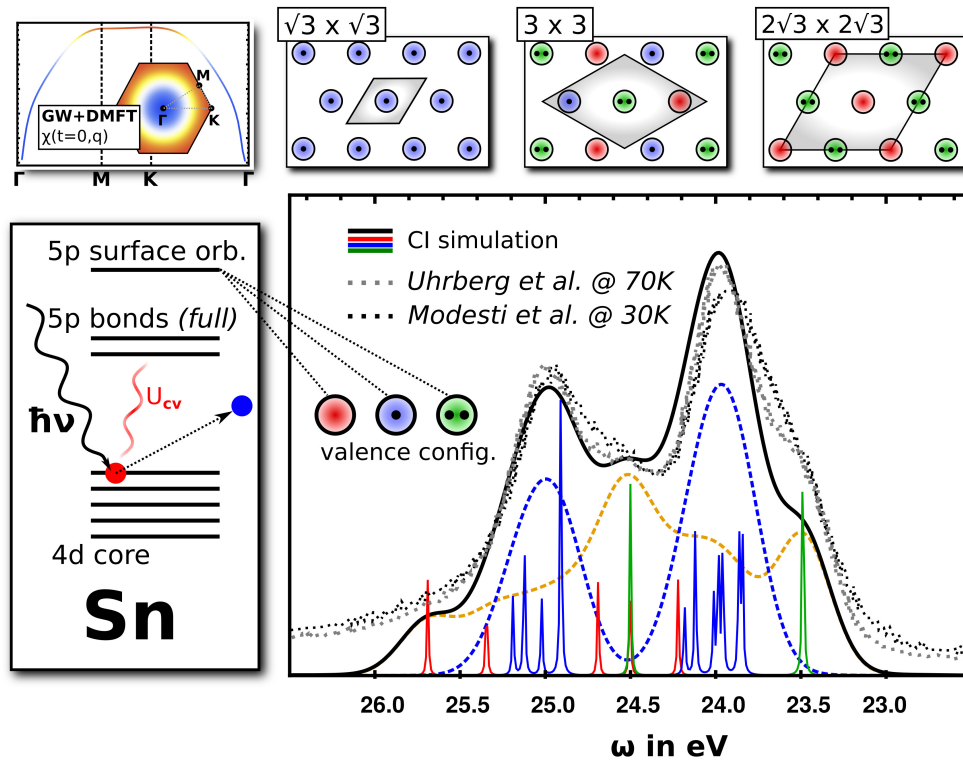


FIG. 1: Core-level photoemission spectroscopy of the Sn adatom 2p-shell. Left hand side (top): GW+DMFT Charge susceptibility plotted along the $\Gamma - M - K - \Gamma$ path in the Brillouin zone (see inset). Left hand side (bottom): Cartoon of the Sn 4d core electron emission process. Right hand side (top): Sketches of the three surface configurations ($\sqrt{3} \times \sqrt{3}$)R30°, 3×3 , and $(2\sqrt{3} \times 2\sqrt{3})$ R30°. Right hand side (bottom): comparison between experimentally obtained spectra (black and gray dots) and theoretical simulations with full multiplet cluster calculations (dashed and solid lines): The black solid line is the final theoretical result broadened by a Gaussian of width 0.37eV. It is the sum of the weighted contributions of the two coexisting phases close to the Mott-CO insulator transition (blue and orange dashed lines). The solid narrow lines (narrow peaks) resolve the contributions to the total spectrum by empty surface orbitals (red), singly occupied surface orbitals (blue) and fully occupied surface orbitals (green) incorporating respective multiplet splittings.

phase diagram in direct vicinity of the phase transition between a Mott insulating and a charge-ordered phase is the key to elucidating the above puzzles. As an order to order transition the first-order nature of this transition leads to phase coexistence with short characteristic time scales, which we extract from combined many-body perturbation theory and dynamical mean field calculations to be of the order of femto seconds: STM is too “slow” to detect such fluctuations, while ARPES and core-level photoemission spectroscopy (cPES) capture them.

Results: Our starting point is the charge-charge correlation function computed within combined many-body perturbation theory and dynamical mean field theory (GW+DMFT), see upper left-hand side of Fig. 1, reference [52], and the method section. This quantity suggests the presence of three major *dynamic* charge-fluctuation symmetries, which are represented in a cartoon-like fashion in the upper right-hand side of Fig. 1): a 3×3 charge-

ordered state, where three inequivalent sites are respectively doubly occupied, half-filled and empty (a “210” charge distribution), a $(2\sqrt{3} \times 2\sqrt{3})$ R30° reconstructed state where stripes of empty sites alternate with stripes of doubly occupied sites, and the conventional Mott insulating state where all sites are half-filled. Its structure (as a function of time/frequency) indicates fluctuations between these configurations with a characteristic timescale of the order of femto seconds, long enough for the cPES process to capture the fluctuations in a “snapshot”-like measurement.

With these insights, we now turn to a discussion of the different observables measured in cPES, STM and ARPES.

Core-level spectroscopy: The first probe we consider is core electron emission from the Sn 4d-shell. Core-level spectroscopy is a local Sn probe as sketched on the left-hand side of Fig. 1 where a 4d core electron is emit-

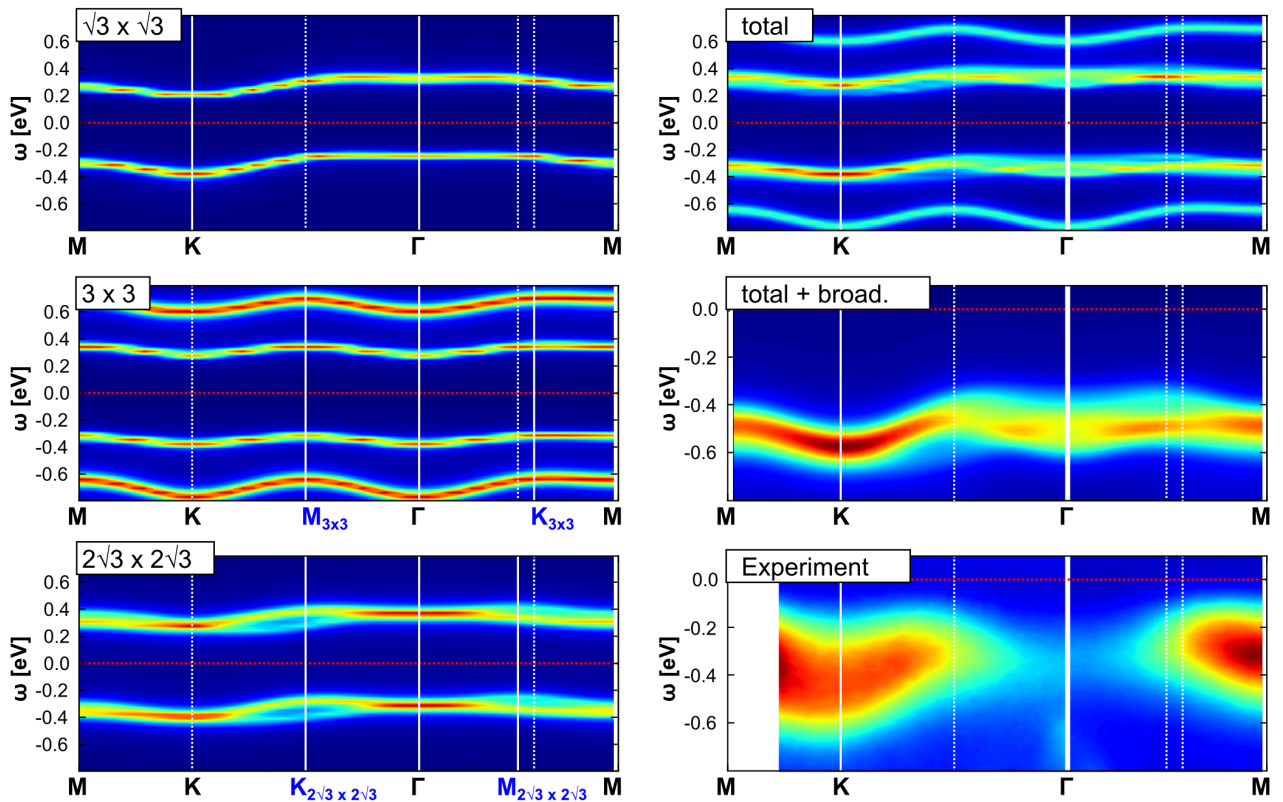


FIG. 2: Left hand side panels: Correlated $A(\mathbf{k}, \omega)$ simulations plotted along the $\Gamma \rightarrow M \rightarrow K \rightarrow \Gamma$ path in the $(\sqrt{3} \times \sqrt{3})R30^\circ$ -Brillouin zone for the three relevant surface configurations $(\sqrt{3} \times \sqrt{3})R30^\circ$ (top), 3×3 (middle), and $(2\sqrt{3} \times 2\sqrt{3})R30^\circ$ (bottom) - note the backfoldings of the lower two spectral functions around the high-symmetry points of the corresponding Brillouin zones marked by white vertical lines and blue labels (For sketches of the respective unit cells see top panel of Fig. 1). The red dashed line marks the Fermi energy ($\varepsilon_F = 0$). Electron removal shown on the left hand side (top). Right hand side panels: Weighted sum of $A(\mathbf{k}, \omega)$ of the contributions shown on the left hand side (top). Electron removal part of the total spectral function with additional broadening (middle) for comparison with experimental ARPES data (bottom). Note that our simulation has no information about \mathbf{k} -dependent matrix elements of the actual ARPES measurement so that relative intensities of theory and experiment are not expected to be comparable.

ted out of the solid by an incoming photon. Due to the Coulomb interaction of this 4d core hole with the 5p valence electrons (U_{cv}) the spectrum is sensitive to the Sn valence configuration which consists of an either empty, half-filled, or full surface orbital. It is therefore a most efficient probe for charge-ordered states or charge-fluctuations on timescales slower than the experimental process. To arrive at a first principles description of the core-level spectra we first determine the core-level emission spectra corresponding to the three different valence configurations (blue, red and green curves in the central panel of Fig. 1 corresponding to singly occupied, empty and full surface orbital configurations respectively) from cluster multiplet simulations (see methods section). The main energy scale for each contribution is the spin orbit coupling of the core hole which splits each spectrum into two main peaks associated to a core hole with to-

tal angular momentum $J_{ch} = 5/2$ or $J_{ch} = 3/2$. On a smaller energy scale (below experimental resolution), the core-valence interaction (U_{cv}) leads to multiplet splittings within each J_{ch} subspace¹.

If the system were homogeneously in the CO state determined above the resulting core-level spectra would be given by the superposition of the spectra determined for the different valence states with contributions of $\approx 13\%$ of the $(\sqrt{3} \times \sqrt{3})R30^\circ$ phase, $\approx 56\%$ of the 3×3 phase, and $\approx 31\%$ of the $(2\sqrt{3} \times 2\sqrt{3})R30^\circ$ phase. Translated into Sn valence contributions this corresponds to $\approx 32\%$ half-filled and $\approx 68\%$ empty/doubly-occupied sites. The resulting spectrum is plotted as yellow-dashed line in

¹ Note that for a filled valence shell (green) and its fully spherical charge distribution such multiplet splittings cannot occur.

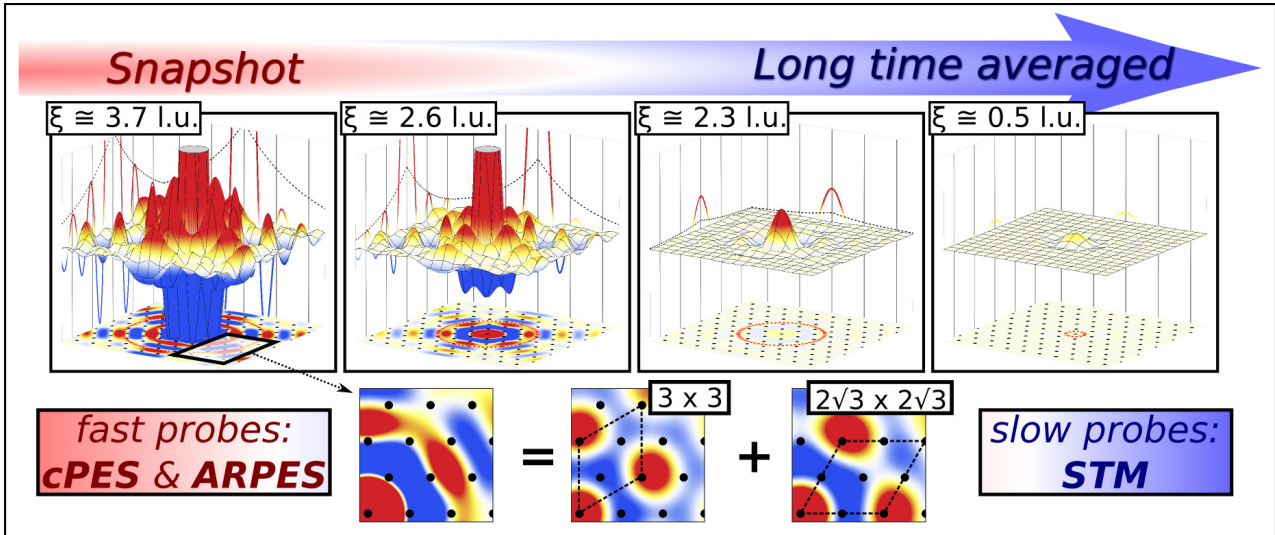


FIG. 3: Upper panels: GW+DMFT charge susceptibility $\chi(\mathbf{R}, \tau)$ plotted on the real space surface lattice (in the xy -plane - indicated by the black dots on the bottom of the respective plots) for four different values of τ . At $\tau = 0.0$ we find large charge fluctuations of correlation lengths ξ exceeding 3.5 lattice units (l.u.) which are picked up by core-level and photoemission spectroscopies. Due to decay on a fs timescale (see evolution with τ) they are invisible to slow probes like STM. Lower panels: The charge fluctuations can be decomposed into two dominant contributions related to 3×3 (“210”) and $(2\sqrt{3} \times 2\sqrt{3})R30^\circ$ (stripes) symmetry.

Fig. 1), and is found to give a bad description of the experimental data (black[55] /gray[34] dots).

If on the other hand, the system were in a pure Mott insulating state, our estimate of the core-level spectrum would be given by the contribution of the half-filled surface orbital only, broadened by the experimental resolution (blue dashed line in Fig. 1). Obviously, this assumption does not hold either, confirming our analysis of the charge-ordered state to contribute to the core-level spectrum.

Closer inspection of the spectra corresponding to the two possible states and comparison to the experimental spectra however shows that while neither the homogeneous CO state of the type determined above nor the Mott state yield theoretical spectra in agreement with experiment, the sum of the two (*ab-initio* calculated) spectra with weights 0.7 for the CO state and 0.3 for the Mott state, does. Such an incoherent superposition can be interpreted as simulating a spatial averaging of the two phases, that is, a state where phase separation leads to a spatial coexistence of Mott-insulating and charge-ordered patches with ratio 3/7. The obviously good agreement with the experimental measurement gives support to our interpretation of the sample being in an inhomogeneous state where Mott insulating islands are embedded into a dynamical CO background, and the spatial averaging done by the core-level spectroscopy results in a weighted average of the two contributions with weights 3:7. These results thus confirm –

from first principles – previous speculations about a possible inhomogeneous state [55], albeit rather as a superposition of the Mott state with the CO precursor we have described as the one observed in Sn/Ge(111) above the stabilization temperature of the COI state[16] and locate Sn/Si(111) in the phase coexistence region of a first-order phase transition between these two phases.

Comparison to the related compound Sn/Ge(111) [15–17] yields further insight: experiments unambiguously find Sn/Ge(111) in a fully static charge-ordered phase of 3×3 symmetry. In this case the phase coexistence has disappeared and the CO-fluctuating patches have grown to macroscopic lengthscales at temperatures below 60 K. Moreover, for the static case the experimental timescale is irrelevant and direct comparison of cPES and STM is unproblematic. In Sn/Si(111), on the other hand, such comparison can only be made by considering the snapshot-like nature of cPES measuring the spatial average of coexisting phases. Before turning to a quantitative discussion of the time and spatial extent of the charge fluctuations, based on the charge-charge correlation function $\chi_{\text{GW+DMFT}}$ as obtained from GW+DMFT (see methods section) we revisit another experiment – complementary to STM and cPES – of Sn/Si(111) that has caused recent controversies.

Angle-resolved photoemission (ARPES): Just as in core-level spectroscopy, the comparison of ARPES with STM surface images (suggesting absence of any charge

order) is not straightforward. More specifically, previous interpretations of ARPES spectra assumed the breaking of some kind of spin- [50] or charge- [33] symmetry of the ground state in order to account for backfolded features of the momentum-resolved spectral function. The origin of such a symmetry breaking has however been unclear so far, since there is no other experimental evidence for it: a static charge-ordered state would contradict STM results, and no experimental probe has found any direct indication for spin-ordering. In the light of the previous discussion on the core-level spectroscopy and by comparison of experimental ARPES spectra with theoretical calculations, we will argue in the following that assuming such symmetry breaking is unnecessary when taking into account the typical timescale of the experiment: just like core-level spectroscopy, ARPES can be understood as a “snapshot” probe that spatially averages over the surface. Hence, short-lived charge fluctuations of specific symmetry and finite but sufficient spatial extension (see next paragraph for details and quantification) will be picked up by ARPES and incoherently averaged (such effect has been recently shown for AF spin fluctuations and their impact on ARPES experiments for the high T_c cuprates [57]). For a quantitative comparison and reference spectra, we have carried out theoretical calculations for the spectral functions in the $(\sqrt{3} \times \sqrt{3})R30^\circ$ -, the 3×3 -, and the $(2\sqrt{3} \times 2\sqrt{3})R30^\circ$ -phase. In Fig. 2 we show in the bottom right panel the experimentally obtained ARPES signal along a specific path in the $(\sqrt{3} \times \sqrt{3})R30^\circ$ Brillouin zone (BZ). If we now take the mixture (and subsequent broadening) of the three theoretically calculated spectra (left panels in in Fig. 2) with weights determined from our cluster calculation and core-level study (upper and central right panel in Fig. 2), the agreement between experimental spectra and theory becomes satisfactory. To be precise, we can identify certain symmetry features, i.e. backfoldings, to be related to a specific charge fluctuation.

For this purpose, and as reference for future experiments, we have plotted the theoretical spectral functions (including also the electron addition part above the Fermi energy $\varepsilon_F = 0.0$ in t) in the left hand side panels of Fig. 2 within the $\sqrt{3} \times \sqrt{3}$ BZ.

The common feature of all shown spectra is their insulating nature, i.e. a finite gap. In the $(\sqrt{3} \times \sqrt{3})R30^\circ$ -phase (upper left) the gap separates an upper and lower Hubbard band of the Mott insulating state. In the 3×3 phase (center left), we find (as expected from the 3×3 occupations) the combination of a band-insulating (empty and doubly occupied sites) and Mott-insulating (singly occupied sites) gap. Finally, the spectral function of the $(2\sqrt{3} \times 2\sqrt{3})R30^\circ$ -stripe phase (lower left) separates the bands of the doubly occupied and empty lattice sites and, hence, represents a band-insulating spectrum. While the momentum-structure of the $(\sqrt{3} \times \sqrt{3})R30^\circ$ Hubbard bands closely resembles the dispersion of a free electron

on the surface lattice, the CO phases display characteristic backfolding features in the $(\sqrt{3} \times \sqrt{3})R30^\circ$ BZ. Particularly noteworthy are maxima of the spectral functions along the $\bar{K} - \bar{\Gamma}$ and $\bar{M} - \bar{\Gamma}$ directions that were subject to discussions in previous studies [33, 50].

Time and spatial resolution of the charge fluctuations: In the previous two paragraphs we have seen that spectroscopies such as core electron emission and ARPES seem to suggest charge order and, hence, are in contradiction to STM images of the Sn/Si(111) surface. As alluded to before, this contradiction can be resolved by considering the typical timescales of the experiments: While the spectroscopies are spatially averaged but quasi instantaneous snapshot probes, the STM complementarily yields time-averaged but spatially resolved information. We will now report on the details of time and spatial resolution of the charge fluctuations relevant to the phase coexistence. Indeed, the discussion on the different experiments above and their interpretation is based on a result from our theoretical ab-initio treatment of Sn/Si(111) within self-consistent GW+DMFT applied to a low energy Hamiltonian (see Methods section and Supplementary material). The most relevant quantity for the present discussion is the charge-charge correlation function $\chi(\mathbf{q}, \omega)$ resolved in momentum \mathbf{q} and frequency ω and its respective Fourier transforms. In our framework this quantity is self-consistently obtained and can be employed as a sensitive probe for charge-order instabilities. More specifically, the vicinity to a transition into an ordered phase of a specific symmetry would be signaled by the behaviour of $\chi(\mathbf{q}, \omega = 0)$ at the corresponding \mathbf{q} vector. Intuitive insight can be obtained from the Fourier transformed correlation function in real space and time $\chi(\mathbf{R}, \tau)$ plotted in Fig. 3. With this quantity we can find the typical correlation length ξ and timescale $\Delta\tau_0$ of a charge fluctuation. Since the Mott to CO phase transition is not a second order transition, $\chi(\mathbf{R}, \tau)$ does not become continuously long range (i.e. $\chi(\mathbf{q}, \omega = 0)$ does not diverge at a given \mathbf{q}) but the correlation length $\xi \rightarrow \infty$ only increases up to a finite value of the order of a few lattice constants before entering the symmetry-broken phase.

In Fig. 3 we plot the calculated $\chi_{\text{GW+DMFT}}(\mathbf{R}, \tau)$ for Sn/Si(111) on the z -axis at three different imaginary time slices which correspond to averages over increasingly large timescales. Four panels show the evolution from instantaneous measurements to averages roughly over some femtoseconds. x - and y - axes present the 2D surface indicated also by the black dots at the respective adatom sites. From these plots we can conclude that the Mott phase coexists with *short-lived finite size lattice-commensurate charge fluctuations*. To quantify this claim we extract a correlation length at $\tau = 0$ of about $4l.u.$ (enough for backfolded bands to be occu-

pied in the ARPES experiment [57]). These numbers immediately resolve the spectroscopy vs. microscopy puzzle: Sn/Si(111) is found in close vicinity but not yet in a charge-ordered phase (which can actually be reached by substituting the Si substrate by a Ge one). However, the ordered phase is preceded by quickly decaying charge fluctuations that can be picked up by fast core-level and photoemission spectroscopies but not by STM.

DISCUSSION

In this work, we have demonstrated that the apparent contradictions between STM, ARPES and core-level spectroscopy for two-dimensional systems of adatoms adsorbed on semiconductor surfaces can be resolved by considering that i) specific compounds like Sn/Si(111) are located in the phase coexistence region of the first-order phase transition from a Mott insulator to a charge-ordered insulator, and ii) the timescales intrinsic to the different experiments matter: quickly decaying charge fluctuations (of specific symmetries) can be seen by fast snapshot-like spectroscopies (core-level spectroscopy, ARPES) while slow microscopy (STM) detects only a time-averaged image in which the charge modulations are averaged out. We have shed light on the history of controversial interpretations of Sn/Si(111) by quantifying these statements, based on first principles many-body calculations using combined many-body perturbation theory and extended dynamical mean-field theory (GW+DMFT). In order to provide a direct theory-experiment comparison, we have computed the observables of core-level spectroscopy and angular resolved photoemission. Moreover, we have visualized and discussed the key observable for dynamically fluctuating surface compounds: the charge susceptibility. Our analysis underlines the need for a very careful analysis of experimental results in circumstances where characteristic timescales of the material (i.e. fluctuations) and the experimental probe coincide.

METHODS

Charge correlation function: The correlation function in the charge channel $\chi(\mathbf{R}, \tau)$ displayed in Fig. 3 has been obtained by spatial and temporal Fourier transformation of the charge correlation function $\chi(\mathbf{k}, i\omega)$. The latter is computed from the polarization function $P(\mathbf{k}, i\omega)$ through the relation:

$$\chi(\mathbf{k}, i\omega) = \frac{-P(\mathbf{k}, i\omega)}{1 - v(\mathbf{k})P(\mathbf{k}, i\omega)}$$

Here, $v(\mathbf{k})$ is the Fourier transform of the interactions

$v(\mathbf{R}_i - \mathbf{R}_j) = U\delta_{ij} + V \cdot \frac{a}{|\mathbf{R}_i - \mathbf{R}_j|}$ (a in the lattice constant and \mathbf{R}_i denotes a lattice site.). The polarization function is computed in the GW+DMFT approximation [60–63], namely as the sum of the impurity polarization $P_{\text{imp}}(i\omega)$ and of the nonlocal part of the bubble $\sim 2GG$, more specifically

$$P(\mathbf{k}, i\omega) = P_{\text{imp}}(i\omega) + 2 \left[\sum_{\mathbf{q}, i\nu} G(\mathbf{q} + \mathbf{k}, i\omega + i\nu)G(\mathbf{q}, i\nu) \right]_{\text{nonloc}}$$

where $G(\mathbf{q}, i\nu)$ is the fully self-consistent Green’s function from a converged GW+DMFT calculation.

The factor of 2 stems from spin degeneracy. The values of interaction parameters are calculated within the constrained random phase approximation [52, 53], namely $U = 1.0$ eV and $V = 0.5$ eV.

Ground-state wave function of charge-ordered state In order to determine the weight with which the “210”, stripe and Mott configurations contribute to the ground-state wave function in the charge-ordered state, we have solved – by exact diagonalization – a six-site cluster with periodic boundary conditions. Subsequent projection of the ground state on the three relevant configurations of interest results in the estimates for the coefficients shown in Fig. 4 as a function of non-local interaction. The qualitative behaviour of the curves shown here can be understood as follows: For small non-local interaction the Mott-like $(\sqrt{3} \times \sqrt{3})R30^\circ$ phase is dominant and un-mixed with energetically high-lying configurations. However, upon increasing the nonlocal interactions some of these high-lying configurations (in particular the 3×3 and $(2\sqrt{3} \times 2\sqrt{3})R30^\circ$ states) become lower in energy with respect to the ground state and for nonlocal interactions exceeding ~ 0.34 even replace the $(\sqrt{3} \times \sqrt{3})R30^\circ$ configuration as the main contribution for the ground state (note that mixing of the different configurations is driven by the gain of kinetic energy, i.e. electron hopping).

According to the cRPA calculations, the physical values for the nonlocal interactions lead to a ground state composed of the above three components with coefficients 0.13 ($(\sqrt{3} \times \sqrt{3})R30^\circ$), 0.56 (3×3), and 0.31 ($(2\sqrt{3} \times 2\sqrt{3})R30^\circ$) - normalized values extracted from results shown in Fig. 4.

Multiplet cluster calculations: In order to simulate the Sn 4d core-level spectra (shown in Fig. 1) we employ full multiplet cluster calculations using the code introduced in Ref. [58]. As common practice for such cluster simulated spectra we estimated the strength of the core hole spin-orbit coupling (SOC), and the multipole part of the core-valence interaction from atomic Hartree-Fock calculations[59]. For valence and core SOC we use $\zeta_{5p} = 0.40$ eV, and $\zeta_{4d} = 0.41$ eV; for the multipole moments of the core valence interaction we use the Slater integrals $F^1 = 0.46$ eV, $F^2 = 1.47$

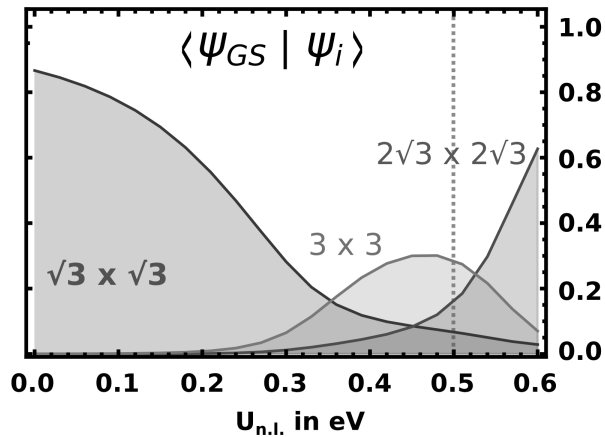


FIG. 4: Projection of the many body ground state in a 6-site cluster on its three most relevant contributions as function of the non-local interaction. The red dashed line indicates the cRPA value for Sn/Si(111).

eV, and $F^3 = 0.42$ eV. The monopole part of the core-hole valence interaction is (in combination with the onsite U of Sn) responsible for the relative shift of the three spectra and fixed by the overall width of the spectrum. The spectral functions are calculated with exact diagonalization in the cluster limit and broadened by convoluting with a Gaussian of width 0.37eV.

Theoretical ARPES spectra: The theoretical ARPES spectrum (top-right and middle-left panels of Fig. 2) is computed as a weighted average of the spectra ($A^\alpha(\mathbf{k}, \omega) \equiv \frac{1}{N_{\text{el}}^\alpha} \text{Tr} \left[-\frac{1}{\pi} \text{Im} \hat{G}^\alpha(\mathbf{k}, \omega + i\eta) \right]$) for the 3 symmetries $\alpha = \{\sqrt{3} \times \sqrt{3}, 3 \times 3, 2\sqrt{3} \times 2\sqrt{3}\}$:

$$A(\mathbf{k}, \omega) = \sum_{\alpha} \lambda_{\alpha} A^{\alpha}(\mathbf{k}, \omega) / \sum_{\alpha} \lambda_{\alpha}$$

The relative weights λ_{α} are determined from the cluster diagonalisation and the cPES spectra (see above). N_{el}^{α} denote the number of electrons per unit cell for each

symmetry (respectively 1, 3, 2). In the top-right panel, this spectrum is broadened with a Gaussian distribution of mean deviation $\sigma = 0.3$ to account for ARPES uncertainties. The individual spectra are shown in the remaining three panels. The self-energy of the $(\sqrt{3} \times \sqrt{3})R30^\circ$ symmetry is obtained by MaxEnt analytical continuation of the imaginary-frequency impurity self-energy $\Sigma_{\text{imp}}(i\omega)$ computed self-consistently through an EDMFT scheme [52, 63]. We find this self-energy well reproduced by an atomic self-energy with a renormalized interaction given by the self-consistently computed effective impurity interaction $\mathcal{U}(\omega = 0)$ as obtained from GW+DMFT. For the 3×3 symmetry, we take the atomic self-energy for the half-filled band, while for the empty and full bands we take the Hartree estimates for the self-energy:

$$\Sigma^{3 \times 3}(\omega) = \begin{pmatrix} \frac{U}{2} - 3V & 0 & 0 \\ 0 & \frac{U^2}{4\omega} & 0 \\ 0 & 0 & -\frac{U}{2} + 3V \end{pmatrix}$$

For the $2\sqrt{3} \times 2\sqrt{3}$ symmetry, we also take Hartree estimates:

$$\Sigma^{2\sqrt{3} \times 2\sqrt{3}}(\omega) = \begin{pmatrix} \frac{U}{2} - 2V & 0 \\ 0 & -\frac{U}{2} + 2V \end{pmatrix}$$

ACKNOWLEDGEMENTS

We thank the authors of Refs. [50] and Daniel Malterre, Yannick Fagot-Revurat, Alessandro Toschi, Georg Rohringer, Thomas Schaefer for useful discussions. We are particularly indebted to Ralph Claessen and Jörg Schäfer for providing us with the ARPES data of Ref.[37] and allowing us to replot them. This work was supported by the French ANR under project SURMOTT, IDRIS/GENCI under project 091393 and the European Research Council under its Consolidator Grant scheme 2013 (project number 617196).

AUTHORS CONTRIBUTIONS

PH performed the DFT, cRPA and cluster calculations. TA performed the GW+DMFT calculations, TA and PH performed the calculations of the k-resolved spectra. All authors contributed to the planning of the study, the interpretation of the results and the writing of the manuscript.

-
- [1] R. Comin, A. Frano, M. M. Yee, Y. Yoshida, H. Eisaki, E. Schierle, E. Weschke, R. Sutarto, F. He, A. Soumyanarayanan, Y. He, M. Le Tacon, I. S. Elfimov, J. E. Hoffman, G. A. Sawatzky, B. Keimer and A. Damascelli. Science **343**,390-392 (2014).

- [2] Eduardo H. da Silva Neto, Pegor Aynajian, Alex Frano, Riccardo Comin, Enrico Schierle, Eugen Weschke, Andrs Gyenis, Jinsheng Wen, John Schneeloch, Zhijun Xu, Shimpei Ono, Genda Gu, Mathieu Le Tacon, and Ali Yazdani, *Science* **343** (6169), 393-396 (2013)
- [3] Darius H. Torchinsky, Fahad Mahmood, Anthony T. Bollinger, Ivan Bozovi, and Nuh Gedik, *Nature Materials* **12**, 387391 (2013).
- [4] R. Comin, R. Sutarto, F. He, E. H. da Silva Neto, L. Chauviere, A. Frano, R. Liang, W. N. Hardy, D. A. Bonn, Y. Yoshida, H. Eisaki, A. J. Achkar, D. G. Hawthorn, B. Keimer, G. A. Sawatzky and A. Damascelli, *Nature Materials*, 1476 (2015)
- [5] W. Tabis, Y. Li, M. Le Tacon, L. Braicovich, A. Kreyssig, M. Minola, G. Dellea, E. Weschke, M. J. Veit, M. Ramazanoglu, A. I. Goldman, T. Schmitt, G. Ghiringhelli, N. Barisic, M. K. Chan, C. J. Dorow, G. Yu, X. Zhao, B. Keimer and M. Greven, *Nature Comm.* **5**, 5875 (2014).
- [6] See e.g. A. Girlando, M. Masino, J. A. Schlueter, N. Drichko, S. Kaiser, M. Dressel, *Phys. Rev. B* **89**, 174503 (2014); H. Shinaoka, T. Misawa, K. Nakamura, M. Imada, *J. Phys. Soc. Jpn.* **81**, 034701 (2012).
- [7] S. Doniach. *Phase Diagram for the Kondo Lattice*, Springer US (1977).
- [8] Y. Quan, V. Pardo, W. E. Pickett, *Phys. Rev. Lett.* **109**, 216401 (2012).
- [9] A. Ralko, J. Merino, S. Fratini, arxiv1412.4696
- [10] H.W. Yeom, S. Takeda, E. Rotenberg, I. Matsuda, K. Horikoshi, J. Schaefer, C. M. Lee, S. D. Kevan, T. Ohta, T. Nagao, and S. Hasegawa, *Phys. Rev. Lett.* **82**, 4898 (1999).
- [11] C. Gonzalez, F. Flores, and J. Ortega, *Phys. Rev. Lett.* **96**, 136101 (2006).
- [12] S. Wippermann and W. G. Schmidt, *Phys. Rev. Lett.* **105**, 126102 (2010).
- [13] J. M. Carpinelli, H. H. Weitering, E. W. Plummer, and R. Stumpf, *Nature (London)* **381**, 398 (1996).
- [14] J. M. Carpinelli, H. H. Weitering, M. Bartkowiak, R. Stumpf, and E.W. Plummer, *Phys. Rev. Lett.* **79**, 2859 (1997).
- [15] J. Avila, A. Mascaraque, E. G. Michel, M. C. Asensio, G. LeLay, J. Ortega, R. Pérez, and F. Flores, *Phys. Rev. Lett.* **82**, 442 (1999).
- [16] R. Cortés, A. Tejada, J. Lobo-Checa, C. Didiot, B. Kierren, D. Malterre, J. Merino, F. Flores, E.G. Michel, and A. Mascaraque, *Phys. Rev. B* **88**, 125113 (2013).
- [17] R. Cortés, A. Tejada, J. Lobo, C. Didiot, B. Kierren, D. Malterre, E. Michel, and A. Mascaraque, *Phys. Rev. Lett.* **96**, 126103 (2006).
- [18] S. C. Erwin, *Nature (London)* **441**, 295 (2006).
- [19] W. Srour, D.G. Trabada, J.I. Martinez, F. Flores, J. Ortega, M. Abuín, Y. Fagot-Revurat, B. Kierren, A. Taleb-Ibrahimi, D. Malterre, and A. Tejada, *Phys. Rev. Lett.* **114**, 196101 (2015).
- [20] F. Ronci, S. Colonna, A. Cricenti, and Guy Le Lay, *Phys. Rev. Lett.* **99**, 166103 (2007).
- [21] K. Takubo, R. Comin, D. Ootsuki, T. Mizokawa, H. Wadati, Y. Takahashi, G. Shibata, A. Fujimori, R. Sutarto, F. He, S. Pyon, K. Kudo, M. Nohara, G. Levy, I. S. Elfimov, G. A. Sawatzky and A. Damascelli. *Phys. Rev. B* **90**,081104 (2014).
- [22] B. F. Hu, B. Cheng, R. H. Yuan, T. Dong and N. L. Wang. *Phys. Rev. B* **90**,085105 (2014).
- [23] E. Tosatti and P. W. Anderson, *Charge and Spin Density Waves on Semiconductor Surfaces*, *Japanese Journal of Applied Physics* **252**,381-388 (1974).
- [24] R. I. G. Uhrberg, G. V. Hansson, J. M. Nicholls, P. E. S. Persson and S. A. Flodström. *Phys. Rev. B* **31**,3805–3810 (1985)
- [25] T. M. Grehk, L. S. O. Johansson, U. O. Karlsson and A. S. Flödstrom. *Phys. Rev. B* **47**,13887–13890 (1993)
- [26] H. H. Weitering, J. Chen, N. J. DiNardo and E. W. Plummer. *Phys. Rev. B* **48**,8119–8135 (1993)
- [27] J. M. Carpinelli, H. H. Weitering, E. W. Plummer and R. Stumpf. *Nature* **381**,398–400 (1996)
- [28] J. M. Carpinelli, H. H. Weitering, M. Bartkowiak, R. Stumpf and E. W. Plummer. *Phys. Rev. Lett.* **79**,2859–2862 (1997)
- [29] H. H. Weitering, X. Shi, P. D. Johnson, J. Chen, N. J. DiNardo and K. Kempa. *Phys. Rev. Lett.* **78**,1331–1334 (1997)
- [30] G. L. Lay, M. G. Rad, M. Gathelid, U. Karlsson, J. Avila and M. Asensio. *Applied Surface Science* **175-176**,201–206 (2001)
- [31] C. A. Pignedoli, A. Catellani, P. Castrucci, A. Sgarlata, M. Scarselli, M. De Crescenzi and C. M. Bertoni. *Phys. Rev. B* **69**,113313 (2004)
- [32] M. H. Upton, T. Miller and T.-C. Chiang. *Phys. Rev. B* **71**,033403 (2005)
- [33] J. Lobo, A. Tejada, A. Mugarza and E. G. Michel. *Phys. Rev. B* **68**,235332 (2003).
- [34] S. Modesti, L. Petaccia, G. Ceballos, I. Vobornik, G. Panaccione, G. Rossi, L. Ottaviano, R. Larciprete, S. Lizzit, and A. Goldoni, *Phys. Rev. Lett.* **98**, 126401 (2007)
- [35] L. A. Cardenas, Y. Fagot-Revurat, L. Moreau, B. Kierren and D. Malterre. *Phys. Rev. Lett.* **103**,046804 (2009)
- [36] T. Zhang, P. Cheng, W.-J. Li, Y.-J. Sun, G. Wang, X.-G. Zhu, K. He, L. Wang, X. Ma, X. Chen, Y. Wang, Y. Liu, H.-Q. Lin, J.-F. Jia and Q.-K. Xue. *Nat Phys* **6**,104–108 (2010)
- [37] C. Tournier-Colletta, L. Cardenas, Y. Fagot-Revurat, A. Tejada, B. Kierren and D. Malterre. *Phys. Rev. B* **84**,155443 (2011)
- [38] E. Kaxiras, K. C. Pandey, F. J. Himpsel and R. M. Tromp. *Phys. Rev. B* **41**,1262–1265 (1990)
- [39] K. D. Brommer, M. Needels, B. Larson and J. D. Joannopoulos. *Phys. Rev. Lett.* **68**,1355–1358 (1992)
- [40] C. S. Hellberg and S. C. Erwin. *Phys. Rev. Lett.* **83**,1003–1006 (1999)
- [41] H. Aizawa, M. Tsukada, N. Sato and S. Hasegawa. *Surface Science* **429**,L509–L514 (1999)
- [42] G. Profeta, A. Continenza, L. Ottaviano, W. Mannstadt and A. J. Freeman. *Phys. Rev. B* **62**,1556–1559 (2000)
- [43] H. Q. Shi, M. W. Radny and P. V. Smith. *Phys. Rev. B* **66**,085329 (2002)
- [44] H. Q. Shi, M. W. Radny and P. V. Smith. *Phys. Rev. B* **70**,235325 (2004)
- [45] G. Profeta and E. Tosatti. *Phys. Rev. Lett.* **95**,206801 (2005)
- [46] G. Profeta and E. Tosatti. *Phys. Rev. Lett.* **98**,086401 (2007)
- [47] S. Schuwalow, D. Grieger and F. Lechermann. *Phys. Rev. B* **82**,035116 (2010)
- [48] L. Chaput, C. Tournier-Colletta, L. Cardenas, A. Tejada, B. Kierren, D. Malterre, Y. Fagot-Revurat, P. Le Fèvre, F. Bertran, A. Taleb-Ibrahimi, D. G. Trabada, J. Ortega and F. Flores. *Phys. Rev. Lett.* **107**,187603 (2011)

- [49] G. Li, M. Laubach, A. Fleszar and W. Hanke. Phys. Rev. B **83**,041104 (2011)
- [50] G. Li, P. Höpfner, J. Schäfer, C. Blumenstein, S. Meyer, A. Bostwick, E. Rotenberg, R. Claessen, and W. Hanke, Nat. Commun. **4**, 1620 (2013).
- [51] G. Santoro, S. Scandolo and E. Tosatti. Phys. Rev. B **59**,1891–1901 (1999).
- [52] P. Hansmann, T. Ayrál, L. Vaugier, P. Werner and S. Biermann. Phys. Rev. Lett. **110**,166401 (2013).
- [53] P. Hansmann, L. Vaugier, H. Jiang and S. Biermann. Journal of Physics: Condensed Matter **25**,094005 (2013).
- [54] I. Brihuega, O. Custance, Rubén Pérez, and J. M. Gómez-Rodríguez, Phys. Rev. Lett. **94**, 046101 (2005).
- [55] R. I. G. Uhrberg, H. M. Zhang, T. Balasubramanian, S. T. Jemander, N. Lin and G. V. Hansson. Phys. Rev. B **62**,8082–8086 (2000).
- [56] T. Ayrál, P. Hansmann, and S. Biermann *unpublished; in preparation*.
- [57] R. Wallauer, E. Lahoud, P. Carretta, S. Sanna, and A. Kanigel arXiv:1506.02932 (2015) *accepted for Phys. Rev. B*.
- [58] M. W. Haverkort, M. Zwierzycki and O. K. Andersen. Phys. Rev. B **85**,165113 (2012).
- [59] R. D. Cowan. *The theory of atomic structure and spectra*, (1970).
- [60] S. Biermann, F. Aryasetiawan, and A. Georges, Phys. Rev. Lett. **90**, 086402 (2003)
- [61] S. Biermann, F. Aryasetiawan, and A. Georges, Physics of Spin in Solids: Materials, Methods, and Applications (Kluwer Academic Publishers B.V, 2004), pp. 4365, NATO Science Series II, available electronically as arXiv:0401653
- [62] P. Sun and G. Kotliar, Phys. Rev. Lett. **92**, 196402 (2004)
- [63] Ayrál, T., Biermann, S., Werner, P. (2013), Phys. Rev. B **87**, 125149 (2013); Ayrál, T., Werner, P., Biermann, S., (2012), Phys. Rev. Lett. **109**, 226401 (2012)



TRILEX: formalism and first implementation

Q.1 Paper 5: Ayrat and Parcollet (2015)

Mott physics and spin fluctuations: A unified frameworkThomas Ayrál^{1,2,*} and Olivier Parcollet²¹*Centre de Physique Théorique, Ecole Polytechnique, CNRS-UMR 7644, 91128 Palaiseau, France*²*Institut de Physique Théorique (IPhT), CEA, CNRS, UMR CNRS 3681, 91191 Gif-sur-Yvette, France*

(Received 30 March 2015; published 3 September 2015)

We present a formalism for strongly correlated electron systems which consists in a local approximation of the dynamical three-leg interaction vertex. This vertex is self-consistently computed using a quantum impurity model with dynamical interactions in the charge and spin channels, similar to dynamical mean field theory approaches. The electronic self-energy and the polarization are both frequency and momentum dependent. The method interpolates between the spin-fluctuation or *GW* approximations at weak coupling and the atomic limit at strong coupling. We apply the formalism to the Hubbard model on a two-dimensional square lattice and show that as interactions are increased towards the Mott insulating state, the local vertex acquires a strong frequency dependence, driving the system to a Mott transition, while at low enough temperatures the momentum dependence of the self-energy is enhanced due to large spin fluctuations. Upon doping, we find a Fermi arc in the one-particle spectral function, which is one signature of the pseudogap state.

DOI: 10.1103/PhysRevB.92.115109

PACS number(s): 71.10.Fd, 71.27.+a, 71.30.+h

Strongly correlated electronic systems such as high-temperature cuprate superconductors are a major challenge in condensed-matter physics. One theoretical approach to cuprates emphasizes the effect of long-range bosonic fluctuations on the electronic fluid, for example, long-range antiferromagnetic (AF) fluctuations due to a quantum critical point [1–6]. These bosonic fluctuations are also central to approaches such as the two-particle self-consistent approximation (TPSC [7–11]), the *GW* approximation [12], and the fluctuation-exchange approximation (FLEX [13]).

Another approach focuses, following Anderson [14], on describing the Mott transition and the doped Mott insulator. In recent years, dynamical mean field theory (DMFT) [15] and its cluster extensions such as cellular DMFT (CDMFT) [16,17] or the dynamical cluster approximation (DCA) [18–20] have allowed for tremendous theoretical progress on the Mott transition both for models and realistic computations of strongly correlated materials [21]. In particular, numerous works have been devoted to the one-band Hubbard model, mapping out its phase diagram, studying the *d*-wave superconducting order and the pseudogap [22–45]. Cluster DMFT is one of the few methods designed for the strong-interaction regime to have a simple control parameter, namely, the size N_c of the cluster or the momentum resolution of the electronic self-energy. It interpolates between the DMFT solution ($N_c = 1$) and the exact solution of the Hubbard model ($N_c = \infty$). Despite its success, this method nonetheless suffers from severe limitations: (i) It does not include the effect of long-range bosonic modes of wavelengths larger than the cluster size; (ii) the negative sign problem of continuous-time quantum Monte Carlo has so far precluded the convergence of the cluster solutions with respect to N_c in the most important regimes, such as the pseudogap; and (iii) the \mathbf{k} resolution of the self-energy is still quite coarse in DCA (typically eight or 16 patches in the Brillouin zone—see, e.g., Refs. [31,33,45,46]), or it relies on uncontrolled *a posteriori* “periodization” techniques in CDMFT [17].

Several directions beyond cluster DMFT methods are currently under investigation to address these issues, such as *GW*+DMFT [47–53], the combination of DMFT with functional renormalization group methods [54], the dynamical vertex approximation (D Γ A) [55–58], and the dual fermion (DF) or boson methods [59–61]. D Γ A and DF require the manipulation of four-leg vertices and, in their ladder version, require the summation of selected classes of ladder diagrams. Simpler yet controlled methods are needed: Except for one-dimensional chains [62], neither D Γ A nor DF has been applied to multiorbital systems to date.

In this Rapid Communication, we discuss a simple formalism that unifies the two points of view mentioned above while remaining comparatively lightweight. It is designed to encompass both Mott physics in the manner of DMFT and the effect of medium- and long-range bosonic modes. It interpolates between the atomic and the “fluctuation-exchange” limits upon going from strong to weak interactions. It consists in decoupling the electron-electron interaction by Hubbard-Stratonovich bosonic fields and making a local and self-consistent approximation of the lattice’s electron-boson one-particle irreducible three-leg vertex, using a quantum impurity model similar to the one used in DMFT. Since this method approximates three-leg objects with a local expansion, we will call it TRILEX. Already at the single-site level, it produces, in some parameter regimes, a momentum-dependent self-energy and polarization, at a small computational cost, similar to solving extended DMFT (EDMFT) [63–65]. In the following, we introduce the method and then present the solution of its single-site version for the two-dimensional Hubbard model.

We focus on the Hubbard model defined by the following Hamiltonian:

$$H = \sum_{ij,\sigma} t_{ij} c_{i\sigma}^\dagger c_{j\sigma} + U \sum_i n_{i\uparrow} n_{i\downarrow}. \quad (1)$$

The indices i, j denote lattice sites, $\sigma = \uparrow, \downarrow$, $c_{i\sigma}^\dagger$ ($c_{i\sigma}$) is a fermionic creation (annihilation) operator, and $n_{i\sigma} \equiv c_{i\sigma}^\dagger c_{i\sigma}$. t_{ij} is the tight-binding hopping matrix [$t_{ij} = t(t')$ for (next-)

*thomas.ayral@polytechnique.edu

nearest neighbors], while U is the on-site Coulomb interaction. We rewrite the operators of the interaction term as

$$U n_{i\uparrow} n_{i\downarrow} = \frac{1}{2} \sum_I U^I n_i^I n_i^I, \quad (2)$$

where U^I is the bare interaction in channel I , and $n_i^I \equiv \sum_{\sigma\sigma'} c_{i\sigma}^* \sigma_{\sigma\sigma'}^I c_{i\sigma'}$, where $\sigma^0 = \mathbf{1}$ and $\sigma^{x,y,z}$ are the Pauli matrices. Here, we consider one possible decoupling¹ which preserves the rotation symmetry of the action: The index I runs on $0, x, y, z$, $U^x = U^y = U^z \equiv U^{\text{sp}}$, and $U^0 \equiv U^{\text{ch}}$, and U^{sp} and U^{ch} satisfy $U = U^{\text{ch}} - 3U^{\text{sp}}$. We have two channels, denoted as $\eta = \text{ch, sp}$. We fix the ratio to $U^{\text{ch}} = U/2$ and $U^{\text{sp}} = -U/6$.² We now decouple (2) using real bosonic Hubbard-Stratonovich fields $\phi_i^I(\tau)$ in each channel and at each lattice site, so that the action now describes a lattice problem with a local electron-boson coupling:

$$S_{\text{latt}} = \int_0^\beta d\tau \sum_{ij} c_{i\sigma\tau}^* \{ \partial_\tau + t_{ij} \} c_{j\sigma\tau} + \sum_{i,I} \left[\frac{1}{2} (-U^I)^{-1} \phi_{i\tau}^I \phi_{i\tau}^I + \lambda^I \phi_{i\tau}^I n_i^I \right]. \quad (3)$$

$c_{i\sigma\tau}^*$ and $c_{i\sigma\tau}$ are conjugate β -antiperiodic Grassmann fields, and $\lambda^I = 1$. The lattice Green's functions $G(\mathbf{k}, i\omega)$ and $W^\eta(\mathbf{q}, i\Omega)$ (the Fourier transforms of $-(c_{i\sigma\tau} c_{j\sigma 0}^*)$ and $-(\phi_{i\sigma\tau}^\eta \phi_{j\sigma 0}^\eta)$, respectively) are given by Dyson equations,

$$G(\mathbf{k}, i\omega) = [i\omega + \mu - \varepsilon(\mathbf{k}) - \Sigma(\mathbf{k}, i\omega)]^{-1}, \quad (4a)$$

$$W^\eta(\mathbf{q}, i\Omega) = U^\eta [1 - U^\eta P^\eta(\mathbf{q}, i\Omega)]^{-1}. \quad (4b)$$

\mathbf{k} and \mathbf{q} are momentum variables, $i\omega$ ($i\Omega$) stands for a fermionic (bosonic) Matsubara frequency, $\varepsilon(\mathbf{k})$ is the Fourier transform of t_{ij} , and μ is the chemical potential. The fermionic and bosonic self-energies Σ and P^η are given by the exact expressions (in the paramagnetic, normal phase) (see, e.g., Ref. [67])

$$\Sigma(\mathbf{k}, i\omega) = - \sum_{\substack{\mathbf{q}, i\Omega \\ \eta=\text{ch, sp}}} m_\eta \lambda^\eta G_{i\omega+i\Omega}^{\mathbf{q}+\mathbf{k}} W_{\mathbf{q}, i\Omega}^\eta \Lambda_{i\omega, i\Omega}^\eta, \quad (5a)$$

$$P^\eta(\mathbf{q}, i\Omega) = 2 \sum_{\mathbf{k}, i\omega} \lambda^\eta G_{i\omega+i\Omega}^{\mathbf{q}+\mathbf{k}} G_{\mathbf{k}, i\omega} \Lambda_{i\omega, i\Omega}^\eta. \quad (5b)$$

Here, $m_{\text{ch}} = 1$ and $m_{\text{sp}} = 3$. $\Lambda^\eta(\mathbf{k}, \mathbf{q}, i\omega, i\Omega)$ is the exact one-particle irreducible electron-boson coupling (or Hedin) vertex, namely, the effective interaction between electrons and bosons renormalized by electronic interactions.

The main point of this Rapid Communication consists in approximating the vertex $\Lambda^\eta(\mathbf{k}, \mathbf{q}, i\omega, i\Omega)$ by the local, but two-frequency-dependent, $\Lambda_{\text{imp}}^\eta(i\omega, i\Omega)$ computed from a

¹Other decouplings are possible, for instance, index I can run only on $0, z$ (charge and longitudinal spin channel only). In this case, U^{ch} and U^{sp} obey the relation $U = U^{\text{ch}} - U^{\text{sp}}$. This decoupling breaks the rotation symmetry of the action.

²The influence of this choice is investigated in Supplemental Material D [66].

self-consistent quantum impurity problem:

$$\Lambda^\eta(\mathbf{k}, \mathbf{q}, i\omega, i\Omega) \approx \Lambda_{\text{imp}}^\eta(i\omega, i\Omega). \quad (6)$$

This strategy differs radically from DMFT, EDMFT, and $GW+DMFT$ which approximate the self-energy Σ (and P), and $D\Gamma A$, which approximates four-leg vertices, not Λ . It implies that our Σ and P [computed from Eqs. (5a) and (5b)] are, in some parameter regimes, strongly *momentum dependent* while containing *local* vertex corrections essential to capture the Mott physics [50].

The action of the impurity model reads

$$S_{\text{imp}} = - \iint_0^\beta d\tau d\tau' \sum_\sigma c_{\sigma\tau}^* \mathcal{G}^{-1}(\tau - \tau') c_{\sigma\tau'} + \frac{1}{2} \sum_{I=0,x,y,z} \iint_0^\beta d\tau d\tau' n_\tau^I \mathcal{U}^I(\tau - \tau') n_{\tau'}^I. \quad (7)$$

This is an Anderson impurity with retarded charge-charge ($I = 0$) and spin-spin ($I = x, y, z$) interactions. The bosonic fields ϕ^I have been integrated out to obtain a fermionic action with retarded interactions amenable to numerical computations. We compute the fermionic three-point correlation functions to reconstruct the electron-boson vertex $\Lambda_{\text{imp}}^\eta$ (as shown in Supplemental Material B [66]). Finally, \mathcal{G} and \mathcal{U}^η derive from the self-consistency conditions as follows,

$$\mathcal{G}^{-1}(i\omega) = G_{\text{loc}}^{-1}(i\omega) + \Sigma_{\text{loc}}(i\omega), \quad (8a)$$

$$[\mathcal{U}^\eta]^{-1}(i\Omega) = [W_{\text{loc}}^\eta]^{-1}(i\Omega) + P_{\text{loc}}^\eta(i\Omega), \quad (8b)$$

where, for any X , $X_{\text{loc}}(i\omega) \equiv \sum_{\mathbf{k}} X(\mathbf{k}, i\omega)$. At convergence, this ensures that $G_{\text{loc}} = G_{\text{imp}}$ and $W_{\text{loc}}^\eta = W_{\text{imp}}^\eta$. W^η and the susceptibility χ^η are related by

$$W^\eta(\mathbf{q}, i\Omega) = U^\eta - U^\eta \chi^\eta(\mathbf{q}, i\Omega) U^\eta. \quad (9)$$

The computational scheme is illustrated in Fig. 1. From $\Lambda_{\text{imp}}^\eta(i\omega, i\Omega)$, we compute $\Sigma(\mathbf{k}, i\omega)$ and $P^\eta(\mathbf{q}, i\Omega)$, which are then used to compute \mathcal{G} and \mathcal{U}^η for (7). We solve Eq. (7) exactly by a continuous-time quantum Monte Carlo algorithm [69] in the hybridization expansion [70] with retarded density-density [71] and vector spin-spin interactions [72]. The computation of the three-point functions is implemented following Ref. [73]. We iterate until convergence is reached. Our implementation is based on the TRIQS library [74]. Equation (7) could also be solved by an interaction-expansion solver.

This construction makes TRILEX exact in two limits: (i) at small interaction strengths, the local vertex reduces to the bare, frequency-independent vertex λ^η so that Σ is given by one-loop diagrams, as in spin-fluctuation theory in its simplest form (spin channel only), the GW approximation (charge channel only), or in FLEX limited to particle-hole diagrams; similarly, P^η turns into the ‘‘bubble’’ diagram; (ii) in the atomic limit ($t = 0$), the effective local action turns into an atomic problem, $\Lambda_{\text{imp}}^\eta$ into the atomic vertex Λ_{at}^η [Eq. (A1)], and Σ and P^η become local, atomic self-energies.

Let us now apply the TRILEX method to the Hubbard model on a square lattice. All energies are given in units of

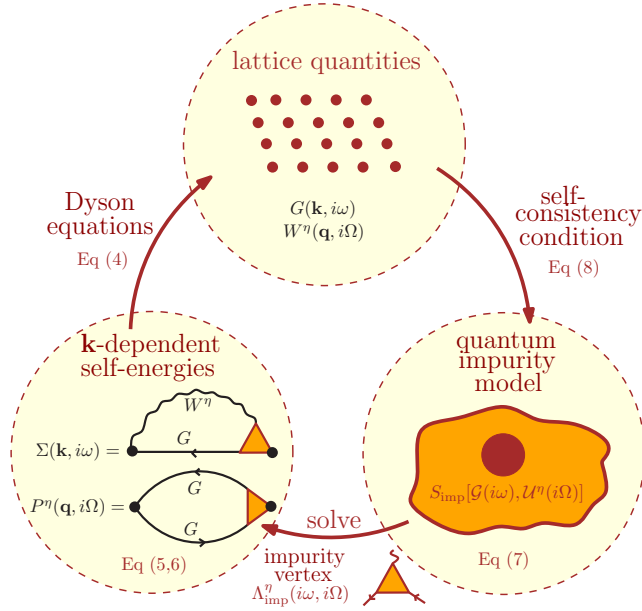


FIG. 1. (Color online) The TRILEX self-consistency loop.

the half bandwidth $D = 4|t|$. The Brillouin zone is discretized on a 64×64 momentum mesh.³ We restrict ourselves to the paramagnetic normal phase.

³We have checked that the 64×64 discretization yields the same results as the 32×32 discretization.

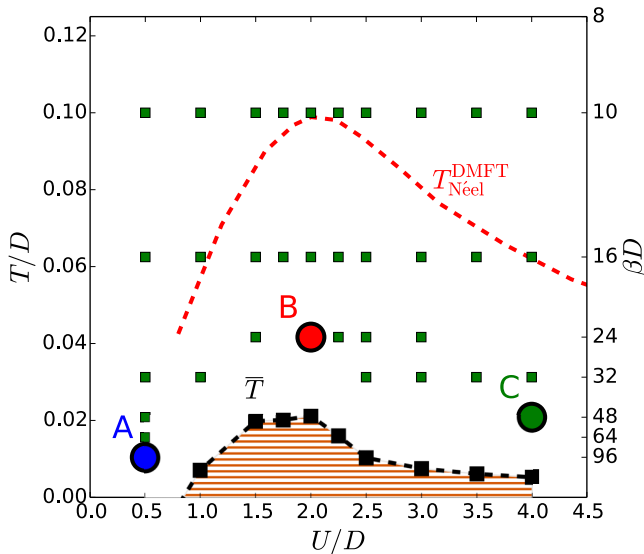


FIG. 2. (Color online) (T, U) phase diagram (half filling, $t' = 0$). The green squares denote converged TRILEX solutions. A, B, and C are defined as (A) $\beta D = 96$, $U/D = 0.5$, (B) $\beta D = 24$, $U/D = 2$, and (C) $\beta D = 48$, $U/D = 4$. The red dotted line denotes $T_{\text{Néel}}^{\text{DMFT}}$ for the square lattice (from Ref. [68]). The black squares denote \bar{T} (temperature below which one cannot obtain stable solutions, hatched region); the black dashed line is a guide to the eye.

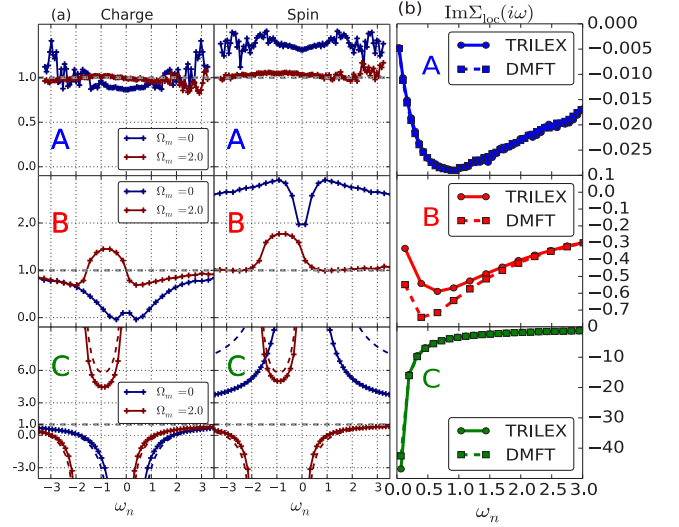


FIG. 3. (Color online) Left: Evolution of the local vertex $\text{Re } \Lambda_{\text{imp}}^{\eta}(i\omega_n, i\Omega_m)$ as a function of ω_n (half filling, $t' = 0$). A, B, and C are defined in Fig. 2. The dashed lines denote the atomic vertex $\Lambda_{\text{at}}^{\eta}$ [Eq. (A1)]. Right: $\text{Im } \Sigma_{\text{loc}}(i\omega_n)$ for TRILEX and DMFT (paramagnetic phase).

In Fig. 2, we present the phase diagram in the (T, U) plane at half filling. We obtain converged solutions until a temperature \bar{T} (see below). The evolution of the local vertex and self-energy (respectively lattice self-energy and polarization) is presented in Fig. 3 (respectively Fig. 4) for the points A, B, and C of Fig. 2. At weak coupling (point A), the local vertex $\Lambda_{\text{imp}}^{\eta}(i\omega, i\Omega)$ reduces to the bare vertex $\lambda = 1$ at large frequencies, up to numerical noise [Fig. 3(a), upper panels]. The spin polarization

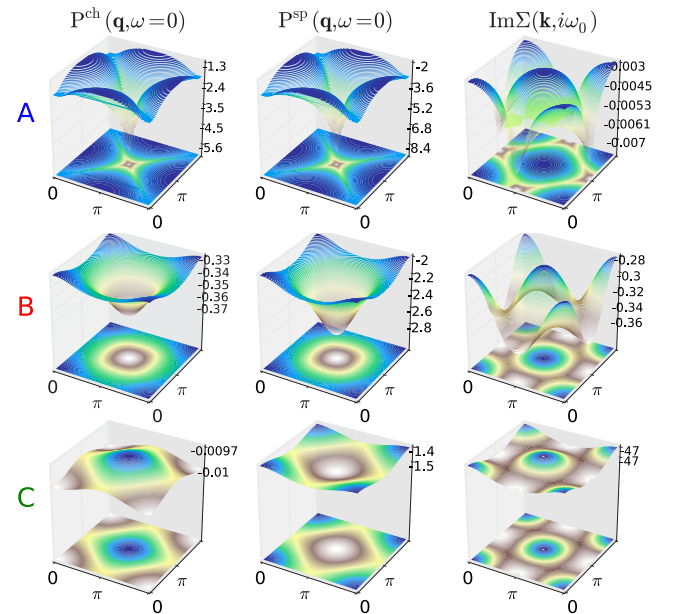


FIG. 4. (Color online) Momentum dependence of the self-energy and polarization (half filling, $t' = 0$). A, B, and C are defined in Fig. 2. Left: $\text{Re } P^{\text{ch}}(\mathbf{q}, \omega = 0)$. Middle: $\text{Re } P^{\text{sp}}(\mathbf{q}, \omega = 0)$. Right: $\text{Im } \Sigma(\mathbf{k}, i\omega_0)$.

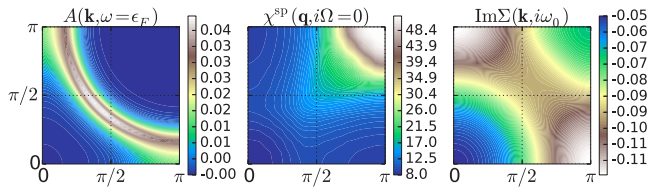


FIG. 5. (Color online) From left to right: $A(\mathbf{k}, \omega = \epsilon_F)$, $\chi(\mathbf{q}, i\Omega = 0)$, and $\text{Im}\Sigma(\mathbf{k}, i\omega_n)$ in the doped case: $U/D = 1.8$, $t' = -0.4t$, $\beta D = 96$, $\delta = 10\%$.

[hence the spin susceptibility—see Eq. (9)] becomes sharply peaked at the AF wave vector $\mathbf{Q} = (\pi, \pi)$ (Fig. 4, upper panels), reflecting the nesting features of the Fermi surface. As a result, the self-energy acquires a strong \mathbf{k} dependence at $(\pi, 0)$ (Fig. 4), but its local part is the same as the DMFT self-energy [Fig. 3(b)]. At strong coupling (point C), the vertex becomes similar to the atomic vertex [Fig. 3(a), lower panels]. Furthermore, the self-energy and polarization are weakly momentum dependent (Fig. 4, lower panels), in agreement with cluster DMFT calculations; the self-energy of TRILEX is very close to the DMFT self-energy [Fig. 3(b)]. Finally, at intermediate coupling (point B), $\Lambda_{\text{imp}}^{\eta}(i\omega, i\Omega)$ acquires frequency structures which interpolate between A and C [Fig. 3(a), middle panels], while Σ is strongly momentum dependent and its local part departs from the DMFT self-energy [Fig. 3(b), middle panels]. Interestingly, the TRILEX self-energy is more coherent than the DMFT self-energy, contrary to the trend observed in cluster DMFT [75]. This may be due to the absence of short-range singlet physics in TRILEX which may be investigated using a small cluster extension.

Contrary to DMFT, the convergence of metastable paramagnetic solutions below a long-range ordering temperature is not possible, since the susceptibilities are not by-products of the calculation, but directly feed back into the self-consistency loop through W^{η} [see Eq. (9)]. We obtain stable paramagnetic solutions at much lower temperatures compared to the Néel temperature computed in DMFT [68] until \bar{T} , as a result of nonlocal fluctuations beyond DMFT. The temperature \bar{T} is determined by extrapolating the inverse static AF susceptibility (see Fig. A1 in the Supplemental Material [66]). Below and in the vicinity of \bar{T} , we obtain unstable solutions because of very small denominators in W^{sp} . Whether we have, within our approximate scheme, finite but very large correlation lengths (as seen, e.g., in Ref. [57]) or an actual AF transition (thus violating the Mermin-Wagner theorem), is left for future studies.

Let us now turn to the effect of doping. In Fig. 5, we present results for $t' = -0.4t$, $\beta D = 96$, and an intermediate interaction strength ($U = 1.8$, close to point B). The spectral function displays Fermi arcs (Fig. 5, left panel), as observed in experiments [76] and in cluster DMFT [35,37,38,42–44,77]. Let us emphasize that this is obtained by solving a *single-site* quantum impurity problem, a far easier task than solving cluster impurities. The Fermi arc is a consequence of the large static spin susceptibility at the AF wave vector (Fig. 5, middle panel), which translates into a large imaginary part of the self-energy (Fig. 5, right panel). The corresponding variation of the spectral weight on the Fermi surface is rather mild compared to the experimental results due to the moderate correlation length ($\xi_{\text{AF}} \sim 2$ unit spacings) for these parameters. This variation is also smaller than cluster DMFT results, which may indicate that improving the description of short-range correlations will yield closer agreement to experiments.

Finally, we examine the influence of the ratio between the interaction in the charge and the spin channel. We observe that it does not impact either the fact that one can obtain stable solutions much below the DMFT Néel temperature (\bar{T} mildly depends on the ratio), or the fulfillment of sum rules on the charge and spin susceptibility (see Supplemental Material D [66]). We have also tried alternative self-consistency conditions, e.g., $\chi_{\text{loc}}^{\eta} = \chi_{\text{imp}}^{\eta}$ instead of $W_{\text{loc}}^{\eta} = W_{\text{imp}}^{\eta}$. This, however, leads to a positive $\mathcal{U}^{\text{sp}}(\tau)$ and hence to a severe sign problem in the quantum Monte Carlo at low temperatures.

In conclusion, we have presented the TRILEX formalism, which encompasses long-range spin-fluctuation effects and Mott physics. Because the competition between spin fluctuations and Mott physics can be described already at the single-site level, this computationally lightweight method may be a good starting point for studying correlated multiorbital systems where spin fluctuations play an important role, such as pnictide superconductors. Future investigations will include the extension to cluster schemes that interpolate between the single-site approximation and the exact solution of the model. With this extension, TRILEX will capture both long-range and short-range fluctuations. Moreover, the convergence of the method with cluster size may depend on the decoupling channel and, when done in the physically relevant channel, may be faster than cluster DMFT methods.

We acknowledge useful discussions with S. Andergassen, S. Biermann, M. Ferrero, A. Georges, D. Manske, G. Misguich, J. Otsuki, and A. Toschi. We thank H. Hafermann for help with implementing the measurement of the three-point correlation function. This work is supported by the FP7/ERC, under Grant Agreement No. 278472-MottMetals. Part of this work was performed using HPC resources from GENCI-TGCC (Grant No. 2015-t2015056112).

- [1] A. V. Chubukov, D. Pines, and J. Schmalian, in *The Physics of Conventional and Unconventional Superconductors*, edited by K. H. Bennemann and J. B. Ketterson (Springer, Berlin, 2002), Chap. 22, p. 1349.
 [2] K. B. Efetov, H. Meier, and C. Pépin, *Nat. Phys.* **9**, 442 (2013).

- [3] Y. Wang and A. Chubukov, *Phys. Rev. B* **90**, 035149 (2014).
 [4] M. A. Metlitski and S. Sachdev, *Phys. Rev. B* **82**, 075128 (2010).
 [5] F. Onufrieva and P. Pfeuty, *Phys. Rev. Lett.* **102**, 207003 (2009).
 [6] F. Onufrieva and P. Pfeuty, *Phys. Rev. Lett.* **109**, 257001 (2012).

- [7] Y. M. Vilk, L. Chen, and A.-M. S. Tremblay, *Phys. Rev. B* **49**, 13267(R) (1994).
- [8] A.-M. Daré, Y. M. Vilk, and A.-M. S. Tremblay, *Phys. Rev. B* **53**, 14236 (1996).
- [9] Y. M. Vilk and A.-M. S. Tremblay, *Europhys. Lett.* **33**, 159 (1996).
- [10] Y. Vilk and A.-M. S. Tremblay, *J. Phys. I* **7**, 1309 (1997).
- [11] A.-M. S. Tremblay, in *Theoretical Methods for Strongly Correlated Systems*, edited by A. Avella and F. Mancini, Springer Series in Solid-State Sciences Vol. 171 (Springer, Berlin, 2011), pp. 409–453.
- [12] L. Hedin, *Phys. Rev.* **139**, A796 (1965).
- [13] N. Bickers and D. Scalapino, *Ann. Phys.* **193**, 206 (1989).
- [14] P. W. Anderson, *Science* **235**, 1196 (1987).
- [15] A. Georges, G. Kotliar, W. Krauth, and M. J. Rozenberg, *Rev. Mod. Phys.* **68**, 13 (1996).
- [16] A. I. Lichtenstein and M. I. Katsnelson, *Phys. Rev. B* **62**, R9283 (2000).
- [17] G. Kotliar, S. Y. Savrasov, G. Pálsson, and G. Biroli, *Phys. Rev. Lett.* **87**, 186401 (2001).
- [18] M. H. Hettler, A. N. Tahvildar-Zadeh, M. Jarrell, T. Pruschke, and H. R. Krishnamurthy, *Phys. Rev. B* **58**, R7475 (1998).
- [19] M. H. Hettler, M. Mukherjee, M. Jarrell, and H. R. Krishnamurthy, *Phys. Rev. B* **61**, 12739 (2000).
- [20] T. A. Maier, M. Jarrell, T. Pruschke, and M. H. Hettler, *Rev. Mod. Phys.* **77**, 1027 (2005).
- [21] G. Kotliar, S. Y. Savrasov, K. Haule, V. S. Oudovenko, O. Parcollet, and C. A. Marianetti, *Rev. Mod. Phys.* **78**, 865 (2006).
- [22] B. Kyung, D. Sénéchal, and A.-M. S. Tremblay, *Phys. Rev. B* **80**, 205109 (2009).
- [23] G. Sordi, P. Sémon, K. Haule, and A.-M. S. Tremblay, *Phys. Rev. Lett.* **108**, 216401 (2012).
- [24] M. Civelli, M. Capone, A. Georges, K. Haule, O. Parcollet, T. D. Stanescu, and G. Kotliar, *Phys. Rev. Lett.* **100**, 046402 (2008).
- [25] M. Ferrero, O. Parcollet, A. Georges, G. Kotliar, and D. N. Basov, *Phys. Rev. B* **82**, 054502 (2010).
- [26] E. Gull, O. Parcollet, and A. J. Millis, *Phys. Rev. Lett.* **110**, 216405 (2013).
- [27] A. Macridin, M. Jarrell, and Th. Maier, *Phys. Rev. B* **70**, 113105 (2004).
- [28] T. A. Maier, M. Jarrell, A. Macridin, and C. Slezak, *Phys. Rev. Lett.* **92**, 027005 (2004).
- [29] T. A. Maier, M. Jarrell, T. C. Schulthess, P. R. C. Kent, and J. B. White, *Phys. Rev. Lett.* **95**, 237001 (2005).
- [30] T. A. Maier, M. S. Jarrell, and D. J. Scalapino, *Phys. Rev. Lett.* **96**, 047005 (2006).
- [31] E. Gull, M. Ferrero, O. Parcollet, A. Georges, and A. J. Millis, *Phys. Rev. B* **82**, 155101 (2010).
- [32] S. X. Yang, H. Fotsó, S. Q. Su, D. Galanakis, E. Khatami, J. H. She, J. Moreno, J. Zaanen, and M. Jarrell, *Phys. Rev. Lett.* **106**, 047004 (2011).
- [33] A. Macridin and M. Jarrell, *Phys. Rev. B* **78**, 241101(R) (2008).
- [34] A. Macridin, M. Jarrell, T. A. Maier, P. R. C. Kent, and E. D’Azevedo, *Phys. Rev. Lett.* **97**, 036401 (2006).
- [35] M. Jarrell, T. A. Maier, C. Huscroft, and S. Moukouri, *Phys. Rev. B* **64**, 195130 (2001).
- [36] D. Bergeron, V. Hankevych, B. Kyung, and A.-M. S. Tremblay, *Phys. Rev. B* **84**, 085128 (2011).
- [37] B. Kyung, V. Hankevych, A.-M. Daré, and A.-M. S. Tremblay, *Phys. Rev. Lett.* **93**, 147004 (2004).
- [38] B. Kyung, S. S. Kancharla, D. Sénéchal, A.-M. S. Tremblay, M. Civelli, and G. Kotliar, *Phys. Rev. B* **73**, 165114 (2006).
- [39] S. Okamoto, D. Sénéchal, M. Civelli, and A.-M. S. Tremblay, *Phys. Rev. B* **82**, 180511 (2010).
- [40] G. Sordi, K. Haule, and A.-M. S. Tremblay, *Phys. Rev. Lett.* **104**, 226402 (2010).
- [41] G. Sordi, P. Sémon, K. Haule, and A.-M. S. Tremblay, *Sci. Rep.* **2**, 547 (2012).
- [42] M. Civelli, M. Capone, S. S. Kancharla, O. Parcollet, and G. Kotliar, *Phys. Rev. Lett.* **95**, 106402 (2005).
- [43] M. Ferrero, P. S. Cornaglia, L. De Leo, O. Parcollet, G. Kotliar, and A. Georges, *Europhys. Lett.* **85**, 57009 (2009).
- [44] M. Ferrero, P. S. Cornaglia, L. De Leo, O. Parcollet, G. Kotliar, and A. Georges, *Phys. Rev. B* **80**, 064501 (2009).
- [45] E. Gull, O. Parcollet, P. Werner, and A. J. Millis, *Phys. Rev. B* **80**, 245102 (2009).
- [46] N. S. Vidhyadhiraja, A. Macridin, C. Sen, M. Jarrell, and M. Ma, *Phys. Rev. Lett.* **102**, 206407 (2009).
- [47] P. Sun and G. Kotliar, *Phys. Rev. B* **66**, 085120 (2002).
- [48] P. Sun and G. Kotliar, *Phys. Rev. Lett.* **92**, 196402 (2004).
- [49] S. Biermann, F. Aryasetiawan, and A. Georges, *Phys. Rev. Lett.* **90**, 086402 (2003).
- [50] T. Ayrál, P. Werner, and S. Biermann, *Phys. Rev. Lett.* **109**, 226401 (2012).
- [51] T. Ayrál, S. Biermann, and P. Werner, *Phys. Rev. B* **87**, 125149 (2013).
- [52] P. Hansmann, T. Ayrál, L. Vaugier, P. Werner, and S. Biermann, *Phys. Rev. Lett.* **110**, 166401 (2013).
- [53] L. Huang, T. Ayrál, S. Biermann, and P. Werner, *Phys. Rev. B* **90**, 195114 (2014).
- [54] C. Taranto, S. Andergassen, J. Bauer, K. Held, A. Katanin, W. Metzner, G. Rohringer, and A. Toschi, *Phys. Rev. Lett.* **112**, 196402 (2014).
- [55] A. Toschi, A. A. Katanin, and K. Held, *Phys. Rev. B* **75**, 045118 (2007).
- [56] A. A. Katanin, A. Toschi, and K. Held, *Phys. Rev. B* **80**, 075104 (2009).
- [57] T. Schäfer, F. Geles, D. Rost, G. Rohringer, E. Arrigoni, K. Held, N. Blümer, M. Aichhorn, and A. Toschi, *Phys. Rev. B* **91**, 125109 (2015).
- [58] A. Valli, T. Schäfer, P. Thunström, G. Rohringer, S. Andergassen, G. Sangiovanni, K. Held, and A. Toschi, *Phys. Rev. B* **91**, 115115 (2015).
- [59] A. N. Rubtsov, M. I. Katsnelson, and A. I. Lichtenstein, *Phys. Rev. B* **77**, 033101 (2008).
- [60] A. N. Rubtsov, M. I. Katsnelson, and A. I. Lichtenstein, *Ann. Phys.* **327**, 1320 (2012).
- [61] E. G. C. P. van Loon, A. I. Lichtenstein, M. I. Katsnelson, O. Parcollet, and H. Hafermann, *Phys. Rev. B* **90**, 235135 (2014).
- [62] H. Hafermann, S. Brener, A. N. Rubtsov, M. I. Katsnelson, and A. I. Lichtenstein, *J. Phys.: Condens. Matter* **21**, 064248 (2009).
- [63] A. M. Sengupta and A. Georges, *Phys. Rev. B* **52**, 10295 (1995).
- [64] H. Kajueter, Interpolating perturbation scheme for correlated electron systems, Ph.D. thesis, Rutgers University, 1996.
- [65] Q. Si and J. L. Smith, *Phys. Rev. Lett.* **77**, 3391 (1996).
- [66] See Supplemental Material at <http://link.aps.org/supplemental/10.1103/PhysRevB.92.115109> for details on the computation of the vertex, on the estimation of \bar{T} and on the influence of the decoupling choice.

- [67] F. Aryasetiawan and S. Biermann, *Phys. Rev. Lett.* **100**, 116402 (2008).
- [68] J. Kuneš, *Phys. Rev. B* **83**, 085102 (2011).
- [69] A. N. Rubtsov, V. V. Savkin, and A. I. Lichtenstein, *Phys. Rev. B* **72**, 035122 (2005).
- [70] P. Werner, A. Comanac, L. de' Medici, M. Troyer, and A. J. Millis, *Phys. Rev. Lett.* **97**, 076405 (2006).
- [71] P. Werner and A. J. Millis, *Phys. Rev. Lett.* **99**, 146404 (2007).
- [72] J. Otsuki, *Phys. Rev. B* **87**, 125102 (2013).
- [73] H. Hafermann, *Phys. Rev. B* **89**, 235128 (2014).
- [74] O. Parcollet, M. Ferrero, T. Ayrat, H. Hafermann, P. Seth, and I. S. Krivenko, *Comput. Phys. Commun.* **195**, 401 (2015).
- [75] H. Park, K. Haule, and G. Kotliar, *Phys. Rev. Lett.* **101**, 186403 (2008).
- [76] A. Damascelli, Z. Hussain, and Z. Shen, *Rev. Mod. Phys.* **75**, 473 (2003).
- [77] B. Kyung, G. Kotliar, and A.-M. S. Tremblay, *Phys. Rev. B* **73**, 205106 (2006).



Computational developments

R.1 Paper 6: Parcollet *et al.* (2015)



Contents lists available at ScienceDirect

Computer Physics Communications

journal homepage: www.elsevier.com/locate/cpc

TRIQS: A toolbox for research on interacting quantum systems[☆]



Olivier Parcollet^{a,*}, Michel Ferrero^b, Thomas Ayrat^{a,b}, Hartmut Hafermann^a,
Igor Krivenko^c, Laura Messio^{d,a}, Priyanka Seth^b

^a Institut de Physique Théorique (IPhT), CEA, CNRS, 91191 Gif-sur-Yvette, France

^b Centre de Physique Théorique, Ecole Polytechnique, CNRS, 91128 Palaiseau Cedex, France

^c I. Institut für Theoretische Physik, Uni. Hamburg, Jungiusstraße 9, 20355 Hamburg, Germany

^d LPTMC, UMR 7600 CNRS, Université Pierre et Marie Curie, 75252 Paris, France

ARTICLE INFO

Article history:

Received 9 April 2015

Accepted 19 April 2015

Available online 8 May 2015

Keywords:

Many-body physics

Strongly-correlated systems

DMFT

Monte Carlo

ab initio calculations

C++

Python

ABSTRACT

We present the TRIQS library, a Toolbox for Research on Interacting Quantum Systems. It is an open-source, computational physics library providing a framework for the quick development of applications in the field of many-body quantum physics, and in particular, strongly-correlated electronic systems. It supplies components to develop codes in a modern, concise and efficient way: e.g. Green's function containers, a generic Monte Carlo class, and simple interfaces to HDF5. TRIQS is a C++/Python library that can be used from either language. It is distributed under the GNU General Public License (GPLv3). State-of-the-art applications based on the library, such as modern quantum many-body solvers and interfaces between density-functional-theory codes and dynamical mean-field theory (DMFT) codes are distributed along with it.

Program summary

Program title: TRIQS

Catalogue identifier: AEWV_v1_0

Program summary URL: http://cpc.cs.qub.ac.uk/summaries/AEWV_v1_0.html

Program obtainable from: CPC Program Library, Queen's University, Belfast, N. Ireland

Licensing provisions: GNU General Public License (GPLv3)

No. of lines in distributed program, including test data, etc.: 93228

No. of bytes in distributed program, including test data, etc.: 2979367

Distribution format: tar.gz

Programming language: C++/Python.

Computer: Any architecture with suitable compilers including PCs and clusters.

Operating system: Unix, Linux, OSX.

RAM: Highly problem-dependent

Classification: 7.3, 20.

External routines: cmake, mpi, boost, FFTW, GMP, BLAS, LAPACK, HDF5, NumPy, SciPy, h5py, mpi4py, mako.

Nature of problem:

Need for a modern programming framework to quickly write simple, efficient and higher-level code applicable to the studies of strongly-correlated electron systems.

[☆] This paper and its associated computer program are available via the Computer Physics Communication homepage on ScienceDirect (<http://www.sciencedirect.com/science/journal/00104655>).

* Corresponding author.

E-mail addresses: olivier.parcollet@cea.fr (O. Parcollet), michel.ferrero@polytechnique.edu (M. Ferrero), thomas.ayrat@polytechnique.edu (T. Ayrat), hartmut.hafermann@cea.fr (H. Hafermann), ikrivenk@physnet.uni-hamburg.de (I. Krivenko), messio@lptmc.jussieu.fr (L. Messio), priyanka.seth@polytechnique.edu (P. Seth).

Solution method:

We present a C++/Python open-source computational library that provides high-level abstractions for common objects and various tools in the field of quantum many-body physics, thus forming a framework for developing applications.

Running time:

Tests take less than a minute. Otherwise it is highly problem dependent (from minutes to several days).

© 2015 Elsevier B.V. All rights reserved.

1. Introduction

In this paper, we present the 1.2 release of the TRIQS project (Toolbox for Research in Interacting Quantum Systems), a free software library written in Python and C++ for the implementation of algorithms in quantum many-body physics. TRIQS is distributed under the GNU General Public License (GPLv3).

Strongly-correlated quantum systems are a central challenge for theoretical condensed matter physics with a wide range of remarkable phenomena such as metal–insulator transitions, high-temperature superconductivity and magnetism. In the last two decades, tremendous progress has been made in the field of algorithms for the quantum many-body problem, both in refining existing techniques and in developing new systematic approximations and algorithms. Methods to address the quantum many-body problem include dynamical mean-field theory (DMFT) [1,2] and its cluster [3] or diagrammatic extensions [4,5] or the density matrix renormalisation group (DMRG) [6]. DMFT methods can also now be combined with more traditional electronic structure methods such as density functional theory (DFT) leading to *ab initio* realistic computational techniques for strongly-correlated materials [2]. Several collaborative software development efforts have made some of these theoretical developments largely accessible, e.g. Refs. [7–9].

The purpose of the TRIQS project is to provide a modern framework of basic building blocks in C++ and Python. This is needed for the rapid implementation of a broad spectrum of methods. Applications range from simple interactive phenomenological analysis in Python to high-performance quantum impurity solvers in C++. At this stage, TRIQS focuses primarily on, but is not limited to, solid-state physics computations, diagrammatic approximations and methods of the DMFT family (DMFT, clusters and underlying quantum impurity solvers).

A particular emphasis is placed on the documentation, in particular in providing short code examples that can be reused immediately (in Python and C++). Full documentation of the project is available online: <http://ipht.cea.fr/triqs>.

Several applications have already been built with the TRIQS library, and some of them are publicly distributed. Let us mention a state-of-the-art implementation of the hybridisation-expansion quantum impurity solver `CTHYB` (<http://ipht.cea.fr/triqs/applications/cthyb/>) and the `DFT TOOLS` project which provides an interface between DMFT and DFT packages such as `WIEN2K` for realistic computations for strongly-correlated materials (http://ipht.cea.fr/triqs/applications/dft_tools/). Since these applications are not part of the library itself and involve a different set of authors, they will be presented in separate publications. However, they are distributed along with the TRIQS library under GPL license and are available for download on GitHub (<https://github.com/triqs>).

The TRIQS project uses professional code development methods to achieve the best possible quality for the library and the applications, including: (i) *version control* using `git`; (ii) *systematic code review* by the main TRIQS developers; (iii) *test-driven development*: features of the library are first designed with a series of test cases. When the implementation is completed, they become the non-regression tests executed during the installation process.

This paper is organised as follows: we start in Section 2 with the main motivations for the project. In Section 3, we outline the structure of the TRIQS project. Section 4 summarises our citation policy. In Section 5, we discuss the prerequisites to efficient usage of TRIQS and Section 6 describes the portability of the library. In Section 7, we provide two illustrating examples to give a flavour of the possibilities offered by the library: we show that TRIQS makes it possible to write a DMFT self-consistency loop in one page of Python, and, in another example, how equations can be coded efficiently in C++. In Section 8 we review the most important library components. In the Appendix we present the implementation of a fully working, MPI-parallelised, modern continuous-time quantum Monte Carlo algorithm (the so-called CT-INT algorithm [10,11]) in about 200 lines. This example illustrates how TRIQS allows one to design a complex, yet short, readable and extensible code.

2. Motivations

The implementation of modern algorithms for quantum many-body systems raises several practical challenges.

Complexity: Theoretical methods and algorithms are becoming increasingly complex (e.g. quantum Monte Carlo [10–13] and dual boson [14] methods). They are hence more difficult to implement, debug and maintain. This is especially true for realistic computations with methods of the DMFT family, where one has to handle not only the complexity of the many-body problem but also the various aspects (orbitals, lattices) of real materials, which usually require a well-organised team effort.

Versatility/Agility: Algorithms are changing and improving rapidly, sometimes by orders of magnitude for some problems [15]. This can lead to a possibly quick obsolescence of a given implementation. To address new physics problems requires regular and substantial modifications of existing implementations. Moreover, there are numerous possibilities for new algorithms which need to be tested quickly.

Performance: Modern algorithms are still quite demanding on resources, e.g. quantum Monte Carlo methods. Hence, the performance of the codes is critical and a simple implementation in a high-level language is usually not sufficient in practice.

Reproducibility: The central role and the growing complexity of the algorithms in our field reinforces the need for reproducibility, which is central to any scientific endeavour. Therefore, the results obtained by a numerical computation should in principle be published systematically along with the code that produced them, in order to allow others to reproduce, falsify or improve on them. This requires codes to be readable (i.e. written to be read by other people than their author) and relatively quick to produce.

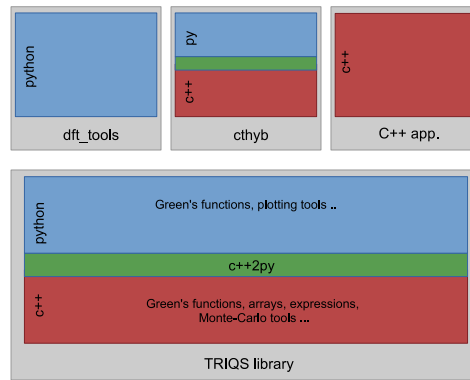


Fig. 1. Structure of the TRIQS project.

To address these challenges, one needs readable, clear and simple implementations with reusable components provided through high-level abstractions. We emphasise that this is *not* in contradiction with the requirement of high performance. The combination of a higher level of abstraction with high performance is achieved using modern programming techniques (e.g. generic programming). The purpose of the TRIQS project is to find and efficiently implement the relevant abstractions, basic components and algorithms for our domain.

3. Structure

The TRIQS framework is depicted in Fig. 1: the core library is at the root (bottom) consisting of basic building blocks, which are used in a series of applications (top). The applications can be in pure python (e.g. DFT TOOLS), in C++ with a Python interface (e.g. CTHYB), or even in pure C++. The subject of this paper is the core library.

The components of the TRIQS library can be used both in Python and in C++: C++ brings the performance needed for applications where speed is critical (like many-body solvers) and the type safety of a compiled language. On the other hand, Python is typically used as a higher-level interface for data analysis, investigation of phenomenological approaches, and tasks related to reproducibility. Most objects of the library are written in C++ and exposed to Python using a specially designed tool described in Section 8.8. As a result, TRIQS can be used together with all the modern scientific tools of the Python community, in particular with IPython notebooks [16] which are recommended for an optimal interactive usage of the library in Python.

4. Citation policy

We kindly request that the present paper be cited in any published work using the TRIQS library directly (e.g. for data analysis) or indirectly (e.g. through TRIQS based applications). In the latter case, this citation should be added to the citations already requested by the application. This helps the TRIQS developers to better keep track of projects using the library and provides them guidance for future developments.

5. Programming requirements

TRIQS can be used *at different levels of expertise*, starting from basic Python interactive usage to development of cutting-edge mixed Python/C++ high-performance and massively parallel codes, and in pure C++.

Most objects, in particular Green's functions, have a rich Python interface, allowing one to easily plot and manipulate them. For example, simple operations such as value assignment, inversion or output to and input from HDF5 files are all one-line operations, as shown in the examples below.

At the C++ level, the required knowledge to make efficient use of the library is minimised. The systematic usage of *modern C++* (C++11 and C++14) very often lead to simpler syntax than old C++. The library often favours a “functional style” programming and the simplest possible constructions for the C++ user. To fully exploit the capabilities of the library, some understanding of the basic notions of generic programming, such as concepts and templates, is helpful, but not required. More traditional object-oriented notions of C++ such as inheritance or dynamical polymorphism (virtual functions) are not necessary to use the TRIQS library.

6. Portability

TRIQS is written in *modern C++*, i.e. using the C++11 ISO standard. The motivation for this choice is twofold: first, we encourage the users of the library to benefit from the new features of C++, in particular those which produce much simpler code (e.g. `auto`, `for` `auto` loop or lambdas). Second, it dramatically reduces the cost of implementing and maintaining the library itself, since many of the new C++ features are designed to facilitate the use of the metaprogramming techniques needed to implement high-level, high-performance libraries.

As a result, TRIQS requires a C++11 *standard-compliant compiler*. The documentation provides an updated list of tested compilers. When it is available, we recommend using a C++14 compiler for development, in particular to get simpler error messages.

At the Python level, we use the 2.7 versions of Python. Support for Python 3 is planned for later releases. We use the binary hierarchical data format (HDF5) to guarantee portability of user generated data in binary form.

IP(y): Notebook `dmft_bethe` (unsaved changes)

```

File Edit View Insert Cell Kernel Help
Code Cell Toolbar: None

In [1]: from pytriqs.gf.local import *
        from pytriqs.archive import *
        import pytriqs.utility.mpi as mpi
        from pytriqs.applications.impurity_solvers.ctint_tutorial import CtintSolver
        from pytriqs.plot.mpl_interface import oplot

        # Parameters
        U = 2.5 # Hubbard interaction
        mu = U/2.0 # Chemical potential
        half_bandwidth=1.0 # Half bandwidth (energy unit)
        beta = 40.0 # Inverse temperature
        n_iw = 128 # Number of Matsubara frequencies
        n_cycles = 10000 # Number of MC cycles
        delta = 0.1 # delta parameter
        n_iterations = 21 # Number of DMFT iterations

        S = CtintSolver(beta, n_iw) # Initialize the solver

        S.G_iw << SemiCircular(half_bandwidth) # Initialize the Green's function

        with HDFArchive("dmft_bethe.output.h5", 'w') as A:
            A['n_iterations'] = n_iterations # Save a parameter

        for it in range(n_iterations): # DMFT loop
            for name, G0 in S.G0_iw:
                G0 <<= inverse(iOmega_n + mu - (half_bandwidth/2.0)**2 * S.G_iw[name]) # Set G0
            # Change random number generator on final iteration
            random_name = 'mt19937' if it<n_iterations-1 else 'lagged_fibonacci19937'

            S.solve(U, delta, n_cycles, random_name=random_name) # Solve the impurity problem

            G_sym = (S.G_iw['up']+S.G_iw['down'])/2 # Impose paramagnetic solution
            S.G_iw << G_sym

            if mpi.is_master_node():
                A['G%i'%it] = G_sym # Save G from every iteration to file

Starting on 1 Nodes at : 2014-10-22 18:06:12.886058

In [2]: A = HDFArchive("dmft_bethe.output.h5", 'r') # Open file
        n_iterations = A['n_iterations'] # Load a parameter
        for it in range(n_iterations): # Use parameter in the analysis
            if not it%2: oplot(A['G%i'%it].imag, '-o', name='Im G%i'%it) # Plot every second result
            xlim(0,5)

Out[2]: (0, 5)

```

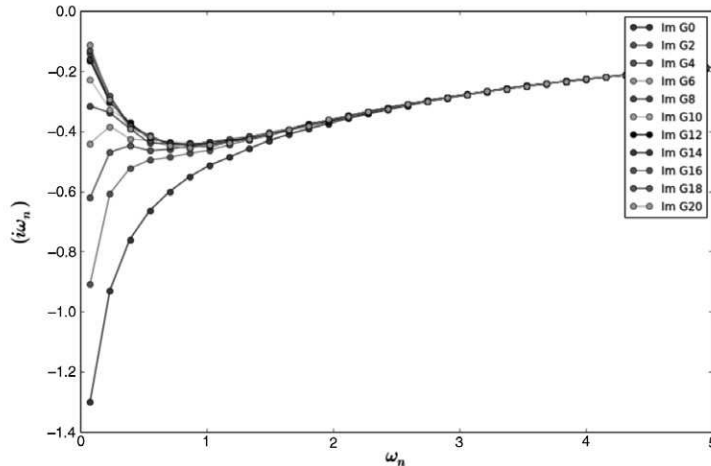


Fig. 2. Screenshot of an IPython notebook executing a DMFT loop using the CT-INT solver.

7. TRIQS in two examples

Here we illustrate the use of the library for two typical tasks encountered in many-body physics; this should give a flavour of the possibilities offered by the library. The first example is a complete DMFT computation implemented in Python, using a continuous-time quantum Monte Carlo solution of the impurity model (which is presented in the Appendix). The second example illustrates the manipulation of Green's functions in C++ within TRIQS.

7.1. A DMFT computation in one page of IPython

This example requires the CT-INT tutorial application to be installed. The installation procedure is described in Section 9.2.

Fig. 2 shows a screenshot of an IPython notebook implementing a DMFT self-consistency loop. The essential steps are to load the solver module, set parameters and an initial guess for Green's function and to loop over the DMFT iterations. The solver module, for which performance is critical, is written in C++ but used from Python. This notebook is available in the sources of the `ctint_tutorial` application (in the `examples` subdirectory) along with the corresponding python script that is suitable for parallel execution.

The Python framework is *highly flexible*. In this example, we exchange the random number generator in the final DMFT iteration to consolidate the result. We could also turn on additional measurements, or implement more sophisticated stopping criteria for the loop. Using the IPython notebook, results can be plotted and analysed interactively. As a minimal example, we load the HDF5 archive from the disk and plot the imaginary part of Green's functions in the second cell of the notebook. Parameters used in the calculation can easily be saved to file and retrieved for data analysis. On a parallel machine, the first part of the script is executed in Python (without the notebook), on multiple cores, while the analysis can still be done in the IPython notebook.

Within this framework, DMFT can readily be explored and practised by non-experts. The major part of the calculation is of course performed by the solver module. In this example, we have used the interaction-expansion continuous-time quantum Monte Carlo (CT-INT) solver. We can easily switch to a more sophisticated hybridisation-expansion continuous-time quantum Monte Carlo algorithm (CT-HYB) solver by loading the appropriate solver module instead. The complete listing of the C++ implementation of the solver module is given and explained in Appendix, as a more detailed illustration of the library's features.

7.2. Easy manipulation of Green's functions in C++

Here, we show how to compute in C++ a hybridisation function $\Delta(\tau)$ in imaginary time given the bare dispersion of a two-dimensional square lattice with nearest neighbour hopping, at chemical potential μ . This is a typical task which is usually performed at the beginning of a DMFT calculation. The necessary steps are the following:

$$G_0(i\omega_n) = \frac{1}{N} \sum_{\mathbf{k}} \frac{1}{i\omega_n + \mu - 2(\cos k_x + \cos k_y)} \quad (1)$$

$$\Delta(i\omega_n) = i\omega_n + \mu - G_0^{-1}(i\omega_n) \quad (2)$$

$$\Delta(\tau) = \frac{1}{\beta} \sum_n \Delta(i\omega_n) e^{-i\omega_n \tau}. \quad (3)$$

The sum over $\mathbf{k} = (k_x, k_y)$ is taken over the Brillouin zone, ω_n is a fermionic Matsubara frequency and β is the inverse temperature. Using the library, these equations are implemented as follows:

Listing 1 Computing the hybridisation

```
#include <triqs/gfs.hpp> 1
using namespace triqs::gfs; 2
using namespace triqs::lattice; 3
int main() { 4
  5
  double beta = 10, mu = 0; 6
  int n_freq = 100, n_pts = 100; 7
  8
  // Green's function on Matsubara frequencies, 1x1 matrix-valued. 9
  auto Delta_iw = gf<imfreq>{{beta, Fermion, n_freq}, {1, 1}}; 10
  auto Gloc = gf<imfreq>{{beta, Fermion, n_freq}, {1, 1}}; 11
  12
  // Green's function in imaginary time, 1x1 matrix-valued. 13
  auto Delta_tau = gf<itime>{{beta, Fermion, 2 * n_freq + 1}, {1, 1}}; 14
  15
  auto bz = brillouin_zone{bravais_lattice{{ {1, 0}, {0, 1} }}}; 16
  auto bz_mesh = regular_bz_mesh{bz, n_pts}; 17
  18
  triqs::clef::placeholder<1> k_; 19
  triqs::clef::placeholder<2> iw_; 20
  21
  // The actual equations 22
  Gloc(iw_) << sum(1/(iw_ + mu - 2*(cos(k_[0]) + cos(k_[1]))), k_ = bz_mesh) 23
  /bz_mesh.size(); // (1) 24
  Delta_iw(iw_) << iw_ + mu - 1 / Gloc(iw_); // (2) 25
  Delta_tau() = inverse_fourier(Delta_iw); // (3) 26
  27
  // Write the hybridization to an HDF5 archive 28
  auto file = triqs::h5::file("Delta.h5", H5F_ACC_TRUNC); 29
  h5_write(file, "Delta_tau", Delta_tau); 30
  h5_write(file, "Delta_iw", Delta_iw); 31
} 32
```

In the implementation of Eqs. (1) and (2) (lines 23–25), we use a compact syntax for the assignment to Green's function container provided by the TRIQS library (the CLEF library, Section 8.5). By definition, this is equivalent to assigning the evaluation of the expression on the right-hand side to the data points of “Green's function”¹ `Delta_iw` on the left and for all Matsubara frequencies in its mesh. `iw_` is a *placeholder*, i.e. a dummy variable standing for all points in Green's function's mesh.

¹ Here we refer Green's function containers and objects representing hybridisation functions or functions with the same signature simply as “Green's functions”.

In line 23, the formal expression made of i_w and $k_$ is summed over the values of $k_$, and assigned to the function for each i_w . Note that no copy is made by this statement, the computation is inlined by the compiler, as if it was written manually. This technique is more concise than writing a for-loop on each variable, reduces the risk of errors and simultaneously increases the readability. Moreover, such techniques come with *no performance penalty* (as indicated by our tests on several standard compilers).

In line, we assign the inverse Fourier transform of $\Delta(\omega)$ to $\Delta(\tau)$ [Eq. (3)]. Note that the high-frequency expansion is part of Green's function container and so is *automatically* computed in lines 23 and 25 (see Section 8.2 for details). It is used to properly treat the discontinuity in the Fourier transformation in line 26.

Finally, Green's functions are stored in an HDF5 file with a simple interface, in a portable manner. The storage conventions are detailed in the reference documentation.

This example is interesting for two reasons: firstly, it shows that the TRIQS library performs a lot of low-lying operations. There is no need to reimplement them and the user can concentrate on the physics; secondly, it shows that one can write quite complex operations concisely, which is necessary in order to write readable codes.

8. Library components

In this section, we provide an overview of the TRIQS library components. We illustrate them either with small examples or in the CT-INT impurity solver example presented in Appendix. The description is neither meant to be complete nor exhaustive; the online reference documentation (<http://ipht.cea.fr/triqs>) will fill the gaps.

8.1. Multidimensional arrays (C++)

TRIQS provides its own multidimensional arrays, with an emphasis on flexibility, performance and the Python interface. It is a fundamental building block for higher-level containers, such as Green's functions. Listing 2 below illustrates some of their features.

Listing 2 Array / matrix example

```
#include <triqs/arrays.hpp>
using namespace triqs::arrays;
int main() {
    auto a = matrix<double>(2, 2); // Declare a 2x2 matrix of double
    auto b = array<double, 3>(5, 2, 2); // Declare a 5x2x2 array of double
    auto c = array<double, 2> {{1,2,3}, {4,5,6}}; // 2x3 array, with initialization
    triqs::clef::placeholder<0> i_;
    triqs::clef::placeholder<1> j_;
    triqs::clef::placeholder<2> k_;
    // Assignment of values using CLEF
    a(i_, j_) << i_ + j_;
    b(i_, j_, k_) << i_ * a(k_, j_);
    std::cout << "a = " << a << std::endl; // Printing
    matrix<double> i = inverse(a); // Inverse using LAPACK
    double d = determinant(a); // Determinant using LAPACK
    auto ac = a; // Make a copy (the container is a regular type)
    ac = a * a + 2 * ac; // Basic operations (uses BLAS for matrix product)
    b(0, range(), range()) = ac; // Assign ac into partial view of b
    // Writing the array into an HDF5 file.
    auto f = triqs::h5::file("a_file.h5", H5F_ACC_TRUNC);
    h5_write(f, "a", a);
    auto m = max_element(abs(b)); // maximum of the absolute value of the array.
    // A more "functional" example: compute the norm sum_{i,j} |A_{ij}|
    auto lambda = [](double r, double x) { return r + std::abs(x); };
    auto norm = fold(lambda)(a, 0);
}
```

The library provides three types of containers: *array* (for multidimensional arrays), *matrix* and *vector* with the following main characteristics:

- **Regular-type semantics:** Just like `std::vector`, these containers have regular-type semantics.
- **Views:** Each container has a corresponding view type (e.g. `array_view`) to e.g. work on slices and partial views.
- **CLEF:** The containers are compatible with CLEF (Section 8.5 and Listing 2) for fast assignment techniques.
- **Python interface:** These containers can be easily converted to and from Python NumPy arrays.
- **Interface to HDF5:** See Section 8.6 and Listing 2.
- **Arithmetics:** Arithmetic operations are implemented using expression templates for optimal performance.
- **BLAS/LAPACK:** A BLAS/LAPACK interface for matrices and vectors is provided for the most common operations.
- **STL compatible iterators:** The containers and views can be traversed using such iterators, or with simple `foreach` constructs.
- *Optionally*, a (slower) debug mode checks for out-of-range operations.

8.2. Green's functions (C++ and Python)

The library provides a special set of containers that allow one to store and manipulate the various Green's functions used in the quantum many-body problem and its algorithms. They are defined on meshes for various domains, they are tensor-, matrix-, or scalar-valued and can be block-diagonal.

Domains currently implemented include real and imaginary frequencies, real and imaginary times, Legendre polynomials, and Brillouin zones. Multiple variable Green's functions are also part of the library, but are restricted to C++14 mode only and are of alpha quality in release 1.2. We will not discuss them in this paper.

Green's functions optionally include a description of their high-frequency behaviour in terms of their moments. Storing this information is important for several operations (e.g. Fourier transformation, frequency summation) where the high-frequency behaviour needs to be treated explicitly. Being part of the object, the singularity is consistently recomputed in all arithmetic operations so that the user need not work out the high-frequency asymptotics. Listing 3 illustrates some basic usage of Green's functions, while a Python example has been given above (Fig. 2).

Listing 3 Green's function example

```
#include <triqs/gfs.hpp>
using namespace triqs;
using namespace triqs::gfs;
using namespace triqs::lattice;
int main() {
    double beta = 10;
    int n_freq = 1000;
    clef::placeholder<0> iw_;
    clef::placeholder<1> k_;
    // Construction of a 1x1 matrix-valued fermionic gf on Matsubara frequencies.
    auto g_iw = gf<imfreq>{{beta, Fermion, n_freq}, {1, 1}};
    // Automatic placeholder evaluation
    g_iw(iw_) << 1 / (iw_ + 2);
    // Inverse Fourier transform to imaginary time
    auto g_tau = gf<imtime>{{beta, Fermion, 2 * n_freq + 1}, {1, 1}};
    g_tau() = inverse_fourier(g_iw); // Fills a full view of g_tau with FFT result
    // Create a block Green's function composed of three blocks,
    // labeled a,b,c and made of copies of the g_iw functions.
    auto G_iw = make_block_gf({"a", "b", "c"}, {g_iw, g_iw, g_iw});
    // A multivariable gf: G(k,omega)
    auto bz = brillouin_zone{bravais_lattice{{{1, 0}, {0, 1}}}};
    auto g_k_iw = gf<cartesian_product<brillouin_zone, imfreq>>{
        {{bz, 100}, {beta, Fermion, n_freq}}, {1, 1}};
    g_k_iw(k_, iw_) << 1 / (iw_ - 2 * (cos(k_(0)) + cos(k_(1))) - 1 / (iw_ + 2));
    // Writing the Green's functions into an HDF5 file.
    auto f = h5::file("file_g_k_iw.h5", H5F_ACC_TRUNC);
    h5_write(f, "g_k_iw", g_k_iw);
    h5_write(f, "g_iw", g_iw);
    h5_write(f, "g_tau", g_tau);
    h5_write(f, "block_gf", G_iw);
}
```

The main characteristics of Green's functions are:

- **Arithmetics:** Just like arrays, Green's functions implement arithmetic operations using **expression templates**.
- **Quick assignment:** The class uses the CLEF component of the TRIQS library for quick assignment (see Section 8.5 and Listing 3).
- **Python interface:** Green's functions are easily shared between Python and C++, see Section 8.8, and can thus be used in conjunction with the Python visualisation tools.
- **Fourier transforms:** TRIQS provides a simple interface to fast Fourier transforms (FFTW). For Green's functions the information about the high-frequency behaviour is used to avoid numerical instabilities.
- **Interface to HDF5.**

8.3. Monte Carlo tools (C++)

The TRIQS library provides several classes for writing Metropolis-like (quantum) Monte Carlo algorithms. In addition to some basic analysis tools, like binning or jackknife, the library mainly contains the `mc_generic` class that implements the Metropolis algorithm (choose a move, try the move, compute Metropolis ratio, reject or accept, etc.) in terms of completely generic *moves* (configuration updates) and *measurements*.

In practice, one just needs to implement the moves and measurements. The only requirement is that they must model their respective *concepts*.² For example, the concept of a move is given by Listing 4. Note in particular that they do not require inheritance or virtual functions, which makes them particularly simple to use.

Listing 4 Concept of a Monte Carlo move

```
struct my_monte_carlo_move {
    // propose a change in the configuration and return the Metropolis ratio
    double attempt();
    // the move has been accepted: modify configuration
    double accept();
    // the move has been rejected: undo configuration changes
    void reject();
};
```

A concrete usage of the class is shown in the CT-INT solver example (Appendix). The class is particularly convenient for complex Monte Carlo algorithms with several moves: the moves are isolated from the implementation of the Metropolis algorithm itself and each move can be implemented independently.

The Monte Carlo is of course automatically MPI-enabled. Furthermore, random number generators can easily be changed dynamically to ensure there is no subtle correlation effect.

Listing 5 illustrates a basic application of the tools for statistical analysis on a correlated random series. Let us assume we have two long vectors V1 and V2 storing (possibly correlated) samples of the random variables X and Y and that we wish to compute estimates of $\langle X \rangle$ and $\langle X \rangle / \langle Y \rangle$, together with the corresponding error bars. In both cases, the correlation between samples has to be removed using a *binning* procedure. This being done, the first computation is quite straightforward, while the second one further requires a jackknife procedure to remove the bias introduced by the nonlinearity. In TRIQS, all these operations are performed by the following code snippet, using a little library similar to e.g. ALPS/alea [7]:

Listing 5 Statistics: error analysis

```
//fill observable with the series
observable<double> X, Y;
for(auto const & x : V1) X << x; //V1: a vector of statistical samples
for(auto const & y : V2) Y << y; //V2: a vector of statistical samples
std::cout << "<X> is approximately " << average_and_error(X) << std::endl;
std::cout << "<X>/<Y> is approx. " << average_and_error(X/Y) << std::endl;
```

$X << x$ fills the observable X (a stack of the samples) with the values x of V1. `average_and_error(X)` computes an estimate of $\langle X \rangle$ and of the error $\Delta \langle X \rangle$, while `average_and_error(X/Y)` computes an estimate of $\langle X \rangle / \langle Y \rangle$ and of $\Delta \langle X \rangle / \langle Y \rangle$.

8.4. Determinant manipulations (C++)

The manipulation of determinants is central to many Monte Carlo approaches to fermionic problems, see e.g. [10–13]. Several cases can be abstracted from the following mathematical problem. Let us consider a function $F(x, y)$ taking real or complex values (the type of the arguments x and y is arbitrary) and the square matrix M defined by

$$M_{ij} = F(x_i, y_j), \quad (4)$$

for two sets of parameters $\{x_i\}$ and $\{y_j\}$ of equal length. The problem consists in quickly updating M and its inverse M^{-1} following successive insertions and removals of one or two lines (labelled by x_i) and columns (labelled by y_j) using the Sherman–Morrison and Woodbury formulas [17,18].

This generic algorithm is implemented in the TRIQS `det_manip` class, using BLAS Level 2 [19,20] internally. The class provides a simple API, in order to make these manipulations as straightforward and efficient as possible.

For optimal efficiency within a Monte Carlo framework, the modifications to the matrices can be done in two steps: a first step which only returns the determinant ratio between the matrix before (M) and after the modification (M'), i.e. $\xi = \det M' / \det M$ (which is generally used in the acceptance rate of a Metropolis move) and a second step which updates the matrix and its inverse. This computationally more expensive step is usually done only if the Monte Carlo move is accepted. An example of this class employed is the CT-INT solver discussed in the Appendix.

8.5. CLEF (C++)

CLEF (Compile-time Lazy Expressions and Functions) is a component of TRIQS which allows one to write expressions with placeholders and functions, and to write quick assignments. For example, the following – quite involved – equation

$$\chi_{\nu\nu'\omega}^{0\sigma\sigma'} = \beta(g_{\nu}^{0\sigma} g_{\nu'}^{0\sigma'} \delta_{\omega} - g_{\nu}^{0\sigma} g_{\nu+\omega}^{0\sigma} \delta_{\nu\nu'} \delta_{\sigma\sigma'}) \quad (5)$$

can be coded as quickly as (variables with underscores denote placeholders)

² In the sense of C++ concepts.

```
chi0(s_, sp_)(nu_, nup_, om_) <<
    beta * (g[s_](nu_) * g[sp_](nup_) * kronecker(om_))
    - beta * (g[s_](nu_) * g[s_](nu_ + om_)
              * kronecker(nu_, nup_) * kronecker(s_, sp_));
```

This writing is clearly much simpler and less error-prone than a more conventional five-fold nested `for`-loop. At the same time, these expressions are inlined and optimised by the compiler, as if the code were written manually. The library also automatically optimises the memory traversal (the order of `for` loops) for performance based on the actual memory layout of the container `chi0`.

The CLEF expressions are very similar to C++ lambdas, except that their variables are found by name (the placeholder) instead of a positional argument (in calling a lambda). This is much more convenient for complex codes.

The precise definition of the automatic assignment is as follows. Any code of the form (e.g. with three placeholders):

```
A(i_, j_, x_) << expression;
```

where `expression` is an expression involving placeholders³ is rewritten by the compiler as follows:

```
trigs_auto_assign(
    A, [](auto& i, auto& j, auto& x) {
        return eval(expression, i_=i, j_=j, x_=x);
    }
);
```

where `trigs_auto_assign` is a free function defined by the container `A`, which fills the container with the result of the evaluation of the lambda, and `eval` evaluates the expression (`eval` is a function and is part of CLEF). The precise details of this operation, such as the memory traversal order, are encoded in this function. The CLEF quick assignment mechanism can therefore easily and efficiently be extended to any object of the library. The library provides adapters to allow standard mathematical functions such as `cos` or `abs` and `std::vector` to be used in expressions. User-defined functions and class methods can conveniently be made compatible with the CLEF quick assignment through macros.

8.6. HDF5 (C++ and Python)

HDF5 is a standard, portable and compact file format, see <http://www.hdfgroup.org>. Almost all objects in the TRIQS library (including arrays or Green's functions) can be stored in and retrieved from HDF5 files, from C++ and/or Python, with a simple and uniform interface. For example, in C++:

```
auto a = array<double, 2> {{1,2,3}, {4,5,6}}; // some data
{
    auto f = h5::file("data.h5", 'w'); // open the file
    h5_write(f, 'a', a); // write to the file
} // closes the file
```

or, the corresponding code in Python:

```
a = numpy.array([[1,2,3],[4,5,6]])
with HDFArchive("data.h5", 'w') as f:
    f['a'] = a
```

In Python, the `HDFArchive` behaves similarly as a `dict`. Therefore, one can reload a complex object (e.g. a block Green's function) in a single command in a script. An example can be seen in Listing 1.

An HDF5 file can be seen as a tree whose leaves are “basic” objects (multidimensional rectangular arrays, double, integer, strings, ...). More complex objects are usually decomposed by the library into a subtree of smaller objects, which are stored in an HDF5 subgroup. For example, a block diagonal Green's function (of type *BlockGf*) is stored with subgroups containing Green's functions it is made of; a Green's function is stored as a subgroup containing the array of data, the mesh, and possibly the high frequency singularity. This *format*, i.e. the precise conventions for the names and types of the small objects and the storage order of the data in the arrays, is described in the reference documentation. The HDF5 files can be read *without the TRIQS library* from C, C++, Fortran, Python codes, the HDF5 command line tools and with any tool supporting this format. This enables publishing data and facilitates sharing them across different groups and platforms. The HDF5 format is indeed widely used, e.g. by the ALPS project [7].

Note also that the HDF5 files written from C++ or Python have exactly the same format. Hence one can straightforwardly load some Green's functions in Python that have been computed and written using a C++ code, or vice-versa.

8.7. Second-quantised operators (C++ and Python)

The theories of strongly-correlated electron systems often use a language of second-quantised operators to formulate the problems under consideration. The model Hamiltonians as well as the observables of interest are routinely written as polynomials of fermionic operators c^\dagger and c .

The TRIQS library implements a C++ template class `many_body_operator`, which abstracts the notion of a second-quantised operator. The purpose of this class is to make expressions for second-quantised operators *written in the C++ or Python code as close*

³ For a precise list of what is allowed in expressions, the reader is referred to the reference documentation.

```

In [1]: %reload_ext pytriqs.magic

In [2]: %%triqs
#include <string>
std::string hello(){ return "Hello, world!"; }

In [3]: print hello()

Hello, world!

In [4]: type(hello())

Out[4]: str

```

Fig. 3. Using C++ directly within the IPython notebook.

as possible to their analytical counterparts. In order to pursue this goal, the class implements the standard operator algebra. The library stores the expression in normal order, so it performs automatically basic simplifications, for example when an expression vanishes. Any operator can be constructed as a polynomial of the elementary operators carrying an arbitrary number of integer/string indices (defined at compile time). The coefficients of the polynomials may be real, complex or of a user-defined numeric type in advanced use scenarios.

There is also a Python version of the same class (called `Operator`), specialised for the case with real coefficients and the fermionic operators with two indices (this particular choice is made for compatibility with Green's function component). Anyone writing a TRIQS-based many-body solver may benefit from this class. For example, the user of the solver could define a model Hamiltonian in a Python script and subsequently pass it to the solver:

```

from pytriqs.operators.operators import Operator, n, c_dag, c
# Spin operators
Sp = c_dag("up",0)*c("dn",0)      # S_+
Sm = c_dag("dn",0)*c("up",0)      # S_-
Sz = 0.5*(n("up",0) - n("dn",0))  # S_z
S2 = Sz*Sz + (Sp*Sm + Sm*Sp)/2    # S^2
# The Hamiltonian of a half-filled Hubbard atom: four equivalent forms
U = 1.0
H1 = -U/2*(n("up",0) + n("dn",0)) + U*n("up",0)*n("dn",0)
H2 = U*(n("up",0) - 0.5)*n("dn",0) - 0.5) - U/4
H3 = -2.0*U*Sz*Sz
H4 = -2.0/3.0*U*S2
print H1, '\n', H2, '\n', H3, '\n', H4
# All four forms are indeed equivalent
print (H1-H2).is_zero() and (H2-H3).is_zero() and (H3-H4).is_zero()

```

8.8. C++/Python wrapping tool

The tool that glues together the C++ components to Python is a crucial piece of the TRIQS project. Indeed the C++/Python architecture of the project is very demanding in this aspect: we need to expose diverse components from C++ to Python. These range from simple functions to complex objects with methods, overloaded arithmetic operators, the interface to HDF5, and so on. The tool must be very flexible, while being as simple as possible to use in the most common cases.

The TRIQS library proposes such a tool in version 1.2. From a simple Python-written *description* of the classes and functions to expose to Python, it generates the necessary C wrapping code to build the Python module. Utilities are also included to actually compile and setup the modules with `cmake`.

In most cases, the process can be fully automatised, using a second tool based on the `Clang` library, which parses the C++ code using `libClang` and retrieves the description of the classes and functions along with their documentation. As an example, the automatically produced description files for the CT-INT algorithm is provided in the [Appendix](#).

In more complex cases, some information can be added manually to the class description, for example the fact that the object forms an algebra over the doubles. In such a case, by adding *a single line* to the description file, the tool automatically generates all the necessary operators for the algebra structure in Python by calling their C++ counterparts.

As a consequence, this tool also allows the TRIQS user to *write C++ code directly within the IPython notebook and use it immediately*, using a so-called “magic cell command”, in IPython terminology. This is illustrated in [Fig. 3](#). In this case, the command `%%triqs` extracts the prototype of the C++ `hello()` function, writes, compiles and loads the Python module to be used in the next cell. TRIQS objects, along with STL containers (e.g. `vector`, `tuple`), can be used as function arguments or return values.

Using this feature one can tinker with C++ codes directly inside a Python environment, without having to set up a C++ project. It is suitable for debugging, quick testing, or executing short C++ code. For longer codes, it is better to set up a Python/C++ project along the lines shown for the CT-INT in the [Appendix](#). Note that this feature is experimental in release 1.2 and currently limited to a single C++ function per cell (even though generalisation is quite straightforward).

9. Getting started

Detailed information on installation can be found on the TRIQS website and current issues and updates are available on GitHub.

9.1. Obtaining TRIQS

The TRIQS source code is available publicly and can be obtained by cloning the repository on the GitHub website <https://github.com/TRIQS/triqs>. As the TRIQS project is continuously evolving, we recommend that users always obtain TRIQS from GitHub. Fixes to possible issues are also applied to the GitHub source.

9.2. Installation

Installing TRIQS is straightforward. We use the `cmake` tool to configure, build and test the library. Assuming that all dependencies have been installed (refer to the online documentation), the library is simply installed by issuing the following commands at the shell prompt:

```
$ git clone https://github.com/TRIQS/triqs.git src
$ mkdir build_triqs && cd build_triqs
$ cmake ../src
$ make
$ make test
$ make install
```

By default, the installation directory `INSTALL_DIR` will be located inside the build directory. Further installation instructions and help on installing the dependencies can be found in the online documentation.

9.3. Usage

There are different ways of using TRIQS. In the following, we assume that the location of the `INSTALL_DIR/bin` folder is in the search path. We recommend starting with one of the interactive IPython notebook examples provided with this paper (see below). The interactive IPython notebook is started using the command

```
$ ipytriqs_notebook
```

which will open the browser and allow one to open an existing or a new notebook. Providing a notebook name as an argument will open the notebook directly.

The IPython example in Fig. 2 uses the CT-INT solver of Appendix, which is shipped as a separate application. Installing external applications is straightforward. The CT-INT application, for example, is installed as follows:

```
$ git clone https://github.com/TRIQS/ctint_tutorial.git src_ctint
$ mkdir build_ctint && cd build_ctint
$ cmake -DTRIQS_PATH=INSTALL_DIR_ABSOLUTE_PATH ../src_ctint
$ make
$ make test
$ make install
```

where `INSTALL_DIR_ABSOLUTE_PATH` is the (absolute) path to the TRIQS installation directory. The application will be installed into the `applications` subdirectory in this TRIQS installation directory. Assuming that `INSTALL_DIR_ABSOLUTE_PATH/bin` is in the UNIX search path, one can then execute the example notebook in Fig. 2. To this end, navigate to the `examples` directory of the `ctint_tutorial` application sources and issue the following command:

```
$ ipytriqs_notebook dmft_bethe.ipynb
```

This will load the notebook inside a browser. Individual cells can be executed by pressing [Shift+ENTER] (refer to the IPython notebook documentation). The same directory contains a Python script to execute the same DMFT loop from the command line, which is another mode to use TRIQS that is better suited for long computations on a parallel machine. It can be executed by typing

```
$ pytriqs dmft_bethe.py
```

or in parallel by running, e.g.,

```
$ mpirun -np 4 pytriqs dmft_bethe.py
```

These commands produce a file `dmft_bethe.output.h5`. To plot Green's function from the final iteration, we can launch `ipytriqs` and type:

```
$ ipytriqs
...
In [1]: from pytriqs.archive import *

In [2]: from pytriqs.gf.local import *

In [3]: from pytriqs.plot.mpl_interface import oplot, plt

In [4]: A = HDFArchive("dmft_bethe.output.h5", "r")

In [5]: oplot(A["G20"].imag, "-o", name="Im G20")

In [6]: plt.show()
```

As a starting point for developing an external application, we provide a minimal skeleton application called `hello_world`. It can be installed in the same way as the CT-INT solver. The C++ examples of this paper, various IPython notebooks and the `hello_world` are provided in a dedicated GitHub repository <https://github.com/TRIQS/tutorials.git>.

10. Contributing

TRIQS is an open source project and we encourage feedback and contributions from the user community to the library and the publication of applications based on it. Issues should be reported exclusively via the GitHub web site at <https://github.com/TRIQS/triqs/issues>. For contributions, we recommend to use the *pull request* system on the GitHub web site. Before any major contribution, we recommend to coordinate with the main TRIQS developers.

11. Summary

We have presented the TRIQS library, a Toolbox for Research on Interacting Quantum Systems. This open-source computational physics library provides a framework for the quick development of applications in the field of many-body quantum physics. Several applications have been built on this library already. They are available at <https://github.com/TRIQS> and will be described in other publications.

Acknowledgements

The TRIQS project is supported by the ERC Grant No. 278472–*MottMetals*. We acknowledge contributions to the library and feedbacks from M. Aichhorn, A. Antipov, L. Boehnke, L. Pourovskii, as well as feedback from our user community. I.K. acknowledges support from Deutsche Forschungsgemeinschaft via Project SFB 668-A3. P.S. acknowledges support from ERC Grant No. 617196–*CorrelMat*.

Appendix. A sample application: interaction expansion continuous-time quantum Monte Carlo algorithm

In this appendix, we present the implementation of a simple interaction expansion continuous-time quantum Monte Carlo algorithm (CT-INT). We have used this solver in the DMFT IPython example in Fig. 2. We first briefly recall the formalism of the CT-INT algorithm before discussing the code.

A.1. Formalism

We consider the following single-orbital impurity action

$$S = - \sum_{\sigma} \int_0^{\beta} \int_0^{\beta} d\tau d\tau' \bar{d}_{\sigma}(\tau) \tilde{G}_{0\sigma}^{-1}(\tau - \tau') d_{\sigma}(\tau') + \int_0^{\beta} d\tau \mathcal{H}_{int}(\tau), \quad (\text{A.1})$$

whose interaction term is a slightly modified Hubbard term

$$\mathcal{H}_{int} = \frac{U}{2} \sum_{s=\uparrow, \downarrow} (\hat{n}_{\uparrow} - \alpha^{s\uparrow}) (\hat{n}_{\downarrow} - \alpha^{s\downarrow}) \quad (\text{A.2})$$

with

$$\alpha^{s\sigma} = \frac{1}{2} + (2\delta_{s\sigma} - 1)\delta. \quad (\text{A.3})$$

Here δ is a free small parameter which reduces the sign problem and $\delta_{s\sigma}$ is a Kronecker symbol. This rewriting of the interaction term results in a shift of the chemical potential (absorbed in the bare Green's function \tilde{G}_0): $\tilde{\mu} = \mu - \frac{U}{2}$. The α 's only appear in the interaction term.

The CT-INT algorithm consists in expanding the partition function $Z = \int \mathcal{D}[\bar{d}, d] e^{-S}$ in powers of \mathcal{H}_{int} . One obtains:

$$Z = Z_0 \sum_{k=0}^{\infty} \frac{(-U)^k}{k!} \int_0^{\beta} d\tau_1 \dots d\tau_k \frac{1}{2^k} \sum_{s_1 \dots s_k = \uparrow, \downarrow} \langle T_{\tau} (n_{\uparrow}(\tau_1) - \alpha^{s_1\uparrow}) \dots (n_{\uparrow}(\tau_k) - \alpha^{s_k\uparrow}) (n_{\downarrow}(\tau_1) - \alpha^{s_1\downarrow}) \dots (n_{\downarrow}(\tau_k) - \alpha^{s_k\downarrow}) \rangle_0 \quad (\text{A.4})$$

where T_{τ} is the time ordering operator. In the original CT-INT algorithm proposed in Ref. [10], $\alpha^{\uparrow\uparrow} = 1 - \alpha^{\uparrow\downarrow} = \alpha$ and $\alpha^{\downarrow\uparrow} = \alpha^{\downarrow\downarrow} = 0$. This choice can be shown to eliminate the sign problem for the half-filled single band Anderson model. Here we sum over the indices to make the formulation slightly more symmetric. It has the advantage that the non-interacting Green's function \tilde{G} does not explicitly depend on α 's. Note that in the case of all $\alpha^{s_i\sigma}$ being the same, the sum over s_i produces a factor 2^k , which cancels the 2^k in the denominator. The non-interacting Green's function has no off-diagonal up/down terms, so that the average factorises into product of two correlation functions for each spin. Let us furthermore introduce time ordering by replacing the integrals over the complete time intervals into a product of time-ordered integrals,

$$\int_0^{\beta} d\tau_1 \dots d\tau_k \left\langle \prod_{i=1}^k \prod_{\sigma} (n_{\sigma}(\tau_i) - \alpha^{s_i\sigma}) \right\rangle_0 = k! \int_0^{\beta} d\tau_1 \int_0^{\tau_1} d\tau_2 \dots \int_0^{\tau_{k-1}} d\tau_k \times \langle (n_{\uparrow}(\tau_1) - \alpha^{s_1\uparrow}) \dots (n_{\uparrow}(\tau_k) - \alpha^{s_k\uparrow}) \rangle_0 \langle (n_{\downarrow}(\tau_1) - \alpha^{s_1\downarrow}) \dots (n_{\downarrow}(\tau_k) - \alpha^{s_k\downarrow}) \rangle_0. \quad (\text{A.5})$$

Using Wick's theorem and the usual definition for Green's function

$$G_0^\sigma(\tau) = -\langle T_\tau d_\sigma(\tau) \bar{d}_\sigma(0) \rangle_0, \quad (\text{A.6})$$

the averages can be represented by determinants. We hence arrive at

$$Z = Z_0 \sum_{k=0}^{\infty} \int_{>} d\tau_1 \dots d\tau_k \sum_{s_1 \dots s_k} \frac{(-U)^k}{2^k} \det D_k^\uparrow \det D_k^\downarrow. \quad (\text{A.7})$$

The determinants explicitly read

$$D_k^\sigma = \begin{bmatrix} \bar{G}_0^{s_1\sigma}(0^-) & \bar{G}_0^{s_1\sigma}(\tau_1 - \tau_2) & \dots & \bar{G}_0^{s_1\sigma}(\tau_1 - \tau_k) \\ \bar{G}_0^{s_2\sigma}(\tau_2 - \tau_1) & \bar{G}_0^{s_2\sigma}(0^-) \dots & \bar{G}_0^{s_2\sigma}(\tau_2 - \tau_k) & \\ \dots & \dots & \dots & \dots \\ \bar{G}_0^{s_k\sigma}(\tau_k - \tau_1) & \bar{G}_0^{s_k\sigma}(\tau_k - \tau_2) & \dots & \bar{G}_0^{s_k\sigma}(0^-) \end{bmatrix}, \quad (\text{A.8})$$

where we have defined Green's function $\bar{G}_0^{s\sigma}$ as

$$\bar{G}_0^{s\sigma}(\tau_1 - \tau_2) = \begin{cases} \bar{G}_0^\sigma(0^-) - \alpha^{s_1\sigma} & \tau_1 = \tau_2 \\ \bar{G}_0^\sigma(\tau_1 - \tau_2) & \tau_1 \neq \tau_2. \end{cases} \quad (\text{A.9})$$

We can sample the partition function (A.7) by defining a Monte Carlo configuration as $\mathcal{C} := \{\{\tau_1, s_1\}, \dots, \{\tau_k, s_k\}\}$ and the Monte Carlo weight of a configuration according to $\omega(\mathcal{C}) = |(-U/2)^k \det D_k^\uparrow D_k^\downarrow|$. The Metropolis acceptance rate for an insertion of a vertex is

$$A_{x,y} = \min \left[1, \frac{-\beta U \det D_{k+1}^\uparrow D_{k+1}^\downarrow}{k+1 \det D_k^\uparrow D_k^\downarrow} \right], \quad (\text{A.10})$$

while for a removal, it is

$$A_{x,y} = \min \left[1, \frac{-k \det D_{k-1}^\uparrow D_{k-1}^\downarrow}{\beta U \det D_k^\uparrow D_k^\downarrow} \right]. \quad (\text{A.11})$$

Green's function can be calculated as

$$G_\sigma(\tau) = -\frac{1}{\beta} \frac{\delta \ln Z}{\delta \Delta^\sigma(-\tau)}. \quad (\text{A.12})$$

Carrying out the functional derivative and Fourier transforming yields

$$G^\sigma(i\omega_n) = \tilde{G}_0^\sigma(i\omega_n) - \frac{1}{\beta} (\tilde{G}_0^\sigma(i\omega_n))^2 \sum_{\mathcal{C}} \sum_{ij} [D_k^\sigma]_{ij}^{-1} e^{i\omega_n(\tau_i - \tau_j)} \text{sign}[\omega(\mathcal{C})] \omega(\mathcal{C}). \quad (\text{A.13})$$

Separating the Monte Carlo weight, we need to accumulate

$$M^\sigma(i\omega_n) \equiv -\frac{1}{Z\beta} \sum_{\mathcal{C}} \sum_{ij} [D_k^\sigma]_{ij}^{-1} e^{i\omega_n(\tau_i - \tau_j)} \times \text{sign}[\omega(\mathcal{C})], \quad (\text{A.14})$$

$$Z = \sum_{\mathcal{C}} \text{sign}[\omega(\mathcal{C})], \quad (\text{A.15})$$

From M , we can compute Green's function as follows [13]:

$$G^\sigma(i\omega_n) = \tilde{G}_0^\sigma(i\omega_n) + \tilde{G}_0^\sigma(i\omega_n) M^\sigma(i\omega_n) \tilde{G}_0^\sigma(i\omega_n). \quad (\text{A.16})$$

A.2. Implementation

As an example of an application of the library, we discuss here the complete code listing of a fully working, parallelised implementation of the weak-coupling CTQMC algorithm described above. How this code can be used in an actual computation is illustrated in the DMFT example of Section 7.1. Through the use of the various components of the library, including `gf`, `mc_tools`, `det_manip` and `CLEF`, the full implementation takes about 200 lines; it comes with a Python interface. Note that this simple implementation can easily be extended: further measurements and moves may be added, or it may be generalised to multi-orbital case or to a retarded interaction.

We divide the code into several listings that we discuss briefly. The purpose is to give an illustration of the possibilities of the TRIQS library without entering into all the details. We start with the main header file (Listing 6) of the code. It mainly defines and provides access to Green's functions that are used in the code, in particular in the main member function `solve`.

Listing 6 CT-INT: the header file

```

1  #include <triqs/gfs.hpp>
2  #include <boost/mpi.hpp>
3
4  // ----- The main class of the solver -----
5
6  using namespace triqs::gfs;
7  enum spin {up, down};
8
9  class ctint_solver {
10
11     block_gf<imfreq> g0_iw, g0tilde_iw, g_iw, M_iw;
12     block_gf<imtime> g0tilde_tau;
13     double double_occ, percent_done_, beta;
14     int n_matsubara, n_times_slices;
15
16     public:
17
18     // Accessors of the class
19     block_gf_view<imfreq> G0_iw() { return g0_iw; }
20     block_gf_view<imtime> G0_tau() { return g0tilde_tau; }
21     block_gf_view<imfreq> G_iw() { return g_iw; }
22
23     ctint_solver(double beta_, int n_iw = 1024, int n_tau = 100001);
24
25     // The method that runs the qmc
26     void solve(double U, double delta,
27               int n_cycles, int length_cycle = 50, int n_warmup_cycles = 5000,
28               std::string random_name = "",
29               int max_time = -1);
30
31 };

```

Listing 7 defines the Monte Carlo configurations through a simple vector of determinants (A.8) (instances of the `det_manip` class). They contain all the necessary information to completely determine a configuration $\mathcal{C} := \{\{\tau_1, s_1\}, \dots, \{\tau_k, s_k\}\}$. The determinants are constructed from a function object `g0bar_tau`, also declared in this listing, that is used to fill the elements of the matrix (A.8).

Listing 7 CT-INT: define the configurations

```

1  // ----- The QMC configuration -----
2
3  // Argument type of g0bar
4  struct arg_t {
5     double tau;    // The imaginary time
6     int s;        // The auxiliary spin
7  };
8
9  // The function that appears in the calculation of the determinant
10 struct g0bar_tau {
11     gf<imtime> const &gt;
12     double beta, delta;
13     int s;
14
15     double operator()(arg_t const &x, arg_t const &y) const {
16         if ((x.tau == y.tau)) { // G_\sigma(0^-) - \alpha(\sigma s)
17             return 1.0 + gt[0](0, 0) - (0.5 + (2 * (s == x.s ? 1 : 0) - 1) * delta);
18         }
19         auto x_y = x.tau - y.tau;
20         bool b = (x_y >= 0);
21         if (!b) x_y += beta;
22         double res = gt[closest_mesh_pt(x_y)](0, 0);
23         return (b ? res : -res); // take into account antiperiodicity
24     }
25 };
26
27 // The Monte Carlo configuration
28 struct configuration {
29     // M-matrices for up and down
30     std::vector<triqs::det_manip::det_manip<g0bar_tau>> Mmatrices;
31
32     int perturbation_order() const { return Mmatrices[up].size(); }
33
34     configuration(block_gf<imtime> &g0tilde_tau, double beta, double delta) {

```

```

35 // Initialize the M-matrices. 100 is the initial matrix size
36 for (auto spin : {up, down})
37     Mmatrices.emplace_back(g0bar_tau{g0tilde_tau[spin], beta, delta, spin}, 100);
38 }
39 };

```

Now that the configuration is declared, the next step is to define the Monte Carlo *moves* that are going to act on this configuration. In Listing 8, two moves are implemented: the insertion of an interaction vertex at a random imaginary time and the removal of a randomly chosen vertex. They are described by classes that must model the concept of a Monte Carlo move. In other words they must have the three members `attempt`, `accept`, `reject`. The `attempt` method tries a modification of the configuration and returns a Metropolis acceptance ratio (e.g. for the insertion this ratio is given by (A.10)). The Monte Carlo class will use this ratio to decide whether to accept or reject the proposed configuration and then call `accept` or `reject` accordingly. Note that for efficiency reasons the update of the determinants is done in two steps: in the `attempt` method only the ratio of the new to the old determinant is computed (via `try_insert`). The actual update of the full inverse matrix is performed only if the move is accepted (see the `complete_operation` call in `accept`).

Listing 8 CT-INT: define the moves

```

1 // ----- QMC move : inserting a vertex -----
2
3 struct move_insert {
4     configuration *config;
5     triqs::mc_tools::random_generator &rng;
6     double beta, U;
7
8     double attempt() { // Insert an interaction vertex at time tau with aux spin s
9         double tau = rng(beta);
10        int s = rng(2);
11        auto k = config->perturbation_order();
12        auto det_ratio = config->Mmatrices[up].try_insert(k, k, {tau, s}, {tau, s}) *
13            config->Mmatrices[down].try_insert(k, k, {tau, s}, {tau, s});
14        return -beta * U / (k + 1) * det_ratio; // The Metropolis ratio
15    }
16
17    double accept() {
18        for (auto &d : config->Mmatrices) d.complete_operation(); // Finish insertion
19        return 1.0;
20    }
21
22    void reject() {}
23 };
24
25 // ----- QMC move : deleting a vertex -----
26
27 struct move_remove {
28     configuration *config;
29     triqs::mc_tools::random_generator &rng;
30     double beta, U;
31
32     double attempt() {
33         auto k = config->perturbation_order();
34         if (k <= 0) return 0; // Config is empty, trying to remove makes no sense
35         int p = rng(k); // Choose one of the operators for removal
36         auto det_ratio = config->Mmatrices[up].try_remove(p, p) *
37             config->Mmatrices[down].try_remove(p, p);
38         return -k / (beta * U) * det_ratio; // The Metropolis ratio
39     }
40
41     double accept() {
42         for (auto &d : config->Mmatrices) d.complete_operation();
43         return 1.0;
44     }
45
46     void reject() {} // Nothing to do
47 };

```

The measurement of Green's function is shown in Listing 9. It is a simple transcription of Eq. (A.15). Again, the measurements are described by classes that obey the concept of a Monte Carlo measurement: they have a method `accumulate` which is called during the Monte Carlo chain and accumulates data, and a `collect_results` method that is called at the very end of the calculation. Typically the `collect_results` MPI-reduces the results from several cores in a parallelised calculation. Note that `std14::plus` in lines 34 and 35 is the C++14 version of `std::plus`, which does not require a type, and which is provided by TRIQS for backward compatibility to C++11.

Listing 9 CT-INT: define the measures

```

1 // ----- QMC measurement -----
2
3 struct measure_M {
4
5     configuration const *config; // Pointer to the MC configuration
6     block_gf<imfreq> &Mw;       // reference to M-matrix
7     double beta, Z = 0;
8
9     measure_M(configuration const *config_, block_gf<imfreq> &Mw_, double beta_)
10         : config(config_), Mw(Mw_), beta(beta_) {
11         Mw() = 0;
12     }
13
14     void accumulate(double sign) {
15         Z += sign;
16
17         for (auto spin : {up, down}) {
18
19             // A lambda to measure the M-matrix in frequency
20             auto lambda = [this, spin, sign](arg_t const &x, arg_t const &y, double M) {
21                 auto coeff = std::exp(-1_j * M_PI * (x.tau - y.tau) / beta);
22                 auto fact = coeff * coeff;
23                 for (auto const &om : this->Mw[spin].mesh()) {
24                     this->Mw[spin][om](0, 0) += sign * M * coeff;
25                     coeff *= fact;
26                 }
27             };
28
29             foreach(config->Mmatrices[spin], lambda);
30         }
31     }
32
33     void collect_results(boost::mpi::communicator const &c) {
34         boost::mpi::all_reduce(c, Mw, Mw, std14::plus<>());
35         boost::mpi::all_reduce(c, Z, Z, std14::plus<>());
36         Mw = Mw / (-Z * beta);
37     }
38 };

```

The above components are put together in the main solver body shown in Listing 10. The first part is the constructor that only defines the dimension of Green's functions. The second part is the solve method that actually runs the Monte Carlo simulation. It first constructs the Fourier transform $\tilde{G}_0(\tau)$ of the non-interacting Green's function given by the user (it is stored in `g0_iw`). Then a Monte Carlo simulation is created by adding the relevant moves and measures. This is done via the `add_move` and `add_measure` methods. Note that both the moves and the measurements are constructed with a reference to the Monte Carlo configuration `config`. The simulation is launched with `start` and final results are collected at the end of the simulation with `collect_results`. In line 50, we finally compute the actual Green's function through a compact CLEF expression that implements (A.15).

Listing 10 CT-INT: the main solver body

```

1 // ----- The main class of the solver -----
2
3 ctint_solver::ctint_solver(double beta_, int n_iw, int n_tau) : beta(beta_) {
4
5     g0_iw =
6         make_block_gf({"up", "down"}, gf<imfreq>{{beta, Fermion, n_iw}, {1, 1}});
7     g0tilde_tau =
8         make_block_gf({"up", "down"}, gf<imtime>{{beta, Fermion, n_tau}, {1, 1}});
9     g0tilde_iw = g0_iw;
10    g_iw = g0_iw;
11    M_iw = g0_iw;
12 }
13
14 // The method that runs the qmc
15 void ctint_solver::solve(double U, double delta, int n_cycles, int length_cycle,
16                         int n_warmup_cycles, std::string random_name,
17                         int max_time) {
18
19     boost::mpi::communicator world;
20     triqs::clef::placeholder<0> spin_;
21     triqs::clef::placeholder<1> om_;
22
23     for (auto spin : {up, down}) { // Apply shift to g0_iw and Fourier transform

```

```

24  g0tilde_iw[spin](om_) << 1.0 / (1.0 / g0_iw[spin](om_) - U / 2);
25  g0tilde_tau()[spin] = triqs::gfs::inverse_fourier(g0tilde_iw[spin]);
26  }
27
28  // Rank-specific variables
29  int verbosity = (world.rank() == 0 ? 3 : 0);
30  int random_seed = 34788 + 928374 * world.rank();
31
32  // Construct a Monte Carlo loop
33  triqs::mc_tools::mc_generic<double> CTQMC(n_cycles, length_cycle,
34                                          n_warmup_cycles, random_name,
35                                          random_seed, verbosity);
36
37  // Prepare the configuration
38  auto config = configuration{g0tilde_tau, beta, delta};
39
40  // Register moves and measurements
41  CTQMC.add_move(move_insert{&config, CTQMC.rng(), beta, U}, "insertion");
42  CTQMC.add_move(move_remove{&config, CTQMC.rng(), beta, U}, "removal");
43  CTQMC.add_measure(measure_M{&config, M_iw, beta}, "M measurement");
44
45  // Run and collect results
46  CTQMC.start(1.0, triqs::utility::clock_callback(max_time));
47  CTQMC.collect_results(world);
48
49  // Compute the Green function from Mw
50  g_iw[spin_](om_) << g0tilde_iw[spin_](om_) + g0tilde_iw[spin_](om_) *
51                                          M_iw[spin_](om_) *
52                                          g0tilde_iw[spin_](om_);
53  }

```

The listings above give a complete implementation of the CT-INT algorithm in C++: the `ctint_solver` class is ready to be used from within other C++ programs. It is however convenient to control calculations on the Python level. As discussed above, TRIQS provides a tool to easily expose C++ to Python. Starting from a descriptor written in Python (shown in Listing 11), it automatically generates a C wrapping code that constructs the Python modules for the `ctint_solver`. The descriptor basically lists the C++ elements that need to be exposed to Python. In most cases, this descriptor can be generated automatically by a small analysing tool provided with TRIQS. Here the script 11 has been generated automatically using this tool.

Listing 11 CT-INT: Python wrapper descriptor

```

1  # Generated automatically using the command :
2  # c++2py.py ../c++/ctint.hpp -p -m pytriqs.applications.impurity_solvers.
   ctint_tutorial -o ctint_tutorial
3  from wrap_generator import *
4
5  # The module
6  module = module_(full_name = "pytriqs.applications.impurity_solvers.
   ctint_tutorial", doc = "")
7
8  # All the triqs C++/Python modules
9  module.use_module('gf')
10
11 # Add here all includes beyond what is automatically included by the triqs
   modules
12 module.add_include("../c++/ctint.hpp")
13
14 # Add here anything to add in the C++ code at the start, e.g. namespace using
15 module.add_preamble("""
16 using namespace triqs::gfs;
17 """)
18
19 # The class ctint_solver
20 c = class_(
21     py_type = "CtintSolver", # name of the python class
22     c_type = "ctint_solver", # name of the C++ class
23 )
24
25 c.add_constructor("""(double beta_, int n_iw = 1024, int n_tau = 100001)""",
26                  doc = "" """)
27
28 c.add_method("""void solve (double U, double delta, int n_cycles, int
   length_cycle = 50, int n_warmup_cycles = 5000, std::string random_name = "",
   int max_time = -1)""",
29              doc = "" """)

```

```

30
31 c.add_property(name = "GO_iw",
32               getter = cfunction("block_gf_view<imfreq> GO_iw ()"),
33               doc = "" "" "")
34
35 c.add_property(name = "GO_tau",
36               getter = cfunction("block_gf_view<imtime> GO_tau ()"),
37               doc = "" "" "")
38
39 c.add_property(name = "G_iw",
40               getter = cfunction("block_gf_view<imfreq> G_iw ()"),
41               doc = "" "" "")
42
43 module.add_class(c)
44
45 module.generate_code()

```

After the code has been compiled and installed a new Python module is available in `pytriqs.applications.impurity_solvers.ctint_tutorial`. The solver can then be used as illustrated in Fig. 2. As this example shows, C++ members like `gO_iw` can directly be initialised from a Python script and the `solve` method is also accessible. Controlling the solver, or any other C++ code directly from Python makes it very easy to change parameters, plot results, build flexible control structures around it, etc., without the need to recompile the codes.

References

- [1] A. Georges, G. Kotliar, W. Krauth, M.J. Rozenberg, Dynamical mean-field theory of strongly correlated fermion systems and the limit of infinite dimensions, *Rev. Modern Phys.* 68 (1) (1996) 13. <http://dx.doi.org/10.1103/RevModPhys.68.13>.
- [2] G. Kotliar, S.Y. Savrasov, K. Haule, V.S. Oudovenko, O. Parcollet, C.A. Marianetti, Electronic structure calculations with dynamical mean-field theory, *Rev. Modern Phys.* 78 (2006) 865–951. <http://dx.doi.org/10.1103/RevModPhys.78.865>.
- [3] T. Maier, M. Jarrell, T. Pruschke, M.H. Hettler, Quantum cluster theories, *Rev. Modern Phys.* 77 (2005) 1027–1080. <http://dx.doi.org/10.1103/RevModPhys.77.1027>.
- [4] A. Toschi, A.A. Katanin, K. Held, Dynamical vertex approximation: A step beyond dynamical mean-field theory, *Physical Review B (Condensed Matter and Materials Physics)* 75 (4) (2007) 045118. <http://dx.doi.org/10.1103/PhysRevB.75.045118>. URL <http://link.aps.org/abstract/PRB/v75/e045118>.
- [5] A.N. Rubtsov, M.I. Katsnelson, A.I. Lichtenstein, Dual fermion approach to nonlocal correlations in the hubbard model, *Phys. Rev. B* 77 (2008) 033101. <http://dx.doi.org/10.1103/PhysRevB.77.033101>.
- [6] U. Schollwöck, The density-matrix renormalization group, *Rev. Modern Phys.* 77 (2005) 259–315. <http://dx.doi.org/10.1103/RevModPhys.77.259>.
- [7] B. Bauer, L.D. Carr, H.G. Evertz, A. Feiguin, J. Freire, S. Fuchs, L. Gamper, J. Gukelberger, E. Gull, S. Guertler, A. Hehn, R. Igarashi, S.V. Isakov, D. Koop, P.N. Ma, P. Mates, H. Matsuo, O. Parcollet, G. Pawłowski, J.D. Picon, L. Pollet, E. Santos, V.W. Scarola, U. Schollwöck, C. Silva, B. Surer, S. Todo, S. Trebst, M. Troyer, M.L. Wall, P. Werner, S. Wessel, The alps project release 2.0: open source software for strongly correlated systems, *J. Stat. Mech. Theory Exp.* 2011 (05) (2011) P05001.
- [8] L. Huang, Y. Wang, Z.Y. Meng, L. Du, P. Werner, X. Dai, iqist: An open source continuous-time quantum Monte Carlo impurity solver toolkit. *arXiv:1409.7573*, URL <http://arxiv.org/abs/1409.7573>.
- [9] M. Stoudenmire, S. White, URL <http://itensor.org>.
- [10] A.N. Rubtsov, V.V. Savkin, A.I. Lichtenstein, Continuous-time quantum monte carlo method for fermions, *Phys. Rev. B* 72 (3) (2005) 035122. <http://dx.doi.org/10.1103/PhysRevB.72.035122>.
- [11] E. Gull, A.J. Millis, A.I. Lichtenstein, A.N. Rubtsov, M. Troyer, P. Werner, Continuous-time monte carlo methods for quantum impurity models, *Rev. Modern Phys.* 83 (2) (2011) 349–404. <http://dx.doi.org/10.1103/RevModPhys.83.349>.
- [12] P. Werner, A. Comanac, L. de' Medici, et al., Continuous-time solver for quantum impurity models, *Phys. Rev. Lett.* 97 (7) (2006) 076405. <http://dx.doi.org/10.1103/PhysRevLett.97.076405>.
- [13] E. Gull, P. Werner, O. Parcollet, M. Troyer, Continuous-time auxiliary-field monte carlo for quantum impurity models, *Europhys. Lett.* 82 (5) (2008) 57003. URL <http://stacks.iop.org/0295-5075/82/i=5/a=57003>.
- [14] E.G.C.P. van Loon, A.I. Lichtenstein, M.I. Katsnelson, O. Parcollet, H. Hafermann, Beyond extended dynamical mean-field theory: Dual boson approach to the two-dimensional extended hubbard model, *Phys. Rev. B* 90 (2014) 235135. <http://dx.doi.org/10.1103/PhysRevB.90.235135>.
- [15] A.M. Läuchli, P. Werner, Krylov implementation of the hybridization expansion impurity solver and application to 5-orbital models, *Phys. Rev. B* 80 (2009) 235117. <http://dx.doi.org/10.1103/PhysRevB.80.235117>.
- [16] F. Pérez, B.E. Granger, IPython: a system for interactive scientific computing, *Comput. Sci. Eng.* 9 (3) (2007) 21–29. <http://dx.doi.org/10.1109/MCSE.2007.53>. URL <http://ipython.org>.
- [17] Abstracts of papers, *Ann. Math. Statist.* 20 (4) (1949) 620–624. <http://dx.doi.org/10.1214/aoms/1177729959>.
- [18] J. Sherman, W.J. Morrison, Adjustment of an inverse matrix corresponding to a change in one element of a given matrix, *Ann. Math. Statist.* 21 (1) (1950) 124–127. <http://dx.doi.org/10.1214/aoms/1177729893>.
- [19] C.L. Lawson, R.J. Hanson, D.R. Kincaid, F.T. Krogh, Algorithm 539: basic linear algebra subprograms for fortran usage [F1], *ACM Trans. Math. Software* 5 (3) (1979) 324–325.
- [20] L.S. Blackford, J. Demmel, I. Duff, G. Henry, M. Heroux, L. Kaufman, A. Lumsdaine, A. Petitet, R.C. Whaley, An updated set of basic linear algebra subprograms (blas), *ACM Trans. Math. Software* 28 (2) (2002) 135–151. <http://dx.doi.org/10.1145/567806.567807>.

R.2 Paper 7: van Rookeghem *et al.* (2014)

Dynamical Correlations and Screened Exchange on the Experimental Bench: Spectral Properties of the Cobalt Pnictide BaCo_2As_2

Ambroise van Roekeghem,^{1,2,*} Thomas Ayrat,^{2,3} Jan M. Tomczak,⁴ Michele Casula,⁵ Nan Xu,^{1,6} Hong Ding,^{1,7}

Michel Ferrero,² Olivier Parcollet,³ Hong Jiang,⁸ and Silke Biermann^{2,9}

¹*Beijing National Laboratory for Condensed Matter Physics, and Institute of Physics, Chinese Academy of Sciences, Beijing 100190, China*

²*Centre de Physique Théorique, Ecole Polytechnique, CNRS UMR 7644, 91128 Palaiseau, France*

³*Institut de Physique Théorique (IPhT), CEA, CNRS, URA 2306, 91191 Gif-sur-Yvette, France*

⁴*Institute of Solid State Physics, Vienna University of Technology, A-1040 Vienna, Austria*

⁵*CNRS and Institut de Minéralogie, de Physique des Matériaux et de Cosmochimie, Université Pierre et Marie Curie, case 115, 4 place Jussieu, FR-75252 Paris Cedex 05, France*

⁶*Swiss Light Source, Paul Scherrer Institut, CH-5232 Villigen, Switzerland*

⁷*Collaborative Innovation Center of Quantum Matter, Beijing 100190, China*

⁸*College of Chemistry and Molecular Engineering, Peking University, 100871 Beijing, China*

⁹*Collège de France, 11 place Marcelin Berthelot, 75005 Paris, France*

(Received 13 August 2014; published 24 December 2014)

Understanding the Fermi surface and low-energy excitations of iron or cobalt pnictides is crucial for assessing electronic instabilities such as magnetic or superconducting states. Here, we propose and implement a new approach to compute the low-energy properties of correlated electron materials, taking into account both screened exchange beyond the local density approximation and local dynamical correlations. The scheme allows us to resolve the puzzle of BaCo_2As_2 , for which standard electronic structure techniques predict a ferromagnetic instability not observed in nature.

DOI: 10.1103/PhysRevLett.113.266403

PACS numbers: 71.27.+a, 71.10.-w, 71.45.Gm, 74.70.Xa

The discovery of unconventional superconductivity in iron pnictides in 2008 has aroused strong interest in the Fermi surfaces and low-energy excitations of transition metal pnictides. Angle-resolved photoemission spectroscopy (ARPES) has been used to systematically map out quasiparticle dispersions, and to identify electron and hole pockets potentially relevant for low-energy instabilities [1–7]. Density functional theory (DFT) calculations have complemented the picture, yielding information about orbital characters [8], or the dependence of the topology of the Fermi surface on structural parameters or element substitution [9,10]. DFT within the local density approximation (LDA) or generalized gradient schemes has also served as a starting point for refined many-body calculations (see, e.g., Refs. [11–18]). Its combination with dynamical mean field theory (LDA + DMFT) [19–25] is nowadays the state-of-the-art *ab initio* many-body approach to low-energy properties of transition metal pnictides. Despite tremendous successes, however, limitations have also been pointed out, e.g., in the description of the Fermi surfaces. Prominent examples include $\text{Ba}(\text{Fe}, \text{Co})_2\text{As}_2$ [26,27] or LiFeAs [14,26]. Interestingly, many-body perturbation theory approximating the self-energy by its first order term in the screened Coulomb interaction W (so-called “ GW approximation”) results in a substantially improved description: calculations using the quasiparticle self-consistent (QS) GW method [28] have pinpointed nonlocal self-energy corrections to the LDA Fermi surfaces not captured in LDA + DMFT as pivotal

[26]. Yet, as a perturbative method, the GW approximation cannot describe materials away from the weak coupling limit [29], and the description of incoherent regimes [13,17] including coherence-incoherence crossovers [30], local moment behavior [15], or the subtle effects of doping or temperature changes [17] are still reserved for DMFT.

In this Letter, we propose and implement a new approach to the spectral properties of correlated electron materials taking into account screened exchange beyond the LDA and correlations as described by DMFT with frequency-dependent local Hubbard interactions. The approach can be understood as a simplified and extremely efficient version of the combined GW + DMFT method [31], as a nonperturbative dynamical generalization of the popular “Coulomb-hole-screened-exchange” (“COHSEX”) scheme [32], or as a combination of generalized Kohn-Sham schemes [33,34] with DMFT. We demonstrate the validity of our combined “screened exchange+dynamical DMFT” (SEx+DDMFT) scheme by calculating the spectral function of BaCo_2As_2 for which detailed ARPES results are available [35,36]. Finally, our work sheds new light on the physical justifications of electronic structure techniques that combine DFT with DMFT, by revealing a subtle error cancellation between nonlocal exchange and dynamical screening effects, both neglected in standard methods.

Our target compound BaCo_2As_2 is isostructural to the prototypical compound of the so-called 122 iron-based superconductors, BaFe_2As_2 . Replacing Fe by Co, however,

increases the filling to a nominal $3d^7$ configuration, with drastic consequences: whereas compounds with filling around the d^6 configuration exhibit characteristic power law deviations from Fermi liquid behavior above often extremely low coherence temperatures [17], in BaCo_2As_2 ARPES identifies clearly defined long-lived quasiparticle bands with relatively weak mass renormalizations [35]. Nevertheless, the electronic structure of this compound raises puzzling questions concerning its paramagnetic behavior: DFT calculations predict a huge density of states (DOS) at the Fermi level, which, given the large Stoner parameter of Co, would be expected to trigger a ferromagnetic instability [37]. The DOS of the isoelectronic compound SrCo_2As_2 presents the same features, but the maximum lies just below the Fermi level [38]. Still, in SrCo_2As_2 —also a paramagnet—important antiferromagnetic fluctuations have been measured, possibly competing with ferromagnetic order [38,39]. CaCo_2As_2 , $\text{Ca}_{0.9}\text{Sr}_{0.1}\text{Co}_2\text{As}_2$, and $\text{CaCo}_{1.86}\text{As}_2$ exhibit magnetic phases with in-plane ferromagnetism at low temperatures [40–42]. ARPES data of BaCo_2As_2 show that there is indeed a flat band (dominantly of $d_{x^2-y^2}$ character) close to the Fermi surface, albeit less filled than predicted by LDA calculations [35,36], suggesting BaCo_2As_2 to be on the verge of a transition [43]. This compound is thus an ideal benchmark system, on which to test new theoretical approaches.

We start our analysis by comparing results for the spectral function calculated within standard LDA + DMFT and LDA + DMFT with frequency-dependent local Hubbard interactions $\mathcal{U}(\omega)$ to the ARPES spectral function of Ref. [35] (Fig. 1). The latter scheme will be abbreviated in the following as LDA + DDMFT to stress the doubly dynamical nature of the theory, which determines a frequency-dependent self-energy in the DMFT spirit, extended, however, to frequency-dependent interactions [17,44,45]. The effective local interactions used in the DMFT calculations were obtained within the constrained random phase approximation in the implementation of Ref. [53]. For LDA + DDMFT, the full frequency-dependence of the monopole term $F_0(\omega)$ is retained in the calculation. The effective local problem with dynamical \mathcal{U} is solved self-consistently by means of a continuous-time Monte Carlo algorithm [54,55] that we have implemented within the TRIQS toolbox [56].

Electronic bands in the energy window between the Fermi level and -2 eV binding energy are states of predominant Co-3d character, and undergo—even in this quite moderately correlated compound—a non-negligible band renormalization, as compared to the LDA band structure [Fig. 1(a)]. Standard LDA + DMFT [Fig. 1(b)] captures this effect, leading to a reduced bandwidth in good agreement with the ARPES results. When dynamical screening effects are taken into account [Fig. 1(c)], additional renormalizations occur, corresponding to the electronic polaron effect discussed in Ref. [57], and the overall

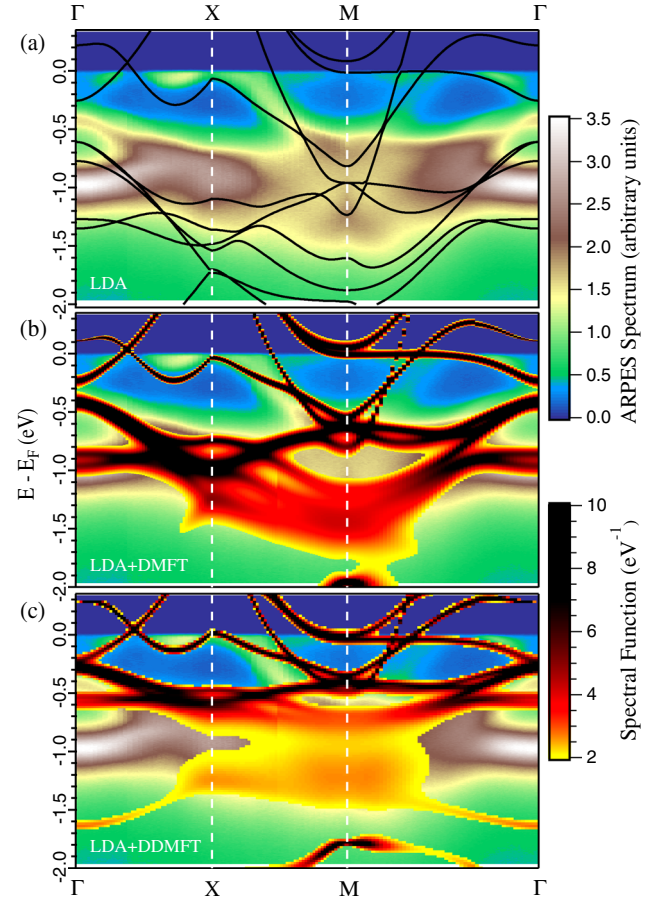


FIG. 1 (color online). BaCo_2As_2 photoemission spectra, replotted from Ref. [35]. Superimposed are (a) the Kohn-Sham band structure of the DFT LDA, (b) the spectral function of standard LDA + DMFT [only those parts that exceed 2 states/eV are shown], (c) the spectral function within LDA + DDMFT [same representation as in (b)].

bandwidth reduction appears to be overestimated. However, one should not conclude from this analysis that dynamical screening effects are absent. Rather, nonlocal exchange—routinely neglected in DFT-based techniques—reshapes and widens the quasiparticle band structure, and the apparent success of LDA + DMFT in obtaining the correct quasiparticle bandwidth relies on an error cancellation when both dynamical screening and nonlocal exchange are neglected in the calculation of the spectral function. We will now substantiate this claim by explicitly including screened exchange, and performing a DMFT calculation with dynamical Hubbard interactions based on the following one-particle Hamiltonian: $H_0 = H_{\text{Hartree}} + H_{\text{SEX}}$, where the first term denotes the Hamiltonian of the system at the Hartree mean-field level, evaluated at the self-consistent DFT-LDA density. H_{SEX} is a screened Fock exchange term, calculated from the Yukawa potential $e^2 \exp(-k_{\text{TF}}|r - r'|)/|r - r'|$ with screening wavevector k_{TF} . This scheme can be understood as the next generation after the recent LDA + DDMFT scheme, by replacing the

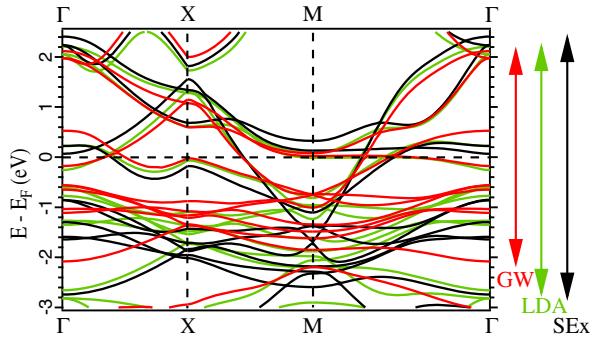


FIG. 2 (color online). Comparison of band structures of BaCo_2As_2 in the $k_z = 0$ plane calculated within the QS GW (red), LDA (green), and screened-exchange (black) schemes.

local Kohn-Sham exchange-correlation potential of DFT by a nonlocal screened Fock exchange term [58].

We first analyze the band structure corresponding to H_0 alone, in comparison to the LDA band structure and the one obtained from the QSGW method (in the implementation of Ref. [61]), see Fig. 2. As expected, the inclusion of nonlocal exchange in H_0 increases the delocalization of electrons, and thus widens the bands as compared to the LDA electronic structure. In the QSGW method, this effect is overcompensated by correlation-induced band narrowing, and the bandwidth of $3d$ -like bands is about 15% smaller than in the LDA. These comparisons highlight the fact that—taking the screened exchange band structure as a reference—the effective exchange-correlation potential of DFT not only incorporates exchange (in a local fashion), but also mimics band renormalizations due to correlations (yet without keeping track of the corresponding spectral weight transfers).

We finally turn to the results of our new scheme: Fig. 3 displays the spectral function within SEEx + DDMFT [panel (a)], superimposed on the ARPES data [panel (b)]. The overall spectrum from SEEx + DDMFT is very close to the experiment: the bandwidth, Fermi surface, and band renormalizations close to the Fermi level are correctly predicted.

The orbital-resolved electron count obtained with SEEx + DDMFT is displayed in Table I and compared to the one within the other schemes. The orbital polarization from the LDA is reduced by correlations, and nearly suppressed within LDA + DDMFT. Conversely, screened exchange increases the orbital polarization, and the final SEEx + DDMFT result still displays stronger orbital polarization than the LDA. This trend can be related to the weakly dispersive $d_{x^2-y^2}$ states discussed above: as in the SEEx band dispersion of Fig. 2, the effect of screened exchange is to push the flat $d_{x^2-y^2}$ -like band away from the Fermi level, to the point of suppressing the electron pocket at the Γ point. This does not correspond to the experimental spectrum, and indeed it is corrected by including correlations. Figure 4 displays the low-energy spectra along the ΓM direction

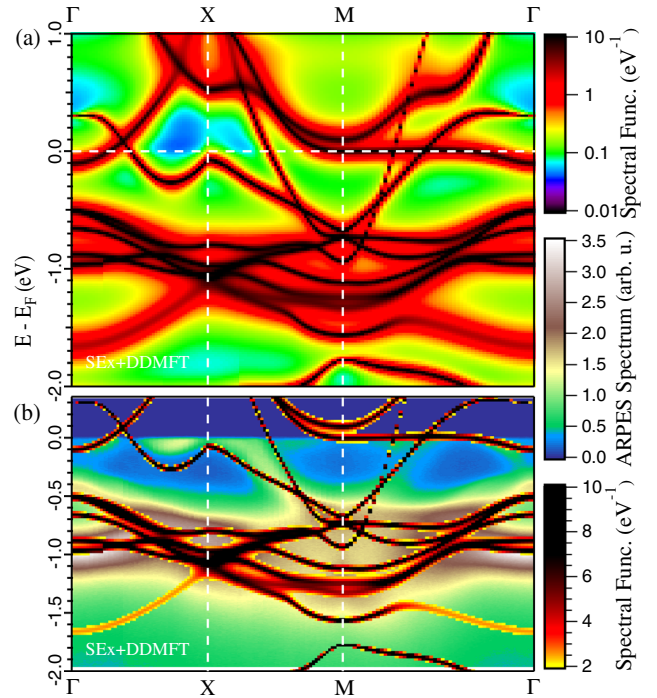


FIG. 3 (color online). BaCo_2As_2 within screened exchange + DDMFT: (a) spectral function and (b) bands extracted from the maxima of panel (a) and superimposed on ARPES data as in Fig. 1.

comparing SEEx + DDMFT and LDA + DMFT overlaid onto the second derivative of the ARPES data [62], together with the QSGW band dispersion. The electron pocket at Γ is recovered in SEEx + DDMFT, and the fraction of $d_{x^2-y^2}$ electrons increases. Within the LDA, the flat band is nearly filled along the ΓM direction, and even more so when we take into account correlations. According to ARPES, this flat band should be occupied only in a small electron pocket at Γ , containing about $0.18 e^-$. This result is consistent with the absence of ferromagnetism. Indeed, this flat band lying on the Fermi surface would imply a high density of states at the Fermi level that could trigger a Stoner instability. We extract from the SEEx + DDMFT calculations a DOS at the Fermi energy of 0.97 states/eV/Co/spin. Assuming a Stoner parameter of ~ 0.9 eV, this leaves us slightly below the onset of Stoner ferromagnetism [63].

TABLE I. Number of electrons in cobalt- d Wannier functions within the LDA, SEEx, SEEx+DDMFT, LDA + DMFT, and LDA + DDMFT schemes.

| | n_{LDA}^e | n_{SEEx}^e | $n_{\text{SEEx+DDMFT}}^e$ | $n_{\text{LDA+DMFT}}^e$ | $n_{\text{LDA+DDMFT}}^e$ |
|-----------------|--------------------|---------------------|---------------------------|-------------------------|--------------------------|
| d_z | 1.64 | 1.66 | 1.63 | 1.61 | 1.62 |
| $d_{x^2-y^2}$ | 1.49 | 1.27 | 1.37 | 1.53 | 1.59 |
| d_{xy} | 1.74 | 1.78 | 1.72 | 1.67 | 1.63 |
| d_{xz}/d_{yz} | 1.69 | 1.73 | 1.68 | 1.64 | 1.62 |
| Total | 8.24 | 8.16 | 8.08 | 8.09 | 8.09 |

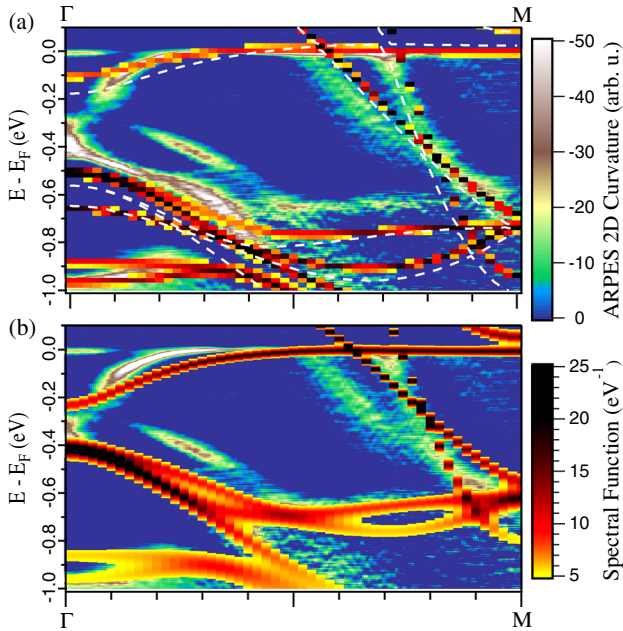


FIG. 4 (color online). Bands along the ΓM direction, extracted from the spectral function calculated by (a) SEx + DDMFT and (b) LDA + DMFT, superimposed on ARPES data from Ref. [35] (represented as a second derivative of the photoemission intensity). The QSGW band structure is also given (white dashed lines).

The QSGW scheme also provides an overall good description, including the position of the $d_{x^2-y^2}$ band, its filling, and its related Fermi wave vector. Taking nonlocal exchange into account is thus necessary to capture the physics of BaCo_2As_2 , and our SEx + DDMFT scheme performs well for these subtle effects.

Finally, we put our new computational scheme in perspective. As far as coarse features such as the bandwidth are concerned, standard LDA + DMFT and the new SEx + DDMFT give comparable results, providing an *a posteriori* explanation for the success of LDA + DMFT calculations with static interactions. For total energy calculations within DFT, it is well known that there are subtle error cancellations between the exchange and correlation contributions in approximate density functionals. Here, we evidence a similar behavior for spectral properties. The effect of dynamical screening as incorporated in the high-energy tail of the dynamical Hubbard interaction $\mathcal{U}(\omega)$ can roughly be understood as a band narrowing by a factor $Z_B = \exp[-\int_0^\infty d\omega \Im \mathcal{U}(\omega)/(\pi\omega^2)]$ [64]. For BaCo_2As_2 , we find dynamical screening to be non-negligible, with $Z_B \sim 0.6$. LDA + DMFT double counts this narrowing effect, as the bandwidth has already been decreased by correlations hidden in the exchange-correlation functional, with respect to the Hartree-Fock or SEx band structure. Thus, starting a many-body calculation from the LDA raises not only the usual well-known double counting questions related to the energetic position of correlated

versus itinerant states, but even more serious ones related to the double counting of screening processes. SEx + DDMFT avoids these issues, providing a more solid foundation for the investigation of dynamical screening effects. On a more pragmatic level, the similarity of the LDA + DMFT and SEx + DDMFT spectral functions suggests that error cancellations between dynamical screening and nonlocal exchange, both absent in LDA + DMFT, make this scheme suitable at least for questions concerning the overall bandwidth reduction of correlated electron systems. Finer details related to the very low energy behavior or Fermi surface topologies, on the other hand, might require explicit exchange corrections as introduced in the present work.

In summary, we have shown that screened exchange combined with dynamical correlations provides an excellent description of the low-energy physics in BaCo_2As_2 . In contrast to perturbative schemes, it can be expected that our nonperturbative method can be extended to regimes with arbitrarily strong correlations, making it a promising tool for probing the finite temperature normal state of iron based superconductors. For BaCo_2As_2 , we show that the flat $d_{x^2-y^2}$ band in the immediate vicinity of the Fermi level is extremely sensitive to an accurate treatment of screened exchange, and that this effect is key to the paramagnetic nature of the compound. Pump-probe photoemission would be useful to experimentally locate the flat band and guide the search for new ways to tune its exact energetic position, thus directly playing on possible Fermi surface instabilities.

We acknowledge useful discussions with V. Brouet, T. Miyake, and the authors of Ref. [35]. This work was supported by the French ANR under project PNICTIDES, IDRIS/GENCI under Projects No. 091393 and No. 96493, the Cai Yuanpei program, and the European Research Council (Projects No. 617196 and No. 278472). J. M. T. acknowledges the hospitality of CPHT within a CNRS visiting position. H. J. acknowledges support by the National Natural Science Foundation of China (Projects No. 20973009 and No. 21173005).

*vanroeke@cpht.polytechnique.fr

- [1] H. Ding, P. Richard, K. Nakayama, K. Sugawara, T. Arakane, Y. Sekiba, A. Takayama, S. Souma, T. Sato, T. Takahashi *et al.*, *Europhys. Lett.* **83**, 47001 (2008).
- [2] C. Liu, G. D. Samolyuk, Y. Lee, N. Ni, T. Kondo, A. F. Santander-Syro, S. L. Bud'ko, J. L. McChesney, E. Rotenberg, T. Valla *et al.*, *Phys. Rev. Lett.* **101**, 177005 (2008).
- [3] V. Brouet, M. Marsi, B. Mansart, A. Nicolaou, A. Taleb-Ibrahimi, P. Le Fèvre, F. Bertran, F. Rullier-Albenque, A. Forget, and D. Colson, *Phys. Rev. B* **80**, 165115 (2009).
- [4] T. Shimojima, K. Ishizaka, Y. Ishida, N. Katayama, K. Ohgushi, T. Kiss, M. Okawa, T. Togashi, X.-Y. Wang, C.-T. Chen *et al.*, *Phys. Rev. Lett.* **104**, 057002 (2010).
- [5] S. de Jong, Y. Huang, R. Huisman, F. Massee, S. Thirupathiah, M. Gorgoi, F. Schaefer, R. Follath,

- J. B. Goedkoop, and M. S. Golden, Phys. Rev. B **79**, 115125 (2009).
- [6] J. Fink, S. Thirupathiah, R. Ovsyannikov, H. A. Dürr, R. Follath, Y. Huang, S. de Jong, M. S. Golden, Y.-Z. Zhang, H. O. Jeschke *et al.*, Phys. Rev. B **79**, 155118 (2009).
- [7] W. Malaeb, T. Yoshida, A. Fujimori, M. Kubota, K. Ono, K. Kihou, P. M. Shirage, H. Kito, A. Iyo, H. Eisaki *et al.*, J. Phys. Soc. Jpn. **78**, 123706 (2009).
- [8] D. J. Singh, Physica (Amsterdam) **469C**, 418 (2009).
- [9] V. Vildosola, L. Pourovskii, R. Arita, S. Biermann, and A. Georges, Phys. Rev. B **78**, 064518 (2008).
- [10] I. I. Mazin, D. J. Singh, M. D. Johannes, and M. H. Du, Phys. Rev. Lett. **101**, 057003 (2008).
- [11] K. Haule, J. H. Shim, and G. Kotliar, Phys. Rev. Lett. **100**, 226402 (2008).
- [12] M. Aichhorn, L. Pourovskii, V. Vildosola, M. Ferrero, O. Parcollet, T. Miyake, A. Georges, and S. Biermann, Phys. Rev. B **80**, 085101 (2009).
- [13] M. Aichhorn, S. Biermann, T. Miyake, A. Georges, and M. Imada, Phys. Rev. B **82**, 064504 (2010).
- [14] J. Ferber, K. Foyevtsova, R. Valentí, and H. O. Jeschke, Phys. Rev. B **85**, 094505 (2012).
- [15] P. Hansmann, R. Arita, A. Toschi, S. Sakai, G. Sangiovanni, and K. Held, Phys. Rev. Lett. **104**, 197002 (2010).
- [16] V. I. Anisimov, D. Korotin, M. A. Korotin, A. V. Kozhevnikov, J. Kunes, A. O. Shorikov, S. L. Skornyakov, and S. V. Streltsov, J. Phys. Condens. Matter **21**, 075602 (2009).
- [17] P. Werner, M. Casula, T. Miyake, F. Aryasetiawan, A. J. Millis, and S. Biermann, Nat. Phys. **8**, 331 (2012).
- [18] G. T. Wang, Y. Qian, G. Xu, X. Dai, and Z. Fang, Phys. Rev. Lett. **104**, 047002 (2010).
- [19] V. I. Anisimov, A. Poteryaev, M. Korotin, A. Anokhin, and G. Kotliar, J. Phys. Condens. Matter **9**, 7359 (1997).
- [20] A. I. Lichtenstein and M. I. Katsnelson, Phys. Rev. B **57**, 6884 (1998).
- [21] G. Kotliar and D. Vollhardt, Phys. Today **57**, No. 3, 53 (2004).
- [22] S. Biermann, in *Encyclopedia of Materials: Science and Technology*, edited by K. H. J. Buschow, R. W. Cahn, M. C. Flemings, B. Ilshner (print), E. J. Kramer, S. Mahajan, and P. Veyssi re (updates) (Elsevier, Oxford, 2006), pp. 1–9.
- [23] K. Held, I. A. Nekrasov, G. Keller, V. Eyert, N. Bl umer, A. K. McMahan, R. T. Scalettar, T. Pruschke, V. I. Anisimov, and D. Vollhardt, Phys. Status Solidi B **243**, 2599 (2006); psi-k Newsletter, **56** (65) 2003.
- [24] G. Kotliar, S. Y. Savrasov, K. Haule, V. S. Oudovenko, O. Parcollet, and C. A. Marianetti, Rev. Mod. Phys. **78**, 865 (2006).
- [25] J. Min ar, L. Chioncel, A. Perlov, H. Ebert, M. I. Katsnelson, and A. I. Lichtenstein, Phys. Rev. B **72**, 045125 (2005).
- [26] J. M. Tomczak, M. van Schilfhaarde, and G. Kotliar, Phys. Rev. Lett. **109**, 237010 (2012).
- [27] V. Brouet, P.-H. Lin, Y. Texier, J. Bobroff, A. Taleb-Ibrahimi, P. Le F evre, F. Bertran, M. Casula, P. Werner, S. Biermann *et al.*, Phys. Rev. Lett. **110**, 167002 (2013).
- [28] M. van Schilfhaarde, T. Kotani, and S. Faleev, Phys. Rev. Lett. **96**, 226402 (2006).
- [29] T. Ayr al, P. Werner, and S. Biermann, Phys. Rev. Lett. **109**, 226401 (2012).
- [30] K. Haule and G. Kotliar, New J. Phys. **11**, 025021 (2009).
- [31] S. Biermann, F. Aryasetiawan, and A. Georges, Phys. Rev. Lett. **90**, 086402 (2003).
- [32] L. Hedin, Phys. Rev. **139**, A796 (1965).
- [33] D. M. Bylander and L. Kleinman, Phys. Rev. B **41**, 7868 (1990).
- [34] A. Seidl, A. G orling, P. Vogl, J. A. Majewski, and M. Levy, Phys. Rev. B **53**, 3764 (1996).
- [35] N. Xu, P. Richard, A. van Roekeghem, P. Zhang, H. Miao, W.-L. Zhang, T. Qian, M. Ferrero, A. S. Sefat, S. Biermann *et al.*, Phys. Rev. X **3**, 011006 (2013).
- [36] R. S. Dhaka, Y. Lee, V. K. Anand, D. C. Johnston, B. N. Harmon, and A. Kaminski, Phys. Rev. B **87**, 214516 (2013).
- [37] A. S. Sefat, D. J. Singh, R. Jin, M. A. McGuire, B. C. Sales, and D. Mandrus, Phys. Rev. B **79**, 024512 (2009).
- [38] A. Pandey, D. G. Quirinale, W. Jayasekara, A. Sapkota, M. G. Kim, R. S. Dhaka, Y. Lee, T. W. Heitmann, P. W. Stephens, V. Ogloblichev *et al.*, Phys. Rev. B **88**, 014526 (2013).
- [39] W. Jayasekara, Y. Lee, A. Pandey, G. S. Tucker, A. Sapkota, J. Lamsal, S. Calder, D. L. Abernathy, J. L. Niedziela, B. N. Harmon *et al.*, Phys. Rev. Lett. **111**, 157001 (2013).
- [40] B. Cheng, B. F. Hu, R. H. Yuan, T. Dong, A. F. Fang, Z. G. Chen, G. Xu, Y. G. Shi, P. Zheng, J. L. Luo *et al.*, Phys. Rev. B **85**, 144426 (2012).
- [41] J. J. Ying, Y. J. Yan, A. F. Wang, Z. J. Xiang, P. Cheng, G. J. Ye, and X. H. Chen, Phys. Rev. B **85**, 214414 (2012).
- [42] V. K. Anand, R. S. Dhaka, Y. Lee, B. N. Harmon, A. Kaminski, and D. C. Johnston, Phys. Rev. B **89**, 214409 (2014).
- [43] Indeed, a presentation of the ARPES spectra in a second derivative plot of the intensities reveals the presence of a flat band just above the Fermi level [35], as pointed out in Ref. [36].
- [44] M. Casula, A. Rubtsov, and S. Biermann, Phys. Rev. B **85**, 035115 (2012).
- [45] See Supplemental Material at <http://link.aps.org/supplemental/10.1103/PhysRevLett.113.266403>, which includes Refs. [46–52], for technical details.
- [46] P. Blaha, K. Schwarz, G. Madsen, D. Kvasnicka, and J. Luitz, *Wien2k, An Augmented Plane Wave+Local Orbitals Program for Calculating Crystal Properties* (Tech. Universit at Wien, Austria, 2001).
- [47] F. O. Tran and P. Blaha, Phys. Rev. B **83**, 235118 (2011).
- [48] L. Vaugier, Ph.D. thesis, Ecole Polytechnique, France, 2011.
- [49] V. I. Anisimov, J. Zaanen, and O. K. Andersen, Phys. Rev. B **44**, 943 (1991).
- [50] L. Hedin, J. Phys. Condens. Matter **11**, R489 (1999).
- [51] K. Morikawa, T. Mizokawa, K. Kobayashi, A. Fujimori, H. Eisaki, S. Uchida, F. Iga, and Y. Nishihara, Phys. Rev. B **52**, 13711 (1995).
- [52] A. van Roekeghem and S. Biermann, Europhys. Lett. **108**, 57003 (2014).
- [53] L. Vaugier, H. Jiang, and S. Biermann, Phys. Rev. B **86**, 165105 (2012).
- [54] P. Werner, A. Comanac, L. de’ Medici, M. Troyer, and A. J. Millis, Phys. Rev. Lett. **97**, 076405 (2006).
- [55] P. Werner and A. J. Millis, Phys. Rev. Lett. **104**, 146401 (2010).

- [56] M. Ferrero and O. Parcollet, TRIQS: A Toolbox for Research on Interacting Quantum Systems, <http://ipht.cea.fr/triqs>.
- [57] M. Casula, P. Werner, L. Vaugier, F. Aryasetiawan, T. Miyake, A. J. Millis, and S. Biermann, Phys. Rev. Lett. **109**, 126408 (2012).
- [58] We note that in SEx + DMFT nonlocal and dynamical renormalizations are by construction separated on the self-energy or Hamiltonian level. This separability was recently justified for iron pnictides [26] and found to hold also for metallic transition metal oxides [59,60].
- [59] J. M. Tomczak, M. Casula, T. Miyake, and S. Biermann, Phys. Rev. B **90**, 165138 (2014).
- [60] J. M. Tomczak, M. Casula, T. Miyake, F. Aryasetiawan, and S. Biermann, Europhys. Lett. **100**, 67001 (2012).
- [61] T. Kotani, M. van Schilfgaarde, and S. V. Faliev, Phys. Rev. B **76**, 165106 (2007).
- [62] P. Zhang, P. Richard, T. Qian, Y.-M. Xu, X. Dai, and H. Ding, Rev. Sci. Instrum. **82**, 043712 (2011).
- [63] However, slight electron doping would bring us close to the maximum value of 1.04 states/eV/Co/spin that we find at $\omega = 44$ meV, at the peak of the Co $d_{x^2-y^2}$ DOS, possibly triggering a ferromagnetic instability.
- [64] In the antiadiabatic limit, where the characteristic frequency of variations in $\mathcal{U}(\omega)$ is larger than the other energy scales of the system, this statement can be made rigorous via a Lang-Firsov transformation [57].

Abstract for the general public

This thesis deals with the description of the electronic properties of solids.

In materials where electronic Coulomb correlations are strong, exact methods are limited to small system sizes. For large systems, dynamical mean field theory (DMFT) reduces the description of the extended solid to a local problem. Applicable to models with local interactions, it captures the correlation-induced phase transition from a metal to a Mott insulator, despite the neglect of nonlocal fluctuations.

In this work, the effects of nonlocal fluctuations coming from local or nonlocal interactions are investigated. In systems of atoms adsorbed on semiconducting surfaces, *nonlocal interactions* are shown to be crucial to explain experimental observations.

A new method is then introduced that captures *nonlocal effects of local interactions* on electronic propagation at a reduced computational cost compared to previous DMFT extensions. The results are discussed in relation to photoemission in cuprate materials.

Résumé “grand public”

Cette thèse porte sur la description des propriétés électroniques des solides.

Dans les matériaux où les corrélations de Coulomb sont fortes, les méthodes exactes sont limitées aux petits systèmes. Une approche dénommée théorie du champ moyen dynamique (DMFT) ramène la description du solide étendu à un problème local. Applicable à des modèles avec des interactions locales, elle rend compte de la transition de phase métal-isolant de Mott, quoiqu'elle néglige les fluctuations nonlocales.

Dans ce travail, j'étudie les effets des fluctuations non locales provenant d'interactions locales et non locales. Dans les systèmes d'atomes adsorbés sur des surfaces semiconductrices, je montre que les *interactions non locales* sont nécessaires pour expliquer les résultats expérimentaux.

Ensuite, je présente une nouvelle méthode; elle tient compte des *effets non locaux des interactions locales* sur la propagation des électrons et a un coût de calcul numérique réduit par rapport aux précédentes extensions de DMFT. Les résultats sont discutés en lien avec la photoémission dans les matériaux cuprates.